DOE/ER-0045/14

Alloy Development for Irradiation Performance

Semiannual Progress Report
For Period Ending March 31, 1985

U.S. Department of Energy
Office of Fusion Energy

Printed in the United States of America. Available from
National Technical Information Service
U.S. Department of Commerce
5285 Port Royal Road, Springfield, Virginia 22161
NTIS price codes—Printed Copy: All Microfiche A01

This report was prepared as an account of work sponsored by an agency of the United States Government Neither the United States Government nor any agency thereof, nor any of their employees, makes any warranty, express or implied, or assumes any legal liability or responsibility for the accuracy, completeness, or usefulness of any information. apparatus. product, or process disclosed. or represents that its use would not infringe privately owned rights Reference herein to any specific commercial product. process, or service by trade name. trademark. manufacturer. or otherwise. does not necessarily constitute or imply its endorsement. recommendation, or favoring by the United States Government or any agency thereof. The views and opinions of authors expressed herein do not necessarily stale or reflect those of the United States Government or any agency thereof.

DOE/ER-0045/14
Distribution
Category
uc-20. 20c

ALLOY DEVELOPMENT FOR IRRADIATION PERFORMANCE
SEMIANNUAL PROGRESS REPORT FOR PERIOD ENDING MARCH 31,1985

ARGONNE NATIONAL LABORATORY

AUBURN UNIVERSITY

GA TECHNOLOGIES, INC.

McDONNELL DOUGLAS ASTRONAUTICS COMPANY

MASSACHUSETTS INSTITUTE OF TECHNOLOGY

NAVAL RESEARCH LABORATORY

OAK RIDGE NATIONAL LABORATORY

WESTINGHOUSE HANFORD COMPANY

Date Published: July 1985

Prepared by
OAK RIDGE NATIONAL LABORATORY
Oak Ridge, Tennessee 37831
operated by
MARTIN MARIETTA ENERGY SYSTEMS, INC.
for the
U. S. DEPARTMENT OF ENERGY
Under Contract No. DE-AC05-840R21400

c

Reports previously issued in this series are as follows:

DOE/ET-0058/1	Period Ending March 31, 1978
DOE/ET-0058/2	Period Ending June 30, 1978
DOE/ET-0058/3	Period Ending September 30, 1978
DOE/ET-0058/4	Period Ending December 31, 1978
DOE/ET-0058/5	Period Ending March 31, 1979
DOE/ET-0058/6	Period Ending June 30, 1979
DOE/ET-0058/7	Period Ending September 30, 1979
DOE/ER-0045/1	Period Ending December 31, 1979
DOE/ER-0045/2	Period Ending March 31, 1980
DOE/ER-0045/3	Period Ending June 30, 1980
DOE/ER-0045/4	Period Ending September 30, 1980
DOE/ER-0045/5	Period Ending Deceinber 31, 1980
DOE/ER-0045/6	Period Ending March 31, 1981
DOE/ER-0045/7	Period Ending September 30, 1981
DOE/ER-0045/8	Period Ending March 31, 1982
DOE/ER-0045/9	Period Ending September 30, 1982
DOE/ER-0045/10	Period Ending March 31, 1983
DOE/ER-0045/11	Period Ending September 30, 1983
DOE/ER-0045/12	Period Ending March 31, 1984
DOE/ER-0045/13	Periud Ending September 30, 1984

FOREWORD

This report is the twenty-first in a series of Technical Progress Reports on "*Alloy Development for Irradiation* Performance" (ADIP), which is one element of the Fusion Reactor Materials Program, conducted in support of the Magnetic Fusion Energy Program of the U.S. Department of Energy. Other elements of the Materials Program are

- *Damage Analysis and Fundamental Studies (DAFS)*
- *Plasma-Materials Interaction (PMI)*
- *Special-Purpose Materials (SPM)*
- *High Heat Flux Components*

The first seven reports in this series are numbered DOE/ET-0058/1 through 7. This report is the fourteenth in a new numberinq sequence that begins with DOE/ER-0045/1.

The ADIP program element is a national effort composed of contributions from a number of National Laboratories and other government laboratories, universities, and industrial laboratories. It was organized by the Materials and Radiation Effects Branch, Office of Fusion Energy, DOE, and a Task Group on *Alloy Development for Irradiation Performance*, which now operates under the auspices of the Reactor Technologi es Branch. The purpose of this series of reports is to provide a working technical record of that effort for the use of the program participants, for the fusion energy program in general, and for the Department of Eneryy.

This report is oryanized along topical lines with Chapters 3 through 8 devoted to the various alloy classes that are currently under investigation. Thus the work of a given laboratory may appear at several different places in the report. The materials compatibility and environmental effects work on all alloy classes is collected together in Chapter 9. The Table of Contents is annotated for the convenience of the reader.

This report has been compiled and edited under the guidance of the Chairman of the Task Group on *Alloy Development for Irradiation Performance.* A. F. Rowcliffe, Oak Ridge National Laboratory, and his efforts and those of the supporting staff of ORNL and the many persons who made technical contributions are gratefully acknowledged. T. C. Reuther, Reactor Technologies Branch, is the Departinent of Energy Counterpart to the Task Group Chairman and has responsibility for the ADIP Program within DOE.

G. M. Haas, Chief
Reactor Technologies Branch
Office of Fusion Energy

CONTENTS

FOREWORD iii

1. ANALYSIS AND EVALUATION STUDIES 1

1.1 Materials Handbook for Fusion Energy Systems (McDonnell Douglas Astronautics Company) 2

Substantial progress has been made towards reducing the backlog of data pages with the release of the tenth and eleventh data packages. In addition, the handbook now has the capability of total computer generation of data pages with a quality suitable for printing.

2. TEST MATRICES, EXPERIMENT DESCRIPTIONS, AND METHODS DEVELOPMENT 4

2.1 Operation of the ORR Spectral Tailoring Experiments ORK-MFE-4A AND -48 (Oak Ridge National Laboratory) 5

The specimens contained in the ORR-MFE-4A experiment have operated for a total of 1077 d at 30 MW reactor power with temperatures of 330 and 400°C. The specimens contained in the ORR-MFE-4B experiment have operated for an equivalent of 916 d at 30 MW reactor power lthrough March 24, 19851 with temperatures of 500 and 600°C.

2.2 Irradiation Experiments for The U.S./Japan Collaborative Testing Program in HFIK and ORR (Oak Ridge National Laboratory) 6

The assembly of JP-7 and -8 was completed. Capsules JP-2 through -8 are being irradiated in the HFIR. Capsule JP-I completed its irradiation for a total of 336.40 d at 100 MW reactor power.

The fabrication and assembly of ORR-MFE-6J are in progress. The assembly of MFE-7J is nearing completion. The specimens are expected to be delivered for loading by the end of March.

2.3 Preparation for Postirradiation Examination of U.S./Japan HFIR Capsules (Oak Ridge National Laboratory) 10

The first U.S./Japan HFIR capsule, JP-I, has completed its irradiation campaign and is cooling down. Preparations for PIE are under way. The new Japan Electron Optical Laboratory, Inc. (JEOL) JEM-2000FX microscope has been delivered to ORNL and is operational.

2.4 Description of the U.S./Japan Spectral Tailoring Experiment in ORR (Oak Ridge National Laboratory and Japan Atomic Energy Research Institute) 12

Two spectral tailoring capsules MFE-6J and -7J are being assembled and irradiated in ORR a8 a part of the U.S./Japan program of collaborative testing in mized-spectrum fission reactors. The test matrix includes conventional U.S. and Japanese structural alloys plus a wide variety of research alloys that lead to a basic understanding of alloy response to the fusion reactor environment.

2.5 Neutronics Calculations in Support of the ORR-MFE-4A and -48 Spectral Tailoring Experiments (Oak Ridge National Laboratory) 20

The calculated fluences from the ongoing three-dimensional neutronics calculations are being scaled to agree with experimental data. A8 of March 32, 1985, this treatment yields 201.9 at. ppm He (not including 2.0 at. ppm He from ^{10}B) and 13.19 dpa for type 316 stainless steel in ORR-MFE-4A arid 155.9 at. ppm He and 10.60 dpa in ORR-MFE-4B.

2.6 Neutron Dosimetry and Damage Calculations for the HFIR-CTR-30, -36, and -46 Experiments (Argonne National Laboratory) 22

Dosimetry measurements and damage calculations have been completed for the CTR 30, 36, and 46 experiments in HFIR. CTR 30 and 36 have the highest exposures seen to date with fluences of $1.95\times10^{23}n/cm^2$ and $1.61\times10^{23}n/cm^2$, respectively. Work is in progress on the RB2 and T3 experiments in HFIK and a prototype of the Japanese experiments in OHR.

2.7. Overview of MIT, ADIP Irradiation Experiments (Massachusetts Institute of Technology) . . . 27

Various rapidly solidified austenitic, ferritic and copper alloys have been produced at MIT for inclusion in ADIP neutron irradiation experiments. A brief summary of the alloys and their preparation and the achieved or projected irradiation parameters is provided.

2.8 Analysis of Damage Exposure Rates in the Materials Open Test Assembly of the Fast Flux Test Facility (Westinghouse Hanford Company) 31

The axial distribution of dpa/sec in stainless steel (Fe18Cr10Ni) and flux E > 0 MeV and E > 0.1 MeV Were determined from the analysis of dosimetry measurements made during MOTA Cycles 1A and 1B.

3. AUSTENITIC STAINLESS STEELS 36

3.1 Minor Compositional Variations of the Austenitic PCA to Explore MC Formation and Stability Characteristics for Improved Radiation Resistance (Oak Ridge National Laboratory and Japan Atomic Energy Research Institute) 37

The original PCA exclusively forms MC carbides in the matrix and grain boundaries during short-term aging, with a small amount of Laves appearing at longer times. The MC phase shows a surprisingly high solubility for chromium. Small laboratory melts were made which vary C, Si, Mo, and Ti alloy concentrations together with F and Nb additions. Solution-annealed (SA) alloys with (Ti t Nb), or Nb and lower Si levels, exhibited grain boundary MC formation after 166 h at 800°C, whereas other alloys formed only coarse $M_{23}C_6$. None formed intermetallics. Alloys with stable grain boundary MC formation in the SA condition showed excellent resistance to recrystallization when cold worked (CW). The MC phase composition was quite sensitive to alloying changes; combinations of Nb, C, and P alloying additions lowered the (Mo + Cr) content of the Ti-rich MC phase, particularly in small particles.

3.2 Microstructural Development in Manganese-Stabilized Austenitic Steel Irradiated in HFIR at 500 ANU 600°C TO 19 dpa (Oak Ridge National Laboratory) 49

The 12Cr/13Mn/4Ni steel (heat EP-838, made available through an exchange with the Soviet Union) was irradiated in HFIK to 19 dpa and 220 ut. ppm He. A spatially nonuniform dispersion of voids (9–19 nm in diameter) developed at 500°C, but none formed at 600°C. Many fine (2.5–6 nm in diameter) matrix bubbles were also observed at both temperatures. A dense tangle of dislocation network and Frank loops was observed at 500°C, but only loose network was found at 600°C. There was considerable precipitation at 600°C, but much less at 500°C. Coarse $M_{23}C_6$ and/or M_6C were found along subgrain boundaries at both temperatures, but many medium-coarse laths (probably Laves) were found in the matrix at 600°C, whereas only some fine particles (probably MC) were found at 500°C.

4. HIGHER STRENGTH Fe-Ni-Cr ALLOYS 52

5. REACTIVE AND REFKACTORY ALLOYS 53

5.1 The Tensile Properties of Several Vanadium Alloys After Irradiation in FFTF (Oak Ridge National Laboratory) 54

Irradiation in ^{7}Li-filled capsules at 420 and 520°C in FFTF (MOTA) with damage levels up to 13.6 dpa substantially lowered the ductility of V-15Cr-5Ti, VANSTAR-7, and V-3Ti-1Si alloys by the mechanism of radiation hardening. The VANSTAR-7 and V-3Ti-1Si alloys resisted the embrittling effects of irradiation better than the V-15Cr-5Ti alloy, regardless of the implanted helium level. Control specimens of all three alloys were not appreciably affected by thermal aging in ^{7}Li at the respective irradiation temperatures. The mechanism causing the low ductility and transgranular cleavage fracture in one V-15Cr-5Ti specimen without implanted helium requires further investigation.

5.2 Comparison of Swelling for Neutron- and Ion-Irradiated MFK Structural Materials (Argonne National Laboratory) 62

The swelling of vanadium and vanadium-base alloys, 316 stainless steel, Fe-25Ni-15Cr alloy, ferritic steels, and copper on neutron irradiation is compared with the swelling for these mterials on ion irradiation in this report. The results of this comparison are taken to show that utilization of the ion-irradiation technique provides for a discriminative assessment of the potential for swelling of candidate MFR materials.

6. INNOVATIVE MATERIAL CONCEPTS 68

7. FERRITIC STEELS 69

7.1 Microstructure of Alloy HT-9 and Modified 9Cr-1Mo Alloy Irradiated in the UBR (Naval Research Laboratory) 70

TEM disks Were prepared from tested Charpy-V specimens of Alloy HT-9 and Modified 9Cr-1Mo which had been irradiated at 149C to –0.8 × 10^{20} n/cm^2, E > 0.1 MeV. Examination of these disks showed that the irmdiation had produced small defect clusters, <10 nm in diameter, in both alloys. These defect clusters Were the apparent source of the hardening and thus the shift in ductile–brittle transition temperature previously observed for these materials. No change8 in precipitate structure could be observed for either alloy.

7.2 Microstructural/Microcompositional Analysis of Normalired-and-Tempered 9Cr-1MoVNb and 12Cr-1MoVW Steels Uoped With 2 wt % Nickel (Oak Ridge National Laboratory) 74

Normalized-and-tempered 9Cr-1MoVNb and 12Cr-1MoVW steels are tempered rmrtensite that have recovered ferrite subgrain structures with $M_{23}C_6$ and MC precipitate and a few dislocations. The 12Cr steel has more precipitate, which is almost exclusively $M_{23}C_6$; the 9Cr steel has less precipitation, but a larger fraction of fine MC. Both steels doped with 2 ut % Ni have more refined precipitate and/or subgrain structures and higher dislocation concentrations, but these changes **are** *consistent with their lower tempering temperatures relative to undoped materials. Nickel doping does not change the precipitate phases observed ($M_{23}C_6$ and MC) or the relative phase fractions, and does not appreciably affect phase compositions.*

7.3 Some Effects of Increased Helium Generation on Microstructure and Swelling of Nickel-Uoped 9Cr-1MoVNb Steel Irradiated in HFIR (Oak Ridge National Laboratory) 81

Considerable void formation was found at 400 and 500°C in 9Cr-1MoVNb-2Ni after –38 dpa (~400 at. ppm He) in HFIR, whereas some voids were found only at 400°C for similar irradiation of the same steel without nickel doping (only –30 at. ppm He). Increased helium generation tremendously increased bubble nucleation over the **mnge** *from 300 to 600°C. The irradiation also produced considerable precipitation in the 9Cr-1MoVNb-2Ni at 400 and 500°C in conjunction with void formation.*

7.4 Postirradiation Tensile Behavior of Nickel-Doped 9Cr-1MoVNb and 12Cr-1MoVW Steels (Oak Ridge National Laboratory) 87

Tensile specimens of normalized-and-tempered 9Cr-1MoVNb, 9Cr-1MoVNb-2Ni, 12Cr-1MoVW, 12Cr-1MoVW-1Ni, and 12Cr-1MoVW-2Ni steels were irradiated in EBR-II to –16 dpa at 390 to 550°C. Tests were conducted at room temperature and the irradiation temperature on unirradiated, thermally aged, and irradiated specimens. The effect of irradiation depended on temperature and on the tempering treatment that the steel was given.

7.5 Elevated-Temperature Tensile Properties of 2 1/4 Cr-1Mo Steel Irradiated in the EBR-II, AD-2 Experiment (Oak Ridge National Laboratory) 99

The effect of irradiation on the tensile properties of 2 1/4 Cr-1Mo steel was determined for specimens irradiated in EBR-11 to 23 dpa at 390 to 550°C. Unirradiated control specimens and specimens aged for 10,000 h at the irradiation temperature Were also tested. Irradiation at 390°C increased the strength and decreased the ductility of the samples while softening occurred in those irradiated and tested at 450, 500, and 550°C.

7.6 Irradiation Effects in Ferritic Steels (GA Technologies) 109

Since 1980 the Alloy Development for Irradiation Performance (ADIP) task funded by the U.S. Department of Energy has been studying the 2-12Cr class of ferritic steels to establish the feasibility of using them in fusion reactor first wall/breeding blanket (FW/B) applications. The advantages of ferritic steels include superior swelling resistance, low thermal stresses compared to austenitic stainless steels, attmctive mechanical properties up to 600°C, and service histories exceeding 100,000 hours. These steels are commonly used in a mnge of microstructural conditions which include ferritic, martensitic, tempered martensitic, tainitic, etc. Throughout this paper where the term "ferritic" is used **it** *should be taken to mean any of these microstructures. The ADIP task is studying several candidate alloy systems including 12Cr-1MoWV (HT-9), modified 9Cr-1Mo, and dual. phased steels such as EM-12 and 2 1/4Cr-1Mo. These mterials are ferromagnetic (FM), body centered cubic (BCC), and contain chromium additions between 2 and 12 wt.% and molybdenum additions usually below 2%. The perceived issues associated*

with the application of this class of steel to fusion reactors are the increase in the ductile-brittle transition temperature (DBTT) with neutron damage, the compatibility of these steels with liquid metals and solid breeding mterials, and their weldability. The ferromagnetic character of these steels can also be important in reactor design. It is the purpose of this paper to review the current understanding of these BCC steels and the effects of irradiation. The major points of discussion will be irradiation induced or enhanced dimensional changes such as swelling and creep, mechanical properties such as tensile strength and various measurements of toughness, and activation by neutron interactions with structural materials.

7.7 Melting and Fabrication of Low Activation Ferritic Alloys for FFTF Irradiations (GA Technologies) 117

Two experimental heats of W-stabilized low activation ferritic steels have been melted, the chemistries analyzed, arid the heats fabricated into specimens to be included in an FFTF irradiation. A control heat of HT-Y was melted and fabricated in the Same my. Specimens include 1/3 PCVN specimens for toughness and DBTT evaluations and TEM disks. All specimens were given a heat treatment of 1050°C for 1 hr followed by an air cool, 700°C for 1 hr followed by an air cool.

7.8 Preliminary Evaluation of Microstructure and Mechanical Properties on Low Activation Ferritic Steels (GA Technologies) 120

A preliminary evaluation of the microstructure and mechanical properties of a 9Cr-2.5W-0.3V-0.15C (GA3X) low activation ferritic steel has been performed. An optimum heat treatment condition has been defined for GA3X steel. The properties and microstructure of the quenched and tempered specimens were characterized via hardness measurement and optical metallographic observation.

Quenched (1000°C/1hr) and tempered (700°C/1hr) specimens were thernully aged at 600°C up to 1,000 hrs to examine the phase stability of the alloy. X-ray diffraction analysis of the precipitates extracted from the thermally aged samples revealed nearly 100% $M_{23}C_6$ carbides la = 10.64A), with no indication of Fe_2W-type Laves phase which may cause embrittlement via segregation of detrimental impurity elements and strengthening. The impurity elements (P, S, Sb) are in small, concentration and this, combined with a fine grain size, lead us to conclude little temper embrittlement will occur.

The hot-microhardness and ductility parameter measurements were used to estimate the tensile properties at elevated temperatures. The estimated tensile strengths of GAJX steel at elevated temperatures are comparable to both 9Cr-1Mo and the modified 9Cr-1Mo steels. These preliminary results are encouraging in that they suggest that suitable low activation alloys can be successfully produced in this ferritic alloy class.

7.9 Microstructural Comparison of HT-9 Irradiated in HFIK and EBR-II (Westinghouse Hanford Company) 129

A series of specimens of HT-Y heat $1354 have been examined following irradiation in HFIH to 39 dpa at 300, 400, 500 and 600°C and following irradiation in EBR-II to 29 dpa at 390 and 500°C. HFIR irradiation was found to have promoted helium bubble formation at all temperatures and voids at 400°C. Cavitation had not been observed at lower fluence, nor was it found in EBR-II irradiated specimens. The onset of void swelling in HFIR is attributed to helium generation. The observations provide an explanation for saturation of ductile-brittle transition temperature shifts with increasing fluence.

7.10 Fractograhic Examination of Ferritic Alloy Charpy Specimens at a Fluence of 6×10^{22} n/cm^2 (Westinghouse Hanford Company) 137

The fracture surfaces of thirteen Charpy specimens have been examined by scanning electron microscopy and several of these have been measured for hardness. The specimen series irradiated in the AD-2 test, second discharge includes HT-Y base metal in two product forms, and Modified 9Cr-1Mo base metal and weld metal, fluences include 13 and 26 dpa and irradiation temperatures cover the range 390°C to 550°C. Fracture appeamnce is found to be insensitive to irradiation fluence, whereas significant differences could be found in product form. It is concluded that irradiation does not encourage a new fracture mechanism such as temper embrittlement. Failure is controlled by the microstructure generated prior to irradiation.

8. COPPER AND ITS ALLOYS 151

8.1 Swelling and Tensile Properties of Neutron Irradiated Copper Alloys for High Heat Flux Applications (Los Alamos National Laboratory) 152

Four commercial copper alloys and two elemental coppers were irradiated to EBR-11 fluences of 3 and 15 dpa at 385°C. The AMZIRC alloy and the two elemental coppers showed large swelling at the high fluence. The two precipitation hardened and cold worked alloys (AMZIRC and MZC) were softened significantly by the irradiation. The two alumina-dispersed alloys (AI-20 and Al-601 retained their mechanical strength after irradiation.

8.2 Neutron-Radiation Induced Changes in Electrical Resistivity of Copper Alloys for MFE Applications (Los Alamos National Laboratory) 161

Values of ρ_e were measured for two elemental (high-purity) coppers and four commercial copper alloys subjected in EBR-11 to neutron fluences of 0.4 arid 2.0 × 10^{26} n/m^2 at 658K. Relative to annealed controls, two alumina-dispersed alloys gave the best results: Increases in ρ_e (and 1/K) of 6-7% at the high fluence, with no significant changes (per paper 8.1 preceding) in the corresponding yield stresses.

8.3 Dual Ion Irradiation Studies of High Strength Copper Alloys (Westinghouse R&D Center and University of Pittsburgh, and McDonnell Douglas Company) 168

Microstructural changes are reported for a precipitation strengthened Cu-0.4 wt % Be-1.9 wt % Ni alloy and a dispersion hardened Cu-0.6 wt % Al (Al_2O_3) alloy after dual ion irradiation at fluences up to -20 dpa at 250°C, 300°C and 350°C. Both alloys show good swelling resistance. Peak swelling temperature for the alumina dispersion hardened alloy (AI-601 is ~350°C. For fluences of 10-20 dpa average swelling rates of 0.01% per dpa and 0.05% per dpa have been measured for irradiation without simultaneous helium injection and with a gas atom implantation Pate of K_g ~3 × 10^{-3} appm·s^{-1}. Void formation is heterogeneous and is most pronounced in grains with low no. densities of Al_2O_3 particles. The beryllium-copper alloy shows almost no swelling with the exception of a few narrow and widely spaced transgranular bands of voids at 250°C-350°C. Loss of the (100) relrod reflections in the Latter alloy is fluence and temperature dependent and reflects loss of coherency of the C.P. zones, particle restructuring and/or loss of imaging conditions due to strain field overlap from the dislocation network. Recoil resolution of the cubic γ-Al_2O_3 particles in the Al-60 is observed under certain conditions. The impact of these phase instabilities on mechanical and thermal properties is not known. It is recommended that neutron irradiation studies at 105°C-300°C be conducted to assess their importance.

9. MATERIALS COMPATIBILITY AND HYDROGEN PERMEATION STUDIES 176

9.1 Environmental Effects on the Properties of Vanadium-Base Alloys (Aryonne National Laboratory) 177

Exposures of V-15Cr-5Ti, V-20Ti, and VANSTAR-7 specimens to pressurized flowing water containing 0.03 ppm dissolved O_2 at 288°C indicate that V-15Cr-5Ti again has the best corrosion resistance. Further scanning Auger microprobe studies of sulfur segregation in vanadium-base alloys reveal no clear correlation between segregation and the variables examined.

9.2 Corrosion of Austenitic and Ferritic Steels in Flowing Lithium Environment (Argonne National Laboratory) 182

Corrosion data on weight loss and internal penetration are presented for ferritic and austenitic steels in flowing lithium at 372, 427, and 482°C. Results from metallographic examination of the lithium-exposed specimens are presented. The influence of time, temperature, and lithium purity on the dissolution behavior of the alloys is discussed.

9.3 Environmental Effects on Properties of Structural Alloys in Flowing Pb-17Li (Argonne National Laboratory) 192

Corrosion data are presented for ferritic HT-9 and Fe-9Cr-1Mo and austenitic Type 316 stainless steel in flowing Pb-17Li at 423, 427, and 454°C. Tensile properties of HT-9 alloy in a flowing Pb-17Li environment at temperatures between 270 arid 450°C are also reported.

9.4 Thermal Convection Loop Studies of the Lithium Corrosion of Low Activation Austenitic Alloys and Standard Fe-12Cr-1MoVW Steel (Oak Ridge National Laboratory) 197

Further data for Cr-Mn steels in thermally convective lithium showed that corrosion in such systems was complicated by multiple simultaneous corrosion processes. The dominant corrosion reaction during higher temperature exposure of 12Cr-1MoVW steel to thermally convective lithium ms thermal gradient mass transfer.

9.5 Corrosion of Type 316 Stainless Steel and 12Cr-1MoVW Steel in Thermally Convective Pb-17 at. % Li (Oak Ridge National Laboratory) 205

Observations of the effects of the cleaning procedure used to remove residual Pb-17 at. % Li from type 316 stainless steel revealed a considerable variability in the amount of corrosion layer that was also removed. No localized corrosion or lead-lithium penetration was noted for 12Cr-1MoVW steel exposed to thermally convective Pb-17 at. % Li for 3078 h at temperatures up to 500°C.

10. STATUS OF IRRADIATION EXPERIMENTS AND MATERIALS INVENTORY 208

10.1 Irradiation Experiment Status and Schedule (Oak Ridge National Laboratory) 209

10.2 Fusion Program Research Materials Inventory (Oak Ridge National Laboratory, McDonnell Douglas Astronautics Company, and GA Technologies) 216

1. ANALYSIS AND EVALUATION STUDIES

1.1 MATERIALS HANDBOOK FOR FUSION ENERGY SYSTEMS--J. W. Davis (McDonnell Douglas Astronautics Company-St. Louis)

1.1.1 ADIP Task

Task Number I.A.I, Define material property requirements and make structural life predictions.

1.1.2 Objective

To provide a consistent and authoritative source of material property data for use by the fusion community in concept evaluation, design, and performance/verification studies of the various fusion energy systems. A second objective is the early identification of areas in the materials data base where insufficient information or voids exist.

1.1.3 *Summary*

During the past six months the handbook has undergone a series of changes which will hopefully help to improve it and also to speed up the release of data pages. Two of the more significant changes are a consolidation of the handbook responsibilities under one organization and the incorporation of total computer generation of the approved data pages with a quality suitable for direct printing.

1.1.4 Progress and Status

When the handbook was originally conceived, approximately five years ago, the responsibility for publication and distribution was assigned to T. K. Bierlein of the Hanford Engineering and Development Laboratory and the responsibility for management and handbook scope was assigned to J. W. Davis of McDonnell Douglas Astronautics Company. This arrangement was a profitable one in the sense that the handbook was able to take advantage of the experience gained by Ted Bierlein over the years in the publication and distribution of data pages for other handbooks. His experience and efforts helped to avoid the costly learning curve that usually accompanies the launching of new initiatives. Unfortunately, about two years ago, Ted decided to retire from HEDL and since that time it has been difficult to locate someone with the experience and dedication to continue on in this area and as a result the publication of the data pages went into a temporary hiatus with the last release of data pages in January 1984. To rectify this situation and to reduce costs through efficiency of operation, it was decided by the Reactor Technologies branch of OFE to consolidate all of these activities with the exception of page preparation under the responsibility of one organization.

Therefore, the orimary thrust of the handbook activities for the past six months has been directed towards consolidating the files between the two organizations and to determine the exact status of the roughly 40 data pages that have been approved and awaiting publication along with the roughly 80 data pages that were in various stages of the preparation, review, and approval cycle. Some progress has been made in these areas with the release in June of the 10th publication package. This publication package was divided into two separate releases, one in June and the other in July. The June release was primarily devoted to the unirradiated properties of the Fe-12 Cr-1Mo alloy known as HT-9 and were prepared by J. B. Wattier of GA Technologies, Inc., D. S. Gelles of HEDL, and C. Y. Ho of TPRC at Purdue University. These data pages covered the temperature dependence of the ultimate tensile strength, yield strength, modulus of elasticity, shear modulus, time to 1% creep, time to tertiary creep, and stress rupture as well as the thermal conductivity and the thermal emissivity. The July data package contained information developed by C. E. Klabunde of ORNL and included the addition of more data to the fiberglass epoxy data sheets previously prepared by him along with new data pages on fiberglass polyimides. Also included in this release are predictive equations for the swelling of HT-9, which were prepared by D. S. Gelles, and the swelling and densification of 20% cold worked type 316 stainless steel which was a joint contribution between F. A. Garner (HEDL), A. F. Rowcliff (ORNL), and R. W. Clark (University of Missouri-Rolla). An 11th publication package is planned for late August which will contain information on magnet structural materials.

For those who receive the handbook data packages, you will notice a slight change in the format and the type fonts. This change was brought about by completely computerizing the handbook to the extent that we can either input equations or data into the code and generate data sheets and tables in a form suitable for direct printing. This capability offers several advantages particularly in the area of savings in production costs since changes and revisions can easily be incorporated. Secondly, the handbook can offer a service of generating comparison curves with different materials plotted on the same curve. This capability is useful for people doing design studies and the information can be rapidly transferred to the user via the MFE network. Even though we are changing some of the style of the handbook, the method of review and approval of the data sheets and equations has not changed.

1.1.5 Conclusions

With the release of the 10th and 11th data packages, substantial progress should be made towards reducing the backlog of data pages. At this time efforts will again be directed towards the generation of data pages. Currently, F. W. Wiffen is assisting in this area by developing data sheets on the effects of irradiation on materials which is one area in which the handbook can use data sheets. Also, to be

responsive to the new design studies, the handbook is in the process of developing data sheets on high conductivity copper alloys which should be of use in compact reactor studies and high heat flux component studies.

2. TEST MATRICES, EXPERIMENT DESCRIPTIONS, AND METHODS DEVELOPMENT

2.1 OPERATION OF THE ORR SPECTRAL TAILORING EXPERIMENTS ORR-MFE-4A AND -48 — I. I. Siman-Tov, J. A Conlin, and I. T. Dudley — (Oak Ridge National Laboratory)

2.1.1 ADIP Task

ADIP Task I.A.2, Define Test Matrices and Test Procedures

2.1.2 Objectives

Experiments ORR-MFE-4A and -48, which irradiate austenitic stainless steel, use neutron spectral tailoring to achieve the same helium-to-displacement-per-atom (He/dpa) ratio as predicted for fusion reactor first-wall service. Experiment ORR-MFE-4A contains mainly type 316 stainless steel and Path A Prime Candidate Alloy (PCA) at irradiation temperatures of 330 and 400°C. Experiment ORR-MFE-48 contains similar materials at irradiation temperatures of 500 and 600°C.

2.1.3 *Summary*

The specimens contained in the ORR-MFE-4A experiment have operated for a total of 1077 d at 30 MW reactor power with temperatures of 330 and 400°C. The specimens contained in the ORR-MFE-48 experiment have operated for an equivalent of 916 d at 30 MW reactor power (through March 24, 1985) with temperatures of 500 and 600°C.

2.1.4 Progress and Status

The details of the Oak Ridge Research Reactor (ORR) spectral tailoring experiments have been documented previously.[1-9]

The MFE-4A irradiation experiment was terminated on January 5, 1985. The capsule was removed from the core, disconnected, and is now stored in the ORR pool awaiting disassembly. The capsule operated for a total equivalent of 1071 d at 30 MW reactor power.

A hafnium sleeve was fabricated for the ORR-MFE-4B experiment to continue irradiation starting in January 1985. However, since the hafnium sleeve of -4A was used for only seven of the projected twelve months, it was decided to use it for the -48 experiment. R. A Lillie estimated this sleeve to be usable for at least four months. The ORR-MFE-48 continues to operate with the hafnium sleeve at the specified temperatures of 500 and 600°C.

2.1.5 References

1. K. R. Thoms and M. L. Grossbeck, "Operation of the ORR Spectral Tailoring Experiment ORR-MFE-4A," pp. 20—24 in ADIP Quart. Prog. Rep. Sept. 30, 1980, DOE/ER-0045/4, U.S. DOE, Office of Fusion Energy.

2. K. R. Thoms, "Operation of the ORR Spectral Tailoring Experiment ORR-MFE-4A," pp. 18-21 in ADIP Quart. Prog. Rep. Mar. 31, 1981, DOE/ER-0045/6, U.S. DOE, Office of Fusion Energy.

3. I. T. Dudley, "Operation of the ORR Spectral Tailoring Experiments ORR-MFE-4A and ORR-MFE-4B," pp. 24—29 in ADIP Semiannu. Prog. Rep. Sept. 30, 1981, DOE/ER-0045/7, U.S. DOE, Office of Fusion Energy.

4. I. T. Dudley and J. A Conlin, "Operation of the ORR Spectral Tailoring Experiments ORR-MFE-4A and MFE-4B," pp. 10—12 in ADIP Semiannu. Prog. Rep. Mar. 31, 1982, DOE/ER-0045/8, U.S. DOE, Office of Fusion Energy.

5. J. A Conlin, I. T. Dudley, and E. M. Lees, "Operation of the ORR Spectral Tailoring Experiments ORR-MFE-4A and ORR-MFE-4B," pp. 17—20 in AOIP Semiannu. Prog. Rep. Sept. 30, 1982, DOE/ER-0045/9, U.S. DOE, Office of Fusion Energy.

6. J. A Conlin, I. T. Dudley, and E. M. Lees, "Operation of the ORR Spectral Tailoring Experiments ORR-MFE-4A and ORR-MFE-4B," pp. 21—22 in ADIP Semiannu. Prog. Rep. Mar. 31, 1983, DOE/ER-0045/10, U.S. DOE, Office of Fusion Energy.

7. J. A Conlin, I. T. Dudley. and E. M. Lees, "Operation of the ORR Spectral Tailoring Experiments DRR-MFE-4A and ORR-MFE-48," pp. 40—41 in ADIP Semiannu. Prog. Rep. Sept. 30, 1983, DOE/ER-0045/11, U.S. DOE, Office of Fusion Energy.

8. J. A Conlin and J. W. Woods, "Irradiation Experiments for the U.S./Japan Collaborative Testing in HFIR and ORR," p. 37 in ADIP Semiannu. Prog. Rep. Mar. 31, 1984, DOE/ER-0045/12, U.S. DOE, Office of Fusion Energy.

9. J. A Conlin and J. W. Woods, "Irradiation Experiments for the U.S./Japan Collaborative Testing Program in HFIR and ORR," pp. 66-67 in ADIP Semiannu. Prog. Rep. Sept. 30, 1984, DOE/ER-0045/13, U.S. DOE, Office of Fusion Energy.

2.2 IKKADIATION EXPERIMENTS FOR THE U.S./JAPAN COLLABORATIVE TESTING PROGRAM IN HFIR AND ORK –

I. I. Siman-Tov, J. A. Conlin, and J. W. Woods [Oak Ridge National Laboratory)

2.2.1 ADIP Task

ADIP Task 1.A.2, Define Test Matrices and Test Procedures

2.2.2 Objectives

The experiments in the U.S./Japan collaborative testing program for HFIK and ORR irradiate austenitic stainless steel candidate alloys for use as first-wall and blanket structural materials in fusion reactors. They will be irradiated with mixed-spectrum neutrons and with spectral tailoring to achieve helium-to-displacement-per-atom (He/dpa) ratios predicted for fusion reactor service.

2.2.3 Summary

The assembly of JP-7 and -8 was completed. Capsules JP-2 through -8 are being irradiated in the HFIR. Capsule JP-I completed its irradiation for a total of 336.40 d at 100 MW reactor power.

The fabrication and assembly of ORR-MFE-6J are in progress. The assembly of MFE-7J is nearing completion. The specimens are expected to be delivered for loading by the end of March.

2.2.4 Progress and Status

The details of the U.S./Japan collaborative irradiation program have been described previously.[1-2]

HFIR capsules JP-7 and -8 were assembled and installed ahead of schedule. Capsule JP-1 completed its irradiation period on February 7, 1985. It is now stored in the pool going through a cooldown process.

ORR-MFE-6J: The "dummy" capsule was removed, disassembled, and the flux monitors were shipped to L. R. Greenwood at ANL for analysis. Minor changes in design have been incorporated mainly to facilitate assembly. Components for the -6J capsule are being fabricated.

~~OKR-MFE-7J~~: Fabrication and procurement of parts were completed. Assembly is nearing completion [see Figs. 2.2.1, 2.2.2, and 2.2.3 for some of the assembled components). A difficulty in assembling the outer tube (Item 1 on DWG. X2E-11837-084) over the inner tube (Item 1 on DWG. X2E-11837-082) has been slowing the assembly down considerably; however, if the next attempt at the assembly is successful, it is expected that the originally planned insertion date will be met. The specimens are being assembled and are expected to be ready for loading by the end of March.

The facilities for both MFE-6J and -7J are being modified to incorporate the use of *an* LEN Speedomax 2500 multipoint temperature recorder. This change will provide state-of-the-art capability in the temperature inonitoring and control system.

The preparation of the second facility is proceeding as planned. Preparation of most of the tubing in the valve box, coupling box, and experiment room is complete. Identification of available wiring and junction points was completed, and the wiring of instruments and safety system circuits is in progress. Figures 2.2.4, 2.2.5, and 2.2.6 show a general view of the valve box on the balcony and the panels in the experiment room.

2.2.5 References

1. J. A. Conlin and J. W. Woods, "Irradiation Experiinents for the U.S./Japan Collaborative Testing in HFIK and ORR," p. 37 in ADIP Semiannu. Prog. Rep. Mar. 31, 1984, DOE/ER-0045/12, U.S. DOE, Office of Fusion Energy.

2. J. A. Conlin and J. W. Woods, "Irradiation Experiments for the U.S./Japan Collaborative Testing Program in HFIK and ORR," pp. 66–67 in ADIP Semiannu. Prog. Rep. Sept. 30, 1984, DOE/ER-0045/13, U.S. DOE, Office of Fusion Energy.

ORNL-PHOTO 6766-85

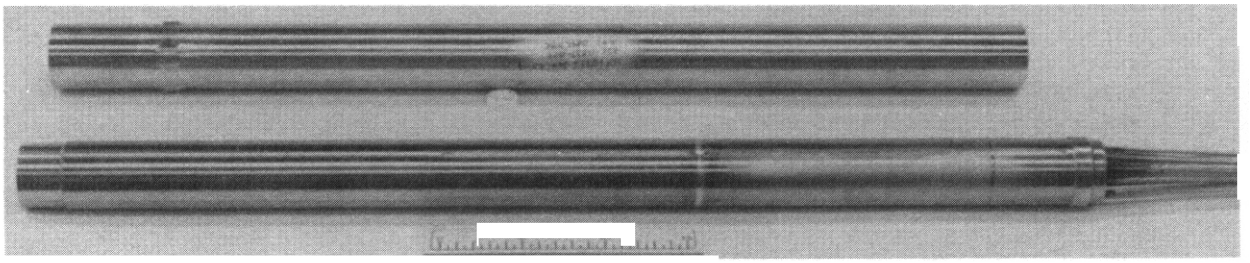

Fig. 2.2.1. Partial assembly — ORR-MFE-7J capsule test region.

ORNL-PHOTO 6768-85

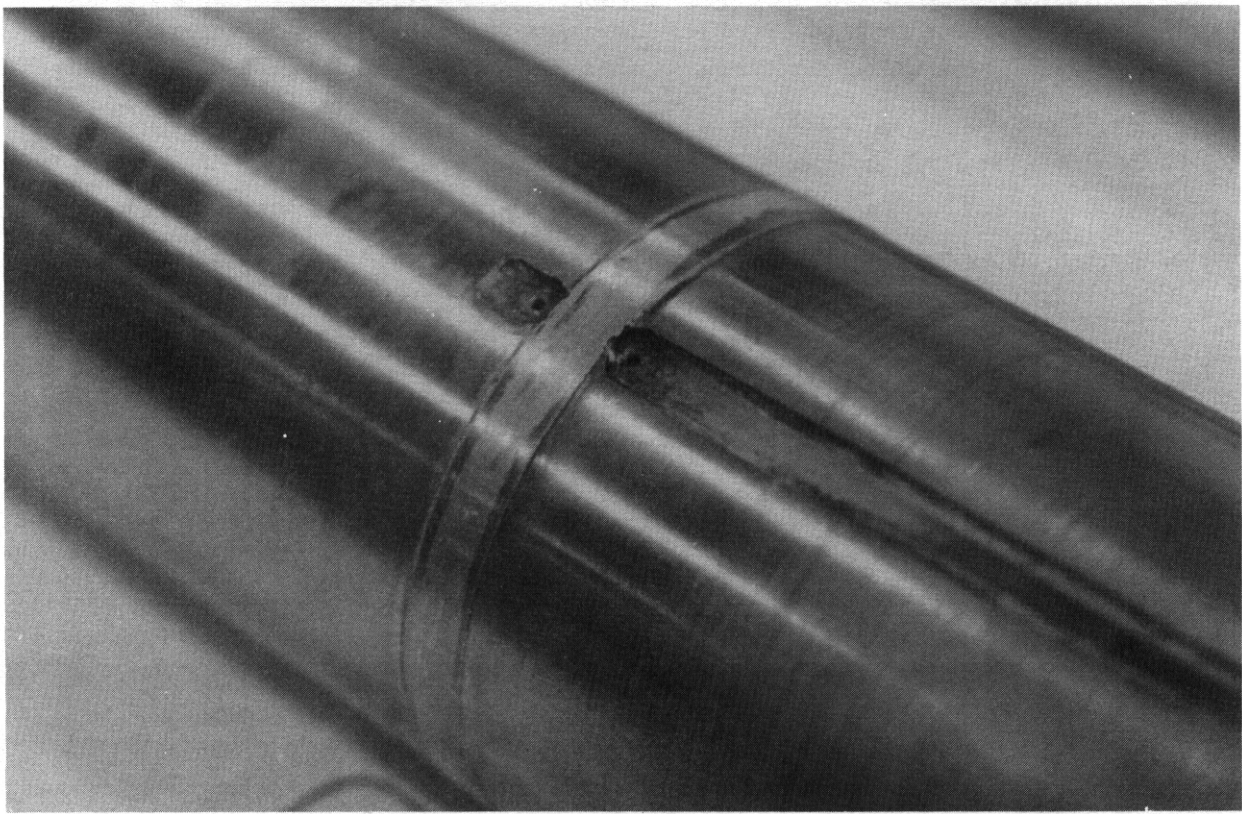

Fig. 2.2.2. Partial assembly — inner tube with sealing ring and return control gas groove.

ORNL-PHOTO 6764-85

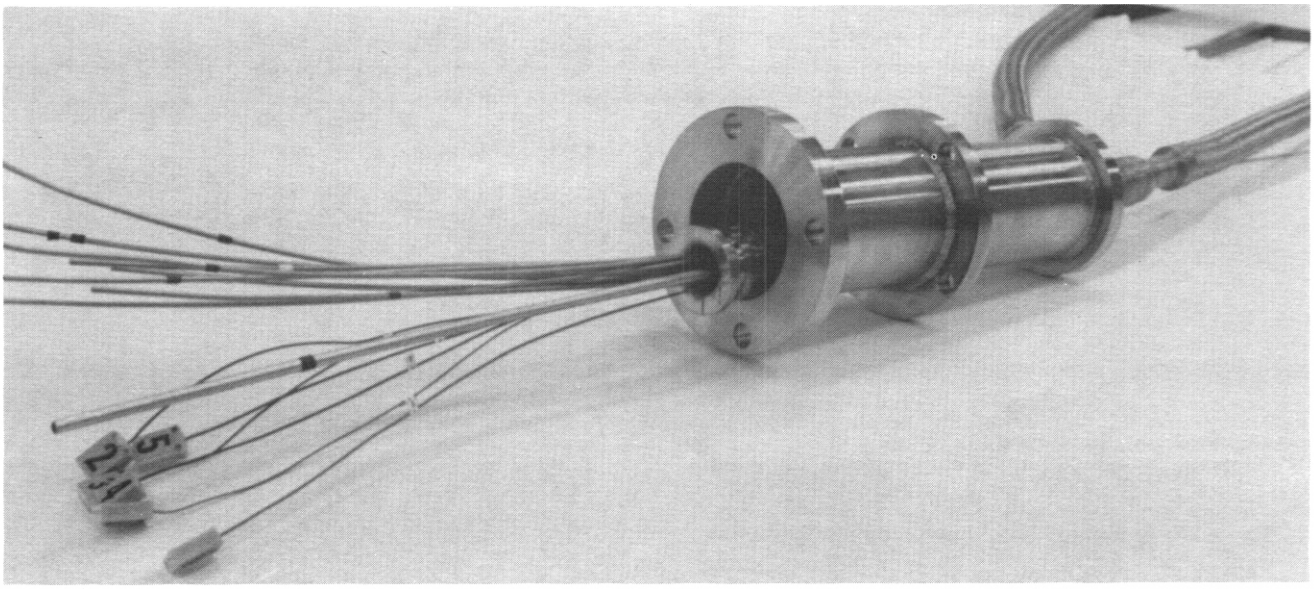

Fig. 2.2.3. Partial assembly — out-of-core leads assembly.

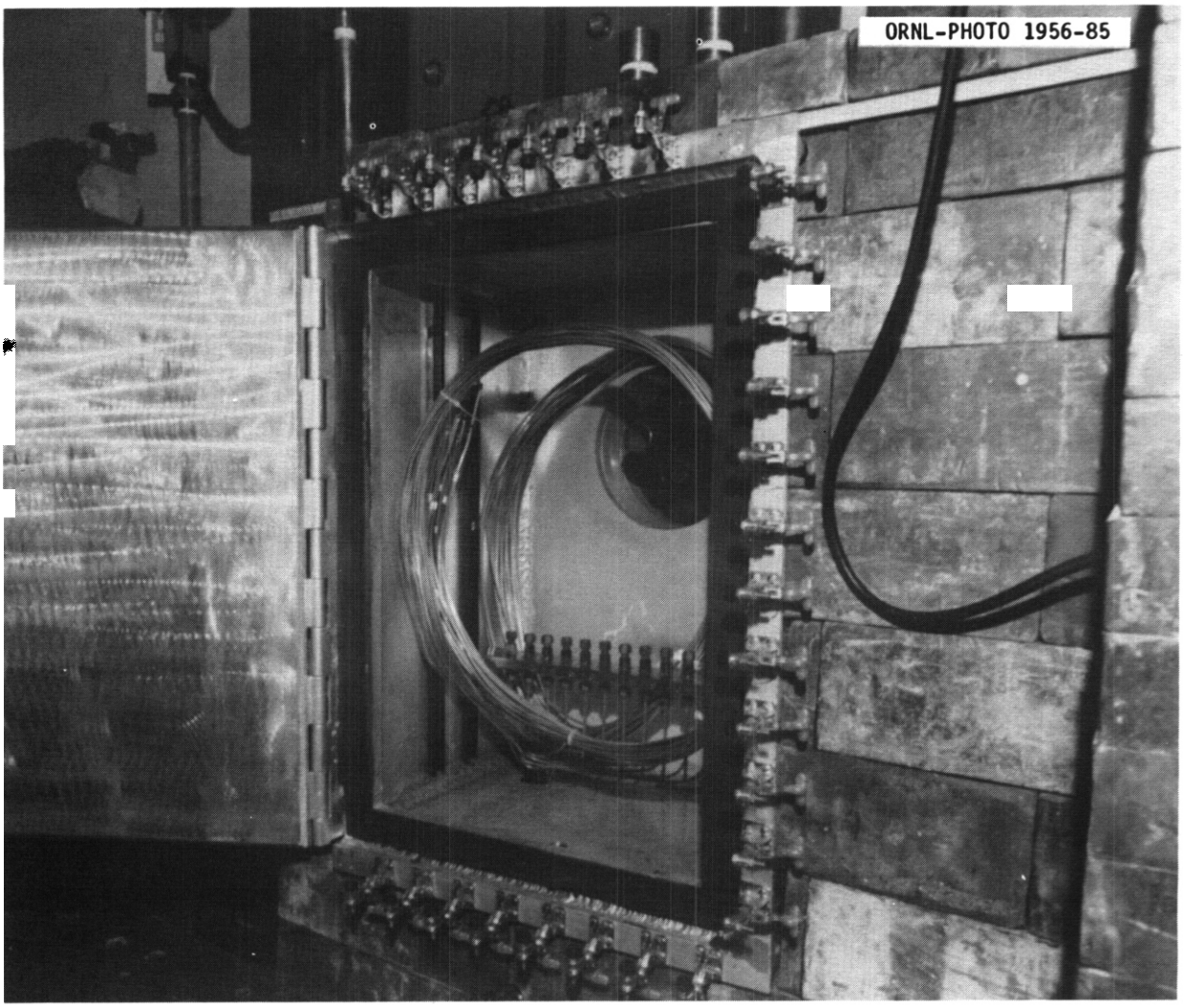

Fig. 2.2.4. Coupling box from experiment to valve box A(3).

ORNL-PHOTO 1959-85

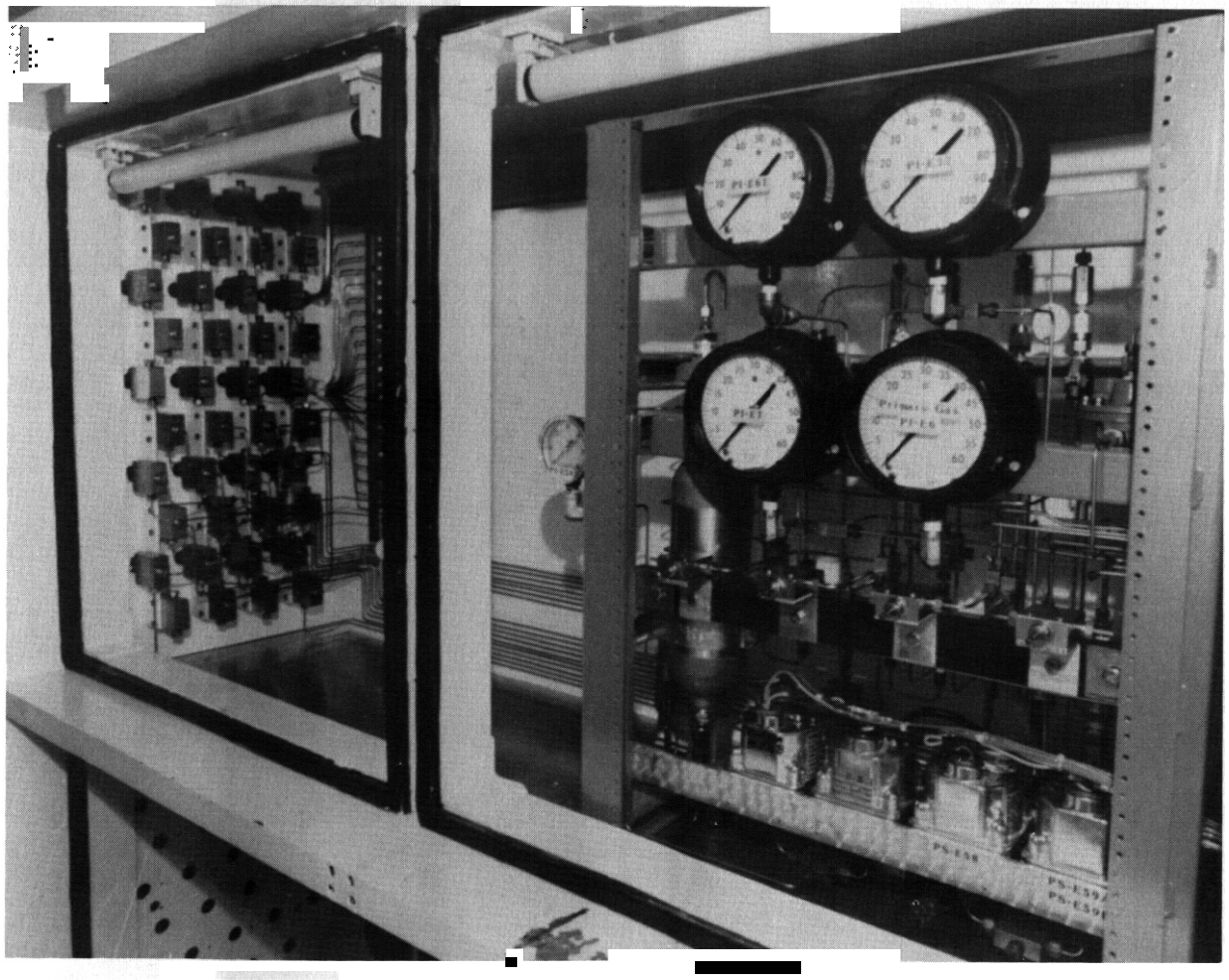

Fig 2.2 5 box A(3) on the s

ORNL-PHOTO 1953-85

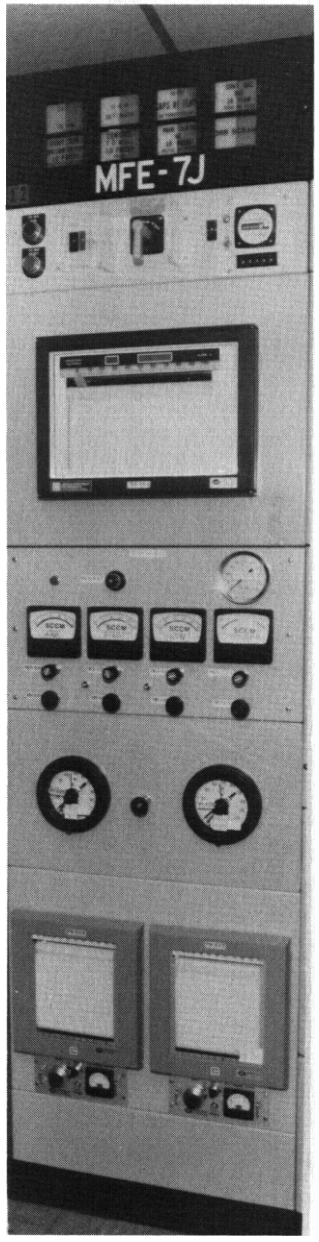

Fig 2.2.6 MFE-7J instrument panel in experiment room

2.3 PREPARATION FOR POSTIRRADIATION EXAMINATION OF U.S./JAPAN HFIR CAPSULES — J. L. Scott (Oak Ridge National Laboratory) and M. P. Tanaka (Japan Atomic Energy Research Institute, assigned to ORNL)

2.3.1 AOIP Task

ADIP Task 1.A.2, Define Test Matrices and Test Procedures

2.3.2 Objectives

The objective of this work is to carry out the postirradiation examination (PIE) of U.S./Japan capsules JP-1 to -8 irradiated in HFIR for the purpose of investigating the irradiation response of Japanese and U.S. structural alloys to high levels of atomic displacement and helium content.

2.3.3 Summary

The first U.S./Japan HFIR capsule, JP-1, has completed its irradiation campaign and is cooling down. Preparations for PIE are under way. The new Japan Electron Optical Laboratory, Inc. (JEOL) JEM-2000FX microscope has been delivered to ORNL and is operational.

2.3.4 Progress and Status

The scope of the collaborative program was reported previously.[1-2] The status of the work for the different phases is reported separately below.

2.3.4.1 HFIR Irradiation Experiments and Postirradiation Examination

The first HFIR capsule, JP-1, completed its campaign February 1, 1985, and is now cooling down in the HFIR pool. The exposures received by the specimens in JP-1 are shown in Table 2.3.1. The status of the other seven capsules, which are still being irradiated. is shown in Table 2.3.2. The present irradiation schedule for the HFIR capsules is shown in Fig. 2.3.1. After irradiation, each capsule is allowed to cool down at least three months prior to disassembly. The disassembly schedule is shown in Fig. 2.3.2. After disassembly, the PIE requires four to six months exclusive of transmission electron microscopy (TEM) examination. A typical PIE schedule indicating individual tasks is shown in Fig. 2.3.3. The present schedule for the eight HFIR capsules is shown in Fig. 2.3.4. All capsules are now on schedule.

Table 2.3.1. Displacements per atom and helium contents in HFIR JP-1 capsule

Position	Distance from HFIR centerline (cm)	Specimen type	Alloy	Displacements per atom (dpa)	Helium content (at. ppm)
1	23.20	Tensile	PCA	15.90	1062
2	18.76	Tensile	PCA	22.19	1621
3	14.31	Tensile	PCA	27.14	2049
4	9.59	Fatigue	316	30.00	1891
5	4.58	Fatigue	316	32.27	2049
6	0.00	TEM disks	J316[a]	33.22	2224
7	4.58	Fatigue	JPCA	33.12	2522
8	9.59	Fatigue	JPCA	30.77	2326
9	14.31	Tensile	JPCA	27.01	2008
10	18.76	Tensile	JPCA	22.09	1585
11	23.20	Tensile	JPCA	15.84	1046

[a]This holder contained several alloys.

2.3.4.2 JEOL Microscope Installation

The new JEOL JEM-2000FX analytical electron microscope was delivered to ORNL on February 7, 1985. It has been assembled and is now operational. An acceptance ceremony was held March 15, 1985, with M. W. Rosenthal and T. Kondo as speakers.

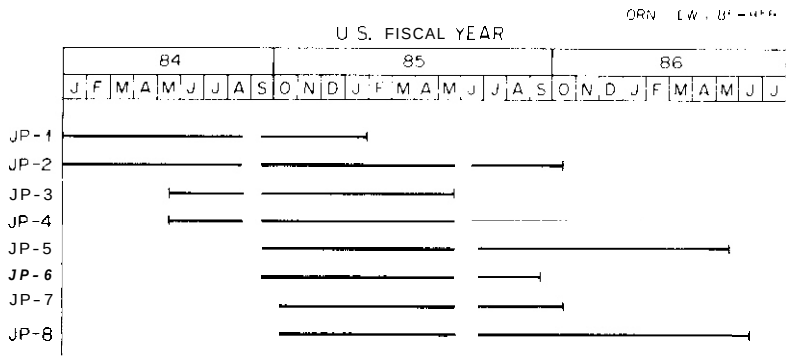

Fig. 2.3.1. HFIR-JP irradiation schedule.

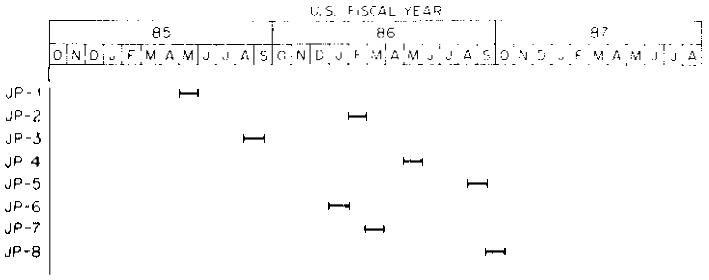

2.3.5 Conclusions

Preparations for the PIE of U.S./Japan JP capsules are now under nay. A schedule has been developed for the eight capsules.

2.3.6 References

1. J. L. Scott and T. Kondo, "Introduction to the U.S./Japan Collaborative Testing Program in HFIR and ORR," pp. 35–36 in ADIP Semiannu. Prog. Rep. Mar. 31, 1984, DOE/ER-0045/12, U.S. DOE, Office of Fusion Energy.

2. A. F. Rowcliffe, M. L. Grossbeck, M. Tanaka, and S. Jitsukawa, "The U.S./Japan Collaborative Testing Program in HFIR and ORR: Specimen Matrices for HFIR Irradiation," pp. 61-62 in ADIP Semiannu. Prog. Rep. Sept. 30, 1984, DOE/ER-0045/13, U.S. DOE, Office of Fusion Energy.

Table 2.3.2. Status of U.S./Japan HFIR capsules

Capsule	Reactor Exposure[a,b] (MWd)	Present Level[c] (dpa)	Goal Level[d] (dpa)
JP-1[e]	33,644	33.22	30
JP-2	40,206	39.77	50
JP-3	29,818	29.38	30
JP-4	29,818	29.38	50
JP-5	19,459	18.96	50
JP-6	19,459	18.96	30
JP-7	17,351	16.84	30
JP-8	17,351	16.84	50

[a]Date: April 11, 1985.

[b]Reactor power: 100 MW.

[c]Peak dpa level in type 5316 stainless steel (13.5% Ni).

[d]Average.

[e]Removed from reactor February 1, 1985.

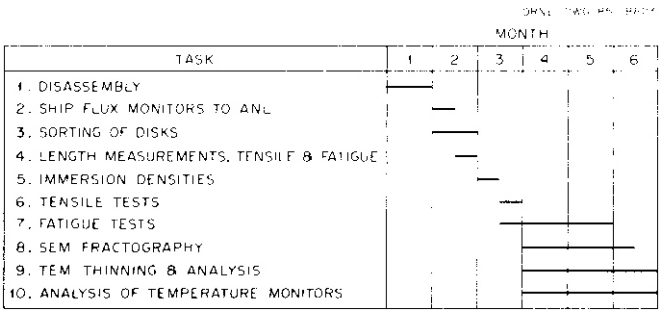

Fig. 2.3.3. PIE schedule for JP capsules (typical).

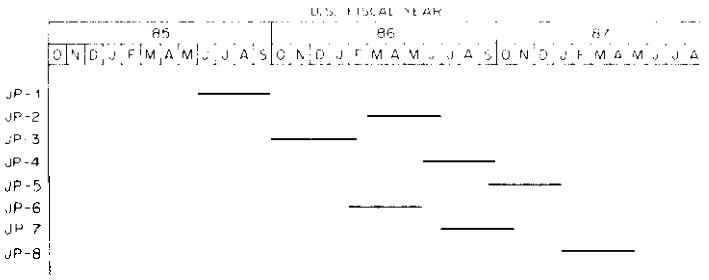

Fig. 2.3.4. HFIR-JP PIE schedule.

2.4 DESCRIPTION OF THE U.S./JAPAN SPECTRAL TAILORING EXPERIMENT IN ORR — J. L. Scott, L. K. Mansur, M. L. Grossbeck, E. H. Lee, K. Farrell, L. L. Horton, and A. F. Rowcliffe (Oak Ridge National Laboratory) and M. P. Tanaka (Japan Atomic Energy Research Institute, assigned to ORNL)

2.4.1 ADIP Task

ADIP Task I.A.2, Define Test Matrices and Test Procedures

2.4.2 Objectives

The primary objective of this experiment is to study the response of U.S. and Japanese fusion structural alloys to high fluences with a helium/dpa ratio similar to that expected in a fusion reactor. In addition, the experiment is used to study fundamental radiation processes under well-controlled conditions.

2.4.3 Summary

Two spectral tailoring capsules MFE-6J and -7J are being assembled and irradiated in ORR as a part of the U.S./Japan program of collaborative testing in mixed-spectrum fission reactors. The test matrix includes conventional U.S. and Japanese structural alloys plus a wide variety of research alloys that lead to a basic understanding of alloy response to the fusion reactor environment.

2.4.4 Progress and status

2.4.4.1 Introduction

Spectral tailoring experiments in the ORR are a part of the program of U.S./Japan collaborative testing in HFIK and ORR. This experimental technique was established earlier as a part of the ADIP program.[1-2] The principle of the technique is shown in Fig. 2.4.1. Initially, the speciinen-containing capsule is surrounded with water to thermalize as many neutrons as possible. The thermal neutrons react with nickel to form helium. Later a solid aluminum corepiece surrounds the specimen capsule, making the flux somewhat harder. Finally, in the third phase, a hafnium sleeve is placed around the capsule to absorb thermal neutrons. The effects of spectral tailoring in ORR on helium generation in type 316 stainless steel are shown in Fig. 2.4.2. In a fusion reactor the He/dpa ratio has a constant value dependent upon the blanket design of about 14. In a fast reactor, such as EBR-II, very little helium is produced, and in HFIR too much helium is produced after about 3 dpa. In the ORR, a close approximation to the correct He/dpa ratio can be achieved.

Under the U.S./Japan collaboration, two new spectral tailoring capsules are being irradiated. Capsule MFE-7J will operate at 330 and 400°C and has the same basic design of MFE-4A (ref. 3). The only difference is that each temperature zone has been lengthened by 4.4 cm to accommodate additional specimens. Capsule MFE-6J will operate at 60 and 200°C. The 60°C region is the reactor coolant temperature, and the specimens are in contact with ORR cooling water.

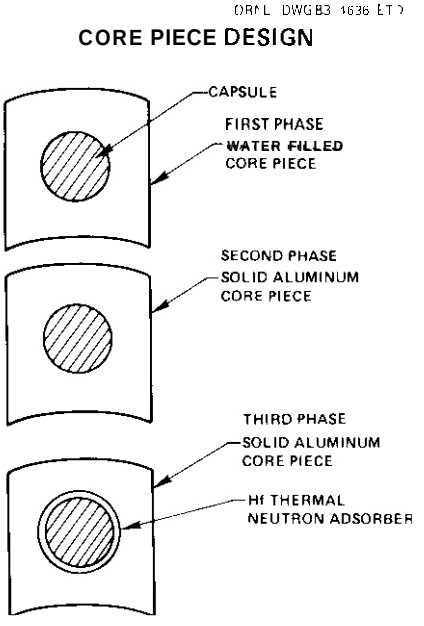

Fig. 2.4.1. Principle of the spectral tailoring method.

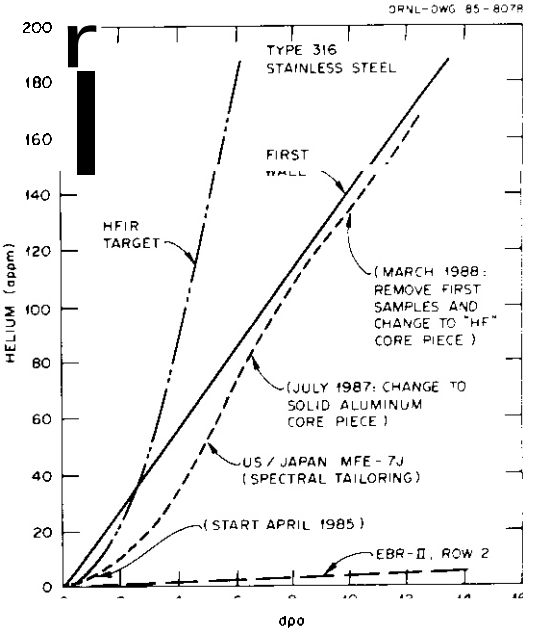

Fig. 2.4.2. Helium/dpa ratio in type 316 stainless steel in ORR with spectral tailoring and in other fission reactors.

The 200°C region is especially challenging. Since NaK does not wet stainless steel below 300°C. it would not be a good heat-transfer medium. The design approach selected was to use a solid piece of aluminum as the heat-transfer medium with carefully machined slots to contain flat tensile specimens and round holes containing pressurized tubes and TEM disk packets. It was also found convenient to put the 60°C region outside the 200°C zone instead of having one above the other. A schematic representation of MFE-6J is shown in Fig. 2.4.3.

ORNL-DWG 84-6518R ETD

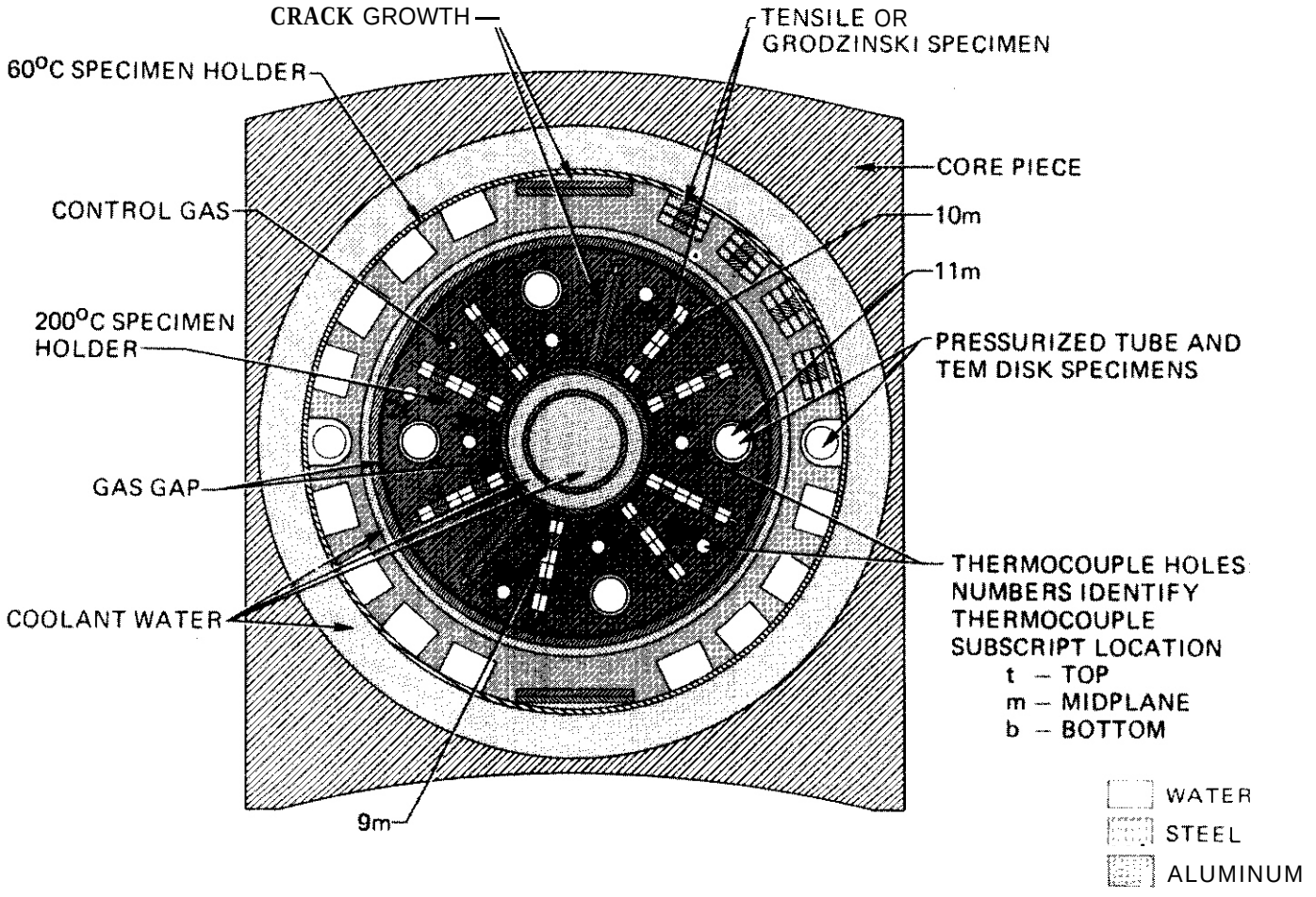

Fig. 2.4.3. Cross section of the MFE-6J capsule with typical test specimen locations.

2.4.4.2 Experiment Objectives

When the U.S./Japan spectral tailoring capsules were originally conceived (October 1981), the emphasis in the United States was focused on obtaining an engineering data base for the next-generation fusion reactor, especially the Engineering Power Reactor (EPR). Likewise in Japan the focus was to obtain a data base for the structural alloy to be used in the Fusion Engineering Reactor (FER). On the U.S. side the low-temperature capsule (60/200°C) was especially important because the higher temperature data (300/400/500/600°C) were already being obtained in the U.S. spectral tailoring capsules MFE-4A and -4B. Thus, the original objectives were primarily toward an engineering data base and on a direct comparison of U.S. and Japanese alloys under the same test conditions.

More recently (-1984) the focus of the U.S. fusion materials program has been redirected toward basic fusion materials research leading to the development of new materials with properties that enhance the economic and environmental potential of fusion. Low-activation alloys with good irradiation properties which are relatively easy to dispose of are especially attractive environmentally.

The U.S. test matrix for MFE-6J and -75 contains specimens focused at both the original and new objectives. Engineering data are being obtained on type 316 stainless steel, U.S. PCA, and on HT-4. At the same time, data will be obtained on a variety of research and low activation alloys at both ORNL and HEDL. The objectives of the JAERI specimens also encompass both the original and new foci, but priority is given to the engineering data base for the FER. A comparison of results obtained in MFE-6J and -7J with MFE-4A and -48 will provide the needed direct comparison between U.S. and Japanese structural alloys.

The basic studies in the ORNL program are a collaborative effort between the ORNL BES Radiation Effects program, ADIP, and DAFS. As part of this collaboration, the programs have undertaken an effort in preparing a combined experiment to constitute a part of the U.S. side of the U.S./JAPAN ORR test. The experiment consists of a joint effort with the fusion program on fundamental studies of irradiation creep and ceramics irradiation, together with other research on swelling, microstructural development, and mechanical properties research.

Irradiation Creep — The irradiation creep behavior under neutron irradiation of materials of interest is relatively unknown at low temperatures, such as are available in this experiment. As far as we are aware, there are no data at temperatures as low as 60 and 200°C. Furthermore, systematic data covering creep, swelling, and microstructures in high-purity simple alloys are also lacking. Such data are highly desirable in our theoretical efforts toward a quantitative understanding of mechanisms of irradiation creep and in particular in the relationships of irradiation creep to swelling.

Four simple alloys are included in the form of pressurized tubes for this experiment. Also included are tubes of the austenitic stainless steel PCA and the ferritic stainless steel HT-9. Corresponding unstressed tubes and TEM specimen disks are part of the experiment to provide baseline data on swelling and microstructures. The four simple alloys are the ferritic Fe-16Cr and the austenitic8 Fe-13Cr-15Ni, Fe-13Cr-35Ni, and Fe-13Cr-15Ni with Ti and C added.

The ferritic alloy should be particularly interesting at the lower temperatures, since materials of this type exhibit swelling and significant dislocation evolution at lower temperatures than austenitic alloys. A high-purity binary alloy was selected in order to study the irradiation response in an alloy with a simple preirradiation microstructure and thus facilitate interpretation of the experiment with modeling. The chromium content was dictated by the low-corrosion requirements for inaterials placed in the cooling water of ORR (60°C irradiation). A minimum level of 15% Cr was suggested to avoid any possible contamination of the reactor pool. The alloy was arc-melted from starting materials of MARL-grade iron (99.99%+) and IOCHROME chromium (99.996%+). For a preliminary test heat fabricated in the same manner as the final alloy, metallic impurity concentrations were less than 5 wt ppm and total interstitial impurity concentration was about 100 wt ppm. Planned postirradiation analyses include correlation of the creep results with the microstructures.

The simple austenitic alloys similarly were selected to facilitate understanding of the creep-swelling interaction. Comparisons of the 15Ni ternary with the 35Ni ternary will provide information on relative creep rates in two alloys known to exhibit large differences in swelling and microstructure. In our previous work the 35Ni ternary proved highly resistant to Swelling, while the 15Ni ternary swelled readily. The 15Ni ternary will also provide a good comparison with the creep and microstructural behavior of the ferritic alloy. The alloy containing Ti and C is expected to form a fine dispersion of TiC precipitates during irradiation. This is a microstructural feature that imparts swelling resistance, as our previous work has shown. The creep response of this swelling-resistant alloy will therefore be of great interest.

The alloys PCA and HT-9 were included in this creep experiment to provide further detailed information on alloys of direct interest for fusion reactor application.

Embrittlement — Several distinct embrittlement studies are under way. Some of the specimens for irradiation at the 400°C level comprise three experiments on radiation-induced solute segregation embrittlement and helium embrittlement. The first experiment consists of a series of binary nickel-base alloys containing the y'-forming elements Si, Al, and Ti at levels of 1 and 8 at. % (Si only), which are below the solubility limits but which are adequate for radiation-induced formation of the γ' phase. This Ni_3X phase, especially Ni_3Si, is sometimes claimed to be the primary source of embrittlement in irradiated, commercial nickel-base alloys and possibly in stainless steels. The purpose of this experiment is to isolate the Si, Al, and Ti γ' phases and measure their contributions to embrittlement. The second experiment is similar to the first, except that the base material is a nominal Fe-15Ni-15Cr alloy to explore whether the effects of γ' formation are altered when the matrix composition is similar to that of stainless steels. The third experiment is to measure the response of bcc ferritic iron to helium embrittlement. Ferritic iron is claimed widely to be much more resistant to helium embrittlement than is fcc stainless steel, but definitive data are sparse. In particular, there is no information on embrittlement associated with burnup of ^{10}B, which is a major source of helium in commercial ferritic alloys. The present experiment is designed to study embrittlement in pure iron and in two boron-doped melts of the same pure iron. The role of lithium, the sister product of He in ^{10}B burnup, will be explored in a boron-free melt containing a few ppm lithium.

Some of the materials inserted at the 300°C level consist of zirconium-base alloys intended for helium embrittlement studies. Zirconium is known to be highly resistant to intergranular creep cavitational failure. This raises the question of whether zirconium will also resist intergranular helium embrittlement which shares many characteristics of creep cavity embrittlement. The only data on helium embrittlement of zirconium are reported by C. E. Ells of Atomic Energy of Canada who irradiated Zircaloy-2 doped with ^{10}B and found severe embrittlement in tensile tests even when the specimens were tested at room temperature. No post-test studies or microstructurdl data were reported. Since helium embrittlement is usually worse under slow, elevated temperature creep tests, these results suggest that something other than simple helium bubble

coalescence is involved. Two possibilities are matrix hardening and embrittlement by lithium which is produced as a sister product of the helium created by burnup of the ^{10}B. In the present experiments, embrittlement will be explored in materials Zr-1, Zr-B1, and Zr-B2 which are alloys of pure zirconium and ^{10}B (up to 40 at. ppm). Creep tests, Auger spectroscopy of fracture surfaces, and TEM examinations are planned. The effects of lithium will be proved with materials Zr4 and Zr4-Li3, where Zr4 is a laboratory-made Zircaloy-4 alloy, and Zr4-Li3 is the same material doped with a small quantity of lithium. Understanding the behavior of Zr and its alloys, materials known to be resistant to radiation effects, is expected to lead to principles by which radiation-resistant materials of other classes can be designed.

Also included in this experiment on mechanical properties are tensile specimens of alloys based on Fe-13Cr-15Ni and Fe-15Cr-15Ni. These comprise both single alloys (with one or more minor additions) designated as the B-series, and more complex engineering-type alloys, designated as the E-series, as well as Li-doped alloys. The extensive data that will be produced from these specimens are expected to give information on the fundamental bases of changes in mechanical properties as affected by alloying additions or deletions. We are now accumulating extensive swelling and microstructural data on these alloys under neutron irradiation, ion irradiation, and thermal aging. By comparing this available information, we expect to build a more complete picture of radiation-induced changes.

Microstructures — Microstructural information will be obtained from specimens described above by analytical electron microscopy. Additional specimens are included in the form of TEM disks. These consist of specimens based on the B-series and E-series austenitics described above and a series of high-purity iron-carbon and iron-chromium-carbon alloys. The austenitics are aimed at studies of phase stability and its interactions with swelling and mechanical property changes. In particular, the association of cavities with precipitates and the effects of precipitate interfacial area on swelling for precipitates such as TiC and Fe_2P are of great interest for controlling swelling. The ferritic specimens were included to study the effects of carbon on swelling and dislocation evolution. The dislocation structures are particularly interesting in ferritic materials. Interstitial dislocation loops with $\underline{b} = a\langle 100\rangle$ are often observed in irradiated ferritic materials while loops in other bcc materials have $\underline{b} = a/2\langle 111\rangle$. The effect of the $a\langle 100\rangle$ loops on the nucleation and growth of cavities is not known. The dose to the onset of swelling in ferritic materials is relatively large and may result, in part, from the unusual dislocation evolution. Impurity segregation at the dislocation loops and cavities may also influence the damage evolution. Carbon, in particular, is known to segregate to (100) planes, as evidenced by the observation of carbides on these planes. In this experiment, the effects of both interstitial carbon and carbide precipitates will be determined. The alloys with the higher carbon concentrations approach the carbon levels contained in ferritic steels. These alloys contain precipitates; the alloys with low carbon concentrations contain no precipitates. The relatively low irradiation temperatures 200, 300, and 400°C, complement the irradiation temperatures in a similar experiment conducted in FFTF. For the FFTF experiment, the same alloys were irradiated at temperatures of 470 to 585°C. While the FFTF experiment primarily will address the high-temperature structures and the swelling variation, the lower temperatures in ORR should permit comparisons of the dislocation loop structures and early stages of cavity nucleation.

Ceramics — Ceramics have been proposed for a variety of fusion applications, but there are almost no irradiation data on most ceramics at the fluences and temperatures of interest. Since the spectral tailoring capsules offer the range of fluences (up to 30 dpa) and temperatures (60–400°C) of greatest interest, it was decided to include selected ceramic materials in the form of TEM disks in MFE-6J and -7J. The compositions, forms, and investigators are listed in Table 2.4.1. Ceramic Nos. 1–3 and 6–7 are compositions and forms of direct relevance for fusion application. Ceramics 4 and 5 will provide additional information about the effects of helium on swelling. Helium is produced either by lithium fissions (composition No. 4) or by the two-step neutron-^{58}Ni reaction that produces ^{56}Fe and helium (composition No. 5). Examination by TEM after irradiation will provide important data on swelling and microstructural changes, and microhardness testing will provide information about irradiation-induced changes in the fracture toughness.

Table 2.4.1. Ceramics being irradiated in MFE-6J and -7J

Number	Composition	Form	Investigator
1	Si_3N_4	Polycrystalline	F. W. Clinard, Jr.
2	MgAlO	Polycrystalline	F. W. Clinard, Jr.
3	$MgAlO_2$	Single crystal	F. W. Clinard, Jr.
4	MgO + 0.1Li	Single crystal	L. L. Horton
5	MgO + 0.1Ni	Single crystal	L. L. Horton
6	MgO	Single crystal	L. L. Horton
7	Al_2O_3	Single crystal	P. F. Becher

Objective of the HEDL Test Matrix — The HEDL test matrix consists of crack growth specimens, SS-3 tensile specimens of experimental ferritic alloys, and TEM disks of simple Fe-Ni-Cr and Fe-Cr-Mn ternaries together with solute modifications to these ternaries. The crack growth specimens consist of 20%-CW type 316 stainless steel (X-15893) and 25%-CW PCA (K-280). Since these alloys were irradiated in MFE-4A and -4B, the data can now be expanded over a wider temperature range. The matrix of tensile specimens consists of a series of low-activation ferritic alloys with chromium contents between 2 1/4 and 12%. with V, W, and Mn as alloying additions. These specimens will provide information on irradiation embrittlement of low-activation alloys. The TEM disk arrays are designed to explore the swelling behavior of high-purity

Fe-Ni-Cr and Fe-Cr-Mn alloys with and without low-activation solute additions. These specimens will provide information on the fundamental mechanisms of swelling and the effects of helium. A more detailed description of the fundamental alloy test matrix is given in ref. 4.

Objectives of the JAERI Program — The primary objective of the JAERI part of the ORR spectral tailoring capsule is to obtain engineering data on candidate structural materials for the next fusion reactor in Japan. Major emphasis is placed on the understanding of the irradiation response of type 316 stainless steel and the Japanese Prime Candidate Alloy (JPCA) with respect to swelling, irradiation creep, tensile properties, and fracture behavior. It is expected that JPCA will show more improved resistance to swelling and helium embrittlement at elevated temperature than does type 316 stainless steel. To further enhance its behavior, JPCA is being tested in the 15- to 20%-cold-worked condition and/or heat treated so as to control solutes and precipitate distributions. Solution-annealed JPCA is also being tested. Since welding is required for blanket assembly, welded joints made by the TIG method are a part of the JAERI test matrix.

A second objective of the JAERI test program in ORR is to carry out fundamental studies leading to a further understanding of radiation-induced segregation, swelling, embrittlement, and resistance to stress corrosion cracking. Not only the austenitic stainless steels, but also ferritic and dual-phase alloys are included. Alloys designated C and K are compositional modifications to JPCA with improved resistance to stress corrosion cracking in water, a possible coolant for next-generation fusion reactors. Alloys C and K have lower carbon contents and small amounts of Ti and/or Nb to compensate for strength reduction. The nickel and chromium contents are also adjusted to maintain phase stability. In the case of ferritic steels, 9Cr-2Mo alloys are being compared with Hi-9. One all-martensitic alloy is included to determine the effects of V and W on HT-9.

The fundamental studies include a series of dual-phase alloys. Since austenitic alloys suffer helium embrittlement and ferritic alloys show a ductile-to-brittle transition, one is seeking an alloy resistant to both phenomena. Dual-phase alloys may offer this possibility. Strain-aged and recrystallized (SAR) austenitic steels are also possibly resistant to helium embrittlement; these alloys are cold worked 50% and then aged at 650°C for 15 h and 775°C for 5 h. This treatment reduces the grain size to ASTM 10–11 and provides many grain boundaries to trap helium. A pure Fe-Ni-Cr ternary is being irradiated to determine the swelling behavior of simple ternaries. Finally, low-activation manganese steels and Incoloy 800, a good breeder reactor alloy, are being evaluated.

Because of the limited availability of space the fundamental studies are limited to TEM disks, and microstructural analysis will be the primary evaluation technique.

2.4.4.3 Test Matrix

Alloy compositions are given in Tables 2.4.2 to 2.4.4. The test matrix for the MFE-6J and -7J capsules is shown in Table 2.4.5. A detailed description of the specimens and test array will be given in the next semiannual report after capsule MFE-6J has been loaded.

2.4.5 References

1. M. L. Grossbeck and K. R. Thorns, "ORR-MFE-4: A Spectral Tailoring Experiment to Simulate the He/dpa Ratio of a Fusion Reactor in Austenitic Stainless Steel," pp. 10–23 in ADIP Quart. Prog. Rep. June 30, 1980, DOE/ER-0045/3, U.S. UOE, Office of Fusion Energy.
2. J. A. Conlin and I. T. Dudley, "Operation of the ORR Spectral Tailoring Experiments (ORR-MFE-4A and ORR-MFE-4B)," p. 20 in ADIP Semiannu. Prog. Rep. Sept. 30, 1984, DOE/ER-0045/13, U.S. DOE, Office of Fusion Energy.
3. K. R. Thorns and M. L. Grossbeck, "Operation of the ORR Spectral Tailoring Experiment ORR-MFE-4A," pp. 20–25 in ADIP Quart. Prog. Rep. Sept. 30, 1980, DOE/ER-0045/4, U.S. DOE, Office of Fusion Energy.
4. H. R. Brager and F. A. Garner, "Fundamental Alloy Studies," pp. 93–101 in Damage Analysis and Fundamental Studies Quart. Prog. Rep. Jan.–Mar. 1984, DOE/ER-0046/17, U.S. DOE, Office of Fusion Energy.

Table 2.4.2. Alloys in the ORNL test matrix for MFE-6J and -75

Alloy	Composition, wt %																						
	Li	B	C	N	O	Al	Si	P	S	Ti	V	Cr	Mn	Fe	Co	Ni	Cu	Zr	Nb	Mo	In	Ta	W
316 SS	--	0.0004	0.061	--	- - - -		0.67	0.037	0.02	--	--	17.3	1.7	bal	0.3	12.4	0.3	--	--	2.1	- - - - - -		
PCA	--	0.0005	0.047	0.009	--	0.03	0.42	0.001	0.003	0.24	0.02	14.0	1.8	bal	--	16.2	0.05	--	0.02	2.3	--	0.001	--
MT-9	--	--	0.2	0.027	--	0.006	0.17	0.016	0.003	0.001	0.20	12.1	0.57	bal	--	0.51	- - - - - -			1.04	--	--	0.45
1B	--	--	0.008	0.012	--	--	0.04	0.003	0.007	- - - -		13.5	--	bal	--	15.0	--	--	--	0.01	- - - - - -		
2B	--	--	0.008	0.012	--	--	0.04	0.001	0.007	--	--	13.5	--	bal	--	35.0	- - - - - -			0.01	--	--	--
3B	--	--	0.04	--	--	--	0.04	0.003	0.007	0.25	--	13.5	--	bal	--	15.0	--	--	--	0.01	--	- - - -	
SA	--											16.0	--	bal	- - - - - - - -								
B1	--	--	0.006	0.010	0.03	--	0.04	0.003	0.007	--	--	13.8	--	bal	--	15.0	--	- - - -		0.01	--		
B2	--	--	0.008	0.011	0.01	--	0.04	0.004	0.007	0.17	--	13.7	--	bal	--	15.0	--	- - - -		0.01	--		
B3	--	--	0.009	0.009	0.02	--	0.83	0.003	0.007	--	--	11.7	--	bal	--	15.0	--	- - - -		0.01	--		
B5	--	--	0.04	0.011	0.004	--	0.04	0.003	0.007	0.17	--	13.7	--	bal	--	14.9	--	- - - -		0.01	--		
B6	--	--	0.06	0.011	0.003	--	0.01	0.003	0.007	0.16	--	13.4	--	bal	--	15.0	--	- - - -		1.97	--		
B7	--	--	0.04	0.011	0.004	--	0.83	0.003	0.007	0.10	--	13.6	--	bal	--	15.0	--	- - - -		0.01	--		
B9	--	--	0.005	0.009	0.01	--	0.04	0.049	0.007	--	--	13.7	--	bal	--	15.2	--	- - - -		0.01	--		--
B10	--	--	0.007	0.009	0.020	--	0.84	0.05	0.007	--	--	13.6	--	bal	--	15.2	--	- - - -		0.01	--		
B11	--	--	0.041	0.011	0.013	--	0.04	0.049	0.007	0.18	--	13.6	--	bal	--	15.2	--	- - - -		0.01	--		
B12	--	--	0.044	0.010	0.004	--	0.83	0.049	0.007	0.17	--	13.6	--	bal	--	15.2	--	- - - -		0.01	--		
811	--	--	0.025	0.007	0.005	--	0.04	0.003	0.007	--	--	13.4	--	bal	--	14.9	--	--	0.40	0.01	--		
E1	--	0.001	0.06	0.010	0.004	--	0.82	0.002	0.007	0.19	--	13.1	2.1	bal	--	15.1	- - - -		0.01	1.98	--		
E2	--	--	0.055	0.011	0.003	--	0.80	0.003	0.007	0.19	--	13.4	2.2	bal	--	15.0	--	--	--	0.01	--		
E3	--	--	0.053	0.011	0.004	--	0.82	0.003	0.007	0.17	--	13.2	--	bal	--	15.1	- - - - - -			1.97	--		
t4	--	--	0.040	0.008	0.006	--	0.83	0.003	0.007	--	--	13.2	2.1	bal	--	15.1	- - - - - -			1.98	--		
E5	--	--	0.009	0.010	0.008	--	0.83	0.002	0.007	0.17	--	13.2	2.1	bal	--	15.1	--	--	--	1.98	--		
E6	--	--	0.047	0.010	0.003	--	0.37	0.002	0.007	0.17	--	13.2	2.1	bal	--	15.1	- - - -		0.01	1.97	--	--	
E8	--	--	0.054	0.011	0.004	--	0.84	0.044	0.007	0.17	--	13.1	7.1	bal	--	15.1	- - - -		0.01	1.98	--		
E9	--	--	0.036	0.010	0.003	--	0.35	0.043	0.007	0.17	--	13.2	2.1	bal	--	15.1	- - - - - -			1.97	--		
E10	--	0.001	0.046	0.010	0.004	--	--	0.046	0.007	0.18	--	13.3	2.1	bal	--	15.1	--	--	0.01	1.98	--		
E11	--	--	0.035	0.007	0.003	--	0.84	0.002	0.007	--	--	13.2	2.1	bal	--	15.2	--	--	0.45	1.94	--		
112	--	0.002	0.023	0.007	0.005	--	0.35	0.003	0.007	--	--	13.2	2.1	bal	--	15.1	- - - -		0.42	1.95	--		
E13	--	--	0.019	0.008	0.009	--	0.01	0.002	0.007	--	--	13.2	2.1	bal	--	15.1	--	--	0.41	1.95	--	--	--
E14	--	--	0.044	0.010	0.003	--	0.01	0.002	0.007	0.09	--	11.2	2.1	bal	--	15.1	- - - -		0.23	1.97	--		
M1	--	--	--	--	--	--	--	--	--	- - - -		7.0	--	bal	--	15.0	--	--	--	--	--	--	--
M3	--	--	--	--	--	--	--	--	--	- - - -		7.0	--	bal	--	35.0	- - - -		--	--	--	--	--
M4	--	--	--	--	--	--	--	--	--	--	--	7.0	--	--	--	45.0	--	--	--	--	--	--	--
M6	--	--	--	--	--	--	--	--	--	- - - -		15.0	--	--	--	45.0	- - - -		--	--	--	--	--
M9	--	--	--	--	--	--	--	--	--	- - - -		2.0	--	- - - -		35.0	- - - -		--	--	--	--	--
M11	--	--	--	--	--	--	--	--	--	- - - -		- - - -		bal	--	35.0	- - - -		--	--	--	--	--
C	--	--	0.01	--	--	--	--	--	--	- - - -		--	--	bal	--	--	- - - -		--	--	--	--	--
D	--	--	0.02	--	--	--	--	--	--	- - - -		--	--	bal	--	--	- - - -		--	--	--	--	--
E	--	--	0.04	--	--	--	--	--	--	- - - -		--	--	bal	--	--	- - - -		--	--	--	--	--
H	--	--	0.10	--	--	--	--	--	--	--	--	--	--	bal	--	--	- - - -		--	--	--	--	--
K	--	--	0.15	--	--	--	--	--	--	--	--	--	--	bal	--	--	--	--	--	--	--	--	--
L	--	--	0.20	--	--	--	--	--	--	--	--	--	--	bal	--	--	--	--	--	--	--	--	--
M	--	--	--	--	--	--	--	--	--	--	--	12.0	--	bal	--	--	- - - -		--	--	--	--	--
P	--	--	0.12	--	--	--	--	--	--			12.0	--	bal	--	--	--	--	--	--	--	--	--
Zr1	--	0.1E-4	0.008	0.004	0.14	--	--	--	--	--	--	--	--	--	--	--	--	bal	--	--	--	--	--
ZrB1	--	4.4E-4[a]	--	--	--	--	--	--	--	- - - -		--	--	--	--	--	--	bal	--	--	--	--	--
ZrB2	--	0.22E-4[a]	--	--	--	--	--	--	--	- - - -		--	--	--	--	--	--	bal	--	--	--	--	--
Zr4	--	--	--	--	--	--	--	--	--	- - - -		0.094	--	0.20	--	--	--	bal	--	--	1.51	--	--
Zr4-Li_3	26E-4	--	--	--	--	--	--	--	--			0.10	--	0.20	--	--	--	bal	--	--	1.52	--	--
Ni-1Si	--	--	--	--	--	--	0.48	--	--	--	--	--	--	--	--	bal	--	--	--	--	--	--	--
Ni-1Ti	--	--	--	--	--	--	--	--	--	0.82	--	--	--	--	--	bal	--	--	--	--	--	--	--
Ni-1Al	--	--	--	--	--	0.46	--	--	--	--	--	--	--	--	--	bal	--	--	--	--	--	--	--
Ni-8Si	--	--	--	--	--	--	4.0	--	--	--	--	--	--	--	--	bal	--	--	--	--	--	--	--
Fe-Ni-Cr	--	--	0.006	--	--	--	0.04	--	--	--	--	13.8	--	bal	--	14.9	--	--	--	--	--	--	--
Fe-Ni-Cr-Li_2	9.4E-4	--	0.006	--	--	--	0.04	--	--	--	--	13.8	--	bal	--	14.9	--	--	--	--	--	--	--
Fe-Ni-Cr(1Si)	--	--	--	--	--	--	0.52	--	--	--	--	13.7	--	bal	--	14.8	--	--	--	--	--	--	--
Fe-Ni-Cr(1Ti)	--	--	--	--	--	--	0.04	--	--	0.82	--	13.7	--	bal	--	14.5	--	--	--	--	--	--	--
Fe-Ni-Cr(1Al)	--	--	--	--	--	0.46	0.04	--	--	--	--	13.7	--	bal	--	14.8	--	--	--	--	--	--	--
Fe	- - - - - - - -				- -									bal	--	--	- - - - - - - - - - - - - - - - - -						
Fe-Li_2	8E-4	- - - - - - - -			- -									bal	- -								
Fe-LowB	--	10E-4[a]	- - - -		- -									bal	- -								
Fe-HighB	--	0.010	--	--	- -									bal	- -								
PCA-20	--	0.001	0.083	0.006	--	--	0.42	0.068	0.007	0.25	0.91	13.83	2.06	bal	0.01	16.12	0.01	--	0.10	2.48	--	--	--
PCMA-6	--	--	0.18	0.003	--	--	0.91	--	--	--	--	15.94	14.59	bal	--	0.01	0.03	--	--	0.01	--	--	--

[a] ^{10}B.

Table 2.4.3. Alloys in the HEDL test matrix for MFE-6J and -7J

Alloy	Composition, wt %																	
	O	C	N	Al	Si	P	S	Ti	V	Cr	Mn	Fe	Ni	Cu	Nb	Mo	Ta	W
Low Activation																		
VO-2262	--	0.086	--		0.08	--	0.003	--	0.50	2.32	--	bal	0.02	--	-	-	--	--
VO-2263	--	0.093	--		0.00	--	0.002	--	1.01	2.38	--	bal	0.01	--	--	--	--	--
VO-2264	--	*0.096*	--		0.09	--	0.003	--	0.52	9.13	0.02	bal	--	-	-	-	-	0.01
VO-2265	--	0.197	--		0.09	--	0.003	--	1.23	9.14	1.08	bal	--	--	-	-	--	0.02
VO-2266	--	0.097	--		*0.09*	--	0.003	--	0.51	9.02	2.68	bal	--	--	--	--	--	0.01
VO-2267	--	0.089	--		0.10	--	0.005	--	1.05	12.2	6.47	bal	0.01	--	-	-	--	--
VO-2268	--	0.101	--		0.10	--	0.004	--	0.27	8.82	2.44	bal	--	--	-	-	--	0.89
VO-2269	--	*0.097*	--		0.11	--	0.005	--	0.28	11.8	6.47	bal	--	--	-	-	--	0.89
UC-19	--	0.11	--	0.043	0.30	0.007	0.015	0.043	1.50	2.46	0.30	bdl	0.05	0.04	--	0.02	--	--
GA-3X	--	0.15	--		--	--	--	--	0.30	9.0	--	bal	--	-	-	-	--	2.5
VO-2702	--	0.093	--	--	0.10	--	0.004	--	0.23	12.0	6.56	bal	--	--	--	--	0.14	0.82
VO-2700	--	0.111	--		0.11	--	0.005	--	1.00	12.0	6.50	bal	0.02	--	0.02	--	--	--
VO-2754	--	0.1	--	--	--	--	--	--	0.3	12.0	6.5	bal	--	--	--	--	0.2	1.0
VO-2755	--	0.1		--	--	--	--	--	1.0	12.0	8.0	bal	--	--	--	--	0.2	0.2
10996	--	0.10	--		0.12	0.007	*0.005*	--	0.21	11.8	3.33	bdl	0.01	--	--	--	--	
10998	--	0.11	--		0.10	0.007	0.006	--	0.20	12.0	6.57	bal	--	--	-	-	--	--
Special Alloys																		
E18	--	--	--	--	--	--	--	--	--	15	--	bal	12.0	--	--	--	--	
E90	--	--	--	--	--	--	--	--	--	15.0	--	bal	15.0	--	-	-	--	
E19	--	--	--	--	--	--	--	--	--	15.0	--	bal	20.0	--	-	-	--	
E20	--	--	--	--	--	--	--	--	--	15.0	--	bal	25.0	--	-	-	--	--
E22	--	--	--	--	--	--	--	--	--	15.0	--	bal	35.0	--	--	--	--	
E23	--	--	--	--	--	--	--	--	--	15.0	--	bdl	45.0	--	-	-	--	
R58	--	--	--		--	--	--	--	--	15.0	--	bal	60.0	--	-	-	--	
E37	--	--	--		--	--	--	--	--	8.0	--	bal	35.0	--	--	--	--	--
GE5	--	--	--		--	--	--	--	--	--	--	bal	35.0	--	-	-	--	--
GE10	--	--	--		--	--	--	--	--	--	--	bal	45.0	--	-	-	--	--
GE26	--	--	--		--	--	--	--	--	--	--	bal	60.0	--	-	-	--	--
GE29	--	--	--		--	--	--	--	--	--	--	bal	75.0	--	-	-	--	--
E38	--	--	--		--	--	--	--	--	20.0	--	bal	35.0	--	--	--	--	--
R41	--	--	--			--	--	--	--	5.0	--	bal	45.0	--	-	-	--	--
R48	--	--	--		--	--	--	--	--	10.0	--	bal	45.0	--	-	-	--	--
R72	--	--	--	--	--	--	--	--	--	--	30.0	bal	--	--	--	--	--	--
R73	--	--	--	--	--	--	--	--	--	5.0	30.0	bal	--	--	--	--	--	--
R74	--	--	--		--	--	--	--	--	10.0	30.0	bal	--	--	-	-	--	--
R76	0.005	0.60	0.05		0.4	*0.05*	--	--	--	2.0	30.0	bal	0.5	--	--	--	--	
R66	--	--	--	--	--	--	--	--	--	5.0	15.0	bal	--	--	-	-	--	
R83	*0.005*	0.60	0.05		1.0	*0.05*	--	--	--	5.0	15.0	bal	*0.5*	--	--	--	--	--
R67	--	--	--	--	--	--	--	--	--	15.0	15.0	bal	--	--	-	-	-	-
R87	0.005	0.10	0.10	--	1.0	*0.05*	--	--	--	15.0	15.0	bal	*0.5*	--	-	-	-	-
R69	--	--	--	--	--	--	--	--	--	10.0	20.0	bal	--	--	-	-	--	
R70	--	--	--		--	--	--	--	--	15.0	20.0	bal	--	--	-	-	--	--
R71	--	--	--	--	--	--	--	--	--	--	25.0	bal	--	--	-	-	--	--
R75	--	--	--	--	--	--	--	--	--	--	35.0	bal	--	--	--	--	--	--

Table 2.4.4. Allays in the JAERI test matrix for MFE-6J and -7J

Alloy	Composition, wt %																	
	C	N	O	Al	Si	P	S	Ti	V	Cr	Mn	Fe	Co	Ni	Cu	Nb	Mo	W
JPCA	0.06	0.0039		--	0.50	0.027	0.005	0.24	--	14.2	1.77	bal	0.002	15.6	--	--	2.28	--
C	0.02	0.0018	--	--	0.51	0.017	0.007	0.25	--	15.4	1.56	bal	--	15.6	--	0.08	2.4	--
K	0.02	0.004	--	--	0.48	0.015	0.005	0.29	--	18.0	1.46	bal	--	17.6	--	--	2.6	--
316	0.058	--	--	--	0.61	0.028	0.003	0.005	--	16.7	1.80	bal	--	13.5	--	--	2.46	--
High Ni																		
Alloy I	0.06	--	--	--	0.31	--	--	0.23	--	12.9	1.78	bal	--	24.9	--	0.03	5.43	--
0	0.007	--	--	--	0.16	0.003	0.003	0.01	--	13.0	1.50	bal	--	20.0	--	--	4.94	4.94
Ferritic Steel	0.056	0.0069	--	0.04	0.74	0.008	0.0059	--	0.11	8.9	0.70	bal	--	1.37	0.02	0.06	2.46	0.01
HT-9	0.198	0.0104	--	--	0.32	0.009	0.0013	--	0.22	11.7	0.55	bal	0.01	0.65	--	--	1.06	0.44
Dual Phase																		
A	0.004	0.004	--	0.022	0.13	--	0.005	--	--	23.2	--	bal	0.01	17.9	--	--	--	--
B	0.005	0.007	--	0.016	0.13	--	0.005	--	--	23.2	--	bal	0.01	16.0	--	--	--	--
C	0.004	0.003	--	0.006	0.16	--	0.006	--	--	23.1	0.05	bal	0.01	15.0	--	--	--	--
D	0.003	0.006	--	0.004	0.17	--	0.005	--	--	22.9	0.11	bal	0.01	11.9	--	--	--	--
E	0.002	0.003	--	0.005	0.17	--	0.005	--	--	23.0	0.05	bal	0.01	8.31	--	--	--	--
K	0.012	0.024	--	0.004	0.18	--	0.004	--	--	23.1	0.17	bal	0.01	9.62	--	--	--	--
G	0.004	0.004	--	0.005	0.15	--	0.006	--	--	23.1	0.06	bal	0.01	16.0	--	--	--	--
I	0.004	0.003	--	0.005	0.18	--	0.005	--	--	23.2	0.04	bal	0.01	15.2	--	--	--	--
J	0.004	0.006	--	0.007	0.16	--	0.005	--	--	23.2	0.03	bal	0.01	15.3	--	--	--	--
SAR																		
Type 304	0.06	--	--	--	0.25	0.034	0.023	--	--	18.2	0.75	bal	--	8.1	--	--	0.13	--
Type 316	0.06	--	--	--	0.39	0.032	0.012	--	--	16.1	0.84	bal	--	10.0	--	--	2.01	--
SN-1	0.01	--	--	--	1.22	0.023	0.005	--	--	16.9	0.94	bal	--	13.9	0.07	--	0.09	--
SN-5	0.013	0.01	--	--	0.58	0.028	0.001	--	--	26.7	1.15	bal	--	8.49	--	--	--	--
High Mn																		
Steel 1	0.006	0.30	0.013	--	0.50	0.003	0.004	--	--	18.0	17.2	bal	--	0.01	--	--	0.01	--
Steel 2	0.007	0.32	0.021	--	0.48	0.003	0.002	--	--	18.0	16.8	bal	--	2.01	--	--	0.01	--
All-Martensite	0.007	0.030	--	--	--	--	0.004	--	0.13	8.4	0.83	bal	--	--	0.29	0.055	1.79	--
Incoloy 800	0.02	--	--	--	0.4	--	0.002	0.56	--	20.8	0.9	bal	--	33.3	--	--	--	--
Pure Stainless Steel																		
HP 12 Ni	0.005	0.02	--	--	0.005	--	--	--	--	17.1	--	bal	--	11.8	--	--	--	--
HP 35 Ni	0.003	0.01	--	--	0.006	--	--	--	--	17.1	--	bal	--	35.3	--	--	--	--
HP 50 Ni	0.003	0.007	--	--	0.007	--	--	--	--	17.1	--	bal	--	49.9	--	--	--	--

Table 2.4.5. Test matrix for the MFE-6J and -7J capsules

Specimen type	Source	Number of specimens			
		60°C	200°C	330°C	400°C
Pressurized tubes	ORNL	34	15	39	33
	JAERI	4	10	6	6
Tube blanks	ORNL	6	6	6	6
	JAERI	3	3	3	3
Disk packets	ORNL	4	4	8	9
	HEDL	0	0	4	4
	JAERI	5	7	6	6
SS1 tensiles	ORNL	29	34	11	13
	JAERI	64	56	73	65
553 tensiles	ORNL	44	44	16	22
	HEDL	35	35	30	30
Grodzinski fatigue	JAERI	56	24	56	40
Crack growth	JAERI	18	18	10	10
	HEDL	18	18	0	0
Rod tensiles	JAERI	0	0	4	0
Hourglass fatigue	JAERI	0	0	0	5

2.5 NEUTRONIC8 CALCULATIONS IN SUPPORT OF THE ORR-MFE-4A AND -48 SPECTRAL TAILORING EXPERIMENTS — R. A. Lillie (Oak Ridge National Laboratory)

2.5.1 ADIP Task

ADIP Task I.A.2, Define Test Matrices and Test Procedures

2.5.2 Objectives

The objective of this work is to provide the neutronic design for materials irradiation experiments in the Oak Ridge Research Reactor (ORR). Spectral tailoring to control the fast and thermal fluxes is required to provide the desired displacement and helium production rates in alloys containing nickel.

2.5.3 *Summary*

PCP - 265 ppm

The calculated fluences from the ongoing three-dimensional neutronics calculations are being scaled to agree with experimental data. As of March 31, 1985, this treatment yields 201.9 at. ppm He (not including 2.0 at. ppm He from ^{10}B) and 13.19 dpa for type 316 stainless steel in ORR-MFE-4A and 155.9 at. ppm He and 10.60 dpa in ORR-MFE-4B.

a05

2.5.4 Progress and Status

The operating and calculated data for the ORR-MFE-4A experiment are summarized in Table 2.5.1. The calculated data for Al-H_2O and solid aluminum corepieces are based on the fluence scaling factors given previously.[1] The calculated data for the hafnium corepiece is based on these same scaling factors folded with the experimentally measured hafnium induced fluence reductions reported last period.[2]

The ORR-MFE-4A experiment was reinoved from the ORR on January 20, 1985. The data in Table 2.5.1 are listed for each corepiece. The exposure and full power days indicate the amount of time each corepiece was in the reactor. The thermal and total fluences represent the radiation levels seen by each corepiece. However, the helium level and displacement level represent the cumulative helium production and dpa levels (i.e., the helium production and dpa levels when the respective corepiece was removed). The final entry in Table 2.5.1 indicates the "closeness" of the experimental helium to dpa ratio to that expected in a fusion device first wall. When the Al-H_2O corepiece was replaced, the helium to dpa ratio was approximately 2.6% above that expected in a first wall. The ratio was 10% high at the insertion of the hafnium corepiece, but dropped to 9.6% when the experiinent was removed from the reactor.

Table 2.5.1. Operating and calculated data for the ORR-MFE-4A experiment

Corepiece	Al-H_2O	Aluminum	Hafnium
Exposure, MWh	337,332	277,476	160,124
Full Power Days[a]	468.5	385.4	222.4
Thermal Fluence, neutrons/m^2	8.39×10^{25}	4.57×10^{25}	1.64×10^{25}
Total Fluence, neutrons/m^2	2.21×10^{26}	2.20×10^{26}	1.04×10^{26}
Cumulative Helium, at. ppm[b]	76.1	164.5	201.9
Cumulative dpa[b]	5.35	10.70	13.19
Ratio[c]	1.026	1.100	1.096

[a]Full power for the ORR is 30 MW.

[b]Helium and dpa values are cumulative for type 316 stainless steel.

[c]Ratio represents the experimental He/dpa value divided by calculated fusion device first wall value of 13.97.

The operating and calculated data based on the fluence scaling factors' are summarized in Table 2.5.2 for the ORR-MFE-48 experiment. The hafnium corepiece was inserted in the ORR-MFE-4B experiment on February 5, 1985. This corepiece is the same as that used in the ORR-MFE-4A experiment. Since this corepiece had been exposed to approximately 7.3 full Dower months of irradiation in the ORR, additional burnup calculations were performed to determine its effectiveness in the ORR-MFE-4B experiment. These calculations also took into account the loss in thermal flux reduction brought about by the use of a 12- rather than 24-in. Hf sleeve.

Although the hafnium corepiece has lost some of its effectiveness due to burnup, it is acceptable for use in the ORR-MFE-4B experiment until this experiinent reaches the 13.19 dpa level attained in the ORR-MFE-4A experiment. In fact, at the 13.19 dpa level, the helium to dpa ratio in the ORR-MFE-4B experiment will be only 6.4% above the first wall ratio whereas a value of 9.6% existed in the ORR-MFE-4A experiment at the time of its removal. At present, the ORR-MFE-48 has undergone approximately one full power inonth of irradiation with the hafnium corepiece. Based on the projected data in Table 2.5.2, approximately

Table 2.5.2. Operating and calculated data for the ORR-MFE-4B experiment

Corepiece	Al-H_2O	Aluminum	Hafnium	
			Current[a]	Projected[a]
Exposure, MWh	305,355	324,432	21,470	172,359
Full Power Days[b]	424.1	450.6	29.8	239.4
Thermal Fluence, neutrons/m^2	7.30×10^{25}	5.02×10^{25}	2.07×10^{24}	1.82×10^{25}
Total Fluence, neutrons/m^2	1.86×10^{26}	2.38×10^{26}	1.31×10^{25}	1.09×10^{26}
Cumulative Helium,[c] at. ppm[b]	59.7	151.1	155.9	196.1
Cumulative dps,[c]	4.49	10.28	10.60	13.19
Ratio[d]	0.952	1.052	1.053	1.064

[a]Current and projected columns represent the current values as of March 31, 1985, and the projected values, respectively, for the hafnium corepiece.

[b]Full power for the ORR is 30 MW.

[c]Helium and dpa values are cumulative for type 316 stainless steel.

[d]Ratio represents the experimental He/dpa value divided by calculated fusion device first wall value of 13.97.

7.9 additional full power months of irradiation are needed to reach the dpa level attained in the ORR-MFE-4A experiment. Assuming a 0.86 duty factor, the ORR-MFE-4B experiment should attain the same dpa level as the ORR-MFE-4A in January 1986.

2.5.5 Future Work

The three-dimensional neutronics calculations that monitor the radiation environment in the ORR-MFE-4B experiment will continue with each ORR cycle. The scale factors used to scale the fluences obtained from these calcualtions will be updated as new experimental data become available.

2.5.6 References

1. R. A. Lillie and T. A Gabriel, "Neutronics Calculations in Support of the MFE-4 Spectral Tailoring Experiments," pp. 19–20 *in* ADIP Semiannu. Prog. Rep. Mar. 31, 1983, DOE/ER-0045/10, U.S. DOE, Office of Fusion Energy,

2. R. A Lillie, "Neutronics Calculations in Support of the ORR-MFE-4A and -4B Spectral Tailoring Experiments," pp. 16–19 in ADIP Semiannu. Prog. Rep. Sept. 30, 1984, DOE/ER-0045/13, U.S. DOE, Office of Fusion Energy.

2.6 NEUTRON DOSIMETRY AND DAMAGE CALCULATIONS FOR THE HFIR-CTR-30, -36, and -46 EXPERIMENTS

L. R. Greenuwd (Argonne National Laboratory)

2.6.1 ADIP/DAFS Tasks

AOIP - Task I.A.2 - Define Test Matrices and Procedures
DAFS - Task II.A.l - Fission Reactor Dosimetry

2.6.2 Objective

To characterize neutron irradiation experiments in terms of neutron fluence, spectra. and damage parameters (dpa, gas generation, transnutation).

2.6.3 Summary

Dosimetry measurements and damage calculations have been completed for the CTR 30, 36, and 46 experiments in HFIR. CTR 30 and 36 have the highest exposures seen to date uith fluences of 1.95×10^{23} n/cm^2 and 1.61×10^{23} nlcm^2, respectively. Work is in progress on the RB2 and T3 experiments in HFIR and a prototype of the Japanese experiments in ORR.

The status of all other experiments is summarized in Table 2.6.1.

Table 2.6.1 Status of Dosimetry Experiments

Facility/Experiment		Status/Comments
ORR	- MFE 1	completed 12/79
	- MFE 2	completed 06/81
	- MFE 4A1	Completed 12/81
	- MFE 4A2	Completed 11/82
	- MFE 4B	Completed 04/84
	- TBC 07	Completed 07/80
	- TRIO-Test	Completed 07/82
	- TRIO-I	completed 12/83
	- HF Test	Completed 03/84
	- JP Test	Samples Received 03/85
	- J6, J7	Samples Sent 02/85
HFIR	- CTR 32	Completed 04/82
	- CTR 31, 34, 35	Completed 04/83
	- T2, RB1	Completed 09/83
	- T1, CTR 39	Completed 01/84
	- CTR 40-45	Completed 09/84
	- CTR 30, 36, 46	completed 03/85
	- RB2, T3	Samples Received 11/84
	- CTR L7-56	Irradiations in Progress
	- JP 1-8	Irradiations in Progress
Omega West	- Spectral Analysis	Completed 10/80
	- HEDL1	Completed 05/81
	- HEDL2	Samples Sent 05/83
	- LANL 1	Completed 08/84
EBR II	- X287	Completed 09/81
IPNS	- Spectral Analysis	Completed 01/82
	- LANL1 (Hurley)	completed 06/82
	- Hurley	Completed 02183
	- Coltman	Completed 08/83

2.6.4 Progress and Status

Dosimetry measurements and damage calculations have been completed for the CTH **30, 36,** and **46** experiments in the peripheral target position of the High Flux Isotopes Reactor (HFIR) at Oak Ridge National Laboratory.

The present experiments are designed to study PCA, ferritic alloys, long-range ordered alloys, titanium alloys, and high nickel alloys in CTR **30;** fatigue specimens of austenitic Stainless steels in CTR **36;** and the impact properties of **12** Cr - 1 MoVW steel in CTH *46.* The exposure histories are as follows:

Experiment	Dates-	Exposure, MWD
30	07/80 - 11/81	43,316
36	11/82 - 04/84	38,069
46	02/83 - 06/83	10,620

Dosimetry capsules were located at six vertical positions in CTR 30 and at five positions in CTR **36** and **46.** Each capsule contained Fe, Ti, Co-Al, and Mn-Cu dosimetry wires; CTR 30 also contained additional helium samples in Cu, Fe, and Nb which cwld also be used for dosimetry.

The measured activities are listed in Tables **2.6.2-2.6.3.** The values are normalized to 100 MU and have been corrected for burnups. The very long exposures on CTR **30** and **36** necessitated rather sizeable burnup corrections of nearly 60% for the $^{59}Co(n,\gamma)^{60}Co$ reaction. In fact, the ^{60}Co activity level was found to actually be declining with further exposure due to burnout of the cobalt sample. In the case of ^{54}Mn produced by the $^{54}Fe(n,p)$ and $^{55}Mn(n,2n)$ reactions, burnup corrections are also hampered by our lack of information concerning the thermal cross section of ^{54}Mn. Previous work indicated a value of about 10 b for thermal capture in ^{54}Mn. With these present higher exposure data, we can now determine the proper value more accurately to be **14.6±1.5** b. We were also able to determine a better thermal cross section for ^{94}Nb of about **15.6** b (to $95g_{Nb}$) in good agreement with the ENDF/B-V value[2] of **14.9±1.0** b. A paper is now being written describing these new cross section determinations. In any case, these new Values permit us to correct the activities in Table I with an estimated uncertainty of about ±2% for all reactions except $^{59}Co(n,\gamma)$ which has a larger uncertainty of about ±5%.

All of the data in Tables **2.6.2-2.6.3** agree quite well with previous data[1] and the vertical gradients can be described by the following equation:

$$f(z) = a\,(1 + bz - cz^2) \qquad (1)$$

where a = midplane value, **b** = 5.02×10^{-4}, c = 1.00×10^{-3}, and **z** = height in cm. This equation has been slightly revised from previous work since it represents a global fit to all of the available data. The b term indicates ony a small asymmetry and is not significant near midplane. Some of the data is Shown in Fig. **2.6.1.**

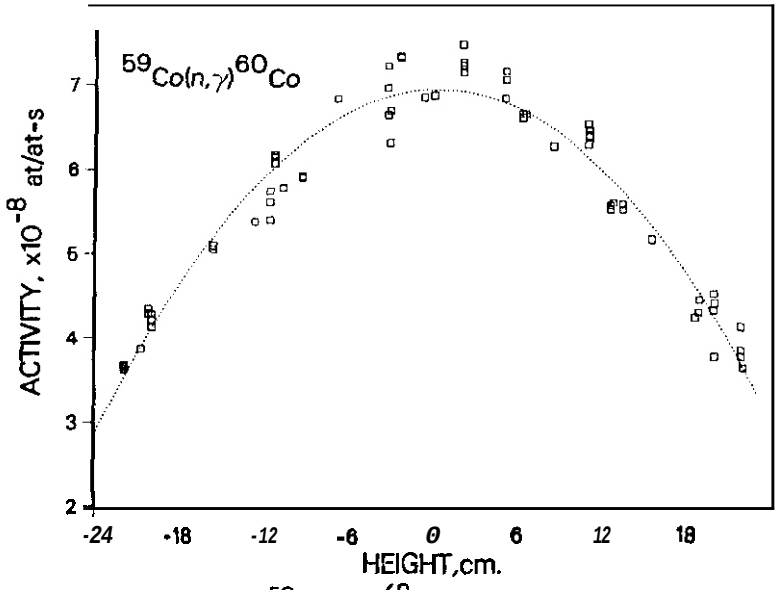

Fig. **2.6.1** Activation Measurements of the $^{59}Co(n,\gamma)^{60}Co$ Reaction are Shown for **63** Locations in HFIR During **14** Different Materials Experiments. The Dotted Line Represents a Least Square Fit to the Data. The Scatter of 5% is Partially Due to Uncertanties in the Burnup Corrections and Partially Due to Physical Differences in the Flux Levels and Experimental Assemblies.

Table 2.6.2. Measured Activities for HFIR-CTR 30

Values at 100 MW With Burnup Corrections
Accuracy ±2% Unless Noted

Heiaht, cm[a]	Activation Rate. at/at-s					
	$^{59}Co(n,\gamma)$[b]	$^{93}Nb(n,\gamma)$	$^{54}Fe(n,p)$	$^{46}Ti(n,p)$	$^{55}Mn(n,2n)$	$^{63}Cu(n,\alpha)$
	($\times10^{-8}$)	($\times10^{-9}$)	($\times10^{-11}$)	($\times10^{-12}$)	($\times10^{-13}$)	($\times10^{-13}$)
20.8	3.83	1.66	4.46	5.94	1.38	2.81
16.7	-	-	5.27	-	-	-
12.5	5.62	2.53	6.20	8.56	1.76	3.86
8.3	-	-	-	-	-	4.44
4.2	6.87	3.03	7.55	10.38	2.27	5.01
0.0	-	-	-	10.72	-	-
-4.2	7.00	3.07	7.40	10.54	2.16	5.04
-8.3	-	-	6.79	-	-	-
-12.5	5.41	2.36	6.89	9.04	1.83	4.63
-20.8	4.13	1.66	4.13	5.61	1.25	3.07
-25.0	-	-	-	4.41	-	-

[a] Height to Bottom of capsule; samples may vary by 1 cm.
[b] Co values ±5% due to large burnup corrections.

Jable 2.6.3. Measured Activities for HFIR-CTR36,46

Values at 100 MU uith Burnup Corrections
Accuracy ±2% Unless Noted

Height, cm	$^{59}Co(n,\gamma)$[a]	$^{58}Fe(n,\gamma)$[a]	$^{54}Fe(n,p)$	$^{55}Mn(n,2n)$
CTR 36:	(10^{-8})	(10^{-9})	(10^{-11})	(10^{-13})
18.5	4.29	1.22	4.55	1.40
8.5	6.31	1.68	6.49	2.10
-0.7	6.88	1.92	7.27	2.23
-10.7	5.80	1.68	6.43	1.93
-20.7	3.88	1.17	4.36	1.36
CTR 46:	$^{59}Co(n,\gamma)$	$^{58}Fe(n,\gamma)$[b]	$^{54}Fe(n,p)$	$^{46}Ti(n,p)$	$^{55}Mn(n,2n)$
	(10^{-8})	(10^{-9})	(10^{-11})	(10^{-12})	(10^{-13})
21.9	3.70	1.06	3.93	5.48	1.14
72.7	5.61	1.56	6.10	8.26	1.80
0.0	6.91	1.91	7.40	9.71	2.13
-12.7	5.38	1.45	6.28	8.64	1.79
-21.9	3.64	1.32	3.13	5.10	1.07

[a] ^{59}Co and $^{58}Fe(n,\gamma)$ values ±5% due to large burnup corrections for CTR 36.
[b] $^{58}Fe(n,\gamma)$ values ±5% on CTR 46.

Neutron fluence and damage parameters are listed in Table 2.6.4. These gradients are also described by equation (1) except for helium production in nickel which is listed separately in Table 2.6.4. The methods used to determine the helium and dpa from nickel are well described in recent papers.[3,4]

In the case of CTR 30, selected samples have been sent to Rockwell International for helium analysis.

Table 2.6.4. Neutron Fluence and Damage Parameters - HFIR-CTR M, 36, 46

Values at midplane; gradients use equation (1)

Energy	Neutron Fluence. x 10^{22} n/cm^2		
	CTR 30	CTR 36	CTR 46
Total	19.5	16.1	4.44
Thermal (<.5 eV)[a]	7.89	6.51	1.79
Fast (>.11 MeV)	5.23	4.31	1.20

Element	CTR 30		CTR 36		CTR 46	
	DPA	He, appm	DPA	He, appm	DPA	He, appm
Al	68.8	31.8	56.7	27.9	15.8	7.62
Ti	43.7	22.1	36.1	18.6	10.1	5.22
V	48.9	1.08	40.3	0.94	11.3	0.26
Cr	43.2	7.39	35.6	6.41	10.0	1.76
Mn[b]	47.4	6.44	39.1	5.65	10.9	1.54
Fe	38.2	13.0	31.5	11.38	8.84	3.12
cob	47.7	6.38	39.4	5.60	11.0	1.53
Ni East[c]	41.0	176.	33.9	151.	9.46	42.
Ni ^{59}Ni	35.0	19,848.	28.5	16,178.	5.02	2845.
Total	76.0	20,024.	62.4	16,329.	14.48	2887.
Cu	37.2	11.6	30.7	10.1	8.59	2.77
Nb	36.9	2.38	30.5	2.08	8.51	0.57
Mo	27.4	-	22.6	-	6.32	-
316SS[d]	44.0	2613.	36.2	2131.	9.75	378.

[a]Multiply X0.866 for 2200 m/s value; temperature effect not included.
[b]Thermal self-shielding important for Mn and Co.
[c]See Table 2.6.4 for Ni gradients.
[d]316SS: Fe(.645), Ni(.13), Cr(.18), Mn(.019), Mo(.026).

The damage parameters listed in Tables 2.6.4 and 2.6.5 shou rather large helium effects for the thermal nickel reaction. For CTR 30, the helium production has reached 2 atom percent and the extra displacements from the ^{56}Fe recoils (He/567) produce 35 dpa, nearly equal to the fast displacements.

Table 2.6.5. Helium and Disolacement Damage for 316 SS*

Helium Includes ^{59}Ni and Fast Reactions
CPA Includes Extra Thermal Kick (He/567)

Heiaht, cm	CTR 30		CTR 36		CTR 46	
	He, appm	DPA	-	DPA	He. appm	CPA
0	2613	44.0	2131	36.2	378	9.75
3	2588	43.5	2109	35.9	372	9.66
6	2515	42.4	2046	34.9	356	9.38
9	2391	40.4	1939	33.3	330	8.93
12	7214	37.6	1786	30.9	295	8.30
15	1983	34.0	15W	28.0	250	7.48
18	1693	29.6	1344	24.2	199	6.48
21	1343	24.3	1052	19.9	144	5.32
24	935	18.2	718	14.9	88	3.99

*316SS: Fe(.645), Ni(.13), Cr(.18), Mn(.019), Mo(.026).

2.6.5 Conclusions

Recent dosim try measurements and helium measurements lor copper also indicate that a thermal helium effect is present.' This effect is now being studied and is not included in Table 2.6.5. Since the effect in copper requires three successive thermal captures, the effect is much smaller than seen for nickel. For CTR 30, we predict that the effect may produce about 75 appm helium and 0.2 dpa in addition to the 12 appm helium and 37.2 dpa produced by fast neutrons. A joint paper uith Rockwell International is now being uritten describing this effect.

2.6.6 References

1. L. R. Greenwood, Alloy Development for Irradiation Performance, Semiannual Progress Reports, DOE/ER-0045/11, p. 30-37, Sept. 1983; DOE/ER-0045/13, p. 13–17, Sept. 1984.

2. S. F. Mughabgbab, M Divadeenam, and N. E. Holden, Neutron Cross Sections, Vol. I, Academic Press, New York, 1981.

3. L. R. Greenwood, A New Calculation of Thermal Neutron Damage and Helium Production in Nickel. J. Nucl. Mater. 115, 137-142 (1983).

4. L. R Greenwood, D. W. Kneff, R. P. Skouronski, and F. M. Mann, A Comparison of Measured and Calculated Helium Production in Nickel Using Newly Evaluated Neutron Cross Sections for ^{59}Ni, J. Nucl. Mater. 122, 1002–1010 (1984).

5. D. W. Kneff, B. M Oliver, R. P. Skowronski, and L. R. Greenwood, Damage Analysis and Fundamental Studies Quarterly Progress Report. DOE/ER-0046/20, pp. 13–16, February 1985.

2.6.7 Publications

L. R. Greenwood, A New Calculation of Thermal Neutron Damage and Helium Production in Nickel, J. Nucl. Mater. 115, 137–142 (1983).

L. R. Greenuwd, D. U. Kneff, R. P. Skouronski, and F. M. Mann, A Comparison of Measured and Calculated Helium Production in Nickel Using Neuly Evaluated Neutron Cross Sections for ^{59}Ni, J. Nucl. Mater. 122, 1002-1010 (1984).

2.7 OVERVIEW OF MIT, AOIP IRRADIATION EXPERIMENTS - G. Kohse, O.K. Harling and N.J. Grant (Massachusetts Institute of Technology)

2.7.1 AOIP Task

AOIP Task I.A.2, Oefine Test Matrices and Test Procedures.

2.7.2 Objective

The objective of this program is to develop and evaluate rapidly soidified alloys for potential fusion reactor applications. Austenitic steels (Path A), ferritic steels (Path E) and copper alloys prepared by various rapid solidification techniques will be analysed after exposure to high levels of atomic displacements and, in some cases, helium production.

2.7.3 Summary

Various rapidly solidified austenitic, ferritic and copper alloys have been produced at MIT for inclusion in AOIP neutron irradiation experiments. A brief summary of the alloys and their preparation and the achieved or projected irradiation parameters is provided.

2.7.4 Progress and Status

2.7.4.1 Introduction

The major objective of the AOIP work at MIT is to evaluate the potential of rapid Solidification (RS) technologies for producing alloys with improved irradiation performance. In support of this objective and other experiments (such as a study of the effects of boron doping), numerous alloys have been prepared and irradiated. Most of the specimens irradiated are in the form of TEM disks, and are analysed by post-irradiation TEM, and by miniature disk bend testing (MORT) for mechanical property estimation. A small number of miniature tensile specimens of the SS-2 type are also being irradiated. This report gives a brief description of the alloys prepared at MIT and other alloys included for comparison. The damaqe levels and helium accumulation achieved or expected in all irradiation experiments in which each alloy is included are sumnarized.

2.7.4.2 Alloy Composition, Preparation and Irradiation Parameters

A titanium modified 316 stainless steel designated PCA is the basis for one class of alloys which have been extensively studied at MIT. PCA (provided by Oak Ridge National Laboratories) has the composition (wt%): 16.59 Ni, 14.27 Cr, 1.96 Mo, 1.62 Mn, 0.53 Si, 0.32 Ti, 0.046 C, 0.008 N, other trace, balance Fe. RS alloys have been prepared by vacuum remelting of PCA with additions of Ti and C to the levels (wt%):

Alloy	Ti	C
PA1	0.32	.046
PA2	0.64	.092
PA3	0.90	.17
PA5	1.50	.25

PCA alloy has been irradiated in two forms, desiqnated AN (1050 °C, 1 h) and CW (20% reduction of area by cold swaging), to provide baseline data for comparison to RS results. Table 2.7.1 describes the thermomechanical treatments (TMT's) which have been applied to the RS materials. In all cases, the melt is solidified by roller quenching at coolinq rates of 10^5 - 10^6 °C/s. The designation "foil" describes material which was cold worked by rolling to the reduction of thickness listed, with annealing as indicated. TEM disks were then punched from the foils. (Such disks are not suitable for bend testing.) All the other material conditions listed were prepared from foils consolidated into rods by cold compaction and extrusion at 1080 °C (under vacuum) with area reduction ratio of 30:1. In these cases, cold work is introduced by swaging to the reduction of area indicated in the table. Additionally, an alloy designated PA3-OPC was prepared from the PA3 melt by the process of dynamic powder compaction.

The irradiation parameters for all irradiations in which these alloys were included are summarized in Table 2.7.2.

Alloys which were irradiated to investigate the effect of boron doping were prepared from an Allegheny Ludlum 316 stainless steel with composition (wt%): 16.67 Cr, 16.36 Ni, 2.26 Mo, 1.25 Mn, 0.51 Si, 0.0036 O_2, 0.0030 N, 0.0027 C, 0.0027 S, balance Fe. The alloy designated 316SS-B1 was melted in argon atmosphere with the addition of 1000 appm ^{10}B and 1000 appm Zr. Roller quenchinq to produce foils was followed by cold compaction, extrusion under vacuum at 1065 °C producing 23:1 reduction of area, cold swaging to 42% reduction of area and annealing at 850 °C for 1 h. Alloy 316SS-B2 was prepared with 5000 appm natural B and 5000 appm Zr and roller quenched as for B1. Specimens were punched from the roller quenched foils following annealing at 980 °C for 112 h. Table 2.7.3 summarizes the irradiation of these alloys.

Table 2.7.1. Therrnomechanical treatment applied to RS PA-type alloys prepared for irradiation experiments.

Material Designation	Thermomechanical Treatment
PAx-foil A	20% CW
-foil B	20% CW + 700 °C, 112 h
-foil C	20% CW + 850 °C, 112 h
-AN	as extruded (see text) + 60% CW + 850 °C, 112 h
-CW 1	as AN + 20% CW
-CW 2	as AN t 40% CW
-REC	as extruded t 60% CW t 700 °C, 112 h

Table 2.7.2. Irradiations of PCA and PA (RS) alloys.

Irradiation Experiment	Materials Irradiated	Temperatures (°C)	Damage (dpa)	Helium Accumulation (appm)
HFIR: CTR-30,31,32 (completed)	PCA-AN, CW PA1-AN, CW 1 PA2-AN	300 400 500 600	4.4, 17, 34 4.4, 17, 34 6.2, 17, 34 6.2, 17, 34	140, 1000, 3100 140, 1000, 3100 210, 1000, 3100 210, 1000, 3100
HFIR: CTR-42,43 (completed)	PA1-foil A,B,C PA3-foil A,B,C PA5-foil A,B,C PA3-REC	500 600	14 14	750 750
EBR-II: AD2 Recon-stitution	PA1-CW 1, CW 2 PA2-CW 1, CW 2 PA3-CW 1, CW 2 PA3-DPC	390 450 500 550	16 15 15 15	
ORR: MFE4 (nomina. - experiment in progress)	TEM: PCA-AN, CW PA1-AN, CW 1 PA2-AN SS2: PA1-AN, CW 1 PA2-AN, CW 1	330 400 500 600	10,20,30 10,20,30 10,20,30 10,20,30	

Oxide dispersion strengthened alloys have also been irradiated. Powders of 316 SS with composition (wt%): 16 Ni, 16 Cr, 2.5 Mo, 1.0 Mn, 0.5 Al, balance Fe, were prepared by vacuum atomization. The powders were attrited to thin flakes, cold compacted and extruded at 1066 °C to 30:1 reduction of area. This produces an alloy with a fine dispersion of Al_2O_3 particles. Material designated 316 SS-A1-AN was irradiated in this as-extruded (extensively recrystallized) state. 316SS-Al-CW was additionally cold swaged to 20% reduction of area. A similar alloy with a dispersion of Y_2O_3 particles was prepared from a 316 stainless steel with composition 16.67 Cr, 2.26 Mo, 1.25 Mn, 0.51 Si, 0.0027 C, 0.003 N, 0.0027 S, 1.0 Al, balance Fe. Vacuum atomized powders were again attrited to thin flakes and 4 volume % of 200 - 400 Å Y_2O_3 powder was mechanically alloyed. Extrusion was at 1150 °C with 16:1 reduction of area. Material designated 316SS-Y-AN was annealed at 1200 °C for 1 h. 316SS-Y-CW was cold swaqed to 25% reduction of area with an intermediate anneal at 850 °C for 1 h after 12% reduction. A third type of dispersion strengthened alloy was similarly prepared from a pure iron base. The powder composition was (wt%): 0.48 Be, 0.001 Al, 0.01 Cr, 0.001 Si, 0.1 Ni, balance Fe. After attrition to flakes a treatment in hydrogen at 800 °C was used for surface reduction and internal oxidation. Extrusion was at 1000 °C with 30:1 reduction of area, producing a fully recrystallized material designated FeBeO-AN. FeBeO-CW was extruded at 750 °C with 30:1 reduction of area. The irradiation of these alloys is also described in Table 2.7.3.

One amorphous alloy composed of 60% Ni, 40% Nb (with impurities at the ppm level) has also been irradiated. Alloy preparation involved levitation melting under arqon atmosphere followed by splat coolinq with a copper piston and anvil, at cooling rates of 10^8 °C/s. The material was irradiated in the as-splatted condition as described in Table 2.7.3.

The MIT ADIP qroup has proposed and investigated copper alloy systems as candidate fusion first wall materials for several years. Twenty copper alloys, both RS and inqot products, have been irradiated in a scopinq experiment. This irradiation has been completed and the specimens are now being analyzed to provide a preliminary assessment of the role of RS technology in enhanced irradiation performance of such alloys. Table 2.7.4 describes the alloys which were irradiated in ERR-I1 to a fluence of 14 dpa at 400 °C.

Table 2.7.3. Irradiation of boron doped 316 SS, oxide dispersion strengthened alloys and amorphous NiNb.

Irradiation Experiment	Materials Irradiated	Temperatures (°C)	Damage (dpa)	Helium Accumulation (appm)
EBR-II: AD2 (completed)	316SS-B1, E2 316SS-A1-AN, CW 316SS-Y-AN, CW FeBeO-AN, CW NiNb	 390 500 550	 13,29 13,29 13,29	
EBR-II: AD2 Reconstitution (completed)	316SS-A1-AN, CW	390 450 500 550	16 15 15 15	
HFIR: CTR-30,31,32 (completed)	NiNb	300 400 500 600	4.4, 17, 34 4.4, 17, 34 6.2, 17, 34 6.2, 17, 34	140, 1000, 3100 140, 1000, 3100 210, 1000, 3100 210, 1000, 3100

Composition (major alloy constituents) is qiven in each case. All the RS alloys were consolidated from gas atomized powders. Those desiqnated flake were attrited to thin flakes to promote oxide formation before the consolidation step. The table qives the extrusion temperature and the reduction in area of the billet during the extrusion step, as well as any subsequent TMT. The inqot products were received in sheet form and cold work referred to was introduced by rolling.

In addition to the above irradiations completed or in proqress, ferritic materials have been prepared for an irradiation planned in FFTF to 20 and 40 dpa. A 2 1/4 Cr-1 Mo steel was rapidly solidified by ultrasonic gas atomization. Consolidation was by extrusion under vacuum at 750 °C with area reduction of 10:1. The final processing step was hot forging (750 °C) to a 50% reduction in thickness. A 9 Cr-1 Mo steel was prepared by liquid dynamic compaction - a process in which the melt is sprayed onto a cooled substrate. The 95% dense material produced was hot isostatic pressed at 765 °C and 207 MPa for 1 h. It was then hot forged to 50% reduction in thickness. One-third size Charpy V-notch specimens were prepared from each of these alloys for irradiation testing.

Table 2.7.4. Composition and preparation of copper alloys irradiated in EBR-II.

1) RS alloys

Alloy	Composition (wt% - balance Cu)	Preparation
$Cu-Al_2O_3$: A1 A2	0.65 Al 2.8 Al	Flake + extrusion: 760 °C, 12:1
B1 E2	0.58 Al 2.65 Al	Flake + internal oxidation + extrusion: 760 °C, 22:1
MZC	0.6 Cr, 0.2 Zr, 0.02 Mg	Extrusion: 650 °C, 25:1
Cu-Ni-Ti	5 Ni, 2.5 Ti	Extrusion: 700 °C, 25:1 Flake + extrusion: 860 °C, 25:1
ZCA	0.57Al, 0.27 Zr, 0.22 Cr	Extrusion: 700 °C, 25:1
ZAC-1 -2B ZA8	0.32 Cr 0.33 Cr, 0.23 Zr 0.8 Zr	Extrusion: 650 °C, 30:1

Table 2.7.4. Composition and preparation of copper alloys irradiated in EBR-II (continued),

Alloy	Composition (wt% - balance Cu)	Preparation
MZC	0.6 Cr, 0.2 Zr, 0.02 Mg	Solution anneal + cold roll 75% + 475 "C, 1/2 h
Cu-Ni-Ti	5 Ni, 2.5 Ti	Solution anneal + cold roll 76% + 500 °C, 1 h
ZCA	0.57 Al, 0.27 Zr, 0.22 Cr	Cast, cold rolled 50%
Cu-Be	1.67 Ni, 0.38 Ni	INESCO proprietary TMT
151	1 Zr	Soft temper
194	2.35 Fe, 0.12 Zn, 0.03 P	Soft temper
195	1.5 Fe, 0.8 Co, 0.6 Sn, 0.1 P	Soft temper
SSC-155	0.11 Mg, 0.034 Ag, 0.06 P	Solution anneal + cold roll 50%
AMZIRC	0.16 Zr	Cold roll 80% + 450°C, 1 h
AMCROM	0.72 Cr	Cold roll SO% + 425 "C, 1 h
OFHC		Annealed Cold roll 20% Cold roll 50%
110 ETP		Cold roll 75%

2.8 ANALYSIS OF DAMAGE EXPOSURE RATES IN THE MATERIALS OPEN TEST ASSEMBLY OF THE FAST FLUX TEST FACILITY - R. L. Simons

2.8.1 ADIP/DAFS Task

ADIP - Task I.A.2-Define Test Matrices and Procedure
DAFS - Task II.A.1 - Fission Reactor Dosimetry

2.8.2 Objective

The objective of this effort is to calculate the irradiation damage parameters for the Materials Open Test Assembly (MOTA) in the Fast Flux Test Facility (FFTF).

2.8.3 *Summary*

The axial distribution of dpa/sec in stainless steel (Fe18Cr10Ni) and flux E > 0 MeV and E > 0.1 MeV were determined from the analysis of dosimetry measurements made during MOTA Cycles 1A and 1B.

2.8.4 Progress and Status

2.8.4.1 Introduction

The FFTF MOTA is an excellent facility for materials irradiation experiments for a number of reasons including: 1) high displacement rate and subsequent dpa, 2) large test volumes, 3) controlled and measured irradiation temperatures, and 4) quick recharging of metallurgical specimens between reactor cycles.

Dosimetry monitors irradiated in MOTA cycles 1A and 1B were analysed and axial distribution of dpa/sec and flux >0 MeV and >0.1 MeV were determined for MOTA.

2.8.4.2 Analysis and Results

The dosimetry in MOTA 1A consisted of seven spectral sets and nine gradient sets which were distributed axially and radially to obtain neutron spectra and flux gradient information. MOTA 1B dosimetry consisted of three spectral sets (two in the below core canister) and five gradient sets distributed axially. For the most part, the dosimetry in MOTA 1A was used to characterize the neutron environment in MOTA and the dosimetry in MOTA 1B was used to normalize the characterized environment. The normalization is justifiable because the neutron environment is expected to change little between reactor operating cycles.

The FFTF power time history (obtained from operations reports) was used as input to the TIMWH code' to determine saturation factors and the total effective full power exposure time. The reaction rates [disintegrations per second per nucleus, (dps/n)] at full power operation (400 MW) are tabulated for MOTA 1A and 1B in Tables 1 and 2 respectively. The uncertainty in the reaction rates was about 3% but they ranged from one to seven percent on standard deviation. The irradiation time for 1A was 1.750×10^7 seconds and for 18 was 9.466×10^6 seconds.

The measured reaction rates are used to adjust the apriori neutron spectrum using the generalized least square code FERRET.' The apriori neutron spectra for MOTA are from a three dimensional, 53 energy group-diffusion theory calculation of the FFTF for the pre-startup fuel loading condition.' The MOTA fluxes used in this analysis are from the subassembly 3404. Subassembly 3404 is a shim subassembly (filled with stainless steel pins) in a location with surrounding fuel and control rods which were nominally the same as those around MOTA. The diffusion theory calculations used six mesh points in each hexagonal subassembly. The fluxes used in this calculation were the average values of the six mesh points for each axial location. The calculation showed no significant radial gradient across the subassembly. The reaction cross sections and fission yields are based on ENDFIB-V nuclear data.

The fluxes (E >0.0 MeV and E >0.1 MeV) and dpa/sec in stainless steel (Fe18Cr10Ni) for MOTA 1A and 18 are shown in Figures 1 thru 3 and are tabulated in Table 3. The symbols are the adjusted values. The curve is an interpolation using the calculated values as a guide. Differences between measured and calculated exposure rates were <25% in core and above core. However, in the below core canister the measured and calculated differed by up to 80%. The accuracy of the adjusted exposures is 5-10% ($\pm 1\sigma$) in the core (levels 1 thru 5) and 10-15% ($\pm 1\sigma$) outside the core (bcc and levels 6 and 8). The analysis of the gradient sets shows that the flux drops <5% across the MOTA subassembly at all levels except in level 6. In level 6 the gradient wires show approximately 10% higher flux on the core center side of MOTA then the core edge side. This may be affected by the mass loading in level 6 or a nearby control rod.

Differences between MOTA 1A and 1B due to cycle to cycle fuel loading and control rod positioning is expected to be less than 5%. The MOTA 1B results generally fall within the one standard deviation uncertainties.

2.8.5 References

1. R. D. Bourquin, "TIMH - A Computer Program for the Determination of Fluence with a TIMH Varying Flux," BNWL-1492, Battelle Northwest (August 1970). TIMWH is a modified version of the TIMH program.

2. F. A. Schmittroth, "FERRET Data Analysis Code," HEDL-TME 79-40, Hanford Engineering Development Laboratory (Sept 1979).
3. D. W. Wooten, J. A. Rawlins, K. D. Dobbins, "Reaction Rates and Neutron Spectra in the FFTF at Full Power," American Nuclear Society, Vol. 16, 743-744, (1984).

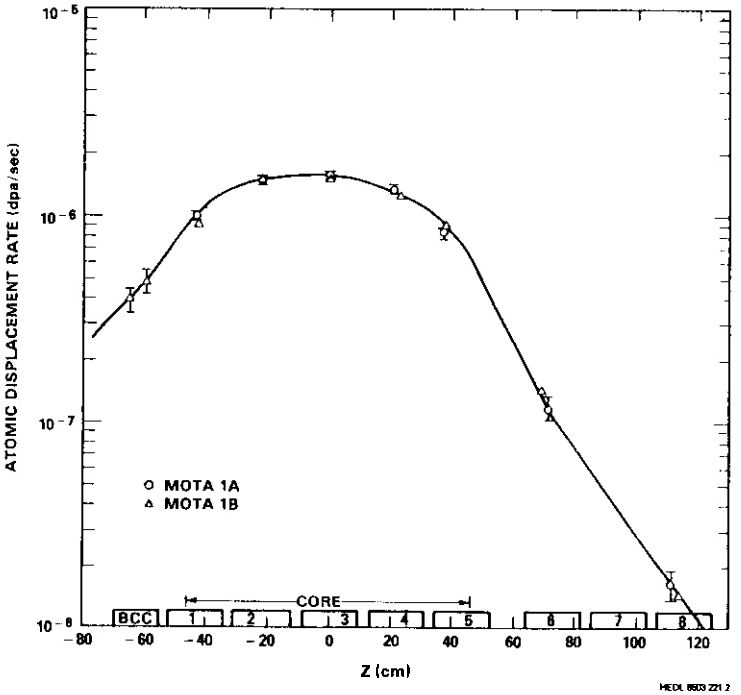

FIGURE 2.8.1. Displacement rate for stainless steel (Fe18Cr10Ni) in FFTF MOTA.

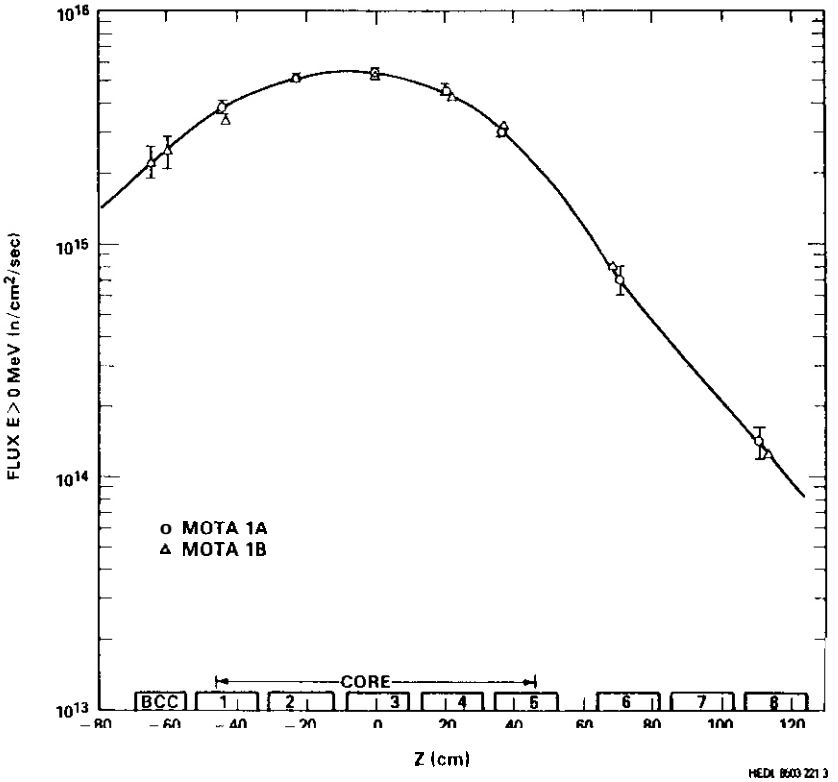

FIGURE 2.8.2. Flux E > 0 MeV in FFTF MOTA.

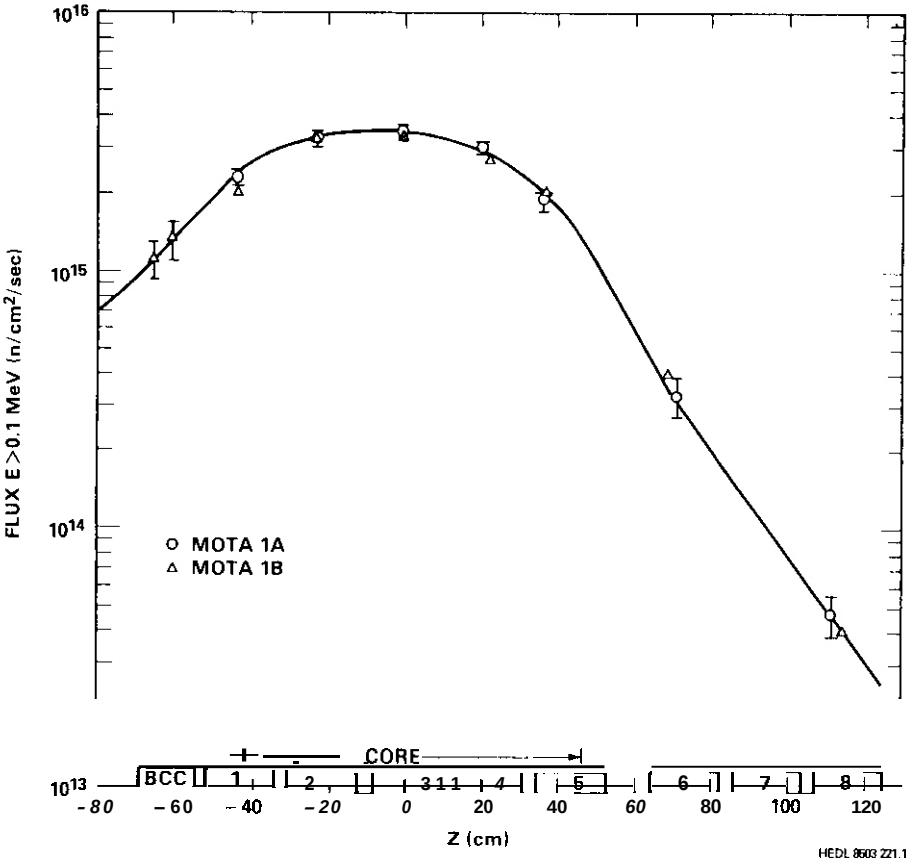

FIGURE 2.8.3. Flux E > 0.1 MeV in FFTF MOTA.

Table 2.8.1 Reaction rates (dps/n) from MOTA 1A which were used to adjust the spectra at various axial locations

Reaction \ Axial location (cm)	-44.27	-22.75	-0.03	+20.27	+36.78	+71.07	+111.46
$^{59}Co(N,\gamma)^{60}Co$	9.489-10	4.522-10	4.248-10	3.668-10	5.694-10	1.021+09	3.306-10
$^{58}Fe(n,\gamma)^{59}Fe$	5.152-11	5.378-11	5.861-11	4.771-11	3.503-11	1.857-11	5.128-12
$^{54}Fe(n,p)^{54}Mn$	2.420-11	4.205-11	4.535-11	3.802-11	2.141-11	6.885-13	3.181-14
$^{63}Cu(n,\gamma)^{60}Co$	1.386-13	2.425-13	2.579-13	2.172-13	1.227-13	3.583-15	2.386-16
$^{58}Ni(n,p)^{58}Co$	3.629-11	6.034-11	6.487-11	5.528-11	3.084-11	1.038-12	5.052-14
$^{45}Sc(n,\gamma)^{46}Ti$	1.757-10	2.031-10	2.152-10	1.787-10	1.237-20	6.195-11	2.015-11
$^{46}Ti(n,p)^{46}Sc$	3.050-12	5.385-12	5.859-12	4.883-12	2.781-12	7.963-14	2.426-15
$^{237}Np(n,f)$	1.433-09	2.289-09	2.613-09	2.038-09	1.166-09	1.369-10	1.393-11
$^{239}Pu(n,f)$	8.056-09	9.371-09	9.808-09	8.496-09	5.965-09	3.108-09	9.156-10
$^{235}U(n,f)$	8.354-09	9.567-09	1.004-08	8.581-09	6.208-09	3.273-09	9.784-10

Table 2.8.2 Reaction rates (dps/n) from MOTA 1B which were used to adjust the neutron spectra at various axial locations

Reaction \ Axial location (cm)	-65.34	-60.10	-43.17	-21.69	-2.38	21.37	t37.37	t68.99	t114.46
$^{59}Co(n,\gamma)^{60}Co$	3.099-09	3.317-09	1.160-09	4.382-10	3.904-10	3.484-10	4.420-10	1.198-09	3.324-10
$^{58}Fe(n,\gamma)^{59}Fe$	5.234-11	5.578-11	4.789-11	5.265-11	5.196-11	4.623-11	3.626-11	2.012-11	4.626-12
$^{54}Fe(n,p)^{54}Mn$	2.458-12	4.702-12	2.407-11	4.409-11	4.586-11	3.961-11	2.409-11	9.987-13	2.868-14
$^{63}Cu(n,\gamma)^{60}Co$	2.471-14	3.557-14							
$^{58}Ni(n,p)^{58}Co$	3.519-12	6.656-12							
$^{46}Ti(n,p)^{46}Sc$	2.814-13	5.630-13							
$^{237}Np(n,f)$	4.646-10	6.305-10							
$^{239}Pu(n,f)$	9.790-09	1.084-08							
$^{235}U(n,f)$	1.038-08	1.073-08							

TABLE 2.8.3 Dpa/sec and Flux E > 0 and > 0.1 MeV in FFTF MOTA 1A and 1B

(cm)	Flux E > 0 MeV (n/cm^2-sec)	Flux E > 0.1 MeV (n/cm^2-sec)	dpa/sec
-77.53	1.51×10^{15}	7.57×10^{14}	2.55×10^{-7}
-72.01	1.85×10^{15}	9.26×10^{14}	3.22×10^{-7}
-65.76	2.19×10^{15}	1.10×10^{15}	3.95×10^{-7}
-60.20	2.57×10^{15}	1.33×10^{15}	4.93×10^{-7}
-55.34	2.96×10^{15}	1.59×10^{15}	6.16×10^{-7}
-50.47	3.34×10^{15}	1.98×10^{15}	7.73×10^{-7}
-47.01	3.61×10^{15}	2.15×10^{15}	9.15×10^{-7}
-43.57	3.88×10^{15}	2.40×10^{15}	1.06×10^{-6}
-38.74	4.26×10^{15}	2.69×10^{15}	1.21×10^{-6}
-33.90	4.61×10^{15}	2.92×10^{15}	1.33×10^{-6}
-29.04	4.98×10^{15}	3.10×10^{15}	1.43×10^{-6}
-24.15	5.11×10^{15}	3.25×10^{15}	1.50×10^{-6}
-19.34	5.26×10^{15}	3.36×10^{15}	1.55×10^{-6}
-14.62	5.44×10^{15}	3.44×10^{15}	1.59×10^{-6}
-9.92	5.50×10^{15}	3.49×10^{15}	1.62×10^{-6}
-5.03	5.50×10^{15}	3.51×10^{15}	1.63×10^{-6}
0.00	5.39×10^{15}	3.48×10^{15}	1.61×10^{-6}
4.95	5.26×10^{15}	3.39×10^{15}	1.57×10^{-6}
9.80	5.02×10^{15}	3.27×10^{15}	1.52×10^{-6}
14.66	4.82×10^{15}	3.13×10^{15}	1.45×10^{-6}
19.51	4.50×10^{15}	2.97×10^{15}	1.35×10^{-6}
24.36	4.18×10^{15}	2.72×10^{15}	1.25×10^{-6}
29.32	3.79×10^{15}	2.47×10^{15}	1.14×10^{-6}
34.10	3.36×10^{15}	2.21×10^{15}	1.02×10^{-6}
38.98	2.91×10^{15}	1.91×10^{15}	8.75×10^{-7}
43.85	2.46×10^{15}	1.58×10^{15}	7.08×10^{-7}
47.32	2.16×10^{15}	1.33×10^{15}	5.80×10^{-7}
50.77	1.87×10^{15}	1.09×10^{15}	4.57×10^{-7}
55.63	1.50×10^{15}	8.17×10^{14}	3.27×10^{-7}
60.50	1.17×10^{15}	6.03×10^{14}	2.33×10^{-7}
67.41	8.06×10^{14}	3.95×10^{14}	1.47×10^{-7}
76.87	5.45×10^{14}	2.48×10^{14}	8.98×10^{-8}
88.33	3.42×10^{14}	1.41×10^{14}	5.01×10^{-8}
100.27	2.18×10^{14}	8.08×10^{13}	2.85×10^{-8}
111.22	1.43×10^{14}	4.77×10^{13}	1.69×10^{-8}
122.16	9.32×10^{13}	2.79×10^{13}	9.96×10^{-9}

3. AUSTENITIC STAINLESS STEELS

3.1 MINOR COMPOSITIONAL VARIATIONS OF THE AUSTENITIC PCA TO EXPLORE MC FORMATION AND STABILITY CHARACTERISTICS FOR IMPROVED RADIATION RESISTANCE — P. J. Maziasz (Oak Ridge National Laboratory) and S. Jitsukawa (Japan Atomic Energy Research Institute)

3.1.1 AOIP Task

ADIP Task I.C.I, Microstructural Stability

3.1.2 Objectives

The objective is to vary the composition of the PCA to further stabilize the MC phase, now that an optimum preirradiation microstructural condition (and appropriate thermal mechanical treatments) has been defined. Minor alloying element concentrations were varied to determine their effect on MC formation characteristics (particularly at grain boundaries) and MC phase composition.

3.1.3 *Summary*

The original PCA exclusively forms MC carbides in the matrix and grain boundaries during short-term aging, with a small amount of Laves appearing at longer times. The MC phase shows a surprisingly high solubility for chromium. Small laboratory melts were made which vary C, Si, Mo, and Ti alloy concentrations together with P and Nb additions. Solution-annealed (SA) alloys with (Ti t Nb), or Nb and lower Si levels, exhibited grain boundary MC formation after 166 h at 800°C, whereas other alloys formed only coarse $M_{23}C_6$. None formed intermetallics. Alloys with stable grain boundary MC formation in the SA condition showed excellent resistance to recrystallization when cold worked (CW). The MC phase composition was quite sensitive to alloying changes; combinations of Nb, C, and P alloying additions lowered the (Mo + Cr) content of the Ti-rich MC phase, particularly in small particles.

3.1.4 Progress and Status

3.1.4.1 Introduction

Previous work outlined the alloy development efforts that led to the selection of the 83 condition (SA t 8 h at 800°C + 25% CW) as the optimum preirradiation microstructural condition of the Path A PCA to provide both void swelling and helium embrittlement resistance.'-3 An essential feature of this void swelling resistance (demonstrated in HFIR) is the formation and stability of a fine dispersion of MC particles in the PCA during irradiation.[4] Likewise, the helium embrittlement resistance is attributed to the formation of medium-coarse MC precipitates at the grain boundaries prior to irradiation which then remain stable during irradiation.[5] Radiation resistance fails when matrix and grain boundary MC particles become unstable and dissolve.' Therefore, it is sensible to seek greater MC stability for improved radiation resistance by appropriate alloy compositional modification.

Modern analytical electron microscopy (AEM) has demonstrated that the titanium-rich MC phase in molybdenum-containing steels, like type 316, can dissolve substantial amounts of Mo and/or Cr.[6-8] The composition and stoichiometry of the titanium-rich MC phase may also vary with particle size.[9] By contrast, the niobium-rich MC phase appears fairly pure. Therefore, two alloying strategies appear viable for manipulating the stability of the MC phase. The first would obviously be to change the alloy in a manner compatible with the phase's natural solute enrichment/depletion characteristics (i.e., increase *Ti*, C, and Mo while reducing Si). The second would be to intentionally add elements that enter the MC phase itself and possibly alter its solubilities for other elements, like niobium in combination with titanium to reduce the solubility of Mo and/or Cr. Toward this end, the first set of a series of small experimental laboratory heats of modified PCA alloys are examined here.

3.1.4.2 Experimental

Compositions of the first nine experimental alloys are given in Table 3.1.1, with compositions of several commercial steels, including the original PCA (K-280 heat), given in Table 3.1.2. The experimental heats were homogenized (24 h at 1275°C) and fabricated the same as the PCA (K-280 heat) with the final SA being 1 h at 1100°C and the final CW level being 25%. Samples were aged at 800°C for 166 h, together with pieces of commercial type 316 and PCA; the samples were wrapped in a tantalum foil and encapsulated in quartz tubes evacuated and backfilled with argon gas. The SA material was intended to test the grain boundary MC-forming characteristics of the various alloys, while recrystallization resistance of the CW material was used to test the stability of fine MC particles.

In addition to conventional transmission electron microscopy (CTEM) performed on thin foils, AEM was used to analyze phase compositions on extraction replicas made from the SA material aged for 166 h at 800°C. The MC phase compositional information was correlated with alloying changes and with the MC microstructural characteristics. AEM was performed on a Philips EM400 equipped with a field emission gun (FEG) for high electron intensity at very small probe sizes. Replicas were also analyzed using a liquid N_2 cold stage (with beryllium holder) to eliminate contamination during analysis. It should be noted that a fine high brightness probe together with the extraction replicas were necessary to accurately analyze phase particles smaller than ~10 nm in diameter.

Table 3.1.1. Compositions of experimental heats of PCA with compositional variations

Alloy designation	Composition,[a] wt %											
	Ni	Cr	Mo	Mn	Si	Ti	Nb	C	P	N	S	B
PCA-1	16	14	2.5	2.1	<0.01	0.13	0.12	0.043	0.001	0.0003	0.008	(0.001
PCA-2	16	14	1.4	2.0	(0.01	0.14	0.11	0.053	0.001	0.0004	0.007	(0.001
PCA-3	15.8	14.3	2.5	2.0	0.42	0.13	0.11	0.056	0.001	0.0005	0.007	(0.001
PCA-4	16	14	2.5	2.1	0.07	(0.01	0.26	0.051	0.001	0.0003	0.007	(0.001
PCA-5	15.9	14.4	1.5	2.1	0.11	<0.01	0.26	0.048	0.001	0.0002	0.007	(0.001
PCA-6	16	13.9	2.4	2.1	0.46	0.25	(0.01	0.081	(0.001	0.0004	0.008	(0.001
PCA-7	16	14	2.6	2.1	0.42	<0.01	<0.01	0.057	0.001	0.0002	0.007	(0.001
PCA-8	16	13.9	2.7	2.1	(0.01	0.17	0.14	0.081	0.001	0.0007	0.008	(0.001
PCA-9	16	13.8	2.5	2.0	0.41	0.25	<0.01	0.073	0.03	0.0005	0.007	<0.001

[a]Balance iron.

Table 3.1.2. Compositions of several commercial heats of austenitic stainless steel

Alloy designation	Composition,[a] wt %											
	Ni	Cr	Mo	Mn	Si	Ti	Nb	C	P	N	S	B
316 (DO-heat)	13	18	2.6	1.9	0.8	0.05	--	0.05	0.01	0.05	0.016	0.0005
316 (N-lot)	13.5	16.5	2.5	1.6	0.5	--	--	0.05	0.01	0.006	0.006	0.0008
316 (heat X-15893)	12.4	17.3	2.2	1.7	0.7	--	0.01	0.05	0.03	--	0.015	0.0004
316 + Ti (R1 heat)	12	17	2.5	0.5	0.4	0.23	--	0.06	0.01	0.006	0.013	--
PCA (K-280 heat)	16.2	14	2.3	1.8	0.4	0.24	--	0.05	0.01	0.01	0.003	--

[a]Balance iron.

3.1.4.3 Results

Microstructural Behavior of Commercial Alloys — SA — In general, type 316 stainless steel forms combinations of $M_{23}C_6$, M_6C, Laves, χ, and σ phases in the temperature range of 650 to 900°C, at aging times of 10 to 100 h or longer.[10] Precipitation kinetics reach a maximum at 800°C. In this work, all three heats of type 316 stainless steel formed coarse $M_{23}C_6$ at grain boundaries after 166 h at 800°C, but matrix precipitation varied considerably from heat to heat, as shown in Fig. 3.1.1. The N-lot 316 had no intragranular precipitation while the DO-heat 316 had copious amounts of coarse Laves and χ phase particles; behavior of the X-15893 heat of 316 was intermediate between these extremes.

The addition of titanium to type 316 stainless steel induced formation of the MC phase during aging. Intragranular MC formation in the R1-heat of 316 + Ti suppressed formation of $M_{23}C_6$, Laves, and χ phases compared to DO-heat 316 after long-time aging at 800°C, as shown in Fig. 3.1.2. Some MC also formed at grain boundaries and suppressed formation of $M_{23}C_6$, but the formation of intergranular σ phase was greatly enhanced in the 316 + Ti relative to 316. By contrast, only MC was observed in the matrix and at grain boundaries in the PCA (K-280 heat) relative to type 316 stainless steel after 166 h at 800°C, as seen in Fig. 3.1.3.

Microstructural Behavior of Commercial Alloys — CW — In general, cold working enhanced precipitation kinetics and the formation of intermetallic relative to carbide phases compared to SA material.[11] The as-cold-worked structure also began to recover in type 316 stainless steels when precipitation occurred; CW 316 (DO-heat) began to recrystallize at ~700°C and above,[12] as seen in Fig. 3.1.4. The formation of very fine MC precipitates pinned dislocations to prevent recovery and recrystallization until higher temperatures in

ORNL-PHOTO 1345-85

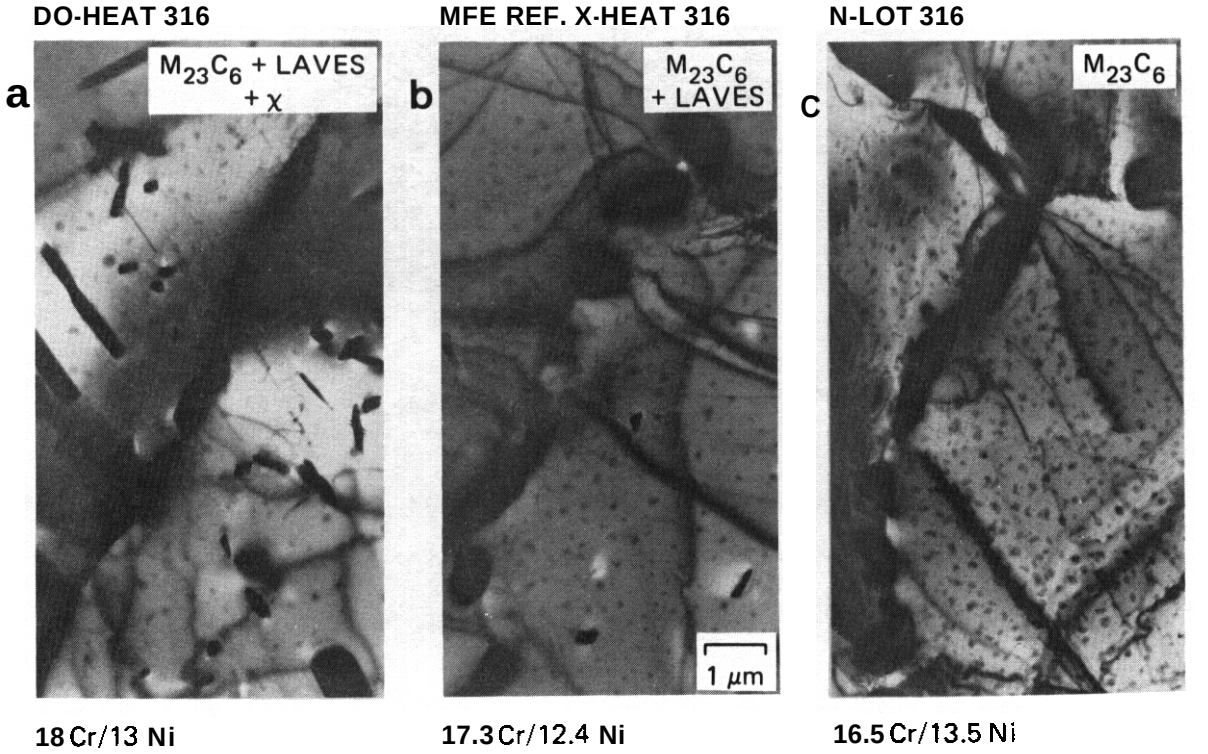

Fig. 3.1.1. Precipitation differences for several different heats of type 316 stainless steel aged for 166 h at 800°C in the solution-annealed condition. (a) DO-heat, (b) X-15893 heat (MFE reference heat), and (c) N-lot type 316.

ORNL-PHOTO 1313-85

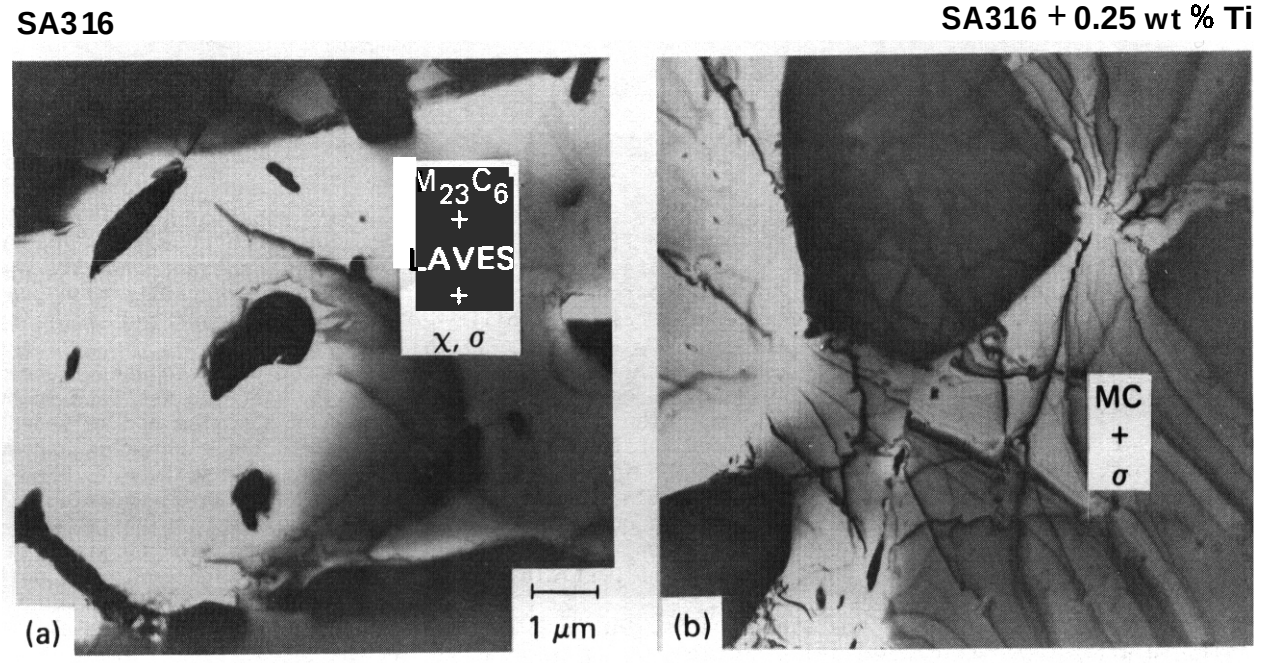

Fig. 3.1.2. Precipitation of σ phase in (a) SA 316 + Ti (R1 heat) compared to (b) SA 316 (DO-heat) for long time aging (2770 h) at 800°C.

ORNL-PHOTO 1777-85

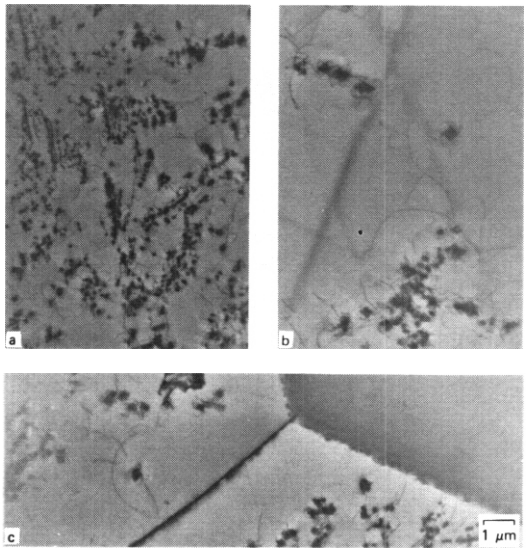

Fig. 3.1.3. The formation characteristics of MC precipitation in SA PCA (K-280 heat) aged for 166 h at 800°C. Nonuniform (a) patches, (b) clusters of MC particles in the matrix, and (c) medium-coarse MC precipitation are found along grain boundaries.

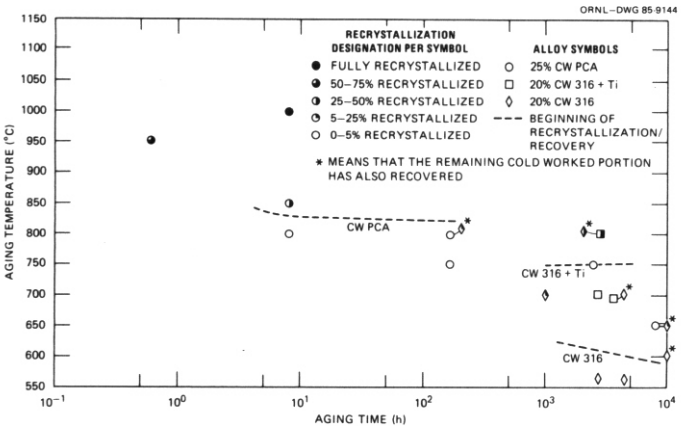

Fig. 3.1.4. Recrystallization data on 25%-CW PCA (K-280 heat), 20%-CW 316 t Ti (R1 heat), and 20%-CW 316 (00-heat) after aging for various times and temperatures. Generally the titanium-modified steels resist recrystallization better than does type 316.

CW 316 + Ti (R1-heat) and CW PCA (K-280 heat) relative to CW 316 (DO-heat),[12,13] as also seen in Fig. 3.1.4. The microstructure of CW PCA (K-280 heat) is shown in Fig. 3.1.5 after aging for 166 h at 800°C. Most of the structure resisted recovery, with fine MC precipitation along the dislocations, but a few small, new dislocation-free grains were also found. Fine MC apparently dissolved during the recrystallization process, to be replaced by coarser clusters of MC in the new grain. Stability of fine MC particles and stability of the dislocation structure appear to be related.

Phase Microcompositional Behavior in Commercial Alloys — SA and CW — The precipitate phases found in type 316 stainless steel were generally rich in molybdenum and chromium. The M_6C carbide was rich in Mo. Si, Cr, and Ni (all other phases were nickel-poor); the $M_{23}C_6$ carbide was rich in chromium and molybdenum. The intermetallic χ, Laves, and a phases contained substantial iron in addition to their chromium and molybdenum enrichments; Laves phase was the richest of the intermetallics in molybdenum and silicon.

Phase amounts varied from heat to heat in type 316 stainless steel and in the titanium-modified steels (R1 and K-280 heats), but phase compositions remained quite constant. These phase compositions showed little change with aging temperature (except Laves) or time and little sensitivity to SA or CW starting condition. Finally, their compositions show little or no particle size dependence, although most were quite coarse.

In contrast to the behavior of the other phases, the MC phase showed considerable compositional sensitivity to alloy composition, initial condition, aging temperature, and particle size. Compositional analyses for the MC phase are presented in Table 3.1.3 for both titanium-modified heats of steel and just for the PCA (K-280) in Fig. 3.1.6. Smaller particles (less than –100 nm in diameter) contained more Cr, Mo, and Fe at the expense of Ti as particle size decreased, particularly at lower temperatures. In both heats of steel, small MC particles were more dilute in the SA relative to the CW material after similar aging. The TiC was of higher purity in particles larger than –150 nm.

ORNL-PHOTO 1314-85

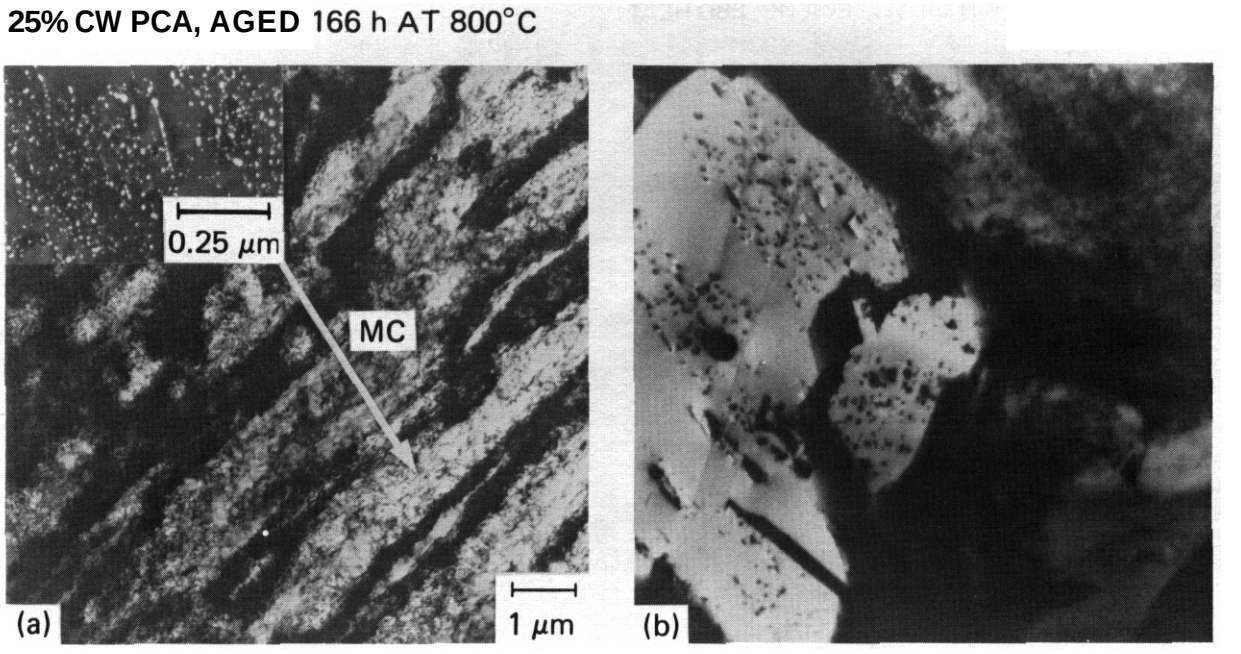

Fig. 3.1.5. Recrystallization behavior of 25%-CW PCR (K-280 heat) after aging for 166 h at 800°C. (a) Unrecrystallized regions (–95 vol % of material) with the as-cold-worked dislocation structure pinned by fine MC precipitate (dark-field inlay) resist recovery; (b) an isolated. recrystallized, dislocation-free grain in which fine MC has dissolved and coarse MC has precipitated.

Table 3.1.3. MC phase compositions in aged comnercial austenitic stainless steels

Aging conditions		Phase composition,[a] at. %								Comments
Temperature (°C)	Time (h)	Si	Mo	Cr	Ti	V	Nb	Fe	Ni	
					SA 316 + Ti (R1 Heat)					
600	2770	3	36	25	31	1	n.d.	4	n.d.[b]	[1][c] 7–10 nm in diameter
		n.d.	18	3	77	n.d.	n.d.	1.7	0.3	[8] 48–100 nm in diameter
700	2770	n.d.	29	5	63.4	0.2	1.2	1	0.2	[6] 48–100 nm in diameter
					20%-CW 316 + Ti (R1 Heat)					
600	4400	n.d.	31	14	43	n.d.	1	11	n.d.	[3] 7-10 nm in diameter or smaller
					SA PCA (K-280 Heat)					
800	166	4.2	4.3	27.3	58.2	4.6	0.1	0.7	0.2	[4] –18 nm in diameter
		0.7	4.0	1.4	93	0.1	0.2	0.2	0.1	[4] –270 nm in diameter
					50%-CW PCA (K-280 Heat)					
800	166	n.d.	12.4	10.3	75.6	n.d.	0.3	1.1	0.8	[2] Small, equiaxed, 5–20 nm in diameter
		n.d.	21.4	9	69	n.d.	0.1	0.3	0.1	[3] Small rods, 35 nm in diameter
		n.d.	13.8	4.1	79.4	n.d.	0.1	2.2	0.4	[3] 90–150 nm in diameter

[a]Normalized analysis of metal atoms, excluding light elements like C, N and O.
[b]n.d. = none deteced.
[c]Numbers in brackets indicate the number of individual particles or small clusters analyzed.

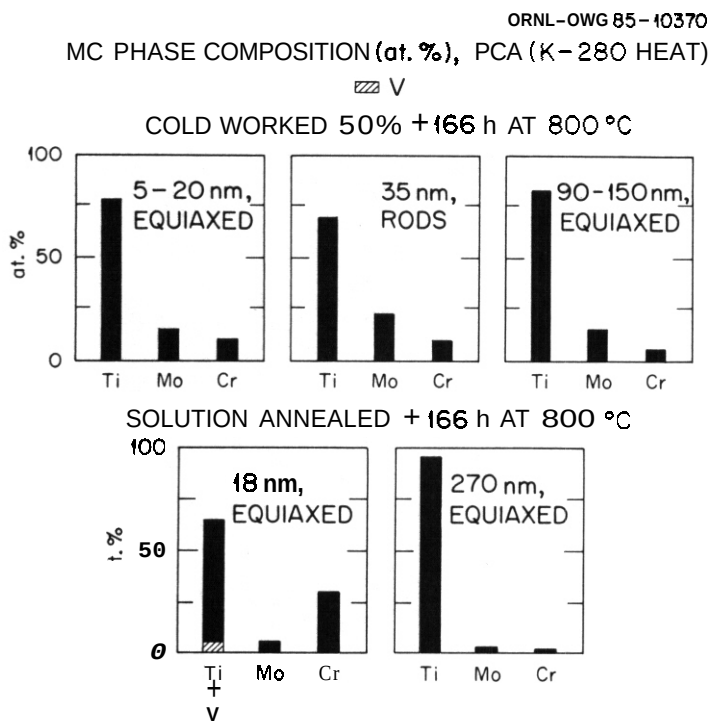

Fig. 3.1.6. Histographs of the MC phase composition of various portions of the total size population of particles formed in either SA or 50%-CW PCA (K-280 heat) aged for 166 h at 800°C. Note the molybdenum and chromium contents of smaller particles.

The variability of the fine MC phase composition supports the alloy development strategy of seeking to manipulate MC phase composition (and possibly phase stability) via alloying.

Microstructural Behavior of Experimental PCA Alloys — SA — Experimental alloys with niobium (PCA-4) or combined Ti and Nb (PCA-1) additions and lower Si levels demonstrated the best grain boundary MC formation characteristics. Detailed microstructural results on all alloys are given in Table 3.1.4. Microstructures from thin foils or replicas for several alloys are shown at lower magnification in Fig. 3.1.7; grain boundary microstructures at higher magnifications are shown in Fig. 3.1.8. Other alloys (i.e., PCA-2 or -6 in Fig. 3.1.8) had little or no grain boundary MC and had coarse $M_{23}C_6$ particles that were either equiaxed or elongated in the plane of the boundary. Even the best experimental alloys had some coarse $M_{23}C_6$ in addition to finer MC at the grain boundaries. whereas the PCA (K-280 heat) had only MC and no $M_{23}C_6$ by comparison. Possibly this is due to the much higher nitrogen in the PCA relative to the experimental alloys (0.01 compared to —0.0005 wt %, respectively).

The BCA-7, without titanium, demonstrated that the 16Ni/14Cr austenite of the PCA alloys was more stable to general precipitate decomposition (either carbides or intermetallics) than the 13Ni/18Cr austenite of type 316 (Table 3.1.4 compared to Fig. 3.1.1). The PCAs-2, -3, -6. and -9 all exhibited stringers of MC particles parallel to and close to grain boundaries, suggesting grain boundary migration away from the MC particles.

Microstructural Behavior of Experimental PCA Alloys — CW — The CW PCA alloys that exhibited the best recrystallization resistance were the same alloys that exhibited grain boundary MC formation in the SA condition (alloys-1, -4, -8). The results are also described in Table 3.1.4. The exception was PCA-5 which, although it formed grain boundary MC in the SA condition, also had lower molybdenum. Both PCA-5 and -2 demonstrated the importance of molybdenum; recrystallization resistance was lost when it was reduced. In general, the alloys showed no hint of recovery in the unrecrystallized regions of the material, regardless of the recrystallization fraction. These unrecovered regions always had the same microstructure of fine MC particle formed along the dense dislocation network. The precise role of fine MC stability in recrystallization resistance is not clear because the alloys that recrystallized most readily also exhibited hints of grain boundary migration in the SA condition (PCAs-2, -3, -6, and -9). However, fine MC formation and stability play an important role because PCA-7 without titanium recrystallized almost completely.

Phase Microcompositional Behavior of Experimental PCA Alloys — SA — The smallest MC particles were most sensitive to alloying changes, with (Ti + Nb) levels varying inversely to (Cr + Mo + Fe) levels. Alloy PCA-2 (Ti + Nb, lower Mo) formed finer MC with lowest amounts of (Cr + Mo), whereas MC in the PCA-6 (Ti, higher Si and C) contained the most (Cr + Mo), nearly 50 at. %. Phase compositions for MC particles analyzed on replicas are given in Table 3.1.5, and histographs that order the compositions from lowest to highest (Cr + Mo) content are shown in Fig. 3.1.9. Particle size and (Ti + Nb) content for the various alloys are correlated in Fig. 3.1.10. MC phase composition and purity did not correlate exactly with best microstructural formation/stability characteristics shown in Table 3.1.4 because phase composition was sensitive to particle size as well as alloy composition. Larger particles in general had higher (Ti + Nb) levels than smaller ones, but both large and small particles showed consistent compositional sensitivities to alloying to suggest that such effects were real.

Table 3.1.4. Microstructural behavior of the experimental PCA alloys after aging for 166 h at 800°C

Alloy identification	Microstructural description				
	Solution-annealed material			25%-cold-worked material	
	Matrix MC formation	Grain boundary phase formation	Relative phase fraction[a]	Recrystallization fraction	Phase formation
PCA (K-280). Ti Baseline	Nonuniform clusters of particles	Medium-sized MC, no $M_{23}C_6$	100% MC	<5%	Fine MC in the matrix and at g.b.s.
PCA-1,. Ti t Nb low Si	Somewhat uniform dispersion of particles and clusters	Medium-fine MC plus a little coarse $M_{23}C_6$	60% MC 40% $M_{23}C_6$	None	Fine MC in the matrix, some coarse g.b. $M_{23}C_6$
PCA-4,. Nb, low Si	Large, ronuniform patches of smaller MC particles	Medium-coarse MC plus coarse elongated $M_{23}C_6$ particles	25% MC 75% $M_{23}C_6$	<5%	Fine MC in the matrix and coarse g.b. $M_{23}C_6$
PCA-5, Nb, low Si and Mo	Somewhat uniform dispersion of coarser MC particles	Medium-coarse MC plus coarse. elongated $M_{23}C_6$ particles	Not measured	5–25%	Fine MC in the CW matrix coarse $M_{23}C_6$ at g.b.s. and coarser MC in recrystallized grains
PCA-8, Ti + Nb, low Si, higher C	Large, nonuniform patches of smaller MC particles	Some coarse MC plus many equiaxed $M_{23}C_6$ particles	30% MC 70% $M_{23}C_6$	None	Fine MC in the matrix, some coarse $M_{23}C_6$ at g.b.s.
PCA-2, Ti t Nb, low Si and Mo	Nonuniform and stringered clusters of medium-sized MC particles	No MC, a little coarse $M_{23}C_6$	20% MC 80% $M_{23}C_6$	25–50%	Fine MC in the CW matrix, coarse $M_{23}C_6$ at g.b.s., coarser MC in recrystallized grains
PCA-3, Ti t Nb. more Si	Nonuniform and stringered clusters of medium-sized MC particles	No MC, plus coarse elongated $M_{23}C_6$ particles	50% MC 50% $M_{23}C_6$	–50%	Same as above
PCA-6, Ti, more Si and C	Nonuniform and very stringered clusters of smaller MC particles	No MC. plus large, equiaxed $M_{23}C_6$ particles	35% MC 65% $M_{23}C_6$	–50%	Same as above
PCA-9, Ti, more Si, C, and P	Nonuniform patches and stringers of finer MC particles	No MC, some finer and some coarser $M_{23}C_6$ particles	30% MC 70% $M_{23}C_6$	~50%	Same as above
PCA-7, no Ti	No precipitation	A few, very coarse $M_{23}C_6$ particles	100% $M_{23}C_6$	>80%	Almost no precipitation in CW regions, and coarse $M_{23}C_6$ at boundaries and within recrystallized regions

[a]Relative phase fractions determined from broad-beam XEDS compositional analysis of large regions of replica, knowing the average compositions of the individual phases.

ORNL-PHOTO 1319-85

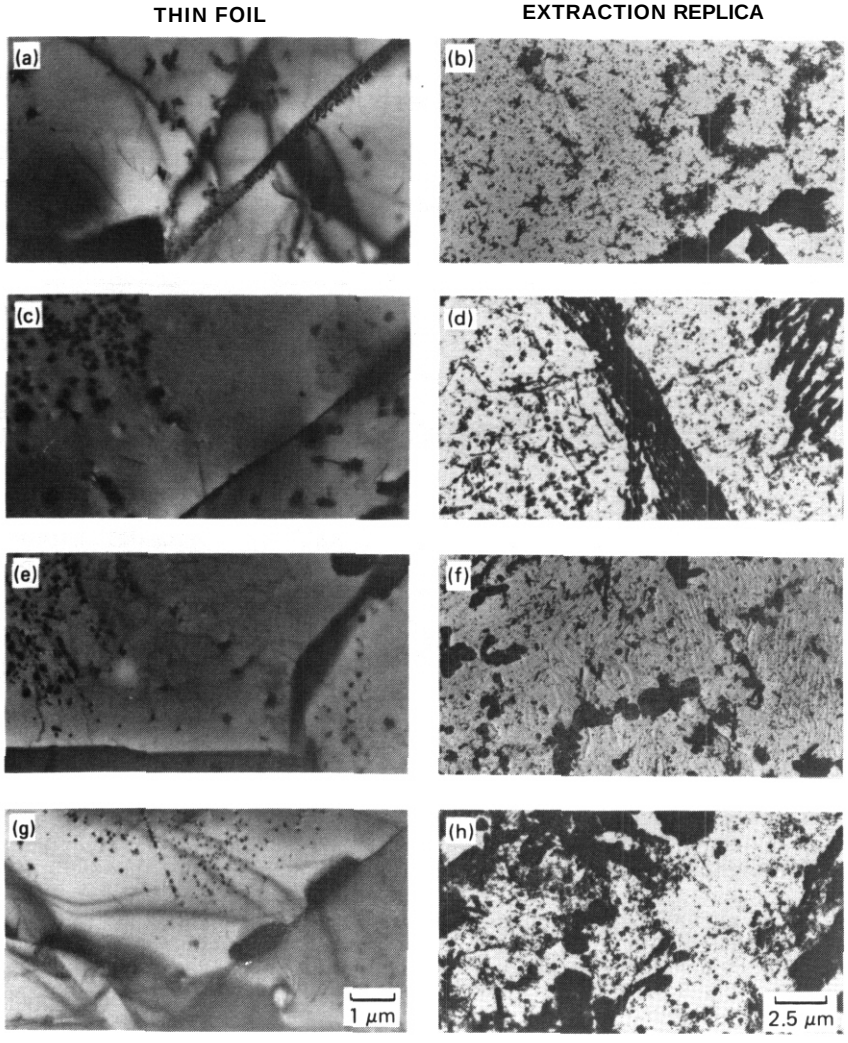

Fig. 3.1.7. Precipitate microstructures of thin foils and replicas respectively. at lower magnifications in SA (a),(b) PCA-1, (c),(d) PCA-4, (e),(f) PCA-2, and (g),(h) PCA-6 after aging for 166 h at 800°C.

Small particles of niobium-rich MC in alloy PCA-4 (Nb, low Si) showed the lowest affinity for molybdenum, but the highest affinity for chromium. This alloy also showed excellent MC formation/stability behavior microstructurally. The purity of MC in PCA-2 (Ti + Nb, lower Si and Mo) demonstrates a tradeoff between incorporation of Nb versus Mo in the phase, but the poor microstructural performance demonstrates the importance of maintaining 2.5 wt % Mo in the alloy. In general, the (Ti + Nb) alloys had higher purity MC than the alloys modified only with Ti (PCA-9, -6). Within the (Ti + Nb) groups, alloys with lower Si and/or higher C had less (Cr + Mo) in the MC phase, but particle size differences made this comparison difficult (see Fig. 3.1.10). For the titanium-containing group, the alloy with phosphorus clearly seemed to form higher purity MC particles because the sizes of small particles were similar in PCA-9 (Ti, higher C, Si. and P) and PCA-6 (Ti, higher C and Si). Again, however, better microstructural performance does not correlate with MC purity in PCA-9 because $M_{23}C_6$ formation is also enhanced.

By contrast to the MC compositional variations, the $M_{23}C_6$ phase shows little or no sensitivity to alloying changes. Compositions of the $M_{23}C_6$ phase in the experimental PCA alloys are listed in Table 3.1.6. Broad-beam XEDS measurements used to determine the relative phase fractions (Table 3.1.4) of MC and $M_{23}C_6$ are found in Table 3.1.7. The chromium content of the broad-beam measurement was the primary indicator of $M_{23}C_6$. The $M_{23}C_6$ phase picked up a little phosphorus in alloy PCA-9 (modified with phosphorus), and showed higher niobium in PCA-4, modified with niobium alone.

In general, alloy microstructural performance was worse as the $M_{23}C_6$ fraction increased, except for PCA-4 which had good grain boundary MC formation despite the presence of the large amount of $M_{23}C_6$.

Finally, the purity of smaller MC particles in PCA (K-280 heat) is lower than most of the experimental alloys, falling in between PCA-3 and PCA-6. However, the excellent microstructural MC formationlstability characteristics suggest that possibly the experimental PCA alloys should also be in a single phase, iso-microstructural regime for a better correlation to be found between MC phase composition and microstructural performance.

ORNL-PHOTO 1318-85

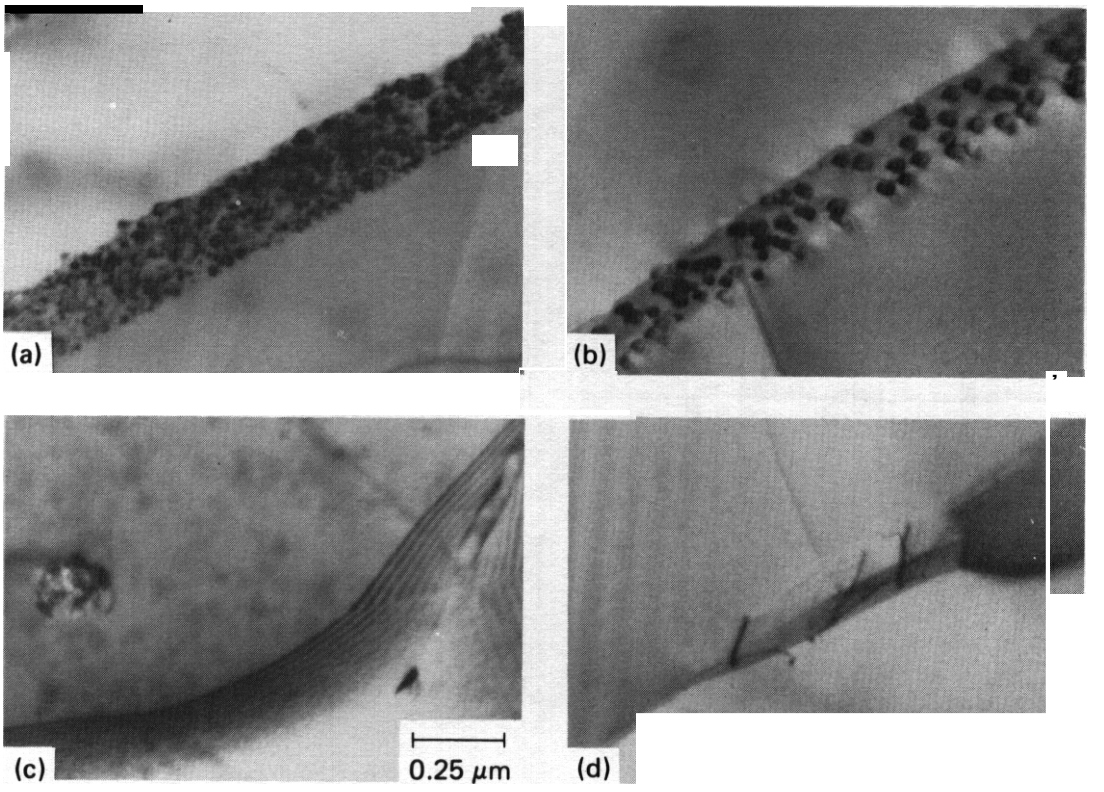

Fig. 3.1.8. Grain boundary precipitate microstructures in SA (a) PCA-1, (b) PCA-4, (c) PCA-2, and (d) PCA-6 after aging for 166 h at 800°C. Note the excellent MC formation in PCA alloys-1 and -4.

Table 3.1.5. MC phase compositions in experimental SA PCA alloys aged for 166 h at 800°C

Alloy designation	Phase composition,[a] at. %									Conent
	Si	P	Mo	Cr	Ti	V	Nb	Fe	Ni	
PCA-1	n.d.[b]	n.d.	12.0	24.0	44.5	n.d.	15.4	3.7	0.5	[5][c] Smaller particles[d]
	n.d.	n.d.	8.6	3.3	53.0	n.d.	35.0	0.2	0.04	[2] Larger particles[e]
PCA-2	0.3	n.d.	3.5	10.0	44.7	n.d.	38.7	1.8	n.d.	[2] Smaller particles
	0.3	n.d.	1.7	6.8	69.6	n.d.	20.2	1.0	n.d.	[4] Larger particles
PCA-3	1.0	0.9	11.3	23.7	44.4	n.d.	15.0	3.4	0.4	[6] Snaller particles
	0.8	0.8	7.0	5.0	56.0	n.d.	28.7	1.2	0.5	[4] Larger particles
PCA-4	n.d.	n.d.	18.2	8.3	n.d.	n.d.	71.7	1.4	n.d.	[3] Snaller particles
	n.d.	n.d.	3.3	2.2	n.d.	n.d.	94.2	0.4	n.d.	[5] Larger particles
PCA-6	2.4	1.0	15.3	25.8	50.6	n.d.	n.d.	4.4	0.6	[7] Smaller particles
	0.5	1.0	18.6	4.5	74.2	n.d.	n.d.	1.0	0.2	[3] Larger particles
PCA-8	4.1	n.d.	4.4	11.5	57	n.d.	17.8	3.2	0.6	[4] Smaller particles
	2.5	n.d.	2.7	11.0	58.7	n.d.	20.5	2.6	0.7	[1] Larger particles
PCA-9	2.7	1.4	8.7	14.8	68.0	n.d.	n.d.	3.3	1.1	[4] Smaller particles
	0.9	0.7	4.8	7.4	85.2	n.d.	n.d.	0.8	0.3	C31 Larger particles

[a]Normalized analysis of metal atoms, excluding light elements like C, N and O.
[b]n.d. = none detected.
[c]Numbers in brackets indicate the number of individual particles or clusters analyzed.
[d]Smaller portion of roughly bimodal particle size distribution, ~5 to 40 nm in diameter.
[e]Larger portion of roughly bimodal particle size distribution, ~80 to 300 nm in diameter.

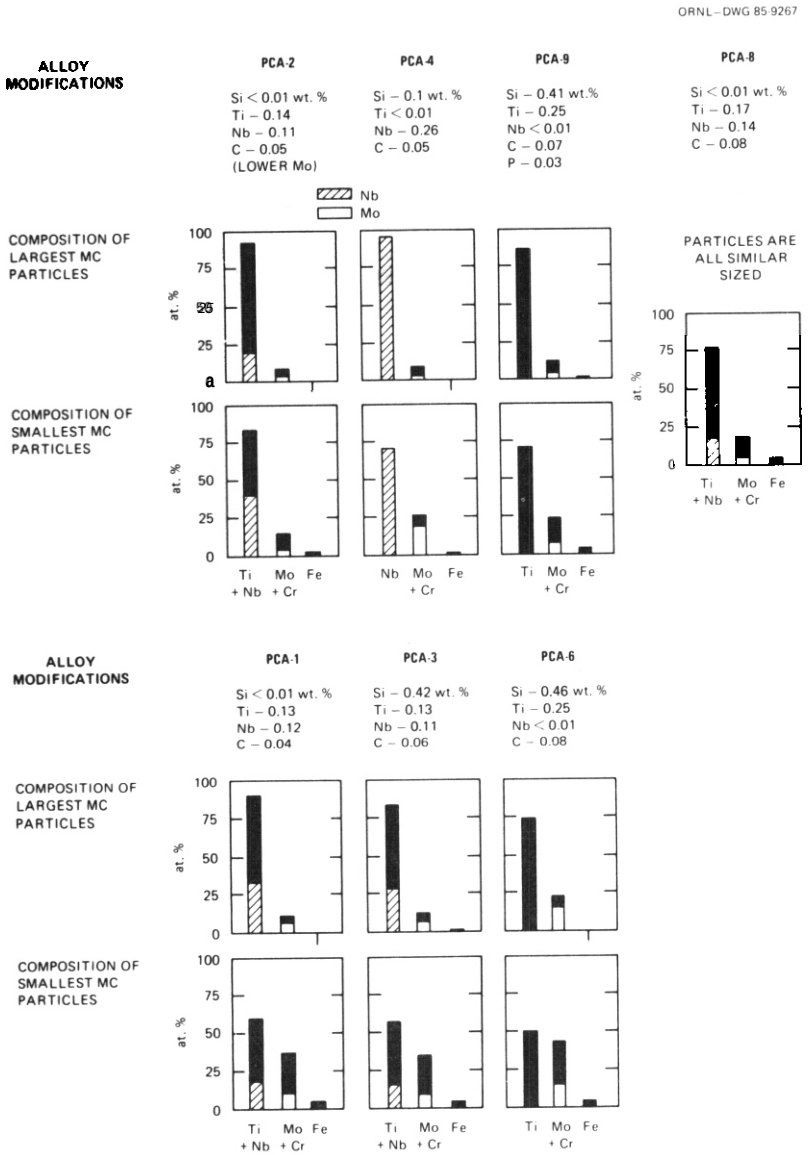

Fig. 3.1.9. Histographs of the MC phase compositions for experimental PCA alloys solution annealed and aged for 166 h at 800°C. Particles were analyzed on extraction replicas. Particle size distributions were generally bimodal, and phase compositions are represented for larger and smaller size components. The alloys are ranked from upper-left to lower-right in order of phase purity [increased (Ti + Nb) and decreased (Cr + Mo + Fe) contents] considering both large- and small-sized particles.

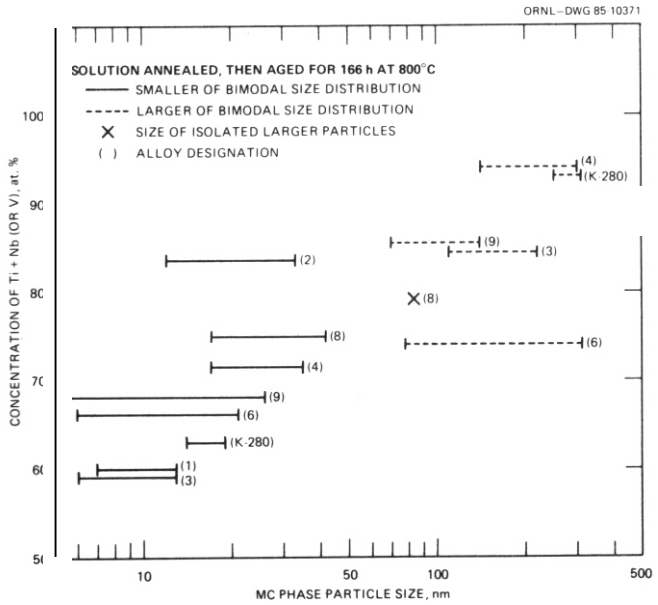

Fig. 3.1.10. A plot of MC phase Ti + Nb content as a function of particle size for PCA (K-280 heat) and experimental PCA alloys aged in the solution-annealed condition for 166 h at 800°C. Phase compositions and particle sizes were measured on extraction replicas.

Table 3.1.6. $M_{23}C_6$ phase compositions in experimental SA PCA alloys aged for 166 h at 800°C

Alloy designation	Phase composition,[a] at. %									Comment
	Si	P	Mo	Cr	Ti	V	Nb	Fe	Ni	
PCA-1	0.7	n.d.[b]	9.0	66.2	3.7	n.d.	1.5	16.5	2.5	[1][c]
PCA-2	0.5	n.d.	7.0	70.6	3.7	n.d.	1.2	14.0	2.5	[5]
PCA-3	0.2	0.4	8.6	65.0	4.6	0.1	2.0	16.4	2.8	[2]
PCA-4	n.d.	n.d.	8.0	68.8	n.d.	n.d.	5.5	15.4	2.4	[4]
PCA-6	0.4	0.2	9.6	66.0	5.6	0.2	0.1	15.5	2.5	[3]
PCA-8	0.6	n.d.	9.0	66.7	4.4	n.d.	1.8	14.5	2.5	[4]
PCA-9	n.d.	0.7	9.0	68.0	2.0	n.d.	n.d.	17.0	3.2	[3]

[a]Normalized analysis of metal atoms, excluding light elements like C, N, and O.
[b]n.d. = none detected.
[c]Numbers in brackets indicate the number of individual particles analyzed.

Table 3.1.7. Broad-beam precipitate compositional averaging in experimental SA-PCA alloys aged for 166 h at 800°C

Alloy designation	Composition,[a] at. %									Comment
	Si	P	Mo	Cr	Ti	V	Nb	Fe	Ni	
PCA-1	4.5	n.d.[b]	9.2	41.4	25.1	n.d.	9.6	8.8	1.4	[1][c] Large[d] — $M_{23}C_6$ + MC
PCA-2	2.3	n.d.	4.0	16.4	51.0	n.d.	18.7	4.0	0.6	[2] Small — MC only
	0.2	n.d.	6.0	60.0	13.0	n.d.	5.0	13.0	2.4	[1] Large — $M_{23}C_6$ + MC
PCA-3	2.0	1.7	8.7	22.0	42.6	n.d.	18.0	4.0	1.2	[1] Small — MC only
	1.0	1.0	8.6	43.3	23.5	n.d.	9.0	11.0	2.6	[1] Large — $M_{23}C_6$ + MC
PCA-4	n.d.	n.d.	12.0	8.5	n.d.	n.d.	71.1	1.6	0.3	[1] Small — MC only
	n.d.	n.d.	9.2	53.7	n.d.	n.d.	23.0	12.4	1.8	[1] Large — $M_{23}C_6$ + MC
PCA-6	3.8	1.7	15.3	2.7	57.6	n.d.	n.d.	2.7	0.4	[1] Small — MC only
	0.7	n.d.	12.0	10.7	26.7	n.d.	0.1	10.8	1.8	[2] Large — $M_{23}C_6$ + MC
PCA-8	5.4	n.d.	4.5	15.0	51.0	0.2	17.4	4.0	0.8	[2] Small — MC only
	1.4	n.d.	7.5	51.3	18.2	0.1	7.6	11.3	2.0	[1] Large — $M_{23}C_6$ + MC
PCA-9	6.0	1.2	7.0	13.3	70.5	n.d.	0.1	1.2	0.5	[1] Small — MC only
	0.8	1.0	8.3	52.4	22.0	n.d.	0.04	13.1	2.6	[1] Large — $M_{23}C_6$ + MC

[a]Normalized analysis of metal atoms, excluding light elements like C, N, and O.
[b]n.d. = none detected.
[c]Numbers in brackets indicate the number of broad-beam spectra analyzed.
[d]Indicates size of area illuminated with electrons: small — 1–3 μm in diameter; large — 15 μm or larger in diameter.

3.1.4.4. Summary and Conclusions

1. The PCA (K-280 heat) and experimental PCA compositional variants were carbide stable with respect to most comnercial heats of type 316 and 316 + Ti, which also form intermetallic phases. The experimental heats of PCA were more prone to grain boundary $M_{23}C_6$ formation than the PCA (K-280 heat) which formed none.

2. Experimental alloys PCA-1 (Ti + Nb, lower Si) and PCA-4 (Nb, lower Si) had good MC formation at grain boundaries, similar to the K-280 heat of PCA after aging for 166 h at 800°C in the SA condition.

3. Experimental alloys PCA-1 (Ti + Nb, lower Si), PCA-4 (Nb, lower Si), and PCA-8 (Ti + Nb, lower Si, higher C) showed excellent recrystallization resistance after aging for 166 h at 800°C in the 25% CW condition, as good as or better than PCA (K-280 heat). All were much better, due to fine MC formation and stability, than alloys with Ti and/or Nb (i.e., PCA-7 or type 316).

4. MC phase composition in the experimental PCA alloys varied with particle size and with alloy composition. Smaller MC particles contained less (Ti + Nb) and more (Mo + Cr). Increased Nb, C, P, and/or lower Si contents in these alloys appeared to lower the (Mo t Cr) content of the MC phase.

5. MC phase composition did not correlate with optimum MC microstructural formationlstability characteristics, possibly because alloy compositional changes also strongly affected MC particle size distributions and the relative balance between $M_{23}C_6$ and MC formation at grain boundaries.

3.1.4.5 Future Work

The experimental PCA alloys 1-9 are currently being irradiated in HFIR (CTRs-42, -43, and JPs-1 through -8), FFTF-MOTA and ORR (MFE-4A and -B reloads) experiments and will be evaluated for swelling resistance and helium effects. The next set of PCA composition variants, Alloys 10—13 and 16—18, will be examined for the effects of higher Ti and Nb levels, V addition, and small changes in Cr and Ni contents on MC phase formation and compositional characteristics.

3.1.5 References

1. P. J. Maziasz and T. K. Roche, "Preirradiation Microstructural Development Designed to Minimize Properties Degradation during Irradiation in Austenitic Stainless Steels," J. Nucl. Mater. 103&104, 797—802 (1982).

2. P. J. Maziasz and D. N. Braski, "Improved Swelling Resistance for PCA Austenitic Stainless Steel under HFIR Irradiation Through Microstructural Control," J. Nucl. Mater. 122&123, 311—16 (1984).

3. D. N. Braski and P. J. Mariasz, "The Tensile Properties and Bend Ductility of PCA after Irradiation in HFIR," pp. 61-63 in ADIP Semiannu. Prog. Rep. Mar. 31, 1984, DOE/ER-0045/12, U.S. DOE, Office of Fusion Energy.

4. P. J. Maziasr, "Swelling and Swelling Resistance Possibilities for Austenitic Stainless Steels in Fusion Reactors," J. Nucl. Mater. 122&123, 472—86 (1984).

5. P. J. Maziasz and D. N. Braski, "Microstructural Design of PCA Austenitic Stainless Steel for Improved Resistance to Helium Embrittlement under HFIR Irradiation," J. Nucl. Mater. 122&123, 305-10 (1984).

6. P. J. Maziasz, "Helium Trapping at Ti-Rich MC Particles in Ti-Modified Austenitic Stainless Steel," pp. 477—92 in Phase Stability During Irradiation, eds., J. R. Holland, L. K. Mansur, and D. I. Potter, Conf. Proc. of The Metallurgical Society of AIME, Warrendale, PA, 1981.

7. H. O. Andren, A. Henjered, and H. Norden, "Composition of MC Precipitates in a Titanium Stabilized Austenitic Stainless Steel." J. Mater. Sci. 15, 2365—68 (1980).

8. P. J. Maziasz, "Molybdenum Solubility Differences in MC Phases Formed in Titanium and Niobium Modified Austenitic Stainless Steels Determined Using AEM," pp. 496—97 in Proc. 42nd. Annual EMSA Meeting, ed., G. W. Bailey, San Francisco Press. San Francisco. 1984.

9. P. J. Maziasz and N. J. Zaluzec, "Application of Quantitative Electron Energy Loss Spectroscopy to Analysis of the Titanium Carbide Phase in Austenitic Stainless Steels," pp. 217—22 in ADIP Semiannu. Prog. Rep. Mar. 31, 1982, DOE/ER-0045/8, U.S. DOE, Office of Fusion Energy.

10. P. J. Maziasz, "Effects of Helium Content on Microstructural Development in Type 316 Stainless Steel under Neutron Irradiation," Ph.D. Dissertation. to be aublished as ORNL-6121, Oak Ridge National Laboratory report, 1985.

11. B. Weiss and R. Stickler, "Phase Instabilities during High Temperature Exposure of 316 Austenitic Stainless Steel," Met. Trans. 3, 851—66 (1972).

12. P. J. Maziasz, "Microstructural Development on 20%-Cold-Worked Types 316 and 316 + Ti Stainless Steels Irradiated in HFIR: Temperature and Fluence Dependencies of the Dislocation Component," pp. 54-37 in ADIP Semiannu. Prog. Rep. Sept. 30, 1981, DOE/ER-0045/7, U.S. DOE, Office of Fusion Energy.

13. P. J. Maziasz, B. L. Cox, and J. A. Horak, "The Influence of Both Helium and Neutron Irradiation on Precipitation in 20%-Cold-Worked Austenitic Stainless Steel," pp. 271—92 in Phase Stability Durin Irradiation, eds., J. R. Holland, L. K. Mansur, and D. I. Potter, Conf. Proc. of The Metallurgica? Society of AIME, Warrendale, PA, 1981.

in Table 3.2.1. The steel was annealed for 1 h at 1050°C, prior to the final 20% reduction by cold rolling. Transmission electron microscopy (TEM) disks (3 mm in diameter) were punched from the 20%-cold-worked (CW) 0.254-mm-thick sheet. The disks were irradiated in HFIR-CTR-42 and -43 at 500 and 600°C, respectively. to an estimated neutron fluence producing 19 dpa and 220 at. ppm He. Disks were thinned remotely and examined on a JEM 100CX analytical electron microscope (AEM), employing standard TEM techniques.

Element	Composition[a] (wt %)	Element	Composition[a] (wt %)
Cr	11.6	cu	0.1
Mn	13.5	V	0.01
Ni	4.2	Ta	0.01
Mo	0.9	Ti	<0.018
Si	0.42	B	0.001
C	0.02	S	0.02
Al	0.72	P	0.003

3.2.4.3 Results

Irradiation of the EP-838 steel to 19 dpa and 220 at.

ORNL-PHOTO 2904-85

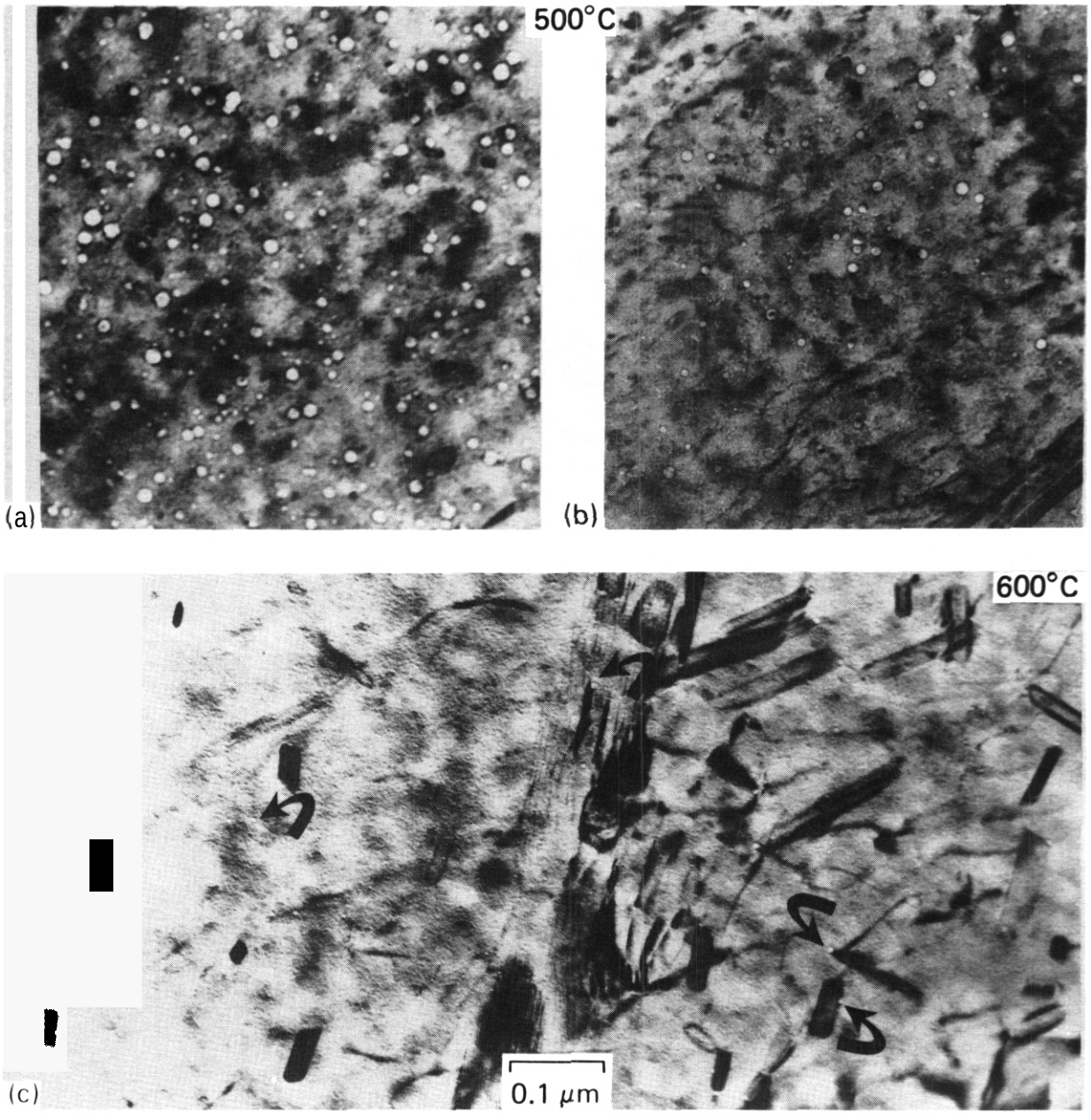

Fig. 3.2.1. Cavity microstructures produced in 20%-CW 12Cr/13Mn/4Ni (EP-838 heat) austenitic steel after HFIR irradiation to about 19 dpa and 220 at. ppm He at (a), (b) 500°C and (c) 600°C. Void formation at 500°C is nonuniform spatially, with (a) and (b) showing patches of high- and low-void concentration, respectively. Bubbles and precipitates are seen at 600°C in (c), and the large arrows point to several of the larger bubbles.

present at 600°C than at 500°C. Some fine matrix precipitation was also found only at 500°C; diffraction evidence suggests MC. The levels of Ti, V, and Nb initially are all quite low, but thermal neutrons transmute Cr into V, so possibly the MC is V-rich and induced by the irradiation. At 600°C, many narrow lath-shaped particles, ranging from 30 to 150 nm in length, were dispersed throughout the matrix [Fig. 3.2.1(c)]; diffraction evidence suggests possibly Laves phase.

In comparing this behavior to that of 20%-CW type 316 stainless steel, neither the DO- nor X-15893 heats of type 316 show void formation in the temperature range of 500 to 600°C after 20 dpa in HFIR. whereas N-lot 316 shows patches of void formation after 10 to 20 dpa. However, in general. there seems to be a similarity in microstructural cavity, dislocation, and precipitation phenomena between the high-inanganese EP-838 steel and various type 316 stainless steels. The 20%-CW EP-838 steel shows less void formation and swelling than found in solution-annealed type 216 similarly irradiated in EBR-II.[2]

3.2.5 Conclusions

1. Voids developed in 20%-CW EP-838 irradiated at 500°C in HFIR to 19 dpa and *220* at. ppm He, but not at 600°C. Void formation was patchy at 500°C. Many fine bubbles were found at both temperatures.
2. A dense dislocation structure of network and Frank loops was produced by irradiation at 500°C, while the structure recovered to form a loose tangle at 600°C.
3. Considerable precipitation was produced at 600°C, much more than found at 500°C. Coarse carbides (probably $M_{23}C_6$ or M_6C) were found along subgrain boundaries at both temperatures. Medium-coarse laths (possibly Laves phase) were found in the matrix at 600°C, whereas only some fine particles (probably MC) were found at 500°C.

3.2.6 Future Work

The EP-838 steel is being irradiated to higher fluences in HFIR, and these experiments should reveal the extent of the transient regime and the post-transient swelling behavior. This steel is also being irradiated in FFTF, thus allowing us to assess the effects of helium on swelling and microstructural evolution.

3.2.7 References

1. R. L. Klueh and E. E. Bloom, "Alloy Development for Fast Induced-Radioactivity Decay for Fusion Reactor Applications," pp. 11–20 in ADIP Semiannu. Prog. Rep. Sept. 30, 1983, DOE/ER-0045/11, U.S. DOE, Office of Fusion Energy.
2. O. S. Gelles and F. A. Garner, "Swelling Behavior of Manganese-Bearing Steel AISI 216," pp. 55–58 in ADIP Semiannu. Prog. Rep. Mar. 31, 1984, DOE/ER-0045/12, U.S. DOE, Office of Fusion Energy.
3. H. R. Brager and F. A. Garner, "Swelling of Fe-Cr-Mn Ternary Alloys in FFTF," pp. 31–33 in DAFS Quart. Prog. Rep. November 1984, DOE/ER-0046/19, U.S. DOE, Office of Fusion Energy.
4. R. L. Klueh and M. L. Grossbeck, "A Comparison of the Irradiated Tensile Properties of a High-Manganese Austenitic Steel and type 316 Stainless Steel," J. Nucl. Mater. 122&123, 294–98 (1984).

4. *HIGHER STRENGTH* ***Fe-Ni-Cr*** **ALLOYS**

5. REACTIVE AND REFRACTORY ALLOYS

5.1 THE TENSILE PROPERTIES OF SEVERAL VANADIUM ALLOYS AFTER IRRAOIATION IN FFTF — 0. N. Braski (Oak Ridge National Laboratory)

5.1.1 AOIP Task

AOIP Task I.B.15, Tensile Properties of Reactive and Refractory Alloys.

5.1.2 Objective

The goal of this research is to investigate the effects of displacement damage and helium generation on the properties of vanadium alloys.

5.1.3 *Summary*

Irradiation in ^{7}Li-filled capsules at 420 and 520°C in FFTF [MOTA) with damage levels up to 13.6 dpa substantially lowered the ductility of V-15Cr-5Ti, VANSTAR-7, and V-3Ti-1Si alloys by the mechanism of radiation hardening. The VANSTAR-7 and V-3Ti-1Si alloys resisted the embrittling effects of irradiation better than the V-15Cr-5Ti alloy, regardless of the implanted helium level. Control specimens of all three alloys were not appreciably affected by thermal aging in ^{7}Li at the respective irradiation temperatures. The mechanism causing the low ductility and transgranular cleavage fracture in one V-15Cr-5Ti specimen without implanted helium requires further investigation.

5.1.4 Progress and Status

5.1.4.1 Experimental

Specimens fabricated from several vanadium alloys have been encapsulated in TZM capsules containing ^{7}Li (ref. 1) and irradiated in FFTF. The specimens were preimplanted with different amounts of ^{3}He using the "tritium trick."[2] The tritium was removed by heating the vanadium specimens under vacuum at 700°C for 19 h. Specimens irradiated at 420°C accumulated 1.3 × 10^{22} neutrons/cm^2 (6.0 dpa) while those at 520°C accumulated 2.8 × 10^{22} neutrons/cm^2 (13.6 dpa). The nominal compositions and annealing treatments for V-15Cr-5Ti, VANSTAR-7, and V-3Ti-1Si were presented previously.[3] The SS-3 type tensile specimens[3] were tested at their respective irradiation temperatures using a crosshead speed of 8.5 μm/s (strain rate = 1.1 × 10^{-3} s^{-1}). Unirradiated control specimens were thermally aged in ^{7}Li and tested under similar conditions. The fracture surfaces were examined using a hot-cell scanning electron microscope (SEM).[4] Irradiated disks (3 mm diam) of each alloy were used for transmission electron microscopy (TEM).

5.1.4.2 Results and Oiscussion

The results of tensile tests on V-15Cr-5Ti, VANSTAR-7, and V-3Ti-1Si specimens are presented for each alloy in Table 5.1.1. Since total elongation is a tensile property that may be strongly influenced by implanted helium, thermal aging, and/or neutron irradiation, it was used as a basis for comparison in Figs. 5.1.1 through 5.1.4. Specimens implanted with 3He were aged or irradiated at 420, 520, and 600°C and tensile tested at the same respective temperatures. Some of the specimens were also tested at those temperatures directly after ^{3}He implantation and these are labeled "as-implanted." Note that the "zero" helium level condition of an as-implanted specimen is simply the starting, annealed alloy. There are no data for specimens irradiated at 600°C because that particular capsule experienced a temperature excursion during the irradiation and the specimens were judged as unusable.

Effect of ^{3}He on ductility — The effect of implanted ^{3}He on the ductility of the three vanadium alloys was shown previously.' Figure 5.1.1 summarizes the results for all three alloys at 600°C; the data are also plotted in Figs. 5.1.2 through 5.1.4. The total elongation for V-15Cr-5Ti specimens was observed to drop in a linear fashion to low values with about 300 at. ppm ^{3}He present in the microstructure (Fig. 5.1.1). On the other hand, VANSTAR-7 specimens were able to accommodate up to ~150 at. ppm ^{3}He with no loss of ductility. The data for V-3Ti-1Si fell between those of the other two alloys. These results show that the vanadium alloys differ substantially in their ability to accommodate helium without degrading ductility. From the standpoint of alloy development, it indicates that vanadium alloys with good helium accommodation and embrittlement resistance can Drobably be oroduced.

Effect of thermal aging on ductility — The total-elongation values for specimens aged in ^{7}Li for 100 d are shown for each alloy in Figs. 5.1.2 through 5.1.4 by the "square" data points. With only one exception (Fig. 5.1.4, 0-He, 600°C), all-of the elongation values-were either the same or only slightly lower than those for the as-implanted material. Therefore, it was concluded that thermal aging for 100 d at 420 to 600°C in ^{7}Li does not affect the ductility of the three vanadium allays tested. In light of these results, it is quite reasonable to assume that the alloys did not pick up any significant amounts of oxygen or nitrogen during the aging period. The oxygen content of several specimens will be checked by neutron activation analysis to confirm this assumption.

Table 5.1.1. Vanadium alloy tensile properties

Condition	Helium level (at. ppm)	Test temperature (°C)	Strength, MPa		Elongation, %	
			Yield	Ultimate tensile	Uniform	Total
V-15Cr-5Ti						
Annealed 1 h at 1200°C	0	420	392	517	17.1	28.2
Annealed 1 h at 1200°C	0	520	353	514	14.3	25.9
Annealed 1 h at 1200°C	0	600	323	521	13.6	22.0
Aged 100 d at 420°C	0	420	355	501	14.0	22.8
Aged 100 d at 420°C	0	420	372	516	14.0	23.5
Aged 100 d at 520°C	0	520	372	575	16.3	24.7
Aged 100 d at 600°C	0	600	393	598	10.8	20.0
Aged 100 d at 420°C	80	420	387	541	13.7	20.3
Aged 100 d at 600°C	80	600	412	626	10.6	14.6
Aged 100 d at 420°C	300	420	346	400	--	2.0
Aged 100 d at 520°C	300	520	--	351	--	0
Aged 100 d at 600°C	300	600	--	364	--	0
Irradiated to 6 dpa at 420°C	0	420	--	598	--	0[a]
Irradiated to 6 dpa at 420°C	14	420	--	518	--	0[a]
Irradiated to 6 dpa at 420°C	80	420	--	497	--	0[a]
Irradiated to 6 dpa at 420°C	300	420	--	316	--	0[a]
Irradiated to 13.6 dpa at 520°C	80	520	--	449	--	0[a]
VANSTAR-7						
Annealed 1 h at 1350°C	0	420	278	443	15.0	23.7
Annealed 1 h at 1350°C	0	520	276	442	13.3	24.7
Aged 100 d at 420°C	0	420	314	452	14.5	23.2
Aged 100 d at 420°C	0	420	308	458	14.8	23.6
Aged 100 d at 520°C	0	520	294	493	12.6	18.6
Aged 100 d at 520°C	0	520	292	483	15.2	21.4
Aged 100 d at 600°C	0	600	305	538	14.8	21.8
Aged 100 d at 600°C	42	600	215	503	13.5	21.6
Aged 100 d at 600°C	150	600	314	518	12.3	18.8
Irradiated to 6 dpa at 420°C	0	420	611	703	4.3	11.1
Irradiated to 6 dpa at 420°C	42	420	617	706	4.3	11.0
Irradiated to 6 dpa at 420°C	150	420	621	710	3.8	9.8
Irradiated to 13.6 dpa at 520°C	0	520	810	883	2.3	6.3
Irradiated to 13.6 dpa at 520°C	42	520	812	895	2.7	5.6
Irradiated to 13.6 dpa at 520°C	150	520	922	1006	1.9	2.3
V-3Ti-1Si						
Annealed 1 h at 1050°C	0	420	335	470	14.0	21.0
Annealed 1 h at 1050°C	0	520	290	527	15.0	21.0
Aged 100 d at 600°C	0	600	401	529	7.5	12.0
Aged 100 d at 600°C	135	600	387	531	8.0	12.8
Aged 100 d at 600°C	480	600	418	557	8.2	10.8
Irradiated to 6 dpa at 420°C	0	420	758	806	2.6	5.8
Irradiated to 6 dpa at 420°C	135	420	793	829	1.0	2.3
Irradiated to 13.6 dpa at 520°C	0	520	569	662	4.6	10.6
Irradiated to 13.6 dpa at 520°C	135	520	520	633	7.6	12.1

[a]Specimen failed at the pin in one of the grips.

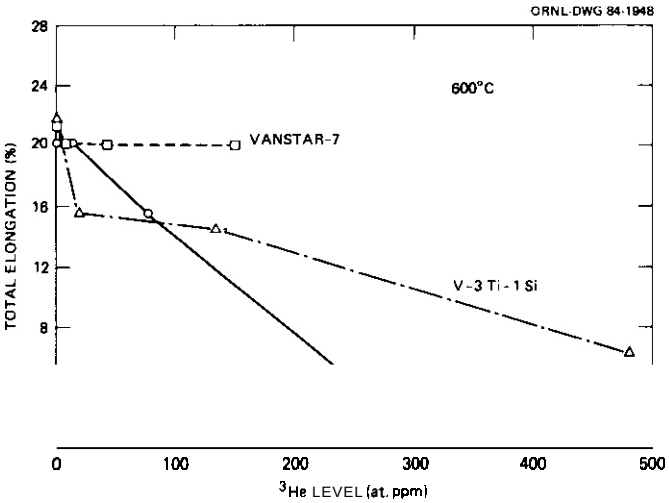

Fig. 5.1.1. Tensile ductility of as-implanted vanadium alloys at 600°C as a function of ^{3}He level implanted by the tritium trick.

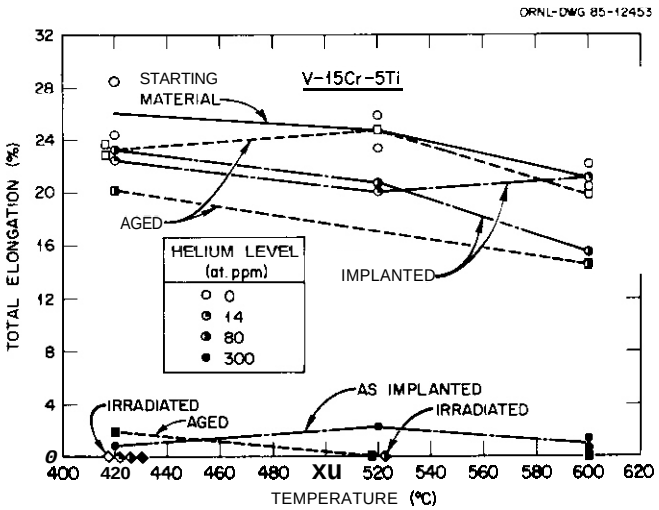

Fig. 5.1.2. Ouctility of V-15Cr-5Ti as a function of temperature. Aged and irradiated specimens were tensile tested at their respective aging or irradiation temperatures. Specimens were irradiated to 6.0 and 13.6 dpa at 420 and 520°C, respectively. Helium levels are indicated by shaded portions of data points.

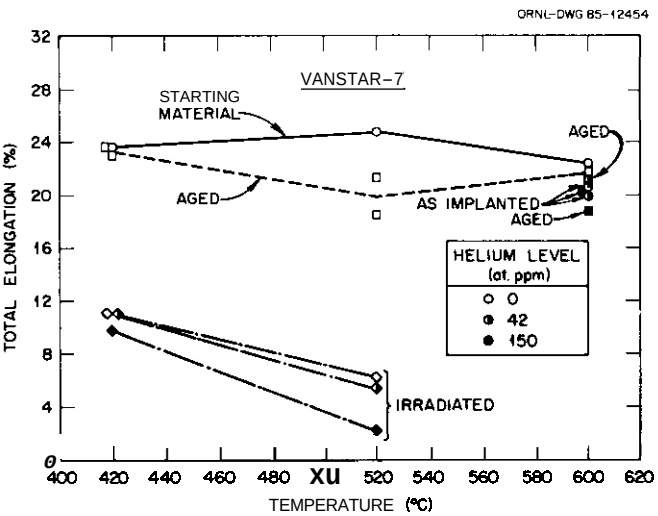

Fig. 5.1.3. Ductility of VANSTAR-7 as a function of temperature. Aged and irradiated specimens were tensile tested at their respective aging or irradiation temperatures. Specimens were irradiated to 6.0 and 13.6 dpa at 420 and 520°C, respectively. Helium levels are indicated by shaded portions of data points.

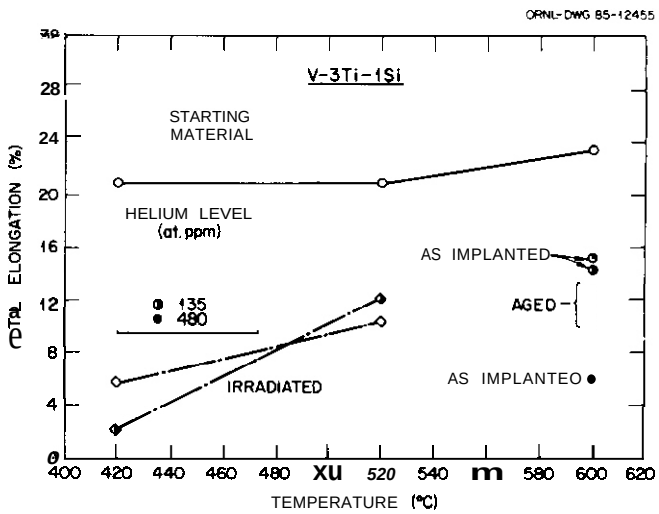

Fig. 5.1.4. Ductility of V-3Ti-1Si as a function of temperature. Aged and irradiated specimens were tensile tested at their respective aging or irradiation temperatures. Specimens were irradiated to 6.0 and 13.6 dpa at 420 and 520°C, respectively. Helium levels are indicated by shaded portions of data points.

Effect of neutron irradiation on ductility — The vanadium alloys were hardened significantly by the neutron irradiation as demonstrated by the increased yield strengths and the ultimate strengths for VANSTAR-7 and V-3Ti-1Si listed in Table 5.1.1. The V-15Cr-5Ti specimens were also hardened, but the effect could not be measured in the tensile tests because of severe embrittlement which caused the specimens to fail prematurely at the pin in the grips. The irradiation hardening was due to the dense, irradiation-induced dislocation structure containing many small dislocation loops, as shown by the example in Fig. 5.1.5. The micrograph shows the dislocation microstructure of a V-15Cr-5Ti specimen irradiated to 6.0 dpa at 420°C. Similar microstructures were observed in the other vanadium alloys that were irradiated under similar conditions. The grain boundaries in all three vanadium alloys with implanted ^{3}He contained many helium bubbles, as shown typically in Fig. 5.1.6. This is not surprising since the boundaries already contained helium bubbles after undergoing the tritium trick (i.e., before irradiation).[5] Helium bubbles were also present in the grain matrices. but were often difficult to see due to their small size. Both grain boundary and matrix bubbles were coarsened by the 100 d irradiation at 420 and 520°C. Large cavities were observed in the vicinity of grain boundaries in the VANSTAR-7 specimens irradiated at 520°C [Fig. 5.1.6(b)]. Large cavities were not observed in other areas of the microstructure nor in the other two alloys. The presence of these cavities in only the VANSTAR-7 alloy is interesting and work is continuing to investigate this phenomenon.

Now let us look at some of the results for each alloy with the help of SEM fractographs. The previous data for V-15Cr-5Ti (Fig. 5.1.1) as well as those in Fig. 5.1.2 show that its ductility is adversely affected by helium implanted to amounts ~300 at. ppm. Although some of the helium was observed in the matrix of V-15Cr-5Ti, the largest bubbles were observed on the grain boundaries and are believed to be the cause of the ductility losses. Indeed, the intergranular nature of fracture surfaces observed for tensile-tested V-15Cr-5Ti specimens containing helium support this conclusion.[5] Similar intergranular failure occurred after irradiation [Fig. 5.1.7(b)] and, in the case of V-15Cr-5Ti, all of the specimens tested at 420°C broke in the shoulder sections (i.e., in the grips). What was surprising, however, was that the V-15Cr-5Ti specimen without helium also broke in the grips during testing at 420°C. The mode of failure for this specimen was mixed, with the major portion being transgranular cleavage and a smaller portion being intergranular [Fig. 5.1.7(a)]. This latter type of failure is similar to that observed by R. Bajaj and R. E. Gold for V-15Cr-5Ti irradiated in an early ORR-MFE-2 experiment where they found relatively high sulfur levels on the cleavage surfaces.[6] In later Auger spectroscopy analyses performed on material from the same heat (unirradiated), Diercks and Smith detected sulfur only on the intergranular portions of the fracture.' They also analyzed the V-15Cr-5Ti material from the same heat as ours (unirradiated), but found only "possible indications of phosphorus and chlorine."[8] Their analysis of an LMFBR heat of V-15Cr-5Ti showed possible traces of sulfur or phosphorus on mostly cleavage surfaces.[8] Therefore. even though sulfur and/or phosphorus have apparently not influenced the tensile properties of the unirradiated V-15Cr-5Ti used in the present study, segregation of one or both elements during irradiation is a possibility. It has also been suggested that irradiation may have caused a significant increase in the ductile-brittle transition temperature (DBTT) for the alloy.[9]

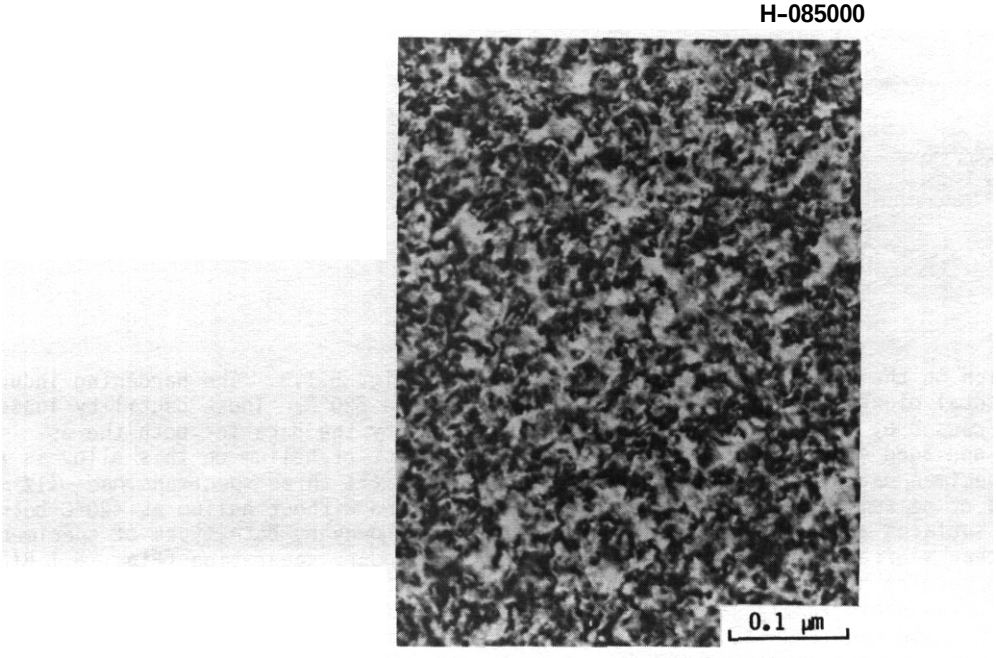

Fig. 5.1.5. Dislocation structure in V-15Cr-5Ti after irradiation in FFTF at 420°C to 6.0 dpa. The specimen contains no implanted helium.

H-085009

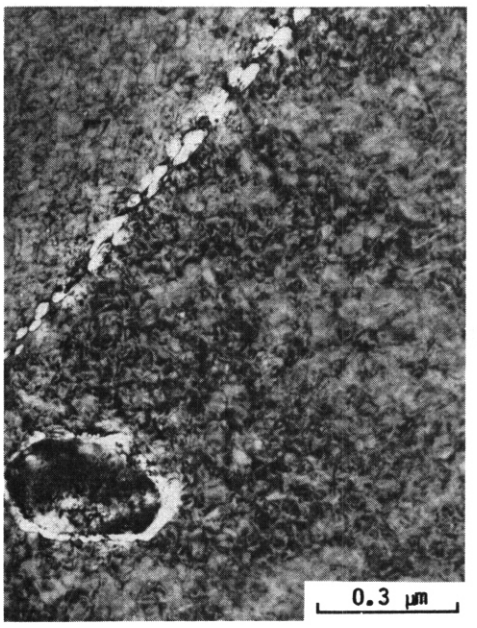

H-085112

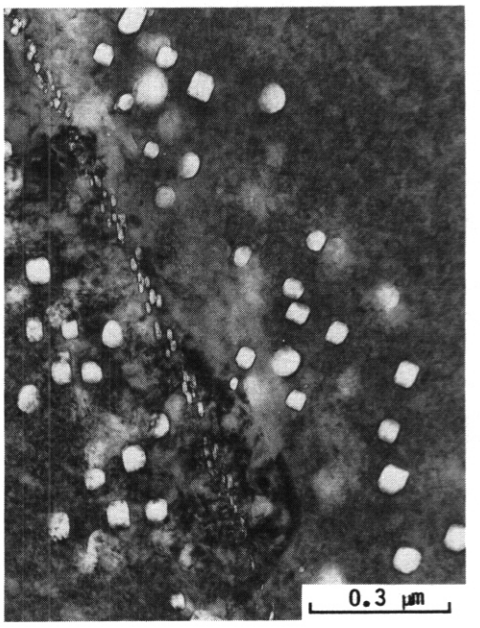

H-085128

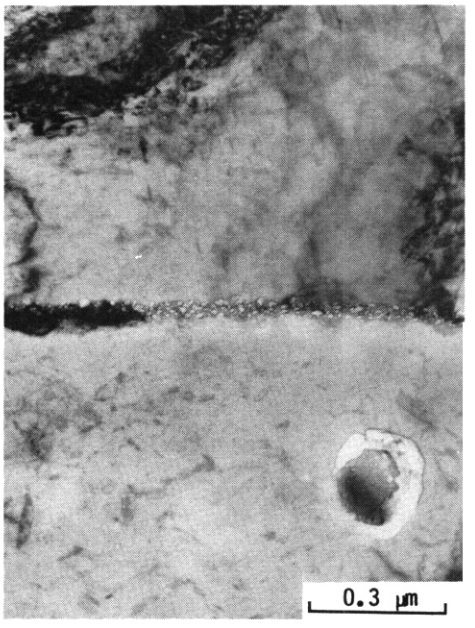

Fig. 5.1.6. Grain boundaries in (a) V-15Cr-5Ti (300 at. ppm ^{3}He), (b) VANSTAR-7 (150 at. ppm ^{3}He), and (c) V-3Ti-1Si (480 at. ppm ^{3}He) after irradiation in FFTF at 520°C to 13.6 dpa.

The effect of irradiation on the ductility of VANSTAR-7 is shown in Fig. 5.1.3. The hardening induced by irradiation lowered the total elongation values substantially at 420 and 520°C. These ductility losses are much greater than those caused by the addition of 3He as demonstrated by the data for both the as-implanted and the implanted and aged specimens. The relatively small effect of helium on this alloy is also evident in the irradiated specimen data itself, especially at 420°C, where all three specimens had ~11% total elongation, regardless of helium level. Irradiated specimens with and without helium at 420°C both had ductile-dimple fracture surfaces as shown in Figs. 5.1.8(a) and (c). However, both types of specimens exhibited numerous surface cracks after testing that were due to grain boundary separation [Figs. 5.1.8(b) and (d)]. At 520°C, the presence of helium in the microstructure changed the failure mode from ductile transgranular to intergranular as shown in Fig. 5.1.9. This in turn caused additional ductility losses up to ~4%; the losses were of the same magnitude as those observed in the unirradiated material tested at 600°C (see Fig. 5.1.3). It should be pointed out that the differences between the 420 and 520°C may not be entirely a temperature effect because the displacement damage in specimens irradiated at 520°C was twice that of those irradiated at 420°C. In any case, the VANSTAR-7 alloy specimens accommodated the effects of irradiation and helium better than V-15Cr-5Ti.

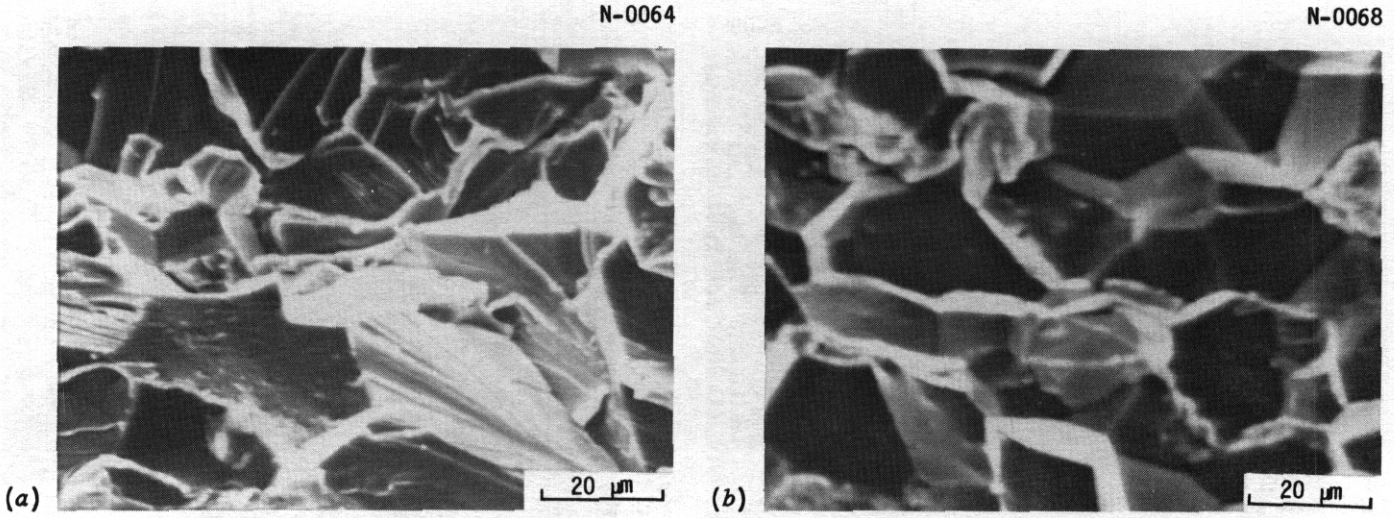

Fig. 5.1.7. Fracture surfaces of tested V-15Cr-5Ti after irradiation in FFTF at 420°C to 6.0 dpa. (a) Mostly transgranular cleavage fracture in specimen without implanted ^{3}He, and (b) intergranular fracture in specimen with 300 at. ppm implanted ^{3}He.

The results for the V-3Ti-1Si alloy, supplied to us by D. Kaletta at the KFK, Karlsruhe, are shown in Fig. 5.1.4. A smaller number of specimens of this alloy were tested due to the limited supply of material and limited space in the MOTA capsule. Like VANSTAR-7, V-3Ti-1Si suffered substantial ductility losses due to irradiation. However, it is not clear whether helium is accommodated as well. Both as-implanted and aged V-3Ti-1Si specimens tested at 600°C exhibit sizable losses in elongation that were not evident in VANSTAR-7 under somewhat similar conditions. One could argue that this was due to the higher levels of helium implanted in the V-3Ti-1Si, but comparison of its 135 at. ppm specimens with the 150 at. ppm for VANSTAR-7 (at 600°C) show that, indeed, helium seems to have a greater effect on the ductility of V-3Ti-1Si. For some reason the ductility of V-3Ti-1Si at 420 and 520°C, after irradiation, is the reverse of that observed for VANSTAR-7 with larger elongations measured at 520°C. All of the fracture surfaces of irradiated V-3Ti-1Si specimens were transgranular ductile. The only difference between the specimens tested at 420 and 520°C was that fewer side cracks were observed to open up along the gage length surfaces of specimens tested at 520°C, as shown in Fig. 5.1.10. Comparison of Figs. 5.1.4 with 5.1.2 shows that V-3Ti-1Si is also more resistant to ductility losses caused by irradiation or helium than V-15Cr-5Ti.

The results indicate that the three vanadium alloys exhibited substantial ductility losses after irradiation that were due primarily to radiation hardening. This effect should saturate with increasing damage level. On the other hand, the ductility losses due to helium were generally less than those from irradiation, but these will almost certainly increase with time in a fusion reactor (or damage level). Fortunately, this second and potentially more serious problem with helium can probably be alleviated, to a great extent, through alloy development. The results in Fig. 5.1.1 showing wide differences in alloy response to implanted helium support this belief.

5.1.5 Conclusions

1. Helium implanted via the tritium trick substantially lowered the ductility of V-15Cr-5Ti, but had little effect on VANSTAR-7. The results for V-3Ti-1Si fell between the other two alloys.
2. Aging in ^{7}Li at 420 and 520°C for 100 d had little or no effect on the ductility of all three vanadium alloys.
3. Vanadium specimens irradiated without implanted helium, at 420 and 520°C, generally exhibited greater ductility losses than unirradiated specimens containing helium. The ductility losses in the irradiated specimens were caused by radiation hardening.
4. Both VANSTAR-7 and V-3Ti-1Si resisted the embrittling effects of irradiation better than V-15Cr-5Ti, regardless of the implanted helium level.
5. The mechanism causing the low ductility and transgranular cleavage fracture in a V-15Cr-5Ti specimen without implanted helium requires further investigation.
6. The production of vanadium alloys with better resistance to helium embrittlement should be possible through alloy development.

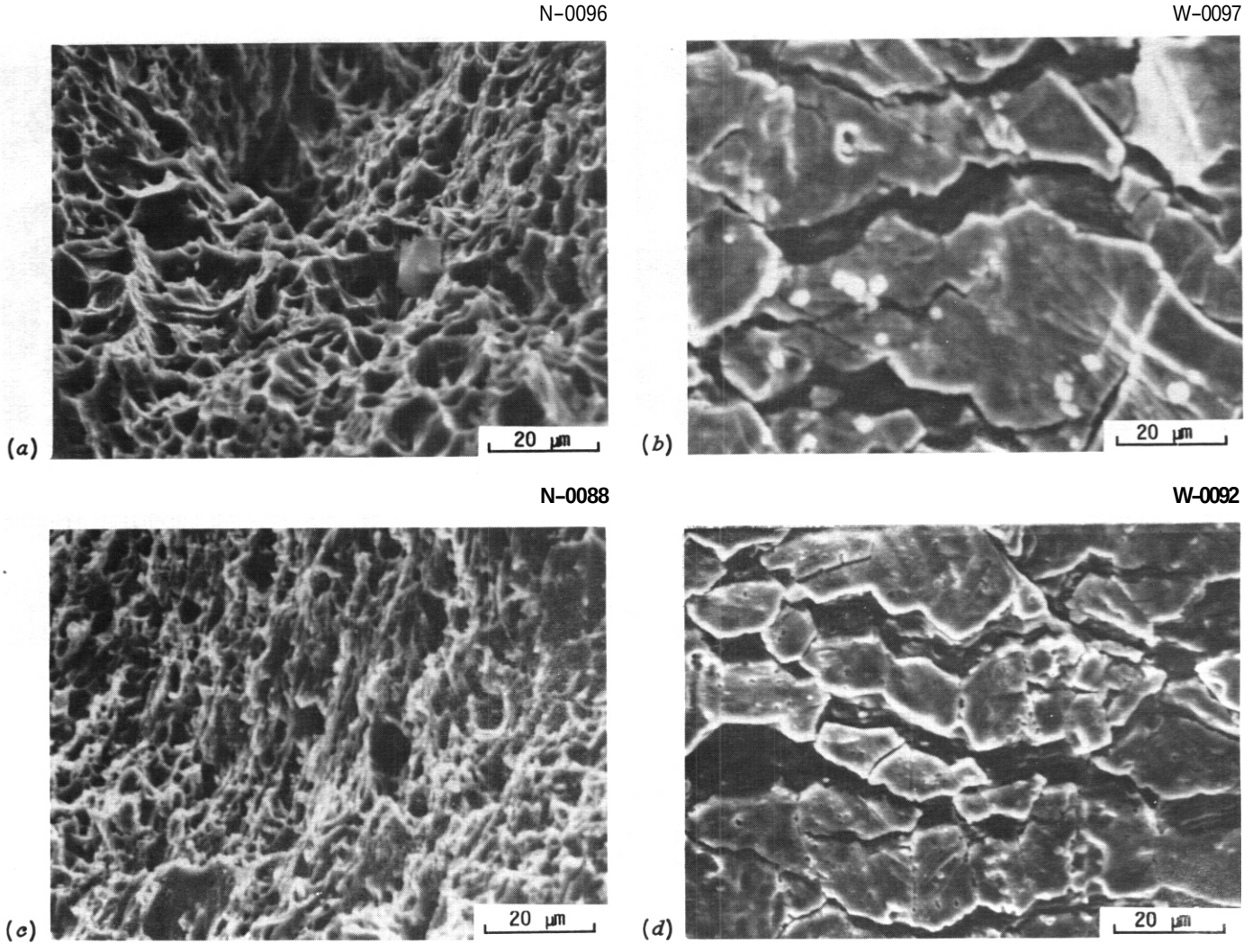

Fig. 5.1.8. (a) Ductile fracture, and (b) surface grain boundary separation in VANSTAR-7 specimen (0-He) irradiated at 420°C to 6.0 dpa. (c) Ductile fracture, and (d) surface grain boundary separation in similar specimens containing 150 at. ppm ^{3}He.

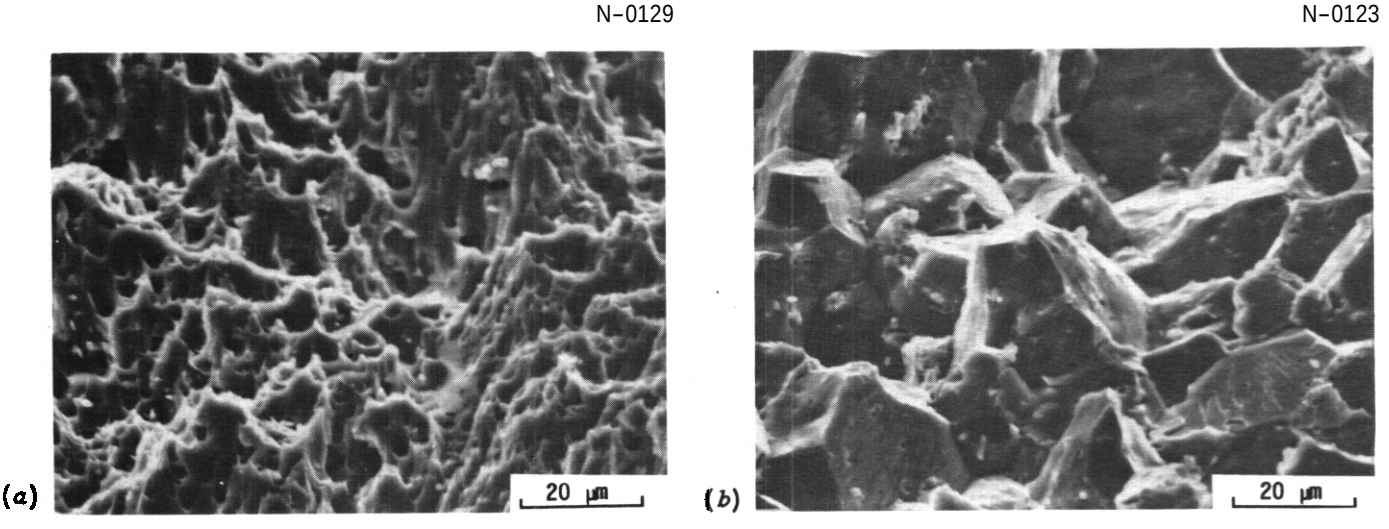

Fig. 5.1.9. (a) Ductile fracture surface of VANSTAR-7 without ^{3}He, and (b) intergranular fracture of VANSTAR-7 with 150 at. ppm ^{3}He. Both specimens were irradiated in FFTF at 520°C to 13.6 dpa and tested at the same temperature.

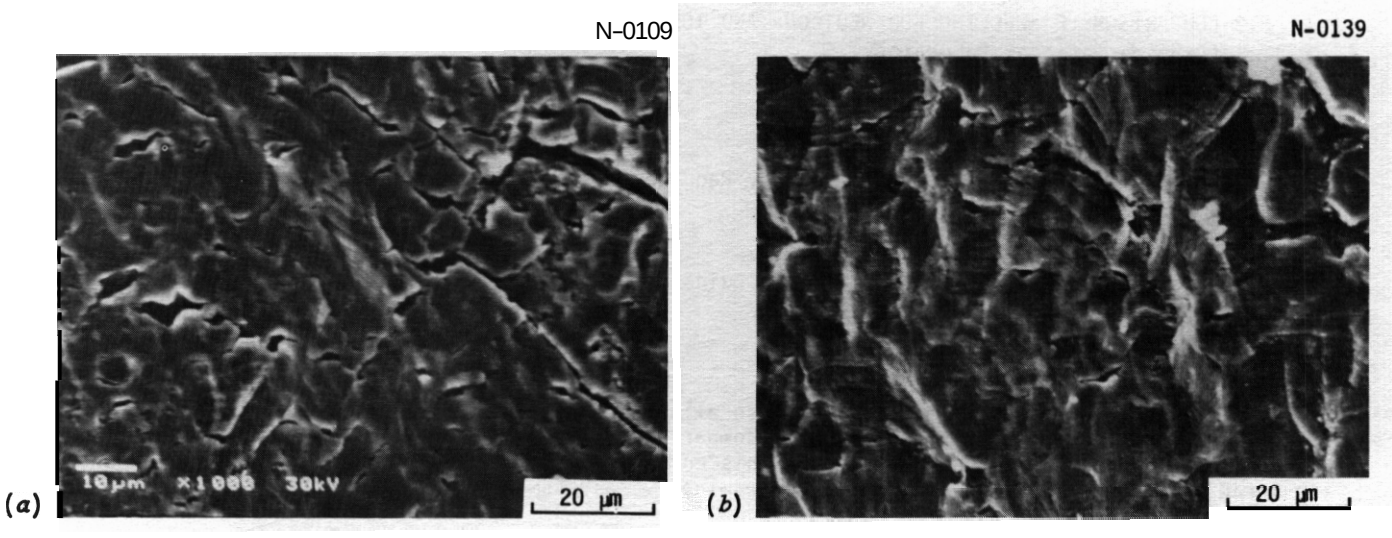

Fig. 5.1.10. Surface grain boundary separation on gage lengths of tested V-3Ti-1Si specimens containing 135 at. ppm ^{3}He that were (a) irradiated at 420°C to 6.0 dpa and (b) irradiated at 520°C to 13.6 dpa.

5.1.6 References

1. A. M. Ermi, "FFTF Fusion Irradiations — FFTF Cycles 4–6," pp. 23–24 in ADIP Semiannu. Prog. Rep. Sept. 30, 1984, DOE/ER-0045/13, U.S. DOE, Office of Fusion Energy.
2. D. N. Braski and D. W. Ramey, "Helium Doping of a Vanadium Alloy by a Modified Tritium Trick," pp. 72–74 in ADIP Semiannu. Prog. Rep. Mar. 31, 1984. DOE/ER-0045/12, U.S. DOE, Office of Fusion Energy.
3. D. N. Braski, "Vanadium Alloy Irradiation Test Matrix in FFTF," pp. 63-65 in ADIP Semiannu. Prog. Rep., Sept. 30, 1984. DOE/ER-0045/13, U.S. DOE, Office of Fusion Energy.
4. J. R. Gibson and D. N. Braski, Scanning Electron Microscope Facility for Examination of Radioactive Materials, ORNL/TM-9451, Oak Ridge National Laboratory Report, (February 1985).
5. D. N. Braski, "The Effect of Helium on the Tensile Properties of Several Vanadium Alloys," pp. 95–98 in ADIP Semiannu. Prog. Rep., Sept. 30, 1984, DOE/ER-0045/13, U.S. DOE. Office of Fusion Energy.
6. R. Bajaj and R. E. Gold, Evaluation of V-15Cr-5Ti Specimens after Neutron Irradiation in the MFE-2 Experiment, Phase I Final Report, Westinghouse Electric Corporation, Advanced Energy Systems Division (August 1983).
7. D. R. Diercks and O. L. Smith, "Environmental Effects on the Properties of Vanadium-Base Alloys," Pp. 75–79 in ADIP Semiannu. Prog. Rep. Mar. 31. 1984, DOE/ER-0045/12, U.S. DOE, Office of Fusion Energy.
8. D. R. Diercks and D. L. Smith, "Environmental Effects on the Properties of Vanadium-Base Alloys." PP. 212–13 in ADIP Semiannu. Prog. Rep. Sept. 30, 1984, DOE/ER-0045/13, U.S. DOE, Office of Fusion Energy.
9. Private communication on May 23, 1985, with J. W. Davis, McDonnell Douglas Astronautics Company, St. Louis Division.

5.2 COMPARISON OF SWELLING FOR NEUTRON- AND ION-IRRADIATEO MFR STRUCTURAL MATERIALS - B. A. Loomis (Argonne National Laboratory)

5.2.1 ADIP Task

ADIP Task I.A.1. Define Material Property Requirements and Make Structural Life Predictions

5.2.2 Objective

The objective of this work is to provide guidance on the applicability of alloys for structural components in a magnetic fusion reactor.

5.2.3 Summary

The swelling of vanadium and vanadium-base alloys, 316 stainless steel, Fe-25Ni-15Cr alloy, ferritic steels, and copper on neutron irradiation is compared with the swelling for these materials on ion irradiation in this report. The results of this comparison are taken to show that utilization of the ion-irradiation technique provides for a discriminative assessment of the potential for swelling of candidate MFR materials.

5.2.4 Progress and Status

5.2.4.1 Introduction

Irradiation-induced microstructural changes in candidate, magnetic fusion reactor (MFR) structural materials will determine their dimensional stability (swelling), mechanical properties, corrosion resistance, and hence the lifetime of the MFR. In the absence of a MFR, it is necessary to utilize existing simulation facilities to determine the effect on microstructural changes of parameters (e.g., helium generation to damage rate ratio, irradiation fluence, and helium generation rate) that pertain to the expected MFR environment. At the present time ideal simulation is not possible since no simulation technique can reproduce simultaneously all the conditions that a MFR structural material will experience. In this report comparisons are presented for the swelling of several candidate MFR structural materials. The data for these comparisons were obtained from use of fission neutron- and ion-irradiation simulation facilities. It remains to be demonstrated that the microstructural changes induced by the use of either of these facilities simulate adequately the microstructural changes in a MFR.

5.2.4.2 Experimental Results

The experimental results on the swelling of vanadium and vanadium-base alloys, stainless steel, Fe-25Ni-15Cr alloy, ferritic steels, and copper that have been reported by several investigators are presented in the following figures. The swelling values that are presented for the different materials do not necessarily include all of the data that have been reported in the literature. The experimental data were selected for this report to show a comparison of swelling using fission neutron- and ion-simulation facilities.

Vanadium and vanadium-base alloys

The swelling of vanadium and several vanadium-base alloys on neutron irradiation is compared with the swelling for these materials on single- and dual-ion irradiation in Fig. 5.2.1. On the basis of limited irradiation data, the alloying of vanadium with 1-20 w/o titanium reduces the swelling rate of vanadium from ~0.05%/dpa to < 0.002%/dpa for neutron- and ion-irradiations in the range of 400 to 800°C. The addition of 10-15 w/o chromium to vanadium causes the swelling rate of vanadium to increase to ~0.2%/dpa for neutron- and ion-irradiations in the range of 650 to 800 C. However, the presence of chromium in a V-15Cr-5Ti allay does not result in significant swelling for radiation damage levels up to ~250 dpa. On the basis of the present data, the steady-state swelling rate for the V-15Cr-5Ti alloy is < 0.001%/dpa. Ion-irradiation results for the V-15Cr-5Ti alloy have also shown that the simultaneous production of radiation damage and implantation of helium impacts significantly on precipitate formation.[16] The data presented in Fig. 5.2.1 suggest that the swelling values obtained for vanadium and vanadium-base alloys on neutron- or ion-irradiation are essentially in agreement.

Fe-25Ni-15Cr and S.A. 316 stainless steel

The swelling of the Fe-25Ni-15Cr alloy on irradiation in the EBR-II reactor is compared with the swelling of this material on irradiation with Ni-ions in Fig. 5.2.2. Also in Fig. 5.2.2, the swelling of solution annealed 316 stainless steel on irradiation in the EBR-II or MIR reactors is compared with the swelling on single- or dual-ion irradiation. The obvious difference between the neutron- and ion-irradiation data for these materials is the damage level required before the attainment of a "steady-state" swelling rate; viz., 10-30 dpa for neutron irradiation and 60-90 dpa for ion irradiation. The

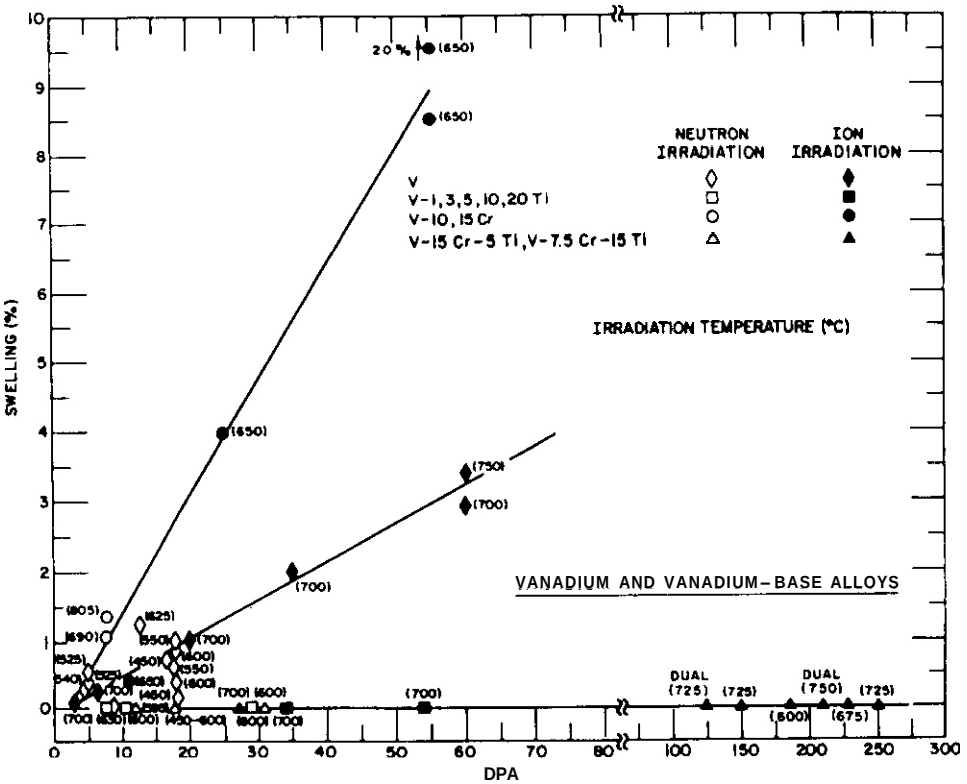

Fig. 5.2.1. Comparison of swelling for vanadium and vanadium-base alloys on neutron and ion irradiation. References for symbols are: ◊-1,2,3,4,5,6; □-3,7,8; ○-3,8,; A-3; ♦-9,10,11,12; ■-11; 0-13; ▲-14,15,16,17.

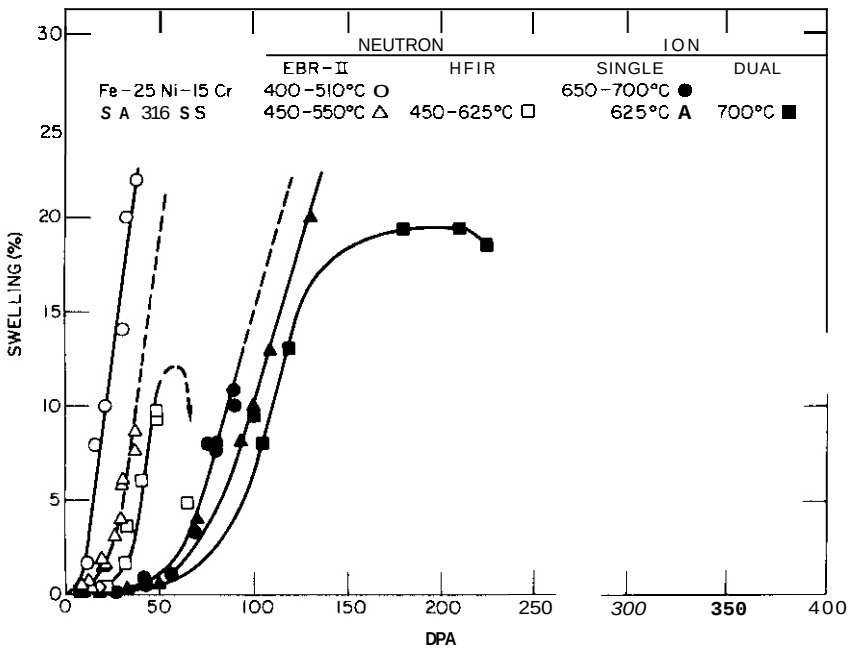

Fig. 5.2.2. Comparison of swelling for the Fe-25Ni-15Cr alloy and solution-annealed 316 stainless steel on neutron and ion irradiation. References for symbols are: ○-18; A-19; □-20; ●-21,22; A-23; ■-24.

neutron irradiation data for the Fe-25Ni-15Cr alloy are interpreted to show a "steady-state" swelling rate of 0.8-1.0%/dpa, whereas the ion-irradiation data suggest a lower rate of 0.2-0.5%/dpa. The neutron irradiation data for the solution annealed 316 stainless steel are interpreted to show a "steady-state" swelling rate of 0.5-0.8%/dpa, and the ion irradiation data suggest a rate of 0.3-0.5%/dpa. On the basis of limited data (especially for the HFIK irradiation), there is evidence for the saturation of swelling in solution annealed 316 stainless steel at high damage levels in the presence of helium. The data presented in Fig. 5.2.2 show that the ion-irradiation technique can be used for a discriminative assessment of potential dimensional instability of these materials in an irradiation environment. Furthermore, the data for solution annealed 316 stainless steel suggest that simultaneous production of radiation damage and helium may have a significant impact on dimensional stability.

Ferritic steels

The swelling of several ferritic steels on neutron irradiation is compared with the swelling of these materials on ion irradiation in Fig. 5.2.3. The neutron- and ion-irradiation data for the ternary ferritic alloys are interpreted to show a "steady-state" swelling rate of 0.01-0.02%/dpa. A lower chromium content in the ternary alloy appears to result in a lower swelling rate, i.e., 0.01%/dpa for EM-12 versus 0.02%/dpa for HT-9. On the basis of the neutron data, the Fe-9,12Cr ferritic alloys may have swelling rates of ~0.06%/dpa. The limited data for the ferritic steels suggest that the swelling values obtained on neutron irradiation or ion irradiation are essentially in agreement.

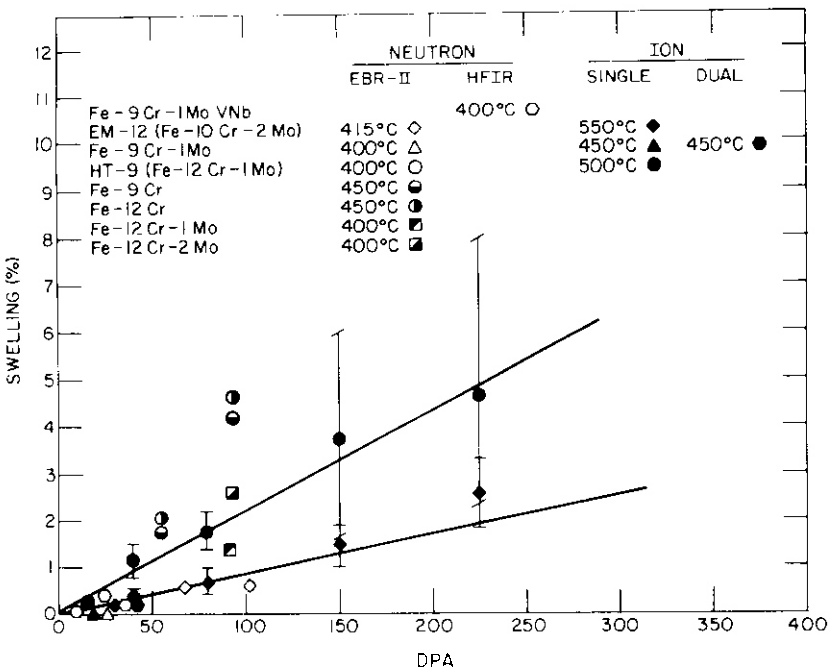

Fig. 5.2.3. Comparison of swelling for ferritic steels on neutron and ion irradiation. References for symbols are: ◇-25,26; ⬡-27; △-28; ◒-29,30; ◑-29,30; 0-30; ◪-30; ◆-31; ●-31; ▲, ⬢-32.

Copper

The swelling of copper on neutron irradiation is compared with the swelling of copper on ion irradiation in Fig. 5.2.4. The extremely limited data on the neutron-induced swelling of copper (100-200 appm oxygen) suggest a swelling rate of ~0.4%/dpa. The ion irradiation data show that the swelling rate is strongly dependent on the oxygen and helium concentration. The swelling rate for copper can be reduced to < 0.001%/dpa by reduction of the oxygen concentration to less than 1 appm for radiation damage levels of < 40 dpa.

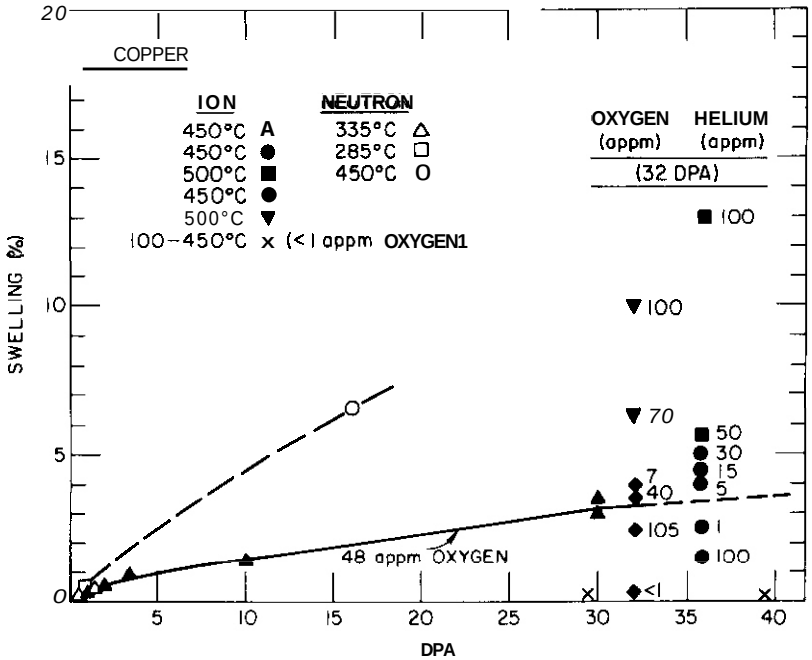

Fig. 5.2.4. Comparison of swelling for copper on neutron and ion irradiation. The references for the symbols are: A-33; ●, ■, ◆, ▼-34; A-35; □-36; O-37.

5.2.5 Discussion

The results of this comparison of experimental swelling data for neutron- and ion-irradiated MFR structural materials are taken to show that the ion-irradiation technique can be utilized for a discriminative assessment of the potential for swelling of these materials. The post-transient (steady-state) swelling rates that were obtained from the experimental data for the structural materials are listed in Table 5.2.1. An apparent difference between the "steady-state" swelling rates for the different materials seems to exist only for the austenitic stainless steels. An additional apparent difference for the stainless steels is a longer incubation period on ion irradiation for the initiation of a 'steady-state" swelling rate. However, insufficient neutron fluence has been accumulated on the stainless steel at the temperature for the ion-irradiations to unambiguously state that the previously mentioned differences are intrinsic to the stainless steels and other materials.[18]

Table 5.2.1. Swelling rate for MFR alloys

Material	Swelling rate (%/dpa) Neutron Irradiation	Ion Irradiation
V-15Cr	~ 0.2	~ 0.2
V-1,5,10,20Ti	< 0.002	< 0.002
V-15Cr-5Ti	< 0.001	< 0.001
Fe-25Ni-15Cr	0.8-1.0	0.2-0.5
S.A. 316 SS	0.5-0.8	0.3-0.5
EM-12 (Fe-10Cr-2Mo)	~ 0.01	~ 0.01
HT-9 (Fe-12Cr-1Mo)	~ 0.02	~ 0.02
Copper (48 appm Oxygen)	--	0.1
Copper (< 1 appm Oxygen)	--	< 0.001
Copper (100-200 appm Oxygen)	~ 0.4[a]	~ 0.3

[a]Estimated oxygen concentration.

On the basis of the data presented for stainless steel and copper, the simultaneous production of radiation damage and implantation of helium has an impact on the microstructural evolution in these irradiated materials. The effect of helium implantation on the microstructural evolution in the vanadium-base alloys and the ferritic steels is less apparent because of their intrinsically low swelling.

It may be considered that structural materials in an MFR can be relatively tolerant of swelling. However, it is possible that high swelling may have an impact on the physical and mechanical properties of a material, *e.g.*, thermal conductivity, elastic moduli, and radiation-induced creep. The ion-irradiation technique can be a useful tool for the rapid evaluation of swelling of candidate MFR materials to high irradiation damage fluence.

5.2.6 Conclusions

1. Ion-irradiation of candidate MFR structural materials can provide a discriminative assessment of the potential for swelling.
2. Ion-irradiation can provide an assessment of the effect of high irradiation damage fluence (100-300 dpa) on the evolution of alloy microstructure.
3. Ion-irradiation can make an assessment of the impact of varying the helium concentration/dpa ratio on swelling of materials.

5.2.7 References

1. J. O. Stiegler, in: Radiation-Induced Voids in Metals, CONF-710601 (1972) 292.
2. F. W. Wiffen, in: Radiation-Induced Voids in Metals, CONF-710601 (1972) 386.
3. R. Carlander, S. D. Harkness, and A. T. bnthanam, in: Effects of Radiation on Substructures and Mechanical Properties of Metals and Alloys, ASTM STP 529 (1973) 399.
4. J. L. Brimhall, H. E. Kissinger, and G. L. Kulcinski, in: Radiation-Induced Voids in Metals, CONF-710601 (1972) 338.
5. Y. Adda, in: Radiation-Induced Voids in Metals, CONF-710601 (1972) 31.
6. A. F. Bartlett, J. H. Evans, E. L. Eyre, E. A. Terry, and J. M. Williams, in: Proceedings of Conference on Radiation Effects and Tritium Technology for Fusion Reactors, CONF-750989 (1975) I-1ZZ.
7. M. P. Tanaka, E. E. Bloom, and J. A. Horak, J. Nucl. Mater. 103 & 104 (1981) 895.
8. J. Eentley and F. W. Wiffen, Nuclear Technology 30 (1976) 376.
9. S. C. Agarwal, D. I. Potter. and A. Taylor, in: Irradiation Effects on the Microstructure and Properties of Metals, ASTM STP 611 (1976) 298.
10. A. T. bnthanam, A. Taylor, and S. D. Harkness, in: Defects and Defect Clusters in B.C.C. Metals and Their Alloys, Nuclear Metallurgy (1973) 302.
11. A. T. bnthanam, A. Taylor, B. J. Kestel, and C. Steves, J. Vac. Sci. Technol. 12 (1975) 529.
12. S. C. Agarwal and A. Taylor, Proceedings of Conference on Radiation Effects and Tritium Technology for Fusion Reactors, CONF-750989 (1975) 1-150.
13. S. C. Agarwal, L. E. Rehn, and F. V. Nolfi, Jr., J. Nucl. Mater. 78 (1978) 336.
14. B. A. Loomis and G. Ayrault, in: Damage Analysis and Fundamental Studies, DOE/ER-0046/12, February 1983, p. 194.
15. B. A. Loomis and D. L. Smith, in: Alloy Development for Irradiation Performance, DOE/ER-0045/13, March 1985, p. 85.
16. B. A. Loomis and D. L. Smith, in: Alloy Development for Irradiation Performance, DOE/ER-0045112, July 1984, p. 66.
17. B. A. Loomis, unpublished results for dual-ion irradiation of three heats of V-15Cr-5Ti alloy.
18. F. A. Garner, J. Nucl. Mater. 117 (1983) 177.
19. J. F. Bates and J. L. Straalsund, Report HEDL-TME-71-139, Hanford Engineering Development Laboratory, 1971.
20. P. J. Maziaz, Ph.D. Thesis, December 1984, p. 195 (to be published as Oak Ridge National Laboratory Report ORNL-6121).
21. M. L. Eleiberg, R. Bajaj, I. M. Baron. A. Chung, R. W. Chickering, and S. Diamond, in: Irradiation Effects on the Microstructures and Properties of Metals, ASTM STP 611 (1976) 315.
22. J. A. Sprague, F. A. Smidt, Jr., J. E. Westmoreland, and P. R. Malmberg, in: Irradiation Effects on the Microstructure and Properties of Metals, ASTM STP 611 (1976) 337.
23. W. G. Johnston, J. H. Rosolowski, and A. M. Turkalo, J. Nucl. Mater. 48 (1973) 330.
24. N. H. Packan and K. Farrell, in: Effects of Radiation on Materials, ASTM STP 782 (1982) 885.
25. D. S. Gelles, J. Nucl. Mater. 122 & 123 (1984) 207.
26. D. S. Gelles, J. Nucl. Mater. 103 & 104 (1981) 975.
27. J. M. Vitek and R. L. Klueh, J. Nucl. Mater. 122 & 123 (1984) 254.
28. D. S. Gelles and L. E. Thomas, in: Alloy Development for Irradiation Performance, DOE/ER-004518, September 1982, p. 343.

29. D. S. Gelles and L. E. Thomas, in: Proceeding of the Topical Conference on Ferritic Alloys for Use in Nuclear Energy Technologies, June 1983, p. 559.
30. D. S. Gelles and R. L. Meinecke. in: Alloy Development for Irradiation Performance, DOE/ER-0045/11, March 1984, p. 103.
31. F. A. Smidt, Jr., P. R. Malmbery, J. A. Sprayue, and J. E. Westmoreland, in: Irradiation Effects on the Microstructures and Properties of Metals, ASTM STP 611 (1976) 227.
32. G. Ayrault, J. Nucl. Mater., 114 (1983) 34.
33. L. D. Glowinski and C. Fiche, J. Nucl. Mater. 61 (1976) 22.
34. L. D. Glowinski and C. Fiche, J. Nucl. Mater. 61 (1976) 29.
35. M. Labbe, G. Brebec, and J. P. Poirier, J. Nucl. Mater. 49 (1973/74) 232.
36. J. L. Brimhall and H. E. Kissinger, Radiation Effects 15 (1972) 259.
31. H. R. Brager and F. A. Garner, in: Damage Analysis and Fundamental Studies, DOE/ER-0046/19, November 1984, p. 131.
38. S. J. Zinkle and G. L. Kulcinski, in: Oamaye Analysis and Fundamental Studies, DOE/ER-0046/20, February 1985, p. 77.

6. **INNOVATIVE MATERIAL** CONCEPTS

7. FERRITIC STEELS

7.1 MICROSTRUCTURE OF ALLOY HT-9 AND MODIFIED 9Cr-1Mo ALLOY IRRADIATED IN THE UBR

J. A. Sprague and J. R. Reed (Naval Research Laboratory)

7.1.1 ADIP Task

The Office for Fusion Energy/Department of Energy has established the need to investigate ferritic alloys under the ADIP program task, Ferritic Steels Development (Path E).

7.1.2 Objective

Alloy HT-9 and Modified 9Cr-1Mo are being evaluated for potential application as first-wall and structural materials in magnetic fusion reactors. The objectives of the current research task were to examine the microstructural changes produced in these alloys by irradiation at 149C (300F) and to correlate these changes with previous notch ductility and fracture toughness data from the same specimens.

7.1.3 Summary

TEM disks were prepared from tested Charpy-V specimens of Alloy HT-9 and Modified 9Cr-1Mo which had been irradiated at 149C to ~0.8 x 10^{20} n/cm^2, E > 0.1 MeV. Examination of these disks showed that the irradiation had produced small defect clusters, <10 nm in diameter, in both alloys. These defect clusters were the apparent source of the hardening and thus the shift in ductile-brittle transition temperature previously observed for these materials. No changes in precipitate structure could be observed for either alloy.

7.1.4 Progress and Status

7.1.4.1 Introduction

As described in previous reports [1-3], Alloy HT-9 and Modified 9Cr-1Mo have been irradiated in the research reactor at State University of New York at Buffalo (UBR) to assess the irradiation embrittlement of these alloys in the temperature range between 100 and 300C. Although the neutron fluence available for practical irradiation times in this reactor are low relative to target fluences for fusion reactor first wall applications, the UBR offers good temperature control in the range below 300C, which is a significant range for some proposed fusion reactor designs. Also, the large irradiation volume available in UBR allowed direct comparison of results from standard and subsize notch ductility and fracture toughness specimens. to aid in the interpretation of data from higher fluence irradiation sources, such as HFIR and FFTF. The overall purpose of the UBR experiments, therefore, was to assess the relative irradiation sensitivity of Alloy HT-9 from both Argon-Oxygen Decarburization (AOD) and Electroslag Remelt (ESR) melt practices and of an ESR heat of Modified 9Cr-1Mo and to determine the mechanisms producing irradiation hardening and embrittlement in the temperature range below 300C in these materials. Subsize Charpy-V specimens were supplied to ORNL for the study of specimen size effects. In the current reporting period, the irradiation-induced microstructural changes in these alloys were studied by TEM, and these were related to the previous tensile and fracture results.

7.1.4.2 Experimental Procedures

The materials studied by TEM were the ESR heats of Alloy HT-9 and Modified 9Cr-1Mo, following irradiation at 149C to a fluence of 0.8 x 10^{20} n/cm^2, E > 0.1 MeV. Details of alloy chemistry, heat treatment, irradiation, and mechanical testing have been well covered in previous reports [1-3] and will not be repeated here. Following testing, TEM specimens were prepared from broken C_V specimens by: (1) cutting off the fracture surface with a low-speed diamond saw; (2) trepanning a 3-mm diameter rod on one end of the remaining stub with an in-cell milling machine; (3) cutting several disks, approximately 250 µm thick, from this rod, using the low-speed diamond saw; (4) mechanically grinding the disks to 100 µm; and (5) electropolishing in a standard dual-jet electropolisher. The thinned specimens were examined with a JEM-200CX electron microscope operating at 200 kV.

7.1.4.3 Results and Discussion

The pre-irradiation heat treatments given to both alloys produced microstructures consisting principally of well-tempered martensite. These general microstructural features, as shown in Figs. 7.1.1 and 7.1.2, were not altered by the irradiation exposure. No significant changes were observed in the carbides at the lath boundaries, or in the low densities of line dislocations present prior to irradiation. When imaged at higher magnification, as illustrated in Figs. 7.1.3 and 7.1.4, both the Alloy HT-9 and the Modified 9Cr-1Mo were found to contain small defect clusters with diameters less than 10 nm. The contrast of these clusters was consistent with their identification as dislocation loops. but the ferromagnetic nature of the specimens prevented the necessary tilting experiments to determine their Burgers vectors and habit planes. The distributions of these defect clusters within the martensite laths were non-uniform, implying some type of heterogeneous nucleation mechanism was operating. In fact,

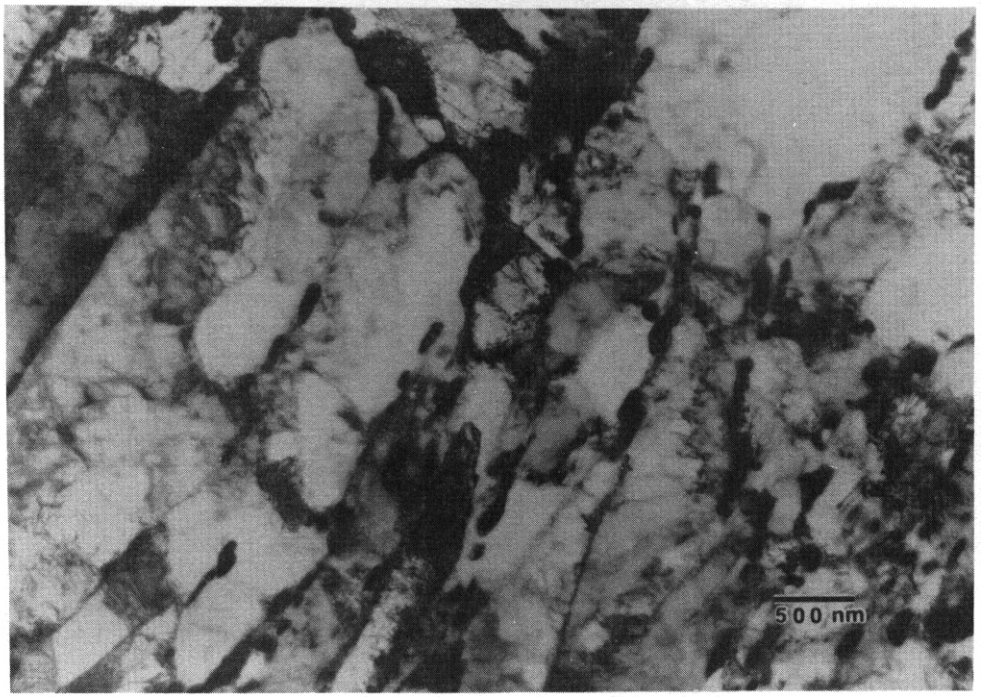

Fig. 7.1.1. Low-magnification electron micrograph of the microstructure of Alloy HT-9 following irradiation at 149C to a fluence of 0.8 x 10^{20} n/cm^2, E > 0.1 MeV.

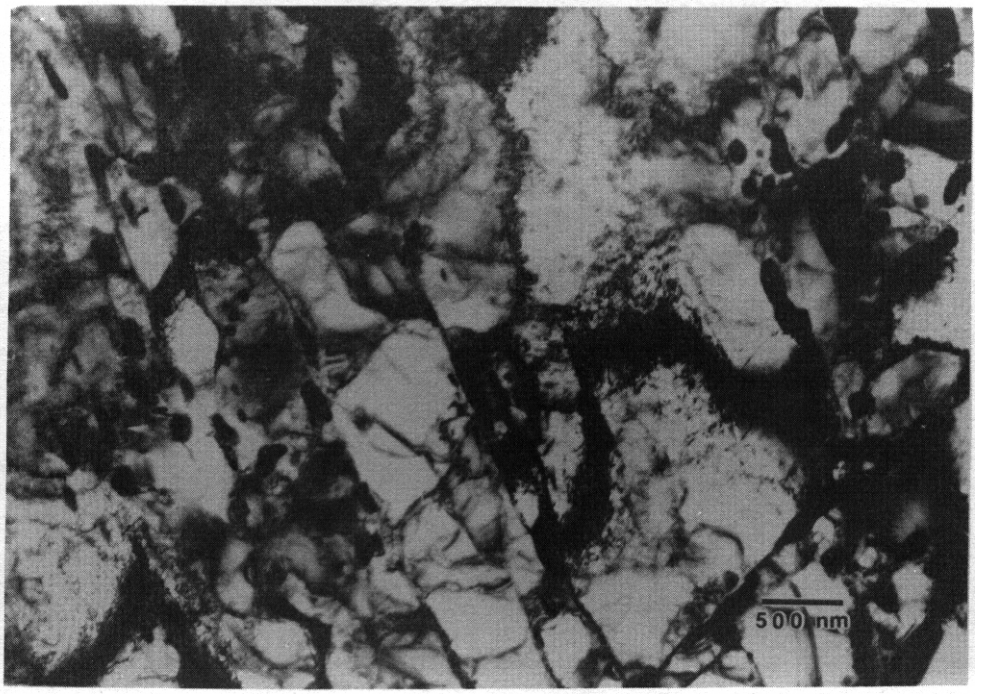

Fig. 7.1.2. Low-magnification transmission electron micrograph of the microstructure of Modified 9Cr-1Mo following irradiation at 149C to a fluence of 0.8 x 10^{20} n/cm^2, E > 0.1 MeV.

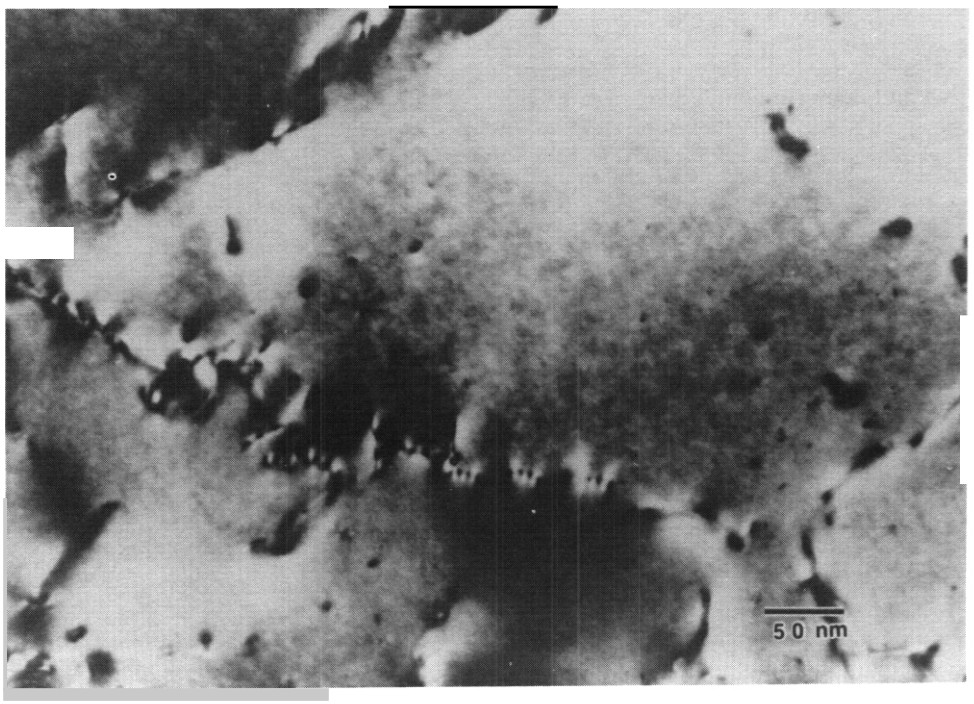

Fig. 7.1.3. Brightfield TEM image of defect clusters formed in Alloy HT-9 by irradiation at 149C to a fluence of 0.8 x 10^{20} n/cm^2, E > 10.1 MeV.

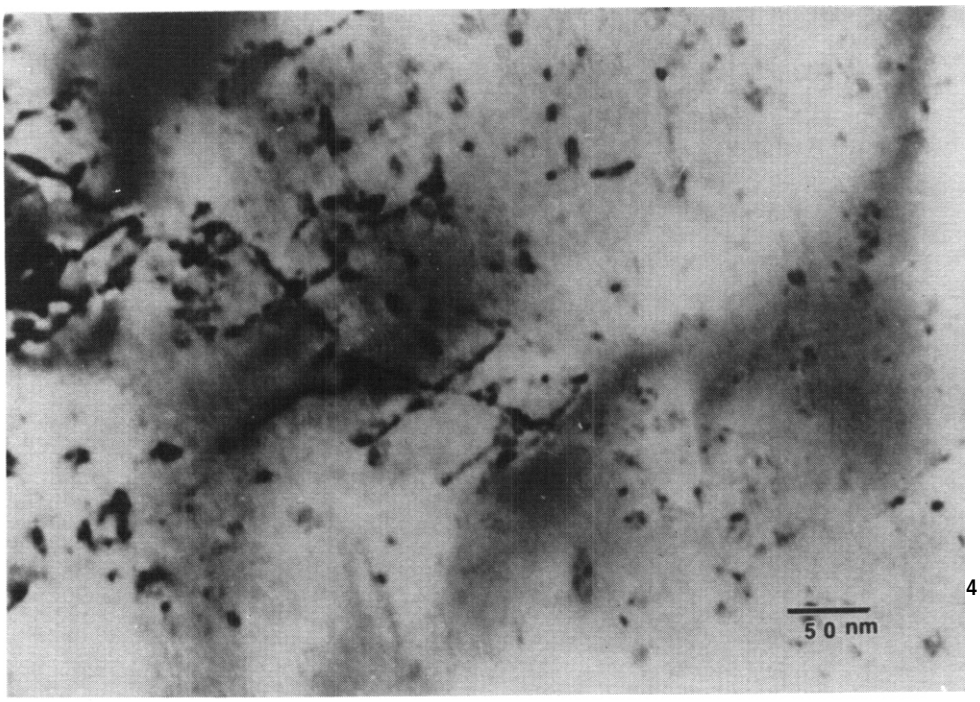

Fig. 7.1.4. Brightfield TEM image of defect clusters formed in Modified 9Cr-1Mo by irradiation at 149C to a fluence of 0.8 x 10^{20} n/cm^2, E > 0.1 MeV.

entire regions, the size of those shown here, containing no visible defect clusters at all could be found in both alloys. Thus, the apparently higher defect density shown here for the Modified 9Cr-1Mo should not be interpreted as representing an overall higher defect concentration.

The observation of defect clusters causing irradiation hardening and embrittlement is consistent with a number of previous investigations (eg Ref. 4) of irradiated iron alloys and pressure vessel steels, for irradiations at temperatures below 300C. The defect distributions observed in the present specimens are also similar to those reported by Gelles. et al[5] for Alloy HT-9 and Modified 9Cr-1Mo irradiated to a higher fluence at 55C in HFIR. The *two* principal differences in the present results were slightly larger defect sizes and lower defect densities, as would be expected for the higher irradiation temperature and lover irradiation exposure. Although it is not possible, from the contrast observed in either of these experiments, to eliminate the possibility that the observed clusters could be small precipitates, their most reasonable identification would be as interstitial dislocation loops, due to the low mobility of vacancies in iron-based alloys at temperatures of 55 - 150C. While it is possible to produce vacancy-type loops by the collapse of vacancy-rich cores of displacement cascades, this collaspe has not been observed to occur in iron[6], for self-ion implantation at room temperature. Thus, the low-temperature vacancy-type irradiation defects are not visible by TEM, although they can produce hardening.

7.1.5 Future Work

Further work on the UBR-irradiated specimens will focus on shear-punch and microhardness measurements on specimens cut from the teated C_v specimens to provide a baseline for predictions of irradiation embrittlement from determinations of flow properties on small specimens.

7.1.6 References

1. J. R. Hawthorne, "Postirradiation Notch hlctility and Fracture Toughness Behavior of AOD Heat of Alloy HT-9," pp. 336-341 in Alloy Development for Irradiation Performance, Semiannual Progress Report for period ending March 31, 1982, DOE/ER 004518.

2. J. R. Hawthorne, "Postirradiation Notch Ductility Tests of ESR Alloy HT-9 and Modified 9Cr-1Mo Alloy from UBR Reactor Experiments," pp. 136-142 in Alloy Development for Irradiation Performance, Semiannual Progress Report for period ending Sept. 30, 1983, DOE/ER-0045/11.

3. J. R. Hawthorne, "Postirradiation Fracture Toughness Tests of ESR Alloy HT-9 and Modified 9Cr-1Mo Alloy from UBR Reactor Experiments," pp. 86-99 in Alloy Development for Irradiation Performance, Semiannual Progress Report for period ending March 31, 1984, DOE/ER-0045/12.

4. P. A. Smidt, Jr. and J. A Sprague, "Property Changes Resulting from Impurity-Defect Interactions in Iron and Pressure Vessel Steel Alloys." Effects of Radiation on Substructure and Mechanical Properties of Metals and Alloys, ASTM STP 529, 1973. pp. 78-91.

5. D. S. Gelles, W. L. Hu, F. H. Huang, and G. D. Johnson, "Effects of HFIR Irradiation at 55C on the Microstructure and Toughness of HT-9 and 9Cr-1Mo," pp. 115-135 in Alloy Development for Irradiation Performance, Semiannual Progress Report for period ending Sept. 30, 1983, DOE/ER-0045/11.

6. M. L. Jenkins, C. A. English, and B. L. Eyre, "Heavy-Ion Irradiation of Iron," Phil. Mag. 38A, 1978, pp. 97-114.

7.2 MICROSTRUCTURAL/MICROCOMPOSITIONAL ANALYSIS OF NORMALIZED-AND-TEMPERED 9Cr-1MoVNb AND 12Cr-1MoVW STEELS DOPED WITH 2 wt % NICKEL — P. J. Maziasz and R. L. Klueh (Oak Ridge National Laboratory)

7.2.1 ADIP Task

ADIP Tasks are not defined for Path E, ferritic steels in the 1978 Program Plan.

7.2.2 Objectives

This investigation was undertaken to evaluate whether or not doping with 2 wt % Ni (to increase helium generation during HFIR irradiation) affected the microstructure or precipitation in the normalized-and-tempered condition prior to irradiation.

1.2.3 *Summary*

Normalized-and-tempered 9Cr-1MoVNb and 12Cr-1MoVW steels are tempered martensite that have recovered ferrite subgrain structures with $M_{23}C_6$ and MC precipitate and a few dislocations. The 12Cr steel has more precipitate, which is almost exclusively $M_{23}C_6$; the 9Cr steel has less precipitation, but a larger fraction of fine MC. Both steels doped with 2 wt % Ni have more refined precipitate and/or subgrain structures and higher dislocation concentrations, but these changes are consistent with their lower tempering temperatures relative to undoped materials. Nickel doping does not change the precipitate phases observed ($M_{23}C_6$ and MC) or the relative phase fractions, and does not appreciably affect phase compositions.

7.2.4 Progress and Status

7.2.4.1 Introduction

Ferritic steels are being investigated for fusion reactor first-wall applications because they demonstrate excellent void swelling resistance during fast breeder reactor (FBR) irradiation.[1-4] However. only minuscule levels of transmutation helium are generated during FBR irradiation compared to the helium to be generated in a fusion reactor first wall. 9Cr-1MoVNb and 12Cr-1MoVW ferritic steels have been doped with 2 wt % Ni to examine the effects of higher helium generation on void swelling resistance and mechanical properties during HFIR irradiation. The purpose of this work is to determine whether or not nickel doping has appreciably altered the normalized-and-tempered microstructure of these steels prior to irradiation. Previous work has characterized the microstructure of the undoped steels in the normalized-and-tempered condition,[5] and has determined tempering conditions for the nickel-doped steels on the basis of hardness changes.[6]

7.2.4.2 Experimental

Alloy compositions are given in Table 7.2.1, and the normalizing-and-tempering heat treatments are listed in Table 7.2.2. Transmission electron microscopy (TEM) disks, 3 mm in diameter, were punched from 0.254-mm-thick sheet prior to normalizing and tempering. Carbon film extraction replicas were produced prior to polishing the disk to electron transparency and suspended on beryllium grids for precipitate analysis. Thin-foil microstructural analysis was performed on a JEM 100C electron microscope equipped with a special objective lens polepiece designed to lower the magnetic field at the specimen (referred to as an AMG polepiece). Analytical electron microscopy (AEM) was performed on a Philips EM400 microscope equipped with

Table 7.2.1. Compositions of 9Cr-1MoVNb and 12Cr-1MoVW heats of steel with and without nickel doping

Alloy designation	Heat number	Concentration,[a] wt %										
		Cr	Mo	Ni	Mn	C	Si	V	Nb	Ti	W	N
9Cr-1MoVNb	(XA 3590)	8.6	1.0	0.1	0.36	0.09	0.08	0.21	0.063	0.002	0.01	0.05
9Cr-1MoVNb + 2% Ni	(XA 3591)	8.6	1.0	22	0.36	0.064	0.08	0.22	0.066	0.002	0.01	0.053
12Cr-1MoVW	(XXA 3587)	12	0.9	0.4	0.5	0.2	0.18	0.27	0.018	0.003	0.54	0.02
12Cr-1MoVW + 2% Ni	(XXA 3589)	11.7	1.0	2.3	0.5	0.2	0.14	0.31	0.015	0.003	0.54	0.02

[a]Balance iron.

a field emission gun (FEG) for very high electron intensity at small probe sizes and with EDAX detector and computer. A beryllium cold stage, cooled with liquid nitrogen, was used to minimize contamination and x-ray background during AEM analysis. Several individual particles were analyzed for each phase and size class, while broad beams (electron probe 2–36 μm in diameter) were used to blend x-ray spectra from many particles into a homogenized spectra for either average phase compositions or relative phase fractions for the total precipitate.[7]

Table 7.2.2. Normalizing and tempering conditions for various steels

Alloy	Normalization	Tempering
9Cr-1MoVNb	0.5 h at 1040°C	1 h at 760°C
9Cr-1MoVNb + 2% Ni	0.5 h at 1040°C	5 h at 700°C
12Cr-1MoVW	0.5 h at 1050°C	2.5 h at 780°C
12Cr-1MoVW + 2% Ni	0.5 h at 1050°C	5 h at 700°C

7.2.4.3 Results

9Cr-1MoVNb – The normalized-and-tempered 9Cr-1MoVNb had a microstructure of polygonized and fairly dislocation-free, small ferrite subgrains, with precipitate particles along the subgrain boundaries, as shown in Fig. 7.2.1(a) and (c). Phase identification and analysis via AEM on an extraction replica indicated predominantly $M_{23}C_6$ precipitation with a minor amount of MC formed as small particles within the small subgrains (Fig. 7.2.2 and Table 7.2.3). Very tiny (<17 nm in diameter) particles of nearly pure copper were also found on the replica among the MC particles (Table 7.2.3). Compositionally, the MC phase was distributed bimodally between vanadium-rich and niobium-rich particles (Fig. 7.2.3 and Table 7.2.3). Despite particle-to-particle variations, there was not a continuous or random variation in MC composition, but a separation into two distinct classes. By contrast the $M_{23}C_6$ phase was very uniform in composition from particle to particle, containing mainly chromium with some iron and lesser amounts of vanadium and molybdenum (4–5 at. %).

The 2 wt % Ni-doped steel shows less recovery during tempering, with lenticular grains which had higher dislocation concentrations than found in the undoped steel [Fig. 7.2.1(c) and (d)]. The amount of precipitation found in the nickel-doped steel seemed to be less than found in the undoped steel, judging from the replicas in Fig. 7.2.1 (a) and (b); however, differences in etching depth during replication could also create such an effect. In-foil analysis, however, also suggested slightly less precipitation in the nickel-doped alloy. Particle sizes were roughly similar, but the undoped alloy contained more of the coarser $M_{23}C_6$ particles. These differences in microstructure and precipitation could easily be accounted for by the differences in tempering conditions and may not be due solely to the nickel doping (see Table 7.2.2).

ORNL PHOTO 2773-85

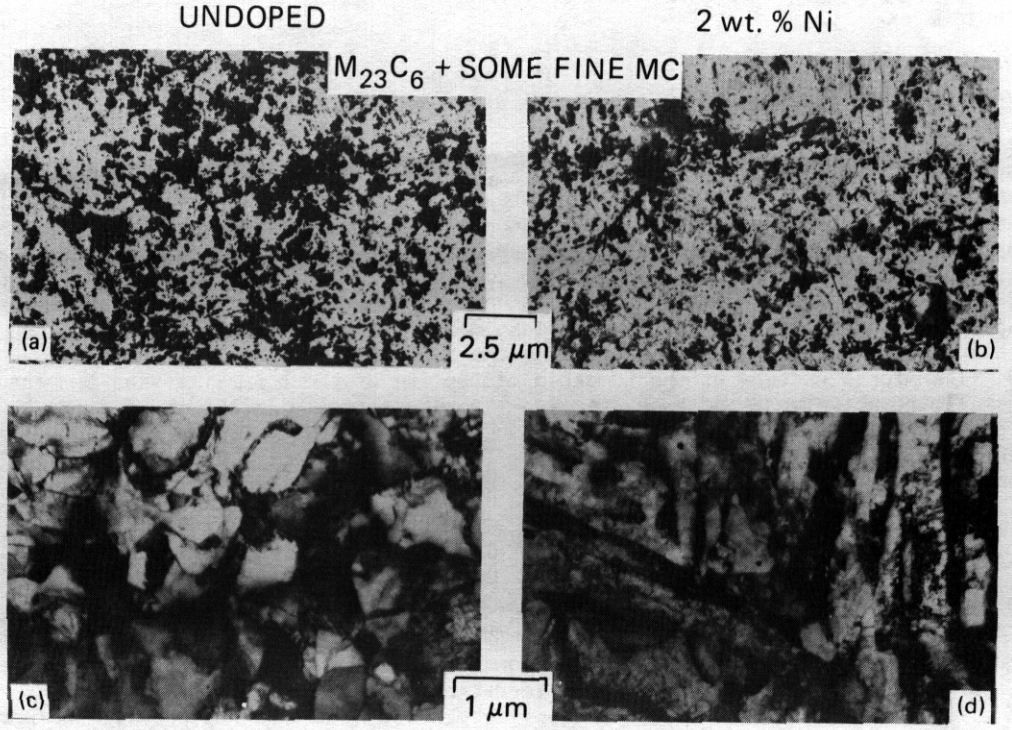

Fig. 7.2.1. Microscopy of precipitation on extraction replicas (a), (b) and of the overall microstructure in-foil (c), (d) of normalized-and-tempered 9Cr-1MoVNb steel after normalizing and tempering (1 h at 760°C).

ORNL PHOTO 2775-85

EXTRACTION REPLICA,
EM 400, FEG

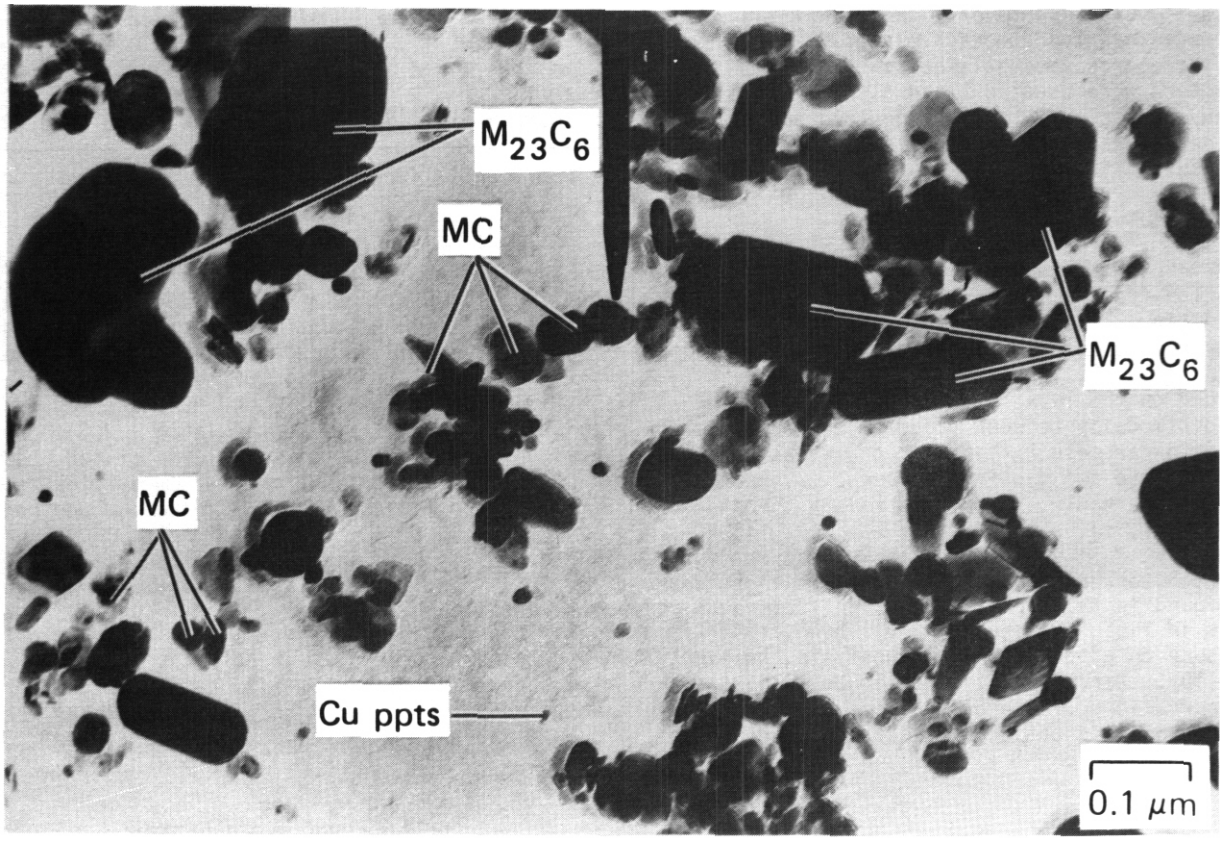

SA + 1 h AT 760°C

Fig. 7.2.2. Higher magnification microscopy of small particles, including MC phases and copper precipitates, on a replica extracted from 9Cr-1MoVNb steel after normalizing and tempering (1 h at 760°C).

The lower tempering temperature of the nickel-doped samples would cause less recovery and possibly less precipitation, if the precipitation kinetics are sluggish and/or temperature sensitive. With this caveat, nickel doping itself does not appear to seriously change the microstructure.

The AEM analysis on replicas also indicates no appreciable effect of nickel-doping on phase compositions or relative phase fractions (Table 7.2.3). The precipitation is still dominated by $M_{23}C_6$ (relative phase fractions 15% MC/85% $M_{23}C_6$). Compositionally, the $M_{23}C_6$ appears to contain a little more chromium, while the MC phase is still bimodally distributed among mainly vanadium-rich carbides with some niobium-rich carbides (possibly these contain more niobium than in the undoped steel).

12Cr-1MoVW — The microstructure of the tempered martensite of the normalized-and-tempered 12Cr-1MoVW steel contains small, relatively dislocation-free ferrite subgrains similar to the 9Cr-1MoVNb steel, but with much more precipitation of $M_{23}C_6$ [Fig: 7.2.4(a) and (c)]. The $M_{23}C_6$ particles more heavily decorate subgrain boundaries or lath packet boundaries in the 12Cr alloy [see Fig. 7.2.5(a)]. AEM replica analysis indicates the presence of very small vanadium-rich MC particles within the subgrains, but the MC is only a minute portion of the total carbide precipitation. The $M_{23}C_6$ is compositionally similar to that found in the 9Cr steel and does not vary with particle size; the $M_{23}C_6$ does contain a trace amount of tungsten in the 12Cr-1MoVW alloy. The vanadium-rich MC in the 12Cr alloy is also very similar to that found in the 9Cr alloy, but with a significant enrichment of titanium, which is present as only a residual element in the 12Cr alloy. The niobium enrichment in the MC phase, despite reduced MC formation and the reduced niobium content (a residual in this alloy), is only present in slightly smaller amounts in the 12Cr-1MoVW steel than the 9Cr-1MoVNb steel. These observations may signal that niobium and titanium additions together are important to MC formation characteristics of these ferritic steels.

The 2 wt % Ni-doped 12Cr-1MoVW steel again shows less recovery microstructurally. and more $M_{23}C_6$ particles which are smaller relative to the undoped steel [Figs. 7.2.4 and 7.2.5(a) and (b)]. Comparison of Fig. 7.2.4(c) and (d) suggests a somewhat smaller subgrain size in the nickel-doped steel; higher magnification microscopy in Fig. 7.2.5(c) and (d) indicates a higher dislocation concentration near precipitates

Table 7.2.3. Compositional analysis via XEDS of precipitates extracted on replicas from normalized-and-tempered 9Cr-1MoVNb and 12Cr-1MoVW steels

Phase analyzed	Phase composition,[a] at. %											Comments
	Si	P	Ti	V	Cr	Fe	Ni	Cu	Nb	Mo	W	
9Cr-1MoVNb												
$M_{23}C_6$	0.6	0.8	n.d.[b]	4.2	58.4	29.6	n.d.	n.d.	1.3	5.2	n.d.	[5][c] large, >350 nm in size
Vanadium-rich MC	1.6	1.3	0.6	62.6(±9)	16.6	1.6	n.d.	0.7	14.2	1.1	n.d.	[6] small, 17–60 nm in size
Niobium-rich MC	2.3	2	2.3	33	9.2	1.1	0.1	n.d.	49(±10)	1.3	n.d.	[2] small, same as above
Copper-rich phase	n.d.	0.8	0.2	0.6	0.2	8.1	n.d.	89.4	0.2	0.5	n.d.	[1] small, <17 nm in diameter
Broad-beam (all precipitates)	0.9	0.7	0.4	9.7	53.3	26.5	0.1	0.4	3.4	4.8	n.d.	[2] r.p.f.[d] — 85% $M_{23}C_6$/15% MC
9Cr-1MoVNb + 2% Ni												
$M_{23}C_6$	0.5	0.2	0.2	3.6	62	25.4	1.2	0.2	0.8	6	n.d.	[6] large, >350 nm in size
$M_{23}C_6$	0.6	0.2	0.2	6.2	68	17.1	1.0	n.d.	0.4	6.2	n.d.	[3] Small, <150 nm in size
Vanadium-rich MC	0.3	0.3	0.6	69.2	14.0	0.8	n.d.	0.2	14.0	0.8	n.d.	[7] small, 17–60 nm in size
Niobium-rich MC	1.3	1.2	2.1	26.5	5.3	0.8	n.d.	0.3	62.4	0.5	n.d.	[2] small, same as above
Broad-beam (small precipitates)	0.8	0.4	0.2	26.8	39.6	13.7	0.6	0.4	13.7	4	n.d.	[1] small, r.p.f. — 55% $M_{23}C_6$/45% MC
Broad beam (all precipitates)	2.2	0.4	0.3	11.5	52.5	22.0	1.0	0.7	4.4	5.0	n.d.	[1] r.p.f.[d] — 85% $M_{23}C_6$/15% MC
12Cr-1MoVW												
$M_{23}C_6$	n.d.	n.d.	n.d.	2.0	64.1	27.8	0.3	n.d.	0.1	4.5	0.9	[7] large, >150 nm in size
$M_{23}C_6$	n.d.	n.d.	n.d.	4.6	65.0	24.0	0.2	n.d.	0.6	4.8	0.9	[1] small, <90 nm in size
Vanadium-rich MC	1.0	n.d.	4.3	64.0	18.4	1.0	n.d.	1.0	9.2	1.1	0.2	[6] small, 35–70 nm in size
Broad-beam (small precipitates)[e]	2.0	n.d.	1.1	25.6	46.4	16.3	0.2	0.7	3.8	3.2	0.6	[1] small, r.p.f. — 60% $M_{23}C_6$/40% MC
Broad-beam (smaller and larger precipitates)	3.1[e]	n.d.	0.4	7.7	58.4	23.1	0.3	1.1	1.2	4.1	0.8	[1] r.p.f. — 90% $M_{23}C_6$/10% MC
Broad-beam (all precipitates)	2.4	n.d.	0.2	2.8	63.1	25.3	0.3	0.3	0.5	4.4	0.8	[1] r.p.f. — 99% $M_{23}C_6$/1% MC
12Cr-1MoVW + 2% Ni												
$M_{23}C_6$	n.d.	n.d.	n.d.	3.0	67	23.1	1.2	n.d.	n.d.	5.0	0.8	[5] large, >150 nm in size
$M_{23}C_6$	0.1	n.d.	n.d.	1.5–6	67.8	19	0.1	n.d	n.d.	5.6	0.8	[4] small, <90 nm in size
Vanadium-rich MC	4.5	n.d.	15.7	60.4	9.0	1.5	0.1	n.d.	9.7	1.0	0.1	[6] small, 30–70 nm in size
Broad-beam (small precipitates)	n.d.	n.d.	1.5	18.0	54.1	17.8	1.0	n.d.	2.2	4.6	0.7	[1] small, r.p.f. — 75% $M_{23}C_6$/25% MC
Broad-beam (smaller and larger precipitates)	n.d.	n.d.	n.d.	2.5	66.3	24.0	1.2	n.d.	n.d.	4.9	0.8	[1] small, r.p.f. — 99% $M_{23}C_6$/1% MC
Broad-beam (all precipitates)	n.d.	n.d.	n.d.	2.6	66.0	24.3	1.3	n.d.	n.d.	5.0	0.8	[1] r.p.f. — 99% $M_{23}C_6$/1% MC

[a]Normalized concentration of metal atoms heavier than aluminum.
[b]n.d. = none detected.
[c]Numbers in brackets indicate the number of individual particles analyzed.
[d]r.p.f. = relative phase fraction.
[e]Small particles analyzed within a small subgrain, outlined by coarser $M_{23}C_6$ particles at the boundaries.

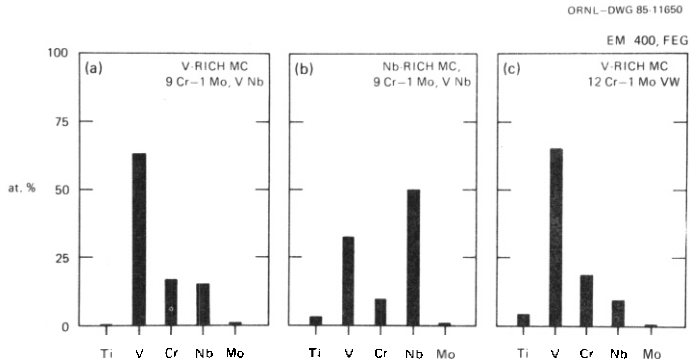

Fig. 1.2.3. Histograms of elemental composition of vanadium-rich MC carbides in normalized-and-tempered (a) 9Cr-1MoVNb, (b) 12Cr-1MoVW, and (c) niobium-rich MC carbides in 9Cr-1MoVNb. These are averaged compositions from analysis of several individual small particles extracted on carbon replicas.

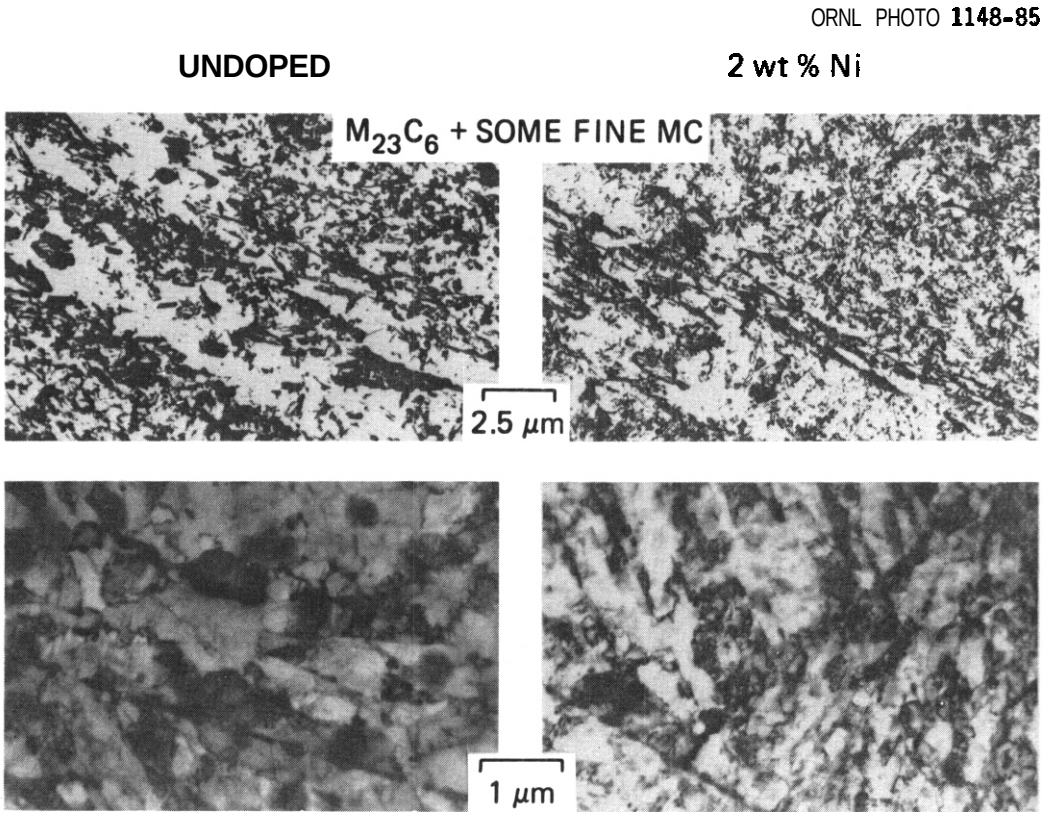

Fig. 1.2.4. Microscopy of precipitation on extraction replicas (a),(b) and of the overall microstructure in-foil (c),(d) of normalized-and-tempered 12Cr-1MoVW steels, undoped (a),(c) and doped with 2 wt % Ni (b),(d).

and/or boundaries in the nickel-doped steel as well. Again, however. such microstructural behavior seems more likely due to the lower tempering temperature of the nickel-doped alloy. If the precipitation kinetics are not sluggish, then lower temperature tempering should cause a refinement in the particle size distribution.

The AEM replica analysis again indicates no appreciable effect of nickel doping on phase compositions and none on phase identities or relative fractions. There is, however, much more titanium in the vanadlum-rich MC formed in the nickel-doped alloy, with a corresponding reduction in the chromium content of that phase. Whether this is due to the difference in tempering temperature is not clear, but it again may suggest a beneficial role of titanium as a strong MC stabilizer together with vanadium and niobium.

ORNL PHOTO 2774-85

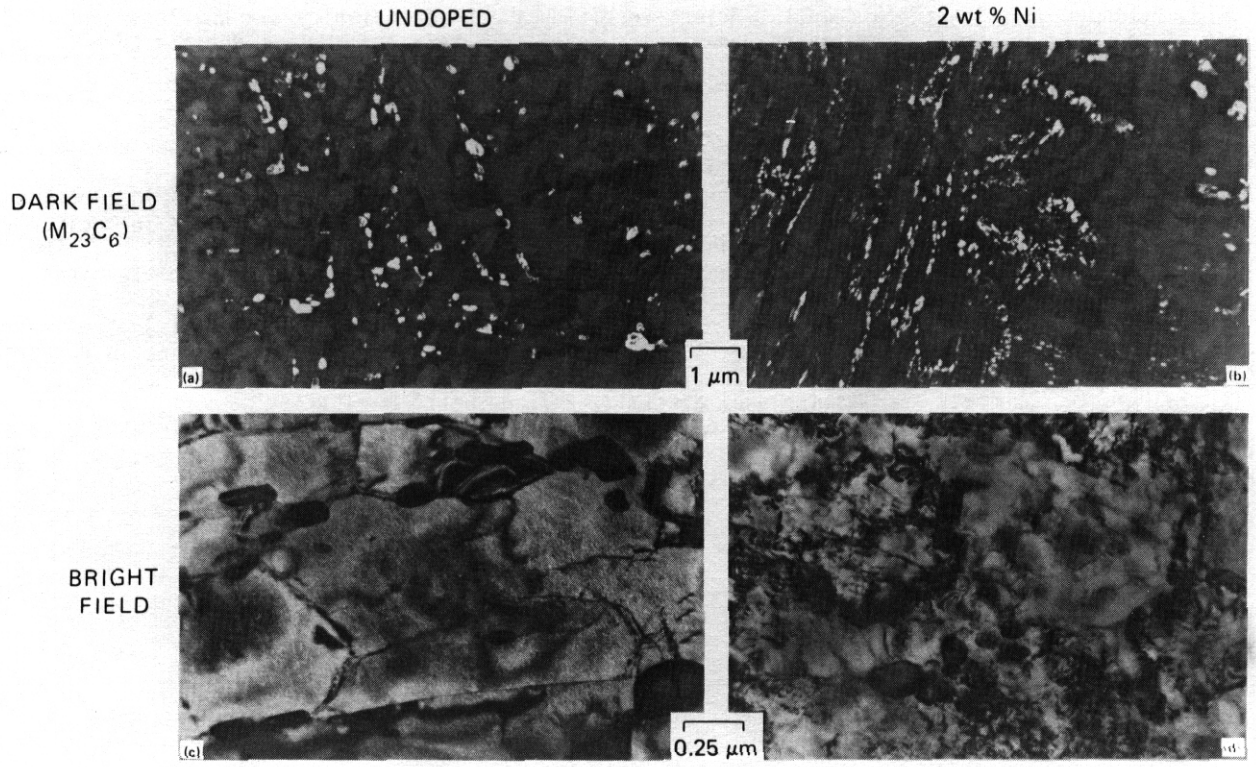

Fig. 7.2.5. Microscopy to illustrate the differences, due to either nickel doping or tempering conditions, in precipitation and dislocation structure observed in 12Cr-1MoVW. Dark-fields (a),(b) show more and finer $M_{23}C_6$ precipitation along cell boundaries in the nickel-doped alloy, whereas bright fields show more dislocations in the nickel-doped material as well. However, such effects are consistent with the different tempering treatments the two alloys received.

7.2.5. Conclusions

1. After normalizing and tempering, the tempered martensitic microstructures of both 9Cr-1MoVNb (tempered 1 h at 760°C) and 12Cr-1MoVW (tempered 2.5 h at 780°C) form polygonized, small subgrains of ferrite that are fairly dislocation free and contain precipitates.
2. The 9Cr-1MoVNb steel contains a mixture of $M_{23}C_6$ and MC carbides (relative phase fractions — 85% $M_{23}C_6$/15% MC); the 12Cr-1MoVW steel contains more precipitation overall, which consists almost exclusively of $M_{23}C_6$ (relative phase fractions — 99% $M_{23}C_6$/1% MC).
3. Compositionally, $M_{23}C_6$ is similar in both 9Cr-1MoVNb and 12Cr-1MoVW. The former, however, contains an MC phase population bimodally distributed between vanadium-rich and niobium-rich particles (the vanadium-rich MC dominates). The 12Cr alloy forms only vanadium-rich MC, which also contains appreciable titanium and niobium, although these are residual elements in the steel.
4. The 2 wt % Ni doped heats of 9Cr-1MoVNb and 12Cr-1MoVW were tempered at lower temperatures for longer times (5 h at 700°C) than the undoped heats of steel. Their structures show less recovery with either lenticular subgrains and/or higher dislocation concentrations within the subgrains than the undoped steels. The nickel-doped 9Cr steel shows less precipitation whereas the nickel-doped 12Cr steel shows more small precipitates than the undoped steels.
5. Nickel doping did not change the phase identities, relative fractions, or appreciably affect phase compositions in either steel in the normalized-and-tempered condition.

7.2.6. Future Work

We plan to examine the effects of similar tempering conditions on the microstructural development in nickel-doped and undoped steels. The present information will also be used to understand further microstructural evolution during either subsequent neutron irradiation and thermal aging. The microstructure will also be correlated with the mechanical behavior of these steels before and after irradiation.

7.2.7. References

1. J. Erler et al., "Le Compartement D'Aciers Ferritiques Sous Irradiation aux Neutrons Rapides," pp. 11–16 in Proc. Inter. Conf. Irradiation Behavior of Metallic Materials for Fast Reactor Core Components, held June 4–8, 1979, Ajaccio, France.

2. E. A. Little et al., "Development of Ferritic-Martensitic Steels For Fast Reactor Applications," pp. 31–37, ibid., ref. 1.

3. R. W. Powell et al., "Swelling of Several Commercial Alloys Following High Fluence Neutron Irradiation," J. Nucl. Mater. 103&104, 969–74 (1981).

4. D. S. Gelles and L. E. Thomas, "Effects of Neutron Irradiation on Microstructures in Experinental and Commercial Ferritic Alloys," pp. 559–68 in Proc. Topical Conf. Ferritic Alloys for Use in Nuclear Energy Systems. eds., J. W. Davis and D. J. Michel, The Metallurgical Society of AIME, Warrendale, PA, 1984.

5. J. M. Vitek and R. L. Klueh, "Precipitation Reactions During the Heat Treatment of Ferritic Steels," Met. Trans. 14A, 1047–55 (1983).

6. R. L. Klueh, J. M. Vitek, and M. L. Grossbeck, 'Nickel-Doped Ferritic (Martensitic) Steels for Fusion Reactor Irradiation Studies: Tempering Behavior and Unirradiated and Irradiated Tensile Properties," pp. 646-64 in Effects of Radiation on Materials: Eleventh Conference, ASTM-STP-782, eds. H. R. Brager and J. S. Perrin, American Society for Testing and Materials, Philadelphia, PA, 1982.

7. P. J. Maziasz and G. R. Cdette, "Wide Area Beam Averaged AEM of Precipitate Particles Extracted on Replicas from Type 316 Stainless Steel," pp. 198–99 in Proc. 41st Annual Meeting of EMSA, ed., G. W. Bailey, San Francisco Press, San Francisco, CA, 1983.

7.3 SOME EFFECTS OF INCREASED HELIUM GENERATION ON MICROSTRUCTURE AND SWELLING OF NICKEL-DOPED 9Cr-1MoVNb STEEL IRRADIATED IN HFIR — P. J. Maziasz, R. L. Klueh, and J. M. Vitek (Oak Ridge National Laboratory)

7.3.1 ADIP Task

ADIP Tasks are not defined for Path E, ferritic steels in the 1978 Program Plan.

7.3.2 Objectives

Ferritic 9Cr-1MoVNb and 12Cr-1MoVW steels have been prepared with additions of up to 2 wt % Ni, with the goal of examining the effects of increased helium generation on microstructural evolution, void swelling, and mechanical properties during HFIR irradiation.

7.3.3 Summary

Considerable void formation was found at 400 and 500°C in 9Cr-1MoVNb-2Ni after ~38 dpa (~400 at. ppm He) in HFIR, whereas some voids were found only at 400°C for similar irradiation of the same steel without nickel doping (only ~30 at. ppm He). Increased helium generation tremendously increased bubble nucleation over the range from 300 to 600°C. The irradiation also produced considerable precipitation in the 9Cr-1MoVNb-2Ni at 400 and 500°C in conjunction with void formation.

7.3.4 Progress and Status

7.3.4.1 Introduction

In the absence of a 14 MeV neutron source, it is necessary to resort to elemental and isotopic tailoring of the composition of ferritic steels, combined with HFIR irradiation, in order to explore the response of these materials to the simultaneous generation of neutron damage and helium generation. Our initial experiments in this area involve heats of 9Cr-1MoVNb and 12Cr-1MoVW steels doped with either 1 or 2 wt % natural nickel. The effects of the nickel additions on the tempering characteristics, tensile, and impact properties have been well established.[1] No effect of enhanced helium generation was found on the tensile properties of these steels following irradiation in HFIR to ~10 dpa at 50°C (ref. 2). Undoped 9Cr-1MoVNb and 12Cr-1MoVW normally contain a small amount of nickel (~0.1–0.4 wt %), which slightly increases the helium generation in HFIR (to ~30 to 90 at. ppm after 40 dpa) above the negligible rate found during fast breeder reactor (FBR) irradiation. Voids have been found in both 9Cr and 12Cr steels only at 400°C after 40 dpa in HFIR, with more swelling in the 9Cr than in the 12Cr steel.[3,4] This work examines the effect of more than an order of magnitude increase in helium concentrations due to the 2 wt % Ni addition to the 9Cr-1MoVNb steel.

7.3.4.2 Experimental

Details of alloy composition and heat treatment are reported elsewhere.[1,2] For this report it is important to note that the undoped 9Cr-1MoVNb contains 0.11 wt % Ni, whereas the doped steel contains 2 wt % Ni. Both were normalized at similar conditions, but the undoped steel was tempered for 1 h at 760°C while the nickel-doped steel was tempered for 5 h at 700°C. Alloys were irradiated side by side in HFIR CTRs-30 through -32 in the form of standard 3-mm-diam transmission electron microscopy (TEM) disks punched from 0.254-mm-thick sheet stock. This work examines only the highest fluence disks from HFIR-CTR-30. Irradiation conditions are given in Table 7.3.1. Irradiation temperatures ranged from 300 to 600°C and have been verified by analysis of temperature monitors.[5] Displacement damage and helium generation were calculated by L. R. Greenwood based on dosimetry performed for this experiment,[6] including dpa due to nickel recoils.

Table 7.3.1. Damage parameters for 9Cr-1MoVNb with and without nickel irradiated in HFIR-CTR-30

Alloy designation	Irradiation temperature (°C)	Displacement damage[a] (dpa)	Helium content[b] (at. ppm He)
9Cr-1MoVNb	300	36.5	30.5
	400	36.5	30.5
	500	38.5	32.2
	600	38.5	32.2
9Cr-1MoVNb + 2 Ni	300	37.2	402.5
	400	37.2	402.5
	500	39.2	424.0
	600	39.2	424.0

[a]Displacement damage calculated from dosimetry measurements performed by L. R. Greenwood ("Fission Reactor Dosimetry — HFIR-CTR-30, -36, -46," Sect. 2.6, this report). The effect of nickel recoils is included.

[b]Helium generation calculated from dosimetry measurements performed by L. R. Greenwood, same reference as above.

Specimens were thinned remotely in an automatic Tenupole twin-jet polishing unit and examined on a JEM 100C TEM, equipped with a special objective lens polepiece designed to lower the magnetic field at the specimen. Standard imaging techniques were used for cavities, dislocations, and precipitates.

7.3.4.3. Results

Cavity Microstructural Evolution — In 9Cr-1MoVNb, matrix voids (9–18 nm in diam) were observed only at 400°C after ~37 dpa (~30 at. ppm He), as reported previously.[4] However, the voids were not spatially uniform, but formed in patches. Some background bubbles (2.5–5 nm in diam) were also observed in the matrix at 400°C and along subgrain boundaries at 600°C, but none were detected at 300 or 500°C.

By contrast, copious fine bubble formation was observed at all temperatures in the 9Cr-1MoVNb-2Ni, and voids were found at both 400 and 500°C after 37 to 39 dpa and 400 to 420 at. ppm He. Low-magnification TEM of 9Cr-1MoVNb-2Ni at 300 to 600°C is shown in Fig. 7.3.1, while comparison of nickel-doped and undoped steels at 400°C is made in Fig. 7.3.2. Higher magnifications of bubble microstructures in the nickel-doped and the undoped 9Cr-1MoVNb are compared in Fig. 7.3.3 at 300 and 600°C, and in Fig. 7.3.4 at 400 and 500°C. The increased bubble nucleation due to increased helium generation is quite obvious at 300, 500, and 600°C from Figs. 7.3.3 and 7.3.4. At 400°C (Fig. 7.3.4), the larger matrix void populations are similar, but many more background matrix bubbles decorate dislocations and precipitates in the nickel-doped steel. At the lower magnification in Fig. 7.3.2, overall void formation appears spatially more uniform in the nickel-doped steel as well. Fine bubble sizes appeared similar at both 300 and 500°C in the 9Cr-1MoVNb-2Ni steel. Bubbles were smaller and more uniformly distributed in the matrix at 300 and 500°C than at 600°C, where they ranged up to ~90 nm in diameter and primarily decorated dislocations and subgrain boundaries [Figs. 7.3.1(d) and 7.3.4(c)].

ORNL PHOTO 2909-85

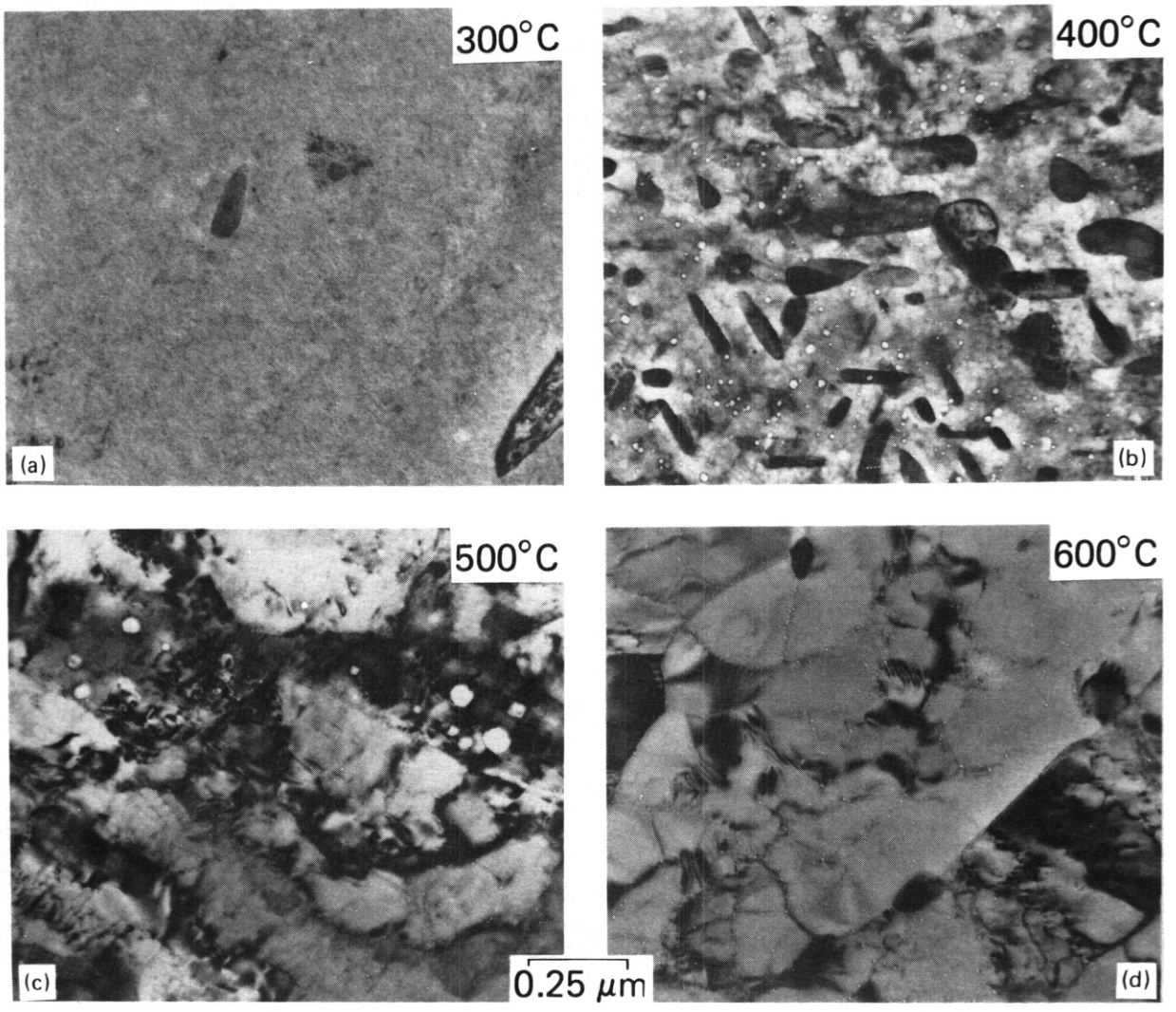

Fig. 7.3.1. A low-magnification comparison of cavity microstructures in 9Cr-1MoVNb-2Ni irradiated in HFIR to 37 to 39 dpa and 400 to 420 at. ppm He at (a) 300°C, (b) 400°C, (c) 500°C, and (d) 600°C. Voids are found only at 400 and 500°C.

ORNL PHOTO 2908-85

400°C, 38–39 dpa

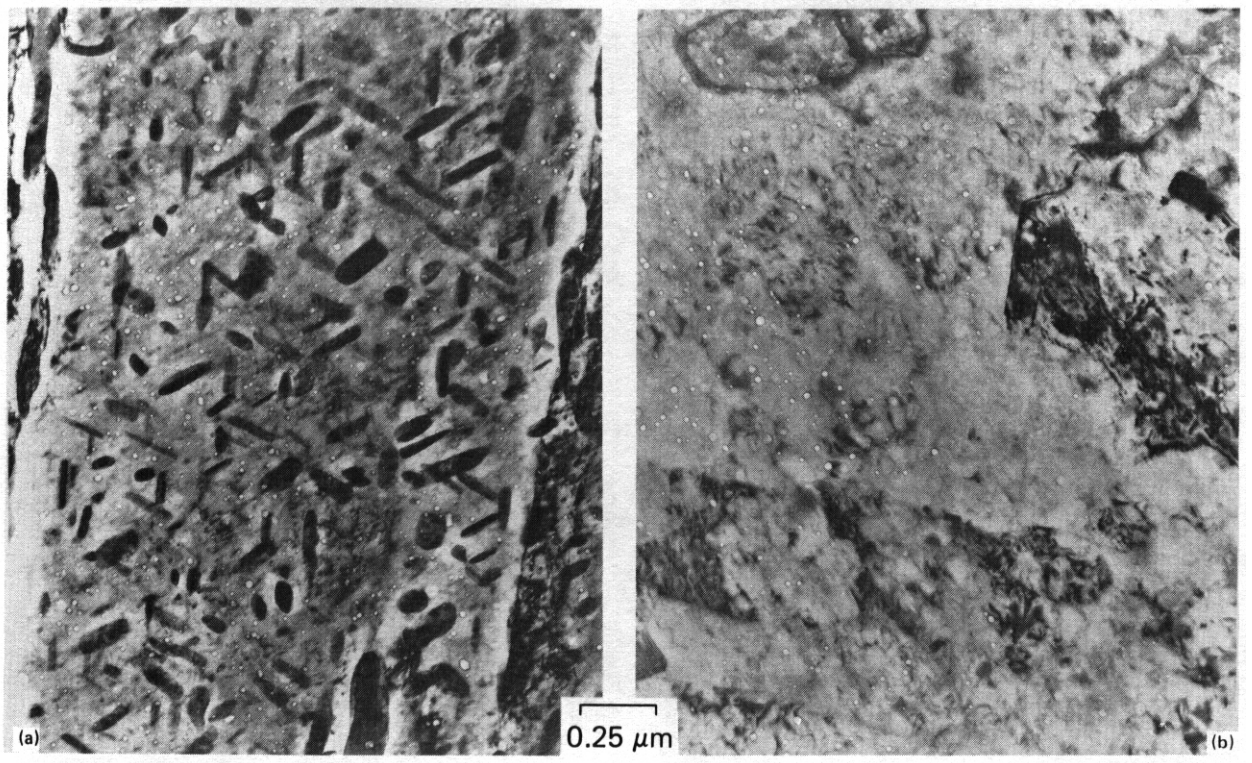

9 Cr–1 MoV Nb + 2 Ni (424 at. ppm He)

9 Cr–1 MoV Nb (32 at. ppm He)

Fig. 7.3.2. A comparison of (a) 9Cr-1MoVNb-2Ni (400 at. ppm He) and (b) 9Cr-1MoVNb (30 at. ppm He) after HFIR irradiation at 400°C to –37 dpa to illustrate the effects of increased helium generation and/or nickel content on void and precipitate formation.

Void formation in 9Cr-1MoVNb-2Ni steel was peculiar at 500°C because all of the voids were exclusively associated with large globular or elongated precipitate phase particles [Fig. 7.3.1(c)]. Void sizes ranged from 14 to 60 nm in diameter and were larger than at 400°C. Stereomicroscopy revealed that the voids at 500°C were within the particles them-selves, with the largest voids being near the center and the smallest ones near the particle interface. A few large particles with voids inside were also observed at 400°C. At 400°C, the voids within precipitates were larger than the average voids in the matrix. This suggests that the voids and their surrounding precipitate phase particle assist each other in growth. However. lower fluence data are required to establish the sequence of void and precipitate development.

Dislocation/Precipitate Microstructural Evolution — Irradiation in HFIR produces obvious changes in the as-tempered microstructures of both nickel-doped and undoped 9Cr-1MoVNb after irradiation at 300 to 500°C to –36 to 39 dpa, but very little change at 600°C. At 600°C in the 9Cr-1MoVNb-2Ni alloy. precipitation and subgrain structures after HFIR irradiation were generally similar to those in the as-temoered condition. but the irradiation definitely caused further recovery of the dislocation network. Nickel doping did not greatly affect dislocation or precipitate microstructures during irradiation at 600°C.

Irradiation in HFIR at 300°C produces a dense dislocation structure of loops and/or network and possibly a somewhat coarser subgrain structure in 9Cr-1MoVNb-2Ni relative to the normalized-and-tempered structure [Fig. 7.3.5(a)]. The as-tempered precipitate structure seemed relatively unaffected by irradiation at 300°C, with little influence of nickel doping.

Irradiation at 400°C produces a tangle of loops and network in the 9Cr-1MoVNb-2 Ni, leaving little evidence of the as-tempered subgrain structure [Fig. 7.3.5(b)]. The dislocation concentration decreased with increasing irradiation temperature; dislocation concentration was considerably higher than as-tempered after irradiation at 400°C, but showed little change from the original structure during irradiation at 500°C. Again, nickel doping appeared to have little effect on dislocation evolution, but by contrast, it tremendously influenced precipitation at 400 and 500°C.

In the 9Cr-1MoVNb, precipitation seemed similar to the as-tempered material after irradiation at 400 and 500°C. However, in the nickel-doped steel, there seemed to be little evidence of the as-tempered precipitate structure (coarse $M_{23}C_6$ + finer MC). Instead, there was considerable irradiation-produced precipitation. At 400°C, a heavy precipitate of medium-coarse lath, rod, and plate-shaped particles was found in

ORNL PHOTO 2906-85

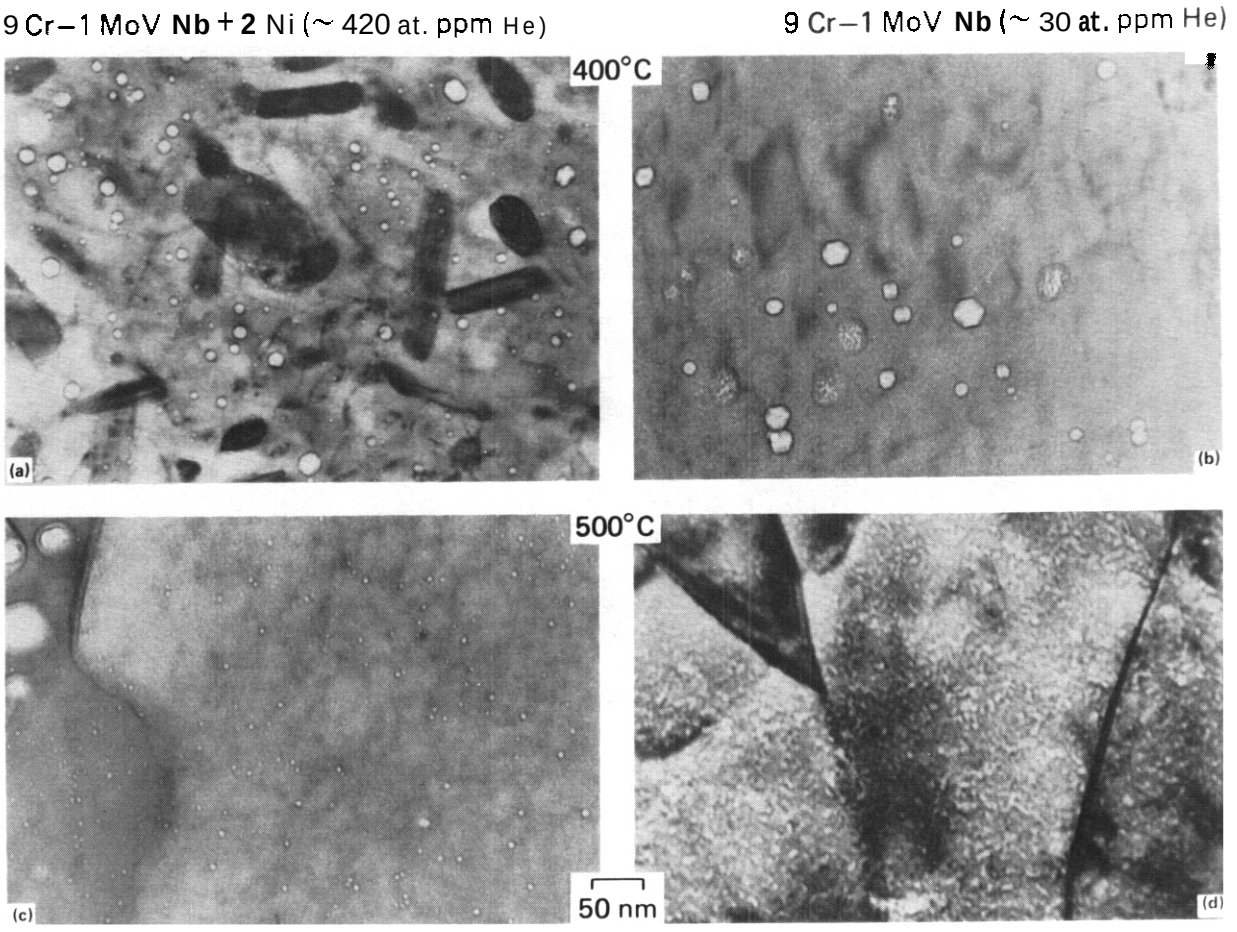

37–39 dpa

Fig. 7.3.3. High-magnification TEM to illustrate the effects of increased helium generation on bubble formation after HFIR irradiation to 37 to 39 dpa at (a) and (b) 400°C and (c) and (d) 500°C. (a) and (c) are 9Cr-1MoVNb-2Ni with 400 to 420 at. ppm He, whereas (b) and (d) are 9Cr-1MoVNb with 30 to 32 at. ppm He.

the matrix, as seen in Fig. 7.3.1(b) and 7.3.2(a), with elongated, almost continuous particles formed along subgrain or packet boundaries; much more fine precipitation was also found relative to the as-tempered condition. The phases at 400°C have not yet been identified. At 500°C, very coarse, globular, or elongated (along boundaries) particles were found with very little matrix (medium-coarse or fine) precipitation. At 500°C, diffraction evidence suggests the body-centered-cubic χ phase. The nature (enhanced thermal, radiation-modified, or radiation-induced) of these precipitation phenomena or their relationship to radiation-induced solute segregation behavior in the steel is under investigation. These precipitate effects were, however, coincident with void formation and confined to the nickel-doped 9Cr-1MoVNb.

7.3.5. Conclusions

1. The addition of 2% Ni to the 9Cr-1MoVNb steel enhances bubble formation over the range 300 to 600°C during HFIR irradiation.
2. Nickel doping to increase helium generation produced considerable void formation at 400 and 500°C after 37 to 39 dpa, whereas the undoped steel formed voids only at 400°C. Voids appeared to form exclusively inside coarse, globular χ phase particles at 500°C.
3. Nickel doping did not seriously affect dislocation evolution during HFIR irradiation at 300 to 600°C. Irradiation-induced dislocation (loops plus network) production in 9Cr-1MoVNb-2Ni was greatest at 300°C, less at 400°C, and negligible at 500°C. The as-tempered dislocation structure actually appeared to recover somewhat after irradiation at 600°C.
4. Considerable amounts of irradiation-produced precipitation occurred in the nickel-doped steel at 400 and 500°C, whereas neither doped nor undoped steels showed much change from the as-tempered precipitate structure after HFIR irradiation at 300 or 600°C.

ORNL PHOTO 2907-85

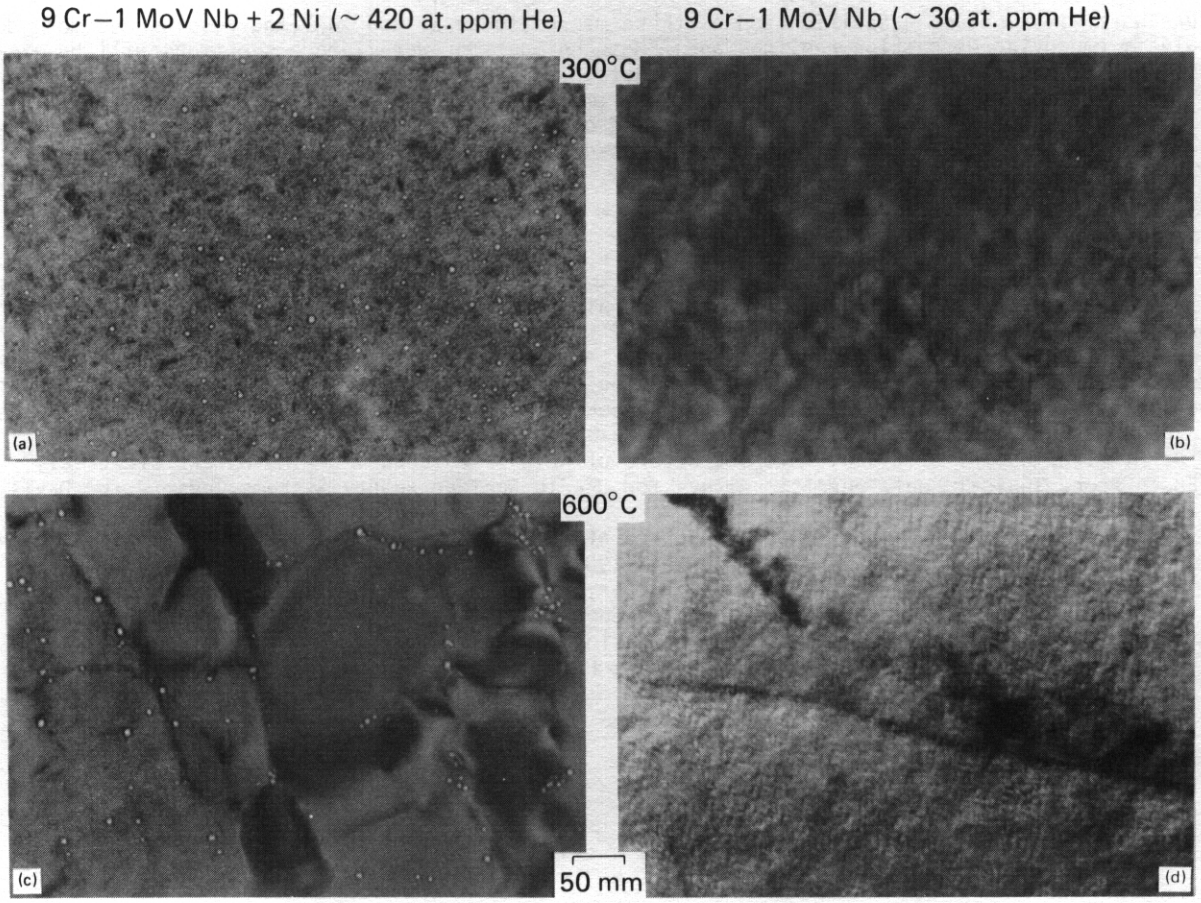

~ 37–39 dpa

Fig. 7.3.4. High-magnification TEM to illustrate the effects of increased helium generation on bubble formation after HFIR irradiation to 37 to 39 dpa at (a)-(b) 300°C and (c)-(d) 600°C. (a) and (c) are 9Cr-1MoVNb-2Ni with 400 to 420 at. ppm He, whereas (b) and (d) are 9Cr-1MoVNb with 30 to 32 at. ppm He.

ORNL PHOTO 2905-85

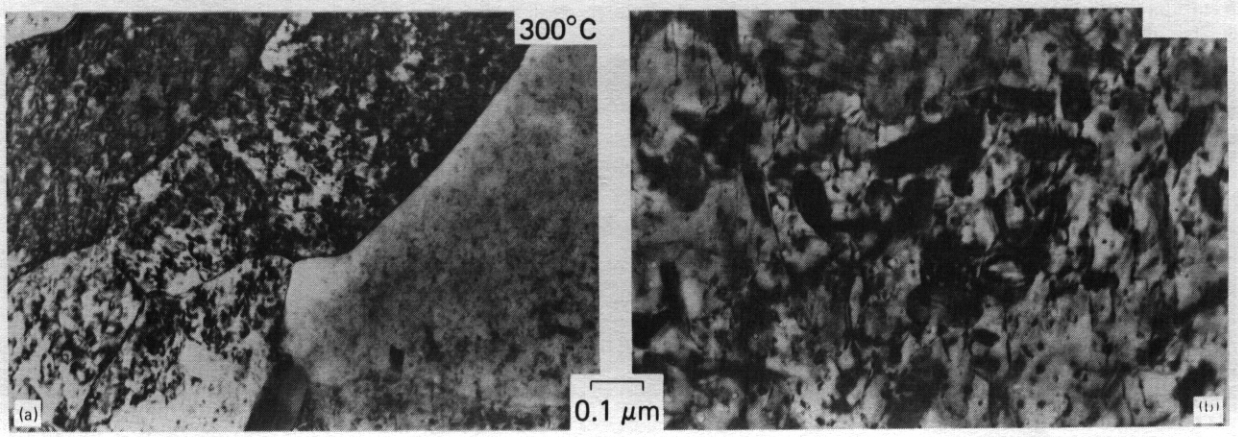

37 dpa, 424 at. ppm He

Fig. 7.3.5. Dislocation microstructures in 9Cr-1MoVNb-2Ni after HFIR irradiation at (a) 300°C and (b) 400°C to 37 dpa and 400 at. ppm He.

7.3.6. Future Work

Future work will include quantification of these microstructural and swelling results and more detailed phase analysis employing extraction replicas and AEM techniques. Lower fluence specimens will be examined to unfold the mechanisms of void evolution in these steels, and higher fluence HFIR irradiations of doped and undoped 9Cr-1MoVNb are in progress. In addition, specimens irradiated to similar conditions in FFTF (minuscule helium generation for both nickel-doped and undoped 9Cr-1MoVNb) will be examined to provide a base line against which to gage the effects of increased helium in both alloys, and a means of separating nickel from helium effects in the 9Cr-1MoVNb. Finally, similar investigations will be extended to both doped and undoped 12Cr-1MoVW steels.

7.3.7 References

1. P. J. Maziasz and R. L. Klueh, "Microstructural/Microcompositional Analysis of Normalized-and-Tempered 9Cr-1MoVNb and 12Cr-1MoVW Steels Doped with 2 wt % Nickel," Chap. 7.2, this report.

2. R. L. Klueh, J. M. Vitek, and M. L. Grossbeck. "Nickel-Doped Ferritic (Martensitic) Steels for Fusion Reactor Irradiation Studies: Tempering Behavior and Unirradiated and Irradiated Tensile Properties." pp. 648–64 in Effects of Radiation on Materials: Eleventh Conference, eds., H. R. Brager and J. S. Perrin. ASTM STP 762. herican Society for Testing and Materials, 1982.

3. J. M. Vitek and R. L. Klueh, "Microstructure of HFIR-Irradiated 12Cr-1MoVW Ferritic Steel," pp. 551–58 in Proc. Topical Conf. Ferritic Alloys for Use in Nuclear Energy Systems, eds. J. W. Davis and D. J. Michel, The Metallurgical Society of AIME, Warrendale, PA. 1984.

4. J. M. Vitek and R. L. Klueh, "Microstructure of 9Cr-1MoVNb Steel Irradiated to 36 dpa at Elevated Temperatures in HFIR," J. Nucl. Mater. 122&123, 254 (1984).

5. M. L. Grossbeck, J. W. Woods, and G. A. Potter, "Experiments HFIR-CTR-30, -31, and -32 for Irradiation of Transmission Electron Microscopy Disk Specimens," pp. 36-44 in ADIP quart. Prog. Rep. Sept. 30, 1980, DOE/ER-0045/4, U.S. DOE, Office of Fusion Energy.

6. L. R. Greenwood, "Fission Reactor Dosimetry — HFIR-CTR-30, -36, -46," elsewhere in this report.

7.4 POSTIRRADIATION TENSILE BEHAVIOR OF NICKEL-DOPED 9Cr-1MoVNb and 12Cr-1MoVW STEELS — R. L. Klueh, P. J. Maziasz, and J. M Vitek (Oak Ridge National Laboratory)

7.4.1 ADIP Task

AOIP Tasks are not defined for Path E, ferritic steels in the 1978 Program Plan.

7.4.2 Objectives

The goal of this project is to measure the tensile properties of Cr-Mo ferritic steels irradiated at elevated temperatures in EBR-II. In the future, the results of this work will be compared with elevated-temperature irradiations of the same steels in HFIR, where much more helium is produced in irradiations to the same dpa level.

7.4.3 Summary

Tensile specimens of normalized-and-tempered 9Cr-1MoVNb, 9Cr-1MoVNb-2Ni, 12Cr-1MoVW, 12Cr-1MoVW-1Ni, and 12Cr-1MoVW-2Ni steels were irradiated in EBR-II to –16 dpa at 390 to 550°C. Tests were conducted at room temperature and the irradiation temperature on unirradiated, thermally aged, and irradiated specimens. The effect of irradiation depended on temperature and on the tempering treatment that the steel was given.

7.4.4 Progress and Status

7.4.4.1 Introduction

To study alloys for fusion reactor first wall applications, it is necessary to have a technique for studying the effect of irradiation-produced displacement damage and transmutation helium in the alloy. To do this in the 9% Cr and 12% Cr Cr-Mo steels, nickel is added to the steels, and they are then irradiated in a mixed-spectrum reactor such as the High Flux Isotope Reactor (HFIR).[1,2] Displacement damage is produced by the fast neutrons in the spectrum and helium is produced by a transmutation reaction of ^{58}Ni with the thermal neutrons in the spectrum. Such a study is in progress on 9Cr-1MoVNb and 12Cr-1MoVW steels to which up to 2% Ni has been added. The steels are being irradiated in HFIR to produce helium and displacement damage. They have also been irradiated in the Experimental Breeder Reactor (EBR-II), a fast reactor where displacement damage occurs but essentially no helium is produced.

This report presents tensile results from specimens irradiated in the AD-2 experiment conducted by HEDL in EBR-II. When the tests on the HFIR-irradiated specimens are completed, the effect of helium on the properties will be determined by comparing the results from the two experiments.

7.4.4.2 Experimental Procedure

Three electroslag-remelted (ESR) heats of 12Cr-1MoVW and two heats of ESR 9Cr-1MoVNb steel were prepared by Combustion Engineering, Inc., Chattanooga, Tennessee. These alloys included the standard 12Cr-1MoVW steel (–0.5% Ni) and this composition with 1 and 2% Ni and the standard 9Cr-1MoVNb (–0.1% Ni) and this steel with 2% Ni. The compositions of the alloys and the designations to be used in this progress report are given in Table 7.4.1.

Sheet tensile specimens in this experiment were of the SS-1 type, with a reduced gage section 20.3 mm long by 1.52 mm wide by 0.76 mm thick. All specimens were machined with their gage lengths parallel to the rolling direction of the sheet. The specimens were normalized and tempered using the heat treatment conditions given in Table 7.4.2.

Table 7.4.1. Chemical composition of 9Cr-1MoVNb and 12Cr-1MoVW steels

Alloy	Heat	Content, wt %							
		Cr	Mo	Ni	V	Nb	W	C	N
9Cr-1MoVNb	XAA-3590	8.62	0.98	0.11	0.21	0.063	0.01	0.09	0.050
9Cr-1MoVNb-2Ni	XAA-3591	8.57	0.98	2.17	0.22	0.066	0.01	0.064	0.053
12Cr-1MoVW	XAA-3587	11.99	0.93	0.43	0.27	0.018	0.54	0.21	0.020
12Cr-1MoVW-1Ni	XAA-3588	11.97	1.04	1.14	0.31	0.015	0.53	0.20	0.016
12Cr-1MoVW-2Ni	XAA-3589	11.71	1.02	2.27	0.31	0.015	0.54	0.20	0.017

Specimens were irradiated in capsules designed to maintain temperatures of 390, 450, 500, and 550°C. Irradiation was in row 4 of EBR-II, and the specimens were exposed to fluences of –3.2 to 3.4 × 10^{26} neutrons/m^2 (E > 0.1 MeV), depending on the position in the reactor. This fluence produced a displacement damage of about 15.4 to 16.2 dpa. The uncertainty in fluence has been estimated as ±10% and the temperature uncertainties are 390 ± 10°C, 450 ± 15°C, 500 ± 20°C, and 550 ± 30°C.

After irradiation, tensile tests were conducted at the irradiation temperature and, where specimens were available, at room temperature. As-heat-treated as well as thermally aged control samples were also tested to separate the effect of irradiation from thermal-aging effects. Thermal aging was at the irradiation temperatures for 5000 h — the approximate time of the irradiation. The tensile tests were made in a vacuum chamber on a 44-kN-capacity Instron universal testing machine at a crosshead speed of 8.5 μm/s, which results in a nominal strain rate of 4.2 × 10^{-4}/s.

Table 7.4.2. Normalizing and tempering conditions for 9Cr-1MoVNb and 12Cr-1MoVW heats of steel[a]

Alloy	Heat treatment conditions[b]
9Cr-1MoVNb	0.5 h 1040°C, AC; 1 h 760°C, AC
9Cr-1MoVNb-2Ni	0.5 h 1040°C, AC; 5 h 700°C. AC
12Cr-1MoVW	0.5 h 1050°C, AC; 2.5 h 780°C, AC
12Cr-1MoVW-1Ni	0.5 h 1050°C, AC; 2.5 h 780°C, AC
12Cr-1MoVW-2Ni	0.5 h 1050°C, AC; 5 h 700°C, AC

[a]Heat treatment was on 5.3-mm-thick plates.
[b]AC = air cool.

Table 7.4.3. Tensile properties of unirradiated normalized-and-tempered 9Cr-1MoVNb steels

Test temperature (°C)	Strength, MPa		Elongation, %	
	Yield	Ultimate	Uniform	Total
		9Cr-1MoVNb		
22	656	757	4.1	7.6
300	611	694	2.8	5.8
400	577	646	2.3	5.3
450	541	610	2.3	5.0
500	565	629	1.6	4.4
550	543	603	1.8	4.5
		9Cr-1MoVNb-2Ni		
22	785	893	3.0	6.1
300	755	828	1.6	4.3
400	708	803	2.5	5.3
450	709	776	1.1	3.4
500	690	740	0.8	2.9
550	653	710	1.1	3.6

7.4.4.3 Results

Details on the heat treatment and the optical microstructures of these steels in the unirradiated conditions have been published.[1,2] All of the steels contained microstructures that were essentially 100% tempered martensite.

The tensile results for the as-heat-treated. thermally aged, and irradiated steels are given in Tables 7.4.3 through 7.4.8. Unaged specimens were tested in the range room temperature to 550°C. When specimens were available, aged and irradiated specimens were tested at room temperature and the irradiation (aging) temperature. Where only one specimen was available, tests were made at the irradiation or aging temperature. In some cases, succimens for a given condition were unavailable, and comparison was difficult.

In Figs. 7.4.1 through 7.4.6, the data are presented for the various-conditions. Figure 7.4.1 and 7.4.2 show the unaged and aged data for the 9Cr-1MoVNb and 12Cr-1MoVW steels, respectively. As-heat-treated, the steels with 2% Ni were considerably stronger than the standard materials and the 12Cr-1MoVW-1Ni steel [Figs. 7.4.1(a) and (b) and 7.4.2(a) and (b)]. This difference was caused by the different tempering treatments used for the steels with 2% Ni (refs. 1,2). These latter steels were tempered at 700°C, where tempering was slower than for the higher temperatures used for the standard steels and the one with 1%Ni (Table 7.4.2). It was not possible to temper the 2%-Ni steels at the same temperatures because those temperatures are above the A_C temperature.

Thermal aging in the range 400 to 550°C had little effect on the strength properties of the 9Cr-1MoVNb [Fig. 7.4.1(a) and (b)] and the 12Cr-1MoVW and 12Cr-1MoVW-1Ni [Fig. 7.4.2(a) and (b)]. There was also no effect of thermal aging on the 9Cr-1MoVNb-2Ni and 12Cr-1MoVW-2Ni steels at 400 and 450°C; however, these steels showed a large decrease in strength after aging at 550°C, where the strength of the 2%-Ni steels approached that of the steels without nickel. There was little effect of aging on the ductility of any of the steels [Figs. 7.4.1(c) and 7.4.2(c)].

The irradiated specimens were compared with the aged specimens for tests at the irradiation (aging) temperatures (Figs. 7.4.3 and 7.4.5) and for tests at room temperature (Figs. 7.4.4 and 7.4.6). An effect of nickel on the response to irradiation could be detected. Strengthening, as determined by an increased yield stress and ultimate tensile strength, occurred for the 9Cr-1MoVNb, 12Cr-1MoVW, and 12Cr-1MoVW-1Ni steels irradiated at 390°C. Little change in strength occurred for the steels with 2% Ni. As a result of the 390°C irradiation, there was considerably less difference in the strengths of the irradiated steels with different nickel contents than there was in the unirradiated condition.

After irradiation at 450°C, the 9Cr-1MoVNb and 9Cr-1MoVNb-2Ni steels had similar strengths (Figs. 7.4.3 and 7.4.4). The strength of the irradiated 9Cr-1MoVNb steel was similar to the strength before irradiation and after aging. However, the strength of the 9Cr-1MoVNb-2Ni steel showed a large decrease over the unirradiated strength. The 12 Cr steels showed similar effects (Figs. 7.4.5 and 7.4.6), with the irradiated strengths of the 12Cr-1MoVW and 12Cr-1MoVW-1Ni steels being similar to the aged strengths, and the steel with 2% Ni showing a significant decrease from the aged values.

Table 7.4.4. Tensile properties of unirradiated normalized-and-tempered 12Cr-1MoVW steels

Test temperature (°C)	Strength, MPa		Elongation, %	
	Yield	Ultimate	Uniform	Total
	12Cr-1MoVW			
22	626	834	7.1	10.5
300	558	735	6.4	9.8
400	551	697	4.5	7.3
450	550	705	4.5	7.1
500	554	691	4.0	6.8
550	485	624	3.5	6.3
	12Cr-1MoVW-1Ni			
22	628	820	6.6	10.1
300	571	728	5.3	8.4
400	535	684	4.1	6.6
450	527	678	4.8	7.8
500	511	670	3.8	6.4
550	458	578	3.8	6.6
	12Cr-1MoVW-2Ni			
22	824	992	3.5	6.0
300	754	908	3.4	5.8
400	726	854	2.4	4.8
450	713	844	2.1	4.1
500	677	798	2.0	4.1
550	652	759	2.6	5.6

Table 7.4.5. Tensile properties of 9Cr-1MoVNb steels thermally aged for 5000 h

Temperature, °C		Strength, MPa		Elongation, %	
Aging	Test	Yield	Ultimate	Uniform	Total
		9Cr-1MoVNb			
400	22	653	767	4.8	8.1
400	400	594	678	2.9	5.9
450	22	651	780	5.3	8.6
450	450	552	628	2.1	4.8
550	22	634	755	4.8	8.3
550	550	522	564	1.4	4.0
		9Cr-1MoVNb-2Ni			
400	22	883	945	4.3	7.1
450	22	849	906	3.5	6.3
450	450	705	761	1.3	3.8
550	22	732	812	4.0	6.8
550	550	540	578	1.4	5.1

Table 7.4.6. Tensile properties of 12Cr-1MoVW steels thermally aged for 5000 h

Temperature, °C		Strength, MPa		Elongation, %	
Aging	Test	Yield	Ultimate	Uniform	Total
		12Cr-1MoVW			
400	22	636	835	6.6	9.8
400	400	545	718	5.4	8.1
450	22	617	825	7.6	11.1
450	450	512	671	4.9	7.8
550	22	632	850	6.4	9.9
550	550	488	612	3.6	7.4
		12Cr-1MoVW-1Ni			
400	22	643	801	6.9	9.8
400	400	557	700	4.6	6.9
450	22	629	798	7.0	10.4
450	450	559	713	4.5	7.0
550	22	633	833	7.6	11.4
550	450	498	590	3.1	7.3
		12Cr-1MoVW-2Ni			
400	22	919	1052	5.5	8.3
400	400	770	886	3.4	5.5
450	22	888	1027	5.0	7.6
450	450	746	859	2.9	5.1
550	22	759	931	5.0	7.9
550	550	556	616	1.9	5.6

Table 7.4.7. Tensile properties of 9Cr-1MoVNb steels irradiated in EBR-II to a displacement damage level of approximately 16 dpa

Temperature, °C		Strength, MPa		Elongation, %	
Irradiation	Test	Yield	Ultimate	Uniform	Total
		9Cr-1MoVNb			
390	22	774	819	3.0	6.1
390	400	687	721	1.5	4.3
450	22	618	708	4.7	8.2
450	450	529	584	2.0	5.0
550	22	582	697	5.7	9.4
550	550	437	494	2.1	5.7
		9Cr-1MoVNb-2Ni			
390	22	874	935	3.6	6.7
390	400	729	787	2.0	4.8
450	22	633	731	5.7	9.8
450	450	539	599	2.1	5.2
500	500	473	534	2.1	5.1
550	22	629	731	7.0	11.7
550	550	444	489	1.5	5.4

Irradiated and aged steels were also compared at 550°C. For the 9Cr-1MoVNb and 9Cr-1MoVNb-2Ni steels, the irradiated specimens had strengths that were below those of the aged steels (Fig. 7.4.3 and 7.4.4). Furthermore, there was little difference between the strength of the 9-Cr steel with no nickel added and 2% Ni. In general, the 12-Cr steels with and without nickel showed similar trends, although there was somewhat more scatter in the data (Figs. 7.4.5 and 7.4.6).

Irradiation appeared to have only a minor effect on ductility. The major effect was at 400°C. where the irradiation-induced strengthening led to a decrease in uniform and total elongation (Figs. 7.4.3 through 7.4.6).

Table 7.4.8. Tensile properties of 12Cr-1MoVW steels irradiated in EBR-II to a displacement damage level of approximately 16 dpa

Temperature, °C		Strength, MPa		Elongation, %	
Irradiation	Test	Yield	Ultimate	Uniform	Total
		12Cr-1MoVW			
390	22	903	1005	4.7	8.0
390	400	794	856	2.0	4.3
450	22	621	810	8.7	13.3
450	450	506	630	3.9	6.6
550	500	452	588	4.2	7.5
550	22	605	811	9.4	14.1
550	550	425	536	4.1	10.2
		12Cr-1MoVW-1Ni			
390	22	932	998	3.9	6.8
390	400	772	807	2.0	4.2
450	22	614	778	7.9	11.7
450	450	472	580	4.0	6.7
550	22	619	797	7.3	11.0
550	550	419	494	2.5	9.6
		12Cr-1MoVW-2Ni			
390	22	908	1003	4.2	6.9
390	400	808	868	2.5	5.2
450	22	713	868	6.0	9.1
450	450	561	661	2.7	5.5
500	500	518	625	2.3	5.7
550	22	647	831	7.0	10.3
550	550	478	569	3.0	8.4

7.4.4.4 Discussion

The unirradiated 9-Cr and 12-Cr steels with and without 2% Ni have been examined by TEM.[3] Both contained a high density of $M_{23}C_6$ precipitates and some fine MC particles. This is shown in Fig. 7.4.7, where micrographs of carbide extraction replicas and foil specimens for the 12Cr-1MoVW and 12Cr-1MoVW-2Ni steels are shown. The 9-Cr steels with and without nickel were also similar. However, they contained more MC particles than were present in the 12-Cr steels, which is due to the niobium in these steels.' The primary difference between the microstructures of the standard steels and the steels with 2% Ni was that the 2%-Ni steel had a finer average precipitate size, a finer cell size, and a higher dislocation density. These observations indicate that the differences in microstructure can be attributed to the different tempering treatments (1 h at 760°C and 2.5 h at 780°C for the 9 Cr and 12 Cr steels, respectively, and 5 h at 700°C for the two steels with 2% Ni). Furthermore, the higher strength for the unirradiated and unaged 2%-Ni steels over the standard steels can be attributed to this difference in microstructure.

The relative effects of aging can also be attributed to the difference in the tempering treatment. The loss of strength of the 2%-Ni steels when aged at 550°C results from a continued tempering of the unstable microstructure of this steel, whereas the highly tempered standard steels and the 12Cr-1MoVW-1Ni steel are relatively stable for the given aging conditions. Note that thermal aging brought the strength of the 2%-Ni steels in line with the other steels. This might be expected, since nickel is not expected to have a significant effect on the strength.[4]

The different relative changes in strength for the different steels can also be attributed to the microstructures. The large increase in strength of the standard 9-Cr and 12-Cr steels and the 12Cr-1MoVW-1Ni steel when irradiated at 390°C is similar to the change previously observed for other heats of 9Cr-1MoVNb and 12Cr-1MoVW steels irradiated to similar fluences in EBR-II.[5,6] The fact that the 2%-Ni steels showed little strength change must reflect the tempering differences of these steels relative to the standard steels. Strengthening by irradiation at 390°C has been attributed to the formation of irradiation-induced dislocation loops and precipitates.[5-7] Similar strengthening effects must be occurring for the standard steels and the steel with 1%Ni. The lack of a significant strength change for the steels with 2% Ni must mean that, in these steels, strengthening caused by the formation of an irradiation-induced structure is offset by an irradiation-aided tempering that helps complete the process started at 700°C.

These same heats of steel were previously irradiated in HFIR at 50°C, and irradiation caused an increase in strength for all of the steels. The 2%-Ni steels were strongest before irradiation and were also strongest after irradiation. For those experiments, hardening was concluded to be caused by irradiation-induced dislocation loop formation. Because of the lower temperature, no precipitation was expected, and no irradiation-aided tempering was possible.

The "irradiation-aided tempering" effect of the 2%-Ni steels is accelerated at the higher irradiation temperatures. When irradiated and aged steels were compared at 450°C, there was little effect of irradiation on the standard steels and the 12Cr-1MoVW-1Ni steel, but the irradiated steels with 2% Ni showed a large strength decrease over the aged specimens. The strength of the irradiated steels with 2% Ni had strengths comparable to the other steels after irradiation. Irradiation at 550°C also resulted in similar strengths for all steels, regardless of the nickel content. The strength of the irradiated steels in this case fell slightly below the strengths of the thermally aged standard steels. (The 2%-Ni steels had a higher strength than the other steels after thermal aging.)

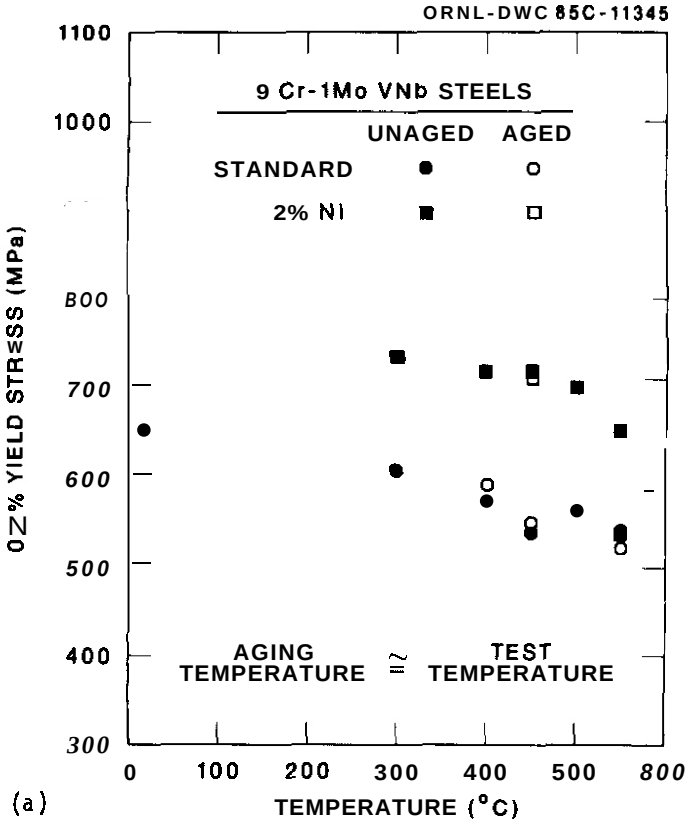

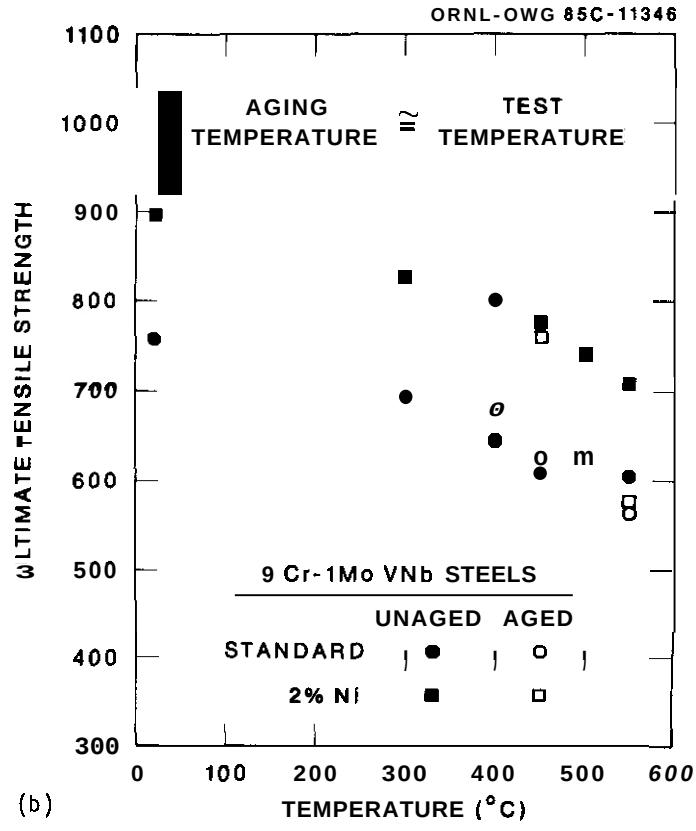

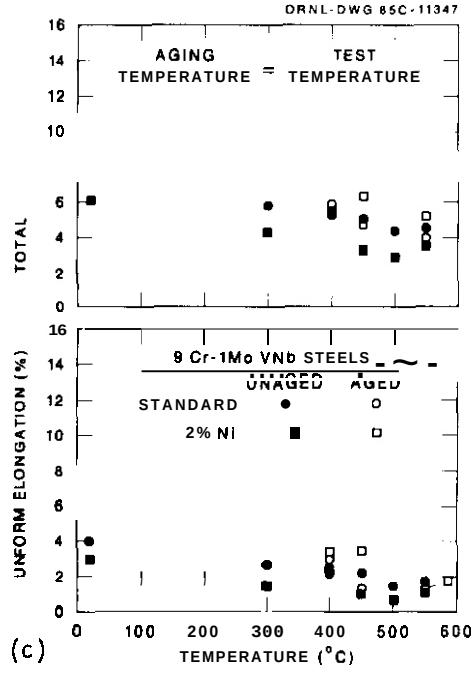

Fig. 7.4.1. The (a) 0.2% yield stress, (b) ultimate tensile strength, and (c) uniform and total elongation as functions of test temperature for normalized-and-tempered and thermally aged (5000 h) 9Cr-1MoVNb and 9Cr-1MoVNb-2Ni steels. The aged steel was tested at the aging temperature.

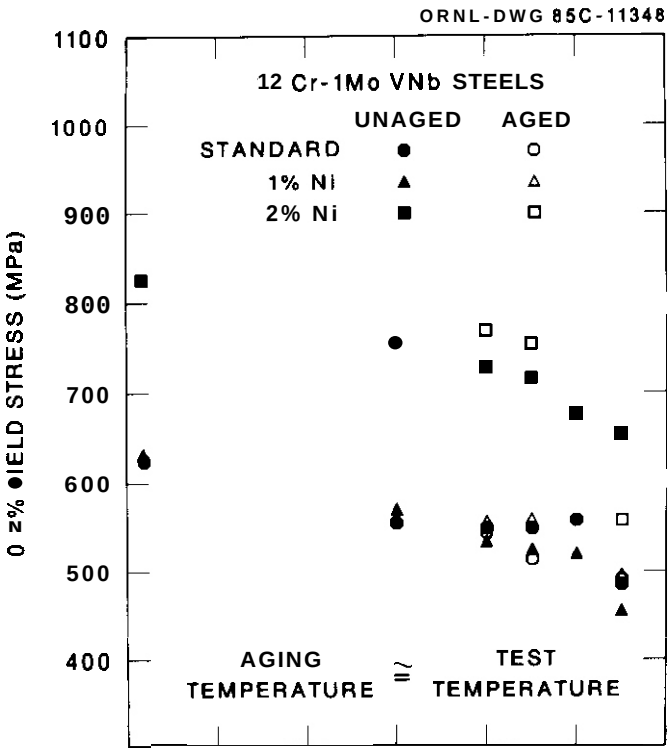

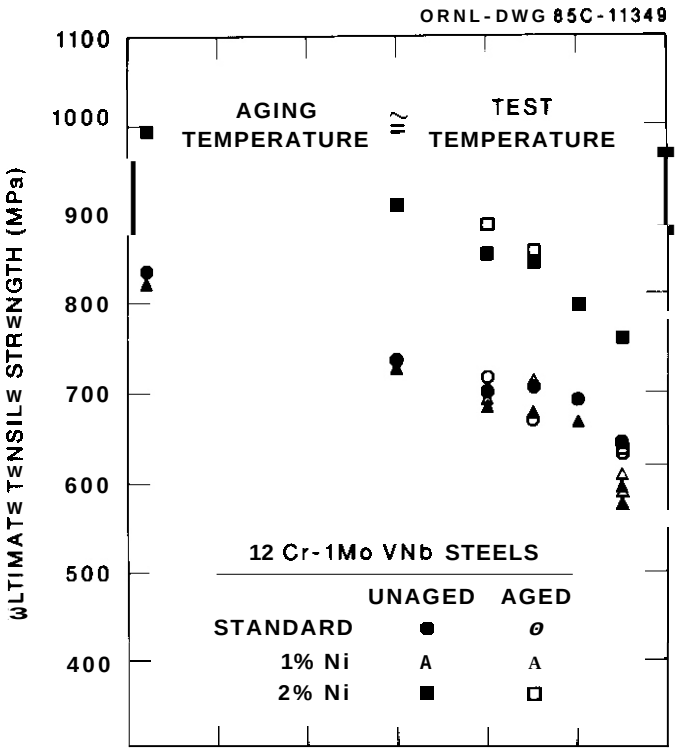

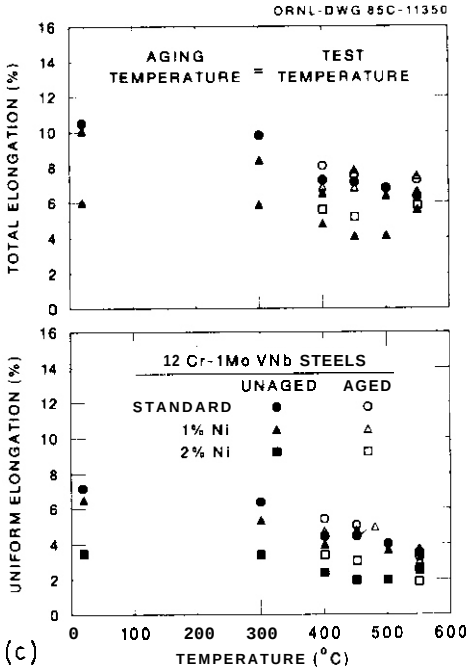

Fig. 7.4.2. The (a) 0.2% yield stress, (b) ultimate tensile strength, and (c) uniform and total elongation as functions of test temperature for normalized-and-tempered and thermally aged (5000 h) 12Cr-1MoVW, 12Cr-1MoVW-1Ni, and 12Cr-1MoVW-2Ni steels. The aged steel was tested at the aging temperature.

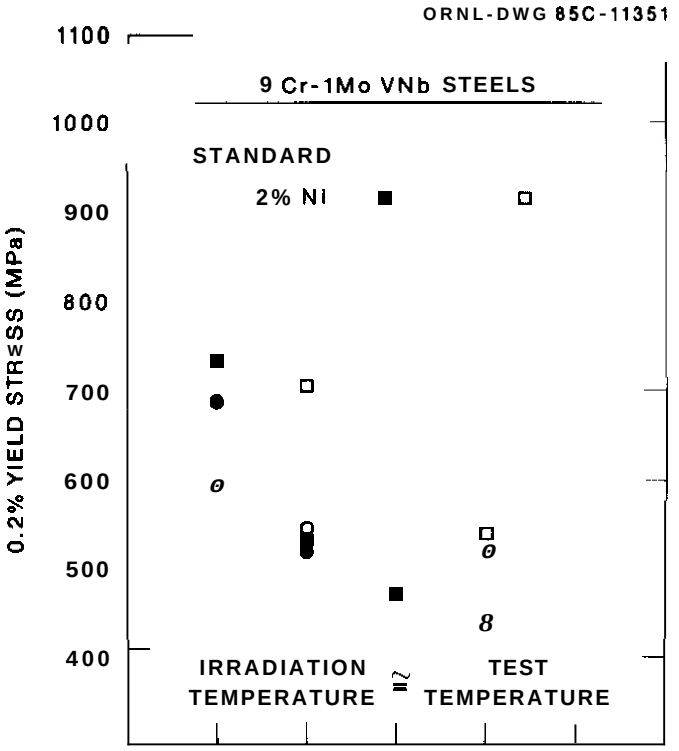

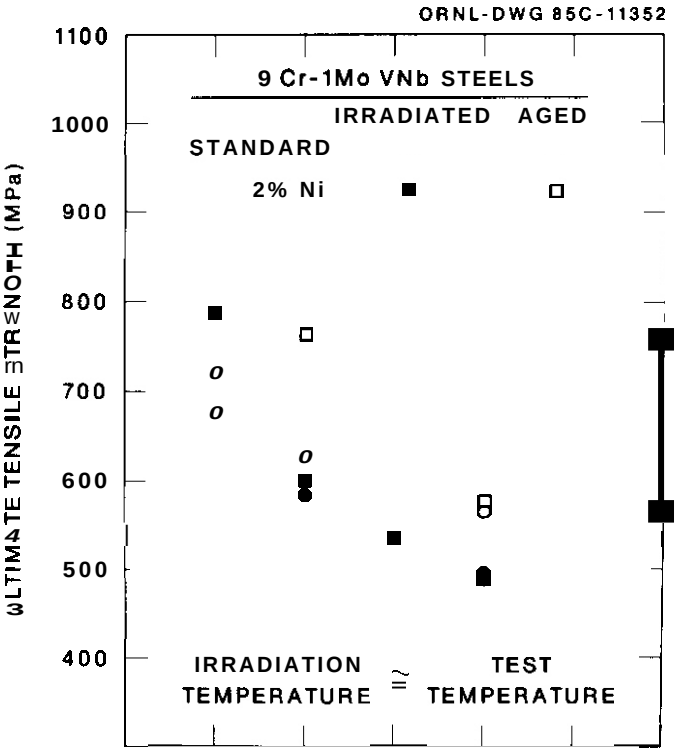

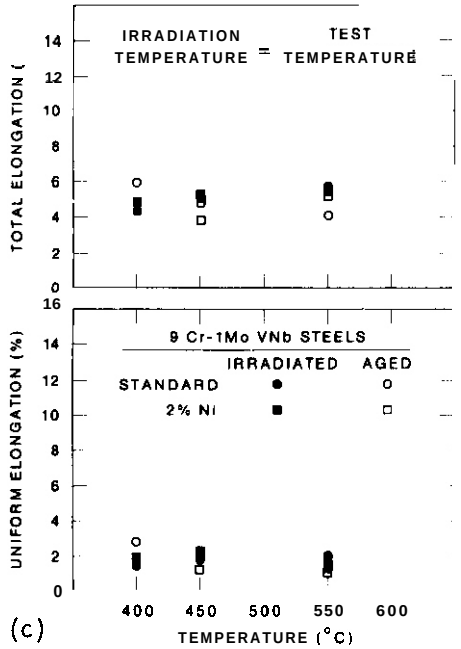

Fig. 7.4.3. The (a) 0.2% yield stress, (b) ultimate tensile strength, and (c) uniform and total elongation as functions of test temperature for thermally aged (5000 h) and irradiated (~16 dpa) 9Cr-1MoVNb and 9Cr-1MoVNb-2Ni steels. Tests were at the aging and irradiation temperatures.

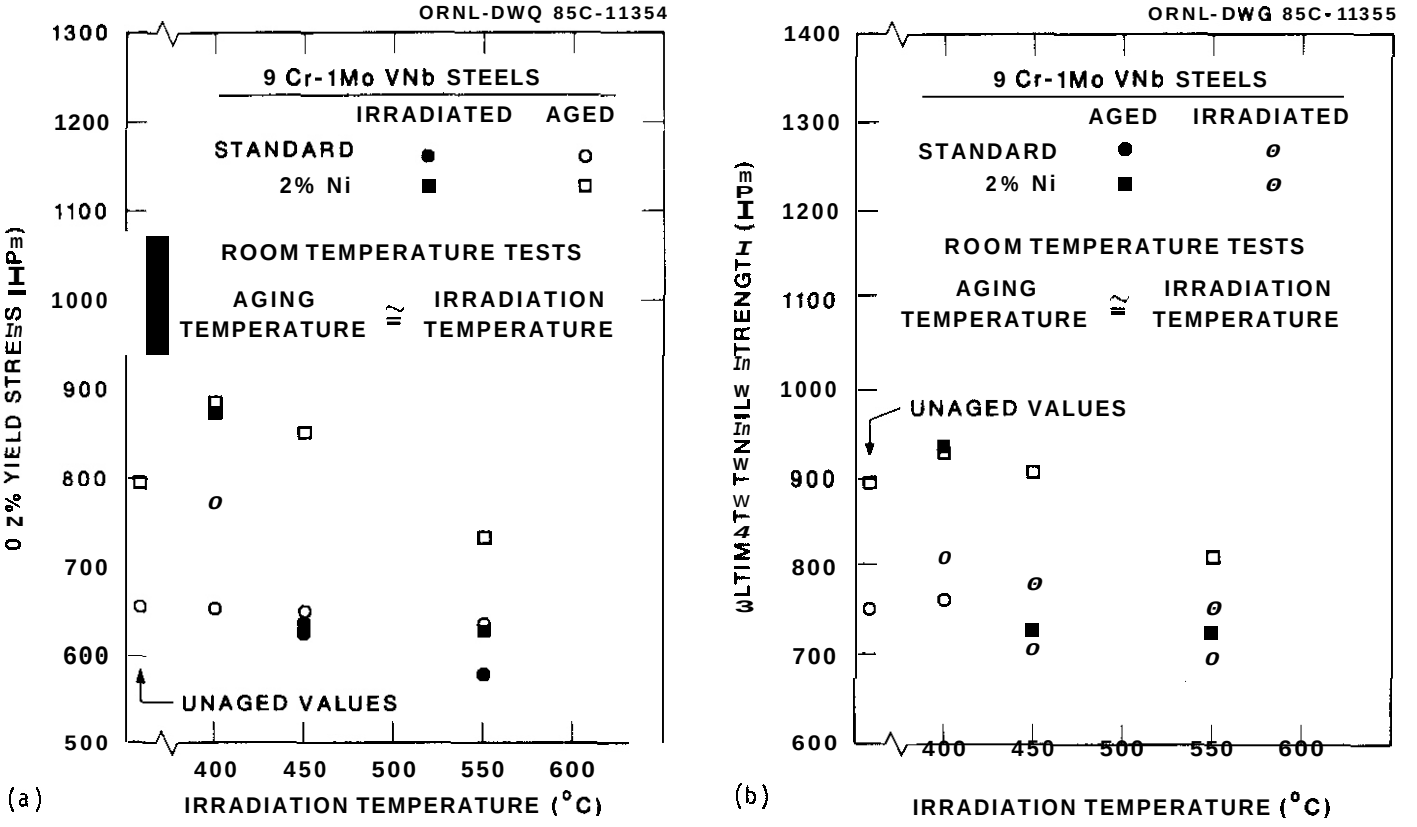

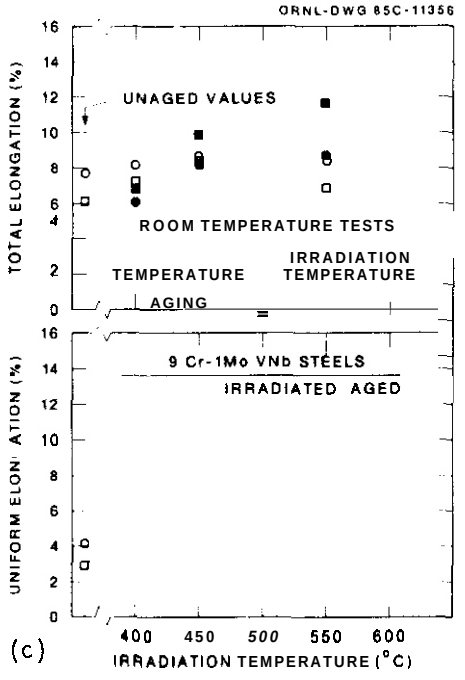

Fig. 7.4.4. The (a) 0.2% yield stress, (b) ultimate tensile strength, and (c) uniform and total elongation as functions of irradiation and aging temperatures for thermally aged (5000 h) and irradiated (–16 dpa) 9Cr-1MoVNb and 9Cr-1MoVNb-2Ni steels tested at room temperature.

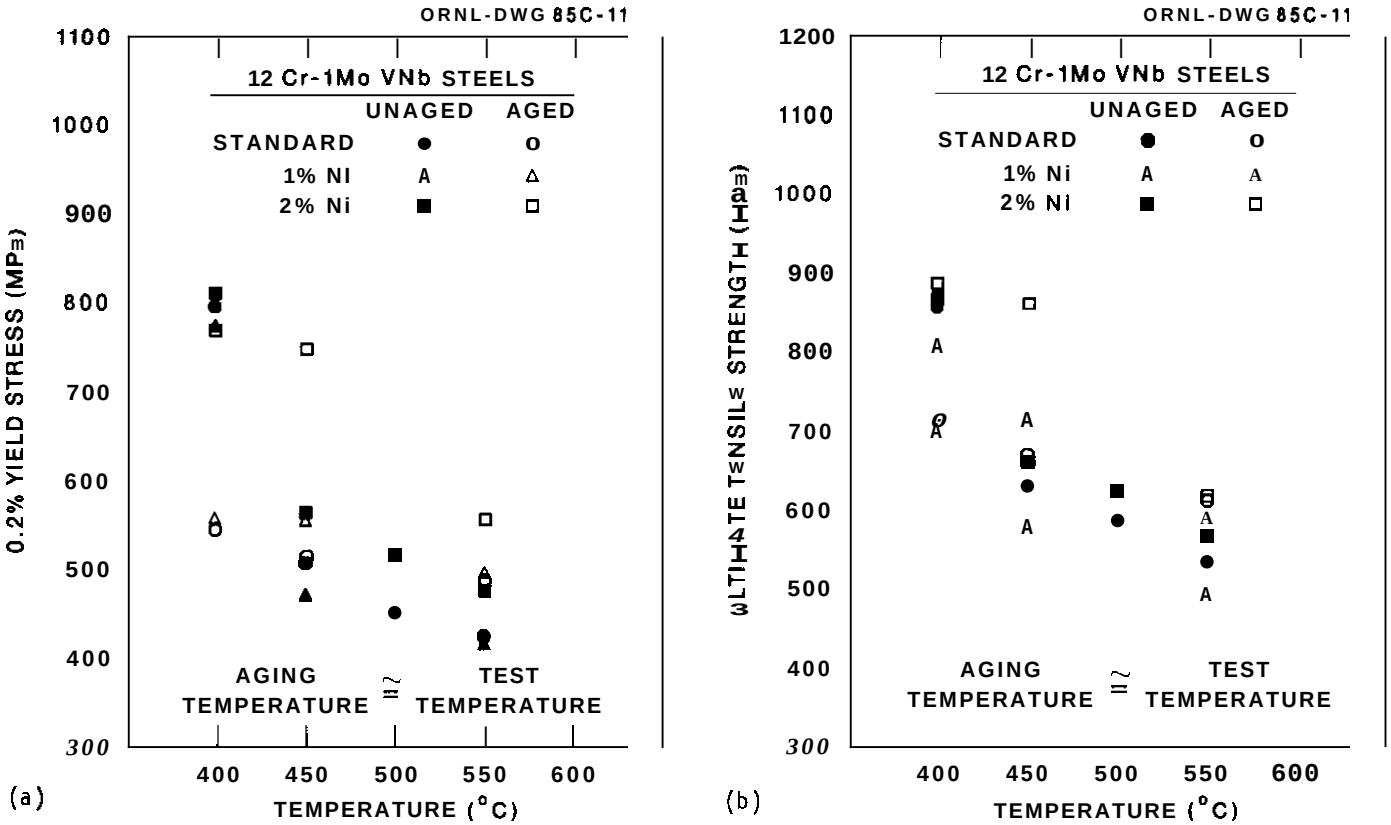

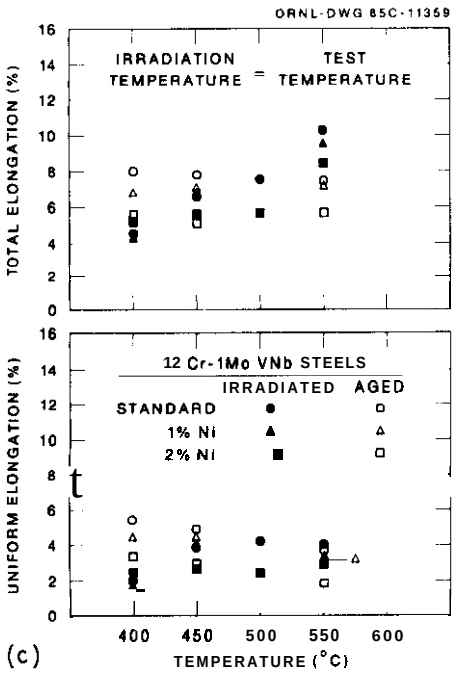

Fig. 7.4.5. The (a) 0.2% yield stress, (b) ultimate tensile strength, and (c) uniform and total elongation as functions of test temperature for thermally aged (5000 h) 12Cr-1MoVW, 12Cr-1MoVW-1Ni, and 12Cr-1MoVW-2Ni steels. Tests were at the aging and irradiation temperatures.

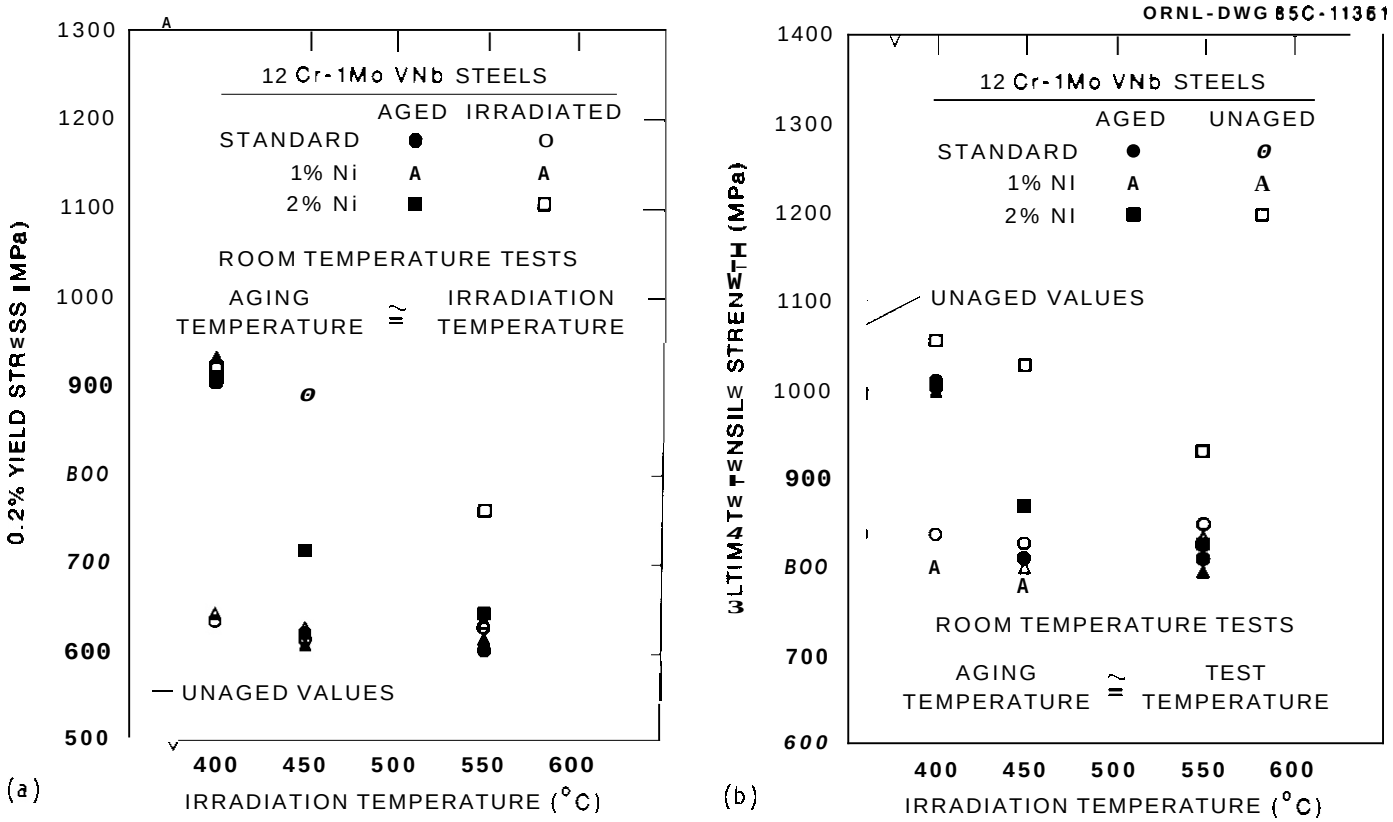

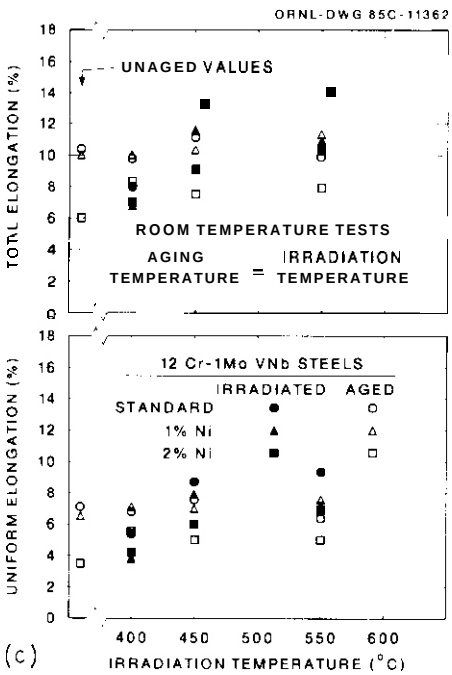

Fig. 7.4.6. The (a) 0.2% yield stress, (b) ultimate tensile strength, and (c) uniform and total elongation as functions of irradiation and aging temperature for thermally aged (5000 h) and irradiated (~16 dpa) 12Cr-1MoVW, 12Cr-1MoVW-1Ni, and 12Cr-1MoVW-2Ni steels tested at room temperature.

ORNL-PHOTO 1148-85

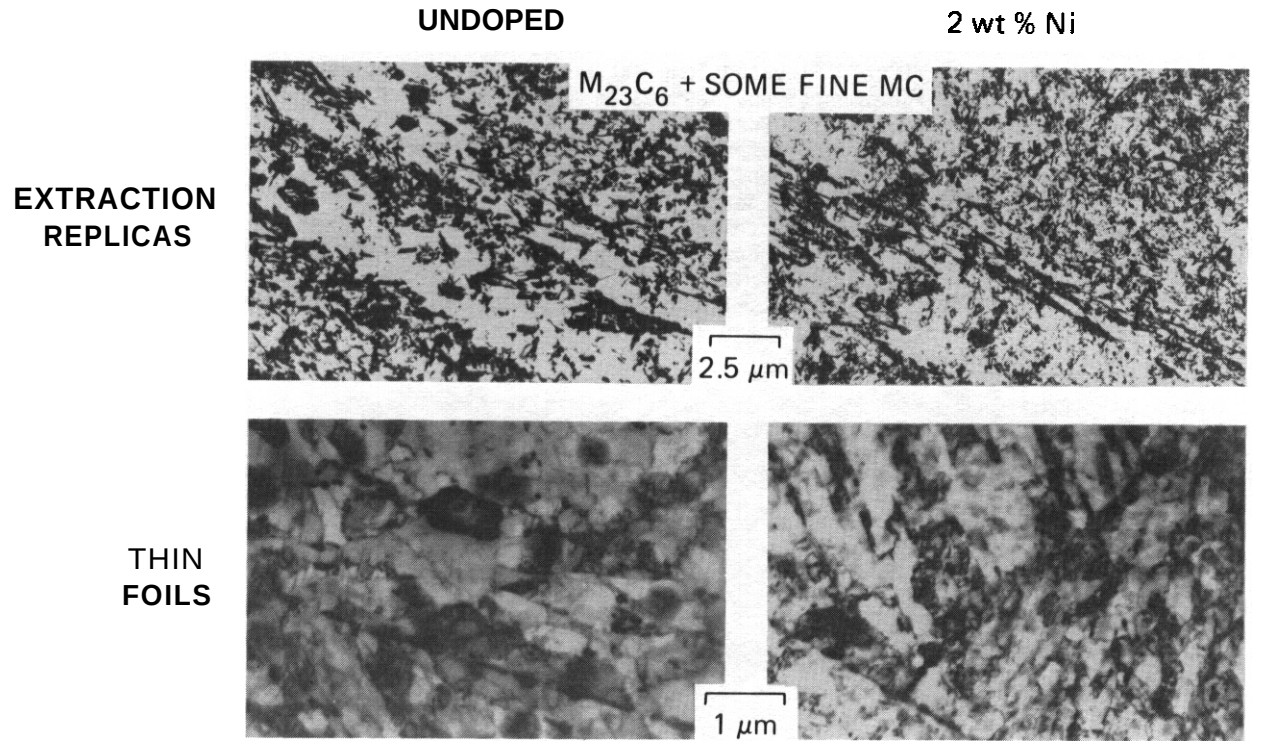

Fig. 7.4.7. Transmission electron micrographs of normalized-and-tempered 12Cr-1MoVW steel (Left) and 12Cr-1MoVW-2Ni steel (right).

In the future, we will examine TEM disks that were irradiated under the conditions of the present experiment. However, even without the information derived from such studies. several interesting observations can be made.

Previous irradiation studies of 12Cr-1MoVW steel indicated that nickel-rich G-phase forms during irradiation in EBR-II at 390°C, and it was concluded that much of the strengthening observed was caused by this precipitate.[7] It was also concluded that the hardening caused by G-phase could lead to an irradiation-induced increase in the ductile-brittle transition temperature (DBTT). If this were true, then the 2%-Ni steels could show a much larger irradiation-hardening effect than the standard steels. Such an enhanced strengthening was not observed for the tensile behavior of the steels with 2% Ni. Neither was a large increase in DBTT observed in these steels.[8] The reason for these observations will need to be determined by TEM studies.

As stated in the Introduction, the primary purpose for investigating the nickel-doped steels is to irradiate the steels in a mixed-spectrum reactor to produce both displacement damage and transmutation helium. However, to use this technique, it is necessary to show that nickel does not cause effects that are not present in the standard alloys. The present results indicate that the nickel has not produced microstructural changes that affect the tensile behavior of the 9-Cr and 12-Cr Cr-Mo steels. The original strength advantage for the 2%-Ni steels was an effect of the different tempering treatments. When aged or irradiated, the steels with and without nickel approached similar strengths; this is consistent with the fact that nickel generally adds little solid-solution strengthening and does not cause the formation of any precipitate phases.* Although TEM on these steels is required, the tensile and impact results indicate that the use of the nickel-doped Steels to simulate the simultaneous production of helium and displacement damage on microstructure and properties appears valid.

1.4.5 References

1. R L Klueh, J. M Vitek, and M L Grossbeck, "Effect of Low-Temperature Irradiation with (n,α) Helium Production on Tensile Properties of 12 Cr-1 MoVW-Type Steels," J. Nucl. Mater. 103&104, 887–92 (1981).

2. R L Klueh, J. M Vitek, and M L Grossbeck, "Nickel-Doped Ferritic (Martensitic) Steels for Fusion Reactor Irradiation Studies: Tempering Behavior and Unirradiated and Irradiated Tensile Properties," pp. 648–664 in Effects of Radiation on Materials: Eleventh Conference, eds., H R Brager and J. S. Perrin, ASTM STP 762, American Society for Testing and Materials, 1982.

3. P. J. Maziasz and R. L. Klueh, "Microstructural/Microcompositional Analysis of Normalized-and-Tempered 9Cr-1MoVNb and 12Cr-1MoVW Steels Doped with 2 wt % Nickel," Chap. 7.2, this report.

4. F. B. Pickering, Physical Metallurgy and the Design of Steels, Applied Science Publishers, Ltd., London, 1978. pp. 10-13.

5. R. L. Klueh and J. M. Vitek, "Elevated Temperature Tensile Properties of 9Cr-1MoVNb Steel Irradiated in the EBR-II AD-2 Experiment," pp. 100–103 in ADIP Semiannu. Prog. Rep. Mar. 31. 1984, DOE/ER-0045/12, U.S. DOE, Office of Fusion Energy.

6. R. L. Klueh and J. M. Vitek, "Elevated Temperature Tensile Properties of 12Cr-1MoVW Steel Irradiated in the EBR-II AD-2 Experiment," pp. 104–106 in ADIP Semiannu. Prog. Rep. Mar. 31, 1983, DOE/ER-0045/10, U.S. DOE. Office of Fusion Energy.

7. D. S. Gelles and L. E. Thomas. "Microstructural Examination of HT-9 and 9Cr-1MoV Contained in the AD-2 Experiment," pp. 343–362 in ADIP Semiannu. Prog. Rep. Mar. 31, 1982, DOE/ER-0045/8, U.S. DOE, Office of Fusion Energy.

8. W. R. Corwin, J. M. Vitek, and R. L. Klueh, "Effect of Nickel Content on the Aging and Irradiation Response of Impact Properties of 9Cr-1MoVNb and 12Cr-1MoVW in the Absence of Internal Helium Effects," pp. 120-127 in ADIP Semiannu. Prog. Rep. Sept. 30, 1984. DOE/ER-0045/13, U.S. DOE, Office of Fusion Energy.

7.5 ELEVATED-TEMPERATURE TENSILE PROPERTIES OF 2 1/4 Cr-1Mo STEEL IRRADIATED IN THE EBR-II, AD-2 EXPERIMENT* — R. L. Klueh and J. M. Vitek (Oak Ridge National Laboratory)

7.5.1 ADIP Task

ADIP Tasks are not defined for Path E, ferritic steels in the 1978 Program Plan.

7.5.2 Objectives

The goal of this project is to measure the tensile properties of 2 1/4 Cr-1Mo steel irradiated at elevated temperatures in EBR-II. In the future, the results from this work will be compared with elevated-temperature irradiations of this steel in HFIR. Comparisons will also be made between 2 1/4 Cr-1 Mo steel and the 9Cr-1MoVNb and 12Cr-1MoVW steels irradiated in the EBR-II, AD-2 experiment.

7.5.3 Summary

The effect of irradiation on the tensile properties of 2 1/4 Cr-1Mo steel was determined for specimens irradiated in EBR-II to 23 dpa at 390 to 550°C. Unirradiated control specimens and specimens aged for 10,000 h at the irradiation temperature were also tested. Irradiation at 390°C increased the strength and decreased the ductility of the samples while softening occurred in those irradiated and tested at 450, 500, and 550°C.

7.5.4 Progress and Status

7.5.4.1. Introduction

Several Cr-Mo steels are considered excellent candidates for first-wall and blanket-structure materials for fusion reactors operating at temperatures up to about 520°C.[1,2] These steels have become of interest relatively recently, and irradiated mechanical properties are now becoming available.

The ferritic steels of primary interest in the U.S. Department of Energy (DOE) Alloy Development for Irradiation Performance (ADIP) program are 12Cr-1MoVW and 9Cr-1MoVNb steels with a secondary interest in 2 1/4 Cr-1Mo steel. Although some 2 1/4 Cr-1Mo steel specimens have been irradiated and tested in the ADIP program studies, the testing of these specimens has a relatively low priority. Because of this, the Electric Power Research Institute (EPRI) is supporting a program to test 2 1/4 Cr-1Mo steel that has been irradiated as part of the ADIP program, but would not be tested in the near future under the normal DOE support. By testing this steel on an accelerated basis, it should be possible to assimilate this information into the program to develop an optimum alloy for fusion reactor applications.

The first phase of the EPRI-sponsored research involved work on the tensile behavior of 2 1/4 Cr-1Mo steel irradiated in EBR-II.[3] These specimens were part of the large AD-2 experiment conducted by Hanford Engineering Development Laboratory (HEDL).[4] Irradiation was to a displacement-damage level of ~9 dpa at 390, 450, 500 and 550°C. The irradiated specimens, as-heat-treated specimens, and thermally aged specimens were tested at the irradiation temperature and, where specimens were available, at room temperature.

The irradiation phase of the AD-2 reconstitution experiment has been completed, and in this report, data will be presented on 2 1/4 Cr-1Mo steel that was irradiated to ~23 dpa. These data will be combined with the data for the 9 dpa irradiation to extend our understanding of the effect of elevated-temperature irradiation on the tensile properties of the steel.

7.5.4.2 Experimental Procedure

The 2 1/4 Cr-1Mo steel used in this experiment was obtained from a section of thick-walled pipe that was fabricated from Mannesman heat 38649.[3] The vendor-certified chemical composition and overcheck are given in Table 7.5.1. Tensile specimens were obtained from 0.76-mm-thick sheet that was produced by cold rolling 11.2-mm-thick sections of the pipe. The specimens were irradiated in the normalized-and-tempered condition: 0.5 h at 900°C, air cooled; 1 h at 700°C, air cooled.[4]

Sheet tensile specimens in this experiment were of the SS-1 type, with a reduced gage section 20.3 mm long by 1.52 mm wide by 0.76 mm thick (Fig. 7.5.1). All specimens were machined with their gage lengths perpendicular to the rolling direction of the sheet.[4]

Specimens were irradiated in capsules designed to maintain temperatures of 390, 450, 500, and 550°C. Irradiation was in row four of EBR-II, and all of the 2 1/4 Cr-1Mo steel specimens were exposed to ~4.9×10^{26} neutrons/m^2 ($E > 0.1$ MeV), which produced a displacement damage of about 23.6 dpa. The uncertainty in fluence has been estimated as ±10% and the temperature uncertainties are 390 ± 10°C, 450 ± 15°C, 500 ± 20°C, and 550 ± 30°C (ref. 5).

---

*Research sponsored by Electric Power Research Institute, Palo Alto, California, under contract No. Y3E053R between McDonnell Douglas Astronautics Company, St. Louis, Missouri, and Martin Marietta Energy Systems, Inc.

After irradiation, tensi1e tests were conducted at the irradiation temperature and. where specimens were available, at room temperature. As-heat-treated as well as thermally aged control samples were also tested to separate the effect of irradiation from thermal-aging effects. Thermal aging was at the irradiation temperatures for 10,000 h — the approximate time of the irradiation. The tensile tests were made in a vacuum chamber on a 44-kN-capacity Instron universal testing machine at a crosshead speed of 8.5 μm/s, which results in a nominal strain rate of 4.2 × 10^{-4}/s.

1.5.4.3. Results

7.5.2(a)]. The prior austenite grain size was estimated as being between ASTM Nos. 8 and 9; the microhardness was 209 DPH (1000-g load). By optical microscopy it was possible to detect a progressive increase in the amount of precipitate with increasing aging time and temperature [Fig. 7.5.2(b) and (c)]. The microhardness showed little

Table 7.5.1. Chemical composition of 2 1/4 Cr-1Mo steel (Heat 38649)

Element	Content (wt %)[a]		Element	Content (wt %)[a]	
	Vendor[b]	Overcheck[c]		Vendor[b]	Overcheck[c]
C	0.093	0.083	Mo	0.95	0.99
Mn	0.52	0.49	cu	0.16	
P	0.011	0.011	Al	0.003	
S	0.011	0.016	AS		0.017
Si	0.17	0.19	Sn		0.0088
Ni	0.40		N		0.010
Cr	2.15	2.17	Sb		0.0024

[a]Balance iron.
[b]Mannesmann Company.
[c]Climax Molybdenum Company, Ann Arbor, Michigan.

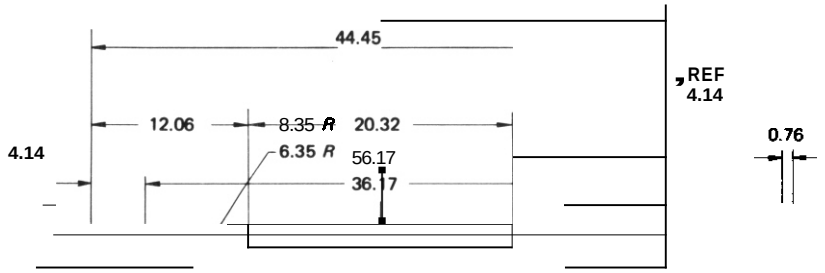

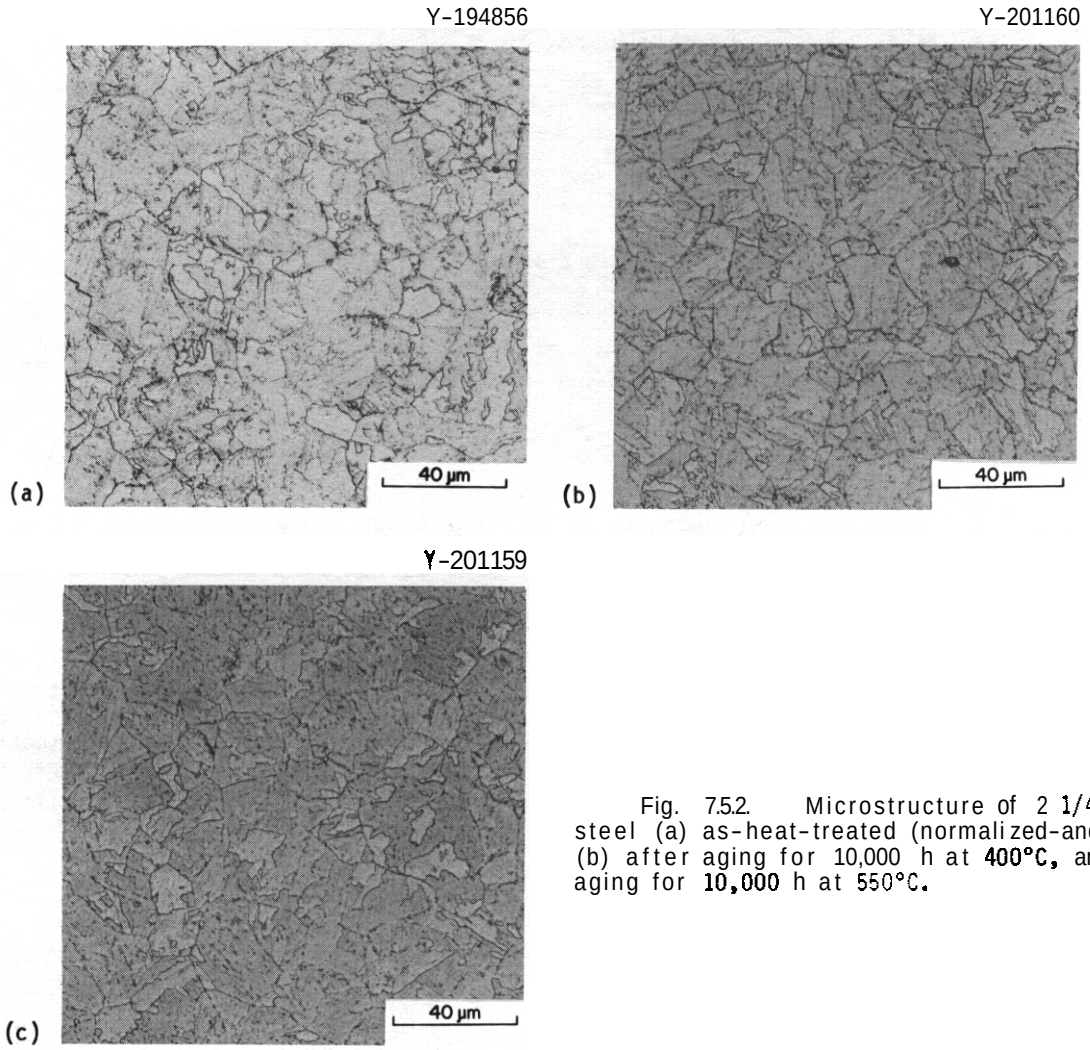

Fig. 7.5.2. Microstructure of 2 1/4 Cr-1Mo steel (a) as-heat-treated (normalized-and-tempered), (b) after aging for 10,000 h at 400°C, and (c) after aging for 10,000 h at 550°C.

Table 7.5.2. Tensile properties of 2 1/4 Cr-1Mo steel thermally aged for 10,000 h

Temperature (°C)		Strength (MPa)		Elongation (%)	
Aging	Test	Yield	Ultimate	Uniform	Total
400	400	452	575	5.3	7.8
450	450	410	471	2.4	4.9
500	500	448	525	3.6	6.5
550	550	383	433	3.1	6.9

Table 7.5.3. Tensile properties of 2 1/4 Cr-1Mo steel irradiated to approximately 23 dpa

Temperature (°C)		Strength (MPa)		Elongation (%)	
Irradiation	Test	Yield	Ultimate	Uniform	Total
390	212	761	799	3.5	6.8
	400	695	715	1.2	3.8
450	22	500	598	7.8	12.5
	450	440	507	4.0	6.8
500	212	482	573	6.2	10.3
	500	373	431	3.1	6.1
550	212	352	452	11.0	15.7
	550	275	311	3.5	7.9

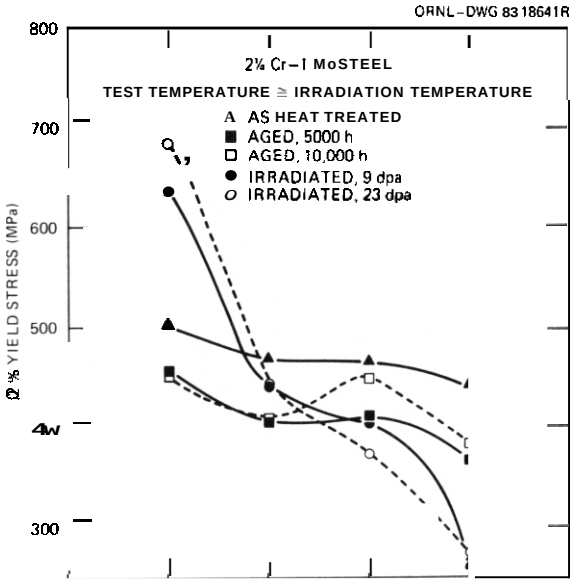

Fig. 7.5.3. The 0.2% yield stress of 2 1/4 Cr-1Mo steel as a function of test temperature for specimens irradiated to 9 and 23 dpa, unirradiated controls, and controls thermally aged for 5000 and 10,000 h. The test temperature equals the irradiation and aging temperatures.

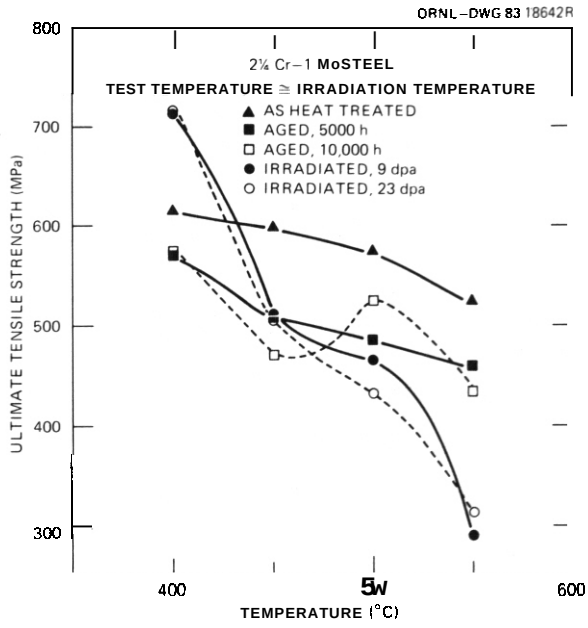

Fig. 7.5.4. The ultimate tensile strength of 2 1/4 Cr-1Mo steel as a function of test temperature for specimens irradiated to 9 and 23 dpa, unirradiated controls, and controls thermally aged for 5000 and 10,000 h. The test temperature equals the irradiation and aging temperatures.

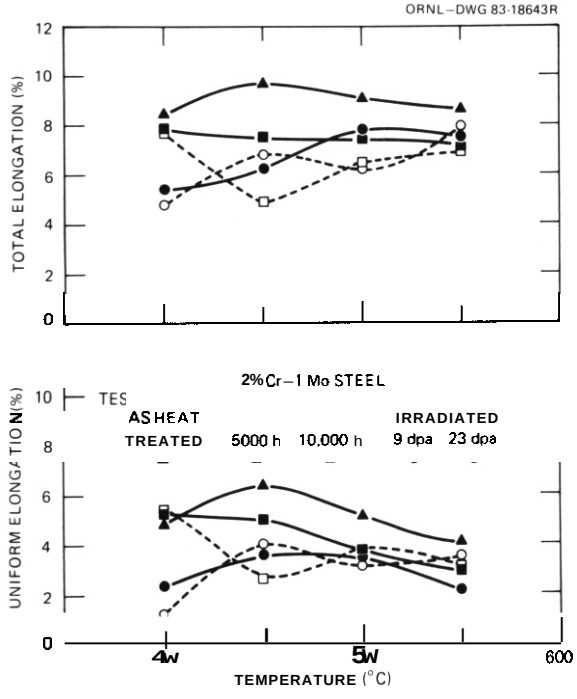

Fig. 7.5.5. The uniform and total elongation of 2 1/4 Cr-1Mo steel as a function of test temperature for specimens irradiated to 9 and 23 dpa, unirradiated controls, and controls thermally aged for 5000 and 10,000 h. The test temperature equals the irradiation and aging temperatures.

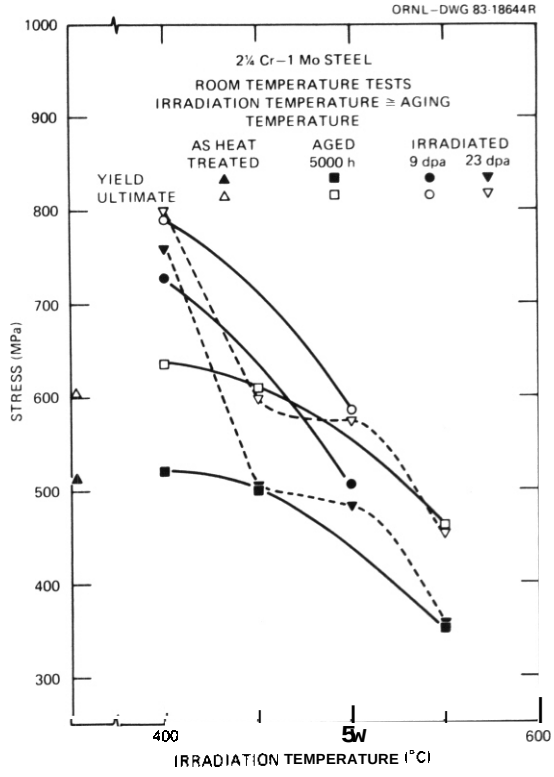

Fig. 7.5.6. The 0.2% yield stress and ultimate tensile strength of 2 1/4 Cr-1Mo steel tested at room temperature plotted against irradiation (aging) temperature for specimens irradiated to 9 and 23 dpa, and specimens thermally aged to 5000 h. Results for unirradiated controls are also shown.

–23 dpa produced no large changes in uniform and total elongation from the values observed after aging for 5000 h and irradiating to 9 dpa, respectively (Fig. 7.5.5). In all cases, adequate ductility remained, even after the large amount of irradiation hardening that occurred when irradiated at 390°C.

Because of the lack of irradiated specimens available for testing at room temperature after the 9 dpa irradiation and the lack of specimens thermally aged to 10,000 h, it is difficult to determine relative changes from these tests beyond stating that the observed behavior is qualitatively similar to that observed on the specimens tested at the elevated temperatures (Figs. 7.5.6 and 7.5.7). If it is assumed that there is little difference

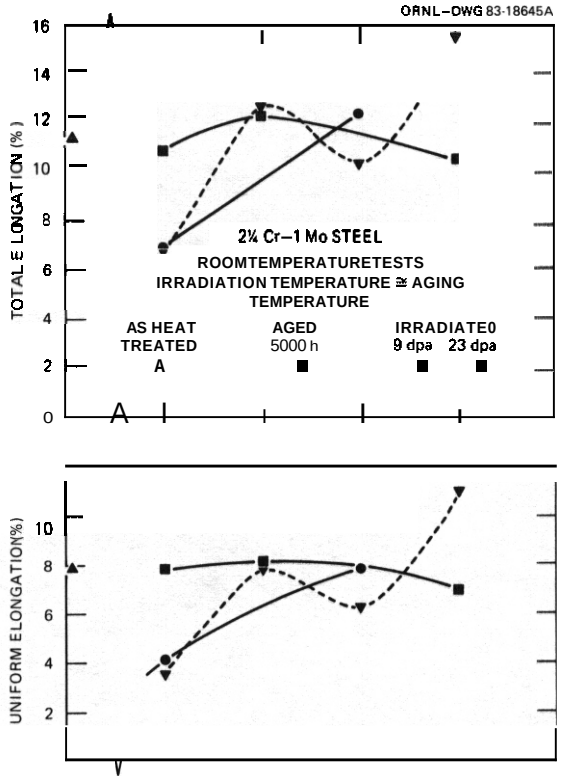

data are available) and those previously aged to 5000 h, it is seen that at 450, 500, and 550°C, there is little difference between the specimens irradiated to 23 dpa and those aged 5000 h at the respective irradiation temperatures. It is not possible to adequately compare specimens irradiated to 9 and 23 dpa because of the lack of specimens for the 9 dpa irradiation. The ductilities of the specimens irradiated to 23 dpa and tested at room temperature were quite large (Fig. 7.7.7); the only significant decrease in uniform and total elongation due to irradiation occurred for the specimen irradiated at 390°C, where the irradiation hardening occurred.

All of the tensile fractures for the specimens were ductile-transgranular. For the unirradiated specimens, the necking was easily observed; selected specimens were also examined by optical metallography. After irradiation, selected fracture specimens were examined by SEM, and only ductile-type failures were observed.

Because of the increase in strength after aging at 500°C (Figs. 7.5.3 and 7.5.4), a qualitative comparison of the effect of thermal aging on the precipitate content was made by examining extraction replicas from the aaed specimens. No attempt was made to identify the precipitates or determine the amounts present.

After the normalizing-and-tempering treatment, there appeared to be a small number of large precipitates present (Fig. 7.5.8). Needlelike precipitates were also present, but they appeared to be quite scattered. Thermal aging for 5000 and 10,000 h at 400°C gave rise to no significant change from the normalized-and-tempered structure. There appeared to be a slight increase in the number of needlelike precipitates.

Aging for 5000 h at 500°C produced an increase in the number of needlelike precipitates [Fig. 7.5.9(a)]. There was a further increase after 10,000 h at 500°C [Fig. 7.5.9(b)] which indicates a probable maximum in the number of particles formed occurs during thermal aging. At 550°C the number of needlelike precipitates also went through a maximum with aging time, but the maximum probably occurred closer to 5000 h than 10,000 h (Fig. 7.5.10).

1.5.4.4. Discussion

The 2 1/4 Cr-1Mo steel develops its elevated-temperature strength properties by solid solution hardening and dispersion strengthening by carbide precipitates.[6-10] The effect of irradiation to 9 dpa and thermal aging for 5000 h on the solid-solution strengthening effects and precipitation processes was used to explain the earlier observations.3 Similar explanations apply to the observations after 23 dpa and 10,000 h

The solid-solution strengthening effect that contributes to the 2 1/4 Cr-1Mo steel was studied by Baird and Jamieson,[6,7] who showed that the effect occurs in steels that contain interstitial and substitutional solutes in supersaturated solution that have an affinity for each other. They termed the effect interaction solid-solution hardening (ISSH) and concluded that the hardening resulted from the formation of atom pairs or atom clusters of carbon and the solute atom. These clusters subsequently form dislocation atmospheres. In mechanical property studies on 2 1/4 Cr-1Mo steel, the effect of ISSH on the strength was examined.[8] For a normalized-and-tempered steel with a tempered-bainite microstructure, it was concluded that ISSH was due to Cr-C interactions.8 The effect of ISSH was found to have a dominant effect on tensile properties between about 250 and 450 to 500°C.[8]

H-83820

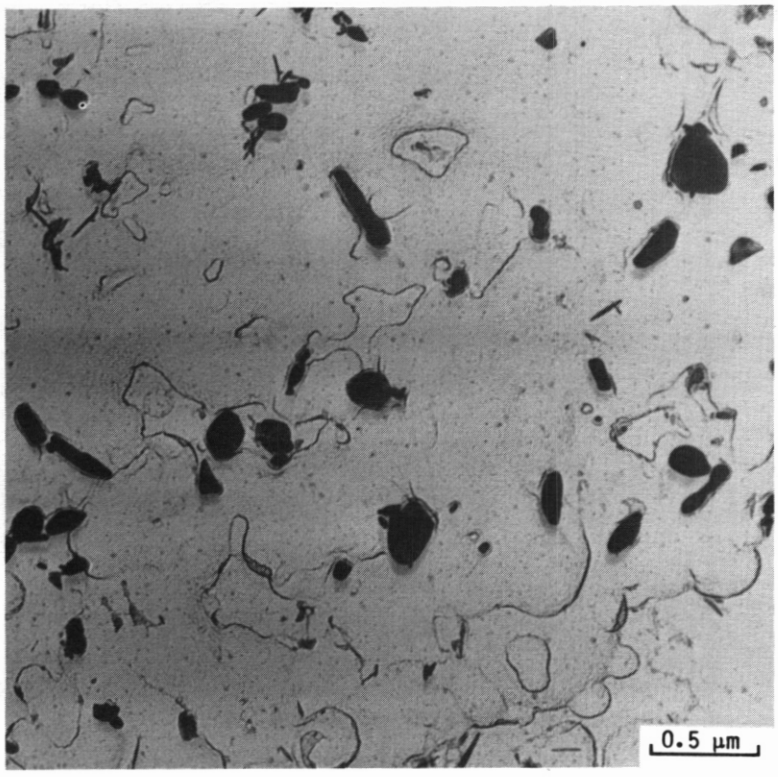

Fig. 7.5.8. Extraction replica of normalized-and-tempered 2 1/4 Cr-1Mo steel.

H-83830

H-83835

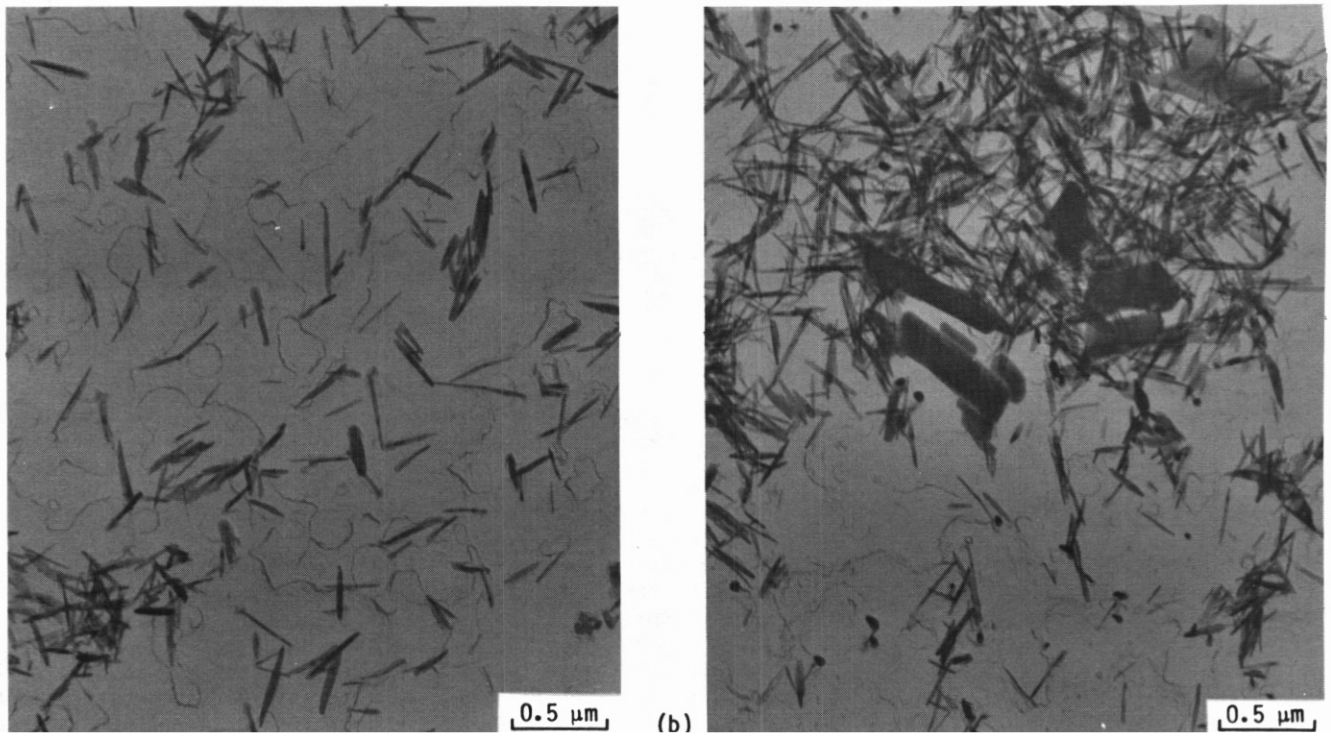

Fig. 1.5.9. Extraction replicas of normalized-and-tempered 2 1/4 Cr-1Mo steel that was thermally aged at 500°C for (a) 5000 h and (b) 10,000 h.

H-83839

H-83841

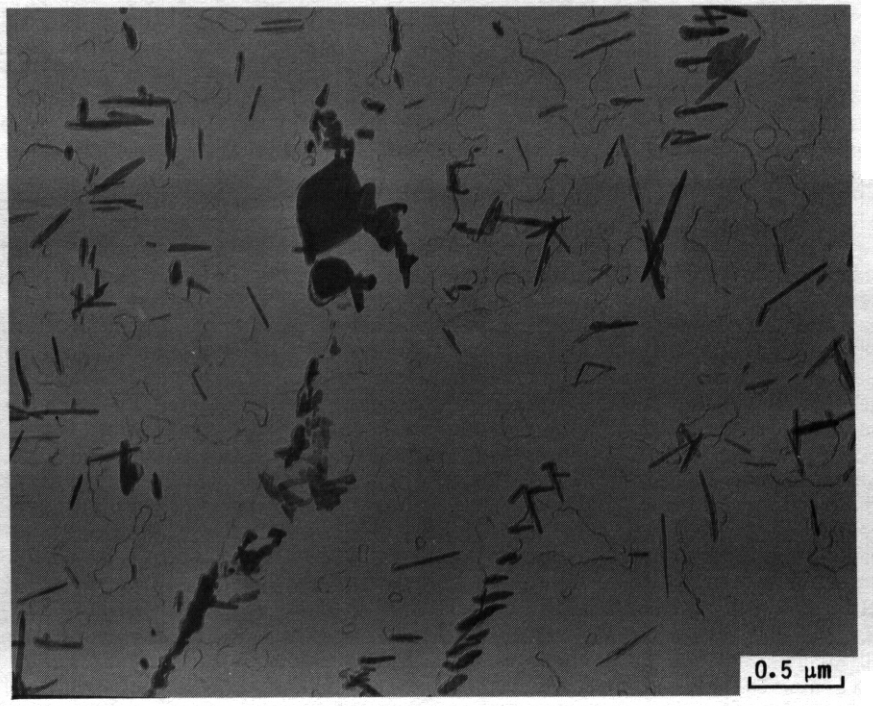

Fig. 7.5.10. Extraction replicas of normalized-and-tempered 2 1/4 Cr-1Mo steel that was thermally aged at 550°C for (a) 5000 h and (b) 10,000 h.

The loss of strength due to thermal aging for 5000 h at 400 and 450°C (Figs. 7.5.3 and 7.5.4) was attributed to the loss of the supersaturation that causes ISSH.[3] At the highest temperature, both the loss of ISSH and changes in dispersion strengthening caused by precipitate changes are expected to play a role in the strength loss. The higher the temperature, the more rapid will be the effect on the precipitate changes that lead to a coarser precipitate, and thus, a lower strength.[3]

Once the supersaturation that caused ISSH is relieved, which occurred during the 5000 h aging treatment, further effects by ISSH are not expected. Thus, the changes noted by thermally aging beyond 5000 h must be attributed to changes in the dispersion hardening due to changes in precipitate type and morphology. The only effect of thermal aging on mechanical properties between 5000 and 10,000 h is the possible increase in strength at 500°C. The electron microscopy observations shed some light on this observation.

The precipitation sequence in 2 1/4 Cr-1Mo steel is complicated. Precipitation curves were first described by Baker and Nutting[9] and recently revised by Gage and Nutting.[10] In the tempered bainite microstructure of the unirradiated specimens, the microstructure can contain M_3C, M_2C, M_7C_3, $M_{23}C_6$, and M_6C, depending on the extent of the tempering and/or aging treatments. At equilibrium, only $M_{23}C_6$ and M_6C are expected to be present.[9,10] The M_2C is felt to be the only carbide that gives rise to significant strengthening.[1]

Because no precipitate identification was carried out, the interpretation of the observed microstructures will be based on the detailed literature observations[9-13] and on work on another heat of 2 1/4 Cr-1Mo steel.[1] The tempered bainite of 2 1/4 Cr-1Mo steel has a lath structure that contains lenticular ("rod-shaped" and "small parallelogram-shaped")[12] carbides that are often found on lath boundaries; these carbides have been identified as M_7C_3 (refs. 12-14). Large carbide particles (globular, and sometimes with a squared or parallelogram shape) are found on prior austenite grain boundaries, with smaller particles on lath boundaries, generally identified as $M_{23}C_6$ in the tempered condition.[12-14] (When the steel is tempered for longer times or after aging, M_6C also appears, and it often has a similar morphology[9,12-14]). The large particles in Figs. 7.5.8 and 7.5.9 are assumed to be M_7C_3 and $M_{23}C_6$. Since they seem little affected by thermal aging, they will not be discussed further.

The Precipitates that showed the greatest amount of change when the specimens were thermally aged were the needlelike precipitates (Fig. 7.5.8). Such precipitates have been identified as M_2C (refs. 10,12), or M_2X, where X accounts for the fact that both carbon and nitrogen can be present. There appeared to be an increase in the number density of the needle-shaped precipitates for the specimen aged 10,000 h at 500°C over that aged for 5000 h. This increase in particle density coincides with the increase in strength with increase in aging time at 500°C (Figs. 7.4.3 and 7.5.4) and is concluded to be the cause of the strength increase. Since the same precipitation processes occur at the other temperatures, continued aging at the lower temperatures would be expected to lead to an increase in strength as M_2C precipitates form. If an increase in strength occurs at 550°C, it peaks before the 5000 h aging treatment is complete. Such an effect of M_2C precipitates on strength has previously been observed on normalized-and-tempered[1] and annealed[15] 2 1/4 Cr-1Mo steel.

During elevated-temperature irradiation, the effect of irradiation damage and precipitation both affect the strength. After irradiation to 9 dpa, the strength changes were explained[3] as follows. The increase in strength at 390°C was attributed to irradiation-induced dislocation-loop formation resulting from displacement damage and any irradiation-enhanced precipitation. The loss of strength from that of the as-heat-treated strength at 450 and 500°C was attributed to the same effects that cause the strength loss due to thermal aging, primarily the loss of ISSH. Finally, the enhanced softening of the irradiated specimen at 550°C over the softening that resulted from thermal aging alone was attributed to enhanced precipitate coarsening due to irradiation-enhanced diffusion.[3]

After irradiation to 23 dpa, there appears to be little change from that observed after 9 dpa (Figs. 7.5.3 –7.5.5). The only change occurred at 500°C, where irradiation to 23 dpa caused a strength decrease over that after 9 dpa. This can be attributed to irradiation-enhanced diffusion similar to that at 550°C after 9 dpa. Because of the lower temperature, a longer time is required to obtain softening. It is interesting that there was no further decrease in strength at 550°C over that observed after 9 dpa. These observations may mean that irradiation hastens the replacement of M_2C by M_6C, after which dispersion strengthening is provided by large $M_{23}C_6$ and M_6C carbides.[16] At that stage, the properties should change quite slowly.

Gelles[13] has performed transmission electron microscopy (TEM) on 2 1/4 Cr-1Mo steel TEM disks irradiated to 23 dpa at 390, 450, and 500°C. Voids formed during irradiation at 390°C; a high density of small spherical particles along with an irradiation-induced dislocation structure also formed. The fine particles were not identified, and it is not known whether they are M_2C, the precipitation enhanced by irradiation, or perhaps an irradiation-induced phase. The needlelike precipitates are present and appear similar to those present in the unirradiated condition. Because of the high density of small precipitate particles, they probably contribute to the hardening along with the irradiation-induced dislocation structure. The strength measurements indicate that this hardening saturates during irradiation to 9 dpa, as there is only a small increase in the YS (Fig. 7.5.3) and no change in UTS (Fig. 7.5.4) between 9 and 23 dpa.

When irradiated at 450 and 500°C, Gelles found no voids and no significant change from unirradiated material.[13] This agrees with the electron microscopy observations made on the thermally aged materials and the interpretation of the results proposed to explain the effect of irradiation on tensile properties.

After the irradiation to 9 dpa, it was concluded that normalized-and-tempered 2 1/4 Cr-1Mo steel irradiated to 9 dpa has good stability when irradiated at temperatures up to 500°C (ref. 3). That conclusion can now be applied for irradiation to 23 dpa. Although the strength deteriorated at 500°C after irradiation to 23 dpa, no gross loss of strength relative to thermal aging was observed. Furthermore, no further deterioration occurred at 550°C, where the large decrease occurred for the 9 dpa irradiation. The observation that ductile failure occurred for the specimens that hardened when irradiated at 390°C agrees with results for 2 1/4 Cr-1Mo steel irradiated at ~50°C in the High Flux Isotope Reactor (HFIR) to ~9 dpa (ref. 17). When tested at room temperature, considerably more hardening was observed, giving rise to a lower uniform and total elongation than observed in this experiment, but nevertheless, a ductile fracture occurred.[17]

7.5.5. Summary and Conclusions

Tensile specimens of normalized-and-tempered 2 1/4 Cr-1Mo steel were irradiated in EBR-II to a fluence of 4.9 × 10^{26} neutrons/m^2 (E > 0.1 MeV), which resulted in a displacement damage level of about 23 dpa. The normalized-and-tempered heat treatment of the 0.76-mm-thick-sheet specimens produced a tempered bainite microstructure. Irradiation was at 390, 450, 500, and 550°C; specimens were tested at the irradiation temperature and at room temperature. In addition to the irradiated specimens, as-heat-treated control specimens and as-heat-treated specimens aged 10,000 h (corresponding to the time in the reactor) at the irradiation temperatures were tested at room temperature and the irradiation temperature. The results were compared with those obtained after irradiation to 9 dpa and thermally aging for 5000 h. The following is a summary of the observations and conclusions.

1. Except at 500°C, thermal aging for 10,000 h at 400, 450, 500, and 550°C caused only slight changes in tensile properties from those observed after aging for 5000 h. An increase in strength occurred after aging at 500°C for 10,000 h was attributed to the precipitation of M_2C.
2. Irradiation at 390°C caused an increase in the strength and a decrease in ductility relative to unirradiated specimens. similar to the changes observed after irradiation to 9 dpa.
3. A strength decrease relative to the unirradiated, aged, and unaged control specimens was noted for specimens irradiated at 450, 500, and 550°C.
4. The hardening at 390°C was attributed to the irradiation-induced dislocation structure resulting from displacement damage along with the irradiation-enhanced precipitation that has been observed.
5. The strength changes caused by irradiation at 450, 500, and 550°C were attributed to changes in the precipitate distribution that were thermally induced, although irradiation enhances these precipitate changes under some conditions.

7.5.6 References

1. S. N. Rosenwasser, P. Miller, J. A. Dalessandro, J. M. Rawls, W. E. Toffolo, and W. Chen, "The Application of Martensitic Stainless Steels in Long Lifetime Fusion First Wall/Blankets," J. Nucl. Mater. 177–82, 85&86 (1979).
2. R. L. Klueh, "Chromium-Molybdenum Steels for Fusion Reactor First Walls — A Review," Nucl. Eng. Design 72, 329 (1982).
3. R. L. Klueh and J. M. Vitek, Elevated-Temperature Tensile Properties of Irradiated 2 1/4 Cr-1Mo Steel," J. Nucl. Mater. 329–44, 126 (1984).
4. R. J. Puigh and N. F. Panayotow, "Specimen Preparation and Loading for the AD-2 Ferritics Experiment," pp. 260–93 in AOIP Quart. Prog. Rep. June 30, 1980, DOE/ER-0045/3, U.S. DOE, Office of Fusion Energy.
5. R. J. Puigh, Hanford Engineering Development Laboratory, Richland, Washington, Private Communication, Oct. 19, 1983.
6. J. D. Baird and A. Jamieson, "High-Temperature Tensile Properties of Some Synthesized Iron Alloys Containing Molybdenum and Chromium," J. Iron Steel Inst. 210, 841–46 (1972).
7. J. D. Baird and A. Jamieson. "Creep Strength of Some Synthesized Iron Alloys Containing Manganese, Molybdenum and Chromium," J. Iron Steel Inst. 210, 847–56 (1972).
8. R. L. Klueh, "Interaction Solid Solution Hardening in 2.25 Cr-1 Mo Steel," Mater. Sci. Eng. 35, 239–53 (1978).
9. R. G. Baker and J. Nutting, "The Tempering of 2 1/4 Cr-1Mo Steel After Quenching and Normalizing," J. Iron Steel Inst. 192, 257–68 (1959).
10. J. Nutting, "The Tempering of Carbon and Alloy Steels," pp. 3–16 in Ferritic Alloys for Use in Nuclear Energy Technologies, American Institute of Mining, Metallurgical, and Petroleum Engineers, Inc., New York, 1984.
11. K. J. Irvine. J. O. Murray. and F. B. Pickering. "Structural Aspects of Creep-Resisting Steel." pp. 246–75 in Structural Processes in Creep, Iron and Steel Institute, London, 1961.
12. J. Pilling and N. Ridley, "Tempering of 2.25 Pct Cr-1 Pct Mo Low Carbon Steels," Met. Trans. 13A, 557–63 (1982).
13. D. S. Gelles, "Evaluation of Ferritic Alloy Fe-2 1/4 Cr-1 Mo after Neutron Irradiation — Microstructural Development," pp. 113–37 in ADIP Semiann. Prog. Rep. March 31, 1984, DOE/ER-0045/12, U.S. DOE, Office of Fusion Energy.
14. J. M. Vitek, Oak Ridge National Laboratory, unpublished research, 1984.

15. R. L. Klueh, "The Thermal Aging of Annealed 2 1/4 Cr-1Mo Steel," pp. 643–51 in Environmental Degradation of Engineering Materials, Virginia Polytechnical Institute, Blacksburg, Virginia, 1977.

16. R. L. Klueh and J. M. Leitnaker, "An Analysis of the Decarburization and Aging Processes in a 2 1/4 Cr-1Mo Steel," Met. Trans. 6A, 2089–2093 (1975).

17. R. L. Klueh and J. M. Vitek, "Tensile Behavior of Three Commercial Ferritic Steels after Low-Temperature Irradiation," pp. 61572 in Ferritic Alloys for Use in Nuclear Energy Technologies, American Institute of Mining, Metallurgical and Petroleum Engineers, Inc, New York, 1984.

7.6 IRRADIATION EFFECTS IN FERRITIC STEELS - T. A Lechtenberg (GA Technologies Inc.)

7 .6.1 ADIP Task

The Department of Energy (DOE) Office of Fusion Energy (OFE) has cited the need to investigate ferritic steels under the Alloy Development For Irradiation Performance (ADIP) task Ferritic Steels Development (Path E).

7.6.2 Objectives

The objective of this paper is to collect and disseminate cohesive information on ferritic steels data and the Path E program. This paper Is a distillation of *two* recent papers given at the 13th Symposium on Fusion Technology (Varese, Italy In Sptember 1984) and the 1st International Conference on Fusion Reactor Materials (Tokyo, Japan In December 1984).

7.6.3 Summary

Since 1980 the Alloy Development for Irradiation Performance (ADIP) task funded by the U-S. Department of Energy has been studying the 2-12Cr class of ferritic steels to establish the feasibility of using them In fusion reactor first wall/breeding blanket (FW/B) applications. The advantages of ferritic Steels include superior swelling resistance. low thermal stresses compared to austenitic stainless steels. attractive mechanical properties up to 600°C. and service histories exceeding 100.000 hours. These steels are commonly used in a range of microstructural conditions which Include ferritic. martensitic, tempered martensitic. bainitic. etc. Throughout this paper where the term "ferritic" Is used It should be taken to mean any of these microstructures. The ADIP task is studying Several candidate alloy systems Including 12Cr-1MoWV (HT-9). modified 9Cr-1Mo. and dual phased steels such as EM-12 and 2 1/4Cr-1Mo These materials are ferranagnetic (FM) body centered cubic (BCC). and contain chromium additions between 2 and 12 wt.% and molybdenum additions usually below 2%. The perceived Issues associated with the application of this class of steel to fusion reactors are the Increase in the ductile – brittle transition temperature (DBTT) with neutron damage. the compatibility of these steels with liquid metals and solid breeding materials. and their weldability. The ferranagnetic character of these steels can also be important In reactor design. It is the purpose of this paper to review the current understanding of these BCC steels and the effects of irradiation. The major points of discussion will be irradiation induced or enhanced dimensional changes such as swelling and creep. mechanical properties such as tensile strength and various measurements of toughness. and activation by neutron interactions with structural materials.

7.6.4 Progress and Status

7.6.4.1. Introduction

The First Wall/Breeding Blanket (FW/B) structures are key cmponents in fusion reactors since their structural life can Impact the reactor's performance which ultimately translates Into the cost of electricity. A number of metals have been proposed for possible use as the structural material in the FW/B and many have been Included in conceptual power reactor design studies. These conceptual designs have helped show that. while each material has attractive properties or features for use in design (low thermal stresses. high temperature strength. or low long-term radioactivity), each also has disadvantages and no one material has emerged as the overwhelming favorite for use in canmercial reactors. The primary uncertainty regarding the use of these materials Is a lack of radiation damage information In fusion relevant conditions. particularly with respect to transmutation-produced helium. In an effort to gain a better understanding of these effects and to ultimately develop Irradiation resistant material, the Office of Fusion Energy (OFE) of the Department of Energy (DOE) created the Alloy Development for irradiation Performance task In 1976 (ADIP). This program has Involved cooperative research between many national laboratories (ORNL. HEDL, ANL, NRL SNLL). Industrial resbarch organizations (GA. McDAC), and universities (MIT Wisconsin. UCSB).

When the ADIP program was created there were more than 10 different alloy systems proposed for study. It was decided to group them Into families or classes and emphasize the most promising material within each group. These groups are referred to as paths and there are currently five in the ADIP program. These are Path A (austenitic stainless steel). Path B (Fe-Ni-Cr precipitation strength alloys) Path C (reactive and refractory metals), Path D (Innovative materials and concepts). and Path E (ferritic steels). The primary objective of the ADIP program is to develop materials capable of operating in a fusion reactor up to a time-Integrated neutron exposure of 40 $MW\text{-}y/m^2$ or approximately 400 dpa. A secondary objective is to provide both materials and design data for use of lower performance, intermediate fusion systems such as an experimental test reactor or a demonstration reactor. In the ADIP studies, each of the candidate alloys are brought through a series of steps Including scoping studies, base research studies, and alloy optimization. This type of approach is necessary since premature selection or rejection of an alloy could severely limit the design options available In the future. Currently, major ADIP program emphases are being placed on modified or Improved austenitics (e.g. PCA) and the ferritic steels, the subject of this paper.

Ferritic steels have a long history of use in the fossil power industry and have been used extensively in Europe[1,2]. They generally have excellent physical and mechanical properties. These steels contain chromium for resistance to elevated temperature corrosion in air (amounts up to 12% for applications up to 600°C) and more aggressive chemical environments. Molybdenum and other carbide forming elements such as tungsten, vanadium, and niobium are sometimes added to increase the creep resistance and the elevated temperature tensile strengths. Keeping carbon below about 0.20% allows these steels to be welded if preheated and followed by a post-weld heat treatment (PWHT) to temper the microstructure. Several commercial alloys are available which are fabricable, weldable and can be used in corrosive environments up to temperatures of 600°C.

Interest in these steels for fusion applicetions was generated first wht it became known that this class had superior resistance to void formation during fission neutron exposure and in bombardment by heavy ions[3,4,5,6]. Experimental data over the last six years in the U.S. fusion materials program has consistently corroborated the resistance of ferritic steels to void swelling[7,8].

7.6.4.2 Irradiation-Induced Dimensional Changes

Ferritic steels have exhibited very low total irradiation-induced swelling to damage levels in excess of 100 dpa in fission reactors such as EBR-II and HFIR. They are expected to behave in a similar fashion to austenitic steels in that there will be an initial transient or incubation period of very low swelling followed by an accelerated steady state swelling rate. Fig. 7.6.1 compares the relative swelling rate of austenitic alloys with simple and commercial ferritic steels utilizing data analyzed by Sniegowski and Wolfer[11], Garner[38], Horton and Bentley[9], and Gelles[39]. It is interesting to note that the steady state swelling rates of austenitic steels is about 1%/ dpa after an incubation period that varies due to metallurgical factors (such as cold working or chemistry), irradiation temperature, or the irradiation source (neutron spectrum or particle energy). The maximum steady state swelling rate of an experimental 10Cr-Fe ferritic alloy was about 0.07% /dpa and had an incubation dose of about 30 dpa. This experiment included a simultaneous injection of He^+ and D^+_2 ions at about 10 appm He/dpa. In the same experiment the swelling rate was 0.02% /dpa at 575°C to damage levels of 100 dpa. In commercial ferritic steels irradiated in EBR-II no significant or measurable swelling has been reported to doses in excess of 120 dpa. 12Cr-1MoWV irradiated in HFIR to 36 dpa and containing 99 appm He had a maximum swelling rate of 0.07%/dpa at 400°C with negligible swelling at 300°, 500°, and 600°C[10] and it appears that the incubation dose has not yet been reached. Sniegowski and Wolfer[11] recently calculated that the theoretical steady state swelling rate for BCC ferritic alloys would be 0.04%/dpa which agrees very well with the data from fission reactor experiments. Because there are no neutron spectra available in which the proper He/dpa ratios can be produced in ferritic steels the effects of helium on the incubation period in ferritics remains unclear. However, the swelling data presented shows that ferritic steels will have much lower total swelling than austenitics. One conceptual study estimated the dose to 5% swelling could be as high 250 dpa, roughly equivalent to 25MW-yr/m^2.[12] Even longer lifetimes would be predicted if the transient period could be increased by manipulating metallurgical factors as has been done with notable success in the austenitic steels[13].

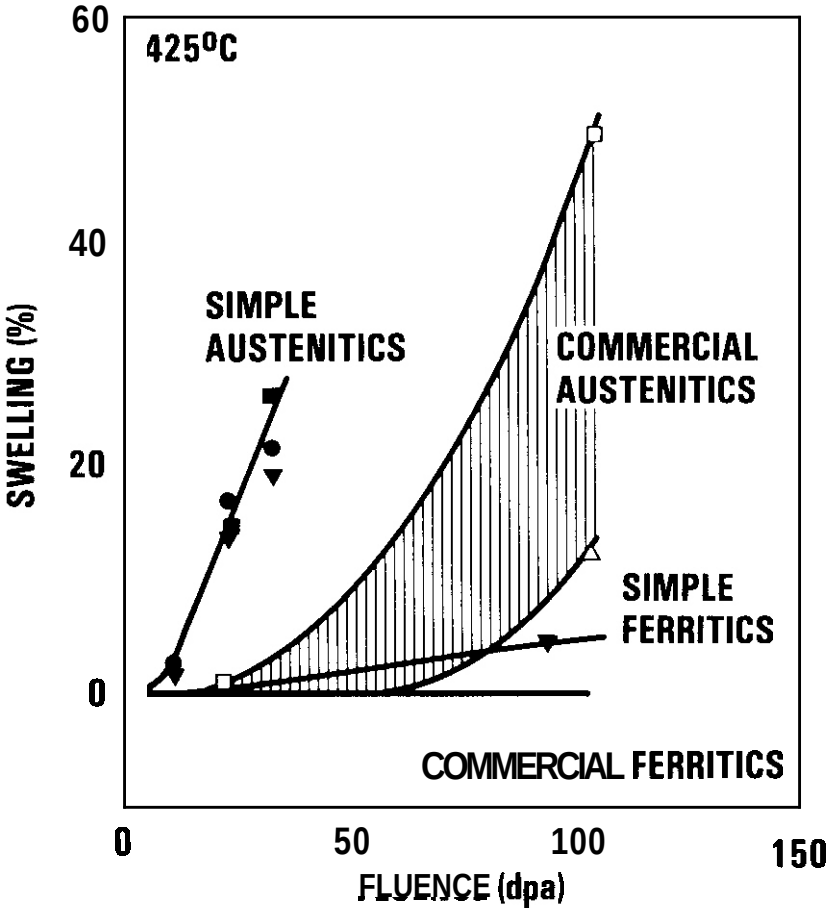

Fig. 7.6.1. A comparison of the swelling behavior of commercial and simple ferritic steels to austenitic steels

Recent in-reactor creep results on selected ferritic alloys to peak fluences to 37 dpa in the temperature range 400° to 500°C and hoop stresses of 205 and 290 MPa show small in-reactor creep strains[14]. Lower dose creep data suggest a linear fluence dependence for the in-reactor creep behavior of

Table 1. Ductile-brittle transition temperature changes of 12Cr-1MoWV and 9Cr-1MoVNb after irradiation

Alloy	T_{irr} (°C)	Fluence (dpa)	DBTT (°C)	DBTT (°C)
12Cr-1MoWV(HT-9)	Unirradiated	-	5	-
	390	15	130	125
		15	110	105
		30	140	135
	450	15	27	22
		15	14	9
		30	78	73
	500	15	30	25
		30	63	58
	500	15	99	93
		15	0	0
		30	60	55
9Cr-1MoVNb	Unirradiated	-	-22	-
	390	15	21	49
		15	43	65
		30	32	54
	450	15	-22	-
		15	-1	23
	500	15	-22	0
		15	0	22
		30	-12	33
	500	30	-11	0
		15	-3	25

change in DBTT. As presented in Fig. 7.6.2 the normalized tensile and hardness data for 12Cr-1MoWV for damage levels up to 30 dpa and irradiation temperatures to 550°C are shown[22]. The DBTT changes seem to mirror those changes in strength seen in Fig. 7.6.2 In that large shifts in DBTT occur at lower temperatures where there are large increases in strength. The maximum change in DBTT observed in 12Cr-1MoWV is 135°C after 30 dpa and 390°C.

While it has not been demonstrated unequivocably that saturation of mechanical properties such as toughness and strength will occur in the 9-12Cr steels, it is strongly suggested by comparison with other bcc and ferritic materials and property measurements such as the tensile data mentioned above. Fig. 7.6.4 contains the most recent DBTT data for HT-9 for fluences up to 30 dpa. Similar to the behavior of ferritic pressure vessel steels, the changes in the DBTT for HT-9 begin to slow at relatively low fluences. At irradiation temperatures of 390°C after 15 dpa the slope for the curve begins to decrease and at 30 dpa there is a slight positive slope indicating that saturation is occurring. As discussed for pressure vessel steels, lower irradiation temperatures produce larger changes in these steels, and the saturation occurs at higher fluences. It is not clear if an increase in the DBTT will preclude the use of ferritic steels in high-fluence fusion cmponents because it may be that these components can be designed to safely operate at temperatures below the DBTT. This possibility is discussed in more detail below. Fig. 7.6.5 shows the effect of irradiation on the plain strain fracture toughness as a function of test temperature. The solid data points indicate unirradiated lower-shelf energy plane-strain fracture toughness data generated on full-sized and miniature compact tension specimens while the open data are plane-strain fracture toughness data generated for HT-9 which has been irradiated between 50° to 500°C and 5 to 10 dpa. These data suggest that to irradiation fluences of 10 dpa and irradiaton temperatures down to 50°C, a lower-shelf fracture toughness has not been measured. The toughness values measured in the irradiated material at test temperatures from 93° to 340°C show that the toughness levels are approximately 125MPa-$m^{1/2}$. The transition temperature measured for the full size and miniature compact tension specimens is approximately -75°C and the lowest energies measured were 30 MPa-$m^{1/2}$ at temperatures below -150°C.

Recent studies by Odette and co-workers[23] and Lechtenberg and Dahms[18] have investigated the plane-strain fracture toughness on the lower-shelf of the 12Cr-1MoWV steel. The increase in transition temperature due to neutron exposure may be largely irrelevant if it could be demonstrated that actual fusion structures can be reliably operated on the lower shelf. This would require that irradiation and other environmental factors do not significantly degrade the lower-shelf toughness. irradiation at typical light water reactor end-of-life conditions (about 0.1 dpa and 300°C) has little or no effect on lower-shelf toughness and no decrease has been measured on HT-9 in conditions irradiated to 30 dpa. On the lower-shelf, the cleavage mechanism appears to be controlled by microstructural features such as grain boundaries and carbides. Precipitation that occurs in ferrite (such as the G-phase) will increase the constraint in the matrix thus causing the shift from ductile-to-cleavage fracture. The cleavage fracture energy is controlled by the features such as carbides at grain boundaries which do not change significantly after the matrix becomes depleted of the chemical specie driving the precipitation. Thus unlike the increase in the DBTT, the lower-shelf fracture energy probably will not decrease significantly as a result of irradiation hardening or high neutron fluences. Plane strain fracture toughness values for 12Cr-1MoVW cooled to below the DBTT are about 50 MPa-$m^{1/2}$. At very low temperatures (<150°C), it is thought the micromechanism of fracture changes from a cleavage to twinning mechanism resulting in a sharp decrease to 30 MPa-$m^{1/2}$.[26] Irradiation did not produce this same shift to a twinning fracture in pressure vessel steels, so it is not expected to do so in the ferritic steels. It has been shown by Odette that the critical micro-cleavage fracture stress, (σ_f*) and critical distance (ℓ*) parameters for HT-9 defined by the Ritchie-Knott-Rice (RKR) critical stress distance criteria is consistent in HT-9 with behavior

an HT-9 material after an Initial rapid transient[15]. Data on HT-9 to a peak fluence of approximately 100 dpa Indicates a linear fluence dependence and a stress dependence with a stress exponent of approximately 1.5 [16,17]. Recent results on a ferritic 12%Cr steel (Din No. 1.4914) similar to HT-9 show that its in-pile creep behavior differed fran that of austenitic steels and fran HT-9. Din. No. 1.4914 has a strong temperature dependence with an unexpectedly high activation energy, which Implies a thermally activated mechanism. but these data show the creep behavior is non-linearly dependent upon the applied stress[15]. These experimentailsts measured a stress dependence exponent of about 3. Furthermore, thermal control samples done in parallel did not show any noticeable creep strain for canparable time periods[35]. However, Puigh and Wire reported that In-reactor creep strains for HT-9 and 9Cr-2Mo were very small and similar to each other at temperatures of 443° and 505°C, while 2-1/4Cr-1Mo begins to loose its strength at 572°C[36]. Pulgh reported In-reactor creep data for HT-9 at 419°C and 490°C which indicated a stress exponent describing the In-reactor creep stress dependence as being between 1 and 2, while at 653°C the HT-9 data suggested a stress exponent of 3 to 7, while 2 1/4Cr-1Mo data Indicated a stress exponent of the order of 2 to 6. Based on the U.S. data fran the EBR-II with a $\alpha = 6.3 \times 10^{18}$ n/cm^2-hr, Dahms and Lechtenberg have suggested an Irradiation Induced creep rate equation of the form:

$$\dot{\varepsilon}_I = B_c \phi \sigma^n$$

where B_c Is a constant which is alloy and temperature dependent, ϕ is the flux or dose rate, σ is the equivalent (or von Mises) stress (MPA), and n is the stress exponent[18]. They suggested for Hi-9 the following values be used;

$$B_c = (6.8581 - 1.8373T + 1.2463T^2) \times 10^{-29} \text{ for } T<737^\circ K$$

$$B_c = 8.6714 \times 10^{-29} \qquad \text{for } T \geq 737^\circ K$$

where ϕ is in n/cm^2-hr, σ is in units of MPa, and $\dot{\varepsilon}$ is in units of strain/ hr.

7.6.4.3 <u>The Effects of Irradiation on Strength and Toughness</u>

In general ferritic steels exhibit radiation hardening below approximately 500°C. There is an Increase in yield and ultimate strengths and an associated decrease in ductility. Fig. 7.6.2 shows the effect of Irradiation temperature on the ratios of the ultimate strength (UTS) and the UTS from hardness correlations for HT-9 from several irradiation experiments. The data was collected fran HFIR and EBR-II Irradiations and range in fluence levels fran approximately 9 to 13 dpa and range in temperatures fran 50° to 550°C[19]. Gelles has suggested that at higher temperatures (<400°C), the strengthening effect in HT-9 may be due to the precipitation of a nickel-silicon rich G-phase[20]. The strength Increase at lower Irradiation temperatures has been associated with the precipitation of defect clusters on the order of 3nm in size[21]. This behavior of an Increase in strength due to Irradiation has been seen also for the 9Cr-1MoVNb and 2 1/4Cr-1Mo as well.

The changes in yield and ultimate strengths have ramifications to other properties such as toughness because the increase in strength is accanpanied by a decrease in ductility. The U.S. fast breeder reactor program and the fusion reactor materials program both maintain major experimental efforts on the Irradiation response of ferritic steels, particularly with regard to toughness. Efforts to date have attempted to Identify potential problems and find solutions. Sane data are now available and more will be available within the next year, Much discussion of the fracture properties of ferritic steels for fusion applications have centered around the measurement of ductile-brittle transition temperature (DBTT). The Impact test furnishes data using a simple method of following the change in the fracture mode of the steel as a function of temperature. The Importance of the Charpy impact test lies in the fact that it reproduces the transition temperature fran the ductile-to-cleavage fracture mode in about the same temperature range as is observed In engineering structures, and has been widely used to measure the effect of a number of variables on the DBTT. A classical Interpretation of the DBTT is that at some temperature, fracture stress is reached during loading of the specimen prior to the onset of yield, resulting in a brittle type cleavage fracture. Above the DBTT the specimen undergoes general yielding prior to the onset of fracture. There is, however, no quantitative method of using the DBTT in design. It is a simple Indication of the toughness In a material which has been empirically related to the behavior of engineering structures. Various standard measures of the DBTT have been used, Including the 40J(30ft-lb) DBTT, predefined lateral expansion values, the fracture appearance transition temperature (FATT), or temperature to half the average or the average energy between the upper-shelf and lower-shelf toughness. For the sake of simplicity and because all these measurements are somewhat arbitrary, the 40J DBTT will be quoted unless otherwise specified.

Table **7.6.1** contains DBTT data for 12Cr-1MoWV and 9Cr-1MoVNb that show irradiations to fluences of 30 dpa fran temperatures of 390° to 500°C. While this will be discussed more canpletely, it may be noted that lower Irradiation temperatures produce larger Increases in the DBTT for both the HT-9 and the 9Cr alloy. Furthermore, the 9Cr-1MoVNb has a lower DBTT. While data on 12Cr-1MoWV and similar ferritic steels are somewhat scarce, there is a significant body of the data on low alloy pressure vessel steels[40]. The data show that the DBTT is generally increased at lower irradiation temperatures, and the change in DBTT saturates at a relatively low fluence. Sane data, Including for the pressure vessel steel A533-B, are shown in Fig. 7.6.3. These data show that lower Irradiation temperatures tend to produce a higher

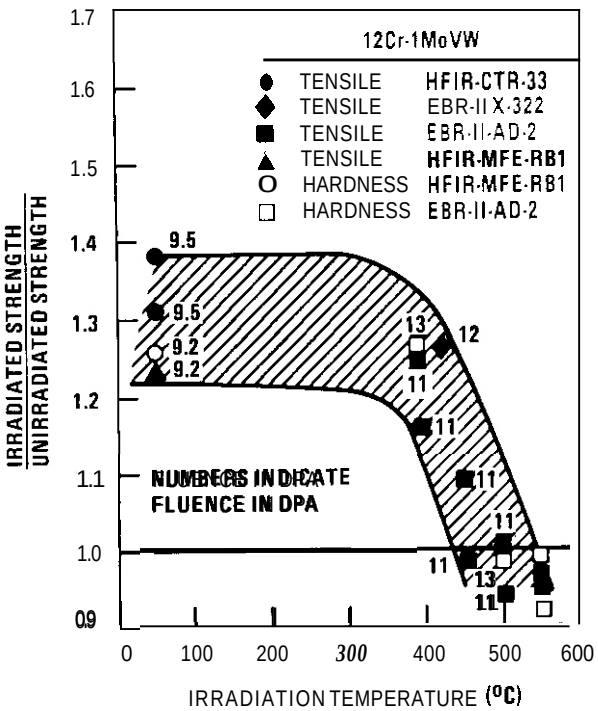

Fig. 7.6.2. The effect of irradiation temperature on the ratio of strength in the irradiated and unirradiated conditions for 12Cr-1MoWV (HT-9) as a function of test temperature.

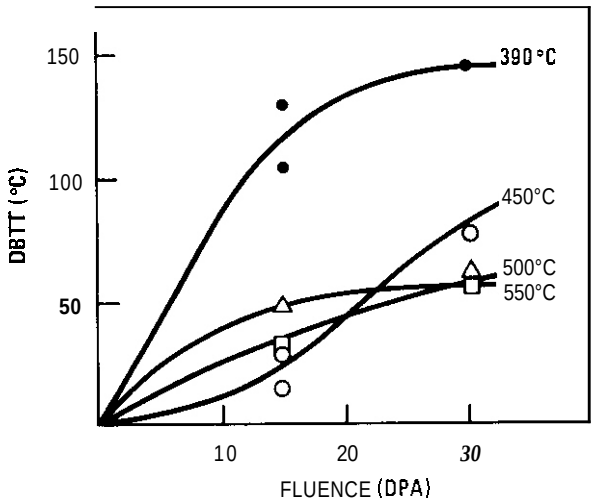

Fig. 7.6.4. The ductile-brittle transition temperature for 12Cr-1MoWV (HT-9) increases with fluence and at lower irradiation temperatures, but the rate of increase slows after about 15 dpa and at lower temperatures.

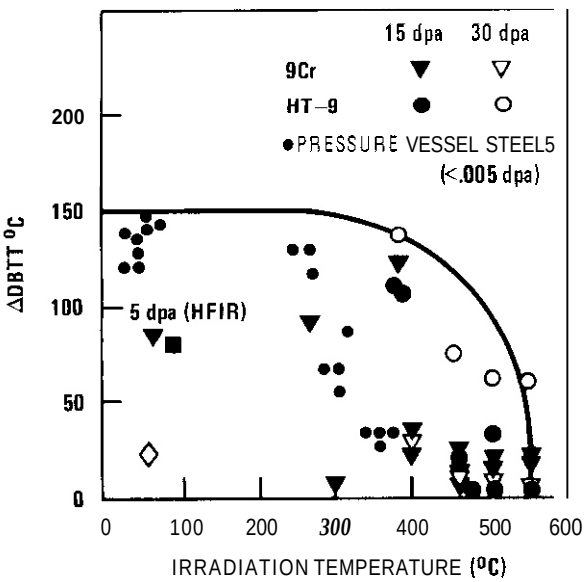

Fig. 1.6.3. The effect of irradiation temperature on the change in ductile-brittle transition temperature on several ferritic steels.

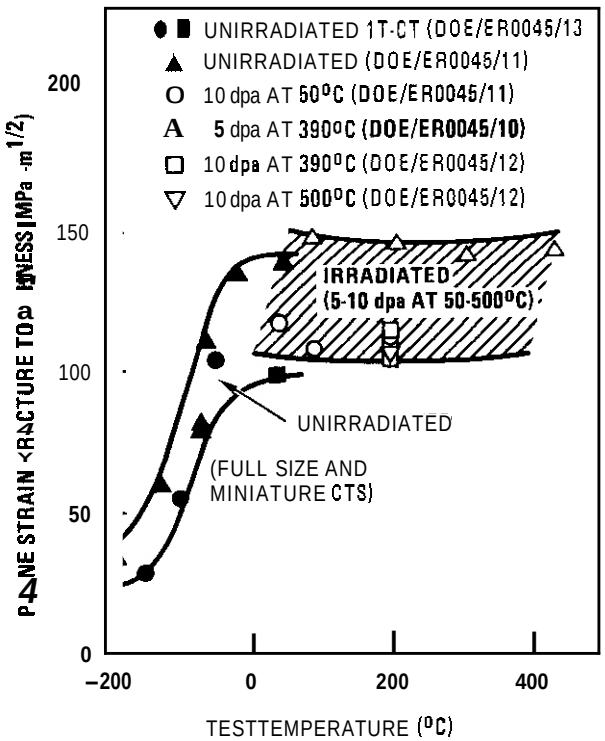

Fig. 7.6.5. Plane-strain fracture toughness of 12Cr-1MoWV steels in the irradiated and unirradiated condition. Irradiation temperatures range from 50 to 500°C and fluences are to 10 dpa.

observed In other tempered bainltic/martensiteic steels based on estlmates of the servlce properties[25,26]. They also calculated that thin fusion structures may fall by plastic collapse following general yield rather than brlttle fractures. Thls was calculated to be true for operatlng at temperatures below the DBTT where large amounts of Irradiation strengthening had occurred. However, calculations showed that under such condltlons, thin-walled fuslon structures (on the order of 2 mm) would experience Increased fallure loads due to Irradlatlon. Thls is In direct contrast to the behavior of thick wall vessels which manifest decreasing fracture loads for these same circumstances.

Based on data currently available, there may be adequate toughness In Irradlated HT-9 to allow for a fracture resistant design. The Increase In DBTT associated with neutron exposure may slow at relatively low damage levels (<20 dpa) as has been seen In other ferrltlc steels. Plain strain fracture toughness tests have been performed on Irradlated materlals to damage levels of approxlmately 125MPa $m^{1/2}$ at temperatures above 0°C. It is likely that the very hlgh neutron fluences needed for economlc fusion FW/B components will increase the DBTT further, although at a slower rate, but one cannot tell whether these calculations predlctlng adequate lower shelf fracture reslstance can be extrapolated to an engineering structure. Investlgatlons are contlnulng to estlmate the lifetlme and fracture mode of various fusion caponents supposlng that the first wall suffers a DBTT shift such that it may operate on the lower-shelf during sane of Its llfetlme.

1.6.4.4 Assessment of the Potential for Low Actlvatlon Ferrltlc Steels

Recently the desirabllity of uslng low activation materlals In fusion machines was assessed by a DOE panel which recommended that reduced activation of structural materlal should remaln one of the primary considerations in the development of fusion reactor materials. The Interactions of neutrons from the fuslon machine with the structural material will cause all conventional alloys to activate[28]. A unique advantage of fuslon Is the fact that this actlvlty Is not Inherent to the fusion process and both the magnltude and half-life of the actlvlty can be controlled by the proper selection of the elements comprising the structural material. Three possible requirements for low actlvatlon materlal are waste disposal, hands on malntenance durlng reactor lifetlme, and safety Issues. The term "low actlvatlon material" recently has been used to described alloys that minimize waste disposal difficulties and costs. Steels under dlscusslon here will are belng dlscussed to meet the guidelines of U.S. Federal Regulation 10CFR61 which specifies four classes of waste. Classes A, B, and C, may be disposed of by near-surface burial. All other wastes, not meetlng A, B, or C requlrements, are not qualified for near-surface disposal and may be required to utilize deep geological disposal. All conventional materials, such as AIS316 or 12Cr-1MoWV, will actlvate such that they do not qualify for surface waste disposal, and could require deep geologic dlsposal for many generations. The relative cost advantages of surface versus geologic disposal has been estlmated to be $7000-20,000/ m^3 [29] Actlvatlon results fran transmutation of major constituent elements and Impurltles. Whlle all elements will actlvate. It is a relatively few that have daughter radlonuclides that decay quickly enough or are weak enough such that they could be dlsposed of as surface wastes. For example, after Irradiation In a theoretical reactor study called Starfire to a fluence of 10 $MW\text{-}yr\text{-}m^{-3}$ followed by 8 yrs storage wlth no dllutlon prlor to disposal, Nb would be restricted in the original alloy to less than 3 ppm and Mo to less than 30 ppm. The llmits on the initial concentrations of Ni, Mo, Cu, Nb and N establlshed by the 10CFR61 guidelines are mutually exclusive. That Is, if any one of the elements Is present at its concentration llmlt, the other elements must not be present, or, alternatively, the sum of the fractional concentratlons must be less than one for the controlled radlonuclides. Common steel elements that could be used for low actlvatlon steels Include Mn, Tl, Cr, Sl, W, V, Ta, and C. The most Important common alloying addltlons that are unsuitable for low actlvatlon material are Ni, Nb, and Mo. In the 9-12Cr class of steels molybdenum Is added to provide solid solutlon hardenlng for Improved hlgh temperature strength and to pranote the preclpltatlon of carblde to Increase the creep strength. Removal of molybdenum for low actlvatlon will therefore degrade hlgh temperature properties. Possible alloy substitutions are tungsten, vanadlum and tantalum[29,30,31]. Tungsten and vanadlum are seen as major replacements for the removal of molybdenum In the ferrltlc alloys. Whlle the Inltlal concepts are still belng developed and data Is scarce on new alloys, the phase space currently belng studled in the U.S. materlals program Includes the alloys ranglng in chranlum composition between 2 and 11%. tungsten between 1 and 5%, vanadlum between 0.2 and 1.58, tltanlum <0.1%, and manganese fran 0.3 to 6.5%[31]. While the metallurgy of the Fe-Cr-W and Fe-Cr-W,V systems have not been studled as extenslvely as the Fe-Cr-Mo systems, analogles can be drawn fran the work done on Cr-Mo-W steels[32,33]. The canpositions mentloned above were formulated based on an assumption of analogous behavior of the FeCrW system and the FeCrMo system and by calculating the chranlum and nickel-equlvalents using such equatlons as those developed by Schnelder[34].

Recently, many of the low actlvatlon alloys were Included in Irradiations In EBR-II to fluences to about 15 dpa. The temperatures ranged fra 420° to 600°C. Gelles[38] has reported the optical and TEM metallography and limited tenslle data on several of the alloys. Prellmlnary results Indicate that bainltlc alloys slmllar to 2 1/4Cr-1Mo and ferrltlc steels analogous to 9Cr-1Mo and HT-9 can be produced which have no constituent elements proscribed by the waste disposal regulations. Initial TEM observation demonstrate that stable mlcrostructres can be designed which behave simllarly to other ferritic steels showing negllglble swelling. Thls data is soon to appear, and the readers are referred to Ref. 38 for further detalls.

7.6.5 Conclusions

Ferritic steels offer significant advantages for use in FW/B components for fusion reactors. It has been shown that the steady state swelling rates of this class are nearly an order of magnitude lower than for austenitic steels. Ferritic steels are expected to exhibit a transient or incubation period similar to austenitic steels and the transient regime is influenced by the microstructure and chemistry of the particular alloys. The effects of helium are unclear primarily due to the lack of a fusion neutron source which would produce the proper helium/dpa ratio. But one effect may be to decrease the transient period. In fission reactors, measured total swelling is very low to over 100 dpa, but the helium content is low also. Optimization of this class may increase the incubation dose thus decreasing the total lifetime swelling.

Our understanding of the effects of irradiation on mechanical properties is becoming more mature as experiments are analyzed. There may be an acceleration of the creep rates in-reactor, but thus far the data for 12Cr-1MoWV shows it Is not severe, and studies have been able to use this alloy for self-consistent designs. The increase in the DBTT remains an area of concern. While it appears that the shift to higher temperatures slows and perhaps saturates at about 30 dpa, the exact influence of very high damage levels and transmuted helium Is not known. By inference fran ferritic pressure vessel steels it may be anticipated that the lower-shelf energy does not degrade, but these data are for very low fluences. Recent studies have been able to show that 12Cr-1MoWV behaves according to the RKR cleavage fracture model and this allowed the lower-shelf toughness to be predicted. This compared favorably to measured values which were used to predict that a thin-walled, embrittled first wall would fail by plastic collapse. not a brittle fracture. Other caiculations predict that there will be a leak-before-break situation even if the material is operating on the lower-shelf.

The public concern about nuclear safety and a recognition that this class of steels might solve part of that problem has led to the initiation of an alloy development program for low activation ferritic steels. Experimental heats of bainitic and martensitic steels have been melted and experiments have been irradiated in EBR-II. Initial results are encouraging. Microstructures appear stable with no severe embrittling precipitation after ~15 dpa.

7.6.6 REFERENCES

1. N. Perrson, Characteristics of Hardenable 12Cr Steels for the 80's, Editor R. Barr, Climax Molybdenum Company, Greenwich, Conn., (1980).
2. J. Briggs, and T. Parker, "The Super 12%Cr Steels", Second Ed., Climax Molybdenum Company. (1982).
3. E. Little, and D. Stowe, Proceedings of the Conference on Radiation Behavior of Metallic Materials for Fast Reactor Component. Corse, France, 4-9 June 1979, pp. 17-24.
4. J. Huett, et al., Ibid, Proceedings, pp. 1-10.
5. E. Little, Ibid. Proceedings, pp. 25-30.
6. W. Johnson et ai., Radiation Damage In Metals, American Society of Metals, Metals Park, Ohio, (1975).
7. E. Little. and D. Stowe, J. Nuc. Mat., 87, p. 25, (1975).
8. D. Gelles, J. Nuc. Mat., 103 & 104, p. 975, (1981).
9. L. Horton, and J. Bentiey, Topical Conference on Ferritic Alloys for Use In Nuclear Energy Technology, Snowbird, Utah, 18 June 1983.
10. J. Vitek, and R. Kiueh, Ibid.
11. J. Snlegowski, and W. Wolfer, Ibid.
12. M. Abdou, "Blanket Comparison and Selection Study, FY83 Final Report", ANL/FPP-83-1, Argon Natonal Laboratory, Argon, Illinois (1983).
13. E. Bloom, J. Nuc. Mat., 85 and 86, p. 795, (1979).
14. A DeBremaeckken, and J. Huet, Dimensional Stability and Mechanical Behavior of Irradiated Metals and Alloys, Brighton, England, (1983), p. 117.
15. K. Herschbach and W. Doser, Dimensional Stability and Mechanical Behavior of Irradicated Metals and Alloys, (British Nuclear Society, London 1983) p. 122.
16. J. Straalsund, and D. Geiles, Topical Confrence on Ferritic Alloys For Use In Nuclear Energy Technology, Snowbird, Utah (1983).
17. R. Pulgh, in proceedings of the Conference on Irradiation Effects In Materials, Williamsburg, Virginia (June 1983).
18. C. Dahms, and T. Lechtenberg, Alloy Development for irradiation Performance Semiannual Progress Report for the Period Ending September 1984, DOE/ER-0045/13, p. 22.
19. J. Vitek, and R. Klueh, Alloy Development For Irradiation Performance Semiannual Progress Report for the period ending March 31, 1984, DOE/ER-0045/12, p. 110.
20. D. Gelles, and L. Thomas, Alloy Development For Irradiation Performance Semiannual Progress Report for the period ending September 30, 1982, DOE/ER-0045/9, p. 162.
21. D. Geiles, W. Hu, W. Huang, and G. Johnson, Alloy Development For Irradiation Performance Semiannual Progress Report for the period ending September 30, 1983, DOE/ER-0045/11, p. 115.
22. T. Lechtenberg, "Irradiation Effecs In Ferritic Steels", presented at U.S.-Japan Seminar on Fusion Reactor Materials. Tskuba, Japan, (December 1983).
23. G. Odette, G. Lucas, R. Matl, and J. Sheckherd, "Fundamental Flow In Fracture Studies Of HT-9". Damage Analysis and Fundamental Studies Quarterly Report for the period ending September 1984.

24. G. Odette, G. Lucas, R. Mattl, and J. Sheckherd, J. Nuc. Mat., **122-123,** p. **442,** (1984).
25. G. Odette, G. Lucas. J. Nuc. Mat., **117** (1983), p. **276.**
26. J. Hyzack. and R. Stolr, J. Nuc. Mat., **103 6 104,** (1981), p. **877.**
27. W. Vogelsang, G. Kulclnskl, **R.** Lott, and T. Sung, Nuc. Tech., **22 (19741,** p. **379.**
28. T. Lechtenberg, J. Nuc. Mat., **122 6 123,** (1984), p. **777.**
29. D. Gel les, H Brager, and F. Garner, "La, Actlvaton Approaches To Materials Development", Al loy Development For Irradiation Induced Radloactlvlty Decay". Al loy Development For Irradlatlon Pertormance Semlannual Progress Report for perlod ending March **31, 1984,** DOE/ER-0045/12.
30. R. Klueh and J. Vltek, ADIP Semlann. Progress Report DOE/ER-0045/12 (1984).
31. T. Lechtenberg, " La Activation Ferrltlc/Matensltlc/Bainltic Alloys, ADIP Pathe E", Private Communlcatl on.
32. T. Wada, "The Effects Of Tungsten On Mechanlcal Properties And Hadenabl lity Of 2.25Cr-1Mo Steel", Cl lmax Molybdenum Canpany of Mlchlgan Report **11-323-02** (July 192).
33. E. Vlneberg. and T. *Cox,* Proceedings Of The Topical Conference On Ferrltlc Al loys For Use In Nuclear Energy Technoloales. AIME. p. **291** (1984).
34. H. Schnelder, Foundry Trade Journal, **108,** (1960) p. **151.**
35. C. Wassllew, K. Herschbach, E. Materna-Morris, and K. Ehrlich, Toplcal Conference on Ferrltlc Alloys for Use In Nuclear Energy Technologles (ASME, Warrendale, PA., **1984)** p. **607.**
36. R. Pulgh and G. Wlre, Ibld., p. **601.**
37. F. Garner, J. Nuc. Mat., 122 **6 123** (1984) p. **459.**
38. D. Gelles, Ibld., p. **207.**

7.6.7 Acknowledgements

As noted earlier the ADIP program Involves many Industrial, national laboratory and unlverslty participants and many of these organlzatlons are Involved In the ferrltlc steel development program. The author wlshes to acknowledge the Ilberal use of data In the open literature and ADIP semiannual progress reporrs and the helpful dlscusslons wlth various partlclpants, Includlng D. Gelles, T. Reuther, R. Klueh, J. Vltek, R. Powell, F. Garner, A Rowcliff, O. Smith, R. Odette; and the crltlcal review of the paper by D. Roberrs, Prof. R. Hasigulti, and Dr. P. Schiller.

7.7 MELTING AND FABRICATION OF LOW ACTIVATION FERRITIC ALLOYS FOR FFTF IRRADIATIONS - T. A. Lechtenberg (GA Technologies)

7.7.1 ADIP Task

The Department of Energy/Office of Fusion Energy has cited the need to investigate ferritic/martensitic alloys under the ADIP Program Task, Ferritic Steel Development (Path E) because of the potential this class of materials appears to have to offer excellent radiation damage resistance, low thermal stresses and good high temperature strength.

7.7.2 Objective

The objective of this work was to prepare experimental heats of tungsten strengthened low activation ferritic steels (LAFS) for incorporation into FFTF MOTA irradiations.

7.7.3 Summary

Two experimental heats of W-stabilized low activation ferritic steels have been melted, the chemistries analyzed. and the heats fabricated into specimens to be included in an FFTF irradiation. A control heat of HT-9 was melted and fabricated in the same way. Specimens include 1/3 PCVN specimens for toughness and DBTT evaluations and TEM disks. All specimens were given a heat treatment of 1050°C for 1 hr followed by an air cool, 700°C for 1 hr followed by an air cool.

7.7.4 Progress and Status

7.7.4.1 Introduction

One potential advantage of fusion energy production is in safety. The fusion process is intrinsically safe in that residual radioactivity in a fusion reactor is not an inherent product of the fusion reaction itself. Instead, radiation results fran the neutron interactions with the materials fran which the reactor is built. Therefore, in principle, induced radioactivity levels can be held very low if structural materials are selected which have appropriately low neutron activation properties. Furthermore, public awareness of safety issues has had a profound effect on the development of the fission nuclear industry. Fusion could be spared much of this travali if it can maintain its perception of being a "clean" energy producing technology. The low activation panel established by the Office of Fusion Energy defined three goals for low activation fusion technology: waste disposal, reactor safety, and maintenance. The Panel recommended that the most pranising goal for near-term applications is to develop structural materials that minimize the problems of waste management. This goal most probably may be attained by modifying conventional ferritic steels to eliminate or severely restrict their content of Ni, Mo, Nb, and other high activation elements. These materials are called "low activation ferritic steels" (LAFS).

Conventional materials being considered for first wall structures, such as the 12Cr-1MoWV alloy, might be modified successfully to eliminate the offending elements, thus reducing the activation species with very long half lives that would require storage for thousands of years. This achievement would have economic advantages in that the cost of geological disposal is much higher that the cost of surface disposal under the less stringent classifications of federal regulation 10CFR61.

The licensing requirements are outlined in the regulation 10CFR Part 61 for land disposal of radioactive waste and are intended to protect the health and safety of the public. Waste classifications A B, and C, are based on the specific activity of various radio nuclides in the waste. The allowable activity limits ana restrictions on disposal increase fran class A to class C waste. All three classes are regarded as low level wastes and 10CFR61 is not intended to cover the higher levels of radioactivity in structures that would be produced, for example, by stainless steel blankets in a fusion reactor. The guidelines are appropriate to the evaluation of materials to be developed with low level or rapid decay of radioactivity, and can be used to judge the potential of materials for simple, inexpensive, near surface disposal. If the material does not meet class A B, or C guidelines, the Nuclear Regulatory Commission may approve other provisions for disposal if it meets the public safety objectives of 10CFR61. Such case-by-case approval may be required for any structural material waste generated in the first wall and blanket region of the fusion reactor if required purity levels turn out to be very difficult or impossible to achieve. Certain martensitic steels, such as HT-9, have been used in design studies and satisfy the strength requirements for use as a first wall or blanket material for a fusion reactor. Because of its body centered cubic microstructure, the martensitic form of steel does not tend to swell, under fusion-relevant radiation, beyond acceptable limits within reasonable lifetimes. Unfortunately, the two common elements used in martensitic steels, molybdenum and nickel, transmutate into daughter nuclides which in the quantities almost certain to be generated would be unacceptable for surface disposal. Molybdenum is used for strength and stability of the microstructure, while nickel is used for increased toughness and hardenability. Although martensitic steels are known which use substitutes for molybdenum and nickel, simple exclusion of problem transmutagenic elements fran the canposition formula is insufficient to render a steel suitable for surface-disposai. All steels manufactured by conventional canmercial techniques

Inherently incorporate Impurltles at levels whlch would make these materlals unsuitable for surface dis-posal after long-term exposure to a neutron flux.

Therefore, It Is very desirable to develop a martensltlc steel havlng the requlslte strength for fuslon reactor havlng sufflclently low concentration of elements whlch transmutate into those daughter nuclides for whlch very low concentratlons are permissfble for surface disposal.

Four separate canposlttons based on the HT-9 class of steels have been proposed as providing tensile strength suitable for use as a fuslon flrst wall or blanket structural materlal, as well as havlng elimin-ated those elements regarded as unacceptable accordlng to current waste dlsposal guidelines. The alloys have tungsten and vanadlum servlng instead of molybdenum and nlckel as strengthenlng alloylng elements. Tungsten may be used In quantltles of equivalent atanlc fractions as molybdenum In conventional Cr-Mo steels. Emplrlcal equations developed for 9-12Cr steels were used to adjust the canposlttlon of chranlum, vanadium, and carbon to Insure an adequate hardenablllty. Furthermore, all Impurltles must be maintained at the lowest level posslble in order to qualify for near-surface dlsposal.

7.7.4.2 Experimental

Three 7 kg (15 lb) Ingots of two experimental canposlttons, and one control canposlttlon of 12Cr-1MoWV have been melted and cast In a GCA vacuum Inductlon meltlng furnace. The nomlnal canpositions are pre-sented In Table 7.7.1 along with the actual chemistrles analyzed. The Ingots were indlvldually encapsu-lated In evacuated quartz tubes and placed In an alr furnace at 1100°C for 24 hr for hanogenizatlon. The Ingots were taken fran the furnace and allowed to cool in alr to approximately 700°C. These hanogenlzed ingots were roiled at 700°C to a plate 0.88 cm thlck by 6.25 cm wide (0.35 in x 2.5 In) in approxlmateiy ten rollng passes. The plate product was allowed to cool to roan temperature and pieces were cut for heat treatments, chemistry, and optlcal microscopy. The flnal yield of experlmental material was between 7 and 9 lbs. Ai i heat treatments were performed for times of 1 hr followed by alr cooling in double wrapped, weld sealed, stainless steel bags to prevent decarburlzatlon. Hardness determinations were performed uslng a Knoop dlamond pyramld hardness Indentor with 100 gms load, or a standard Rockwell hard-ness tester. Optical microscopy was performed after mounting in Bakellght, grlndlng and pollshlng on successlvely finer abrasives, followed by a chemical etching uslng Villelas, nltol, or tltanlum etch, where Indicated.

Chemical analyses for carbon were performed uslng the Leco carbon analyzer, and check analyses Were performed by GA and Smlth-Emery Co. (Los Angeles, Ca) for alloylng elements.

7.7.4.3 Results and Discussion

Fabrication of Ingots

All three Ingots were hanogenlzed after castlng at 1100°C for 24 hr while encapsulated in an evacuated quartz tube. The ingots were allowed to cool to approximately 700°C, were taken out of the quartz tube and rolling began. The 5 cm (2 in) round Ingot was flrst rolled length-wise to 2.5 cm (1 in) Thls requlred about 5 passes, Includlng one reheat to 700°C. It was then cross-rolled to about 1.25 cm (0.5 in), whlch required about 7 passes and 2 reheats. Plates were then flnlshed rolling to 0.89 cm (0.35 In) plate. The flnal dlmensions were approxlmateiy 7 cm wide and 25 cm long (2.75 in x 10 in) .

The as-rolled plates appeared sound with no edge cracking. The LAFS materlal Is as workable as other heats of HT-9. The plates had a thin layer of blulsh-black oxide, but no scaling was observed durlng the entlre process.

Determinatlon of Chemical Composltions

The nomlnal canpositions of the low actlvatlon ferritic steels and the control heat of HT-9 is glven in Table 7.7.1. Because of the scheduling for Incorporatlon of the Irradlatlon experlment only two LAFS heats were melted and chemlcally analyzed. Those are LAFS1 and LAFS3 In Table 7.7.1. These are Indicated by the GA Identification numbers In parentheses. The analyzed chemical canpositions of the experlmental low activation heats are also glven in Table 7.7.1. Chemical analyses were performed at the Smlth-Emery Company, Los Angeles and the Materlals and Chemistry Dlvlslon of GA.

Austenitlzatlon and Tempering Experlments

Samples were cut fran LAFS1 for austenltlzation and tempering experiments. Specimens were austen-ltized at 1025 and 1050°C for 1 hr followed by an air quench. Al I specimens had been placed In a double stainless steel bag and welded in order to minimize decarburlzation. The as-quenched hardness for the 1025°C treatment was 434 DPH. After austenitlzatlon at 1050°C the hardness Increased to 444 DPH. After tempering at 600, 650, and 700°C the hardness decreased fran about 440 DPH down to a low of 256 DPH.

Optical microscopy was performed after pollshlng and etchlng uslng the Tltanlum etch. Oftentimes, in order to delineate the prlor austenlte grain size, successive pol lsh-etch procedures were required. The prlor austenlte grain slze at the two austenltizlng temperatures were ASTM 7-8. The mlcrostructure was fully martensltic and few carblde or nitrlde were observed. After temperlng, sane recovery could be seen optically and carblde had preclpltated, decoratlng martenslte lath packet boundaries and prlor austenlte grain boundaries.

Table 7.7.1 The nominal and chemical ccmpositlon of the low activation ferritic steels

Heat #		C	Cr	W	V	TI	Mn	S
GA3X	Range	0.16 - 0.17	7.4 - 7.6	1.9 - 2.0	0.014 - 0.016	- -	0.002	0.005
	Nominal	0.15	9	2.5	0.3	-	-	-
GA4X	Range	0.017 - 0.019	10.1 - 10.3	1.6 - 1.8	0.28 - 0.30	- -	0.011	<0.003
	Nominal	0.15	11	2.5	0.3	-	-	-

The reader is referred to a companion section (7.8) in this semiannual report for a more detailed dlscusslon of microstructural data and mechanical property evaluations.

7.7.4.5 Conclusions and Future Work

Two experimental heats of 9Cr-2.5W-.3V-.15C and 11Cr-2.5W-.3V-.15C LAFS have been melted and fabricated for Incorporatlon in FFTF irradlatlons. Chemical analyses verified that the canposition was close to the nominal. Limited heat treatments were performed to minimize the prior austenite grain size, yet maximize the as-tempered hardness. It was found that at temperatures between 1000-1100°C the microstructure was fully austenltlc, and after quenchlng to room temperature transformed to 100% martensite. Because there was no apparent Increase in hardness after austenitlzatlon temperatures between 1000-1100°C, the lower austenltizlng temperature was selected. No decrease in hardness occurred between 700-750°C, and, therefore, all tempering treatments were performed using 700°C. 1/3 PCVN pre-cracked to the standard specifications were manutactured and encapsulated for the FFTF irradiations at 400, 450, and 500°C. 70 TEM disks of each alloy were prepared, and also incorporated at those temperatures in the Irradiation capsule.

The Irradiations will be completed in July 1985, at whlch time the ductile/brlttle transition temperatures will be determined and microstructural observations performed.

7.8 PRELIMINARY EVALUATION OF MICROSTRUCTURE AND MECHANICAL PROPERTIES ON LOW ACTIVATION FERRITIC STEELS

- Chen-Yih Hsu and T. A Lechtenberg (GA Technologies Inc.).

7.8.1 ADIP Task

The Department of Energy (DOE), Office of Fusion Energy (OFE), has cited the need to investigate ferritic alloys under the ADIP program task, Ferritic Steel Development (Path E).

7.8.2 Objective

Radioactive waste disposal has become a primary concern for the selection of materials for the structural canponents for fusion reactors. One way to minimize this potential environmental problem Is to use structural materials in which the induced radioactivity decays quickly to levels that allow for near-surface disposal under 10CFR61 rules. The primary objective of this work is to develop low activation ferritic steels that exhibit mechanical and physical properties approximately equivalent to the HT-9 and 9Cr-1Mo steels, but which only contain elements that would permit near-surface disposal under 10CFR61 after exposure to fusion neutrons.

7.8.3 Summary

A preliminary evaluation of the microstructure and mechanical properties of a 9Cr-2.5W-0.3V-0.15C (GA3X) low activation ferritic steel has been performed. An optimum heat treatment condition has been defined for GA3X steel. The properties and microstructure of the quenched and tempered specimens were characterized via hardness measurement and optical metallographic observation.

Quenched (1000°C/1hr) and tempered (700°C/1hr) specimens were thermally aged at 600°C up to 1,000 hrs to examine the phase stability of the alloy. X-ray diffraction analysis of the precipitates extracted from the thermally aged samples revealed nearly 100% $M_{23}C_6$ carbides (a = 10.64A), with no indication of Fe_2W-type Laves phase which may cause embrittlement via segregation of detrimental impurity elements and strengthening. The impurity elements (P, S, Sb) are in small concentration and this. combined with a fine grain size, lead us to conclude little temper embrittlement will occur.

The hot-microhardness and ductility parameter measurements were used to estimate the tensile properties at elevated temperatures. The estimated tensile strengths of GA3X steel at elevated temperatures are comparable to both 9Cr-1Mo and the modified 9Cr-1Mo steels. These preliminary results are encouraging in that they suggest that suitable low activation alloys can be successfully produced in this ferritic alloy class.

7.8.4 Progress and Status

7.8.4.1. Introduction

Commercially available alloys for first wall/and blanket structural components will become activated during service and will pose a waste disposal problem after service. Guideilnes (10CFR61) for the classification of nuclear wastes have been issued by the U.S. Nuclear Regulatory Commission. In 1982, DOE convened a panel to examine the issues and incentives associated with the development of low-activation materials. One of the panel conclusions was that it was Judged desirable and technically feasible to develop reactor material which fell within the 10CFR61 waste disposal criteria after fusion reactor irradiation. To meet these objectives the canpositions of fusion reactor structural materials must be limited in order to control activation levels after service.

The available data show that the 9-12%Cr ferritic/martensitic steels are attractive materials for fusion reactor structural component applications. The objective of this work is to develop low activation ferritic steels with equivaient properties and performance in a fusion environment to the canmercialiy developed ai loys. HT-9 and/or 9Cr-1Mo steels. To achieve the waste disposal objective, Mo, Nb, Ni, and N must be reduced to low levels. W and V can be used to substitute for Mo. W and Mo show similar solid-solution hardening characteristics and Fe-W-C alloys develop analogous precipitates with similar precipitation sequences to Fe-Mo-C alloys. The Cr-W steels offer promise for the development of a replacement for Cr-Mo steels if W replaces Mb in equal atanic fractions. The addition of 0.3% V to Cr-W steels will result in a pronounced effect on the precipitate formation and on elevated-temperature properties. The addition of V, however, may make the steels less weldable due to the formation of carbides. For this reason, the suggested carbon content Is kept below 0.15% in Cr-WV steels. Ti is also a strong carbide-former with an evidence of inhibiting grain coarsening while retaining good notch toughness, so the addition of 0.1% Ti is considered in this work. This work reports preliminary data on two experimental compositions.

7.8.4.2 Experimental Procedures

Two 1 kg (15 lb) experimental heats were melted in vacuum induction furnaces. The melting and fabrication practice of these two low activation ferritic steels were described in Reference (1). The

naninal and actual canposition of the two heats (labeled GA3X and GA4X) are shown in Table 7.8.1. Sections of the material were austenltlzed at 1000°C, 1050°C or 1100°C for one hour followed by water quenching, and then subsequently tempered at 400°C-800°C for one hour followed by an air-cool. Rockwell hardness measurement and optical metallographic examlnatlon were conducted on speclmens after heat treatment.

Electrolytic extraction was performed on quenched and tempered speclmens. The sample was anodically extracted In an electrolyte of 10% HCl-methanol at 100 mA/cm^2 for 3 hours. This condition Insures the selective removal of the matrlx without any dissolution of carbides. Precipitates adherlng to the samples were removed by ultrasonic vibratlon In ethanol, and the sample was then drled and weighted. The preclpltates were separated fran the solutlon. dried, and welghed. Samples for X-ray dlffractanetry were prepared by smearing 5mg of the precipitate and alcohol onto a single crystal quartz slide. A graphite crystal monochrometer-scintillation detector system was used to record count rate every 0.030 29 for Cu K_α radiation.

Table 7.8.1 The Naninal and Chemical Composition of the Low Activation Ferritic Steels

Heat #		C	Cr.	W.	V.	Ti.	Mn.	S.
GA3X	Range	0.16 - 0.17	7.4 - 7.6	1.9 - 2.0	0.014 - 0.016	- -	0.002	0.005
	Nominal	0.15	9	2.5	0.3	-	-	-
GA4X	Range	0.017 - 0.019	10.1 - 10.3	1.6 - 1.8	0.28 - 0.30	- -	0.011	<0.003
	Nominal	0.15	11	2.5	0.3	-	-	-

Specimens for hot-mlcrohardness measurements were ground and polished to 0.6mm thlck, 9mm wide, and 10mm long. A 500g load was used on a sapphire Indentor. The specimens were heated gradually in a pure argon environment, and three Indentlons at each temperature were made. The room temperature Indentations were done before and after the hot hardness test. For the evaluatlon of ductility, a proflianeter with a dlamond stylus was used to measure the pile-up of metal adjacent to the Indentation. The hot-hardness tests were conducted at the Universlty of Cincinnati.

7.8.4.3 Results and Discusslon

It is well known that the varlatlon of austenltizing temperature has a slgnlflcant influence on the mlcrostructure and mechanlcal propertles of quenched and tempered speclmens. Since the GA3X and GA4X steels are new heats. their optimum heat treatment conditions need to be defined.

Flgure 7.8.1 shows the effect of austenltlzing temperature on hardness and prlor austenitic graln size of the GA3X steel held one hour at temperature followed by water quenchlng. The prior austentic grain size varied fran ASTM 9 to ASTM 6 as the austenitlzlng temperature increased fran 1000°C to 1100°C. The hlgher the austenitizing temperature the less the undlssolved carbides were able to pln graln boundaries and grain growth was pranoted. The hardness decreased fran R_C44 to R_C40 as the austenltlzlng temperature Increased fran 1000°C to 1100°C. For a given canposition of martensltlc steel In the as-quenched condltlon the hardness is primarlly controlled by prlor-austenitic graln size and the carbon content of the martensite, and Is also a relative measure of the presence of other phases such as ferrite. In this steel the difference In hardness result is mainly due to the variation in graln slze. Figure 7.8.2 shows optical mlcrographs of the martensltlc structure In the quenched speclmens. The optlcal metallography Indlcates that some part of the decrease In hardness may be due to the presence of ferrite at temperatures above 1050°C, although the amounts are estimated to be low.

The carbon content of GA4X heat is 0.018%. whlch Is much lower than the target value. The hardness of GA4X quenched fran one-hour austenltlzlng at 1000°C was Rockwell B 80. A multiple phase mlcrostructure was obtained and no further study of this heat is necessary, although another heat will be melted and studied whlch is closer to the naninai canposition.

For GA3X steel, the effect of temperlng temperature on hardness as a function of austenltlzlng temperature Is shown In Figure 7.8.3. The hardness profiles show a large decrease after temperlng above 600°C and the tempering characteristics of each austenltlzlng condition appear simllar. Specimens austenitized at 1000°C were harder than speclmens austenitlzed at hlgher temperatures (1050°C and 1100°C) over the entire range of tempering temperature. Thls may be due to a small Increase In ferrite content as reported above.

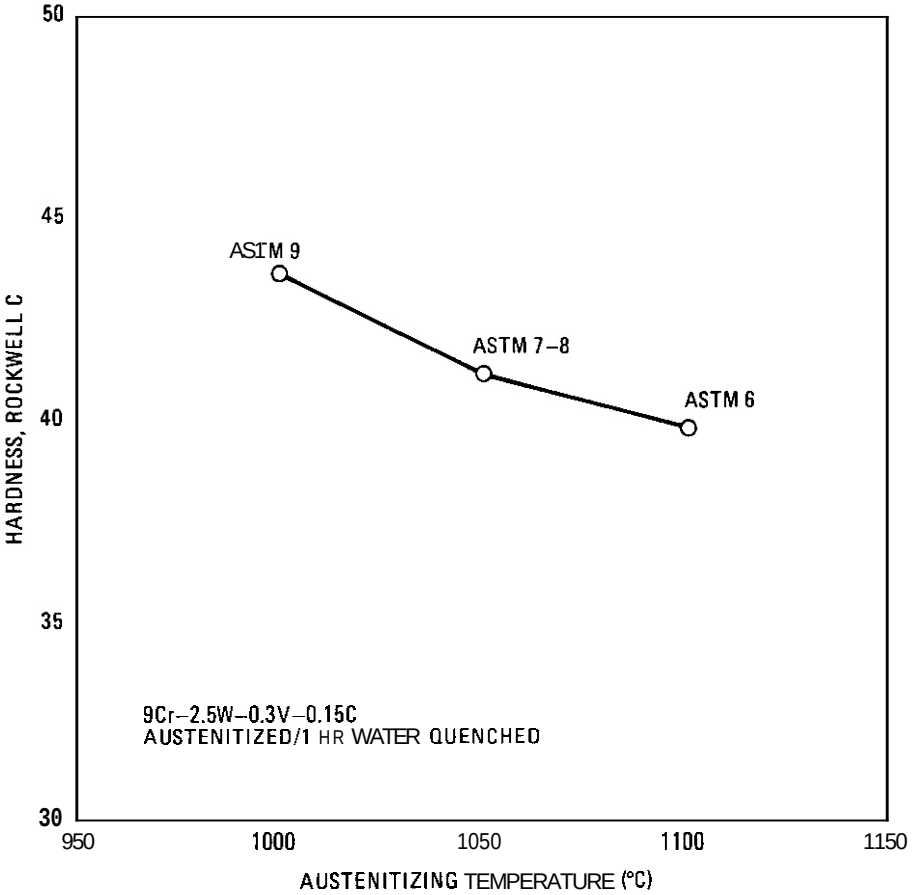

Fig. 7.8.1. The effect of austenitizing temperature on the hardness and microstructure of GA3X Alloy

The variation in tempered hardness between the three austenitizing conditions can be attributed to the effect of grain size and the presence of ferrite and carbides precipitates. This indicates that the prior microstructure can influence the tempering behavior. In HT-9, the secondary hardening peak occurred after tempering at 500°C[2]. For GA3X, no secondary hardening peak was observed after tempering from 400°C to 800°C. This is because this heat contains less carbon and carbide-forming elements than HT-9 steel.

in an attempt to increase the tempered hardness, some material was austenitized at 950°C/1hr and tempered at 700°C/1hr. The measured hardness was R_B95, which does not compare favorably with the hardness at the same tempering temperature for 1000°C/1hr treatment which was R_C20. This may be due to an increased amount of proeutectoid ferrite. Based on these data, the austenitizing treatment recommended for this heat of steel would be 1000-1050°C/1hr.

Resistance to temper embrittlement is controlled by the segregation of impurity elements such as P, Mn, etc. The formation of intermetalilc compounds such as Laves phases may promote the segregation of impurity elements and thus degrade the resistance to temper embrittlement. Furthermore it is known that Fe_2Mo-type Laves phase may form in Cr-Mo steels after a long-term thermal exposure at 500-550°C. So an effort was made to determine if Fe_2W-type Laves phase forms in GA3X steel. The anaiysis of the extracted precipitates is presented in Table 7.8.2. The X-ray diffraction analysis on the GA3X quenched (1000°C/1hr) and tempered (700°C/1hr) specimen revealed nearly 100% $M_{23}C_6$ type carbides, with no indication of Laves phase. Figure 7.8.4 shows the X-ray diffraction of the extracted precipitates, which is a typical diffraction pattern of $M_{23}C_6$ carbide. Additionai thermal aging at 600°C up to 1,000 hrs was done to accelerate the precipitation of any phases. The weight percentages of the extracted precipitates increased from 2.0% to 3.1% after thermal aging for 100 hrs. and then remained nearly unchanged up to 1,000 hrs. Again, the extracted precipitates were dominated by $M_{23}C_6$ carbides and no Laves phase was detected in GA3X steel which contain 2wt% W. However, under irradiation at somewhat higher W concentration, it is possible Fe_2W will precipitate.

The chemical composition of $M_{23}C_6$ carbide was identified by X-ray fluorescence. X-ray analysis indicated that the extracted $M_{23}C_6$ carbides were in the form of $(Fe_{0.21}W_{0.09}Cr_{0.70})_{23}C_6$ with a lattice parameter of 10.64A. No apparent change of the content of metallic elements in $M_{23}C_6$ and its lattice parameters was observed up to 1,000 hrs. thermal aging. The weight percentage of the extracted precipitates increased slightly from 3.1% to 3.3%. Also, the 1,000 hrs. thermally aged specimen exhibited a lower hardness level than the specimen thermally aged for 100 hrs, which is probably due to overaging.

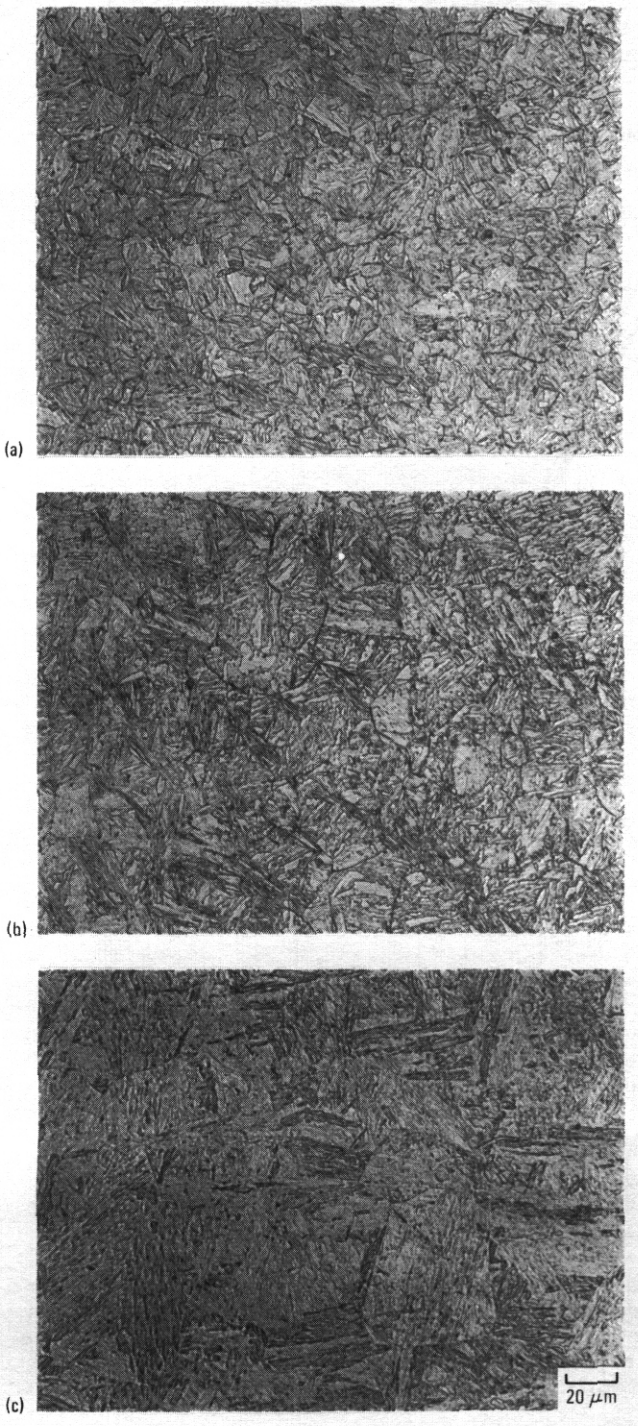

Fig. 7.8.2. The optical micrograph of GA3X Steel (a) 1000°C/1 hr, (b) 1050°C/1 hr and (c) 1100°C/hr.

According to the chemical analysis of GA3X steel seen in Table 7.8.1, the P content is negilgible, the Mn content is less than 0.002% and S content Is only 0.005%. The combined effect of these impurities on the resistance to temper embrittlement can be disregarded based on the analysis proposed by Watanabe et al[3]. We would not expect, therefore, temper embrittlemerit In heat GA3X.

Hot microhardness measurement can be used to estimate other mechanical properties at elevated temperatures and also to screen new material in an alloy development program where only small quantities of materials are avaiiabie. Hot microhardness and ductility parameter measurements were conducted on four quenched (1000°C end 1050°C) and tempered (700°C and 750°C) specimeiis fran room temperature to 650°C. Figure 7.8.5 shows the Vickers microhardness result vs. test temperature for these four specimens. The change in hardness over the test temperature appeared similar for these four specimens and a rapid decrease in hardness was observed at temperature above 400°C. Lower austenitization temperature (1000°C) samples, tempered at 700°C, were harder than samples tempered at 750°C. Higher austenitization temperature (1050°C) samples, tempered at 700°C, were slightly harder than samples tempered at 750°C at test temperature below 450°C and became weaker than samples tempered at 750°C at test temperature above 450°C.

It has been demonstrated that an approximation of the ultimate tensile strength and yield strength (0.2% offset) can be obtained from microhardness measurements through the correlationships (4-6):

$$\sigma_{uts} = C_n \left(\frac{H}{3}\right) \qquad (1)$$

$$\sigma_{ys} = \frac{H}{3} (0.1)^n \qquad (2)$$

where H is the microhardness (kg/mm^2) and C_n is a constraint factor parameter that accounts for straln hardening. C_n is diven in Ref. 4:

$$C_n = (n/0.217)^n \qquad (3)$$

where n is the strain hardening exponent in the classical strain hardening relationship:

$$\sigma = K E^n \qquad (4)$$

where K is the flow stress (σ) at a strain (E) of unity. The strain hardening exponent (n) Is generally equated to the uniform elongation (E_u). The uniform elongation can be expressed as (7):

$$E_u = C/ P^{\alpha} \qquad (5)$$

where α and C are materlals constants and P, the ductility parameter. is given by:

$$P = \frac{h_1 + h_2}{2r} \qquad (6)$$

where h_1 and h_2 are the heights of the plastically deformed metal adjacent to the indentation and 2r is the distance between the peek heights of the deformed metal.

Equation (5) suggests that the uniform elongation increases with a decrease In the ductility parameter. Figure 7.8.6 shows the ductility parameter measurement vs. test temperature for the four specimens. The ductility parameter results increased with increasing test temperature which indicated that uniform elongation decreased with increasing test temperature. An abrupt increase in ductility

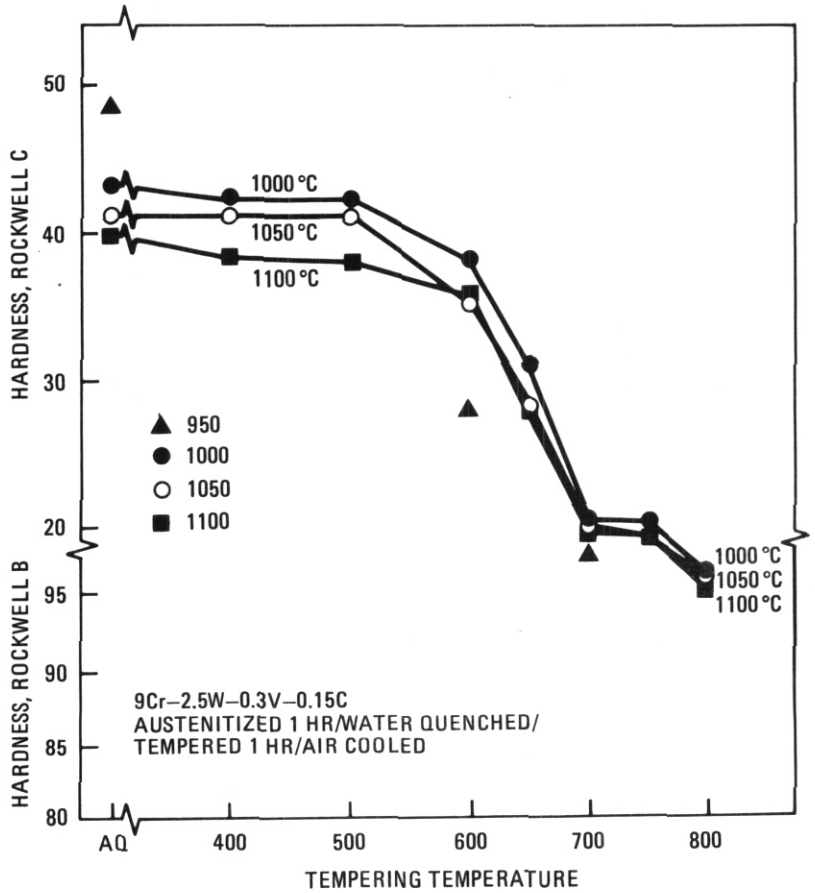

Fig. 7.8.3. The hardness results of GA3X Steel as a function of austenitization and tempering temperature

Table 7.8.2. The Analysis of the Extracted Precipitates of GNX Steel

Specimen Description	Rockwell Hardness	Wt% of the Extracted Precipates	Phase
1000°C/1hr + 700°C/1hr	R_B 99	2.0%	$M_{23}C_6$ a=10.64A
1000°C/1hr + 700°C/1hr + 600°C/100hrs	R_C 20	3.1%	$M_{23}C_6$ a=10.64A
1000°C/1hr + 700°C/1hr + 600°C/1000hrs	R_B 97	3.3%	$M_{23}C_6$ a=10.64A

parameter was observed at test temperatures above 400°C and a peak value was reached at about 600°C for each specimen. The changes in ductility parameter measurements can be rationalized with the changes in microhardness results where an abrupt decrease in hardness occurs. Due to the general scatter of data a solid line is drawn through the general trend of the data points. On closer examination, one may find some second harder/softer phase of grain boundary in the region of identation to cause sane of the scatter in the data.

Current work in progress is directed toward obtaining the materials constants, C and a necessary to determine the yield and ultimate strengths and uniform elongation values for GNX fran the hot microhardness data. In order to estimate the values prior to obtaining the data, the tensile characteristics of similar fully martensitic steels, the 9Cr-1Mo and modified 9Cr-1Mo[8], were compared to the hot hardness curve of GA3X. The shapes were similiar enough to assume, as a first estimate, that the stress-strain behavior of GNX was the same as for the other two steels. This allows the material constants for the 9Cr-1Mo steels to be used in estimating the tensile properties of GNX. By using the available data of uniform elongation fran the modified 9Cr-1Mo steel the ultimate tensile strength and yield strength (0.2% offset) of GNX was estimated according to equations (1) and (2). The estimated ultimate tensile strength and yield strength vs. test temperature are plotted in Figures 7.8.7 and 7.8.8 respectively. The experimental data of the modified 9Cr-1Mo steel and 9Cr-1Mo steel are indicated by solid lines. In canparison with those two 9Cr-1Mo steels, the GNX steal is shown with higher strength at temperatures below 450°C and becomes equivalent to modified 9Cr-1Mo in strength at temperatures above 450°C. Overall. It is shown that the estimated tensile strengths of GA3X steel are very comparable to those two 9Cr-1Mo steels.

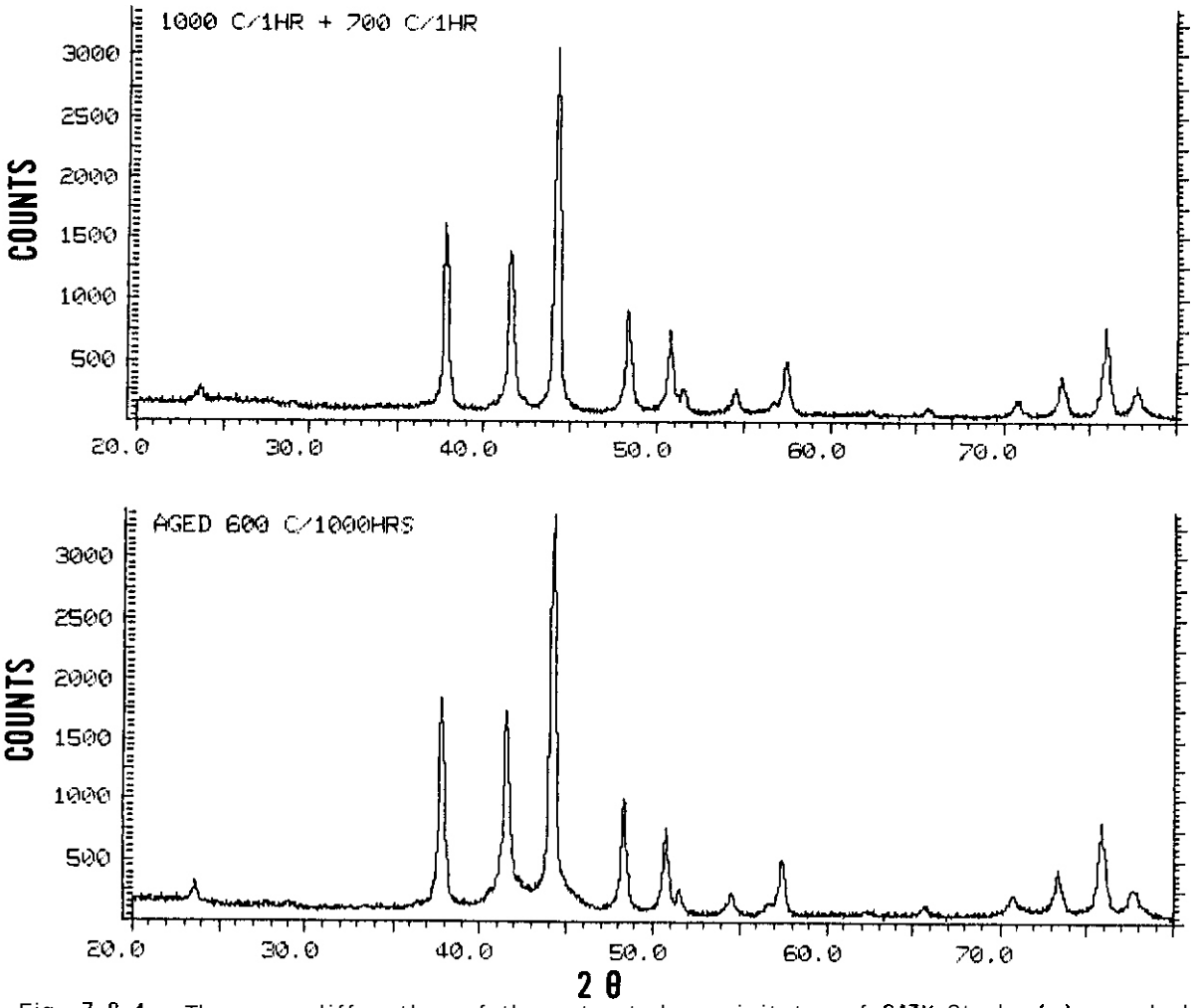

Fig. 7.8.4. The x-ray diffraction of the extracted precipitates of GA3X Steel, (a) quenched (1000°C/1hr) and tempered (700°C/1hr) and (b) aged 600°C/1000 hrs following (a)

The GA3X steel is slightly weaker in tensile strength and almost identical in yield strength as compared with those two 9Cr-1Mo steels at temperature above 450°C. This observation can be explained from the effect of varying alloying element concentrations which determine the carbide stability. The modified 9Cr-1Mo steel contains 0.21% V and 0.01% Ti and the GA3X steel contains only 0.015% V. V and Ti are strong carbide-formers which can enhance carbide stability and maintain fine microstructure for high temperature strength and good notch toughness respectively. Hence, it is expected that the elevated-temperature strength can be improved by increasing V and Ti contents. However, the preliminary results point out a promising potential of the proposed low activation ferritic steels (see Table 7.8.1) for the replacement of the commercially developed heat resistant alloys in fusion reactor structural components.

7.8.5. Future work

The preliminary results demonstrate that a fully martensitic alloy can be successfully produced with an acceptable naninal canposition for surface waste disposal after fusion reactor service. The GA3X steel possesses tensile strengths canparable to both 9Cr-1Mo and the modified 9Cr-1Mo steels. Hence, the preli-minary evaiuation of microstructure and mechanical properties on GA3X low activation ferritic steel is very pranising.

In order to determine the pre-irradiation DBTT, impact tests will be performed. Because of the small quantities of the experimentai heat, 1/2 size Charpy bars will be prepared for impact property measurements. The performance of hot hardness and ductility parameter measurements on HT-9 and 9Cr-1Mo steels will provide a direct canparison with GA3X steel. The post-irradiation mechanical behavior will be evaluated using instrumentation at HEDL. It is suggested that hot hardness and ductility parameter measurements be performed on irradiated specimens for comparison. More candidate alloys will be manufactured to meet the target chemical compositions listed in Table 7.8.1. Future work will also include evaiuation of time-dependent mechanical properties at elevated temperatures.

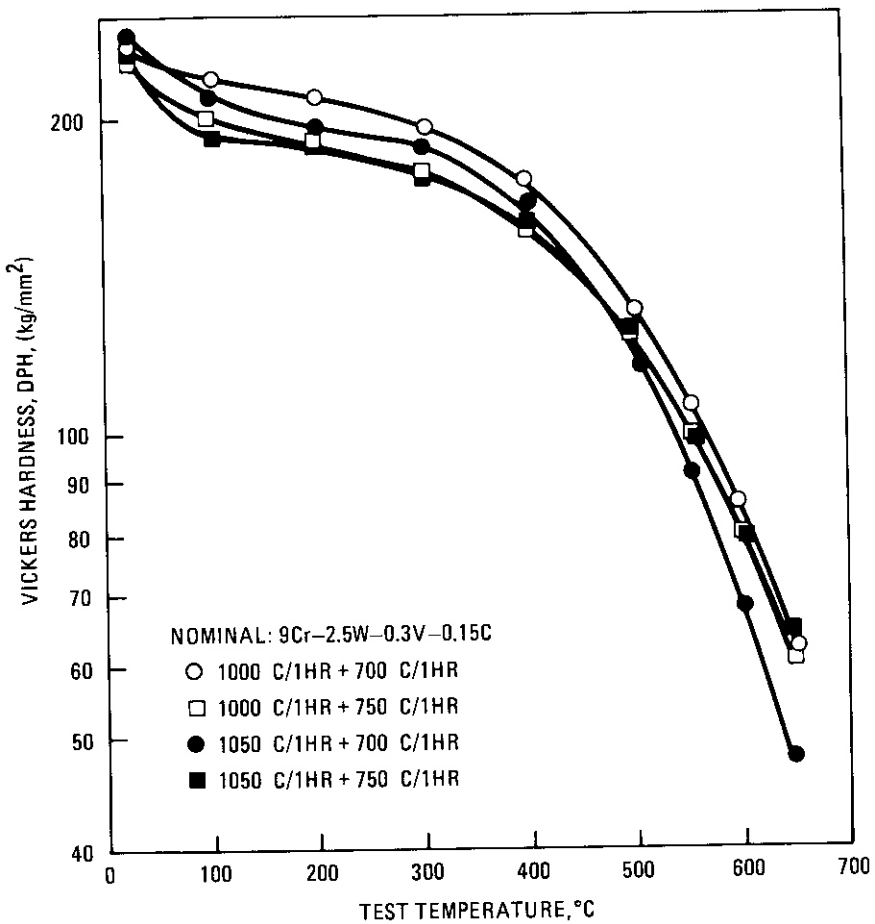

Fig 7.8 5. The Vickers microhardness of GA3X Steel as a function of test temperature

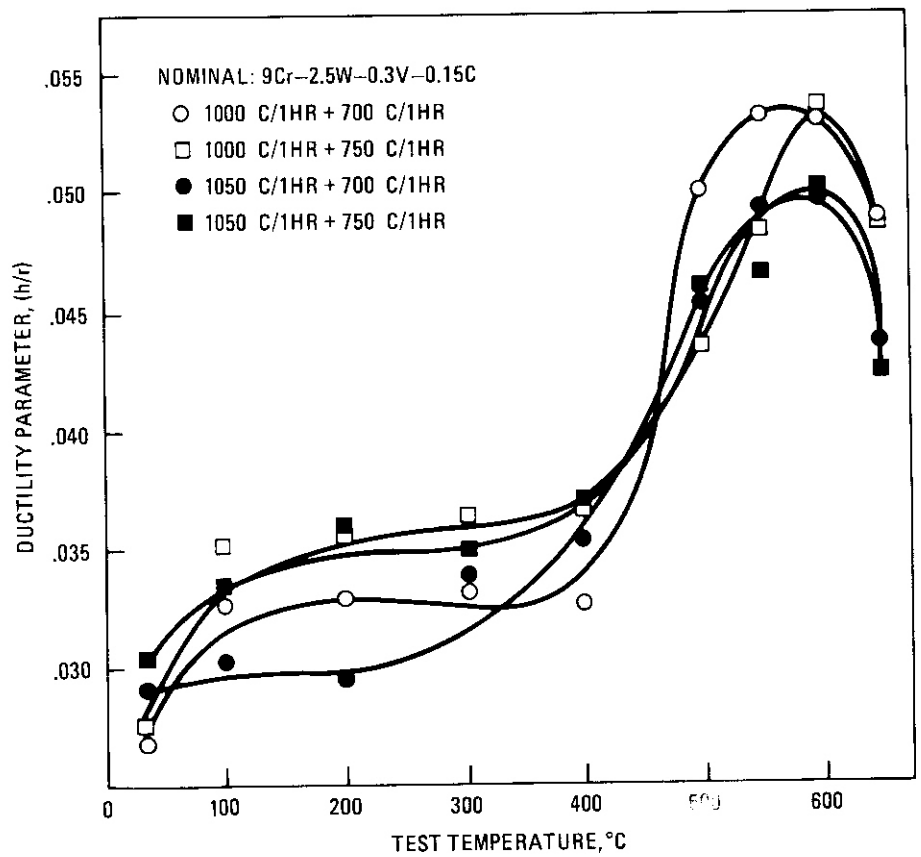

Fig 7.8 6. The ductility parameter of GA3X Steel as a function of test temperature. The parameter is defined as the ratio of the height of the pile formed by indention and half the distance between the peaks

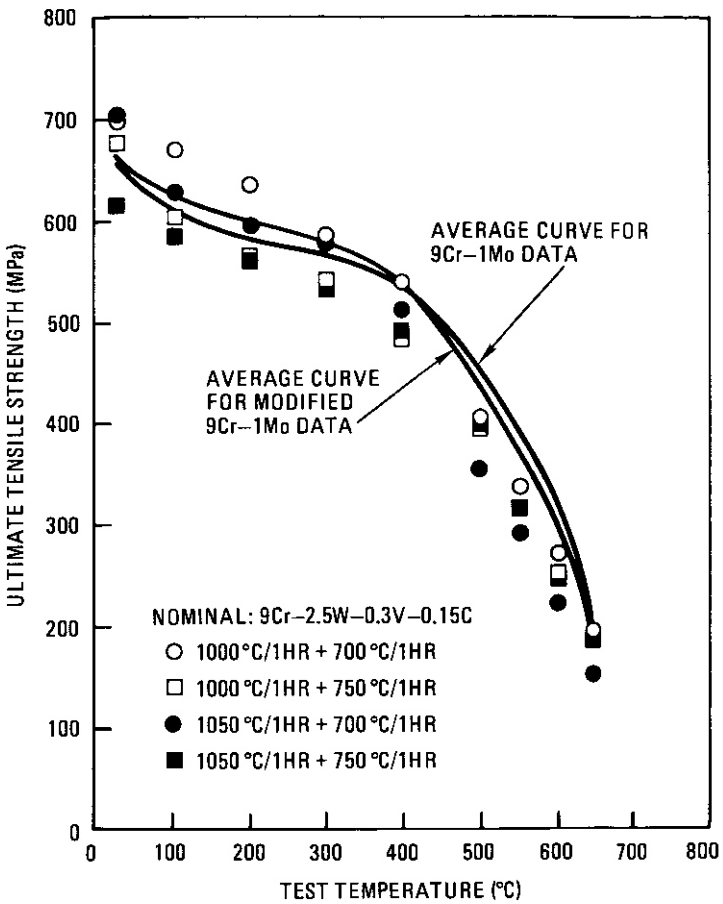

Fig. 7.8.7. The Estimated Ultimate Tensile Strength of GA3X steel as a function of test temperature in comparison with the 9Cr-1Mo and modified 9Cr-1Mo Steels

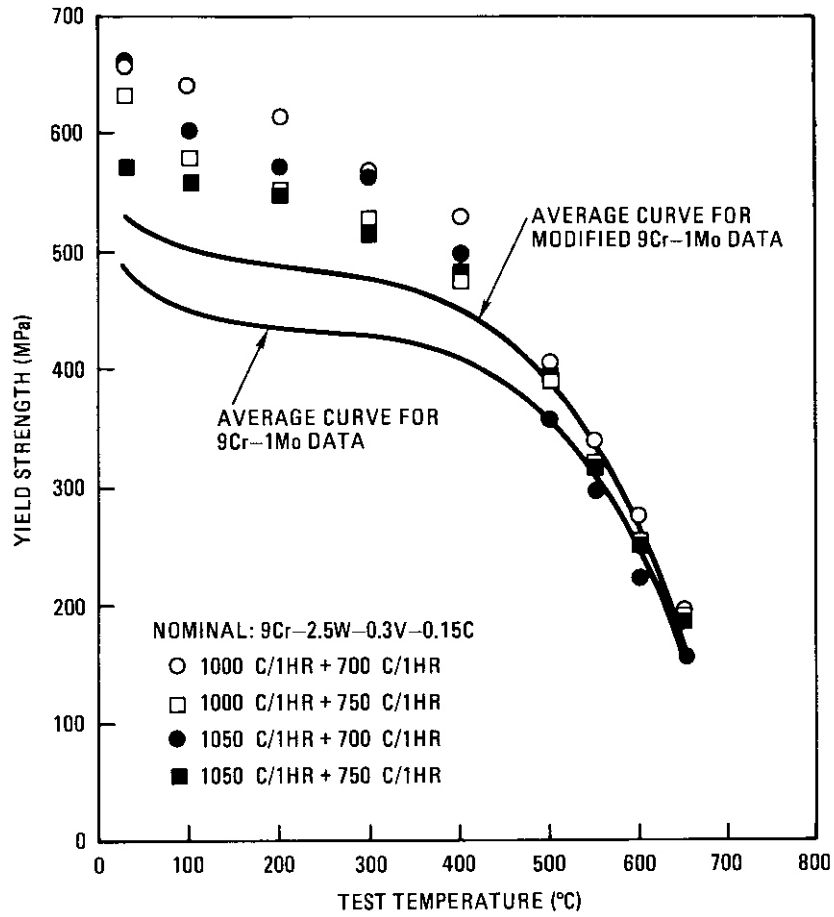

Fig. 7.8.8. The Estimated Yield Strength of GA3X Steel as a function of test temperature in comparison with the 9Cr-1Mo and modified 9Cr-1Mo Steels

7.8.6 REFERENCES

1. T. A. Lechtenberg, "Melting and Fabrication Aspect of Low Activation Ferritic Steels," in this ADIP Semiannual progress report.
2. T. A. Lechtenberg, Journal of Nuclear Materials, 103 & 104 (1981), pp. 1133-1138.
3. J. Watanabe, et al., "Temper Embrittlement of 2 1/4 Cr-1Mo Pressure Vessel Steels," presented at the ASME 29th Petroleum Mech. Engineering Conf., Dallas, Texas, September 15-18, 1974.
4. J. R. Cahwn, Met. Trans. 1972, Vol. 3A, p. 3040.
5. J. Moteff, R.K. Bhargara, and W. L. McCullough, Met. Trans., Vol 6A. May 1975, pp. 1101.
6. J. R. Cahoon, W. H. Broughton, and A. R. Kutzak, Met. Trans. Vol. 2, 1971, pp. 1179-83.
7. R. Bokien, In "The Science of Hardness Testing and Its Application," Eds. J. H. Westbrwk and H. Conrad (ASM 1973). p. 109.
8. V. K. Sikka," Modified 9Cr-1Mo Steel Development Program Progress Report" #ORNL/BRP-79.4, September, 1979.

7.9 MICROSTRUCTURAL COMPARISON OF HT-9 IRRADIATED IN HFIR AND EBR-II - D. S. Gelles (Westinghouse Hanford Company)

7.9.1 ADIP Task

The Department of Energy (DOE)/Office of Fusion Energy (OFE) has cited the need to investigate ferritic alloys under the ADIP program task, Ferritic Steels Development (Path E). The tasks involved are akin to task number 1.C.7, Microstructures and Swelling in Austenitic Alloys and task number I.C.I, Microstructural Stability.

7.9.7 Objective

The objective of this work is to provide guidance on the applicability of martensitic stainless steels for fusion reactor structural materials.

7.9.3 *Summary*

A series of specimens of HT-9 heat 91354 have been examined following irradiation in HFIR to 39 dpa at 300, 400, 500 and 600°C and following irradiation in EBR-II to 29 dpa at 390 and 500°C. In most cases, identical specimens had been previously examined following irradiation to lower dose.

HFIR irradiation was found to have promoted helium bubble formation at all temperatures and voids at 400°C. Helium bubbles were generally associated with subgrain boundaries or dislocations within grains. Void development was typical of the swelling incubation regime. Swelling had not been observed at lower fluence, nor was it found in EBR-II irradiated specimens. The onset of void swelling in HFIR is attributed to helium generation.

The major effect of increasing dose was found to be minor growth of dislocation loops and precipitate particles. All major microstructural features which were present at lower dose were retained. These observations provide an explanation for saturation of ductile-brittle transition temperature shifts with increasing fluence.

7.9.4 Progress and Status

7.9.4.1 Introduction

Following irradiation in HFIR at 400°C to 39 dpa, HT-9 heat XAA3587 was found to have developed void swelling.[1] The swelling was very low, 0.07%, consisting of 16 nm average diameter cavities at densities on the order of 3 x $10^{20}/m^3$ distributed non-uniformly. This represented an unusual observation of swelljng in HT-9 because examination of HT-9 irradiated in EBR-II to 77 dpa showed no tendency for void swelling. The swelling observed in the HFIR irradiated specimens was attributed "to a large extent to the helium produced during irradiation in HFIR."[1] However, an alternate explanation for the observation of swelling in HT-9 was proposed based on the absence of G-phase precipitation in these specimens[3] under the assumption that the presence of G-phase in irradiated HT-9 suppressed void formation.[4] Micrographs of HT-9 heat XAA3587 which contained voids showed no evidence of precipitation and results for heat XAA3587 were not available following irradiation in an environment where helium generation rates were lower, such as ERR-11. Therefore, a second variable, heat-to-heat variation, could explain the results. Note that a heat-to-heat variation in the swelling resistance of HT-9 could significantly affect the applicability of HT-9 for fusion reactor applications. It was therefore considered very important to determine if swelling in HT-9 was due to helium generation or composition variations.

The HFIR-CTR-30, -31 and -32 tests did contain several transmission electron microscopy (TEM) disk specimens of HT-9 heat 91354[5] which had been irradiated in the same capsules as had specimens of heat XAA3587. As this heat was identical to that used in the ADZ test irradiated to 29 dpa (6 x 10^{22} n/cm^2) it was possible to determine the effect of helium generation without introducing heat-to-heat variables. Unfortunately, most of the disks were needed for disk bend ductility tests but one disk from each condition was made available for TEM examination. The present effort therefore centers on the examination of specimens of HT-9 heat 91354 irradiated in HFIR at 300, 400, 500 and 600°C to 39 dpa. For comparison, specimens of HT-9 heat 91354 irradiated in ERR-I1 at 390 and 500°C to 29 dpa (6 x 10^{22} nlcm^2) were also examined. The results show that HT-9 does indeed swell in HFIR but not in EBR-II. Therefore, heat-to-heat variations are not responsible for this difference in behavior supporting the contention that helium encourages void formation in HT-9.

7.9.4.2 Experimental Procedure

Specimens selected for examination are listed in Table 7.9.1, along with corresponding irradiation conditions. All conditions were from the same heat of material, heat 91354 but heat treatments for the different irradiation tests were performed at different laboratories, at ORNL for the HFIR-CTR-30 test and at WHC for the EBR-II AD-7 test. Specimens irradiated in both tests had been examined following earlier discharges, 10 dpa for CTR-32[5] and 13 dpa for AD-2.[4] Experimental procedures in the present study were identical to those in the previous studies except that transmission electron microscopy has been performed only on thin foil specimens and the electron microscope used was a JEOL 1200EX operating at 170 KeV.

Table 7.9.1. Specimen conditions of HT-9 heat 91354 selected for microstructural examination. HFIR-CTR-30 fluences were estimated from reference 6 assuming a midplane position.

Identification Code	Irradiation Experiment	Fluence dpa (10^{22} n/cm^2)	Temperature
SA24	HFIR-CTR-30	39 (19.5)	300°C
SA21	HFIK-CTR-30	39 (19.5)	400°C
SA23	HFIK-CTR-30	39 (19.5)	500°C
SA22	HFIK-CTR-30	39 (19.5)	600°C
2HCP	EBRII-AD-2	29 (6.1)*	390°C
2HCU	EBRII-AD-2	29 (6.1)*	500°C

*E>0.1 MeV, others E TOTAL

7.9.4.3 Results

HFIR-CTR-30

Specimens of HT-9 heat 91354 irradiated to 39 dpa in HFIR were found to retain the carbide and subgrain structure which was generated prior to irradiation and retained following irradiation at 300 and 400°C to 10 dpa.[5] Carbides were large and equiaxed but were not associated with martensite lath structure (lath structure was not found). Also, dislocation and precipitate structures which had been found following irradiation at 300 and 400°C to 10 dpa were retained although growth had occurred. However, a major difference could be identified due to irradiation to higher fluence. HT-9 heat 91354 following irradiation at 400°C was found to contain a non-uniform distribution of faceted cavities at low density (typical of a material in the incubation regime for void swelling), and a higher density of smaller spherical cavities, most prominent at grain boundaries, but also uniformly distributed through the grains (typical of helium bubbles). Specimens irradiated at 500 and 600°C were found to contain larger spherical cavities on grain boundaries and on dislocations within grains (again typical of helium bubble development). The specimen irradiated at 300°C also showed features which were probably helium bubbles. A fine mottled appearance was found which in the under-focused imaging condition appeared to be small bubbles.

Examples of these structures are shown in Figures 7.9.1 through 7.9.3. Figure 7.9.1 shows low magnification examples of each of the specimens examined. The large carbides which can be seen and the lack of martensite lath structure are characteristic of these specimens. It may be noted that irradiation at 500 and 600°C promotes the formation of subgrains and that subgrains which developed at 600°C contain very few dislocations. Careful examination of Figure 7.9.1b reveals that after irradiation at 400°C, small voids and precipitate particles are present.

Figure 7.9.2 provides examples of these microstructures at higher magnification. Figure 7.9.2a shows dislocation and precipitate structures in specimen SA24 irradiated at 300°C to 39 dpa, the region on the left in dislocation contrast and the region on the right showing the presence of a fine array of 4 nm particles. Dislocation loops can be identified that are as large as 13 nm in diameter. Therefore, by comparison with previous results,[5] it can be concluded that both dislocation loops and G-phase precipitate particles have approximately doubled in size when the irradiation dose was increased from 6 dpa to 36 dpa.

Figure 7.9.2b shows similar features for specimen SA21 irradiated at 400°C to 39 dpa. The dislocation structure consists of dislocation tangles and perfect dislocation loops. The loops are as large as 33 nm and are predominantly of type a<100>. The region on the right of Figure 7.9.2b contains a number of faceted cavities typical of higher void swelling regions in this specimen. However, careful examination of this micrograph reveals the presence of a large number of much smaller spherical cavities typical of helium bubbles or very small voids. Precipitate particles are randomly arrayed and as large as 30 nm although most are smaller. In comparison, irradiation to 10 dpa resulted in 8.0 nm particles often in linear arrays. Therefore, it can be concluded that continued irradiation results in coarsening of the G-phase and loss of evidence for heterogeneous nucleation on dislocations.

Figures 7.9.2c and d, showing specimens SA23 and SA22 irradiated at 500 and 600°C to 39 dpa, appear similar. Subgrain boundaries are well defined and spherical cavities can be identified decorating boundaries and within grains, often clearly associated with dislocations which are weakly imaged. The major differences between these conditions are 1) the cavity size and distribution, and 2) the presence of precipitates within subgrains after irradiation at 500°C. Cavities after irradiation at 500°C are as large as 4 nm whereas after irradiation at 600°C the cavities are as large as 10 nm. In all cases, they appear to be helium bubbles. The precipitate particles found following irradiation at 500°C could only be imaged in matrix dark field contrast and therefore the particles are identified as α'.

In order to show the fine structure found in the specimens of HT-9 heat 91354, higher magnification micrographs are given in Figure 7.9.3 for greater clarity. Figure 7.9.3a provides an example of the mottled structure found in specimen SA24 irradiated at 300°C. Note that a well developed subgrain boundary runs diagonally across the micrograph. If the structure is due to helium bubbles the bubbles are no more than 1.6 nm in diameter. Examples of helium bubbles on subgrain boundaries can be found in each of Figure 7.9.3b, c and d. It is apparent that bubble formation at grain boundaries is very non-uniform and is presumably associated with grain boundary dislocations.

Of further note was the observation that substructure was developing in carbide particles due to irradiation. In order to show the range of response found, examples of carbide particles on the edge of foils which had been irradiated at 300 and 600°C are shown in Figure 7.9.4. From Figure 7.9.4 it is apparent that substructure in the form of a second phase, or dislocation loop structure has evolved. (It is unlikely that the structure is due to cavitation.) The structure is on the order of 3 nm after

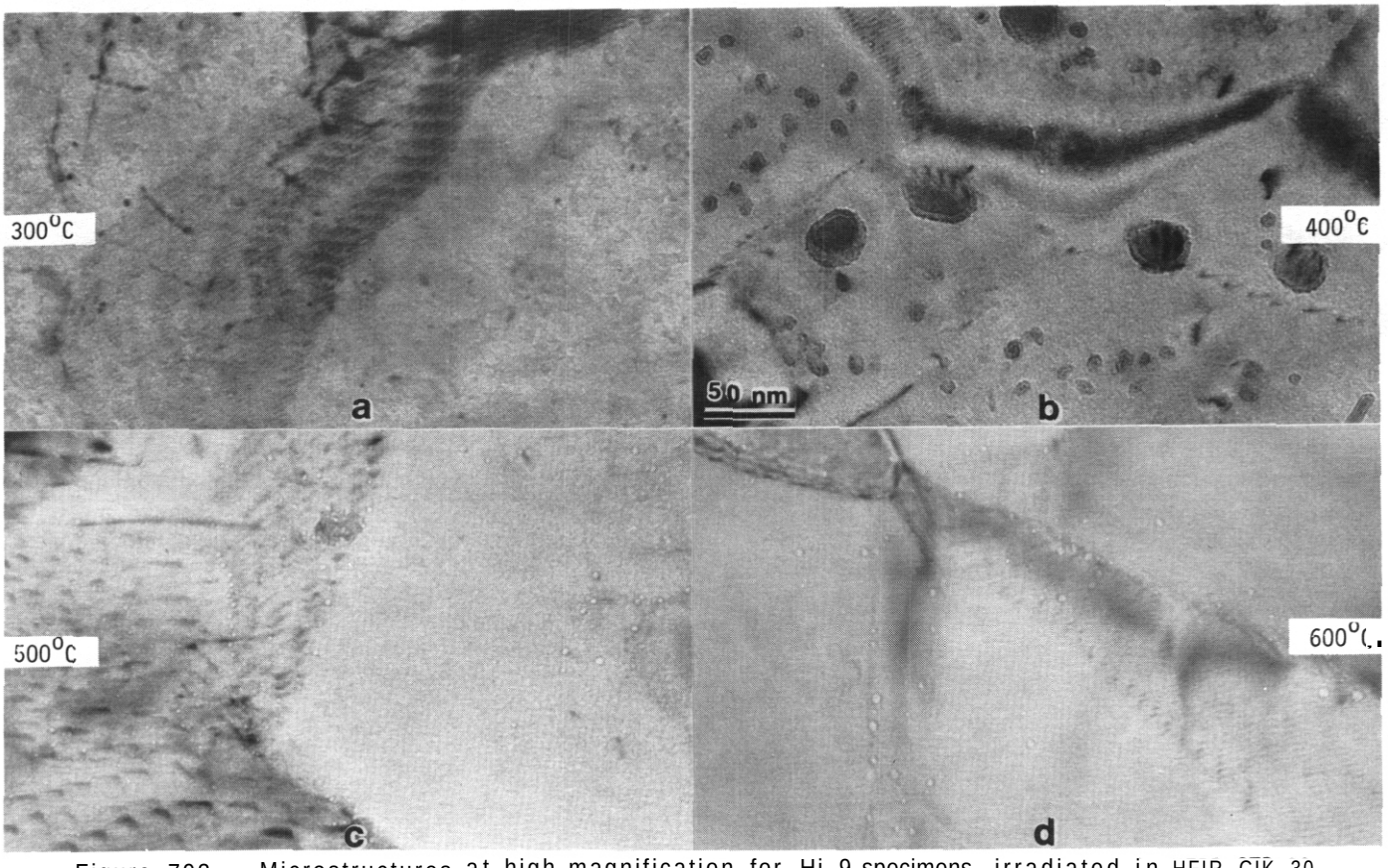

Figure 7.9.3. Microstructures at high magnification for Hi-9 specimens irradiated in HFIR-CTR-30 showing helium bubble structure.

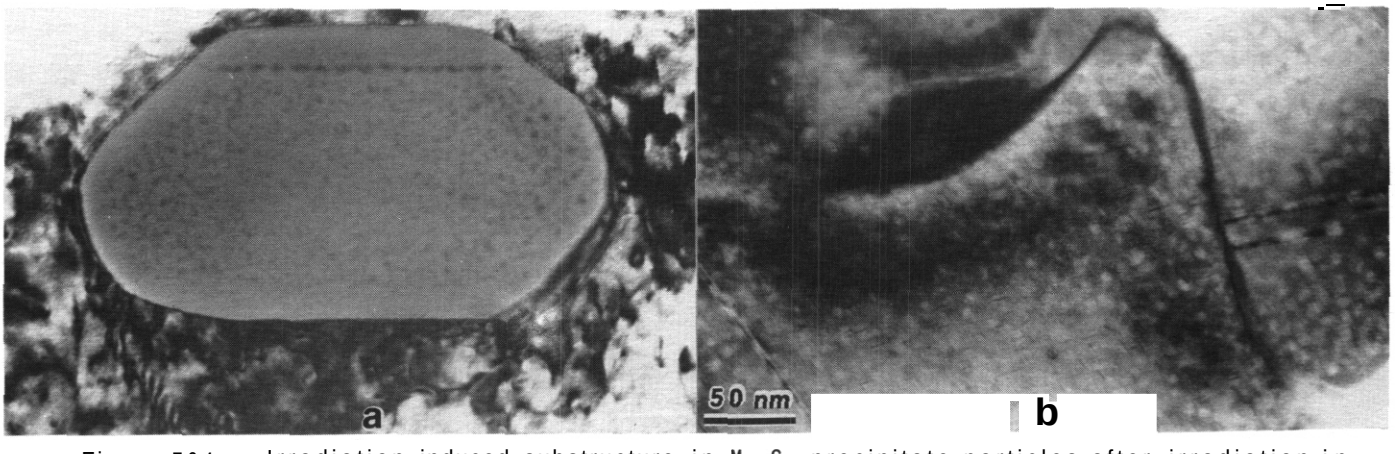

Figure 7.9.4. Irradiation induced substructure in $M_{23}C_6$ precipitate particles after irradiation in HFIR-CTR-30 to 39 dpa at 300 and 600°C.

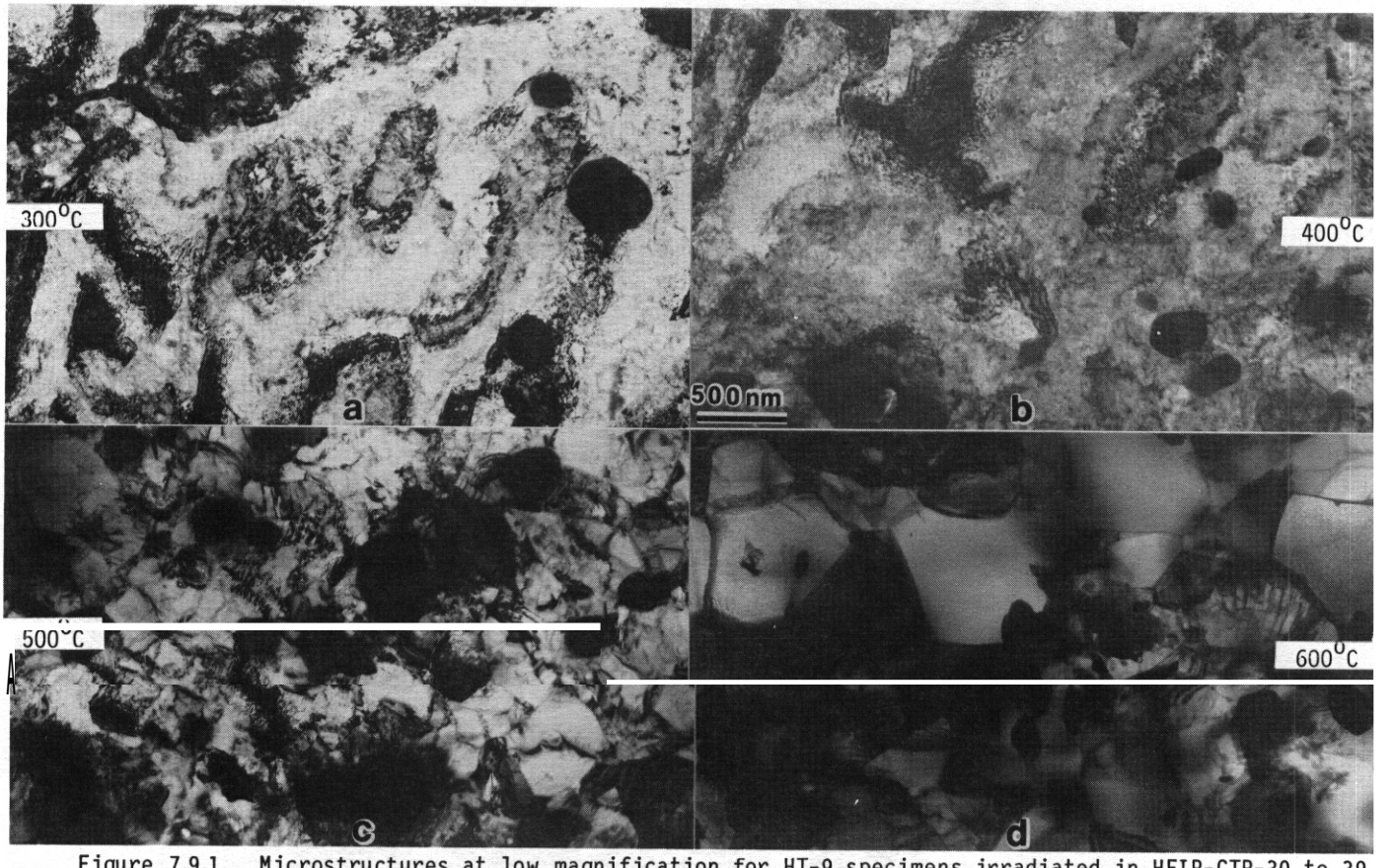

Figure 7.9.1. Microstructures at low magnification for HT-9 specimens irradiated in HFIR-CTR-30 to 39 dpa.

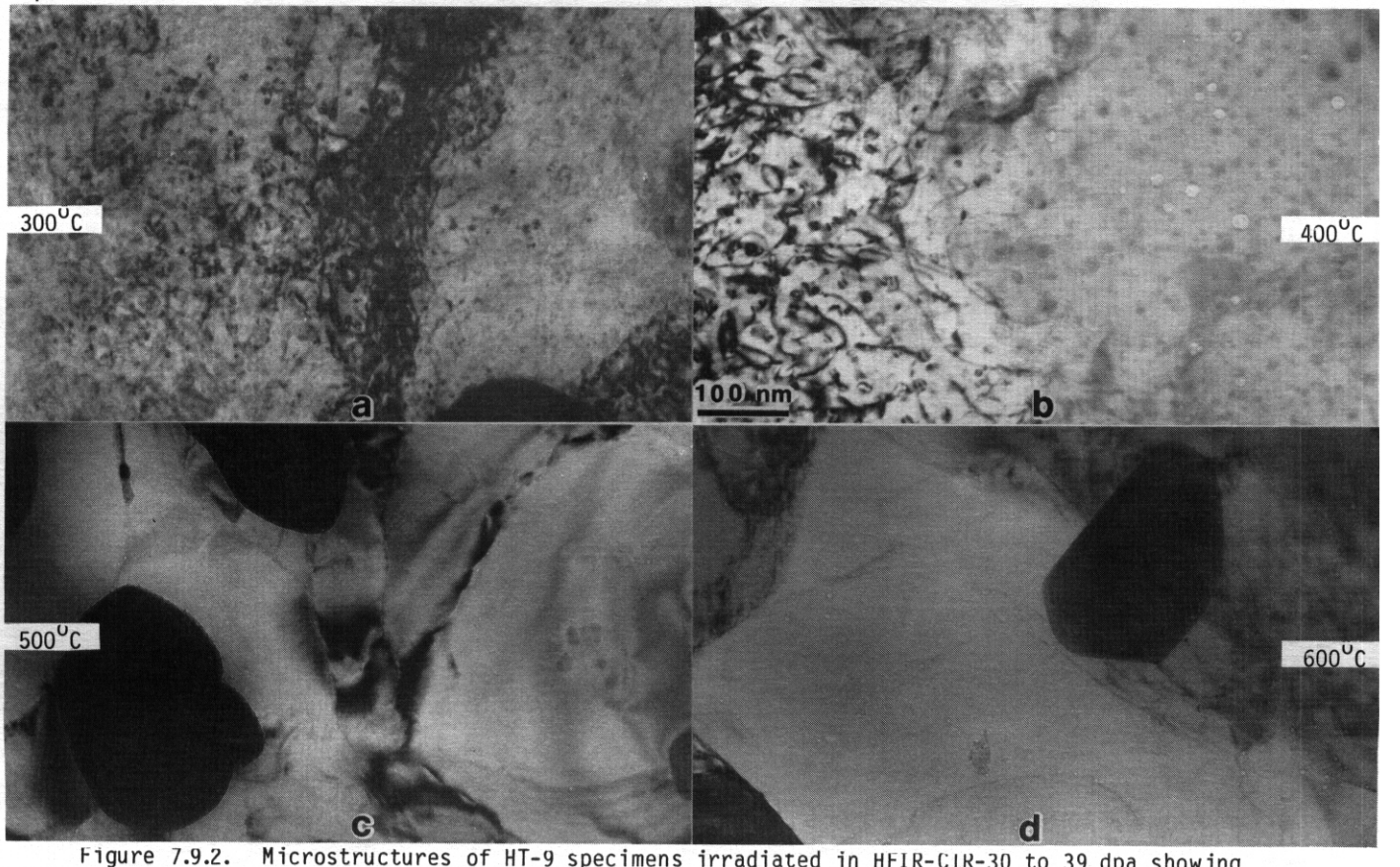

Figure 7.9.2. Microstructures of HT-9 specimens irradiated in HFIR-CTR-30 to 39 dpa showing dislocation, precipitate and cavity structures.

irradiation at 300°C and on the order of 11 nm after irradiation at 600°C. Further work will be needed to characterize this response more completely but is is apparent that such structural changes may result in mechanical properties changes.

EBR-IIIAD-2

Specimens of HT-9 heat 91354 irradiated to 29 dpa in EBR-II were found to be very similar to specimens previously examined following irradiation to 13 dpa.[4] Following irradiation at 390°C, the structure contained a fine distribution of small particles, a moderate density of perfect loops within dislocation tangles and well developed subgrain structure. Following irradiation at 500°C, the precipitate density was drastically reduced and loop structure was not present. Only minor evidence of precipitate coarsening was found.

Examples of these structures are given in Figure 7.9.5. Figures 7.9.5a and c show specimen 2HCP irradiated at 390°C to 29 dpa at low and higher magnification. A typical lath structure can be seen at low magnification. Lath boundaries are decorated with elongated (plate-like) $M_{23}C_6$ precipitate and within the laths radiation-induced precipitate and dislocation structures are present. The precipitate and dislocation structures are shown at higher magnification in Figure 7.9.5c using g = 110 contrast. The largest loops are on the order of 50 nm in diameter and precipitate particles are on the order of 10 nm. Therefore, both dislocation loops and precipitates had grown as a result of further irradiation from 13 to 29 dpa. Cursory examination of $M_{23}C_6$ precipitate particles revealed substructure similar to that shown in Figure 7.9.4.

Figures 7.9.5b and d show specimen 2HCU irradiated at 500°C to 29 dpa at low and higher magnifications. The subgrain boundaries are well defined but subgrains are quite clean with only a few dislocations and small precipitates (possibly carbides) within subgrains. Evidence was found for helium bubble formation at subgrain boundaries. Bubbles were about the same size but the number density was much lower than for specimen SA23.

Void Swelling Measurements

Three areas of specimen SA21 irradiated at 400°C to 39 dpa were selected for quantitative void swelling measurements. All areas contained relatively high densities of voids so it can be assumed that they represent behavior approaching steady state with regard to void density levels. However, the measurements are expected to represent an extreme overestimate of the overall swelling in the specimen

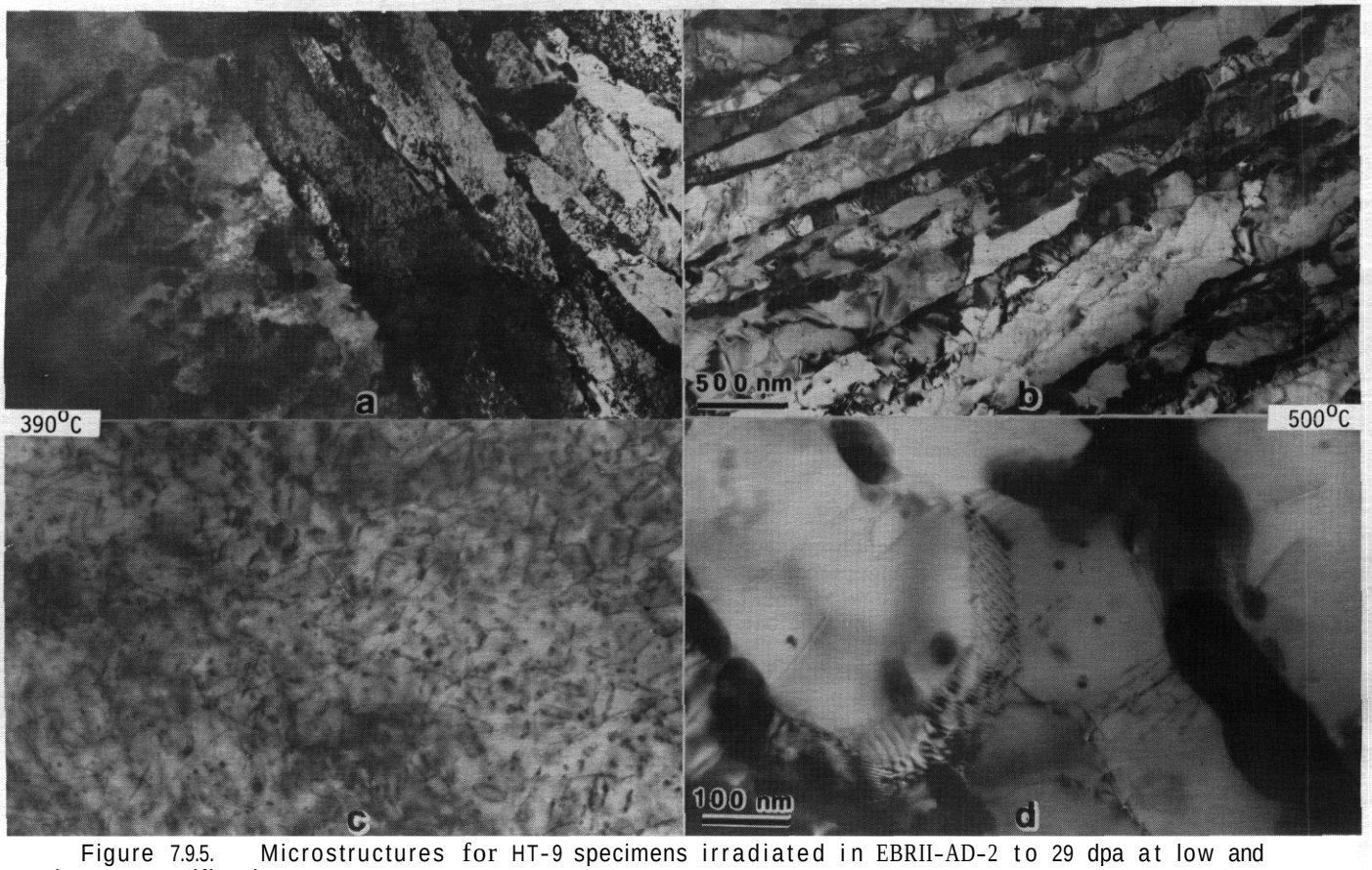

Figure 7.9.5. Microstructures for HT-9 specimens irradiated in EBRII-AD-2 to 29 dpa at low and moderate magnifications.

because many much larger regions contained no voids. The void swelling varied between 0.035 and 0.050% with an average of 0.044%. The void density varied between 5.1 x 10^{14} and 8.4 x 10^{14} cm^{-3} and the mean void size was in the range 10.8 to 11.7 nm. (These measurements excluded features which were characterized as spherical helium bubbles.)

7.9.4.4 Discussion

Several topics for discussion arise from the present work. HT-9 is confirmed to swell as a result of irradiation in HFIR and the behavior can be attributed to the helium produced during irradiation in HFIR as opposed to a heat-to-heat effect. This result not only has implications regarding the fundamental consequences of helium production but also regarding swelling design equation development and heat-to-heat variability on swelling uncertainty predictions. Also, other microstructural changes were found as a result of further irradiation which have bearing on interpretation of fracture toughness measurements.

Helium Effects on Swelling in Ferritics

The present effort appears to show that the swelling response of HT-9 is different in EBR-II and HFIR. Following irradiation in HFIR to 39 dpa at 400°C, cavitation typical of void swelling in the incubation regime was found whereas following irradiation in EBR-II to 29 dpa at 390°C, specimens of the same heat of material showed no evidence of void swelling. It has been noted that the preirradiation microstructures of the specimens for the two different tests were quite different. Therefore, three possible explanations for the different swelling response must still be considered: heat treatment procedure, fluence, and helium production. Heat-to-heat variations can be eliminated.

The preirradiation microstructure of HT-9 specimens irradiated in HFIR-CTR-30, 31, and 32 was atypical due to the absence of martensite lath structure decorated with $M_{23}C_6$ and due to the presence of excessively large carbide structure. It is possible that a consequence of this atypical heat treatment is enhanced swelling. However, this is considered unlikely. It has been proposed that the swelling resistance of HT-9 arises from G-phase precipitation in-reactor.[4] The specimens of HT-9 heat 91354 did indeed contain G-phase following irradiation and therefore it is apparent that swelling resistance does not simply arise from the presence of 6-phase. The mechanism is more complex; either G-phase dilutes the potency of gas atoms thereby preventing void nucleation or else high levels of helium production can overcome the swelling inhibition promoted by 6-phase.

There are differences in accumulated dose; the specimens which swelled were irradiated to approximately 30% higher dose. However, it is unlikely that dose differences can explain the differences in behavior. HT-9 has been irradiated in EBR-II to 75 dpa and the swelling resistance was maintained.[2] A different heat was involved, but the present effort supports the contention that heat-to-heat differences are unimportant. The most likely explanation for the loss of swelling resistance in HFIR for two heats of HT-9 is that helium production promotes void swelling. Note that helium production in the HFIR irradiated specimens was 115 appm He[6] whereas in EBR-II it was on the order of 3 appm He.

The mechanism whereby helium promotes void swelling has received attention using both simulation and theoretical analysis techniques. It has been shown thdt for ferritic alloys irradiation with helium in conjunction with other ion species produces more swelling than when helium is not included.[7,8] Theoretical analyses[9,10] provide explanation based on the concept that a critical cavity size is needed before cavities can grow as voids and that helium additions promote large cavity sizes. Therefore, larger helium additions promote the onset of void swelling at lower fluences and tend to produce higher void densities. The concept of a critical cavity size has been considered experimentally for austenitic sta' less steels[10,11] and for an Fe-10Cr binary alloy preinjected with helium and subsequently ion bombarded.]? The present effort provides the following experimental observations with regard to critical cavity size in neutron irradiated ferritics. At 300°C in an HFIR environment, the critical cavity size is greater than 1.6 nm. At 400°C, the critical cavity size is on the order of 30 nm and at 500 and 600°C, the critical cavity size is greater than 4 nm and 10 nm, respectively. These values are based on helium bubble measurements, and it is not clear that bubbles located on grain boundaries and dislocations can indeed be sites for void growth. Nonetheless, these estimates are most relevant for theoretical analysis.

HT-9 Swelling Design Equation for Fusion

An approach to develop swelling equations for ferritic alloys has been proposed[13] and used to predict swelling in 2-1/4Cr-1Mo.[14] The same approach can be used to predict swelling for HT-9 in a fusion environment. The key parameters for such an equation would be 1) a peak swelling rate of 0.06%/dpa, 2) a peak swelling temperature at 400°C with negligible accumulated swelling to high fluence at 325 and 475°C, and 3) an incubation parameter which defines the onset of steady state swelling (as a bilinear inflection point). A design equation for HT-9 has been included in the MHFES[15] which defines the minimum incubation parameter arbitrarily as 72.

The present results provide further insight regarding the selection of the minimum incubati n parameter. Voids first appear in HT-9 between 20 and 39 dpa as a result of irradiation in HFIR! Helium gener tion in HT-9 irradiated in HFIR is approximately 25% of that expected in a fusion machine first wall! Based on the concept of critivcal cavity size, it can be assumed that void formation will occur in a fusion environment at doses between 5 and 9 dpa. However, the first appearance of voids rarely corresponds to the void incubation dose. The incubation dose is often two to three times longer, and in the case of ferritics. it may be significantly longer than that.[13] However, 72 dpa could well be an overestimate.

Interpretation of Toughness Measurements

The large shifts in ductile-brittle transition-temperature (DBTT) following irradiation at about 400°C are found to saturate with increasing fluence.[16] This behavior could be traced to saturation in hardness increases due to irradiation (in fact a slight softening was found with further irradiation).[17] The present results indicate that irradiation-induced microstructural features such as dislocations and precipitates grow with increasing fluence. Precipitate growth is probably in part a result of coarsening. Therefore, the saturation of DBTT shifts can be ascribed to saturation of the irradiation-induced precipitate microstructures. Furthermore, further large shifts in DBTT with increasing fluence should not be expected.

7.9.5 Conclusions

Microstructural examinations on a series of specimens of HT-9 heat 91354 have been performed in order to determine the effect of spectrum and additional dose on microstructural evolution during irradiation. The following conclusions can be made:

The major difference between EBR-II and HFIR irradiation is the appearance of cavities in all specimens irradiated in HFIR whereas cavities were generally not found in specimens irradiated in EBR-II. Cavities typical of helium bubbles were found following HFIR irradiation at 400, 500 and 600°C and evidence for helium bubbles were found following HFIR irradiations at 300°C. Void swelling typical of incubation response was found following irradiation at 400°C. (Cavities typical of helium bubble formation were found following EBR-II irradiation at 500°C.) The void swelling differences due to irradiation environment are attributed to helium generation; heat-to-heat variations can be ruled out.

Irradiation to increased dose does not significantly alter other microstructural features in either reactor spectrum. The major effect of increased dose was growth of the microstructural features, on the order of a doubling in size when the dose was effectively squared ($d \propto (\phi t)^{1/2}$).

7.9.6 Future Work

This work will be continued.

7.9.7 References

1. J. M. Vitek and R. L. Klueh "Microstructure of 9Cr-1MoVNb and 12Cr-1MoVW Ferritic Steels After Irradiation at Elevated Temperatures in HFIR" p. 108 in Alloy Development for Irradiation Performance Semiannual Progress Report for Period Ending September 30, 1983, DOE/ER-0045/11, Oak Ridge National Laboratory, Oak Ridge, TN.

2. D. S. Gelles and L. E. Thomas "Effects of Neutron Irradiation on Microstructure in Experimental and Commercial Ferritic Alloys" p. 559 in Proceedings of Topical Conference on Ferritic Alloys for Use in Nuclear Energy Technologies, ed. J. W. Davis and D. J. Michel (The Metallurgical Society of AIME), Warrendale, PA, 1984.

3. Alloy Development for Irradiation Performance Program Review Meeting, November 9-10, 1983 at Chicago, IL.

4. D. S. Gelles and L. E. Thomas "Microstructural Examination of HT-9 and 9Cr-1Mo Contained in the AD-2 Experiment" p. 343 in Alloy Development for Irradiation Performance Semiannual Progress Report for Period Ending March 31, 1982, DOE/ER-0045/8, Oak Ridge National Laboratory, Oak Ridge, TN.

5. D. S. Gelles and L. E. Thomas "Microstructural Examination of HT-9 Irradiated in the HFIR-CTR-32 Experiment" p. 162 in Alloy Development for Irradiation Performance Semiannual Progress Report for Period Ending September 30, 1982, DOE/ER-0045/9, Oak Ridge National Laboratory, Oak Ridge, TN.

6. L. R. Greenwood "Fission Reactor Dosimetry - HFIR-CTR 3036, 40" p. 5 in Damage Analysis and Fundamental Studies Quarterly Progress Report for Period Ending March 1985, DOE/ER-0046/21, U.S. Department of Energy, Washington, DC.

7. G. Ayrault "Cavity Formation in Single- and Dual-Ion Irradiated HT-9 and HT-9 + 2 Ni Ferritic Alloys" p. 182 in Damage Analysis and Fundamental Studies Quarterly Progress Report for Period Ending December 31, 1981, DOE/ER-0046/8, U.S. Department of Energy, Washington, DC.

8. L. L. Horton and J. Bentley "Swelling Behavior of a Simple Ferritic Alloy" p. 569 in Proceedings of Topical Conference on Ferritic Alloys for Use in Nuclear Energy Technologies, eds. J. W. Davis and D. J. Michel (AIME), Warrendale, PA, 1984.

9. J. R. Townsend "Critical Cavity Sizes in Dual-Ion Bombarded 304 SS, Part II: Theoretical", J. Nucl. Matl., 108 and 109, 544, (1982).

10. Section 6 "Radiation Effects - Helium" in the Proceedings of the Third Topical Metting on Fusion Reactor Materials, J. Nucl. Matl., 122 and 123, 487, (1984).

11. J. A. Spitznagel, W. J. Choyke, W. J. Doyle, R. 8. Irwin, J. R. Townsend and J. N. McGruer, "Critical Cavity Sizes in Dual-Ion Bombarded 304 SS, Part I: Experiment," J. Nucl. Matl., 108 and 109, 537, (1982).

12. L. L. Horton "Experimental Determination of the Critical Cavity Radius in Fe-10%Cr for Ion Irradiation" p. 148 in Damage Analysis and Fundamental Studies Quarterly Progress Report for Period Ending September 1984, DOE/ER-0046/19, U.S. Department of Energy, Washington, OC.

13. 0. S. Gelles and R. L. Meinecke "Swelling in Simple Ferritic Alloys Irradiated to High Fluence" p. 103 in Alloy Development for Irradiation Performance Semiannual Progress Report for Period Ending September 30, 1983, DOE/ER-0045/11, Oak Ridge National Laboratory, Oak Ridge, TN.

14. D. S. Gelles and R. J. Puigh "Evaluation of Ferritic Alloy Fe 2-1/4Cr-1Mo After Neutron Irradiation - Irradiation Creep and Swelling" ibid. 82.

15. File Code AA01-3304 (E-1) Supplement Package 10, Materials Handbook for Fusion Energy Systems, DOE/TIC-10122.

16. W. L. Hu "Charpy Impact Test Results of Ferritic Alloys at a Fluence of 6 x 10^{22} n/cm^2", p. 106 in Alloy Development for Irradiation Performance Semiannual Progress Report for Period Ending September 30, 1984, DOE/ER-0045/13, Oak Ridge National Laboratory, Oak Ridge, TN.

17. D. S. Gelles and W. L. Hu "Fractographic Examination of Ferritic Alloy Charpy Specimens at a Fluence of 6 x 10^{22} n/cm^2" this reoort.

7.10 FRACTOGRAPHIC EXAMINATION OF FERRITIC ALLOY CHARPY SPECIMENS AT A FLUENCE OF 6 x 10^{22} n/cm² – D. S. Gelles and W. L. Hu (Westinghouse Hanford Company)

7.10.1 ADIP Task

The Department of Energy/Office of Fusion Energy (DOE/OFE) has cited the need to investigate ferritic alloys under the ADIP program task Ferritic Steels Development (Path E). The tasks involved are akin to Task Number 1.B.13, Tensile Properties of Austenitic Alloys, and Task Number 1.C.2, Microstructure and Swelling in Austenitic Alloys.

7.10.2 Objective

The objective of this effort is to provide fractographic data for Charpy specimens of the irradiated ferritic alloys HT-9 and Modified 9Cr-1Mo in order to provide improved understanding of toughness degradation as a result of irradiation for the ferritic alloy class.

7.10.3 *Summary*

The fracture surfaces of thirteen Charpy specimens have been examined by scanning electron microscopy and several of these have been measured for hardness. The specimen series irradiated in the AD-2 test, second discharge includes HT-9 base metal in two product forms, and Modified 9Cr-1Mo base metal and weld metal, fluences include 13 and 26 dpa and irradiation temperatures cover the range 390°C to 550°C. It is found that significant hardening occurs both in HT-9 and 9Cr-1Mo following irradiation at 390°C, but not at 450°C and higher. Hardness decreases slightly with increasing fluences for HT-9 irradiated at 390°C and for 9Cr-1Mo irradiated at 390' and 500°C. Fracture appearance is found to be insensitive to irradiation fluence, whereas significant differences could be found in product form. It is concluded that irradiation does not encourage new fracture mechanism such as temper embrittlement. Failure is controlled by the microstructure generated prior to irradiation.

7.10.4 Progress and Status

7.10.4.1 Introduction

This report describes fractographic examinations and hardness measurements for Charpy specimens of HT-9 and Modified 9Cr-1Mo (T91) which had been irradiated in the AD-2 test to fluences as high as 6 x 10^{22} n/cm² (26 dpa). The Charpy impact test results for these specimens have been described pre iously[1] and the fractographic examinations provide a follow-on to similar examinations reported earlier,' in some cases involving specimens in identical conditions but only irradiated to 3 x 10^{22} n/cm² or 13 dpa. Therefore, the intent of this effort includes: (1) to determine if effects of further irradiation fluence can be identified by fractography, and (2) to determine if observations in the recent Charpy impact test data base can be explained by fractography. Those observations[1] include: (1) for HT-9 base metal as the fluence was raised from 3 to 6 x 10^{22} n/cm² a small additional shift was found in transition temperature when irradiated at 390°C and 450°C and a further reduction in upper shelf energy was found at all irradiation temperatures, (2) no significant change in 9Cr-1Mo base metal response with increased fluence for all irradiation temperatures, (3) a higher transition temperature and a higher upper shelf energy for 9Cr-1Mo weld metal than for base metal at the same irradiation conditions, and (4) a significant improvement in both transition temperature and upper shelf energy for HT-9 base metal specimens fabricated from normalized and tempered plate stock in comparison with the standard specimen condition which was fabricated from mill-annealed bar stock.

7.10.4.2 Experimental Procedure

Specimens selected for fractographic examination are listed in Table 7.10.1 with Charpy test conditions and measured normalized fracture energy. In general, specimens were selected which had been tested at approximately the transition temperature so that both ductile and brittle fracture surface features could be studied. However, from both lots of HT-9 base metal and for 9Cr-1Mo at the higher irradiation temperature, one specimen was also selected for examination to show upper shelf behavior. These specimen conditions are identified by specimen identification number in Figure 7.10.1 which shows the Charpy impact test results for all specimens tested.

Experimental procedures for hardness determination and fractographic examination are identical to those used previously[2].

7.10.4.3 Results

Hardness Measurements

Results of Rockwell C hardness measurements on irradiated specimens were as follows: Specimen TT28, 28.7; TT15, 22.5; TT20, 21.4; KT06, 33.4; KT13, 23.5; KT20, 23.5; KT24, 22.3; TV22, 21.4 and TV11, 12.1.

Table 7.10.1. Charpy specimens selected for fractographic examination from the AD-2 test, second discharge

Alloy	Condition	Code	Irradiation Temperature (°C)	Fluence dpa (10" nlcm')	Test Temperature (°C)	Normalized Fracture Energy[1] (Jouleslcm')
HT-9	Wrought Bar	TT28	390	26 (6)	132	61.63'
		TT15	500	26 (6)	29	78.85
		TT23	500	26 161	93	145.52
		TT20	550	26 (6)	29	64.75
HT-9	Plate	KT06	390	13 131	104	85.70
		KT13	450	13 (3j	-18	117.49
		KT20	550	13 (3)	-7	89.51
		KT24	550	13 (3)	104	285.26
9Cr-1Mo	Base Metal	TV22	390	26 (6)	29	163.67
		TV11	500	26 (6)	29	450.36
9Cr-1Mo	Weld Metal	NL03	390	13 (3)	82	177.59
		NLII	450	13 (3)	43	396.72
		NL31	550	13 (3j	10	409.70

*One of the authors would like to take this opportunity to acknowledge an error presented in the previous report (Reference 1). Instead of normalizing the fracture energy by multiplying by the factor $L/B(w-a)^2$ as stated in the report, it was inadvertently normalized by multiplying by the factor $L/B^2(w-a)$. Consequently, the actual normalized fracture energy should be approximately twice the value reported in Reference 1.

These values are plotted in Figure 7.10.2 and compared with previous results. However, it may be noted that Figure 7.2.2 given in Reference 2 was plotted incorrectly. Specimen TV14 was irradiated at 390°C but was plotted at 500°C. Therefore, specimens TV21 and TV13 were subsequently measured and gave values of 15.5 ± 0.3 and 16.4 ± 0.3 C_r, respectively. These values are included in Figure 7.10.2 to define behavior for 9Cr-1M at 3 x 10^{22} (13 dpa). Examination of Figure 7.10.2 reveals several trends. Significant hardening occurs both in HT-9 and 9Cr-1Mo following irradiation at 390°C whereas following irradiation at higher temperatures of 450°C and above, hardness remains constant or decreases slightly. Hardness decreases with increasing fluence for HT-9 irradiated at 390°C and for 9Cr-1Mo both irradiated at 390 and 500°C. The reduction in hardness with increased fluence suggests a saturation in the DBTT degradation due to neutron exposure and indicates a softening effect due to prolonged aging at the irradiation temperatue. Hardness values for HT-9 appear to be stable at 500 and 550°C (or increase slightly). Finally, HT-9 plate stock appears to be slightly harder than rod stock at all temperatures where direct comparison is possible.

Fractography

Results of fractographic examination are presented as stereo pairs in Figures 7.10.3 through 7.10.15. In each case, a low magnification example of the specimen is given in part (a) showing a small portion of the fatigue surface on the left but primarily showing the fracture surface created prior to irradiation. Part (b) displays a region in the center of the fracture surface immediately adjacent to the fatigue surface with the fatigue surface again showing on the left. The reader is encouraged to view these fractographs with a small stereo viewer in order to appreciate the fracture surface geometries. Also, the reader is encouraged to compare the present fractographs with those given in Reference 2.

HT-9 Base Metal, TT Series. The specimens of condition TT which were examined in the present series of specimens were found to be very similar to those examined previously. All specimens showed evidence of delta ferrite stringers in the fracture surface topography oriented parallel to the initial crack front. The delta ferrite stringer effect could be found in both ductile and brittle regions. For example, Figure 7.10.3 is taken from specimen TT28 which had been irradiated at 390°C to 26 dpa and tested at 132°C which is in the transition temperature range. The normalized fracture energy for this condition was 31.8 Jouleslcm'. The fracture surface created during the Charpy test can be divided into three parts: (1) a ductile region located immediately adjacent to the fatigue surface which forms a narrow band, most easily recognized at the lower left, (2) adjacent to this, a brittle region extending approximately half way across the fracture surface consisting of three distinct levels which are relatively flat, and (3) the remainder which is a ductile region consisting mainly of corrugated structure. These three regions can be identified in Figure 7.10.3a; in Figure 7.10.3b, the transition

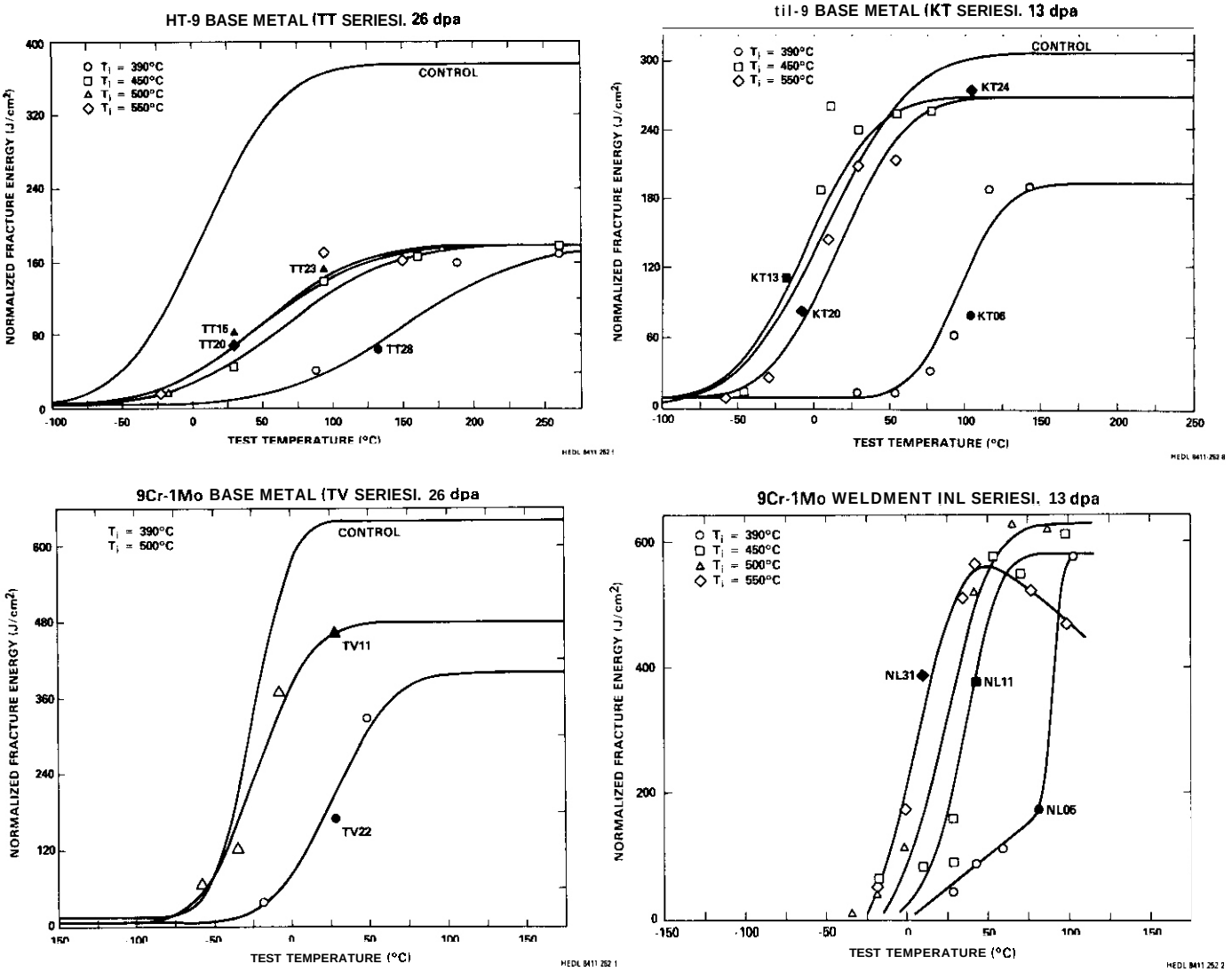

Fig. 7.10.1. Specimen selected for fractographic examination are irradiated by specimen identification number on the various Charpy impact energy curves.

from region (1) to region (2) is shown at higher magnification. In all cases, evidence for the elongated structure due to delta ferrite stringers can be seen.

Figures 7.10.4 and 7.10.5 provide comparison of HT-9 specimens TT15 and TT23 irradiated at 500' to 26 dpa and tested at 29 and 93°C respectively. The normalized fracture energies for these conditions were 41.1 and 76.1 joules/cm²; therefore, specimen TT15 shows a fracture surface at the transition temperature, whereas specimen TT23 shows fracture behavior on the upper shelf. Comparison of the fracture surfaces of specimens TT15 and TT23 reveals that both contain corrugated structure typical of ductile failure in association with delta ferrite stringers, but only specimen TT15 contains a region typical of brittle failure which extends approximately half way across the fracture surface. That this region is brittle can be shown in the higher magnification fractograph of Figure 10.7.4b. Therefore, as expected, the difference in normalized fracture energy between these test conditions is due to brittle failure on almost half the fracture surface area.

The fracture surface of specimen TT20 which was irradiated at 550°C to 26 dpa and tested at 29°C is shown in Figure 7.10.6. This condition gave a normalized fracture energy of 34.0 joules/cm' and represents behavior at the transition temperature. The fracture surface is similar to that in conditions TT28 and 15; a brittle region extending over just under half the specimen is found between two ductile regions. The major difference is that the initial ductile region adjacent to the fatigue surface is wider in specimen TT20.

Comparison of the present results with previous results given in Reference 2 provides two significant points: (1) Upper shelf failure following irradiation is very similar to upper shelf

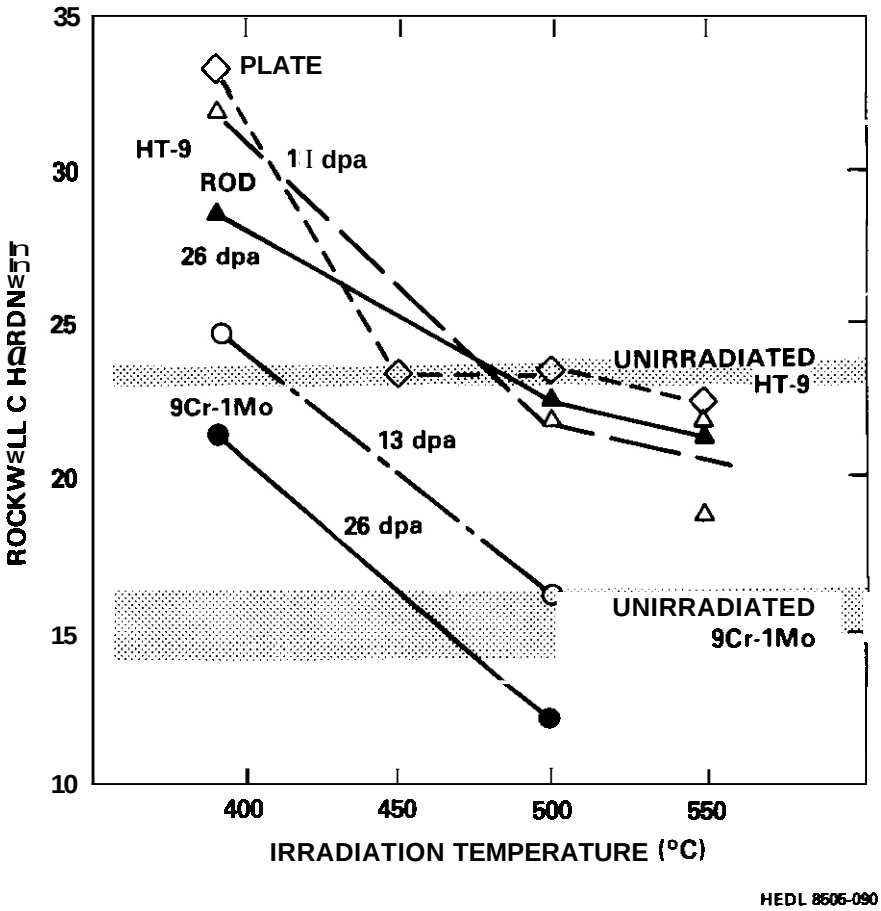

Fig. 7.10.2. Rockwell C hardness measurement as a function of irradiation temperature for HT-9 and modified 9Cr-1Mo base metal Charpy specimens contained in the AD-2 test, second discharge.

response in unirradiated specimens. This can be demonstrated by comparison of Figure 7.10.5 with Figure 7.2.5 from Reference 2. Therefore, the reduction in upper shelf energy due to irradiation is not a consequence of a change in fracture mechanism; (2) The consequences of irradiation at 390°C, as claimed following examination of specimen TT16 in Reference 2, are not corroborated in the present study. Specimen TT16 was found to contain few examples of linear structure due to delta ferrite stringers and shear lips at specimen surfaces were found to be wider but not as steep. Also, the fracture surface appeared to be flatter. These differences were attributed to increased hardness due to irradiation which resulted in reduced likelihood of cavitation at delta ferrite stringers. Specimen TT28 is quite different, however. The shear lips adjacent to specimen surfaces are of normal width and steepness, delta ferrite stringer effects are clearly defined, and the fracture surface is corrugated on the same scale as specimens irradiated at higher temperature. An explanation for these differences is not obvious. It may be due in part to reduced hardness found in specimen TT28 or to the higher fluence which has resulted in greater precipitation at delta ferrite stringers which compensates for the hardness increases found following irradiation at 390°C.

HT-9 Base Metal, KT Series. Specimens in the KT series were found to have fracture surfaces which were very different from those in the TT series. Three significant differences could be identified: (1) The effect of delta ferrite stringers on the fracture surface was not evident. Only specimen KT24 showed any indication of delta ferrite stringer formation, and this indication showed a difference in orientation of the delta ferrite stringers normal to the crack front and in the plane of the fracture surface. This difference in orientation is as expected[5], and the reduced density may be a result of controlling[3]; (2) in regions where brittle failure occurred, the plateau regions in KT series specimens were much smaller than in TT series specimens. This is indicative of prior austenitic grain size differences. However, the sense of the difference is in the reverse order based on specimen fabrication details; TT should have a grain size of ASTM 8 to 9 whereas KT should have a grain size of

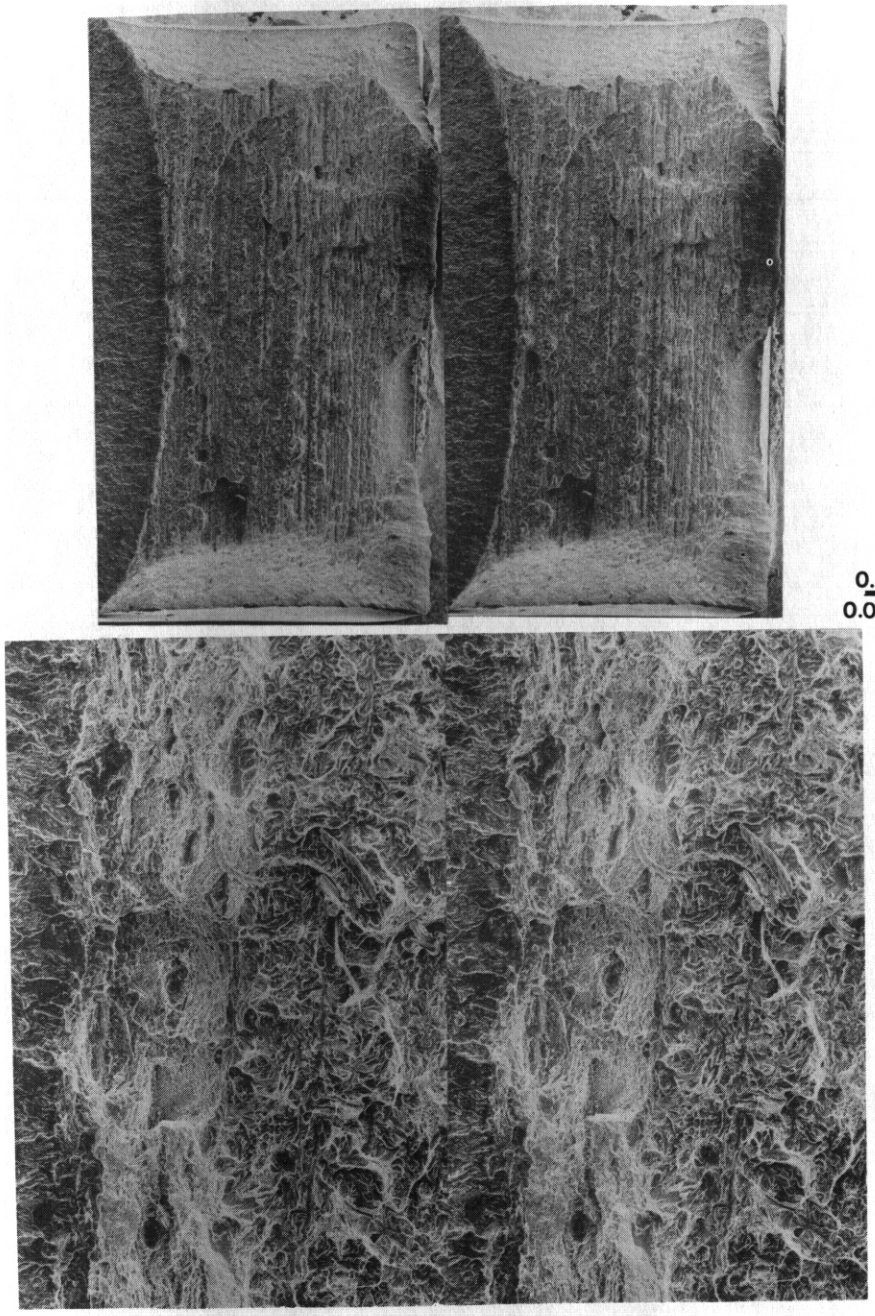

Fig. 7.10.3. Stereo pair fractographs of HT-9 specimen TT28 irradiated at 390°C to 26 dpa and tested at 132°C.

0.5 mm
0.05 mm

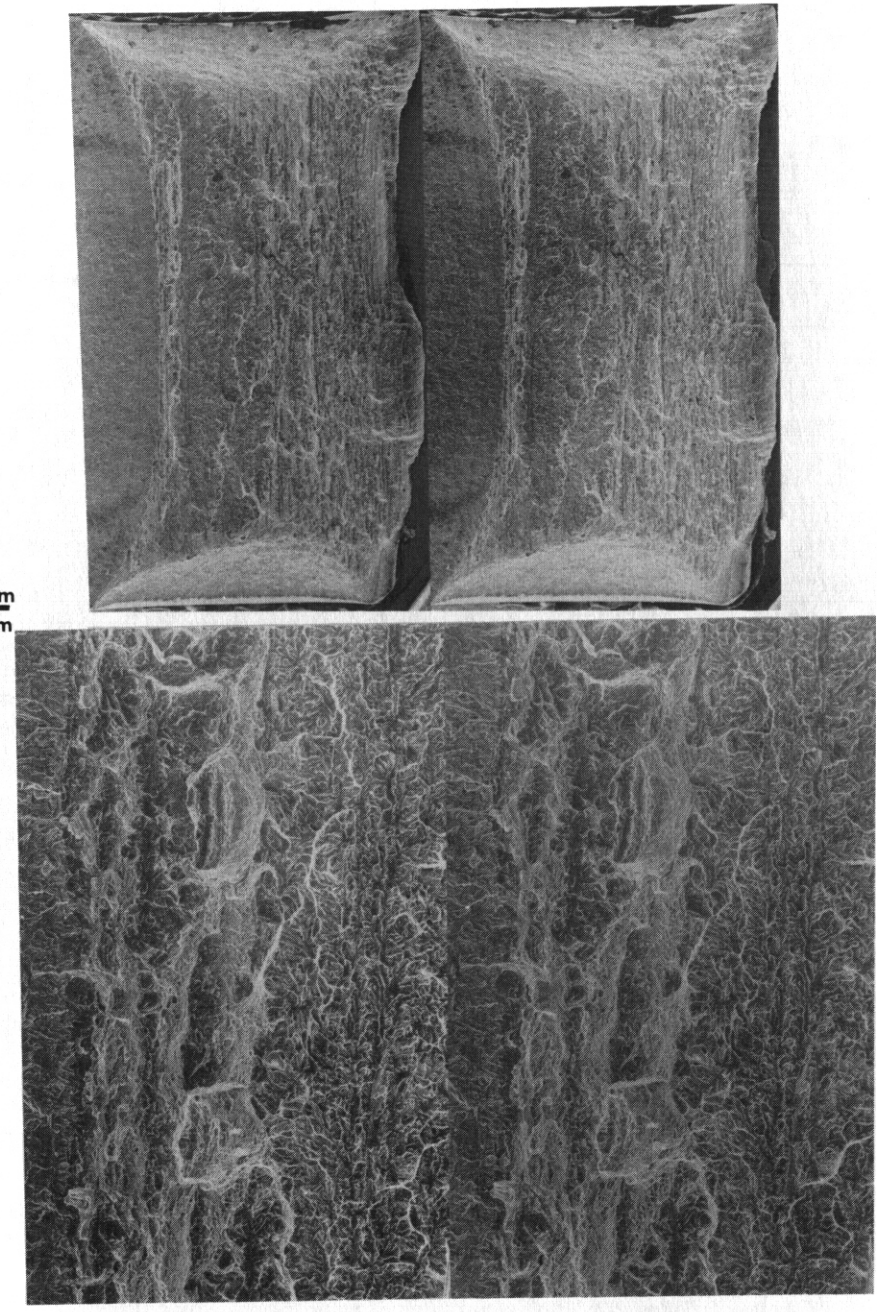

Fig. 7.10.4. Stereo pair fractographs of HT-9 specimen TT28 irradiated at 500°C to 26 dpa and tested at 29°C.

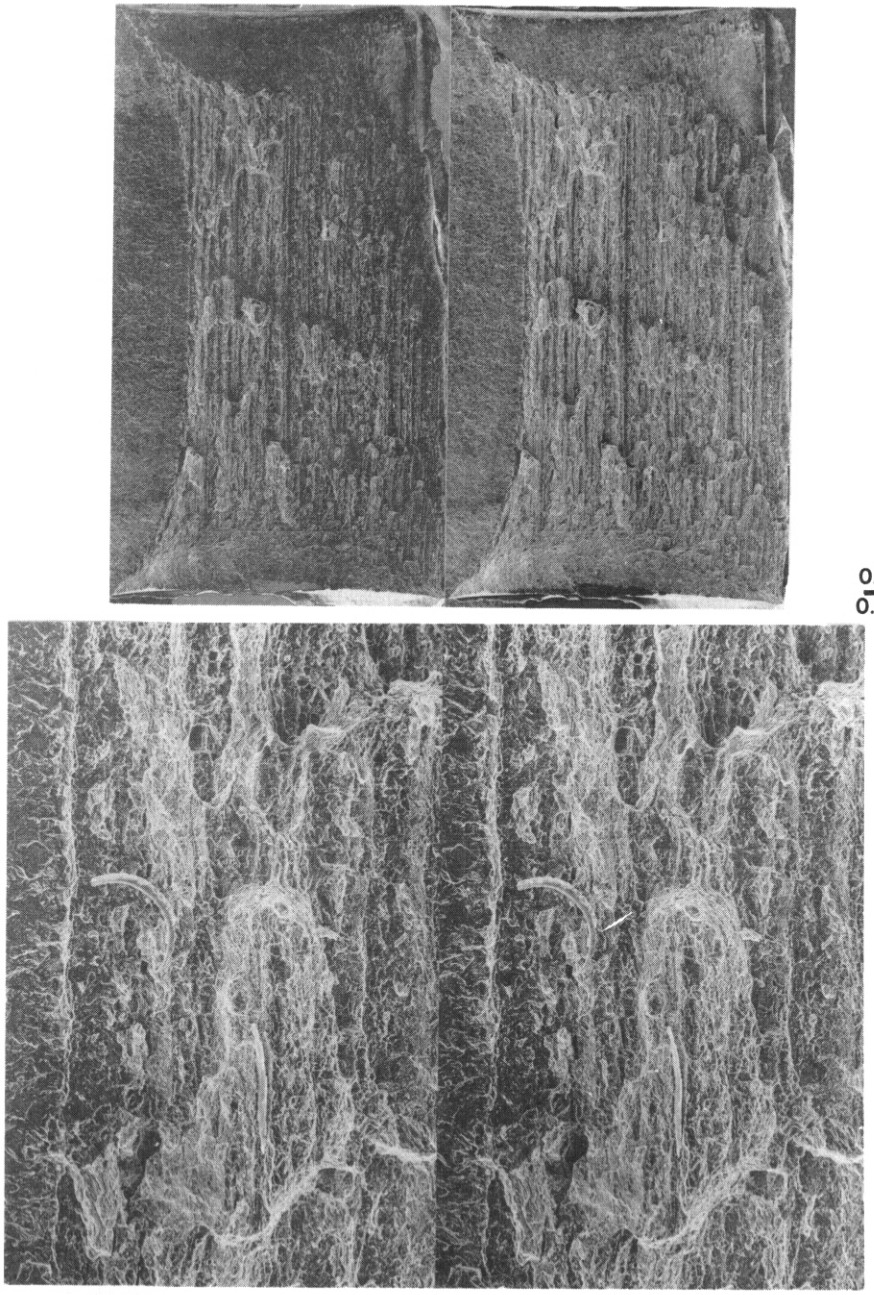

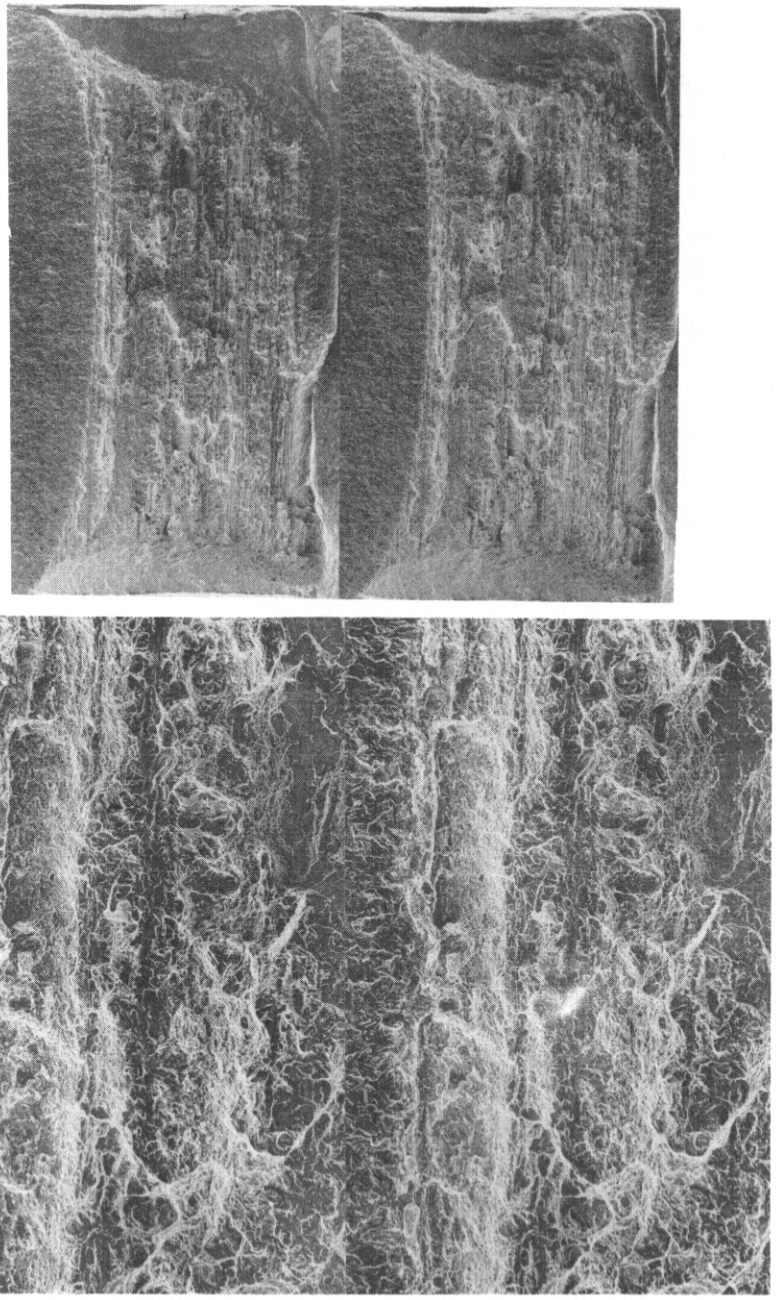

0.5 mm
0.05 mm

Fig. 7.10.5. Stereo pair fractographs of HT-9 specimen TT23 irradiated at 500°C to 26 dpa and tested at 93°C.

Fig. 7.10.6. Stereo pair fractographs of HT-9 specimen TT20 irradiated at 550°C to 26 dpa and tested at 29°C.

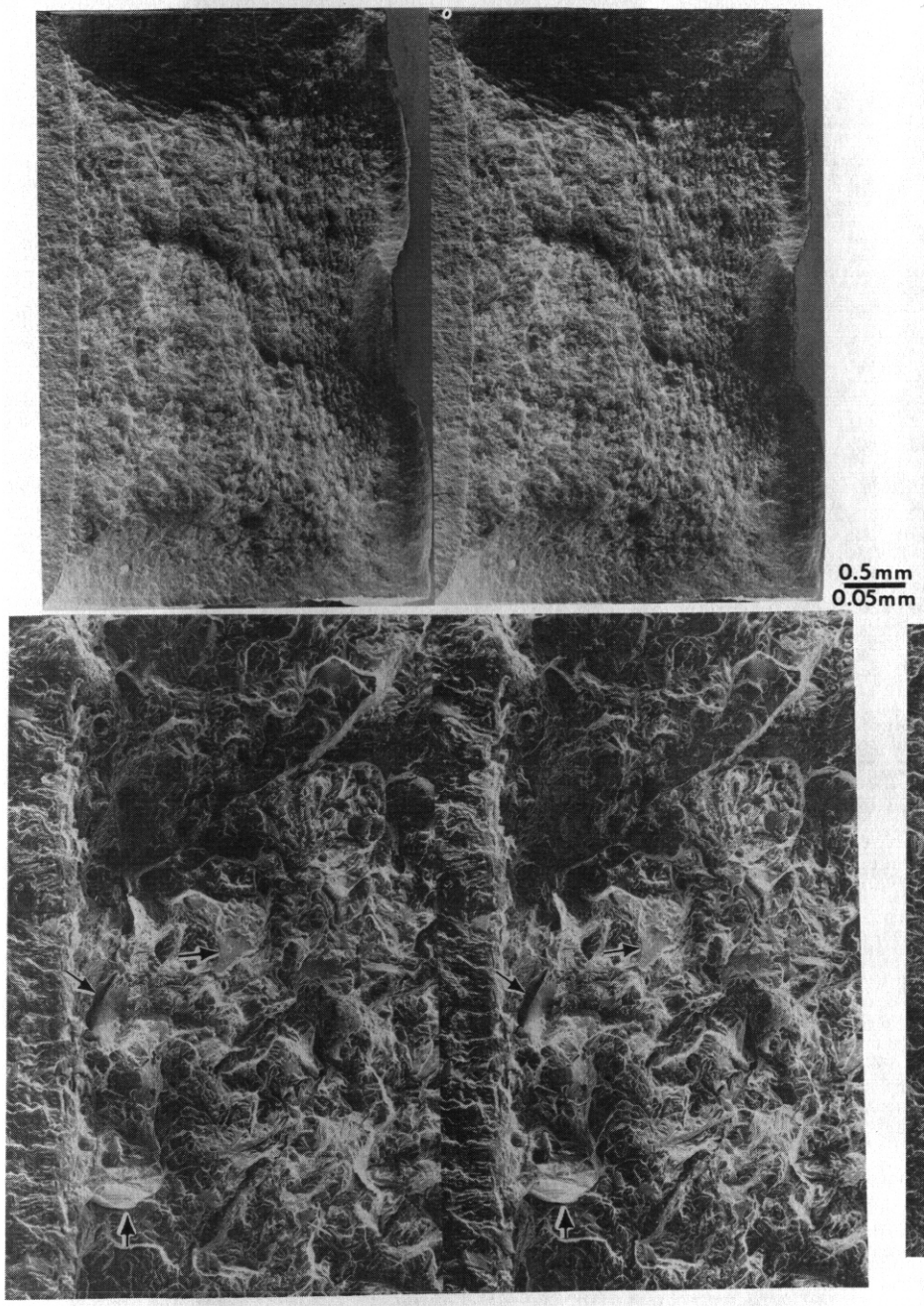

Fig. 7.10.7. Stereo pair fractographs of HT-9 specimen KT06 irradiated at 390°C to 13 dpa and tested at 104°C. Arrows point to features discussed in the text.

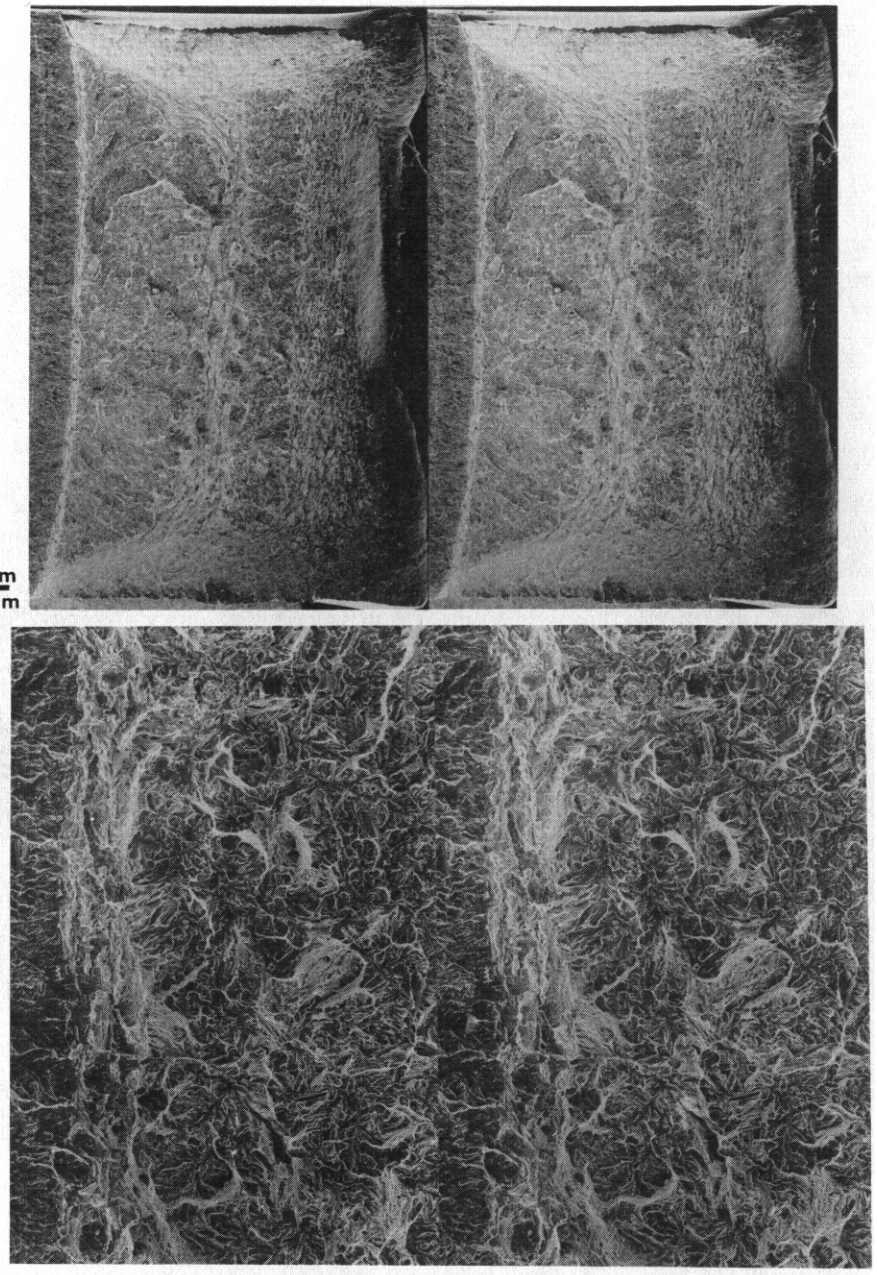

Fig. 7.10.8. Stereo pair fractographs of HT-9 specimen KT13 irradiated at 450°C to 13 dpa and tested at -18°C.

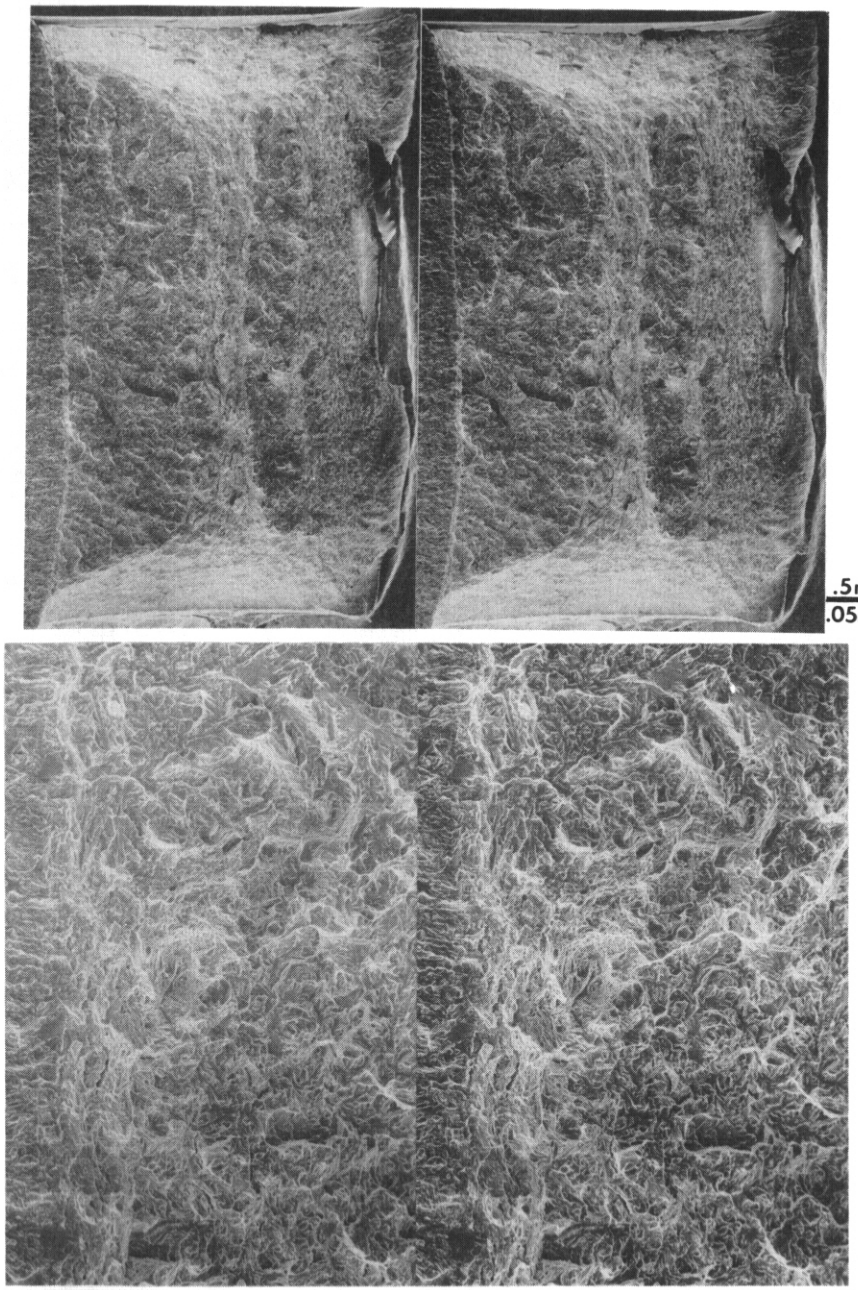

Fig. 7.10.9. Stereo pair fractographs of HT-9 specimen KT20 irradiated at 550°C to 13 dpa and tested at -7°C.

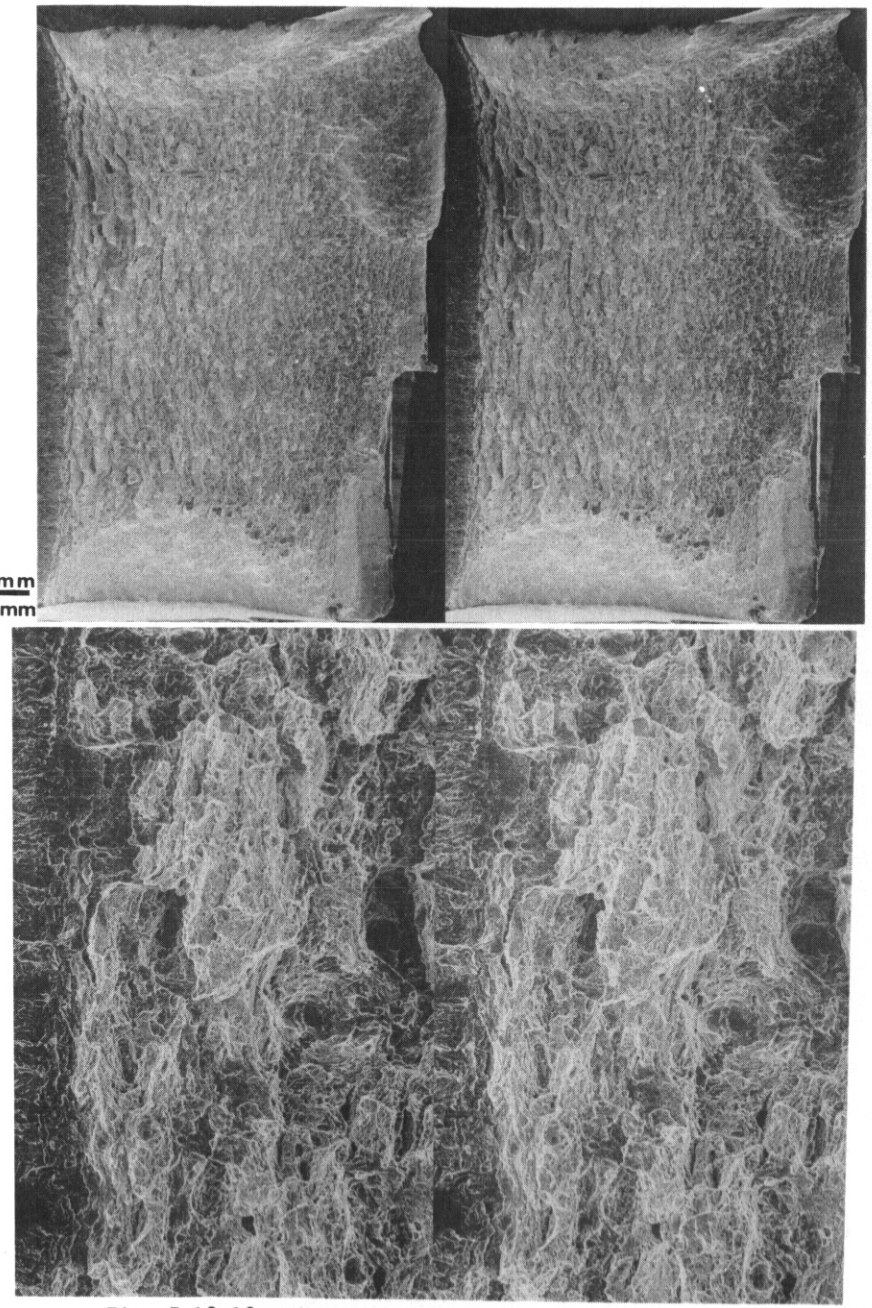

Fig. 7.10.10. Stereo pair fractographs of HT-9 specimen KT24 irradiated at 550°C to 13 dpa and tested at 104°C.

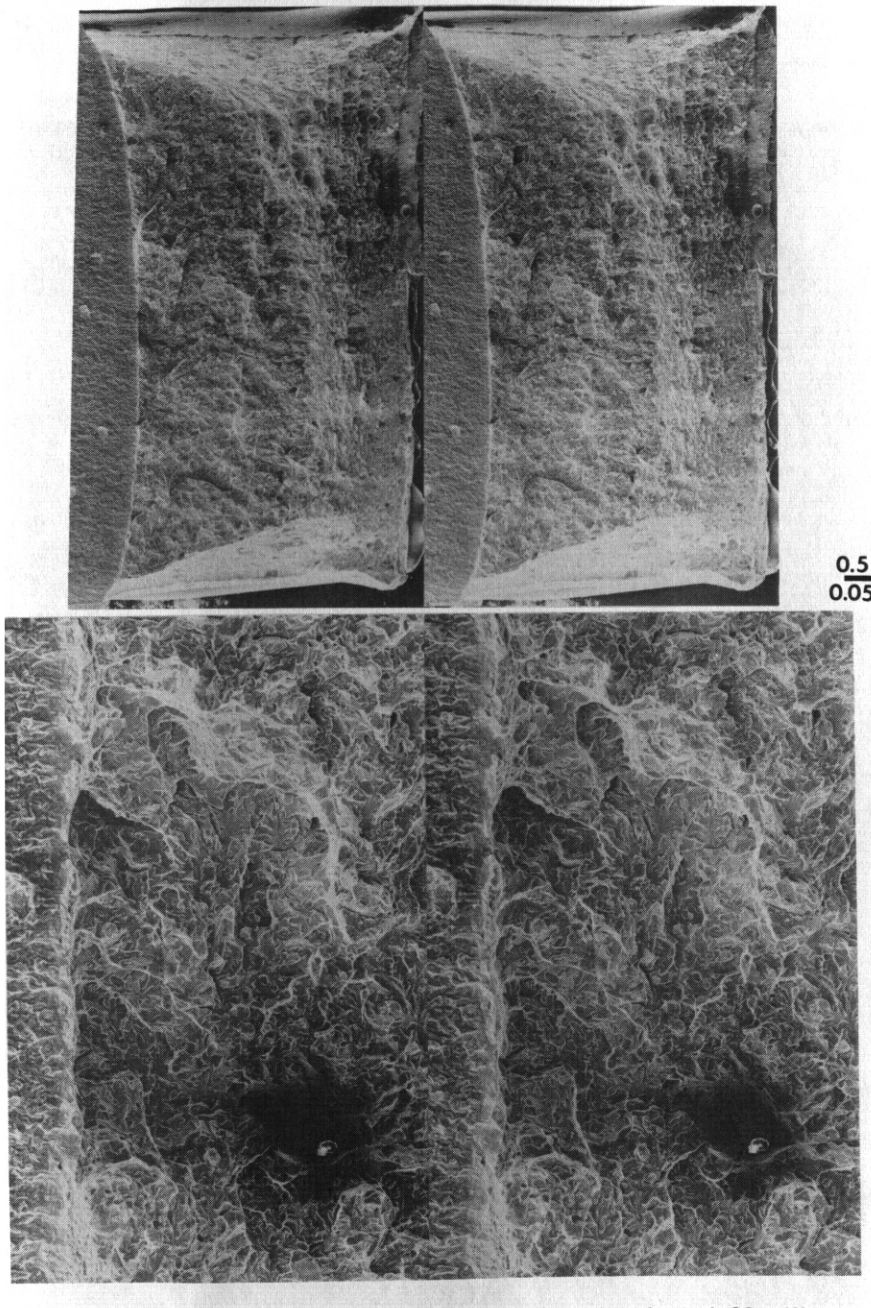

Fig. 7.10.11. Stereo pair fractographs of modified 9Cr-1Mo base metal specimen TV22 irradiated at 390°C to 26 dpa and tested at 29°C.

0.5 mm
0.05 mm

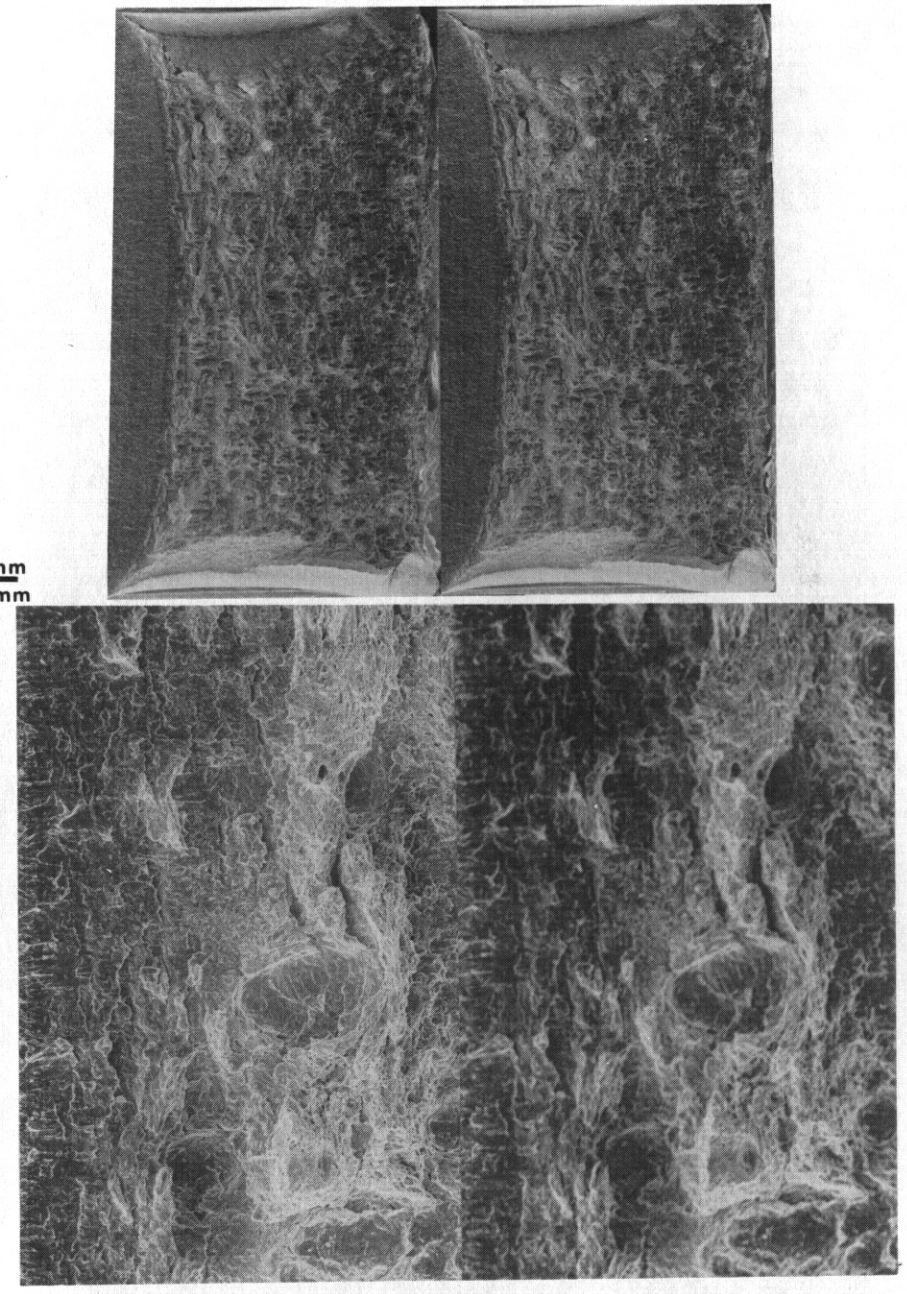

Fig. 7.10.12. Stereo pair fractographs of modified 9Cr-1Mo base metal specimen TV11 irradiated at 500°C to 26 dpa and tested at 29°C.

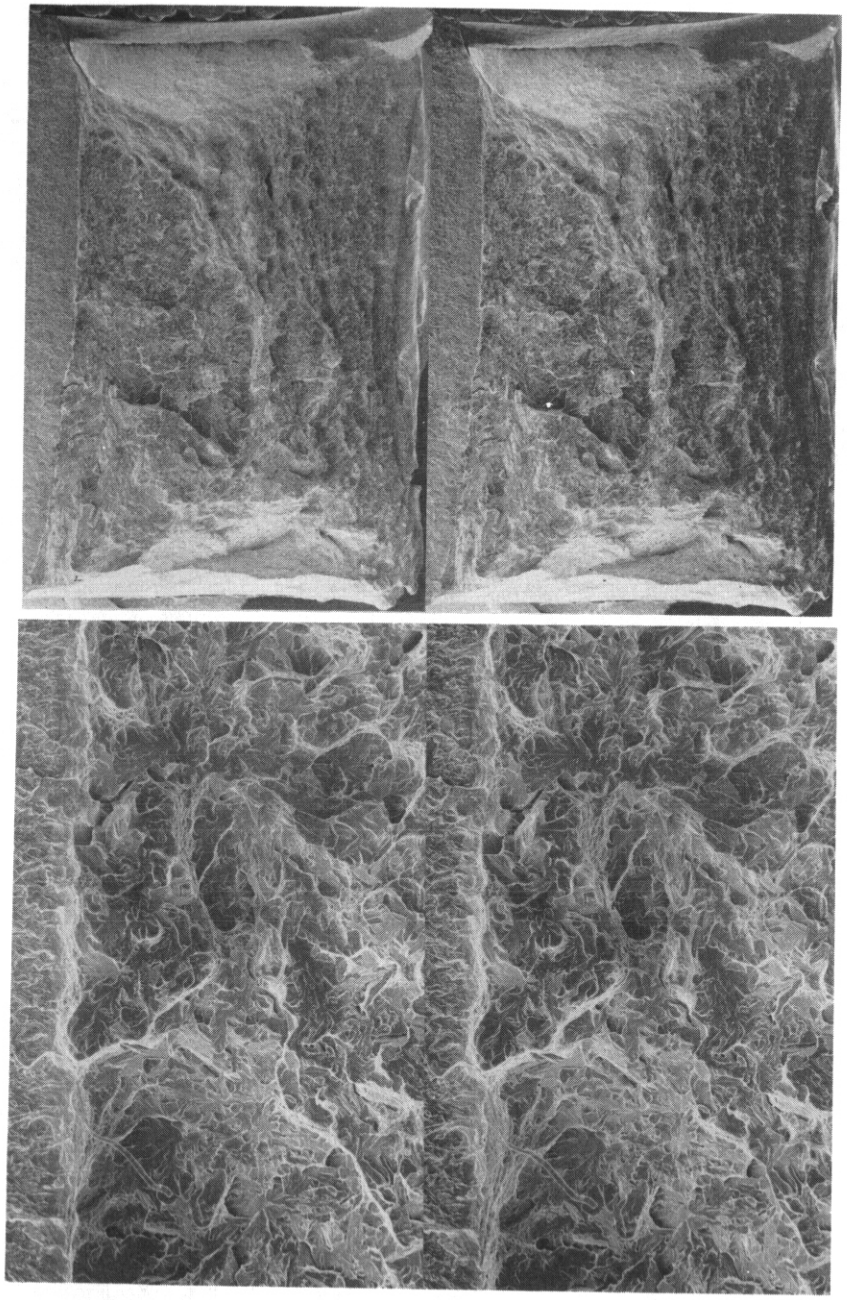

Fig. 7.10.13. Stereo pair fractographs of Modified 9Cr-1Mo weld metal specimen NL05 irradiated at 390°C to 13 dpa and tested at 82°C.

0.5 mm
0.05 mm

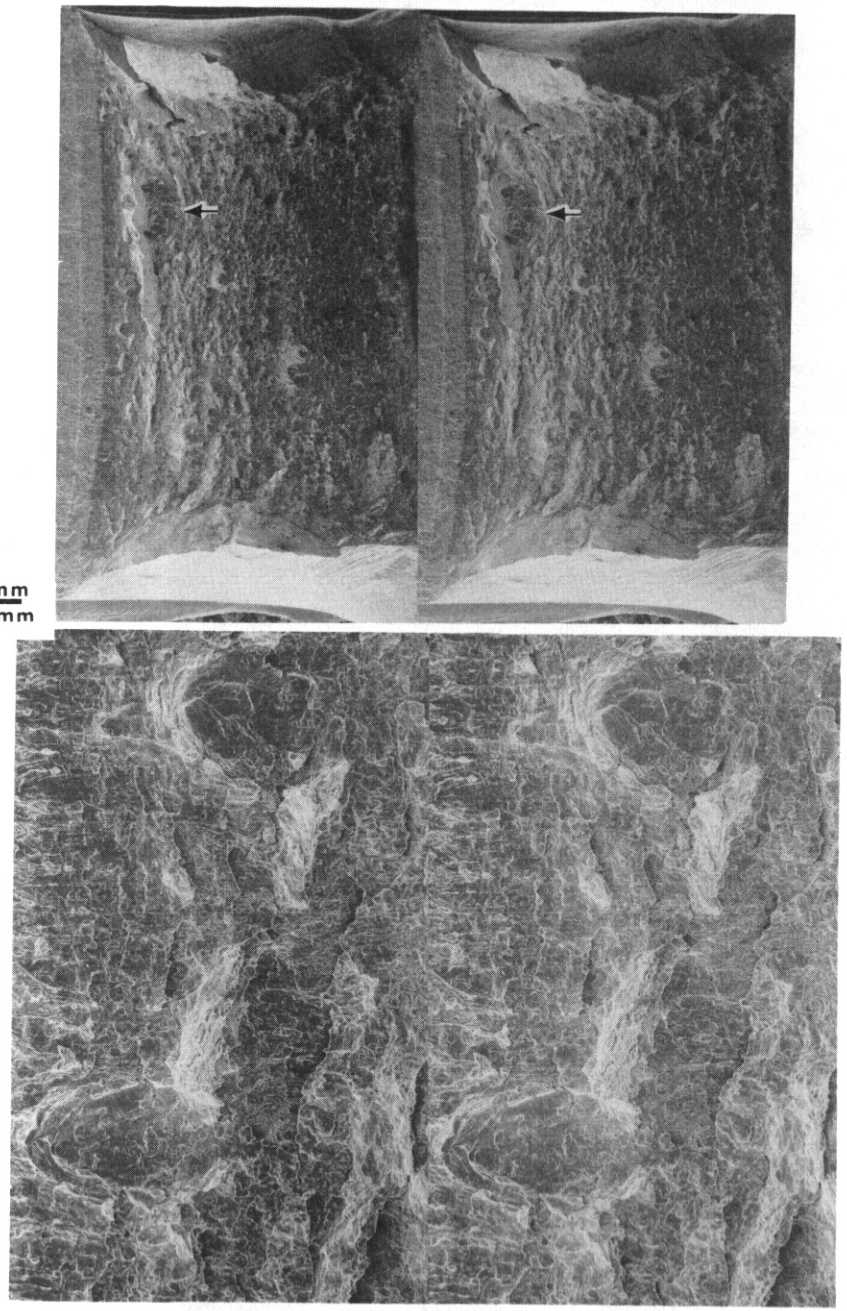

Fig. 7.10.14. Stereo pair fractographs of modified 9Cr-1Mo weld metal specimen NL11 irradiated at 450°C to 13 dpa and tested at 43°C.

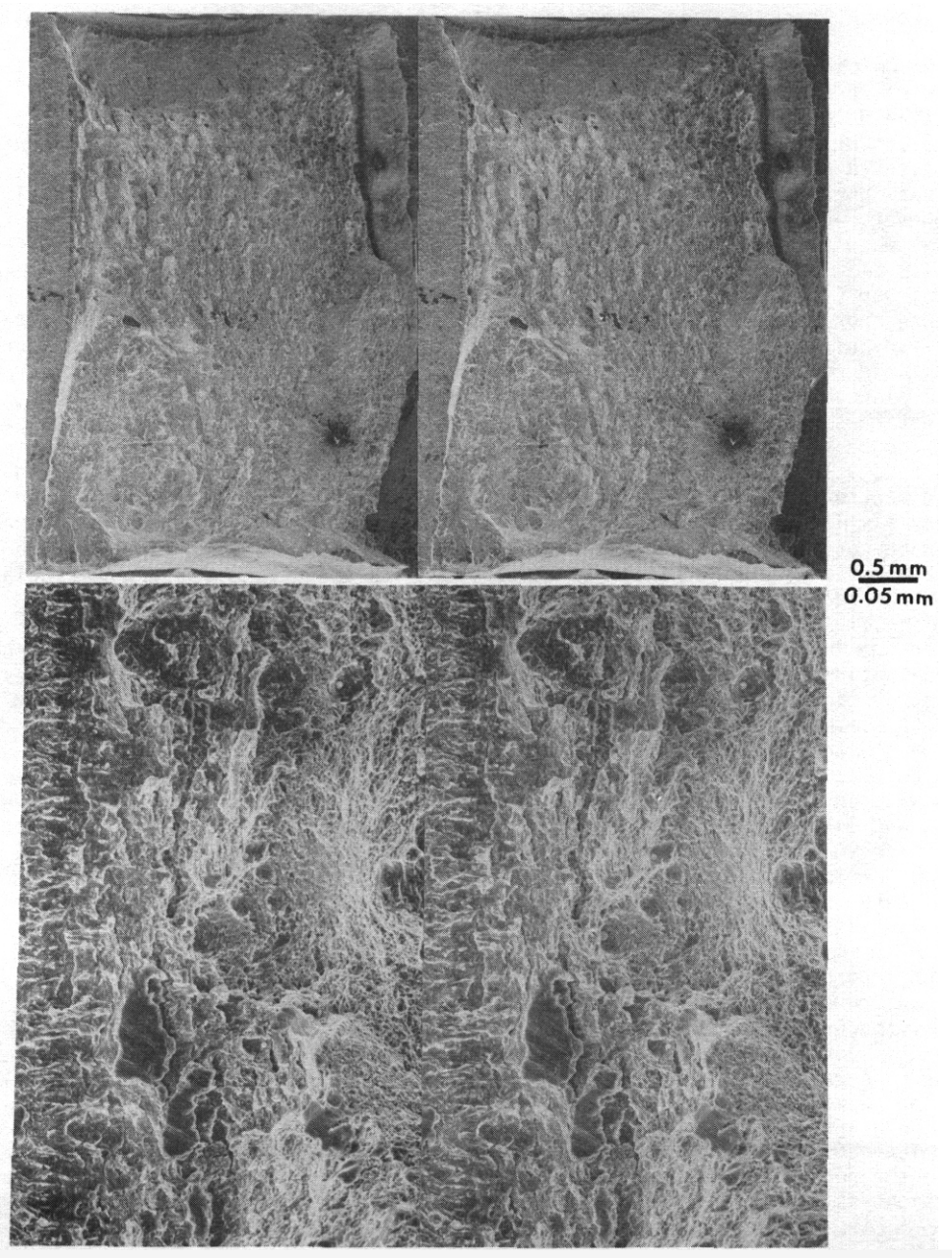

Fig. 7.10.15. Stereo pair fractographs of modified 9Cr-1Mo weld metal specimen NL31 irradiated to 550°C to 13 dpa and tested at 10°C.

ASTM 6 to 8.[3,4] Therefore, this differences is probably a consequence of delta ferrite effects on crack propagation; (3) an unusual banded structure was observed on two of the four specimens of condition KT which were examined. (This banded structure may be present but obscured on the other two specimens by other features.) Such structure is typical of weldmetal specimens where the effect is due to non-uniform internal stresses.

Figure 7.10.7 shows the fracture surface of specimen KT06 which was irradiated at 390°C to 13 dpa and tested at -7°C. The normalized fracture energy for this condition was 50.3 joules/cm' which corresponds to behavior at the transition temperature. The fracture appearance of specimen KT06 is typical of Charpy behavior at the transition temperature. A narrow ductile region is found adjacent to the fatigue surface. Adjacent to it is a brittle region which extends approximately half way across the specimen, and the remainder consists of ductile failure (or shear lips at specimen surfaces). The differences between this material and TT series specimens are the apparent disappearance of delta ferrite stringers effect and the smaller scale of the individual brittle plateau regions. Also of note is the observation of three regions in Figure 7.10.1 Part b (center to lower left) which appear to have a different texture than the remainder of the surface. The regions are uniformly gray in color and have

been marked by arrows. These features are believed to be typical of failure at prior austenite grain boundaries.

Specimen KT13 which was irradiated at 450°C to 13 dpa and tested at -18°C is shown in Figure 7.10.8. The normalized fracture energy measured was 70 joulesfcm' which corresponds to behavior at the transition temperature. Figure 7.10.8 provides an excellent example of ductile failure along a central band which separates two regions which failed by brittle fracture. This ductile band appears to contain seams up to 1 mm in length oriented normal to the fracture surface and parallel to the original crack tip. An explanation is that internal seams were created during rolling, but this is considered highly speculative. However, apart from this ductile bank, the fracture appearance of specimen KT13 is typical of failure in HT-9 when failure is not affected by delta ferrite stringers.

Figures 7.10.9 and 7.10.10 provide comparison of HT-9 plate material specimens KT20 and KT24 which were irradiated at 550°C to 13 dpa and tested at -7'C and 104°C, respectively. Specimen KT20 had a normalized fracture energy of 52 jouleslcm' which corresponds to behavior on the upper shelf. Figure 7.10.9 is very similar in appearance to Figure 7.10.8. Again a ductile central band can be seen separating two brittle regions with evidence for seams in this ductile region. Brittle behavior consists of relative small plateau regions characteristic of this condition. Figure 7.10.10 displays ductile response on the entire surface created during the Charpy test. At higher magnification, a few examples of large dimples can be seen; but, in general, ductile failure is associated with fine dimple rupture. However, in Figure 7.10.10a, three examples of fracture in association with delta ferrite (oriented parallel to the direction of crack propagation) can be identified. The structure on specimen KT24 appears to be very similar to that in the ductile region of specimen KT06, shown in Figure 7.10.7; therefore, it can be concluded that the upper shelf reduction found following irradiation at 390°C is not a result of a change in fracture mechanism in comparison with that found following irradiation at 550°C where the upper shelf reduction was much less severe.

9Cr-1Mo Base Metal. The Charpy test results for Modified 9Cr-1Mo base metal specimens indicated that negligible change in fracture behavior occurred as a result of a fluence increase from 13 to 26 dpa. Fractographic examinations in general confirmed that response, but significant differences were found as regarding the distribution of large dimples in ductile fracture.

Figure 7.10.11 shows the fracture surface of 9Cr-1Mo base metal specimen TV22 which was irradiated at 390°C to 26 dpa and tested at 29°C. The normalized fracture energy measured was 85.4 jouleslcm' which corresponds to a test at the transition temperature. The fracture surface was found to be typical for such a condition with an initial narrow ductile region, a brittle region covering just over half the fracture ligament and with the remaining surface ductile in appearance. The brittle fracture surface was similar in appearance to that for condition KT consisting of small plateau regions linked by steeply inclined transition regions. An example of brittle fracture far from the vicinity of the fatigue crack can be found in Figure 7.10.11b. A steep ledge can be seen separating the fatigue crack from the bottom of a brittle plateau region. However, such observations are not uncommon.

Specimen TV11, which was irradiated at 500°C and tested at 29°C, is shown in Figure 7.10.12. The normalized fracture energy for this specimen was 231.0 jouleslcm' which corresponds to upper shelf behavior. The fracture appearance for this condition was found to be completely ductile. Of particular note, however, was the presence of a large number of large dimples on the order of 50μm in diameter apparently arrayed in lines parallel to the direction of crack propagation. This corresponds to the rolling direction.[3] A re-examination of specimen TV22 (Figure 7.10.11) reveals that similar features were present following irradiation at 390°C to 26 dpa. These features were not found in unirradiated specimens but are prese t in specimen TV13 irradiated at 500°C to 13 dpa although the density of such dimples was much lower.' Therefore, irradiation of 9Cr-1Mo appears to be promoting the growth of cavity nucleation sites, the nucleation site probably associated with stringers in the alloy. Unless the density of such sight is greatly increased, the upper shelf response will not be affected significantly.

9Cr-1Mo Weld Ketal. The fracture surfaces of Modified 9Cr-1Mo weld metal specimens were found to be more contorted (nonplanar) than either base metal specimens of HT-9 and 9Cr-1Mo or weld metal specimens of HT-9.[2] Therefore, the plane strain stress state imposed by the specimen geometry was counteracted by the microstructure thereby allowing more plasticity prior to failure and higher upper shelf energies in 9Cr-1Mo weld metal compared to base metal conditions. Also, brittle failure was less extensive than in other conditions, often occurring in localized regions.

Figure 7.10.13 shows the fracture surface of Modified 9Cr-1Mo weld metal specimen NL05 which was irradiated at 390°C to 13 dpa and tested at 82°C. The normalized fracture energy was 107.5 joulesfcm' which corresponds to a temperature slightly below the transition temperature. Figure 7.10.13 reveals that the usual ductile regions immediately adjacent to the fatigue surface and across approximately half of the remaining part of the specimen ligament. However, a large brittle region does cover about a third of the specimen in a thumb-nail shaped area slightly below the center of the fractograph. Careful inspection showed that brittle failure also occurred in isolated regions "beyond the thumb nail" in the lower part of the fractograph. Also, the fracture surface is somewhat more contorted than those previously examined. A deep step is found in the middle of the thumb nail region, and a tall ridge appears to divide the fracture surface into two parts. Also. the shear lip at the lower part of the micrograph is unusually distorted. Therefore, it is likely that a significant fraction of the energy absorbed in breaking this specimen was due to the formation of this contorted fracture surfaced. In such a case, a fracture appearance transition temperature would be a more meaningful measure of ductile brittle transition behavior.

Specimen NL11 which was irradiated at 450°C and tested at 43°C is shown in Figure 7.10.14. The normalized fracture energy for specimen NL11 was 233.6 joules/cm² which corresponds to a test temperature

close to but somewhat above the transition temperature. Specimen NLll was found to have failed predominantly by dimple rupture; only a few small isolated regions showed brittle fracture. An example of brittle fracture is identified by an arrow in the upper left portion of the fractograph. Therefore, this specimen was tested at a temperature very close to the upper shelf. Evidence for a contorted fracture appearance due to the weldmetal microstructure can be found near the fatigue surface and at the lower left. However, this effect is not very pronounced in specimen NL11.

Figure 7.10.15 shows the fracture surface of specimen NL31 which was irradiated at 550°C to 13 dpa and tested at 10°C. The normalized fracture energy for this specimen was 241.4 which corresponds to a test temperature somewhat above the transition temperature. The fracture appearance of specimen NL31 was again mostly ductile failure, but a region in the lower left was found to be brittle. This fracture surface was also contorted. A large ridge can be seen in the lower left, unusual show lip formation in the lower center, and a raised region in the lower right. Therefore, based on fracture appearance, specimen NL31 would correspond to behavior at temperatures just below the upper shelf regime.

7.10.4.4 Discussion

This section will address the issues raised in Section 7.10.4.1. The purpose is to discuss the results of the examinations with regard to the objectives of the effort and to comment further on the effects of irradiation fluence composition and microstructure on fracture toughness.

Irradiation Fluence

Comparisons can now be made of fracture surface topography as a function of irradiation fluence for both HT-9 and 9Cr-1Mo base metal. Although irradiation does cause significant shift in ductile-brittle transition temperature (DBTT). reductions in upper shelf energy (USE) and hardness increases at 390°C for HT-9 and 9Cr-1Mo, the fracture appearance is relatively unchanged. Both ductile and brittle fracture surfaces on irradiated specimens look similar to fracture surfaces on unirradiated specimens. Therefore, it can be concluded that new mechanisms for failure, such as temperature embrittlement (where phosphorus, lead and antimony segregate to prior austenite grain boundaries) are not significantly enhanced by irradiation, at least to doses on the order of 26 dpa. The changes in fracture toughness must instead be attributed to changes in the microstructure so that failure occurs at lower plastic strain but at the same sites as the ones that operate in unirradiated material. For example, reductions in USE due to irradiation are likely due to enhanced carbide precipitation and intermetallic formation in the vicinity of carbide particles formed during heat treatment which leads to cavity nucleation and growth at lower plastic strains. Also, shifts in DBTT can be due to matrix hardening as a result of G-phase, α' and carbide precipitation and dislocation loop formation. (Voids are not present in HT-9 following irradiation in EBR-II to 26 dpa.) Therefore, it can be concluded, based on fractographic examination, that the effect of irradiation fluence on fracture toughness to 26 dpa is to facilitate cavity nucleation and to reduce the plastic strain prior to cavity nucleation and coalescence. No new mechanisms such as temper embrittlement become dominant.

Weld Metal Response. Weld metal specimens appear to consistently give slightly higher upper shelf energies than do base metal specimens. The present series of tests demonstrates this effect for 9Cr-1Mo,[1] and a similar conclusion can be drawn from results for HT-9 from the lower fluence discharge of AD-2. Fractographic examination provides an explanation. The fracture surfaces are more contorted; therefore, a larger region is plastically deformed ahead of the propagating crack, and more energy is absorbed. As a result, upper shelf energies are higher. This leads to a distorted Charpy impact energy curve, often non-symmetric about the transition temperature. A good example is provided in Figure 7.10.1d for 9Cr-1Mo specimens irradiated at 390°C. This distortion could probably be reduced by using a fracture appearance transition temperature (FATT) rather than an absorbed energy criterion.

Processing Effects for HT-9. Two conditions of HT-9 can be compared from the AD-2 Charpy specimen matrix. Series TT represents a "mi11 annealed" condition for HT-9 which differs from the standard condition in that it was austenitized at 1149°C for one hour and then hot worked prior to cooling to room temperature. It did undergo a full matrensite transformation, and the delta ferrite content remained in the acceptable range of 1%. In comparison, the KT series was given a lower annealing treatment 1038°C for four minutes. but the tempering conditions were similar (760°C for 30 minutes versus 750°C for one hour). Both series came from the same alloy heat. The difference in Charpy fracture behavior can be ascribed, based on the present effort, to the effects on fracture of delta ferrite stringers (and indirectly perhaps on rolling direction). The delta ferrite stringers appear to promote the growth of brittle cracks over large areas, crossing prior austenite grain boundaries. If the delta ferrite stringers are broken up by cross rolling, brittle cracks only extend to prior austenite boundaries; therefore, energy must be absorbed in breaking the ligaments between brittle cracks. Similar argument apply to ductile failure (upper shelf response); therefore, it can be concluded that fabrication procedures can have a measurable effect on toughness and that cross rolling is likely to be beneficial if the heat of HT-9 contains delta ferrite.

7.10.5 Conclusions

Significant hardening occurs both in HT-9 and 9Cr-1Mo following irradiation at 390°C whereas following irradiation at higher temperatures of 450°C and above, hardness remains constant or decreases slightly. Hardness decreases with increasing fluence of Hi-9 irradiated at 390°C and for Modified 9Cr-1Mo irradiated at 390°C and 500°C.

Fracture appearance is not altered significantly by irradiation to increasing fluence; therefore, new fracture mechanisms are not promoted by irradiation. Failure is controlled by the microstructure generated prior to irradiation, but the allowed plastic strain is decreased andlor the nucleation and coalescence of cavities is accelerated.

7.10.6 Future Work

This work will be continued when more Charpy specimens become available for examination.

7.10.7 References

1. W. L. Hu, "Charpy Impact Test Results of Ferritic Alloys at a Fluence of 6 x 10^{22} nlcm'," p. 106 in Alloy Development for Irradiation Performance Semiannual Progress Report for Period Ending September 30, 1985, DOE/ER-0045/13, Oak Ridge National Laboratory, Oak Ridge, TN.

2. D. S. Gelles and W. L. Hu, "Fractographic Examination of HT-9 and 9Cr-1Mo Charpy Specimens Irradiated in the AD-2 Test," p. 178 in Alloy Development for Irradiation Performance Semiannual Progress Report for Period Ending September 30, 1982, DOE/ER-0045/9, Oak Ridge National Laboratory, Oak Ridge, TN.

3. R. J. Puigh and N. F. Panayotou, "Specimen Preparation and Loading for the AD-2 Ferritics Experiment," p. 260 in Alloy Development for Irradiation Performance Semiannual Progress Report for Period Ending September 30, 1980, DOE/ER-0045/3, Oak Ridge National Laboratory, Oak Ridge, TN.

4. A. M. Ermi, "Reconstitution of the AD-2 Ferritics Experiment," p. 431 in Alloy Development for Irradiation Performance Semiannual Progress Report for Period Ending March 31, 1982, DOE/ER-0045/8, Oak Ridge National Laboratory, Oak Ridge, TN.

5. W. L. Hu, "Miniature Charpy Impact Test Results for Irradiated Ferritic Alloys," p. 255 in Alloy Development for Irradiation Performance Semiannual Progress Report for Period Ending September 30, 1982, DOE/ER-0045/9, Oak Ridge National Laboratory, Oak Ridge, TN.

8. COPPER AND ITS ALLOYS

8.1 SWELLING AND TENSILE PROPERTIES OF NEUTRON IRRADIATED COPPER ALLOYS FOR HIGH HEAT FLUX APPLICATIONS

R. J. Livak, T. G. Zocco, and J. C. Kennedy (Los Alamos National Laboratory)

0.1.1 ADIP Task

ADIP Tasks are not defined for copper alloys in the 1978 program plan. The tasks involved are similar to Tasks I.B.13, Tensile Properties of Austenitic Alloys, and I.C.2, Microstructures and Swelling in Austenitic Alloys.

0.1.2 Objective

The objective of this work is to determine the neutron irradiation response of four commercial, high-strength, high-conductivity copper alloys in order to plan future alloy development for high heat flux components.

8.1.3 Summary

Four commercial copper alloys and two elemental coppers were irradiated in EBR-II to fluences of 3 and 15 dpa at 385°C. The AMZIRC alloy and the two elemental coppers showed large swelling at the high fluence. The two precipitation hardened and cold worked alloys (AMZIRC and MZC) were softened significantly by the irradiation. The two alumina-dispersed alloys (A1-20 and A1-60) retained their mechanical strength after irradiation,

8.1.4 Progress and Status

8.1.4.1 Introduction

High-strength, high-conductivity copper alloys are being considered for several applications in fusion reactors such as the first wall in high power-density devices, resistive magnetic coils, and high heat flux components. The high thermal conductivity of copper-base alloys, relative to other candidate structural materials such as stainless steel and refractory alloys, offers the design potential of higher thermal fluxes at the first wall which is especially important for compact, high power-density reactors.[1,2] In support of engineering studies being done at Los Alamos National Laboratory on the Compact Reversed-Field Pinch Reactor (CRFPR), an independently supported research program was initiated at Los Alamos to study radiation damage effects in high-strength, high-conductivity copper alloys with the purpose of developing materials that will be capable of withstanding the operating environment in the fusion power core of the proposed CRFPR.

8.1.4.2 Procedure

Two elemental coppers and four dilute copper alloys were irradiated in the Experimental Breeder Reactor (EBR-II) at 385°C to two fluences ($E_n > 0.1$ MeV) of 0.4 and 2.0 x 10^{26} n/m^2 correspondins to about 3 and 15 displacements per atom (dpa). The nominal compositions of the six copper test materials (in wt%) are Marz-grade copper - 99.999% purity, oxygen-free (OF) copper - 99.95% purity, A1-20 - 0.20% alumina, A1-60 - 0.60% alumina, AMZIRC - 0.17% Zr, and MZC - 0.5% Cr + 0.18% Zr t 0.04% Mg. Control samples were annealed at the same time and temperature (245 days at 385°C) as the full-power days exposure of the irradiated samples. The irradiation temperature used is a realistic near-maximum temperature for high power-density first wall designs based on copper alloys.

The Marz-grade copper was irradiated in the cold rolled condition, and the oxygen-free copper had been annealed 5 minutes at 500°C in argon after cold rolling. The two precipitation-hardened alloys (AMZIRC and MZC) supplied by AMAX Base Metals were irradiated in the 90% cold rolled and aged condition (one hour at 425°C). The two alumina-dispersed copper alloys (A1-20 and A1-60) were supplied by SCM Metal Products that had produced them by the hot extrusion and subsequent fabrication of internally oxidized powders. These two alloys had been cold rolled 83% reduction in thickness followed by an intermediate anneal at 850°C in argon and then given a final cold reduction of 70% with a stress relief anneal at 850°C in argon.

Density changes for the control and irradiated samples were measured using the immersion method with bromobenzene. Room temperature tensile properties were determined for triplicate specimens measuring 35 mm long x 2 mm wide x 0.5 or 0.25 mm thick. Fractographic examination of the broken tensile specimens was conducted using a scanning electron microscope.

8.1.4.3 Results and Discussion

The increasesin volume (or swelling) after irradiation of these copper alloys are given In Table 8.1.1. The results are based on density measurements made of triplicate specimens with a typical standard deviation of about 0.3% for each condition. The two elemental coppers (Marz and OF) exhibited the same swelling response after irradiation within the accuracy of the density measurements. For the two alumina-dispersed copper alloys, the thin copper clad produced by the manufacturing process was chemically removed from the specimens before measuring the densities. The variability of the data for these two samples indicates

relatively little swelling at the high fluence compared to the other tested samples. The two precipitation-hardened copper alloys did not swell at the low fluence, whereas at the high fluence the AMZIRC alloy exhibited a large change in volume. Previous dual-ion irradiation experiments with this AMZIRC sample[3] found non-uniform void formation occurring in the temperature range 300-400°C. An encouraging observation is that the MZC alloy did not swell at the high fluence corresponding to about 15 dpa.

Table 8.1.1. Swelling of Neutron Irradiated Copper Alloys

	Volume % Increase After Irradiation	
Copper	Low Dose[1]	High Dose[2]
Marx-grade (99.999%)	1.8	6.8
Oxygen-free (99.95%)	2.1	6.6
Dispersion-Strengthened[3]		
A1-20	0.8	0.9
A1-60	1.1	0.6
Precipitate-Strengthened		
AMZIRC	nil	3.6
MZC	nil	nil

[1] Low dose exposure was 0.4 x 10^{26} n/m² (E_n > 0.1 MeV) at 385°C giving ∿ 3 dpa in copper.

[2] High dose exposure was 2.0 x 10^{26} n/m² (E_n > 0.1 MeV) at 385°C giving ∿ 15 dpa in copper.

[3] Densities measured after removal of oxygen-free copper clad.

Tensile properties measured at room temperature for the irradiated and control samples are given in Table 8.1.2. The cold worked, Marz-grade copper did not show any pronounced changes in 0.3% offset yield strength or ultimate tensile strength (UTS) due to neutron irradiation, although it did have a lower total elongation at the high neutron dose. The yield strength of the annealed OF copper doubled after the neutron irradiation with no change in the ultimate tensile strength. The two alumina-dispersed alloys exhibited relatively stable tensile properties after irradiation. The A1-20 sample showed greater tensile elongation at the high dose level indicating that some recovery of the cold worked microstructure may have occurred.

The two precipitation-hardened alloys exhibited pronounced softening after irradiation as reflected by the lower strength levels and the higher tensile elongations with the AMZIRC alloy showing larger changes than the MZC alloy. These two alloys were irradiated at a temperature somewhat below their aging temperature range so that radiation-enhanced overaging effects at long times would be anticipated. A previous investigation of the thermal and ion irradiated behavior of these two alloys found that Cu-ion irradiation accelerated dislocation recovery and grain recrystallization processes in the temperature range 300-550°C resulting in significant softening.[4]

The fracture surfaces of broken tensile specimens were examined in a scanning electron microscope. As shown in Figure 8.1.1, the OF copper control sample exhibited a very ductile failure as evidenced by the knife-edge fracture surface that may be associated with voids (see Figure 8.1.1d). The Marz-grade copper had similar fractographic features as the OF copper.

The fracture appearance of the A1-20 (and also A1-60) sample did not change with irradiation as seen in Figure 8.1.2a-b. The small dimples on the fracture surface are characteristic of a microvoid coalescence failure mechanism. The white particles appear to be alumina particles that may have initiated some of the dimples or microvoids. These observations confirm the measured ductility values (elongation and reduction of area) given in Table 8.1.2 that did not change very much with irradiation for the alumina-dispersed alloys.

Irradiation produced large changes in the fracture appearance of the AMZIRC samples (see Figure 8.1.3 a-b). The control specimen showed wavy slip or serpentine glide which characterizes ductile failure. After irradiation, large dimples were observed on the fracture which may be associated with voids formed during neutron irradiation. The large measured tensile elongation for the high dose specimens is partly attributed to the grain boundary fissures that occurred along the length of the specimen (see Figure 8.1.3c).

Table 8.1.2. Tensile Properties of Neutron Irradiated Copper Alloys

Alloy / Condition		Yield Strength (MPa)	UTS (MPa)	Elongation (%)	Reduction of Area (%)
Marz Cu:	Control	31	152	24	89
	Low dose	33	155	25	80
	High dose	41	149	17	48
OF Cu:	Control	26	196	27	90
	Low dose	51	200	30	59
	High dose	49	185	24	46
A1-20:	Control	337	395	14	48
	Low dose	353	411	14	51
	High dose	343	395	20	50
A1-60:	Control	397	466	12	56
	Low dose	402	468	10	43
	High dose	379	449	11	50
AMZIRC:	Control	271	334	9	70
	Low dose	274	317	9	73
	High dose	71	226	34	44
MZC:	Control	431	458	10	61
	Low dose	379	437	13	56
	High dose	284	354	17	57

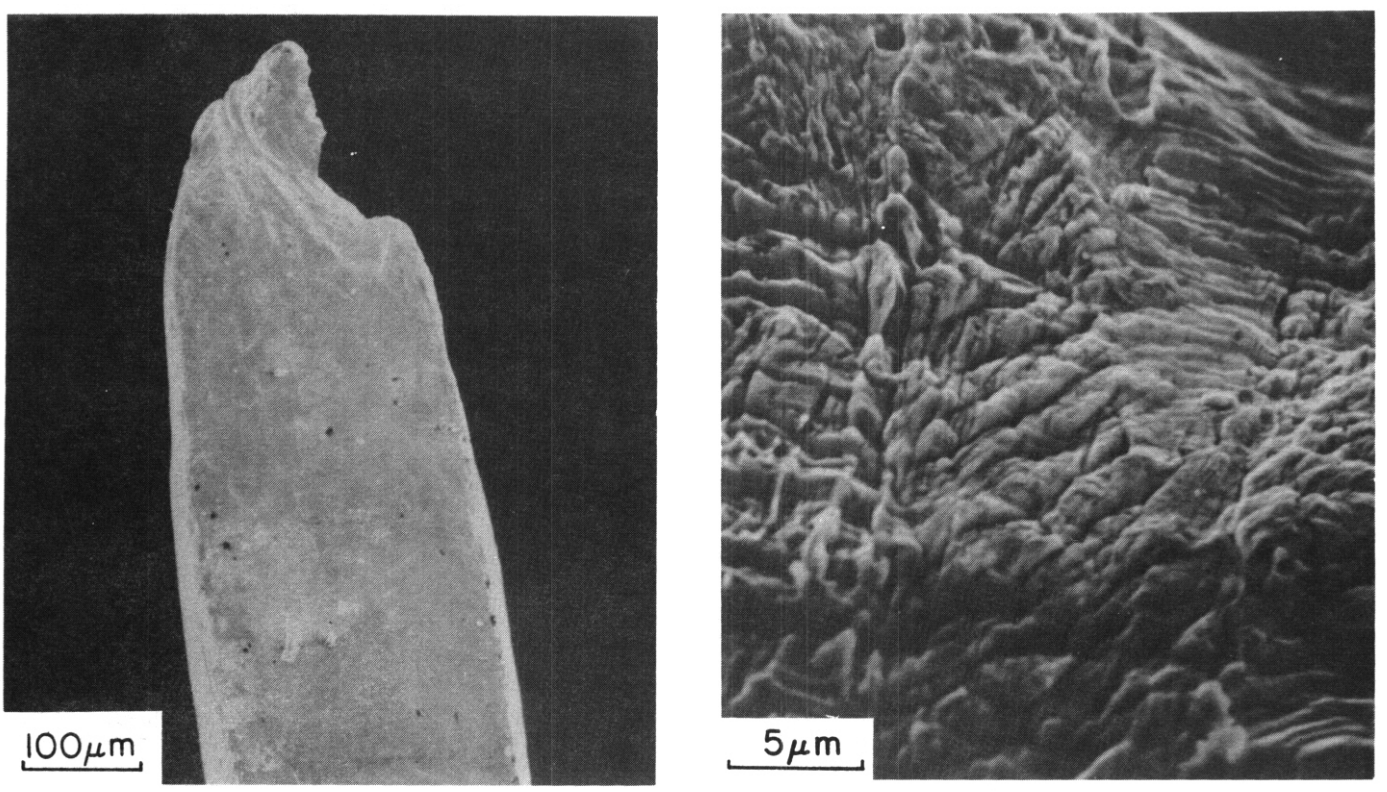

(a) (b)

Fig. 8.1.1a-b. Fractographs of oxygen-free copper sample. (a) Side view showing knife-edge necked region. (b) Wavy slip steps indicative of ductile failure.

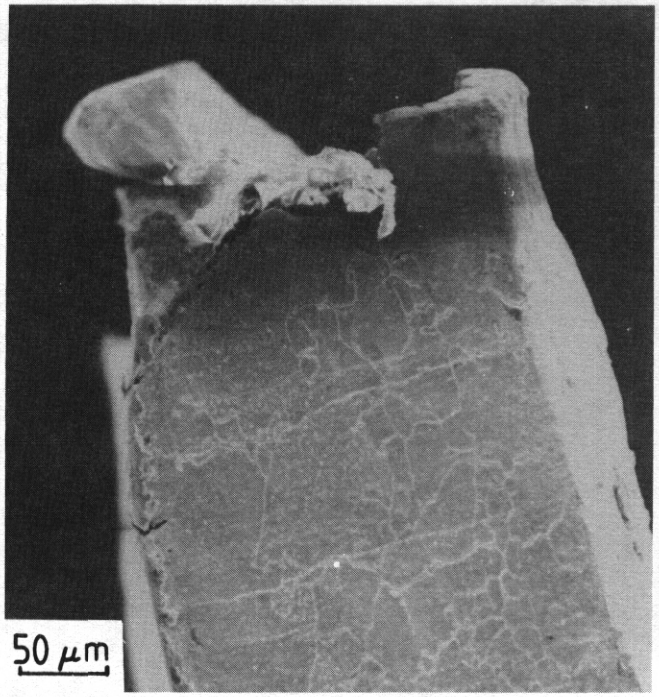

(c).

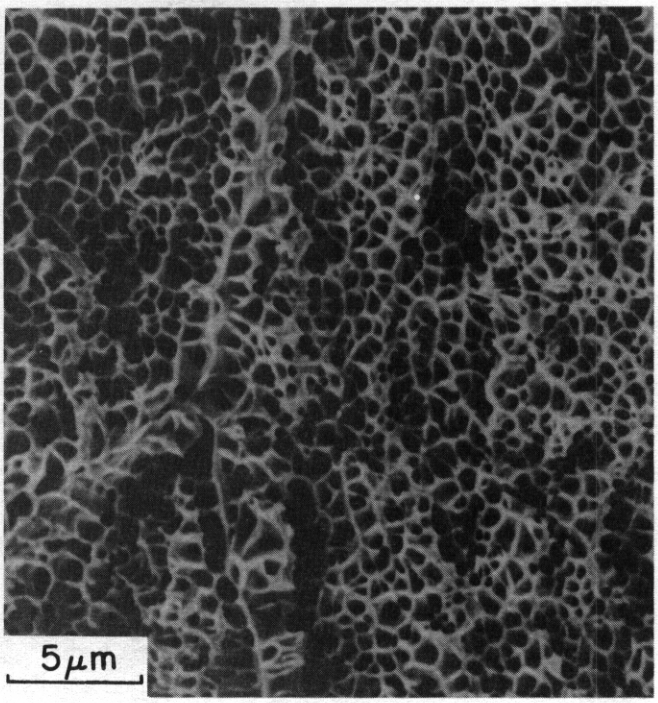

(d)

Fig. 8.1.1c-d. Fractographs of oxygen-free copper, high dose sample. (c) Side view showing reduced necking at the fracture. (d) Large dimples may be associated with voids produced by irradiation.

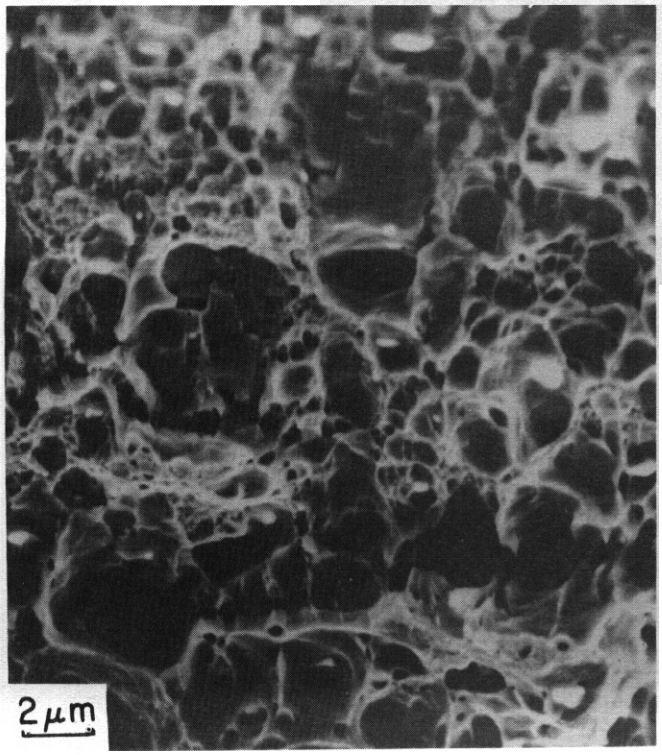

(a)

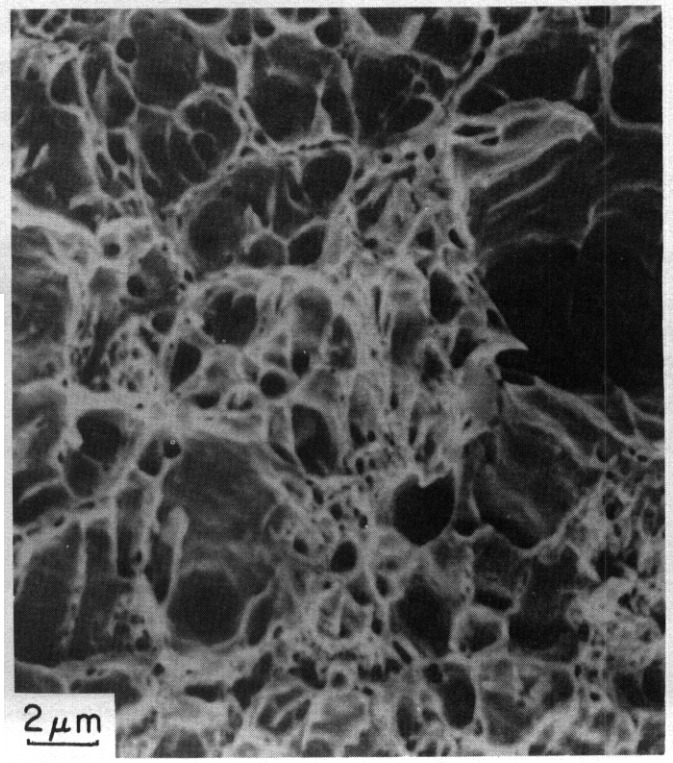

(b)

Fig. 8.1.2a-b. Fractographs of alumina-dispersed A1-20 samples. (a) Control sample showing microvoid coalescence failure. (b) High dose sample with similar fracture appearance as (a).

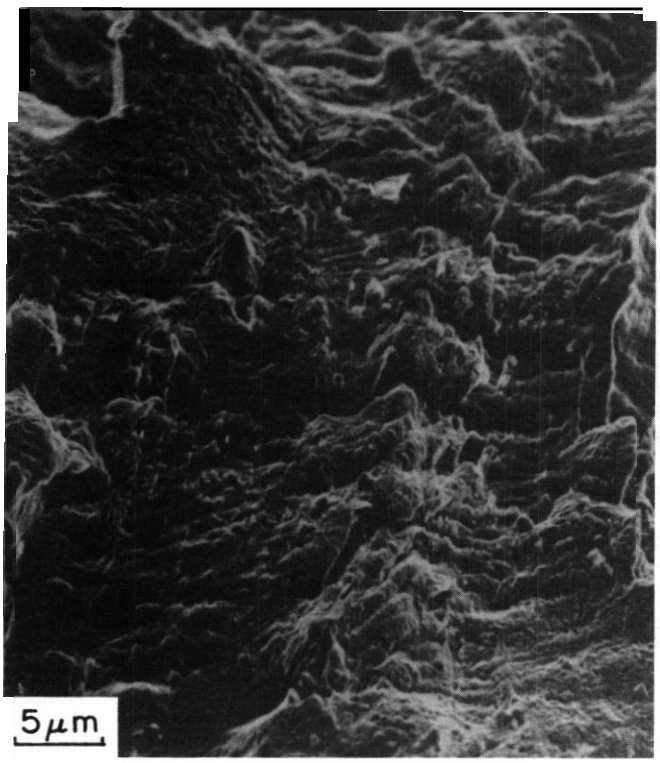

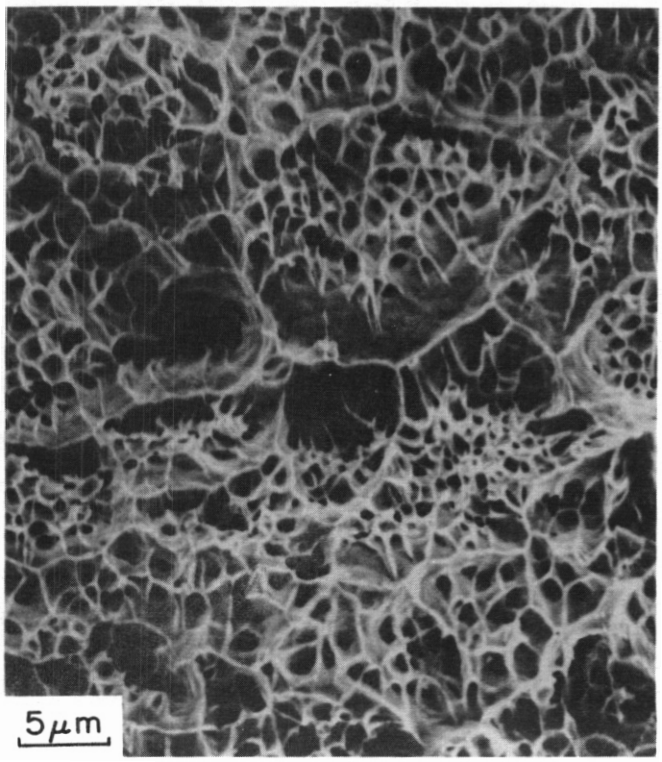

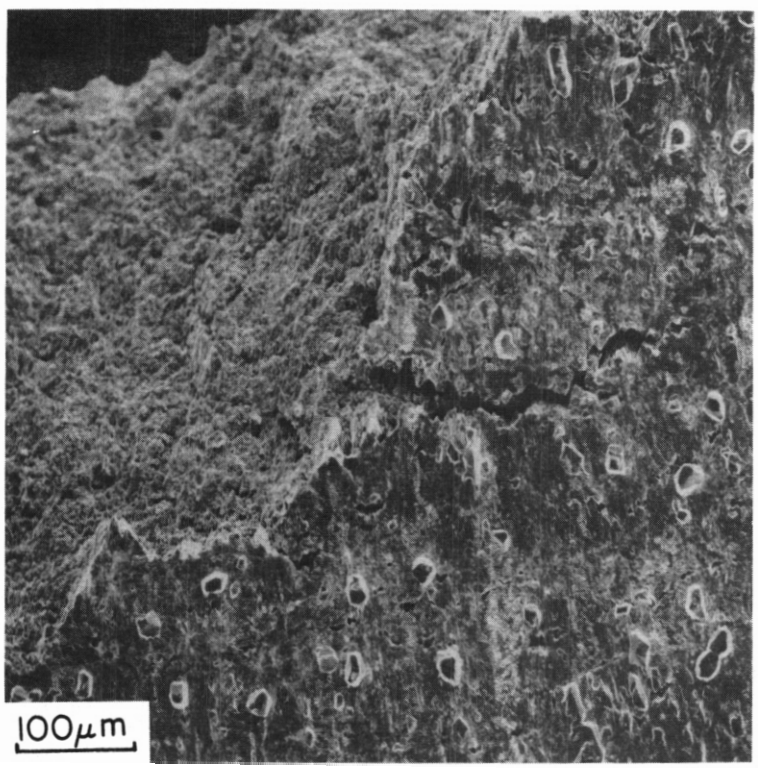

Fig. 8.1.3a-c. Fractographs of AMZIRC samples. (a) Control sample showing serpentine glide on a ductile failure. (b) High dose sample with dimples that may be associated with voids produced by neutron irradiation. (c) High dose sample showing grain boundary fissures and protruding grains on the side surface of the broken tensile specimen.

Chemical analyses for three of the copper test materials are given in Table 8.1.3 for both irradiated and unirradiated samples. Transmutation of copper by neutron irradiation increased the nickel and zinc contents of all three materials by measurable amounts. The major effect of these chemical changes for MFE applications will be to decrease the thermal conductivity of the materials during irradiation with subsequent impact on the design and operating parameters of a fusion energy device.

Table 8.1.3. Chemical Analyses of Neutron Irradiated Copper Alloys

	Marz Cu		A1-60		MZC	
Element	Control*	15 dpa*	Control	15 dpa*	Control	15 dpa*
Ag	<1	<2	20	15	20	15
Al	<1	6	4500	5000	40	<10
As			120*	<400	90*	<400
Be		<1	<1	<1	<1	<1
Bi		<6	<4	6	<4	<6
Ca		1.5		2		<2
Cd		<10	<4	<10	<4	<10
Co		<10	<10	<10	<10	<10
Cr		12	10	6	5100	4000
Fe	<1	80	60	100	70	100
Hg			37*		40*	
Mg		3	1	3	450	500
Mn		<2	<4	<3	4	3
Mo	<1	<10		<10		<10
Na	<1	<40		<30		<30
Ni	<1	600	10	500	10	500
P			6		4	
Pb		<10	<10	12	<10	<10
O	1		4920		110	
S			15		30	
Sb		<40	<40	<40	<40	<40
Se			80*		80*	
Si	8	12	<10	5	<10	100
Sn	<1	<10	30	30	<10	150
Ti	<1	<20	<10	<20	<10	<20
Zn		1000	<40	800	<40	800
Zr	<1	<20	<10	<10	1800	1000

*Analyses done by quantitative emission spectroscopy with a factor of two accuracy and a precision of 50% relative standard deviation.

The control samples of A1-60 and MZC were analyzed using inductively coupled plasma spectroscopy, unless marked with an asterisk, and have an accuracy withing 20% relative of the true value and a precision of 3 to 5% relative standard deviation.

Results are expressed as parts per million (ppm) by weight. Result preceded by a < symbol represents the limit of detection.

Microstructural changes resulting from neutron irradiation were studied using transmission electron microscopy. Thin foils prepared from irradiated and control samples were examined in the Philips 400T and the JEOL 200B electron microscopes. Because the control samples had effectively been annealed for an extended time at 385°C, the two elemental coppers (MARZ and OF) had large grain structures with very few dislocations. After the low dose irradiation, large, faceted voids or bubbles that extended through the thin foils were observed in the elemental coppers as shown in Figure 8.1.4.

The alumina-dispersed copper alloys appear to have relatively stable microstructures under the fast neutron irradiation conditions studied. Both the A1-20 and A1-60 alloys have fine grain sizes of a few micrometers in diameter. The alumina particle dispersion is more uniform in the A1-20 alloy than in the A1-60 alloy which has a few large, isolated particles surrounded by regions of smaller and more numerous particles. The particles range in size from about 10 nm to 60 nm. Extraction replicas made from both irradiated and control samples have not revealed any discernible changes in the alumina particle dispersion as a consequence of neutron irradiation. Figure 8.1.5 shows a typical area of an extraction replica made from an A1-60 control sample. The alumina particle morphology varies from equiaxed particles to flat, triangular ones.

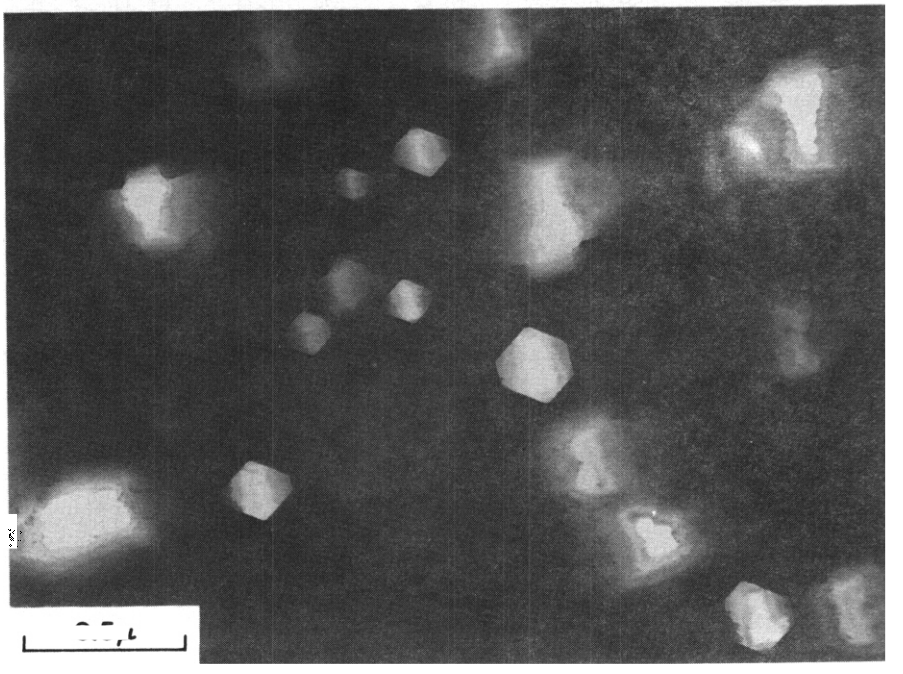

Fig. 8.1.4. Transmission electron micrograph of oxygen-free copper sample exposed to about 3 dpa damage at 385°C. The large, faceted voids extend through the foil thickness.

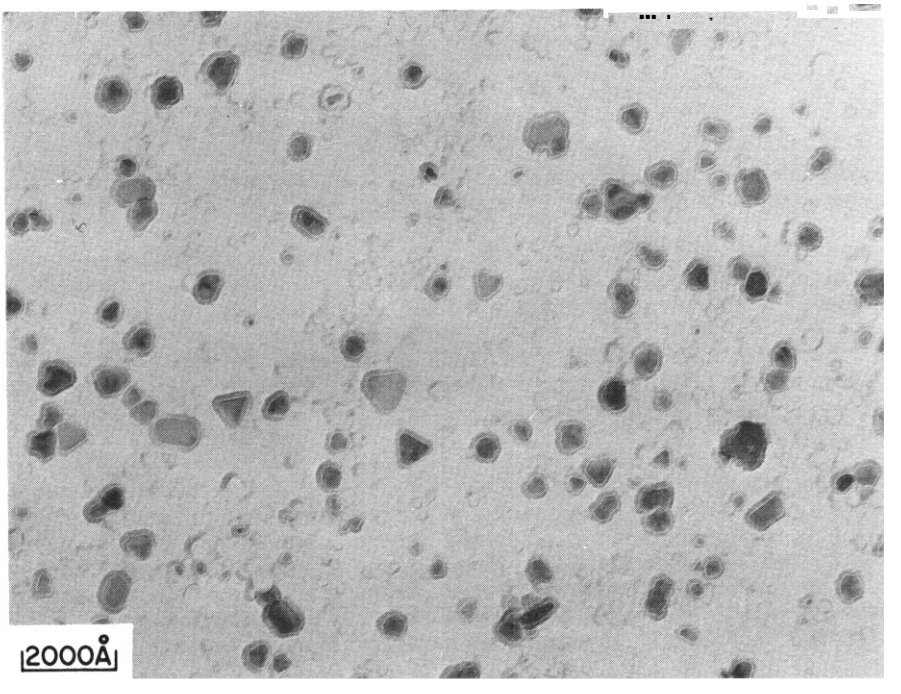

Fig. 8.1.5. Extraction replica prepared from A1-60 control sample showing the alumina particle dispersion.

Examination of the precipitation-hardened MZC alloy has not revealed any microstructural changes nor void formation after neutron irradiation to about 15 dpa at 385°C. Single ion irradiation experiments done at the University of Wisconsin[5] found that the MZC and AMZIRC alloys were resistant to void swelling after irradiation to a calculated peak damage level of 40 dpa at 100-400°C. The absence of void formation was attributed to the low oxygen content in the foils and the absence of helium. The micrograph in Figure 8.1.6 shows a typical area in an MZC sample exposed to 15 dpa damage at 385°C. There are a few large inclusions and numerous small, spherical particles about 50 nm in diameter that are presumably the Cu_5Zr precipitates. The microstructure is polygonized with well defined dislocation cell walls.

Additional examination using analytical electron microscopy will be done to ascertain any microstructural or microchemical changes that may have been produced during neutron irradiation of these copper alloys at 385°C.

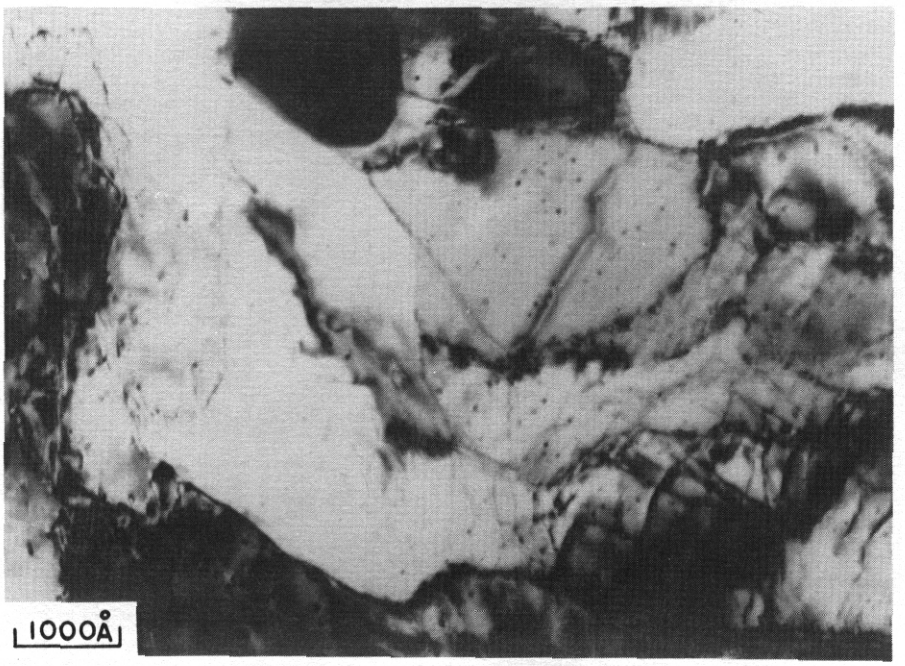

Fig. 8.1.6. Transmission electron micrograph of MZC copper alloy exposed to about 15 dpa damage at 385°C. The small, dark spherical particles are presumably Cu_5Zr precipitates.

8.1.4.4 Conclusions

Fast neutron irradiation at 385°C to a damage level of 15 dpa produced large swelling of elemental copper and the Cu-Zr (AMZIRC) alloy. The other three commercial alloys tested, (MZC, Al-20, and Al-60) did not exhibit pronounced swelling under these irradiation conditions. The two precipitation-hardened alloys softened significantly after irradiation, whereas the two alumina-dispersed alloys showed relatively stable tensile properties after irradiation. Nickel and zinc are produced by transmutation reactions in copper alloys during fast neutron irradiation, and the increased solute content will decrease the thermal and electrical conductivities. Additional evaluation and development of oxide-dispersed copper alloys are needed to establish the viability of using these materials for high heat flux components in MFE applications.

8.1.4.5 References

1. O. K. Harling, G. P. Yu, N. J. Grant and J. E. Meyer, "Application of High Strength Copper Alloys for a Fusion Reactor First Wall," *J. Nucl. Matls.* 103 & 104, 127-132 (1981).

2. R. L. Hagenson et al., *Compact Reversed-Field Pinch Reactors (CRFPF): Preliminary Engineering Considerations*, La-10200-MS, Los Alamos National Laboratory, Los Alamos, New Mexico, 1984.

3. S. J. Zinkle, R. A. Dodd, and G. L. Kulcinski, *Comparison of Thermal and Irradiated Behavior of High-Strength, High-Conductivity Copper Alloys*, University of Wisconsin Fusion Engineering Report UWFDM-581 (June 1984), Madison, Wisconsin.

4. J. A. Spitznagel and J. W. Davis, "Response of Selected High Strength, High Conductivity Copper Alloys to Simulated Fusion Irradiation and Temperature Conditions," to be published in *Alloy Development for Irradiation Performance Progress Report (April-Sept. 1984)*, DOE/ER-0045/13, Oak Ridge National Laboratory, Oak Ridge, Tennessee.

5. S. J. Zinkle, and G. L. Kulcinski, "Ion Irradiation of Copper and Copper Alloys to 40 dpa at 100-400°C," pp. 77-84 in *Damage Analysis and Fundamental studies Quarterly Progress Report October-December 1984*, DOE/ER-0046/20, Office of Energy Research, Washington, DC, February 1985.

8.2 NEUTRON-RADIATION INDUCED CHANGES IN ELECTRICAL RESISTIVITY OF COPPER ALLOYS FOR MFE APPLICATIONS - H. M. Frost and J. C. Kennedy (Los Alamos National Laboratory)

8.2.1 ADIP Task

ADIP Tasks are not defined for copper alloys in the 1978 program plan.

8.2.2 Objective

To identify, by fast-neutron irradiation and post-irradiation testing, one or more mechanically acceptable copper alloys with low yet stable dc electrical resistivity values (ρ_e) and thus with attractive thermal conductivity (K) performance for first-wall applications.

8.2.3 *Summary*

Values of ρ_e were measured for two elemental (high-purity) coppers and four commercial copper alloys subjected in EBR-II to neutron fluences of 0.4 and 2.0 $\times 10^{26}$ n/m^2 at 658K. Relative to annealed controls, two alumina-dispersed alloys gave the best results: Increases in ρ_e (and 1/K) of 6-7% at the high fluence, with no significant changes (per paper 8.1 preceding) in the corresponding yield stresses. Changes in ρ_e for MZC and AMZIRC Cu alloys were smaller than this, but the corresponding yield stresses were strongly diminished at the high fluence. Void swelling and accumulation of transmuted Ni and Zn contributed significantly to the observed changes in ρ_e.

8.2.4 Progress and Status

8.2.4.1 Introduction

Recent trends in magnetic fusion energy (MFE) concepts have evolved toward more compact reactor designs such as the compact reverse-field pinch reactor (CRFPR) being developed at Los Alamos. Such designs incorporate smaller confined plasmas with higher power densities that give more intense first-wall loading by fast neutrons, high thermal fluxes, and other forms of radiation. In addition, thermal energy can be deposited in the first wall by the eddy currents induced either by the toroidal plasma current or by the time-varying magnetic induction field accompanying coil turn-on during pulsed operation. Cyclic mechanical stresses will result from both thermal gradients through the first-wall thickness and induced electromagnetic forces throughout the first-wall volume. The thermal-mechanical fatigue resistance of first-wall materials is thus an important consideration. All other things being equal, this resistance becomes greater the greater the values of K and $1/\rho_e$ of the first-wall material. That is, good heat conduction through the first wall will lead to small gradients in temperature, and high electrical conductivity will result in small temperature increases arising from resistive heating. Further, high K's will reduce the peak surface temperatures of the first wall resulting from sputtered-target heating.

High values of K and $1/\rho_e$ are also desirable in other fusion reactor designs for these same reasons. The absence of magnetically active metals such as Ni and Fe in the first-wall alloy also means the absence of hysteresis losses which could further add to the peak operating temperature requirements of the first wall.

For the preceding reasons, a high-conductivity copper alloy of suitable mechanical strength is an attractive candidate for a first-wall material. At first look, it may not seem as attractive as alloys with better strength at high temperatures. However, a computer simulation has predicted a peak copper first-wall temperature of 0.4 of the melting temperature T_m to arise in CRFPR design'. This is within the nominal limit of 0.5 T_m below which little degradation occurs in the structural performance of most alloys at or above room temperature.

Furthermore, copper alloys strengthened by oxide dispersion or by precipitates have surprisingly good performance (at $T<T_m/2$) relative to high-temperature alloys. If S_y/ρ_e is taken to be an abbreviated figure of merit' -- with S_y the room-temperature yield stress at 0.2% offset -- then (unirradiated) annealed values for any of the four strengthened Cu alloys featured in this report turn out to be nearly an order of magnitude higher than for Type 316 stainless steels or 6-4 Ti alloys. The Cu-alloy values were 150-220 MPa/μΩ-cm, vs. about 20 to 30 MPa/μΩ-cm for (pure) titanium and for 316 stainless steel.[3,4]

A major purpose of this study was thus to see how well these Cu alloys "held up" under irradiation by fast neutrons (E>0.1 MeV).

The elemental coppers used in this study were an oxygen-free high-conductivity (OFHC) copper which' had been annealed 5 min at 775 K in argon after cold rolling, plus a high-purity (99.999%), Marz-grade copper initially in the cold-rolled condition. Two precipitation-hardened alloys, MZC and AMZIRC, were supplied by AMAX Base Metals and were tested in the 90% cold-rolled and aged condition (1 hr, at 700 K). The other two commercial materials studied were the alumina-dispersed copper alloys A1-20 and A1-60 supplied by SCM Metal Products, with nominal concentrations of alumina of 0.2 and 0.6 wt.%, respectively. They were cold rolled to a 83% reduction in thickness, then annealed at 1123 K in argon, and finally given a final cold roll reduction of 70% with a stress-relief anneal at 1123 K in argon.

In the succeeding paragraphs, we present details of the irradiation experiment and the resistivity measurement setup, then results and discussion of the as-measured values and the corresponding porosity and transmutation-product contributions to ρ_e. Finally, we discuss our results in terms of a recent study.

8.2.4.2 Experimental Details

The elemental coppers and copper alloys were irradiated at 385°C as "matchstick" specimens in the Experimental Breeder Reactor (EBR-II) at Idaho Falls at fluences of 0.4 and 2.0 x 10^{26} n/m^2 corresponding to damage levels in copper of 3 and 15 dpa, respectively. Control specimens were annealed for the same time and temperature conditions (245 days at 385°C) as for the full-power irradiation. All specimens were cut from sheet stock to lengths and cross sectional areas of 3.5 cm and ½ to 1 mm^2, respectively.

The setup for the four-point measurements of the (dc) electrical resistivity ρ_e made on these specimens is illustrated in Fig. 8.2.1. A programmable source of current I was connected to the ends of the specimen S while the voltage drop V was measured across an electrical gage length L defined by the spacing between 'knife-edge' contacts. The specimen was pressed against all four contacts by insulated contact weights of weights F, and room temperature was monitored by a thermocouple TC. A number of current "steps" of different amplitudes and of both polarities were included in the current sequence programed in order to remove zero-offset errors in the readings taken from the digital nanovoltmeter. The setup, measurement protocols, and reduction of the resistance data (V/I) to ρ_e values at 20°C were based essentially on ASTM Standard Test Method B193-78.

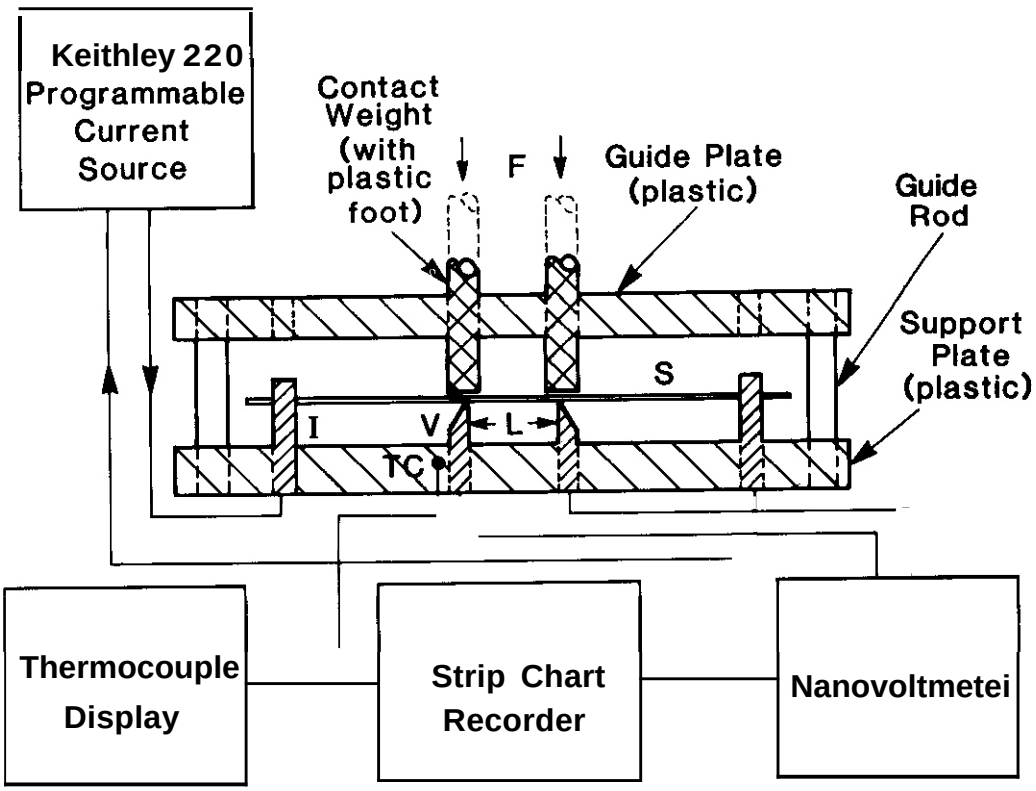

8.2.4.2 Results and Discussion: As-Measured Properties

Table 8.2.1 presents the results for control (C), low-fluence (L), and high-fluence (H) specimens for the elemental coppers OFHC and MARZ and the alloys A1-20, A1-60, MZC, and AMZIRC. Typical standard deviations for the as-measured values of ρ_e are 0.015 μΩ-cm. The ρ_e values were converted to the corresponding IACS values of conductivity σ_{IACS} in percent via the relation σ_{IACS} 172 41/ρ_e. The accuracy of the measurements is indicated by the agreement obtained between measured and tabulated values of ρ_e for the specimens of elemental copper: 1.70 vs. 1.71 μΩ-cm for OFHC and 1.67 vs. 1.67 μΩ-cm for MARZ (pure copper).[5] Furthermore, the control values of σ_{IACS} for MZC and AMZRIC agree to within 1-2% of values published for these alloys annealed at 550°C for 1 hr.[6]

In a limited and artificial sense, the high fluence produced about the same result in five of the six Cu types: The corresponding spread in the values of σ_{IACS} is only 5%, excluding A1-60. Further, it would

seem at first look that the precipitation-hardened alloys gave better results (after the high fluence) than the alumina-dispersed alloys, viz., values of σ_{IACS} in the 90's vs. the 80's.

Table 8.2.1. DC Electrical resistivity results for copper alloys irradiated to two fluences by fast neutrons

Copper Material	Neutron Fluence	Electrical Properties As Measured σ_{IACS} (%)	ρ_e ($\mu\Omega$-cm)	$\delta\rho_e/\rho_e$ (%)	Ratio of Yield Stress[2] to (MPa/μΩ-cm) Resistivity	% Change
OFHC	C	101	1.70	0.0	15	0
	L	95	1.82	7.0	28	87
	H	87	1.98	16.7	25	67
MARZ	C	103	1.67	0.0	19	0
	L	97	1.78	6.6	19	0
	H	87	1.98	18.6	21	1
Al-20[3]	C	94	1.84	0.0	183	0
	L	90	1.91	3.9	184	0
	H	88	1.96	6.1	175	-4
Al-60[3]	C	87	1.99	0.0	199	0
	L	83	2.08	4.3	193	-3
	H	81	2.13	7.1	178	-11
MZC	C	90	1.93	0.0	224	0
	L	89	1.94	0.7	195	-13
	H	92	1.88	-2.4	151	-33
AMZIRC	C	97	1.77	0.0	153	0
	L	97	1.78	0.5	154	0
	H	92	1.87	5.3	38	-75

[1] C=Annealed Control, L=low fluence (0.4 x 10^{26} n/m^2), and H=high fluence (2.0 x 10^{26} n/m^2). Reactor: EBR-II (E>0.1 MeV).

[2] Yield stress data (0.2% offset) from R. Livak et al, preceding paper (8.1).[11]

[3] With a nominal 5% cladding of OFHC Cu on each side.

However, the data column "$\delta\rho_e/\rho_e$" in Table 8.2.1 shows that the greatest percent changes in ρ_e occurred for the elemental coppers and that the ρ_e increases were roughly comparable for Al-20, A1-60, and AMZIRC. Only MZC showed a decrease here -- small but significant. The preceding picture for the alloys is misleading, though, since it leaves out the effects of radiation on other important properties of the alloys. A more reliable way to assess the effects of irradiation on the performance of a first-wall material is via the thermal stress parameter M (with units of W/m):[2]

$$M = 2S_y K(1-\nu)/(\alpha E). \qquad (1)$$

This quantity includes the effects of yield stress S thermal conductivity K, Poisson's ratio v, coefficient of thermal expansion a, and Young's modules E The major effects of neutron irradiation are expected on only S_y and K, however.

For highly conductive metals (such as copper) near or above their DeBye temperatures (θ), K and ρ_e are related to temperature by the equations

$$K = K_e + K_l$$
$$K_e\rho_e = L_oT, \qquad (2)$$

where K_e and K_l are the electronic and lattice contributions to K, and L_o is the Lorenz number. For Cu, θ=310K; also L_o=22.6 nW-Ω/K^2.[7] Since, for Cu, K_l/K_e<<1 at or above room temperature, Eq. (1) can be rewritten approximately as

$$M_R = 2T[(S_y/\rho_e)(1-\nu)L_o/(\alpha E)]_R.$$

Since for a potential first-wall material, M should be evaluated for the case of radiation exposure, a subscript R has also been added to include this case as well.

To a first approximation, Eq. (3) can be rewritten as

$$M_R = 2T(1-\nu)L_o(S_y/\rho_e)_R/(\alpha E).$$

An abbreviated form of M_R is thus $M'=(S_y/\rho_e)_R$, and values of this quantity are accordingly tabulated in Table 8.2.1 (for R=L or R=H). Compared to the ρ_e data **per se**, an entirely different performance pattern now emerges for the Cu alloys. Looking specifically at the high-fluence case (R=H) shows that the radiation-induced changes in M' are much greater for the precipitation-hardened than for the alumina-dispersed alloys. The latter would thus appear to be even more stable under the more intense irradiation conditions (R>H) of a fusion, as opposed to fission, reactor.

In fact, the percent change in M' for either fluence is 3 to 4 times higher for MZC than for A1-60. Relative to Al-20, the M'-changes for MZC are even higher. As a result for MZC, A1-20, and A1-60, the M_R ranking of MZC falls from first (for R=C) to last place (for R=H).

This difference in property stabilities may be due to the non-equilibrium nature of a precipitation-hardened alloy that is quenched (by the manufacturer) from above its solvus temperature. The subsequent cold working and aging, performed by the manufacturer to increase the strength, bring fine precipitates out of solution whose sizes and spacings are optimum and lattice-coherent. Nevertheless, these sizes are still smaller than those which would arise **if** the alloy were aged sufficiently long. The corresponding effect of the neutron irradiation may then be a tendency to drive the alloy towards a new equilibrium compared to the equilibrium tending to result from aging alone (e.g., as from 385°C for 245 days). Inasmuch as the irradiation superimposes on the thermal stress additional stresses, such as of atoms displaced by scattered neutrons, the rate at which this equilibrium is achieved also may be changed, e.g., increased.

A radiation-induced change in the equilibrium state of a precipitation-strengthened alloy could correspond, for example, to a new equilibrium concentration of solute in the Cu matrix (as of Cu_5Zr in AMZIRC). The radiation may have the net effect of producing sinks, in either the matrix or on the grain boundaries, that trap solute atoms from solution. In turn, the corresponding depletion of solute levels may, by mass action, "drive" the diffusion of solute atoms into solution that originate from those fine precipitates having the optimal sizes and interparticle spacings for preventing recrystallization. The neutron irradiation may also speed up the process of precipitate coarsening due to surface-tension effects on the matrix-precipitate interfaces, but limited by the tendency of the fast neutrons to disperse particle aggregates. Some combination, then, of the preceding and/or other processes may have the net effect of reducing the effectiveness of the ability of the alloying elements to both scatter conduction electrons and to strengthen the alloy. This apparently happened with MZC: Both ρ_e and S_y decreased as a result of the high fluence. As seen in the next section (8.2.4.4), the same reasoning appears to apply also to AMZIRC.

To conclude this section, we observe that line charts of M vs. T have been published for various unirradiated alloys, including MZC, for T's of about 0-500°C.[2,8] Our work indicates, however, that such line charts should also be generated and published for M_R Vs. T in order to provide a more realistic basis of comparison for potential first-wall materials.

8.2.4.4 Results and Discussion: Porosity and Transmutation Contributions

The preceding results and discussion have dealt with the as-measured values of ρ_e for irradiated copper alloys and with their impact on an evaluation of the thermal-mechanical performance of first-wall Cu-alloys. However, as is shown in succeeding paragraphs, these values can also be converted into estimates of what the ρ_e values would be **if** the increases due to porosity swelling and transmutation products were subtracted out. The differences between the resulting corrected values and the corresponding (annealed) control values yield ρ_e 'residues', i.e., the remaining changes in ρ_e due to some other mechanism(s) such as a phase change or microstructural damage.

First considered is the effect of porosity swelling of an initially fully dense material on ρ_e. For simplicity, only two phases are considered: The fully dense (FD) copper, assumed for purposes of calculation to be homogeneous, and vacuum or (non-conducting) gas in pores or voids interspersed throughout it. The characteristic dimensions of these pores are also assumed to be sufficiently larger than the electron mean free path Λ so that the extra resistance due to electron scattering from the pores can be regarded as independent of pore size under conditions of fixed total porosity of volume fraction v. (For comparison, $\Lambda \approx 300$Å for pure Cu at 300 K.[9]) Then an appropriate mixing rule for ρ_e can be invoked. If the porosity is in parallel (e.g., as tubules) with the FD Cu, then the mixing rule is simply

$$(\rho_e')_p = (\rho_e)_{FD}/(1-v),$$

where $(\rho_e')_p$ and $(\rho_e)_{FD}$ are the mixture and FD values, respectively. The value of $(\rho_e')_p$ is a lower bound on the correct estimate of ρ_e, the measured value.

A more realistic mixing rule, which we adopt here, gives the higher estimate ρ_e':

$$\rho_e' = (1+\tfrac{1}{2}v)(\rho_e')_p. \qquad (6)$$

Due to Maxwell (1904), this expression assumes the porosity to be randomly distributed in the FD Cu as randomly-sized spheres.[10] The mixture resistivity ρ_e' is identified with the as-measured value ρ_e. Furthermore, the volume fraction v equals $(\rho_{FD}-\rho')/\rho'$ in terms of the FD and as-measured values of mass density ρ_{FD} and ρ', respectively. If ρ_{FD} is taken to be the density of the annealed and unirradiated control, then $(\rho_e)_{FD}$ for the irradiated material can be estimated. Accordingly, the difference $\rho_e'-(\rho_e)_{FD}$ can then be calculated and subtracted from ρ_e. The result of doing this for the high-fluence case R=H is tabulated in Table 8.2.2.

Table 8.2.2. DC electrical resistivity values corrected via subraction of increases due to porosity swelling and dissolved transmutation products

Copper Material	Neutron Fluence[1]	DC Volume Resistivity (μΩ-cm) As-Measured	Corr. for Increases Due to Porosity[2]	+ Transmu.[3]	Residue
OFHC	C	1.70	—	—	0.00
	H	1.98	1.78	1.68	-0.02
MARZ	C	1.67	—	—	0.00
	H	1.98	1.77	1.67	0.00
Al-20[4]	C	1.84	—	—	0.00
	H	1.96	1.94	1.84	0.00
Al-60[4]	C	1.99	—	—	0.00
	H	2.13	2.10	2.00	-0.01
MZC	C	1.93	—	—	0.00
	H	1.88	1.88	1.78	-0.15
AMZIRC	C	1.77	—	—	0.00
	H	1.87	1.76	1.66	-0.11

[1] C=annealed control, L=low fluence (0.4×10^{26} n/m^2), and H=high fluence (2×10^{26} n/m^2). Reactor: EBR-II (E>0.1 MeV).

[2] Based on mixing rule described in text; values given are for fully dense copper,

[3] Based on chemical analysis of transmutation products Ni and Zn and on published ρ_e data on Cu-Ni and Cu-Zn alloys; see text. (This correction includes both porosity and transmutation contributions.)

[4] With a nominal 5% cladding of OFHC Cu on each side.

The second column of numbers in this table gives the estimated values that ρ_e would have had if no swelling had occurred. It is readily apparent that most of the neutron-radiation induced changes in ρ_e for the elemental coppers are due to void swelling. Little or no change occurs for A1-20, Al-60, and MZC. These results are consistent with the high-dose values of swelling in Table 8.1.1 of the preceding paper.

By combining data from chemical analyses of transmuted trace elements present in Cu specimens, together with data published on ρ_e vs. solute concentration in binary Cu alloys, an estimate can be obtained of the increase in ρ_e due to transmutation products. The principal transmutation elements expected are Ni and Zn.[12] Comparing the C and H values given in Table 8.1.3 in the preceding paper, then the average neutron-induced increases in Ni and Zn are found to be 0.053 and 0.087 wt.%, respectively. The rates, on an at.% basis, at which increases in low-level concentrations increase ρ_e in Cu-Ni and Cu-Zn binary alloys, in accordance with Nordheim's rule, are 1.25 and 0.32 μΩ-cm/at.%, respectively.[13] Taking into account the slight differences involved here in at.% vs. wt.%, the corresponding increases expected in ρ_e were calculated and then subtracted from the porosity corrected values. The results are presented in the third column of numbers in Table 8.2.2.

These numbers (in the "Transmu." column) estimate what ρ_e would have been if no swelling or transmutation per se had occurred. The residue, i.e., the difference between the cases of C and corrected H, is essentially zero for the elemental coppers and the alumina-dispersed alloys. This seems to mean that microstructural damage or other types of change has little or no effect on ρ_e. This point of view is consistent with published results on the effect in Cu of point and line defects on ρ_e. For example, Horvak and Blewitt estimated that the ρ_e increase measured at 4.5 K and due to Frenkel-pair production induced by fast neutrons (E>0.1 MeV, T=4.5 K) saturates at 0.33 μΩ-cm.[14] This residual resistivity would certainly anneal out at the 658 K of the present study.

The effect of dislocations on ρ_e is larger, but still smaller in magnitude than the residues for the elemental coppers or alumina-dispersed alloys. A value, for Cu, of the ρ_e increase due to dislocations has been given by Brown as $1.3\ N \times 10^{-13}$ μΩ-cm^3, with N the dislocation density in units of cm^{-2}.[15] Assuming a residue of +0.1 (Table 8.2.2) would then lead to an N value of 7.7×10^{10} cm^{-2}. This is high. Its accumulation is not very likely given the annealing conditions of 385°C (for 245 days) pertinent to the present study.

For MZC and AMZIRC, however, the residue values for both are negative and relatively large in magnitude. This could mean that a single phenomenon not solely related to swelling, transmutation, or thermal annealing tended to produce a small (6-8%) decrease in ρ_e of both these alloys. The most likely candidates for this phenomenon involve the non-equilibrium nature of a precipitation-hardened alloy as discussed in preceding paragraphs.

8.2.4.5 Comparison with Results of a Recent Study

A prior fast-neutron irradiation study of Cu that is close in character to the present one was done in the Materials Open Test Facility (MOTA) in The Fast Flux Test Reactor (FFTF) in Richland, WA, to a fluence of 2.5×10^{26} n/m^2 at 450°C, and a corresponding damage level of 16 dpa.[16] Of interest here are three of the eight materials featured in that study: MARZ (annealed), MZC, and A1-25.

The one material exactly the same in both studies was the 99.999% pure MARZ copper and -- encouragingly -- the measurement results from Brager et al. were nearly identical to those reported here or in the preceding paper on irradiated or unirradiated σ_{IACS}, irradiated S_y, and swelling. However, the differences in the alloy materials and in the experimental conditions bearing on them make it difficult to otherwise correlate the study results. For example, the compositions of the MZC alloys were Cu-0.9Cr-0.1Zr-0.05Mg and Cu-0.5Cr-0.18Zr-0.04Mg in the previous and present studies (concentrations in wt.%), respectively, and significant differences arose in the cold-working and/or aging histories of the MZC and alumina-dispersed alloys. Further, Brager et al. reported σ_{IACS} values on as-is -- and thus unannealed -- unirradiated alloys while we did so on unirradiated alloys subjected to the same annealing conditions as our irradiated specimens. The irradiation temperatures differed (450°C vs. 385°C) as well.

Perhaps for these and other reasons. the ρ_e results differed for the two 'common' alloys in these two studies (as well as for most of the results on swelling). Surprisingly, though, the same type of correlation trend was seen here as it was between S_y and σ_{IACS} for the unirradiated Cu materials (barring the beryllium-containing alloys) in the previous study: S_y was found here to be linearly related to σ_{IACS} (linear correlation coefficient r of -0.94 for six points) such that the slope and intercept values were within a factor of two of those calculated from a corresponding linear regression analysis of the data of Brager et al. Additionally, the hypothesis $S_y \propto \rho_e$ gave nearly the same correlation with our data (r=0.92). A greater range in the values of σ_{IACS}, larger than the 103-87=16 for our controls, is needed, though, to better ascertain anv real functional relationship that exists between $(S_y)_c$ and $(\rho_e)_c$.

A more detaileb look into this matter is of more than academic interest, since the ratio S_y/ρ_e appears in Eq. (4) for M_R or in the quantity M'.

8.2.5 Conclusions

Of the four Cu alloys featured in this study, the alumina-dispersed alloy A1-20 is identified as the most acceptable in terms of stable dc electrical and thermal conductivities combined with relatively high yet stable yield stresses. This performance is reflected in the high value of $M' = (S_y/\rho_e)_H$ given in Table 8.2.1 for the high-fluence case.

By subtracting from the as-measured values of ρ_e the increases due to void swelling and transmutation products, a self-consistent picture emerges for the ρ_e results. Within the estimated experimental error, the subtracted effects entirely explain the ρ_e changes measured for the two high-purity coppers, OFHC and MARZ, and the two alumina-dispersed alloys, A1-20 and A1-60. Additionally, this subtraction procedure yielded negative residues for both of the precipitation-strengthened alloys, MZC and AMZIRC, that indicate an effect of radiation-induced conductivity.

For more meaningful assessments of first-wall alloy candidates, the thermal-mechanical quantity M_R defined in Eg. (4) for irradiated materials should be used, as an adequate data base on radiation effects becomes available.

To "sort out" the dynamics and kinetics of radiation-induced changes in the Cu alloys studies, other types of data need to be gathered. Examples include energy dispersive x-ray spectroscopy of intragranular and intergranular levels of second-phase (e.g., solute) levels and histograms of precipitate particle size distributions in the Cu matrix.

8.2.6 References

1. R. L. Hagenson, R. A. Krakowski, C. G. Bathke, R. L. Miller, M. J. Embrechts, N. M. Schnurr, M. E. Battat, R. J. LaBauve, and J. W. Davidson, "Compact Reversed-Field Pinch Reactors (CRFPR): Preliminary Engineering Considerations," LA-10200-MS (UC-20d), Los Alamos National Laboratory, Los Alamos, NM, August 1984, p. 206.
2. R. W. Conn, "First Wall and Divertor Plate Material Selection in Fusion Reactors," J. Nucl. Mat. 76-77, 103-111 (1978).
3. American Society for Metals (Editorial Staff), ASM Metals Reference Book: A Handbook of Data about Metals and Metalworking, (American Society for Metals, Metals Park, OH, 1981), pp. 194, 199 and 295.
4. D. E. Gray (editor), American Institute of Physics Handbook, 2nd ed., (McGraw-Hill, New York, 1963), p. 9-38.
5. H. E. Boyer and T. L. Gall (editors), Metals Handbook: Desk Edition, (American Society for Metals, Metals Park, OH, 1985), p. 1.53.
6. S. J. Zinkle, D. H. Plantz, G. L. Kulcinski, and R. A. Dodd, "Microstructures and Physical Properties of Cu-Zr and Cu-Cr-Zr-Mg Alloys," pp. 143-145 in "Damage Analysis and Fundamental Studies" Quarterly Progress Report, April-June 1984, DOE/ER-0046/18 (UC-20,20c), U.S. Department of Energy, Offices of Energy Research and Fusion Energy, Washington, D.C., August 1984.
7. H. E. Boyer and T. L. Gall (editors), Metals Handbook: Desk Edition, (American Society for Metals, Metals Park, OH, 1985), p. 2.20.
8. R. L. Hagenson, R. A. Krakowski, C. G. Bathke, R. L. Miller, M. J. Embrechts. N. M. Schnurr, M. E. Battat, R. J. LaBauve, and J. W. Davidson, "Compact Reversed-Field Pinch Reactors (CRFPR): Preliminary Engineering Considerations," LA-10200-MS (UC-20d), Los Alamos National Laboratory, Los Alamos, NM, August 1984, p. 106.
9. C. Kittel, Introduction to Solid State Physics, 4th Ed., (John Wiley & Sons, New York, 1971), p. 259.
10. J. E. Parrott and A. D. Stuckes, Thermal Conductivity of Solids, (Pion Ltd., London, 1985), pp. 131-134.
11. R. J. Livak, T. G. Zocco, and J. C. Kennedy, "Swelling and Tensile Properties of Neutron Irradiated Copper Alloys for High Heat Flux Applications," paper 8.1, "Alloy Development for Irradiation Performance" Semiannual Progress Report for period ending March 31, 1985, DOE/ER-0045/14, (USDOE/OFE).
12. R. L. Hagenson, R. A. Krakowski, C. G. Bathke, R. L. Miller, M. J. Embrechts, N. M. Schnurr, M. E. Battat, R. J. LaBauve, and J. W. Davidson, "Compact Reversed-Field Pinch Reactors (CRFPR): Preliminary Engineering Considerations," LA-10200-MS (UC-20D), Los Alamos National Laboratory, Los Alamos, NM, August 1984, p. 97.
13. A. N. Gerritsen, "Metallic Conductivity, Experimental Part," pp. 137-226 in Encyclopedia of Physics (ed. by S. Flügge), Vol. XIX, (Springer-Verlag, Berlin, 1956).
14. J. A. Horak and T. H. Blewitt, "Fast Neutron Irradiation Induced Resistivity in Metals," Phys. Stat Sol. (A) 9, pp. 721-730 (1972).
15. R. A. Brown, "Electrical Resistivity of Dislocations in Metals," J. Phys. F: Metal Phys. 7, pp. 1283-1295 (1977).
16. H. R. Brager, H. L. Heinisch, and F. A. Garner, "Effects of Neutron Irradiation at 450°C and 16 dpa on the Properties of Various Commercial Copper Alloys," Int. Conf. Fusion Reactor Materials, Tokyo, Japan, December 1984 (proceedings to be published).

8.3 DUAL ION IRRADIATION STUDIES OF HIGH STRENGTH COPPER ALLOYS - J. A. Spitznagel (Westinghouse R&D Center and University of Pittsburgh), and J. W. Davis (McDonnell Douglas Company)

8.3.1 ADIP Task

ADIP Tasks are not defined for copper alloys in the 1978 program plan. The tasks involved are similar to Task Number 1.C.2, Microstructures and Swelling in Austenitic Alloys and Task Number I.C.I, Microstructural Stability.

8.3.2 Objective

The objective of this work is to scope the irradiation response of three classes of high strength, high conductivity copper alloys and to provide guidance for alloy development for fusion reactor structural components.

8.3.3 *Summary*

Microstructural changes are reported for a precipitation strengthened Cu-0.4 wt % Be-1.9 wt % Ni alloy and a dispersion hardened Cu-0.6 wt % Al (Al_2O_3) alloy after dual ion irradiation at fluences up to ~20 dpa at 250°C, 300°C and 350°C. Roth alloys show good swelling resistance. Peak swelling temperature for the alumina dispersion hardened alloy (Al-60) is ~350°C. For fluences of 10-20 dpa average swelling rates of 0.01% per dpa and 0.05% per dpa have been measured for irradiation without simultaneous helium injection and with a gas atom implantation rate of K_g ~3 x 10^{-3} appm·s^{-1}. Void formation is heterogeneous and is most pronounced in grains with low no. densities of Al_2O_3 particles. The beryllium-copper alloy shows almost no swelling with the exception of a few narrow and widely spaced transgranular bands of voids at 250°C-350°C. Loss of the (100) relrod reflections in the latter alloy is fluence and temperature dependent and reflects loss of coherency of the G.P. zones, particle restructuring and/or loss of imaging conditions due to strain field overlap from the dislocation network. Recoil resolution of the cubic γ-Al_2O_3 particles in the A1-60 is observed under certain conditions. The impact of these phase instabilities on mechanical and thermal properties is not known. It is recommended that neutron irradiation studies at 105°C-300°C be conducted to assess their importance.

8.3.4 Progress and Status

8.3.4.1 Introduction

The Electric Power Research Institute of Palo Alto, CA, has funded a program entitled Evaluation of Irradiated Metal Samples for Use in Fusion Components under contract RP-1597-1 with McDonnell Douglas Astronautics Company. Westinghouse R&D Center and the University of Pittsburgh have been participants in that program under contract Y4E034R entitled Radiation Response of Copper. In order to disseminate the results of this work to the fusion materials community in timely fashion, a brief summary covering highlights of work in progress is being included in the Alloy Development for Irradiation Performance Progress Report.

Copper is of interest to fusion for a number of reasons. The two leading applications, however; are as high heat flux components and as first walls in high wall loading devices. Both of these applications require materials that have high thermal conductivity. In this program, dual ion irradiation techniques are being used to study the combined effects of temperature, atomic displacements and helium production in the fusion environment. The emphasis is on scoping the general radiation response of three types of copper alloys: a solid solution and mechanically worked alloy (Cu-0.15 wt % Zr), a precipitation strengthened alloy (Cu-0.4 wt % Be-1.9 wt % Ni), and a dispersion strengthened alloy (Cu-0.6 wt % Al as Al_2O_3 particles).

8.3.4.2 Experimental Procedures

Alloy compositions, thermomechanical processing, specimen preparation and irradiation procedures have been described in a previous AOIP report.[1] Results reported here were obtained by irradiating beryllium-copper and A1-60 specimens at 250°C, 300°C and 350°C to a peak damage level of ~100 dpa. Specimens were run without simultaneous helium injection and with a gas atom injection rate of K_g = 3 x 10^{-3} appm·s^{-1}. After irradiation samples were sectioned by low energy ion milling and electrochemically back-thinned to provide planar TEM specimens at depths corresponding to fluences of 10 dpa and 20 dpa. Selected specimens were also prepared for cross-section TEM to permit full range imaging. The calculated atomic displacement rate over the helium implanted region was ~1 x 10^{-4} dpa/s.

8.3.4.3 Results and Oiscussion

Al-60 Alloy

Regions of the powder metallurgy alloy containing high number densities of the triangular, cubic γ-Al_2O_3 particles are extremely resistant to swelling at fluences up to 20 dpa over the temperature range 250°C-500°C. Conversely, regions with few Al_2O_3 particles exhibit the greatest swelling. At present it has not been possible to define a particle number density corresponding to the transition between high and low swelling regions because of the wide distribution of particle sizes reported previously and the tendency for particles to etch out and collect on the surfaces of the foil during electrothinning.[1] Grain boundary regions are also resistant to void formation over this temperature range indicating that most of the 300 appm to 600 appm of helium is probably trapped within the grains. A peak swelling temperature of ~350°C is obtained by averaging the void volume fraction over the high and low regions, Figure 8.3.1. An average swellino rate of 0.05% oer dpa is seen at 20 dpa with simultaneous implantation of helium. Without helium, the rate is lower by approximately a factor of five, Figure 8.3.2. Over the temperature range where void formation occurs a high dislocation density, (10^9 cm/cm3 to 10^{10} cm/cm^3) develops around the γ-Al_2O_3 Particles. In addition. at ~10 doa. effects of recoil resolution are observed at 10^{-4} dpa·s^{-1} at 250°C-350°C. The process is being analyzed and will be described in detail at the October 1985 AIME Symposium in Toronto. It is manifested by a dose dependent fading of the rings in the SAD patterns corresponding to d-spacings of 0.244 nm, 0.195 nm and 0.142 nm for the cubic Al_2O_3. Fragmentation of the triangular shaped particles seen in bright and dark field accompanies the changes in the SAD patterns. The resolution process is important because it leads to a second stage of void formation in the alloy. The process is not unique to ion irradiation and theory predicts similar effects at ~100°C lower temperatures for neutron irradiation at a displacement rate of 10^{-7} dpa·s^{-1}.[2] The effects of particle resolution on mechanical and thermal properties are not known. Some loss of strength may result. Neutron irradiation studies in the range 100°C-300°C to fluences >20 dpa are required to determine whether such "internal sputtering" processes are important for copper alloys which derive their strength from a dispersion of non-metallic particles.

Beryllium-Copper

This Cu-0.4 wt % Be-1.9 wt % Ni alloy supplied by Rosenwasser, et al. at Inesco[1] is even more swelling resistant than the A1-60 alloy under the current irradiation conditions. Only rarely were voids observed at fluences up to 20 dpa. These tended to lie in rows or long transgranular bands separated by hundreds of microns. No clear evidence was found for structural or chemical heterogeneities responsible for their formation, and it was not possible to calculate a significant value for $\Delta V/V_0$. The bands were most often seen at an irradiation temperature of 300°C; less frequently at 250° and 350°C, and were never observed at higher irradiation temperatures.[1] Grain boundaries and interface regions of large nickel-rich precipitates in the alloy apparently do not serve as preferential helium collection or void nucleation sites since no gas bubbles or voids have been observed at magnifications up to 200,000X at those locations. The grain boundaries appear to resist discontinuous or cellular precipitation both thermally and under irradiation. The principal microstructural instabilities relate to the changes in the G.P. zones as evidenced by irradiation enhanced thermal coarsening at 425°C-500°C and irradiation driven disappearance at temperatures below 350°C, Figures 8.3.3 to 8.3.7. The latter process is accompanied by a disappearance of the (100) relrods at 250°C-350°C. This may indicate loss of coherency of the G.P. zones, particle restructuring and/or formation of overlapping strain fields from the formation of a dislocation network. The role of helium in promoting the process suggests that nucleation of dislocation loops may be an important contributor to the process. It is not possible to determine the sign or magnitude of these effects on yield strength elongation or conductivity and low temperature neutron irradiation studies are needed.

8.3.5 Future Work

Analysis of irradiation results and preparation of the final report are in progress. No additional dual ion experiments are planned for 1985.

8.3.6 References

1. J. A. Spitznagel and J. W. Davis, "Response of Selected High Strength High Conductivity Copper Alloys to Simulated Fusion Irradiation and Temperature Conditions", pp. 171-182 in ADIP Semiannual Progress Report, September 1984, DOE/ER-0045/13.

2. H. J. Frost and K. C. Russell, Acta Metall. 30 953-960 (1982).

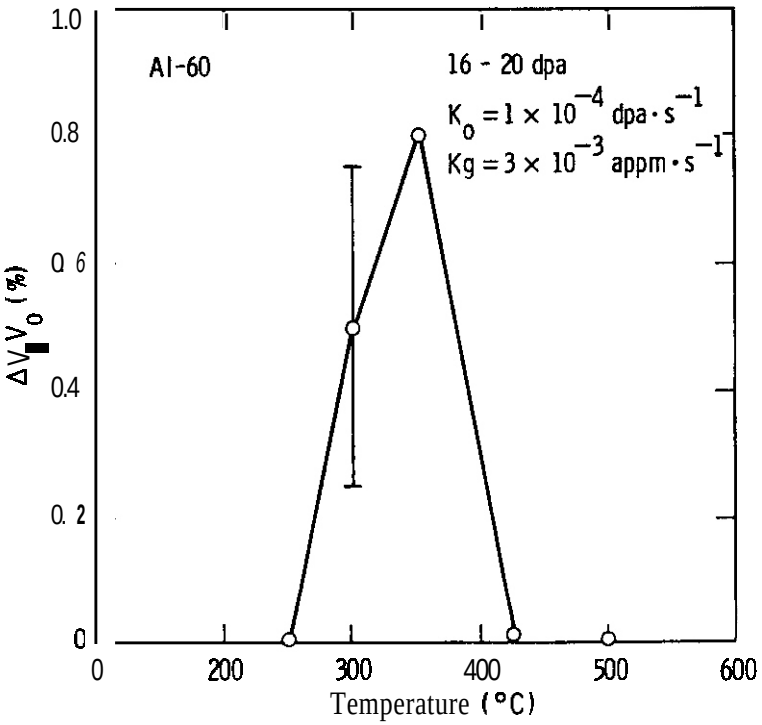

Figure 8.3.1 Temperature distribution of swelling for dual ion irradiated A1-60 alloy at fluences of 16 dpa-20 dpa.

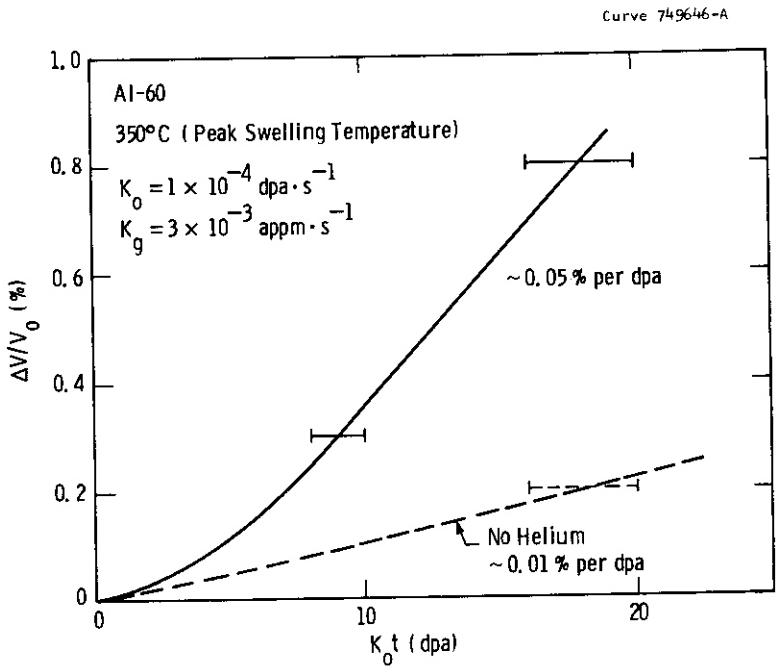

Figure 8.3.2 **Dose** dependence of swelling for A1-60 alloy at the peak swelling temperature.

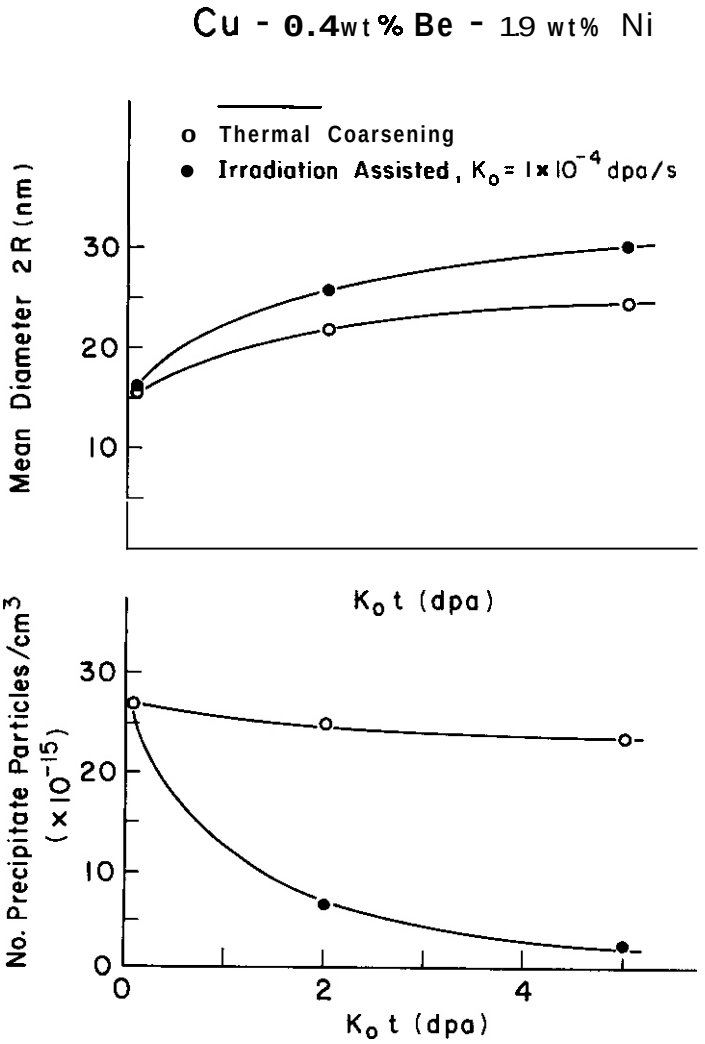

Figure 8.3.3 Effects of thermal aging and dual ion irradiation on precipitates imaged with (100) relrods in beryllium-copper alloy at 500°C.

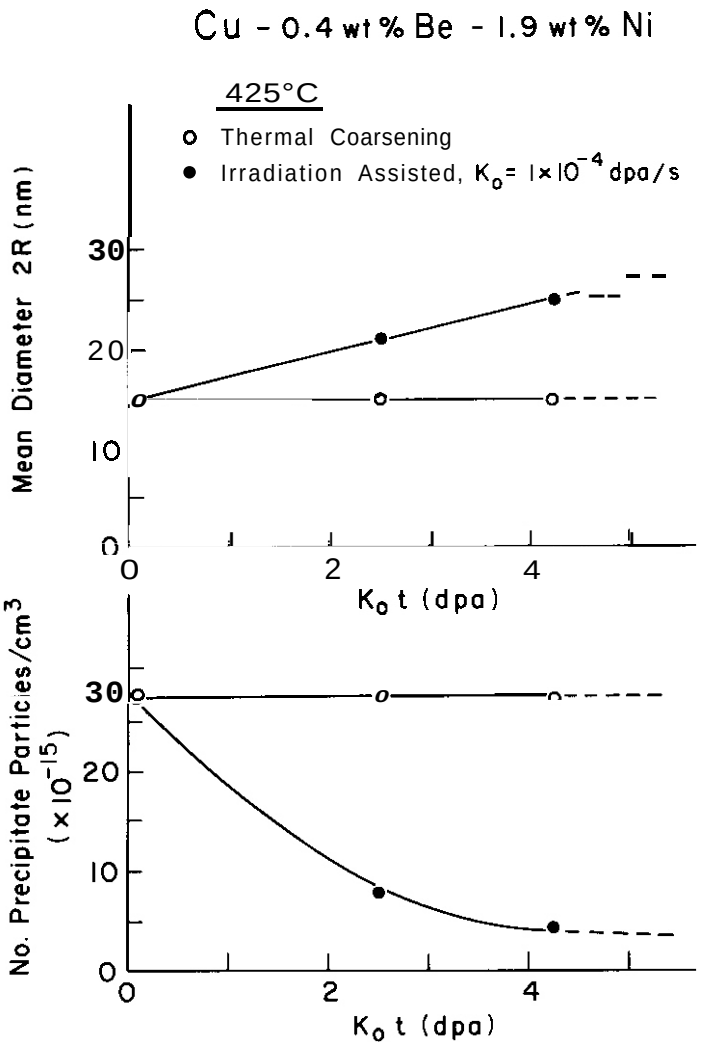

Figure 8.3.4 Effects of thermal aging and dual ion irradiation on precipitate particles imaged with (100) rel-rods in beryllium-copper alloy at 425°C.

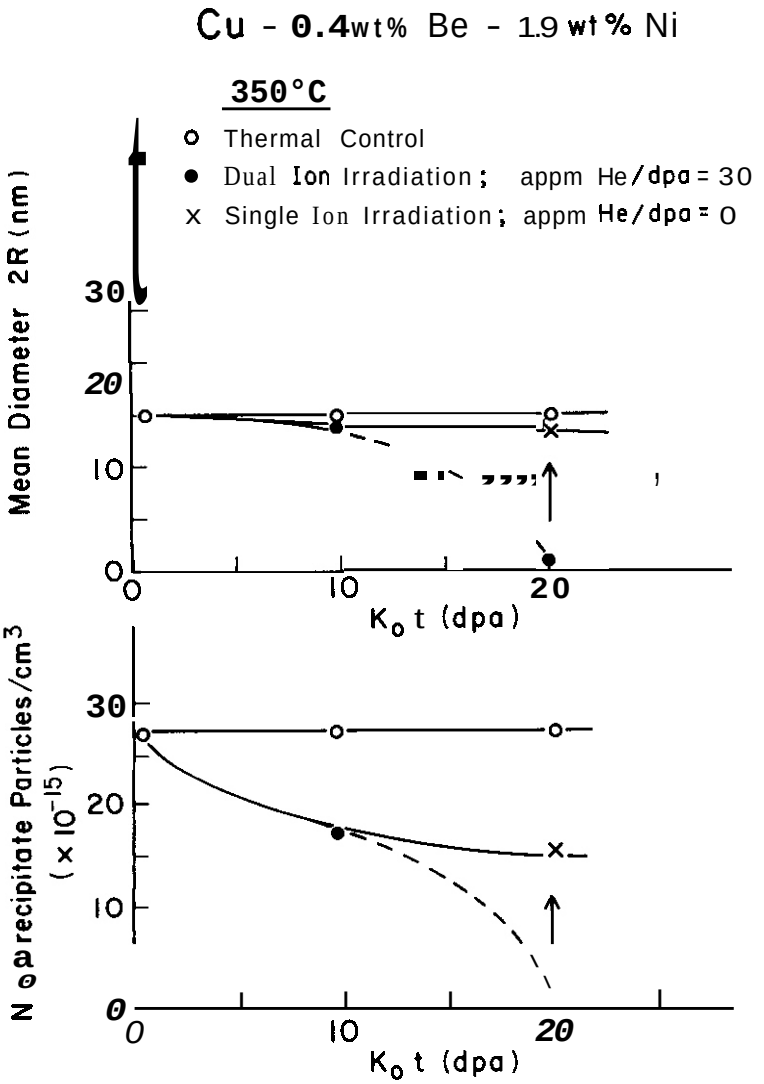

Figure 8.3.5 Effects of thermal aging, single ion irradiation and dual ion irradiation on precipitates imaged with (100) relrods in beryllium-copper alloy at 350°C.

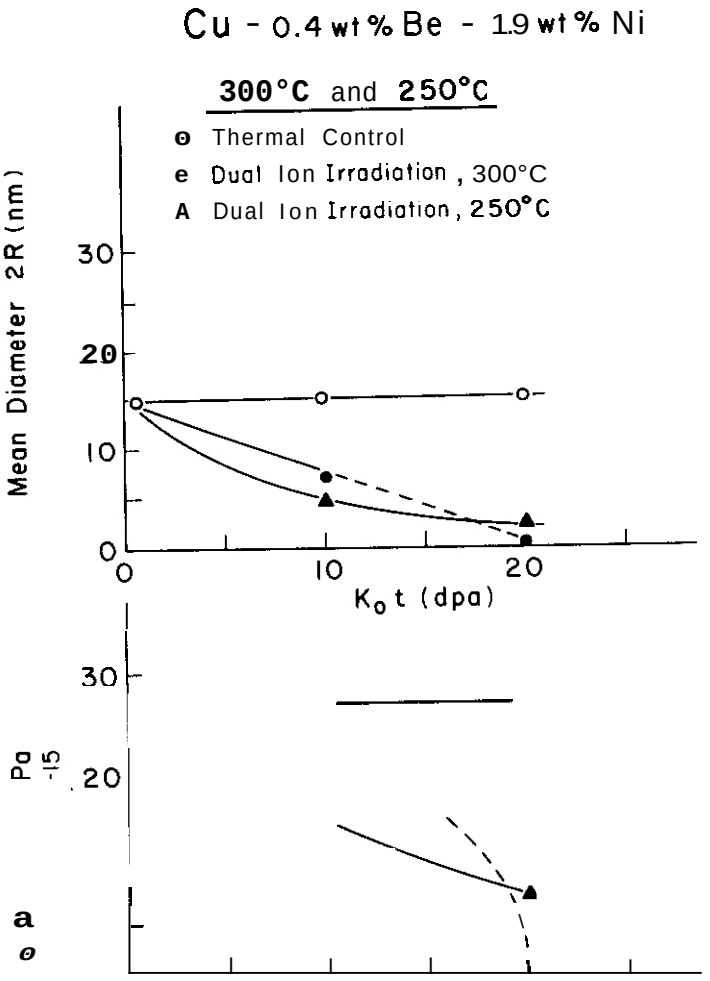

Figure 8.3.6 Effects of thermal aging and dual ion irradiation on precipitates imaged with (100) relrods in beryllium-copper alloy at 300°C and 250°C.

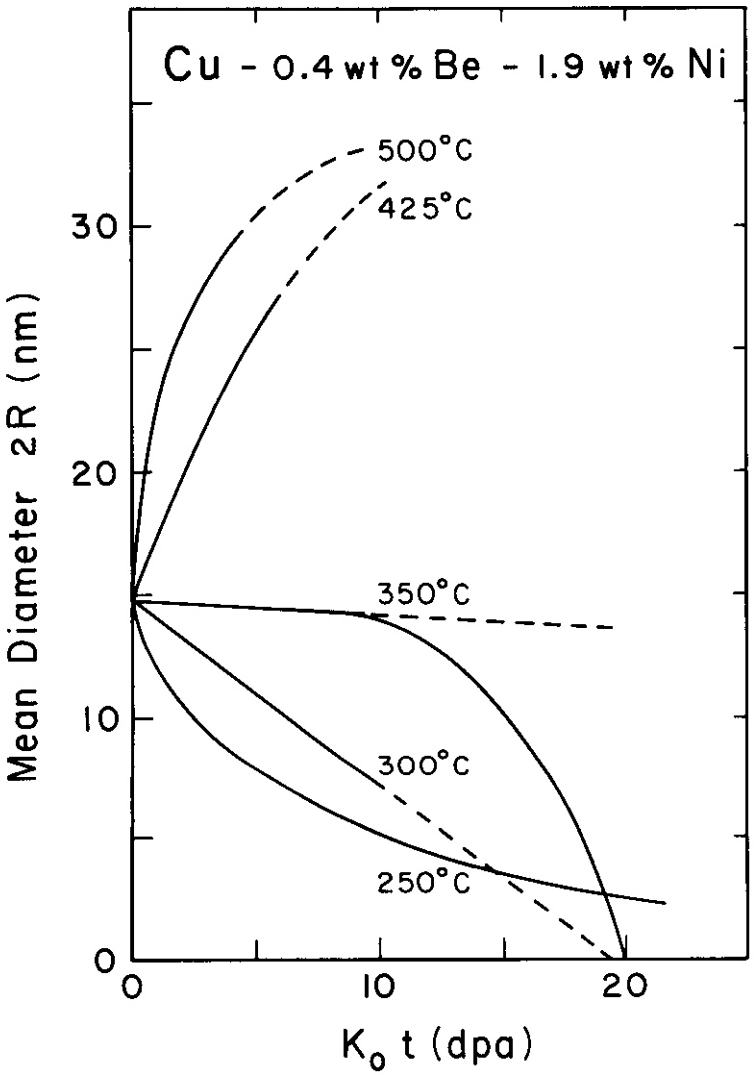

Figure 8.3.7 Combined thermal and irradiation effects on the size of precipitates imaged in dark field with (100) relrods in SAD pattern.

9. MATERIALS COMPATIBILITY AND HYDROGEN PERMEATION STUDIES

9.1 ENVIRONMENTAL EFFECTS ON THE PROPERTIES OF VANADIUM-BASE ALLOYS - D. R. Diercks and D. L. Smith (Argonne National Laboratory)

9.1.1 ADIP Task

ADIP Task I.A.3, Perform Chemical and Metallurgical Compatibility Analyses.

9.1.2 Objective

The objective of this task is to experimentally evaluate the corrosion behavior of selected vanadium-base alloys in a number of aqueous, liquid metal, and gaseous environments. The results of these investigations will be used in the selection of appropriate vanadium-base alloys for structural applications in fusion reactors.

9.1.3 Summary

Exposures of V-15Cr-5Ti, V-20Ti, and VANSTAR-7 specimens to pressurized flowing water containing 0.03 ppm dissolved O_2 at 288°C indicate that V-15Cr-5Ti again has the best corrosion resistance. Further scanning Auger microprobe studies of sulfur segregation in vanadium-base alloys reveal no clear correlation between segregation and the variables examined.

9.1.4 Progress and Status

9.1.4.1 Aqueous Corrosion Behavior of Vanadium-base Alloys

The exposure of vanadium-base alloys to pressurized water at 288°C (550°F) and 8.3 MPa (1200 psi) containing various levels of dissolved oxygen in a refreshed autoclave system is continuing. The three alloys being exposed are V-15Cr-5Ti, V-20Ti, and VANSTAR-7. Samples of all three alloys were obtained from the Fusion Power Program (FPP) materials inventory in the form of 0.76-mm (0.030-in.)-thick sheet, and additional samples of the first two alloys were obtained from the ANL LMFBR inventory in the form of 1.52-mm (0.060-in.)-thick sheet. These alloys were sheared into weight-change specimens approximately 7.1-cm (2.8-in.) long and 1-cm (0.4-in.) wide. Further experimental details, as well as the results of the first series of exposures in water containing 4 ppn dissolved O_2, are described in previous reports.[1,2]

During the present reporting period, a second series of exposures has been completed in water having a dissolved O_2 level of approximately 0.03 ppm at the outlet. This outlet level is considered to be representative of that present in the autoclave in contact with the specimens. The test was initiated using high-purity distilled water (conductivity ~0.1 μS/cm) containing approximately 0.4 ppm dissolved O_2 at the inlet, as obtained by equilibrating the solution with a N_2-1% O_2 blanketing gas mixture. The flow rate through the autoclave system was about 11 cm^3/min, and the oxygen level in the outlet water was monitored on a more or less continuous basis using a Leeds and Northrup Model 7931 dissolved-oxygen meter. Spot checks of the oxygen level in the inlet water were made using the same meter, as well as with Chemetrics dissolved-oxygen test kits.

After about 1300 h of specimen exposure time, the dissolved-oxygen level in the outlet water was observed to be falling below the desired level, and it was necessary to change the blanketing gas to a N_2-2% O_2 mixture. During the majority of the test, the dissolved-oxygen level in the outlet water varied between 0.02 and 0.04 ppm, giving the average 0.03 ppm reported here. However, occasional excursions to oxygen levels as low as 0.01 ppm and as high as 0.055 ppm were experienced.

This second corrosion test was interrupted after exposure times of 192, 500, 1000, and 2000 h to weigh the specimens. The observed weight changes for the alloys and heats tested are summarized in Table 9.1.1 and plotted in Figs. 9.1.1 and 9.1.2. In all cases but one, the specimens lost weight. The exception is one of the two VANSTAR-7 specimens, which exhibited a very slight weight gain after an exposure time of 192 h, but lost weight thereafter. As may be seen in Fig. 9.1.1, the V-20Ti and VANSTAR-7 specimens otherwise showed similar behaviors, with steadily increasing corrosion kinetics and weight losses of the order of 3.5 to 4 mg/cm^2 after 2000 h. Best-fit equations representing all of the data of Fig. 9.1.1 for each of these two alloys were obtained as follows:

$$\text{V-20Ti:} \quad W = 3.100 \times 10^{-5}\, t^{1.544}, \text{ and}$$

$$\text{VANSTAR-7:} \quad W = 3.401 \times 10^{-6}\, t^{1.830},$$

where W is weight change in mg/cm^2, and t is time in hours. As reported previously,[2] the same alloys exposed to water containing 4 ppm dissolved O_2 also showed increasing rates with time (i.e., exponent >1). However, the total weight losses were much greater in the water containing 4 ppm O_2, being of the order of 95 to 110 mg/cm^2 after 2000 h for the V-20Ti and 65 mg/cm^2 for the VANSTAR-7.

Table 9.1.1. Observed weight losses for vanadium-base alloys from Fusion Power Program (FPP) materials inventory and ANL LMFBR inventory exposed to water containing 0.03 ppn dissolved oxygen at 288°C and 8.3 MPa

Alloy	Source	Weight Loss/Unit Area (mg/cm^2) after Indicated Exposure Time			
		192 h	500 h	1000 h	2000 h
V-15Cr-5Ti	FPP	0.140	0.345	0.659	1.498
	FPP	0.168	0.322	0.688	1.528
	LMFBR	0.117	0.226	0.504	0.895
	LMFBR	0.143	0.275	0.493	0.914
V-20Ti	FPP	0.306	0.623	1.105	3.699
	FPP	0.311	0.632	1.082	3.783
	LMFBR	0.276	0.618	1.311	4.093
	LMFBR	0.271	0.621	1.320	3.991
VANSTAR-7	FPP	+0.017[a]	0.387	1.054	3.925
	FPP	0.105	0.363	0.997	3.550

[a]Specimen showed weight gain after 192-h exposure and weight losses thereafter.

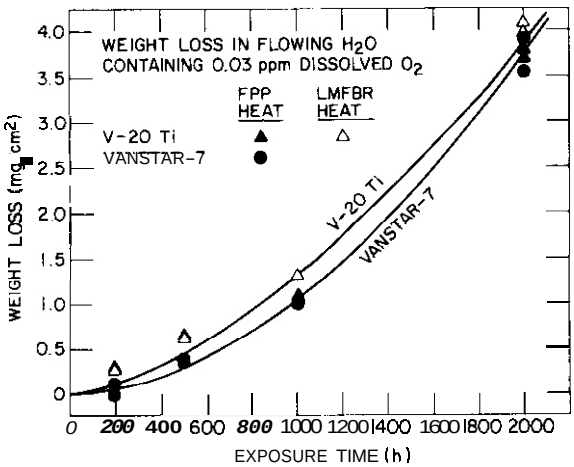

Fig. 9.1.1. Observed weight losses for V-20Ti and VANSTAR-7 exposed to water containing 0.03 ppm dissolved oxygen at 288°C.

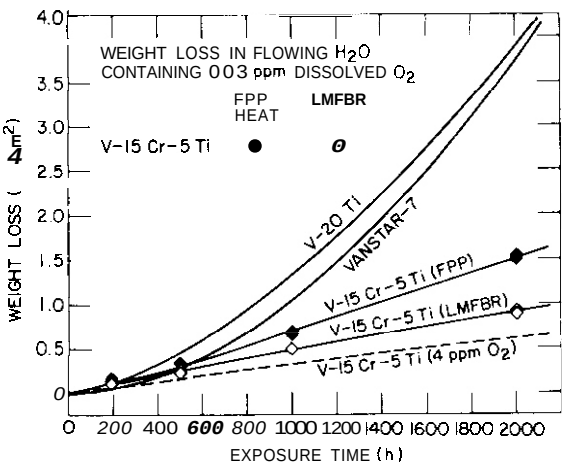

Fig. 9.1.2. Observed weight losses for V-15Cr-5Ti exposed to water containing 0.03 ppm dissolved oxygen at 288°C. The behaviors of V-20Ti and VANSTAR-7 in the same solution, as well as V-15Cr-5Ti in water containing 4 ppm dissolved O_2, are shown for comparison.

The corrosion data obtained in this second test for the V-15Cr-5Ti specimens are plotted in Fig. 9.1.2. The two heats of this alloy exhibit noticeably different corrosion kinetics, in contrast to the two V-20Ti alloys and in contrast to either the V-15Cr-5Ti or V-20Ti specimens in the first test.' The weight loss data for the Fusion Power Program material is described by the relationship

$$\text{V-15Cr-5Ti (FPP):} \quad W = 3.414 \times 10^{-4}\, t^{1.104},$$

whereas the data for the ANL LMFBR heat fit the relationship

$$\text{V-15Cr-5Ti (LMFBR):} \quad W = 1.103 \times 10^{-3}\, t^{0.8829}.$$

For comparison purposes, the best-fit curves to the observed weight losses for the V-20Ti and VANSTAR-7 specimens under the same conditions are replotted in Fig. 9.1.2. In addition, the behavior of the

V-15Cr-5Ti specimens from the first test in water containing 4 ppm O_2 is shown as the dashed curve. Whereas the V-20Ti and VANSTAR-7 specimens showed much smaller weight losses in the 0.03 ppm O_2 water than in the 4 ppm O_2 water, the V-15Cr-5Ti lost somewhat more weight in the former solution.

Wastage rates can be calculated on a linearly extrapolated basis from the observed 2000-h weight loss data of Table 9.1.1, assuming uniform corrosion and an approximate density of 6.16 g/cm^3 for each of the three alloys. These calculated wastage rates are about 0.009 mm/y for V-15Cr-5Ti and about 0.027 mm/y for the V-20Ti and VANSTAR-7 alloys. In the case of the latter two alloys, the observed increasing corrosion rate with time suggests that the actual annual wastage rate may be greater. By way of comparison, a maximum corrosion wastage rate of 0.005 to 0.020 mm/y has been suggested for the fusion reactor first wall.[3]

The nature of the oxide films formed on the surfaces of the exposed specimens was in general agreement with the observed corrosion kinetics. The V-15Cr-5Ti specimens, which showed the slowest corrosion rates and had the smallest exponents on time in the rate equation, were covered by a thin, adherent, and apparently protective oxide. In contrast, the V-20Ti and VANSTAR-7 specimens, which had higher weight losses and showed increasing corrosion rates with time over 2000 h, were covered with heavier powdery oxides that rubbed off readily during handling.

Additional results have been obtained on the identification of the surface oxides formed in the first test after 2000-h exposures to water at 288°C containing 4 ppm dissolved O_2. The surface oxide formed on the V-20Ti specimens was readily identified by x-ray diffraction powder patterns as TiO_2 (rutile). Similar patterns obtained fran the oxide on the V-15Cr-5Ti specimens have identified the tetragonal VO_2 phase on at least one specimen, along with minor amounts of TiO_2. In addition, the possible presence of a mixed (V,Cr) oxide, either in the tetragonal (rutile) or orthorhombic structures, was indicated on some of the patterns. The relatively diffuse patterns produced by the oxide obtained from the VANSTAR-7 specimens could not be satisfactorily indexed.

In order to further identify these oxides, quantitative x-ray microprobe analyses have been performed. In both of the V-15Cr-5Ti alloys, the surface oxide was typically found to contain V, Ti, and Cr in the approximate relative proportions 25% V, 30% Ti, and 45% Cr, although one location noticeably higher in Cr and one higher in Ti were detected. The results, when combined with previous x-ray diffraction data, suggest that the predominant corrosion product phase formed on the surface of the V-15Cr-5Ti specimens is a mixed oxide of the form $(V,Ti,Cr)O_2$, with the three metallic elements present in the approximate proportions indicated above. The surface oxide present on the VANSTAR-7 specimen was found to have a widely varying composition, depending upon the region analyzed. The metallic elements present were Cr, V, Fe, and Zr. It thus appears that more than one oxide is formed on the surface of this alloy.

9.1.4.2 Segregation of Sulfur in Vanadium-base Alloys

The previous report[2] described preliminary results obtained in a series of scanning Auger microprobe (SAM) examinations of selected vanadium-alloy specimens fractured in situ at liquid nitrogen temperature. The purpose of these examinations was to look for possible segregation of sulfur to grain boundary and fracture surface regions and to investigate its influence on the fracture characteristics. This study has now been completed, and the resulting observations are summarized in Table 9.1.2. The specimens examined included (1) V-15Cr-5Ti of uncertain origin utilized in the ORR-MFE-2 experiment and provided by Westinghouse, (2) V-15Cr-5Ti, V-20Ti, and VANSTAR-7 specimens from the FPP materials inventory ("CAM" heats), and (3) V-15Cr-5Ti and V-20Ti material from ANL LMFBR heats.

The first two entries in Table 9.1.2 summarize the observations made by Westinghouse and Argonne, respectively, on unirradiated archival material fran the ORR-MFE-2 experiment. Although some differences in fracture behavior were seen, substantial levels of sulfur were detected on the fracture surfaces by both Westinghouse and Argonne, even though a high-sensitivity sulfur chemical analysis performed by Leco Corp. determined the bulk sulfur content of the alloy to be only about 5 wppm.

The remaining examinations summarized in Table 9.1.2 were conducted at Argonne in an attempt to define the conditions under which and the extent to which sulfur segregation occurred in different alloys after varying heat treatments. Unfortunately, no clear pattern emerges from these observations. Significant sulfur peaks (of the order of 1 to 2 wt % S) were seen on the fracture surfaces of an annealed FPP V-20Ti specimen and a cold-swaged FPP VANSTAR-7 specimen. However, only traces of sulfur or no sulfur at all were seen on the fracture surfaces of the remaining specimens. In some cases, traces of other elements such as C, P, Cl, O, and Si were detected. No clear correlation could be made between the sulfur level on the fracture surface and thermomechanical treatment, fracture characteristics, or bulk sulfur content.

As a follow-on to these SAM studies, specimens of V-15Cr-5Ti fran four heats of material are being prepared for a series of annealing experiments, followed by high-resolution transmission electron microscope examinations to determine the extent of the resulting sulfur and other elemental segregation to grain boundaries.

Table 9.1.2. Results of Auger microprobe analyses of in situ fracture surfaces of vanadium-base alloys

Alloy	Heat	Condition	Auger Microprobe Results	Bulk S Analysis (wppm)
V-15Cr-5Ti	HSV-307, R1301	'Recrystal 1ized"	Transgranular cleavage fracture with ~3 wt % S on fracture surface (Westinghouse)	~5
V-15Cr-5Ti	HSV-307, R1301	"Recrystal1ized"	Mixed intergranular/transgranular cleavage fracture; ~10 wt % S seen on intergranular regions, but none on transgranular regions (ANL)	~5
V-15Cr-5Ti	CAM 835 8-2	Cold-swaged	Transgranular ductile fracture; no S detected	~40
V-15Cr-5Ti	CAM 835 8-2	Annealed 1 h at 850°C	Transgranular cleavage fracture with isolated ductile regions; no S seen, but C, P, and possible Cl detected	~40
V-15Cr-5Ti	ANL LMFBR	Annealed 1 h at 850°C	Transgranular cleavage fracture with some possible intergranular regions; traces of S and P seen	~50
V-20Ti	CAM 832 Top-5	Cold-swaged	Transgranular ductile fracture; C and O seen, but no S detected	~40
V-20Ti	CAM 832 Top-5	Annealed 1 h at 850°C	Transgranular ductile fracture with possible intergranular areas; S detected at 3 locations, with one fairly large peak	~40
V-20Ti	ANL LMFBR	Annealed 1 h at 850°C	Transgranular ductile fracture; possible traces of S, P, and Cl detected	None Detected
VANSTAR-7	CAM 836 Top-4	Cold-swaged	Trangranular ductile fracture; moderate S detected at some locations, along with P, C, and Si	~35
VANSTAR-7	CAM 836 Top-4	Annealed 1 h at 850°C	Transgranular ductile fracture with some transgranular cleavage; no S or P detected	~35

9.1.5 Conclusions

Exposures of V-15Cr-5Ti, V-20Ti, and VANSTAR-7 specimens for 2000 h to pressurized flowing water containing 0.03 ppm dissolved O_2 at 288°C have been completed. The V-15Cr-5Ti specimens obeyed approximately linear corrosion kinetics and showed the least weight loss of the three alloys tested. The V-20Ti and VANSTAR-7 specimens showed increasing corrosion rates with time and had weight losses approximately three times as great as the V-15Cr-5Ti specimens. The V-15Cr-5Ti specimens formed a thin, adherent corrosion product, while that on the other two alloys was somewhat thicker and less adherent. Compared to their corrosion behavior in water containing 4 ppm dissolved O_2, the weight losses for the V-15Cr-5Ti specimens were approximately a factor of two greater after 2000 h in the 0.03 ppm O_2 water, while the losses were less for the V-20Ti specimens by about a factor of 25 and for the VANSTAR-7 specimens by about a factor of 15.

Scanning Auger microprobe analyses have been performed on a number of vanadium-alloy specimens fractured in situ in order to observe possible sulfur segregation in these alloys. Significant sulfur segregation to the fracture surfaces was observed in only a few of the specimens examined, and traces of P, C, O, Cl, and Si were also occasionally seen on the fracture surfaces. No clear correlation could be made between the tendency for sulfur segregation and such factors as alloy composition, thermochemical condition, fracture behavior, or bulk sulfur content.

9.1.6 References

1. D. R. Diercks and D. L. Smith, "Environmental Effects on the Properties of Vanadium-base Alloys," pp. 15–19 in Alloy Developnent for Irradiation Performance: Semiannual Progress Report for Period Ending March 31, 1984, DOE/ER-0045/12, Oak Ridge National Laboratory, Oak Ridge, TN, July 1984.

2. D. R. Diercks and D. L. Smith, "Environmental Effects on the Properties of Vanadium-base Alloys," pp. 209–213 in Alloy Developnent for Irradiation Performance: Semiannual Progress Report for Period Ending September 30, 1984, DOE/ER-0045/13, Oak Ridge National Laboratory, Oak Ridge, TN.

3. Blanket Comparison and Selection Study Final Report, ANL/FPP-84-1, Vol. 2, Argonne National Laboratory, Argonne, IL, pp. 6.2–17 and 6.2–18.

9.2 CORROSION OF AUSTENITIC AND FERRITIC STEELS IN FLOWING LITHIUM ENVIRONMENT - O. K. Chopra and O. L. Smith (Argonne National Laboratory)

9.2.1 ADIP Task

ADIP Task 1.A.3, Perform Chemical and Metallurgical Compatibility Analyses.

9.2.2 Objective

The objective of this program is to investigate the influence of a flowing lithium environment on the corrosion behavior and mechanical properties of structural alloys under conditions of interest for fusion reactors. Corrosion rates are determined by measuring the weight change and depth of internal corrosive penetration as a function of time and temperature. These measurements, coupled with metallographic evaluation of the alloy surface, are used to establish the mechanism and rate-controlling process for the corrosion reactions. Initial effort on mechanical properties is focused on fatigue and tensile tests in a flowing lithim environment of controlled purity.

9.2.3 Summary

Corrosion data on weight loss and internal penetration are presented for ferritic and austenitic steels in flowing lithium at 372, 427, and 482°C. Results from metallographic examination of the lithium-exposed specimens are presented. The influence of time, temperature, and lithium purity on the dissolution behavior of the alloys is discussed.

9.2.4 Progress and Status

The corrosion behavior of several ferritic and austenitic steels is being investigated in a flowing lithium environment. The corrosion tests are conducted in a forced-circulation lithium loop consisting of three vessels and a secondary cold-trap purification loop. A detailed description of the lithium loop has been presented earlier.' Flat corrosion coupons, –70 x 10 x 0.3 mm in size, are exposed to flowing lithium, and the corrosion behavior is evaluated from measurements of weight loss and depth of internal penetration (or internal corrosive attack). Specimens are periodically removed from the loop and cleaned in alcohol and water, and the weight loss data obtained at different exposure times. Tests are conducted in the test vessel, as well as in the specimen exposure vessel. The temperature and time of exposure and the loop operating conditions for the various test runs are given in Table 9.2.1. Lithium was recirculated at –1 L/min in the primary loop, and the concentrations of C and H in lithim were –10 and 120 wppm, respectively.

The weight losses for HT-9 and Fe-9Cr-1Mo ferritic steels, PCA, and annealed and 20% cold-worked (CW) Type 316 stainless steels are shown in Figs. 9.2.1 to 9.2.3. The ferritic steels were exposed in the normalized and tempered condition. Two different thermal-mechanical treatments were employed for the PCA, viz., solution annealed plus 25% CW (treatment A3) and solution annealed plus 8 h at 800°C plus 25% CW plus 2 h at 750°C (treatment B2). The results indicate that the weight losses for ferritic steels follow a linear law with time and yield a constant dissolution rate after a relatively large transient weight loss during the initial –500 h of exposure to lithium. It will be shown later that the transient weight loss results from the "etching effect" of lithium and that the specimens develop a dimpled appearance. The weight losses and dissolution rates of HT-9 and Fe-9Cr-1Mo steel are comparable at all temperatures. Also, specimens exposed at 427°C during test runs 4 and 5 show similar dissolution behavior although the location of these specimens was different, i.e., specimens were placed at the maximum loop temperature in run 5 while the specimens in run 4 were located downstream in the specimen-exposure vessel. The dissolution rates for both steels decrease with a decrease in temperature.

The dissolution behavior of austenitic PCA and Type 316 stainless steel shows considerable scatter. At 427 and 482°C, steady-state dissolution is observed after an initial transient period of –1500 h characterized by very large weight losses. For example, the weight losses after the transient period are comparable to those predicted by the steady-state dissolution rates over the next two years. The transient dissolution stage represents the formation of a ferritic layer due to complete depletion of nickel, and to some extent chromium, from the steel.[1,2] The factors that influence the composition or nature of the ferrite layer are not well known. Limited data indicate that the chromium depletion from Type 316 stainless steel exposed at 427°C is higher than for that exposed at 482°C.[2] An increase in nitrogen content in lithium also increases the depletion of chromium from the steel. Specimens that show greater depletion of chromium exhibit large porosity in the ferrite layer. Minor variations in lithium purity, e.g., nitrogen content, or the system parameters, e.g., temperature, downstream effects, etc., are likely to influence the transient dissolution stage and the steady-state dissolution rates of austenitic steels.

Table 9.2.1. Lithium loop operating conditions for various corrosion tests

Test Run	Loop Temperature (°C) Test Vessel	spec. Exp. Vessel	Supply Vessel	Cold Trap	N Content in Lithium (wppm)	Exposure Time (h) Test Vessel	spec. Exp. Vessel
1	482	482	432	212	<50	1295	5000
2	482/427[a]	482	407	230[b]	–250	-	1997
3	427	482	407	230	–100	11011	-
4	482	427	410	212	<100	5521	6501
5	427	372	372	206	–100	5023	4955

[a]Test vessel temperature changed from 482 to 427°C after 1540 h.
[b]No flow through cold trap after 890 h due to plugging. Plugged sections replaced and flow started after an additional 480 h.

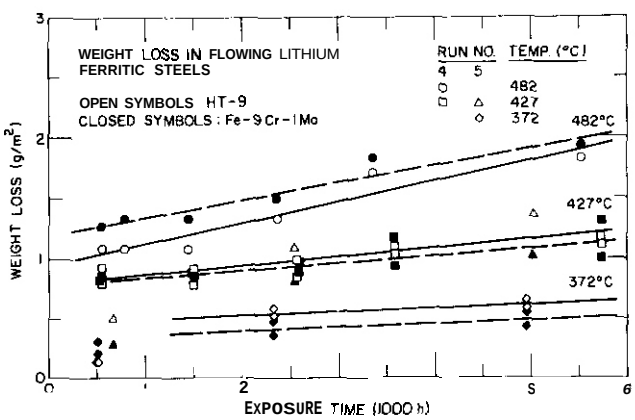

Fig. 9.2.1. Weight loss versus exposure time for HT-9 and Fe-9Cr-1Mo ferritic steels exposed to flowing lithium at 372, 427, and 482°C.

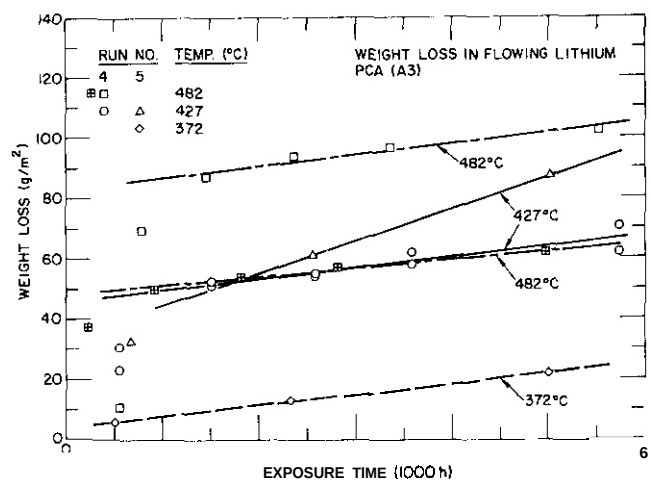

Fig. 9.2.2. Weight loss versus exposure time for PCA exposed to flowing lithium at 372, 427, and 482°C.

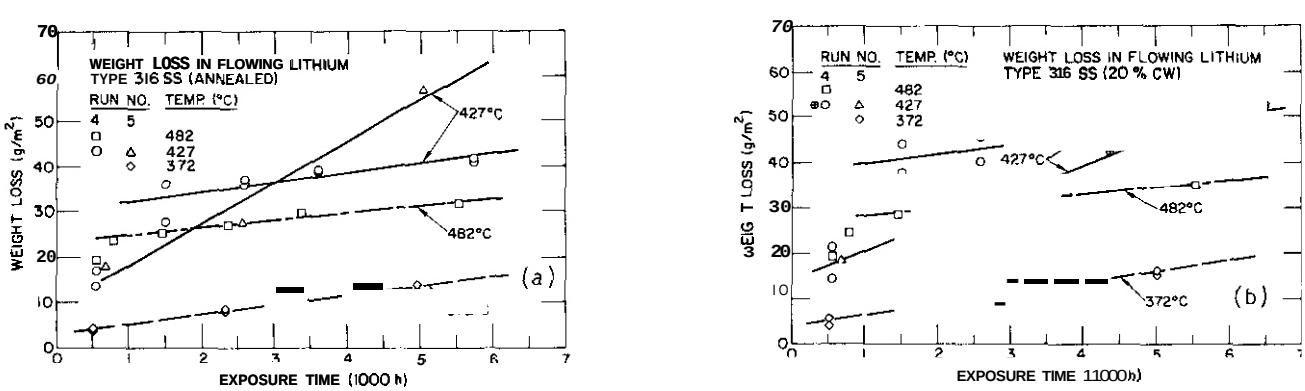

Fig. 9.2.3. Weight loss versus exposure time for (a) annealed and (b) 20% CW Type 316 stainless steel exposed to flowing lithium at 372, 427, and 482°C.

Differences in the transient stage are reflected in the corrosion data shown in Figs. 9.2.2 and 9.2.3. The weight losses and dissolution rates for PCA and Type 316 stainless steel exposed at 427°C are comparable to or higher than those exposed at 482°C. Two PCA specimens which were exposed to lithium at 482°C show a factor of two difference in weight loss; the specimen with smaller weight loss was included in the test run ~550 h after the other specimen. However, duplicate specimens exposed at the same time always show similar dissolution behavior. The austenitic steel specimens exposed at 427°C during run 5 show a different corrosion behavior, e.g., although the weight losses after ~5000 h are not significantly different than those observed at 427 and 482°C during run 4, the dissolution rates are a factor of 3 to 4 higher. Metallographic examination of the specimens, discussed later, indicates that the differences in the dissolution rates for runs 4 and 5 are caused by differences in the ferrite layer which forms on the surface of austenitic steels exposed to lithium.

A transient dissolution stage is not observed for austenitic steels exposed at 372°C. The weight lasses increase linearly with time, and the dissolution rates are comparable with those observed at 427 or 482°C. However, the total weight loss for PCA and Type 316 stainless steel at 372°C is a factor of 3 to 4 lower than at 427 or 482°C.

The dissolution rates of the various sets of ferritic and austenitic steel specimens exposed to flowing lithim at 372, 427, and 482°C are given in Table 9.2.2. These dissolution rates represent the steady-state values shown by the straight lines in Figs. 9.2.1 to 9.2.3. The results indicate that the dissolution rates for HT-9 and Fe-9Cr-1Mo steel decrease by a factor of ~2.5 with each 55°C decrease in temperature. However, the steady-state dissolution behavior of Type 316 stainless steel and PCA is insensitive to changes in temperature; with the exception of run 5 at 427°C, the dissolution rates for Type 316 stainless steel, PCA (A3), and PCA (B2) are ~2.0, 3.4, and 6.0 $mg/m^2 \cdot h$, respectively, at all test temperatures.

After exposure to lithium, the alloy surfaces developed a pebbled or dimpled appearance. Micrographs of Hi-9 alloy exposed to lithim for ~5000 h at 372, 427, and 482°C are shown in Fig. 9.2.4. The size of the dimples decreases with a decrease in temperature. Such dimples form during the initial 2000 h of exposure, and their size does not change with additional exposure. Figure 9.2.5 shows micrographs of the surfaces of HT-9 alloy exposed for 3000 and 5000 h at 482°C. The size and shape of the dimples are identical for the two specimens. The early stage of the surface interactions for HT-9 alloy is shown in Fig. 9.2.6. The micrograph shows that lithium reacts preferentially along the prior austenite boundaries and lathe boundaries. Dimples are beginning to fon in some regions of the surface. Such an etching effect of lithium results in the large weight losses observed during the initial stages of exposure, seen in Fig. 9.2.1.

Table 9.2.2. Dissolution rates of ferritic and austenitic steels exposed to flowing lithium

Test Run	Specimen Location[a]	Temp. (°C)	Maximum Time (h)	Dissolution Rate ($mg/m^2 \cdot h$)					
				HT-9	Fe-9Cr-1Mo	31b SS	316 CW	PCA (A3)	PCA (B2)
4	Test Vessel	482	5521	0.173	0.144	1.61	1.58	3.75	5.11
	Test Vessel	482[b]	4972		-	-	-	2.78	6.57
4	Spec. Exp. Vessel	427[c]	5739	0.064	0.066	2.21	2.18	3.65	6.38
	Spec. Exp. vessel	427[d]	6501	0.070	0.070	-	-	-	-
5	Test Vessel	427	5023	0.077[e]	0.062[e]	9.17	6.34	10.61	-
5	Spec. Exp. Vessel	372[c]	4955	0.029	0.030	2.11	2.48	3.52	-

[a]Corrosion specimens were exposed in the test and specimen exposure vessels of the lithium loop. The lithim flow was from test vessel to specimen exposure vessel.
[b]A second set of PCA specimens was included in run 4 after the first weight change measurements at 549 h of exposure.
[c]Duplicate specimens of each alloy were exposed during the test run.
[d]A set of HT-9, Fe-9Cr-1Mo, and annealed and 20% CW Type 316SS specimens included in test run 4 for long-term exposure. These specimens were removed after 4368 and 6501 h for weight change measurements.
[e]Dissolution rates obtained from the combined data of test runs 4 and 5 at 427°C.

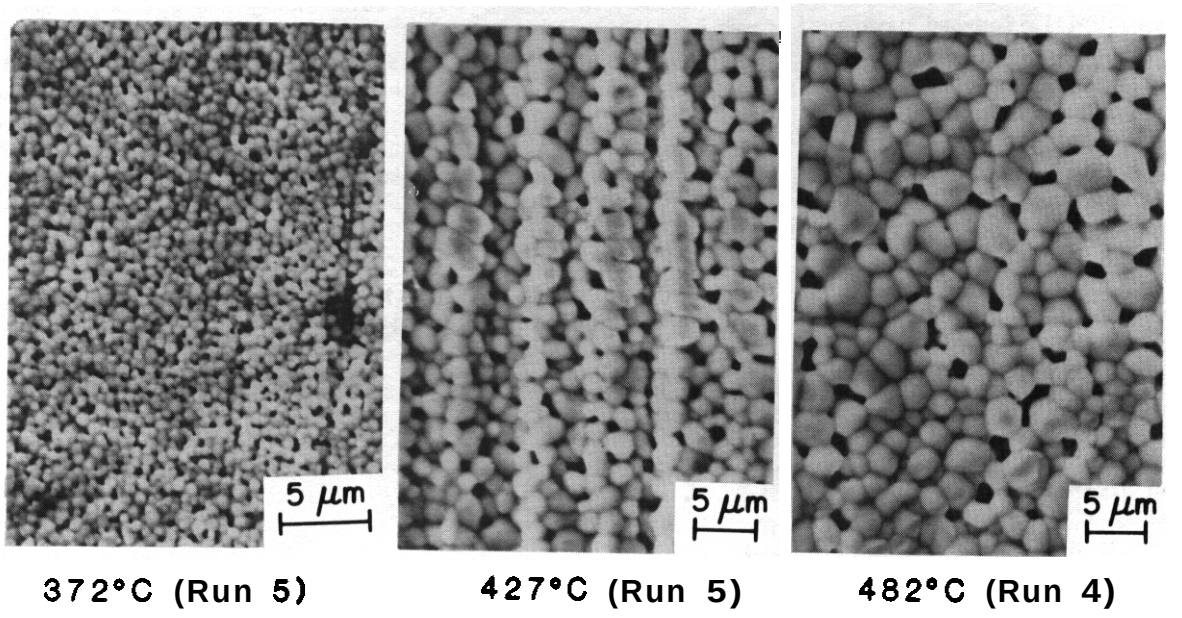

Fig. 9.2.4. Mlcrographs of the HT-9 alloy surface exposed to flowing lithlun for -5000 h at 372, 427, and 482.

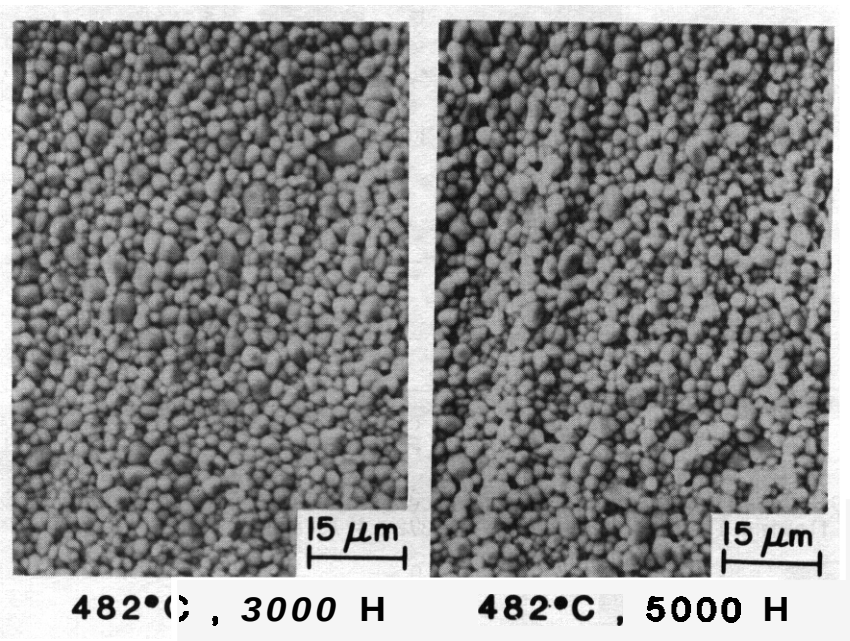

Fig. 9.2.5. Micrographs of the HT-9 alloy surface exposed to flowing lithium for 3000 and 5000 h at 482°C.

Austenitic stalnless steels exposed to lithiun also develop a dimpled appearance. Mlcrographs of annealed Type 316 stainless steel exposed to llthiun for -5000 h at 372, 427, and 482°C are shown in Fig. 9.2.7. The size of the dimples is smaller at 372°C and is not significantly different at 427 and 482°C. The early stage of the formation of dimples for Type 316 stainless steel exposed at 482°C is shown in Fig. 9.2.8; the dimples are small and not fully developed. These results indicate that the transient dissolution stage is not completed even after -5000 h of exposure at 372°C. A true "steady-state" dissolution is not achieved after 5000 h at 372°C, and the dissolution rates are canparable to or higher than the steady-state dissolution rates at 427 or 482°C.

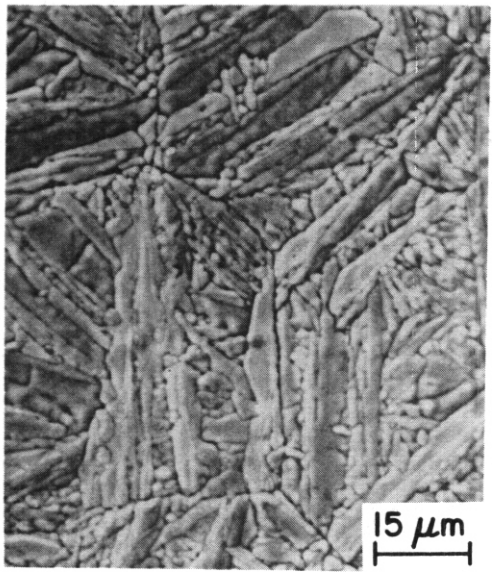

Fig. 9.2.6. **Micrograph of the** HT-9 **alloy surface exposed to flowing lithim for** 1100 h **at** 427°C.

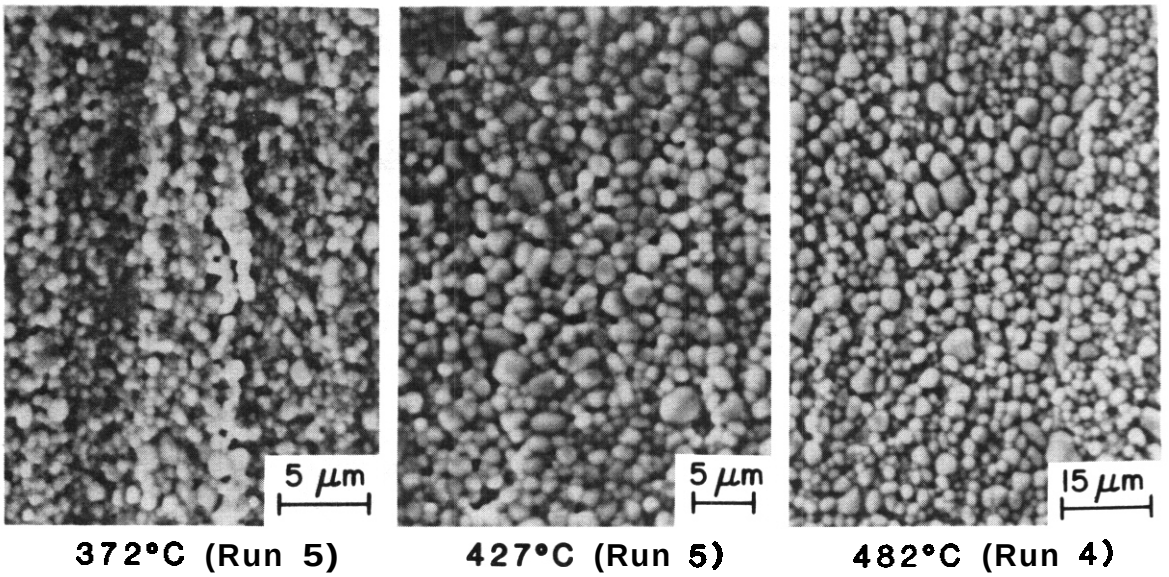

Fig. 9.2.7. **Micrographs of the surface of annealed Type** 316 **stainless Steel exposed to flowing lithim for** ~5000 h **at** 372, 427, **and** 482°C.

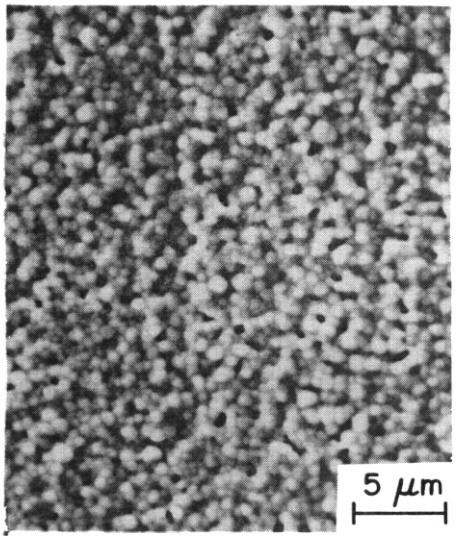

Fig. 9.2.8. **Micrograph of the Type** 316 **stainless steel surface exposed to flowing lithim for** 1300 h **at** 482°C.

In addition to the dimpled appearance, the austenitic steels show surface cavities or porosity. It was shown earlier[2] that specimens with large porosity also show high weight losses. The porosity depends on exposure temperature and nitrogen content in lithium. For example, the Type 316 stainless steel specimens exposed at 427°C show greater porosity and higher loss in weight than the specimens exposed at 482°C, as shown in Figs. 9.2.3 and 9.2.7. Also, Type 316 stainless steel exposed to high-nitrogen lithium (run 21 at 482°C showed large porosity.[2]

The lithium-exposed specimens were examined metallographically for measurements of the depth of internal corrosive penetration and compositional changes of the surface of the specimens. The ferritic steels showed little or no internal corrosion, whereas the austenitic steels developed a porous ferrite layer. The thickness of the ferrite layer was determined from the difference between the initial thickness of the specimen and the sound metal remaining (i.e., the unreacted metal) after exposure to lithium. At least 10 measurements were made to obtain an average value. The thickness of the ferrite layer formed on annealed and 20% CW Type 316 stainless steel exposed to lithium at 427 and 482°C is plotted as a function of time in Fig. 9.2.9. Most of the data can be represented by a power-law relationship with a value of 1.34 for the time constant. Such a relationship yields a growth rate of 22 μm/y at 5000 h. These results indicate that a "stoichiometric" steady-state dissolution is not achieved in a flowing lithium environment, as is generally observed for austenitic steels exposed to flowing sodium environment. A steady-state dissolution rate is attained in sodium when the elements being dissolved from the ferrite layer are in proportion to their concentration in the steel. Consequently, at steady state, the movement of the ferrite/austenite boundary is the same as the recession of the dissolving surface, such that the thickness of the ferrite layer is constant. Data for internal penetration yield a growth rate of ~22 μm/y, whereas the weight loss measurements give an average dissolution rate of ~2 $mg/m^2 \cdot h$, which corresponds to a uniform recession of only ~2.1 μm/y.

Micrographs and distribution of major elements across the ferrite layers of PCA and Type 316 stainless steel are shown in Fig. 9.2.10. Both steels show an ~10-μm-thick surface region depleted in chromium and completely depleted of nickel over the entire ferrite layer. The concentration of nickel decreases abruptly across the ferrite/austenite interface. The weight loss during the transient dissolution stage and steady-state dissolution rate for austenitic steel depend strongly on the nature of the ferrite layer. Figure 9.2.11 shows the ferrite layers formed on 20% CW Type 316 stainless steel exposed during runs 4 and 5 for >5000 h at 427°C. The ferrite layers are significantly different for the two specimens exposed under similar time and temperature conditions. The specimen exposed during run 4 has uniform porosity, while the specimen from run 5 has a layered structure, viz., the outer 15-μm-thick layer has very large cavities and the inner 30-μm-thick layer is relatively free from porosity. A similar layered structure was observed for the annealed Type 316 stainless steel exposed during run 5. The high dissolution rates observed for these specimens from run 5 may be attributed to the large cavities in the ferrite layer that forms on the specimen surface.

Energy dispersive x-ray analyses were performed to determine the differences in surface composition of HT-9 alloy and Type 316 stainless steel specimens exposed to lithium at different temperatures and lithium purity conditions. The weight loss and concentrations of major elements for specimens exposed during different test runs are given in Tables 9.2.3 and 9.2.4. The results for HT-9 alloy indicate that after ~5000 h of exposure at 372, 427, and 482°C, the concentration of chromium in the alloy surface decreases from 12% to between 6 to 8%; the values after exposure at 482°C are lower than those at 372°C. Specimens exposed [illegible] h [illegible] indicati [illegible] ic [illegible] es. Figure 9 [illegible] s [illegible] indicate any correlation between suri [illegible]

The results for Type 316 stainless steel indicate that the depletion of nickel from the steel is quite rapid. The concentration of nickel decreases from 12.9 to <1% after ~5000 h of exposure at 427 or 482°C. The nickel content is slightly higher, e.g., 1.2 to 1.5%, after short-term exposure at 427 or 482°C or after [illegible] p [illegible], and r [illegible] h [illegible] g., -13% a [illegible] ur [illegible] itrogen (run 2) show greater depletion of chromium than those exposed to lithium with <100 wppm nitrogen. The chromium content is lower in specimens exposed at 427°C than those exposed at 482°c (average chromium is 8.4% at 427°C and 9.8% at 482°C). Specimens with greater depletion of chromium also show larger weight loss and internal penetration. Data at 372°C indicate that the transient dissolution stage is not over after ~5000 h at 372°C. The average chromium content for the specimens is ~10.2%.

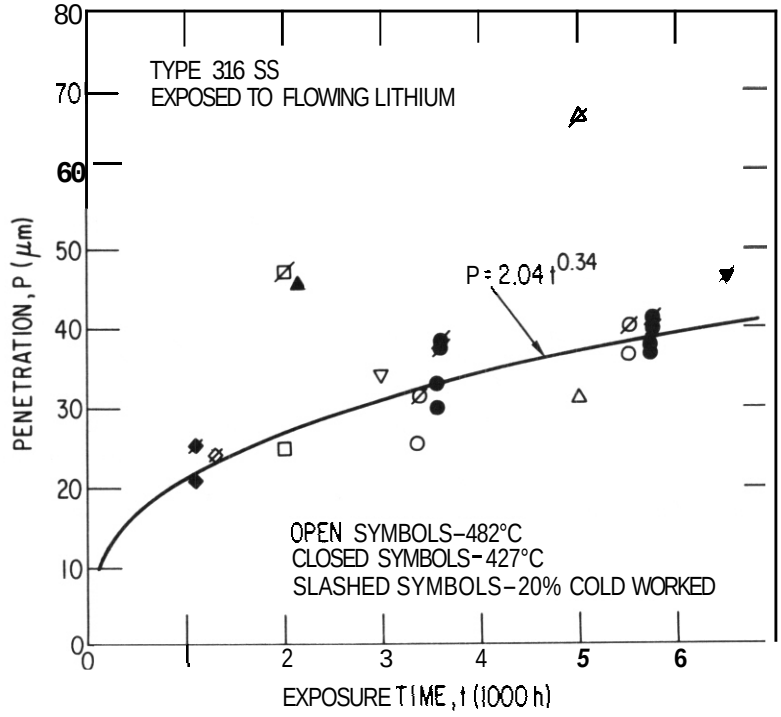

Fig. 9.2.9. **Internal penetration versus exposure time for Type** 316 **stainless steel exposed to lithim at** 427 **and** 482°C.

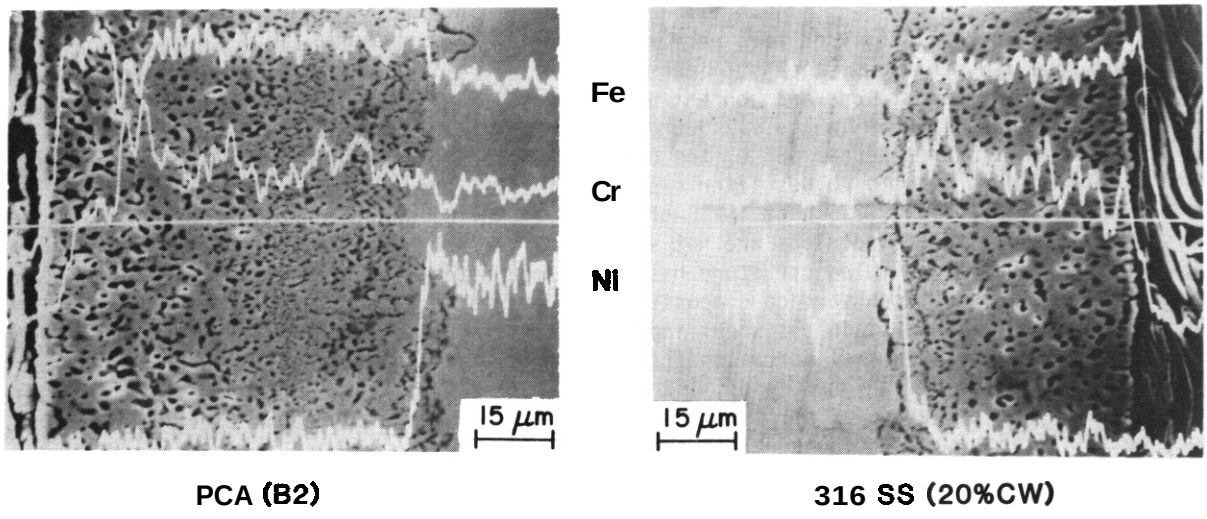

Fig. 9.2.10. **Micrographs and concentration profiles for major elements across the ferrite layer of** PCA **and Type** 316 **stainless steel exposed to lithium at** 427°C.

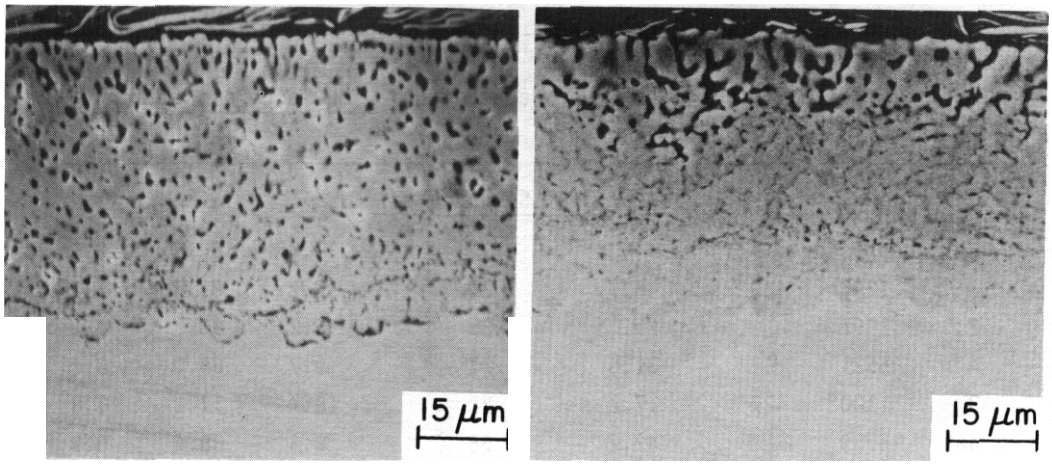

6501 H (Run 4) 5023 H (Run 5)

Fig. 9.2.11. Micrographs of the ferrite layers formed on 20% CW Type 316 stainless steel exposed to lithium for >5000 h at 427°C during runs 4 and 5.

Table 9.2.3. Weight loss and surface composition of HT-9 alloy exposed to flowing lithium

Test Run	Time (h)	Temp. (°C)	Weight Loss (g/m^2)	Surface Composition (%) Cr	Fe
-	Unexposed		-	12.0	85.6
1	1295	482	0.30	10.8	86.8
1	3000		1.35	6.2	91.8
1	5000		0.82	6.6	91.3
2	1997		2.93	7.1	88.5
4	5521		1.83	5.9	88.4
3	1100	427	0.22	11.0	87.0
4	5739		1.17	8.1	87.1
4	5739		1.11	8.7	84.8
4	6501		0.85	7.3	90.7
5	5023		1.37	6.5	88.4
5	4955	372	0.58	8.3	89.7
5	4955	372	0.65	8.0	87.8

Table 9.2.4. Weight loss, depth of internal penetration, and surface compositions of Type 316 stainless steel exposed to flowing lithium

Test Run	Time (h)	Temp. (°C)	Weight Loss (g/m^2)	Penetration (μm)	Surface Composition (%) Cr	Fe	Ni
			Type 316 SS (annealed)				
-	Unexposed		-	-	17.5	64.9	12.9
1	1295	482	6.7	13	12.2	81.6	1.2
2	1997		21.0	25	6.2	90.9	1.1
4	5521		31.8	37	9.7	84.0	0.7
3	1100[a]	427	17.2	21	18.7	77.1	1.8
4a	5739		42.2	38	8.3	88.4	0.9
4b	5739		41.5	37	8.1	86.6	0.8
5	5023		57.2	31	8.0	90.6	0.6
5a	4955	372	14.1	9	10.6	86.0	1.4
5b	4955	372	12.9	13	9.1	87.3	1.5
			Type 316 SS (20% CW)				
1	1295	482	23.8	24	13.9	78.0	0.6
2	1997		46.5	47	5.6	88.1	0.6
4	5521		35.0	40	10.0	85.6	0.7
3	1100	427	24.9	25	14.3	82.6	1.3
4a	5739		47.9	42	8.8	88.3	1.0
4b	5739		51.6	40	8.6	86.8	0.9
4	6501		52.9	46	7.3	87.9	0.8
5	5023		46.0	38	8.5	89.4	0.6
5a	4955	372	16.3	14	-	-	-
5b	4955	372	15.5	13	10.2	86.5	1.4

[a]Large deposits of chromium observed on the specimen. The surface canposition represents regions away fran the deposits.

9.2.5 Conclusions

Corrosion data for ferritic HT-9 and Fe-9Cr-1Mo steel in flowing lithim at 372, 427, and 482°C indicate that the weight losses for ferritic steel increase linearly with time and yield a constant dissolution rate. The dissolution behavior of the HT-9 alloy and Fe-9Cr-1Mo steel is identical at all temperatures. For both steels, the dissolution rates decrease by a factor of ~2.5 with each 55°C decrease in temperature. After exposure to lithim, the alloy surfaces develop a dimpled appearance. The size of the dimples decreases with a decrease in temperature. The dimpled structure is fully developed after ~2000 h of exposure at temperatures between 372 and 482°C, and the size of the dimples does not change with additional exposure. Such an "etching effect" of lithium leads to significant weight loss during the initial period of exposure. The lithim-exposed specimens show some depletion of chromium fran the specimen surface; the surface concentration of chromium is between 6 and 8%.

The austenitic PCA and Type 316 stainless steel show a complex dissolution behavior in flowing lithium. The dissolution rates reach a steady state after a transient period of ~1500 h characterized by rapid dissolution. At 427 and 482°C, the weight losses during the transient dissolution stage are equivalent to those predicted by the steady-state dissolution rates over the next two years. The total weight loss for austenitic steels in lithim at 372, 427, and 482°C is more than an order of magnitude

greater than the ferritic steels. The most significant feature of the corrosion behavior of austenitic steels in lithium is that the steady-state dissolution rates are insensitive to changes in exposure temperature. The average steady-state dissolution rates for Type 316 stainless steel, PCA (A3), and PCA (B2) are –2.0, 3.4, and 6.0 $mg/m^2 \cdot h$, respectively.

The transient dissolution stage for austenitic steels represents the formation of a ferritic surface layer due to depletion of nickel and, to some extent, chromium from the steel. Metallographic examination of the lithim-exposed specimens indicates that the transient dissolution stage plays an important role in controlling the nature and growth of the ferrite layer and, consequently, in the overall dissolution behavior of austenitic steels. Limited data show that an increase in nitrogen content in lithium from –100 to 250 wppn increases the porosity in the ferrite scale as well as the weight loss for the specimen. Austenitic steels exposed at 427°C show greater porosity and weight loss than those exposed for similar times at 482°C. Specimens with higher weight loss also exhibit larger depletion of chromium from the steel. The transient dissolution stage is not over even after –5000 h of exposure in lithium at 372°C.

The results indicate that different mechanisms control the dissolution behavior of austenitic steels. The influence of system parameters, such as temperature, lithium purity, downstream effects, etc., needs to be determined to establish the dissolution/mass transfer behavior of austenitic stainless steels in flowing lithium. Estimates of mass transfer in lithim-austenitic steel systems based on a steady-state dissolution rate do not account for the significant mass transfer that occurs during the initial –1500 h of exposure. Corrosion tests are in progress in flowing lithium at 538 and 482°C to evaluate the dissolution behavior of ferritic and austenitic steels at higher temperatures.

9.2.6 References

1. O. K. Chopra and O. L. Smith, "Environmental Effects on Properties of Structural Alloys in Flowing Lithium," pp. 176-182 in Alloy Developnent for Irradiation Performance: Semiannual Progress Report for Period Ending March 31, 1984, DOE/ER-0045/12, Oak Ridge National Laboratory, Oak Ridge, TN, July 1984.

2. O. K. Chopra and D. L. Smith, "Environmental Effects on Properties of Structural Alloys in Flowing Lithium," pp. 200-204 in Alloy Developnent for Irradiation Performance: Semiannual Progress Report for Period Ending September 30, 1984, DOE/ER-0045/13, Oak Ridge National Laboratory, Oak Ridge, TN, March 1985.

9.3 ENVIRONMENTAL EFFECTS ON PROPERTIES OF STRUCTURAL ALLOYS IN FLOWING Pb-17Li - O. K. Chopra and D. L. Smith (Argonne National Laboratory)

9.3.1 ADIP Task

ADIP Task I.A.3, Perform Chemical and Metallurgical Compatibility Analyses.

9.3.2 Objective

The objective of this program is to investigate the influence of a flowing Pb-17 at. % Li environment on the corrosion behavior and mechanical properties of structural alloys under conditions of interest for fusion reactors. Corrosion behavior is evaluated by measuring the weight change and depth of internal corrosive penetration of alloy specimens exposed to flowing Pb-17Li for various times. The dissolution rates are determined as a function of temperature. Metallographic examination of the alloy surface is used to establish the mechanism and rate-controlling process for the corrosion reactions. Initial effort on mechanical properties is focused on tensile tests in a flowing Pb-17Li environment.

9.3.3 Summary

Corrosion data are presented for ferritic HT-9 and Fe-9Cr-1Mo steel and austenitic Type 316 stainless steel in flowing Pb-17Li at 413, 427, and 454°C. Tensile properties of HT-9 alloy in a flowing Pb-17Li environment at temperatures between 270 and 450°C are also reported.

9.3.4 Progress and Status

The effects of a flowing Pb-17Li environment on the corrosion behavior and mechanical properties of austenitic and ferritic steels are being investigated.[1-3] Tests are conducted in a forced-circulation Pb-17 at. % Li loop consisting of a high-temperature test vessel with a heat exchanger section and a cold-temperature chamber. The eutectic alloy was prepared in a separate vessel and transferred into the loop. A schematic of the loop and mixing vessel is shown in Fig. 9.3.1. The total volume of the loop is ~2 liters. Several analyses of the eutectic alloy show that the concentrations of O, H, and N are 260, 22, and <10 wppm, respectively.

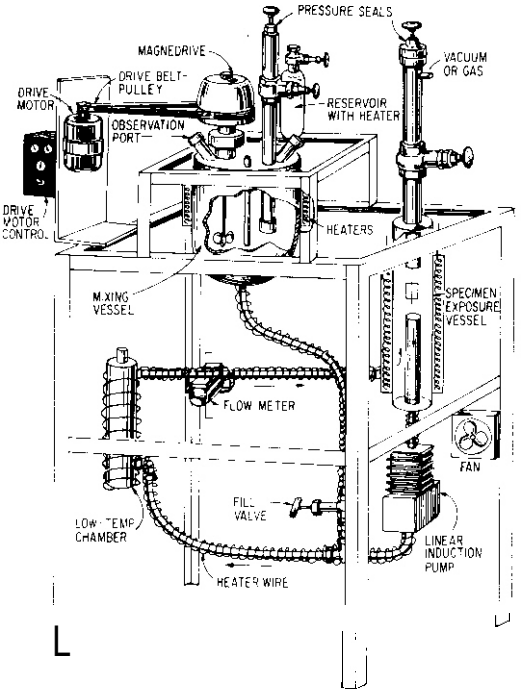

Fig. 9.3.1. Schematic of Pb-17Li Test Loop.

Flat corrosion coupons, ~73 x 10 x 0.26 mm in size, of Type 316 stainless steel, PCA, Fe-9Cr-1Mo, and HT-9 alloy were exposed to flowing Pb-17Li, and the corrosion behavior was evaluated by measurements of weight loss and depth of internal corrosive penetration. Two corrosion test runs of ~4000-h duration each were completed at maximum temperatures of 454 and 427°C. respectively. For each test run, specimens were exposed at two locations, viz., the maximum temperature position in the test vessel and at the entrance of the heat-exchanger tube. The temperature of the latter position was 15 to 25°C lower than the maximum temperature. For both test runs, the Pb-17Li alloy was recirculated at ~350 cm^3/min and the cold-leg temperature was maintained at 300°C. The specimens were periodically removed fran the loop for weight change measurements. After each exposure, the corrosion specimens were cleaned in static lithium at ~300°C. Subsequently, they were washed in alcohol and water. This procedure was repeated several times until no further weight change was observed for the specimens.

Constant extension rate tests (CERT) are also being conducted on HT-9 alloy in a flowing Pb-17Li environment to study the possible embrittlement of the material. The CERT facility and a mechanical test fixture were constructed for performing the tests in the flowing environment. Cylindrical specimens, 2.54-mm diameter and 10.2-mm gauge length (ASTM Standard E8), were tested at temperatures between 270 and 450°C and a constant extension rate of 5.1 x 10^{-5} mm/s.

9.3.4.1 Corrosion Behavior

Figures 9.3.2 and 9.3.3 show the weight losses of ferritic and austenitic steels, respectively, in flowing Pb-17Li at 413, 427, and 454°C as a function of time. The results indicate that the weight losses for HT-9 and Fe-9Cr-1Mo ferritic steels increase linearly with time, whereas the annealed and 20% cold-worked (CW) Type 316 stainless steels achieve a steady-state dissolution behavior after an initial period of ~500 h characterized by very high dissolution rates. The weight losses for austenitic steels are an order of magnitude higher than for the ferritic steels. For austenitic steels, the large weight losses during the initial transient period represent the formation of a ferritic surface layer due to complete depletion of nickel and, to a lesser extent, chromium fran the steel.[3] Generally, the ferrite layer is very porous, and the concentrations of nickel and chromim decrease abruptly across the ferrite/austenite interface. The ferritic steels show a slight depletion of chromium after exposure to flowing Pb-17Li. The distribution of Ni, Cr, and Fe across the surface regions of annealed Type 316 stainless steel and HT-9 alloy is shown in Fig. 9.3.4.

The steady-state dissolution rates for HT-9, Fe-9Cr-1Mo, and annealed and 20% CW Type 316 stainless steels in flowing Pb-17Li are given in Table 9.3.1. The results indicate that the dissolution rates for ferritic steels decrease with a decrease in temperature. However, the data for Type 316 stainless steel show considerable scatter; e.g., the dissolution rates at 454°C fran Run 1 are comparable to those at 427°C from Run 2, and the rates at 427°C from Run 1 are comparable to those at 413°C from Run 2. For both ferritic and austenitic steels, the dissolution rates at 427°C fran Run 2 are significantly higher than those from Run 1. These differences at 427°C may be attributed to specimen location, i.e., the specimens at 427°C fran Run 1 were placed downstream and were not at the maximum loop temperature, whereas the specimens from Run 2 were at the maximum loop temperature of 427°C. The large scatter in dissolution rates for Type 316 stainless steel may also result fran differences in the nature of the ferrite layer, specifically the porosity in the ferrite layer. The ferrite layer is very weak and often breaks off during exposure or the cleaning procedure, adding considerable uncertainty in the weight loss measurements.

9.3.4.2 Tensile Properties

Tensile properties of normalized and tempered HT-9 alloy at temperatures between 213 and 454°C and a constant extension rate of 5.1 x 10^{-5} mm/s in flowing Pb-17Li are given in Table 9.3.2. Prior to testing, all specimens were exposed for ~18 h to flowing Pb-17Li at 427°C to achieve complete wetting of the specimen surface. The results indicate that the ultimate and yield strengths of the steel in Pb-17Li are comparable to those observed in air or a flowing lithim environment.[4] All specimens showed considerable necking and a ductile fracture. The reductions in area at the different temperatures are >50%. The values of total elongation over the gauge length of the specimens were >18%. The specimens tested below 371°C showed serrated flow. Tests are in progress on normalized and tempered HT-9 alloy at a constant extension rate of 1 x 10^{-2} mm/s.

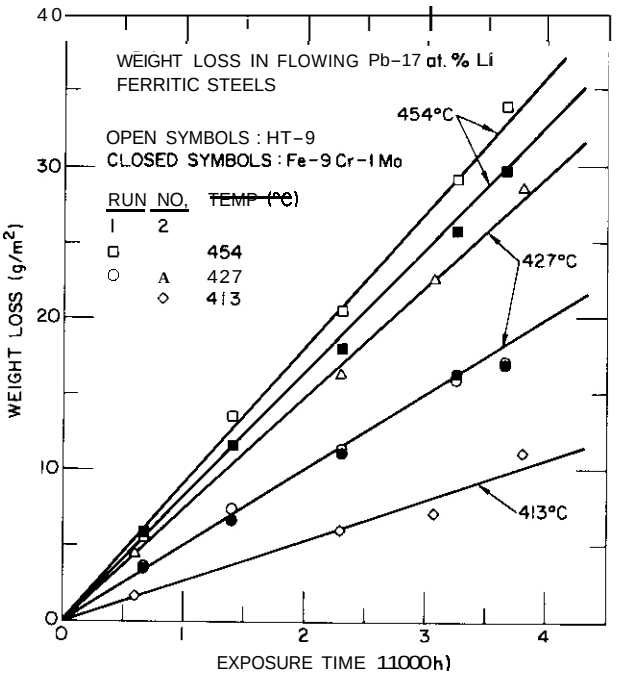

Fig. 9.3.2. Weight loss versus exposure time for HT-9 and Fe-9Cr-1Mo ferritic steel exposed at 413, 427, and 454°C to flowing Pb-17Li. For both test runs, specimens at the higher temperature were located at the maximum loop temperature while the specimens at the lower temperature were placed downstream.

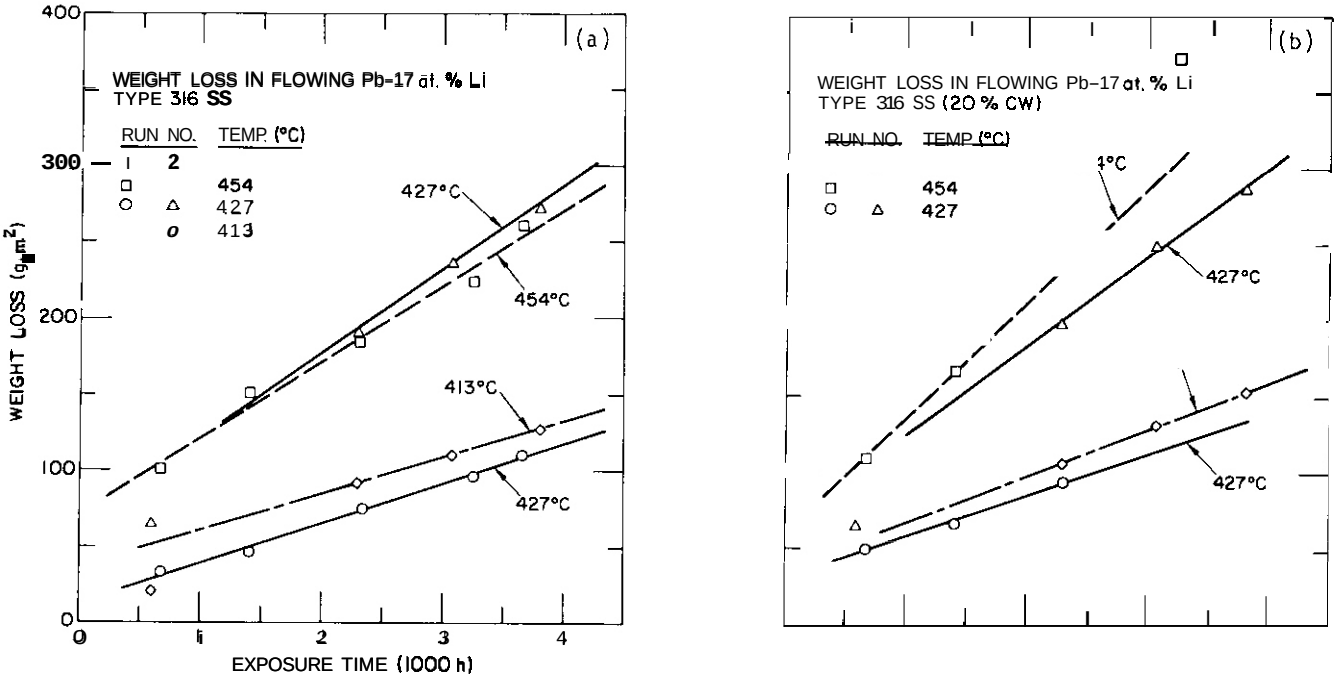

Fig. 9.3.3. Weight loss versus exposure time for (a) annealed and (b) 20% cold-worked Type 316 stainless steel exposed at 413, 427, and 454°C to flowing Pb-17Li. For both test runs, specimens at the higher temperature were located at the maximum loop temperature while the specimens at lower temperature were placed downstream.

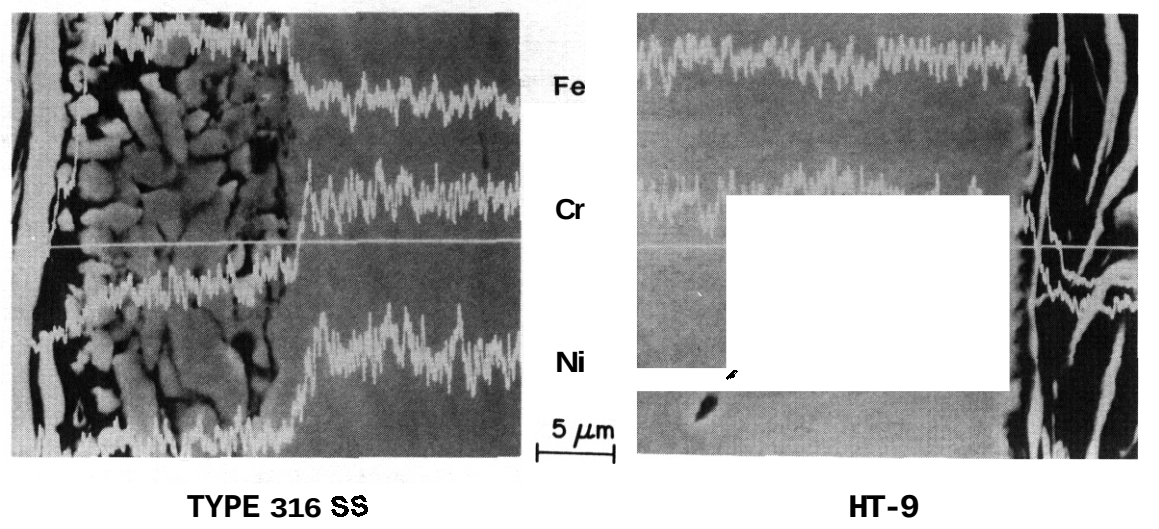

Fig. 9.3.4. Micrographs and concentration profiles for major elements across the ferrite layer of Type 316 stainless steel and the surface region of the HT-9 alloy exposed to Pb-17Li for 3663 h at 454°C.

Table 9.3.1. Dissolution rates for ferritic and austenitic steels exposed to flowing Pb-17Li

Run Number	Temp. (°C)	Maximum Time (h)	Dissolution Rate ($mg/m^2 \cdot h$)			
			T-9	9Cr-1Mo	316 SS	316 CW
1	454	3663	9.0	8.2	50.1	75.9
1	427	3663	5.1	4.9	26.1	27.4
2	427	3808	7.4	-	55.1	58.6
2	413	3808	2.6	-	23.9	31.1

Table 9.3.2. Tensile properties of HT-9 alloy tested in flowing Pb-17Li

Specimen Number[b]	Test Temp.[a] (°C)	Ultimate Strength (MPa)	0.2% Yield Strength (MPa)	Reduction in Area (%)
TH-8	454	596	478	75.0
TH-1	427	644	-	-
TH-3	427	627	486	63.1
TH-4	371	711	550	57.3
TH-5	316	730	534	55.3
TH-6	273	740	556	59.5
TH-7	273	749	573	58.8

[a]All specimens were exposed for ~18 h in flowing Pb-17Li at 427°C before testing. Tests were performed at a constant extension rate of 5.1×10^{-5} mm/s.

[b]Cylindrical specimens, 2.54-mm diameter and 14.3-mm gauge length.

9.3.5 Conclusions

Corrosion data in flowing Pb-17Li at 413, 427, and 454°C indicate that the dissolution rates for austenitic steels are an order of magnitude greater than those for ferritic steels. The dissolution rates for ferritic steels decrease with a decrease in temperature, whereas the rates for austenitic Type 316 stainless steel show considerable scatter. The austenitic steels show large weight losses during the initial ~500 h of exposure and develop a very porous ferrite layer. Differences in the nature of the ferrite layer and downstream effects may cause the scatter in corrosion data for austenitic stainless steels. Corrosion tests are in progress in flowing Pb-17Li at 482 and 465°C to determine the change in dissolution rates with time.

Tensile tests on normalized and tempered HT-9 alloy show that at slow extension rates (5.1×10^{-5} mm/s) a flowing Pb-17Li environment has little or no effect on tensile properties. At temperatures between 270 and 450°C, the material shows good ductility and the ultimate and yield strengths are comparable to those observed in air.

9.3.6 References

1. O. K. Chopra and D. L. Smith, "Environmental Effects on Properties of Structural Alloys," pp. 216-200 in Alloy Development for Irradiation Performance: Semiannual Progress Report for Period Ending September 30, 1983, DOE/ER-0045/11, Oak Ridge National Laboratory, Oak Ridge, TN.

2. O. K. Chopra and D. L. Smith, "Corrosion of Ferrous Alloys in Eutectic Lead-Lithium Environment," J. Nucl. Mater. 122-123, 1219-1224 (1984).

3. O. K. Chopra and D. L. Smith, "Corrosion of Structural Alloys in Flowing Pb-17Li Environment," pp. 183-189 in Alloy Development for Irradiation Performance: Semiannual Progress Report for Period Ending March 31, 1984, DOE/ER-0045/12, Oak Ridge National Laboratory, Oak Ridge, TN, July 1984.

4. O. K. Chopra and D. L. Smith, "Environmental Effects on Properties of Structural Alloys in Flowing Lithium," pp. 176-182 in Alloy Development for Irradiation Performance: Semiannual Progress Report for Period Ending March 31, 1984, DOE/ER-0045/12, Oak Ridge National Laboratory, Oak Ridge TN, July 1984.

9.4 THERMAL CONVECTION LOOP STUDIES OF THE LITHIUM CORROSION OF LOW ACTIVATION AUSTENITIC ALLOYS AND STANDARD Fe-12Cr-1MoVW STEEL — P. F. Tortorelli and J. H. DeVan (Oak Ridge National Laboratory)

9.4.1 ADIP Task

ADIP Task I.A.3, Perform Chemical and Metallurgical Compatibility Analyses.

9.4.2 Objective

The purpose of this task is to determine the corrosion resistance of candidate first-wall materials to slowly flowing lithium in the presence of a temperature gradient. Corrosion and deposition rates are measured as functions of time, temperature, additions to the lithium, and flow conditions. These measurements are combined with chemical and metallographic examinations of specimen surfaces to establish the mechanisms and rate-controlling processes for dissolution and deposition reactions.

9.4.3 Summary

Further data for Cr-Mn steels in thermally convective lithium showed that corrosion in such systems was complicated by multiple simultaneous corrosion processes. The dominant corrosion reaction during higher temperature exposure of 12Cr-1MoVW steel to thermally convective lithium was thermal gradient mass transfer.

9.4.4 Progress and Status

Because of their favorable neutronic (i.e., activation) properties, manganese-containing austenitic stainless steels are currently being investigated as part of the fusion alloy development effort. Consequently, a qualitative assessment of the resistance of such steels to corrosion by molten lithium was begun using a thermal convection loop with removable specimens (of a type described previously[1]). The loop was constructed of type 316 stainless steel which, because of prior operation with lithium and associated preferential leaching of nickel and chromium, was known to have a considerably higher iron concentration at hot leg surfaces than found in the starting material. The manganese-containing alloy specimens were exposed to lithium in a region of the loop near the top of the hot leg. Because of the nonisothermal nature of the loop, the temperatures of these specimens varied from 500°C [maximum loop temperature (T_{max})] to 480°C. However, this temperature difference was small relative to the loop's overall temperature differential (150°C). Coupons of type 316 stainless steel were placed at the other normally used specimen positions around the remainder of the loop.

The first experiment with manganese-containing alloys used specimens provided by Hanford Engineering Development Laboratory (HEDL). (The compositions of these alloys are given in Table 9.4.1.) Weight change data and some scanning electron microscopy/energy dispersive analysis results for these alloys, after a total exposure of 3340 h, were reported in the preceding progress report[2] and revealed a complex overall corrosion process involving chromium transfer among hot leg specimens and substantial manganese depletion from the Cr-Mn steels. The alloys containing 30 wt % Mn (X75, R77, R80, see Table 9.4.1) were severely corroded in lithium at 500°C and suffered large overall weight losses.[2] The weight change data yielded a less definitive result in the case of the alloys containing 15 to 18 wt % Mn due to the competing effects of chromium deposition and manganese dissolution. However, the scanning electron microscopy and energy dispersive x-ray analysis of the exposed surfaces confirmed that such alloys are subject to rather extensive dissolution when exposed to thermally convective lithium at 500°C and, consequently, are not particularly corrosion resistant. These results were consistent with earlier work in static lithium,[3-5] which showed that manganese-containing alloys suffered preferential dissolution and that the high nitrogen concentrations of these steels would accelerate corrosion in lithium.

Table 9.4.1 Compositions of Fe-Mn-Cr and Fe-Ni-Cr steels exposed to thermally convective lithium between 500 and 485°C in the first loop experiment

Alloy	Composition (wt %)						
	Mn	Cr	Ni	C	N	Si	Fe
18-18+	18	18	0.5	0.1	0.4	0.6	bal
AMCR	17	10	0.7	0.2	0.06	0.6	bal
R88	15	15	0.5	0.3	0.30	0.4	bal
X75	30	2	0.5	0.1	0.15	0.4	bal
R77	30	2	0.5	0.6	0.15	0.4	bal
R80	30	10	0.5	0.50	0.10	0.4	bal
CN13	1.7	17	14.0	0.05		0.6	bal
316 SS	2	17	10	0.05		0.4	bal

In the preceding progress report,[2] it was observed that, in the loop containing the Cr-Mn steels, the dissolved manganese from the hot zone specimens tended to be deposited, along with nickel, in the coldest part of the loop. This observation was based on the examination of only one cold leg specimen and, since then, scanning electron microscopy and associated energy dispersive x-ray analysis of the surfaces of additional cold leg specimens have confirmed this initial result. As shown in Table 9.4.2 and Fig. 9.4.1, the amount of deposition on these surfaces increased dramatically with decreasing temperature. The weight gain data and the examination of surface morphology showed that very little deposition occurred on the cold leg specimen at 410°C.

However, extensive deposition was noted for the coldest specimen (350°C) and this is reflected in the large measured weight gain (see Table 9.4.2). In addition, as also shown in Table 9.4.2, a semi-quantitative analysis of energy dispersive x-ray data taken from the surfaces of these cold leg specimens indicated that the overall surface composition increased in manganese and nickel as the temperature decreased. This is consistent with the appearance of more and larger deposits (and greater weight gains per unit area) as the specimen temperature decreased. Figure 9.4.2 shows some higher magnification micrographs of these deposits and includes their corresponding energy dispersive x-ray spectra that indicate high manganese and nickel concentrations relative to the underlying matrix.

Table 9.4.2 Weight gains and surface compositions of cold leg type 316 stainless steel specimens in a lithium thermal convection loop that operate between 500 and 350°C with Cr-Mn steel specimens in its hot zone for 3340 h

T (°C)	Weight gain (g/m^2)	Surface concentration (wt %)[a]			
		Fe	Cr	Ni	Mn
	unexposed	64	18	13	3
410	1.4	60	15	18	3
390	15.1	27	7	40	27
370	23.9	18	4	44	22
350	70.9	7	2	48	43

[a]Semi-quantitative determination based on ZAF-corrected energy dispersive x-ray analysis data.

The observation of a large concentration of manganese in the coldest area of the loop confirms that the manganese being dissolved from a few specimens in the hottest part of the loop is being transported and deposited in the cold zone. Thus, thermal gradient mass transfer of manganese will be a major concern in manganese steel—lithium systems, just as nickel mass transfer is for nickel-bearing alloys exposed to nonisothermal lithium. The lack of significant chromium deposition in the cold zone (see Table 9.4.2) is consistent with the observation, cited in the preceding progress report,' that chromium is preferentially reacting in the hot zone of the loop.

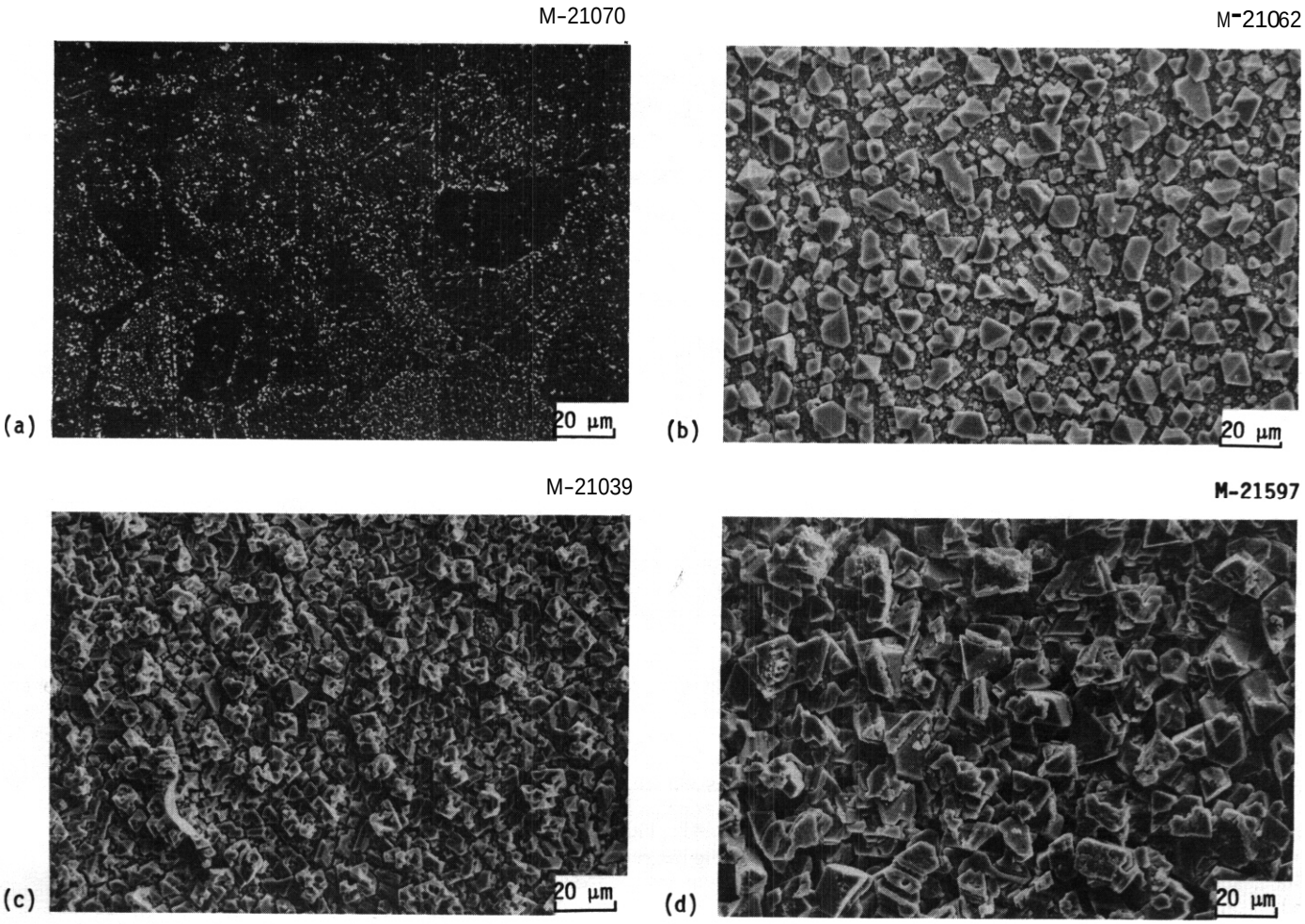

Fig. 9.4.1. Scanning electron micrographs of type 316 stainless steel coupon surfaces located in the cold leg of a lithium thermal convection loop containing Cr-Mn and Cr-Ni austenitic alloy specimens in its hot leg. Maximum loop temperature was 500°C. (a) 410°C. (b) 390°C. (c) 370°C. (d) 350°C.

M-21067

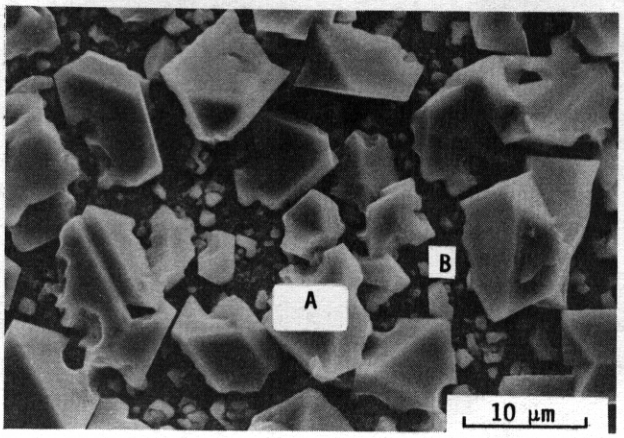

ORNL-DWG 85-1903

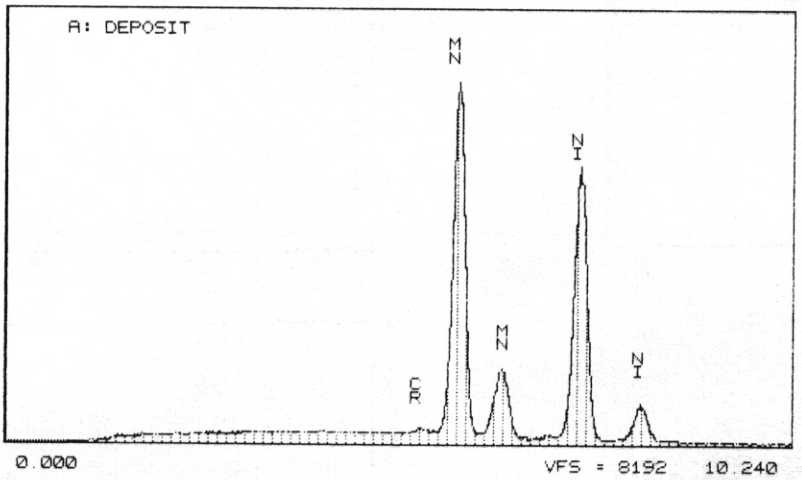

ORNL-DWG 85-1904

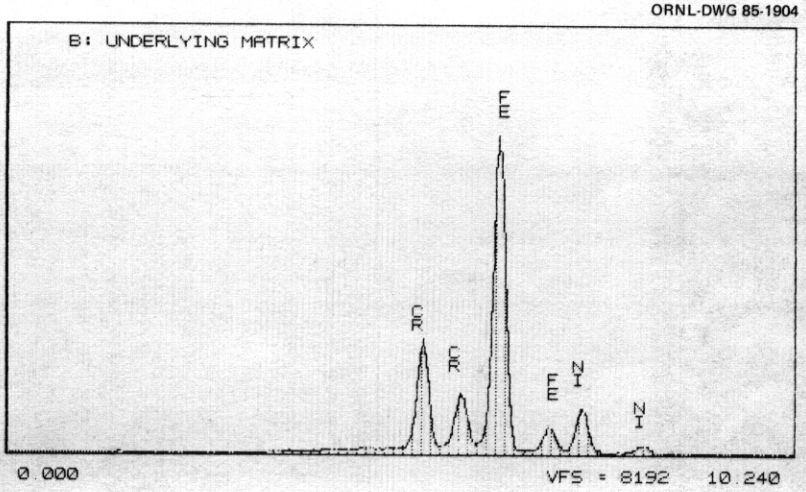

(a)

M-21041

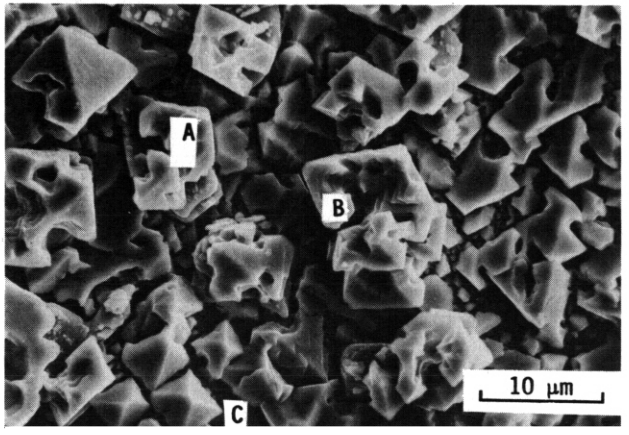

ORNL-DWG 85-1905

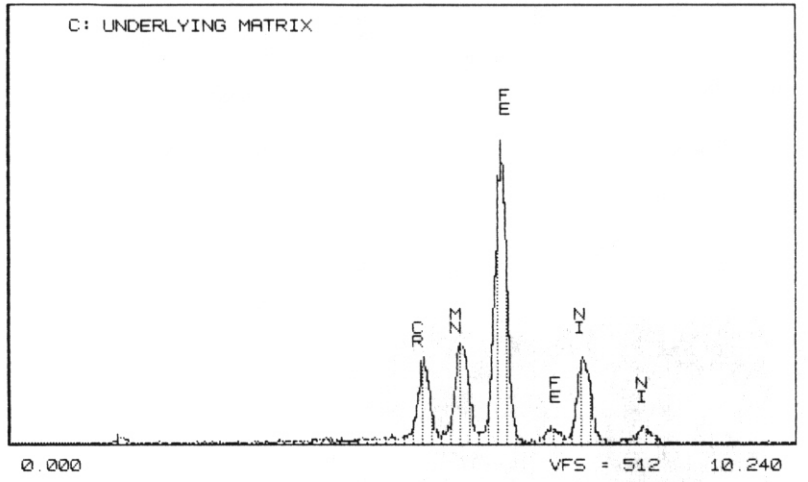

ORNL-DWG 85-1906

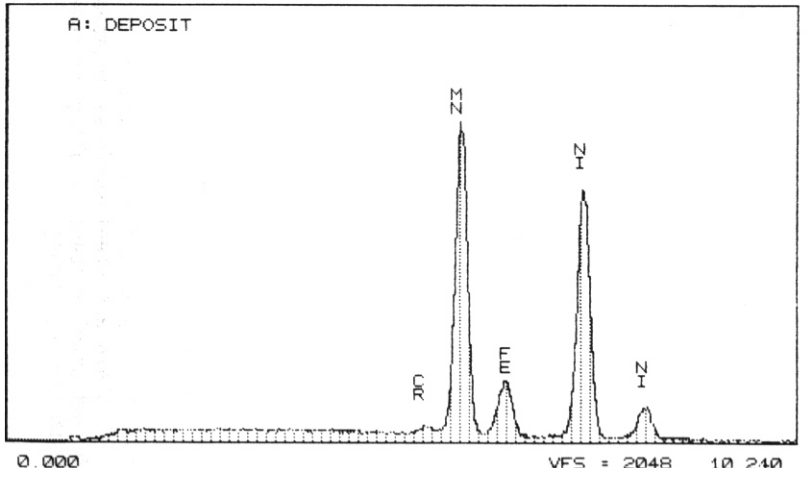

ORNL-DWG 85-1907

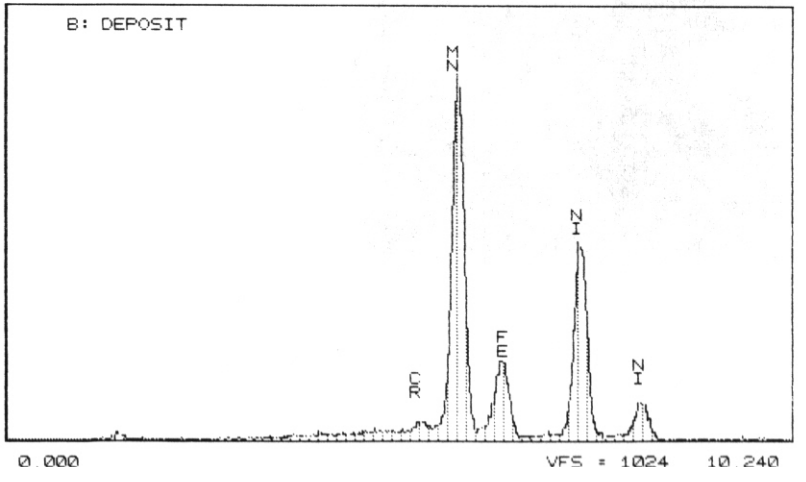

(b)

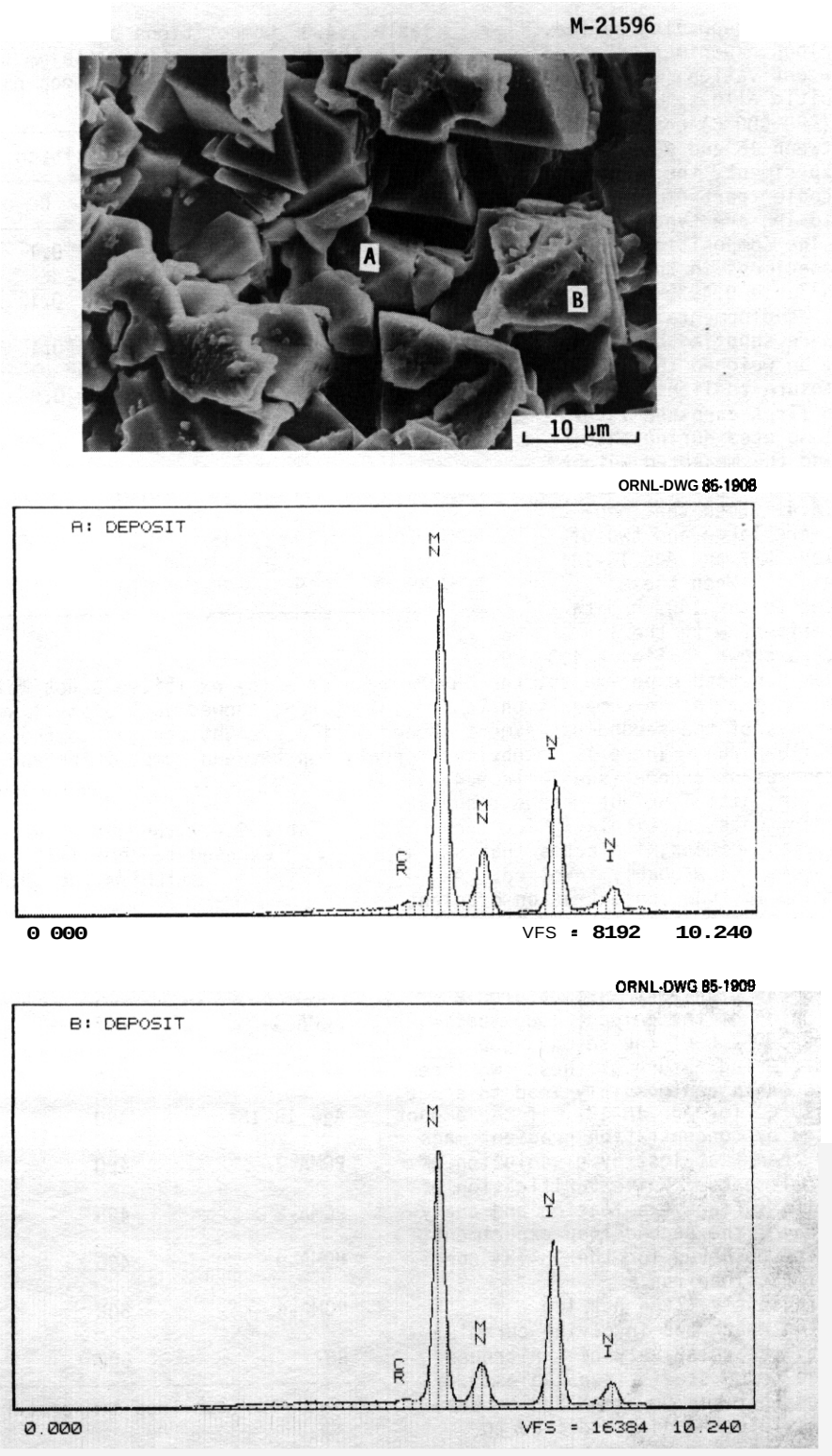

Fig. 9.4.2. Scanning electron micrographs and associated energy dispersive x-ray spectra of deposits formed on type 316 stainless steel surfaces located in the cold leg of a lithium thermal convection loop containing Cr-Mn and Cr-ni austenitic alloy specimens in its hot leg. Maximum loop temperature was 500°C. [a) 390°C. (b) 370°C. (c) 350°C.

During the current reporting period, a second lithium loop experiment started operation with low activation (manganese-containing) austenitic alloys. The hot zone of the loop (480–500°C) contains Cr-Mn steels with between 15 and 20 wt % Mn. As in the first experiment, the remaining specimens in the cooler part of the hot leg and in the cold leg are type 316 stainless steel. The compositions of low activation alloy specimens in the hot zone are listed in Table 9.4.3. The PCMA specimens are ORNL developmental alloys, while the others were supplied by HEDL. The specimens will be weighed thrice during a total exposure to lithium of about 3300 h. The first exposure interval (1037 h) was completed during this reporting period and the measured weight changes for the hot zone specimens are listed in Table 9.4.4. Note that none of the weight losses were large and two of the specimens, alloys R87 and Age 18-18+, actually gained weight. When these results are compared to the 1507 h data from the first experiment with the low activation alloys, as shown in Fig. 9.4.3, it can be noted that, in both experiments, the 18-18+ type of alloy exhibited a net weight gain. Additionally, an alloy similar in composition to R87, alloy R88, showed just a small weight loss. Overall, all of the Cr-Mn steels of the second experiment showed similar weight changes to those measured after 1507 h in the first loop run. There is no obvious correlation between composition and the magnitude and sign of the measured weight change (see Table 9.4.4).

Table 9.4.3 Compositions of Fe-Mn-Cr steels exposed to thermally convective lithium between 500 and 485°C in the second loop experiment

Alloy	Composition (wt %)						
	Mn	Cr	Ni	C	N	Si	Fe
Age 18-18+	18	18	0.5	0.1	0.4	0.6	bal
R87	15	15	0.5	0.1	0.1	0.4	bal
NIT-32	12	18	1.5	0.1	0.4	0.6	bal
PCMA-2	17	15	0.01	0.06	0.001	0.04	bal
PCMA-4	19	10	0.01	0.09	0.002	0.02	bal
PCMA-6	14	16	0.01	0.18	0.003	0.02	bal
PCMA-7	19	15	0.01	0.38	0.005	0.02	bal
PCMA-9	18	20	0.01	0.26	0.006	0.03	bal

The similarity in initial weight change results of the two loop experiments, particularly for the 18-18+ and Age 18-18+ specimens, indicates that similar corrosion processes are probably involved. As discussed above, these include concentration gradient chromium transport among the specimens and loop wall in the hot zone and thermal gradient mass transfer of manganese to the cold zone. (A significant amount of this latter type of mass transport was measured as substantial weight gains of the coldest loop specimens during the first 1037 h of the second loop experiment.) The differing nature of these two types of mass transfer processes can possibly lead to a net weight gain, as measured for Age 18-18+, if the amount of material deposited by concentration gradient mass transfer is greater than that lost by dissolution of manganese and other elements. While verification of these processes awaits surface examination and analysis at the completion of the second loop experiment, similar reactions were observed for the 18-18+ specimen exposed in the first loop run.[2]

Table 9.4.4 Weight changes of specimens exposed to thermally convective lithium for 1037 h

Specimen	Temperature[a] (°C)	Weight change (g/m^2)
PCMA-4	485	-4.8
NIT-32	485	-8.5
Age 18-18+	490	+2.8
PCMA-7	490	–5.7
PCMA-2	495	–0.9
PCMA-9	495	–7.7
PCMA-6	500	–4.0
R87	500	+1.7

[a]Minimum loop temperature = 350°C.

As discussed previously,[2] the hot leg dissolution/deposition reactions involving chromium may be exacerbated by the relatively high nitrogen concentrations of the Cr-Mn steels (see Tables 9.4.1 and 9.4.3). Reactions between Cr and N and between Li, Cr, and N are possible[6,7] and could lead to increased dissolution and/or reaction product formation at specimen surfaces. Such reactions could explain the presence of chromium-enriched nodules on the hot zone specimens in the first loop experiment.[2] Evidence for a similar chromium reaction was also observed[2] in a loop experiment in which 12Cr-1MoVW steel was exposed to thermally convective lithium circulating between 600 and 450°C, where chromium-rich nodules formed on the surface of a 12Cr-1MoVW steel that suffered net dissolution at 600°C. Such reactions may become even more important at lower temperatures.[8] At the higher temperatures of this loop experiment, thermal gradient mass transfer appears to become the dominant corrosion mechanism.

The 12Cr-1MoVW steel loop experiment has now been completed after a total specimen exposure of 6962 h. The updated (and now final) weight loss data for the 12Cr-1MoVW steel specimen located at the maximum temperature position in the loop are shown in Figs. 9.4.3 and 9.4.4. The former figure compares the data from

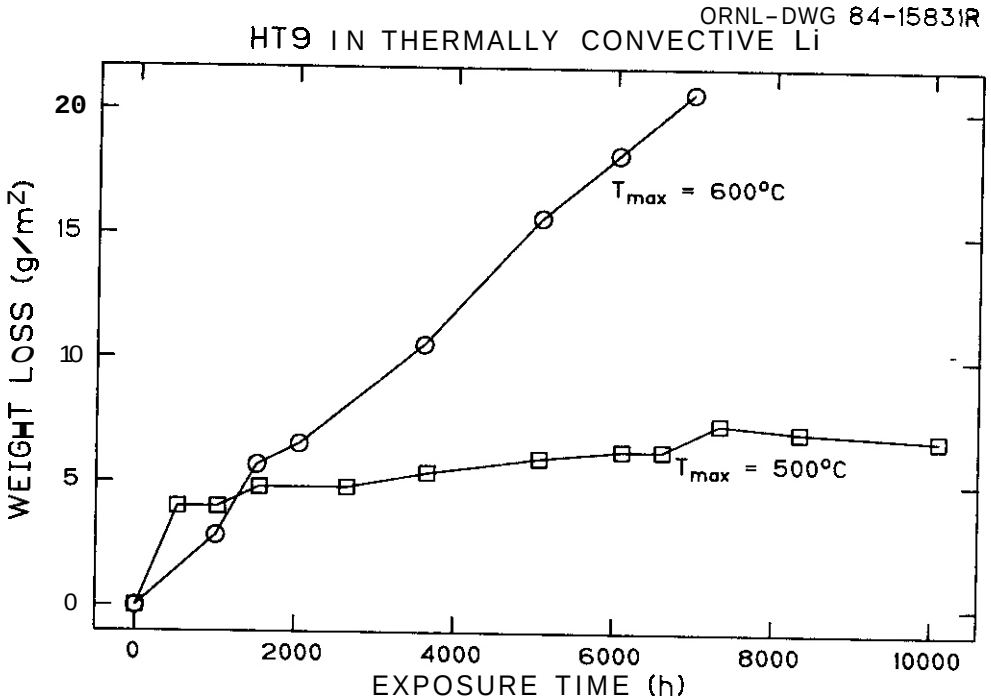

Fig. 9.4.3. Weight loss versus exposure time for 12Cr-1MoVW steel in thermally convective lithium.

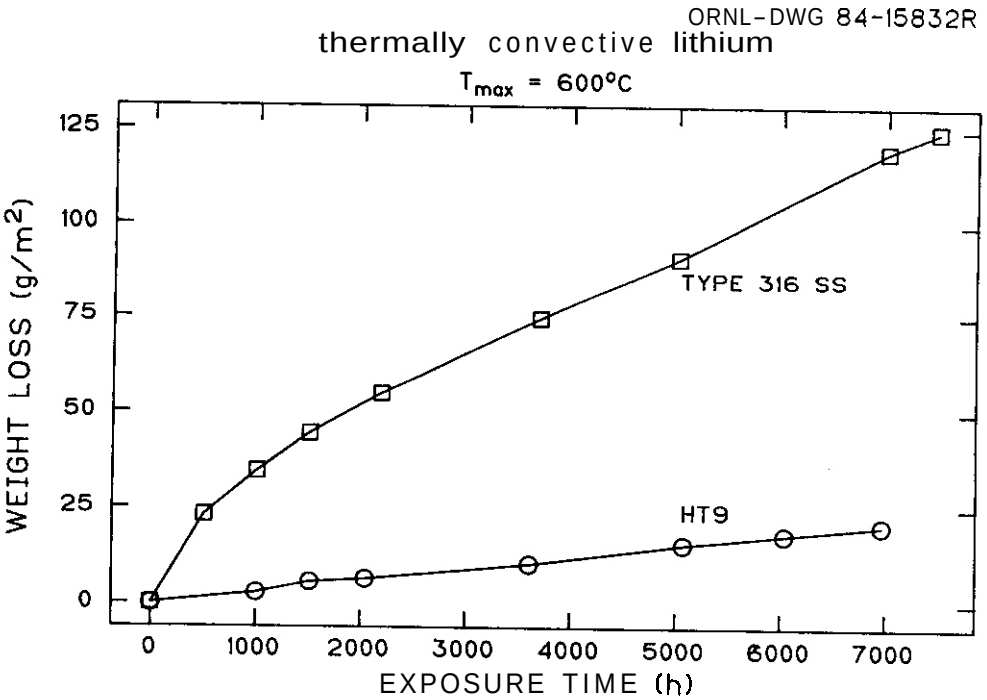

Fig. 9.4.4. Weight loss versus exposure time for 12Cr-1MoVW steel and type 316 stainless steel exposed to thermally convective lithium at 600°C.

the present experiment with that from an earlier lithium loop study conducted at a maximum temperature of 500°C.[8] The 600°C data yielded a dissolution rate of 3.0 $mg/m^2 \cdot h$ determined on the basis of linear dissolution kinetics (that is, the rate obtained from the slope of the curve). This rate is significantly higher than that obtained from the 500°C data at longer times. (Of course, based on the discussion above, it must be remembered that the data being compared in Fig. 9.4.3 could very well be representative of two different corrosion regimes.) Figure 9.4.4 compares weight loss data for 12Cr-1MoVW steel exposed to thermally convective lithium at 600°C in a 12Cr-1MoVW steel loop to that for type 316 stainless steel exposed under the same conditions in a type 316 stainless steel loop. As noted previously with the earlier data,' the dissolution rate of the 12Cr-1MoVW steel is significantly less than that of the type 316 stainless Steel. To determine the extent of thermal gradient mass transfer in this loop experiment, vis-a-vis other reactions involving chromium, scanning electron microscopy with associated energy dispersive x-ray analysis will be used to examine surfaces of specimens in both the hot and cold legs.

9.4.5 Conclusions

1. Initial weight change measurements for lithium exposure of a second set of Cr-Mn steels containing 15-20 wt % Mn yielded values consistent with earlier results for other alloys of similar composition. The relatively modest weight losses and weight gains after 1037 h at about 500°C indicated that the corrosion was not severe. However, pending surface examination and analysis at the end of the loop experiment, the actual extent of the corrosion reactions cannot be established due to the possibility of competing processes that may lead to relatively low net weight changes.

2. Analyses of thermal gradient mass transfer deposits from a lithium loop containing Cr-Mn steels of varying (15-30 wt % Mn) concentrations showed transport of manganese, but not chromium, to the coldest part of the circuit. Such evidence is consistent with earlier indications that, while manganese underwent thermal gradient mass transfer, chromium transport occurred between components in the hot leg.

3. Weight change data obtained at the completion of a 6962 h loop experiment with 12Cr-1MoVW Steel confirmed prior indications that, (1) thermal gradient mass transfer is the dominant corrosion process for this steel when exposed to thermally convective lithium circulating between 600 and 450°C and *(2)* the dissolution rate of 12Cr-1MoVW steel in this lithium at 600°C was significantly less than that measured for type 316 stainless steel measured under similar conditions.

9.4.6 References

1. J. H. DeVan and J. R. DiStefano, "Thermal-Convection Loop Tests of Type 316 Stainless Steel in Lithium," pp. 200–208 in ADIP Quart. Prog. Rep. Mar. 31, 1978, DOE/ET-0058/1, U.S. DOE, Office of Fusion Energy.

2. P. F. Tortorelli and J. H. DeVan, "Corrosion of Low Activation Austenitic Alloys and Standard Fe-12Cr-1MoVW Steel in Thermally Convective Lithium," pp. 189–195 in ADIP Semiann. Prog. Rep. Sept. 30, 1984, DOE/ER-0045/13, U.S. DOE, Office of Fusion Energy

3. E. Ruedl. V. Coen. T. Sasaki. and H. Kolbe. "Intergranular Lithium Penetration of Low-Ni, Cr-Mn Austenitic Stainless Steel," J. Nucl. Mater. 110 (1982) 28–36.

4. E. Ruedl and T. Sasaki, "Effect of Lithium on Grain Boundary Precipitation in a Cr-Mn Austenitic Steel," J. Nucl. Mater. 116 (1983) 112–122.

5. E. Ruedl, V. Coen, T. Sasaki, and H. Kolbe, "Phase Stability and Corrosion of Cr-Mn Austenitic Steels Exposed to Pure Lithium," J. Nucl. Mater. 122&123 (1984) 1247–51.

6. W. F. Calaway, "The Reaction of Chromium with Lithium Nitride in Liquid Lithium," pp. 18-8–18-26 in Proc. Second. Int. Conf. on Liq. Metal Technol. in Energy Production, U.S. DOE, CONF-800401-P2, 1980.

7. M. G. Barker et al., "The Interaction of Chromium with Nitrogen Dissolved in Liquid Lithium," J. Nucl. Mater. 114, 143–49 (1983).

8. P. F. Tortorelli and J. H. DeVan, "Corrosion of an Fe-12Cr-1MoVW Steel in Thermally Convective Lithium," pp. 215–221 in Proc. Topical Conf. on Ferritic Alloys for Use in Nuclear Energy Technologies, J. W. Davis and D. J. Michel (eds.), AIME, 1984.

9.5 CORROSION OF TYPE 316 STAINLESS STEEL AND 12Cr-1MoVW STEEL IN THERMALLY CONVECTIVE Pb-17 at. % Li — P. F. Tortorelli and J. H. DeVan (Oak Ridge National Laboratory)

9.5.1 ADIP Task

ADIP Task I.A.3, Perform Chemical and Metallurgical Compatibility Analyses.

9.5.2 Objective

The purpose of this task is to determine the corrosion resistance of candidate first-wall materials to slowly flowing Pb-17 at. % Li in the presence of a temperature gradient. Dissolution and deposition rates are measured as functions of time, temperature, and additions to the lead-lithium. These measurements are combined with chemical and metallographic examinations of specimen surfaces to establish the mechanisms and rate-controlling processes for the dissolution and deposition reactions.

9.5.3 *Summary*

Observations of the effects of the cleaning procedure used to remove residual Pb-17 at. % Li from type 316 stainless steel revealed a considerable variability in the amount of corrosion layer that was also removed. No localized corrosion or lead-lithium penetration was noted for 12Cr-1MoVW steel exposed to thermally convective Pb-17 at. % Li for 3078 h at temperatures up to 500°C.

9.5.4 Progress and Status

During the current reporting period, separate studies of type 316 stainless steel and 12Cr-1MoVW steel in Pb-17 at. % Li have continued using thermal convection loops (TCLs). The loop design' allows corrosion coupons to be withdrawn and inserted without interrupting the lead-lithium flow. The type 316 stainless steel coupons are contained in a loop of the same base composition; however, the loop circulated lithium for over 10,000 h prior to operation with lead-lithium. The TCL containing the 12Cr-1MoVW steel specimens is made from 9Cr-1Mo steel and had not seen previous service. Both loops are circulating Pb-17 at. % Li at a maximum temperature of 500°C, but the temperature differential is higher in the case of the 12Cr-1MoVW steel (150°C) than the type 316 stainless steel (100°C). The details of the procedure for the preparation of the lead-1ithium were given previously.[2]

As discussed in previous progress reports,[3,4] the use of lithium to remove residual lead-lithium from exposed stainless steel specimens can result in the stripping of the corrosion layer[5,6] and must therefore be taken into account in weight loss determinations and in any subsequent metallographic examinations. Such an effect of the lithium rinse procedure can be used to explain earlier observations of minimal microstructural and compositional changes on exposed surfaces[3] (since most of the corrosion layer was probably removed) and the very high weight loss versus time data for loop specimens that were repeatedly exposed, rinsed, weighed, and re-exposed.[3] As described in the preceding progress report,[4] the examination of an as-exposed (that is, unrinsed) stainless steel specimen that had been exposed for 2015 h revealed an intact corrosion layer, which contained a significant amount of lead-lithium. Since then, we have had the opportunity to examine type 316 stainless steel loop specimens exposed to the lead-lithium for 2472 h. A direct comparison between rinsed and unrinsed specimens was made using two specimens exposed at 500°C (see Fig. 9.5.1). Interestingly, the micrographs in Fig. 9.5.1 indicate that the lithium rinsing of the exposed type 316 stainless steel did not completely strip the corrosion layer from the base alloy, although it did remove a significant amount of material. This mass loss is obvious from the "holes" in the corrosion layer shown in Fig. 9.5.1(b). Presumably, the lithium rinse removed most of the lead-lithium that had penetrated the steel. However, the significant weight loss for this rinsed specimen (311 g/m^2) indicates that a significant portion of the steel's constituents were dissolved during loop exposure and/or removed as part of the corrosion layer during lithium rinsing. (The lithium used for rinsing was not at a sufficiently high temperature to cause significant corrosion by itself.) The present results thus show that the corrosion layer on austenitic alloys is not always released during a lithium cleaning procedure. The amount of the layer removed obviously depends on the depth of the corrosion layer (and thus, on the severity of the corrosion reactions), the morphology of the reaction zone, and the microstructural aspects of the interface between the corroded surface region and the unaltered base metal.

Three type 316 stainless steel specimens were exposed at 500°C to Pb-17 at. % Li for 2472 h in the current loop experiment. Two of these were then rinsed in lithium until their weights became constant (indicating removal of the residual lead-lithium). The third was metallographically examined without any rinsing and was used for the comparison discussed above (see Fig. 9.5.1). For the two rinsed specimens, weight losses were 311 and 338 g/m^2, respectively. These losses are substantially greater than what would be expected for type 316 stainless steel in thermally convective lithium under similar conditions. Indeed, these 500°C data for lead-lithium are about seven times greater than what is measured for lithium loop exposures at 600°C.' It is also interesting to note that a calculated corrosion loss based on only sound metal remaining [as determined from cross-sectional micrographs as shown in Fig. 9.5.1(b)] yielded values that were about 50% higher than the measured weight losses quoted above. These calculated corrosion losses should be representative of losses incurred if the entire corrosion layer had been stripped during the cleaning process.

During the current reporting period, the 12Cr-1MoVW steel specimens completed 3078 h of exposure to thermally convective Pb-17 at. % Li in the loop fabricated from 9Cr-1Mo steel. Metallographic examination

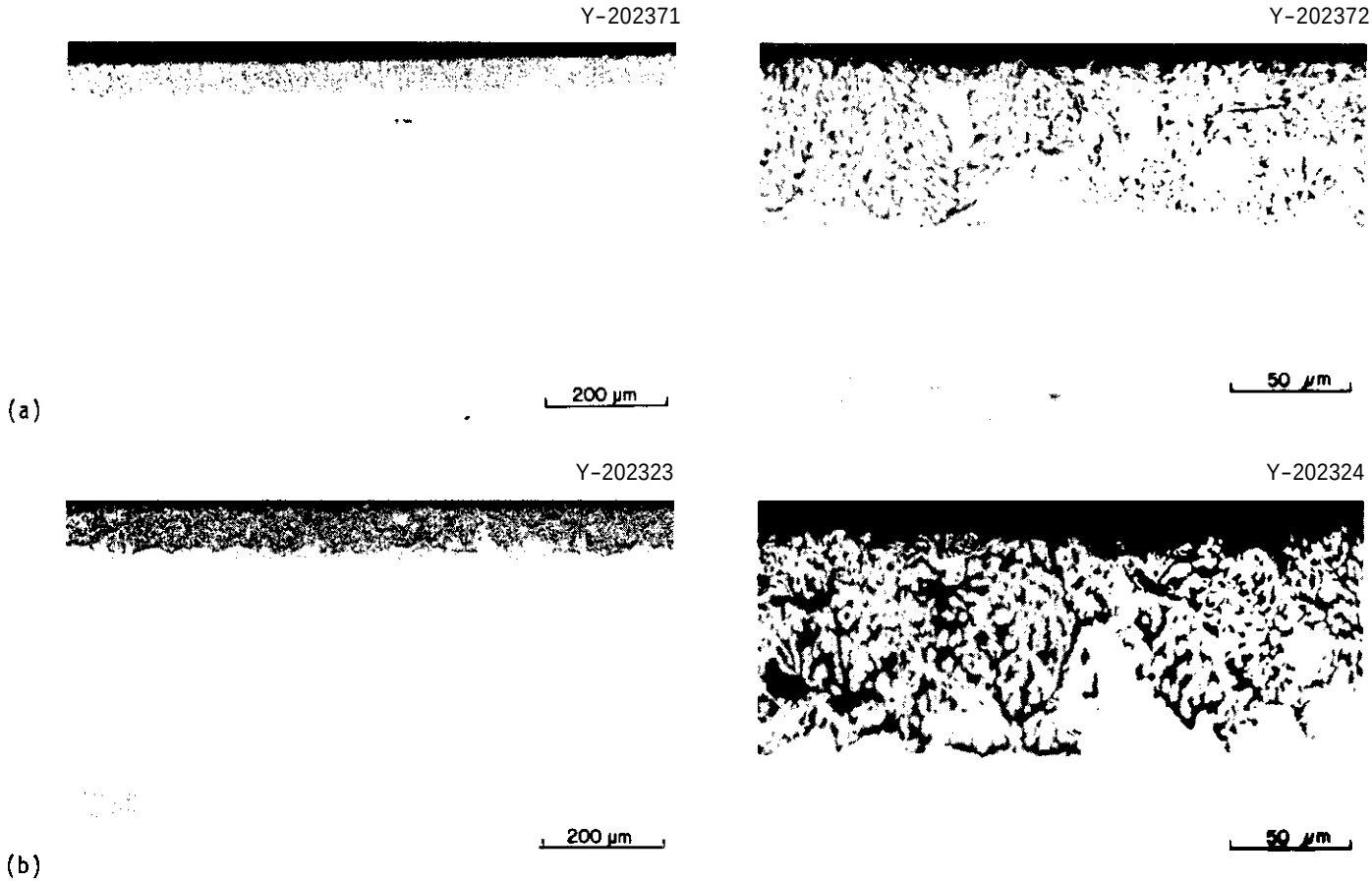

Fig. 9.5.1. Polished cross sections of type 316 stainless steel exposed to thermally convective Pb-17 at. % Li for 2472 h at 500°C. (a) Polished without attempting to remove residual lead-lithium. (b) Rinsed in lithium prior to polishing.

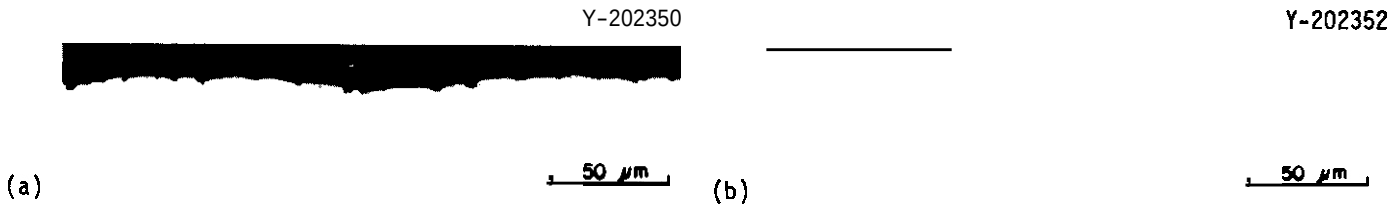

Fig. 9.5.2. Polished cross sections of 12Cr-1MoVW steel exposed to thermally convective Pb-17 at. % Li for 3078 h; polished without attempting to remove residual lead-lithium. (a) 500°C (maximum loop temperature). (b) 475°C.

of polished cross sections revealed a corrosion process that resulted in uniform thinning. Unlike similarly exposed type 316 stainless steel, no evidence of localized attack or lead-lithium penetration was observed (see Fig. 9.5.2). As such, corrosion of austenitic and ferritic alloys in lead-lithium induces similar morphological features (albeit with much greater severity) to those observed for lithium: the development of porous, irregularly attacked corrosion layers on nickel-bearing alloys and uniform dissolution of Cr-Mo steels.

The two lead-lithium thermal convection loops will be used during the next reporting period to start generating corrosion data as a function of time for type 316 stainless steel and 12Cr-1MoVW steel, respectively. In view of our observations of the difficulty of characterizing a true corrosion loss, a series of coupons will be exposed at 500°C in each loop in order to obtain carefully measured weight losses.

9.5.5 Conclusions

1. The lithium rinse procedure used to remove residual lead-lithium from exposed Pb-17 at. % Li may remove just part or most of the corrosion layer in addition to the adhering lead-lithium. The variability

of the effect of the lithium cleaning process necessitates careful characterization of the way weight or corrosion losses are determined for austenitic alloys exposed to molten Pb-17 at. % Li.

2. 12Cr-1MoVW steel exposed to thermally convective Pb-17 at. % Li for 3078 h corroded uniformly: metallographic examination of specimens exposed between 500 and 350°C revealed that, unlike the case with austenitic alloys, dissolution occurred without localized corrosion reactions and penetration by the lead-1ithium.

3. Weight losses of type 316 stainless steel exposed to thermally convective Pb-17 at. % Li at 500°C were substantially greater than when this steel is exposed to molten lithium under similar conditions.

9.5.6 References

1. J. H. DeVan and J. R. DiStefano, "Thermal-Convection Loop Tests of Type 316 Stainless Steel in Lithium," pp. 200–208 in ADIP Quart. Prog. Rep. Mar. 31, 1978, DOE/ET-0058/1, U.S. DOE, Office of Fusion Energy.

2. P. F. Tortorelli and J. H. DeVan, "Corrosion of Type 316 Stainless Steel in Flowing Pb-17 at. % Li," pp. 203–203 in ADIP Semiannu. Prog. Rep. Sept. 30, 1983, DOE/ER-0045/11, U.S. DOE, Office of Fusion Energy.

3. P. F. Tortorelli and J. H. DeVan, "Corrosion of Type 316 Stainless Steel in Flowing Pb-17 at. % Li," pp. 190–92 in ADIP Semiannu. Prog. Rep. Mar. 31, 1984, DOE/ER-0045/12, U.S. DOE, Office of Fusion Energy.

4. P. F. Tortorelli and J. H. DeVan, "Corrosion of Type 316 Stainless Steel and 12 Cr-1 MoVW Steel in Flowing Pb-17 at. % Li," pp. 196–99 in AOIP Semiannu. Prog. Rep. Sept. 30, 1984, DOE/ER-0045/13, U.S. DOE, Office of Fusion Energy.

5. P. Fauvet, J. Sannier, and G. Santarini, "Corrosion of 316L Stainless Steel in Flowing 17Li83Pb Alloy," Proc. 13th Symp. Fusion Technol., Varese, Sept. 1984.

6. O. K. Chopra and D. L. Smith. "Corrosion of Ferrous Alloys in Eutectic Lead-Lithium Environment," J. Nucl. Mater. 122&123 1219–24 (1984).

7. P. F. Tortorelli and J. H. DeVan, "Mass Transfer Kinetics in Lithium-Stainless Steel Systems." to be published in Proc. Third Int. Conf. on Liquid Metal Eng. and Technol. in Energy Production, British Nuclear Energy Society, April 1984.

10. STATUS OF IRRADIATION EXPERIMENTS AND MATERIALS INVENTORY

10.1 IRRADIATION EXPERIMENT STATUS AND SCHEDULE — M. L. Grossbeck (Oak Ridge National Laboratory)

A large number of planned, in-progress, and completed reactor irradiation experiments support the AOIP program. Table 10.1.1 summarizes the parameters that describe completed experiments. Experiments that have been removed from the reactor recently, that are now undergoing irradiation, or that are planned for future irradiation are shown in the schedule barcharts of Table 10.1.2.

Experiments were under way during the reporting period in the Oak Ridge Reactor (ORR) and the High Flux Isotope Reactor (HFIR), which are mixed-spectrum reactors, and in the Fast Flux Test Facility (FFTF), which is a fast reactor.

Three capsules completed irradiation in the HFIR and one in the ORR during the reporting period. Two were capsules containing Charpy impact specimens of ferritic alloys at elevated temperatures. The displacement damage was 40 dpa to complement the earlier 10 dpa data. The third capsule was the first of the cooperative irradiation program for fusion reactor materials between Japan and the United States. This is the first of eight capsules in the HFIR comprising Phase I of the program.

The ORR spectral tailoring capsule was removed for major reconstitution. It is planned to continue irradiation in the HFIR following completion of an instrumented spectral tailoring position in the HFIR, making possible a significantly higher flux.

Two capsules began irradiation in the HFIR. Both contained ferritic alloys as well as low neutron activation alloys. Damage levels will be 50 and 100 dpa, reflecting the need to explore the behavior of the ferritic alloys at higher damage levels.

Table 10.1.1. Descriptive parameters for completed ADIP program fission reactor irradiation experiments

Experiment	Major objective	Alloy	Temperature (°C)	Displacement damage (dpa)	Helium (at. ppm)	Ouration (months)	Date completed
		Experiments in ORR					
ORR-MFE-1	Scope the effects of composition and microstructure on tensile, fatigue, and irradiation creep	Paths A, B, C	25—00	2	<10	4	6/78
ORR-MFE-2	Scope the effects of composition and microstructure on tensile, fatigue, and irradiation creep	Paths A, B, C	300—600	6	<60	15	4/80
ORR-MFE-5	In-reactor fatigue crack growth	Path A	325—460	1	<10	2	2/81
		Experiments in EBR-II					
Subassembly X-264	Effect of preinjected helium on microstructure, tensile properties, and irradiation creep	316, PE-16, V—20%Ti, V—15%Cr—5%Ti, Nb—1%Zr	500—825	8	2-200	4	1/77
AA-X, Subassembly X-287	Effect of preinjected helium on microstructure, tensile properties, and irradiation creep	316, PE-16, V—20%Ti, V—15%Cr—5%Ti, Nb—1%Zr	4OG-700	20	2—200	23	12/78
Subassemblv X-217D	Stress relaxation	Ti alloys	450	2		I	1/78
Pins 8285, 8286. and 8284	Swelling, fatigue crack growth, and tensile properties	Ti alloys	370—550	25		14	9/79
		Experiments in HFIR					
HFIR-CTR-3	Swelling and tensile properties	PE-16, Inconel 600	3OG-700	4.3—9	350—1800	3	2/75
HFIR-CTR-4	Swelling and tensile properties	PE-16	300—700	2.2-4.5	100—350	2	3/77

Table 10.1.1. (continued).

Experiment	Major objective	Alloy	Temperature (°C)	Displacement damage (dpa)	Helium (at. ppm)	Duration (months)	Date completed
HFIR-CTR-5	Swelling and tensile properties	PE-16, Inconel 600	300-700	4.3-9	350-1800	3	4/75
HFIR-CTR-6	Swelling and tensile properties	PE-16, Inconel 600	300-700	4.3-9	350-1800	3	4/75
HFIR-CTR-7	Swelling and tensile properties	PE-16	300-700	9-18	1250-3000	7	8/77
HFIR-CTR-8	Swelling and tensile properties	PE-16	300-700	9-18	1250-3000	7	8/77
HFIR-CTR-9	Swelling and tensile properties	316, 316 + Ti	280-680	10-16	400-1000	6	5/77
HFIR-CTR-10	Swelling and tensile properties	316, 316 + Ti	280-680	10-16	400-1000	6	5/77
HFIR-CTR-11	Swelling and tensile properties	316, 316 + Ti	280-680	10-16	400-1000	6	5/77
HFIR-CTR-12	Swelling and tensile properties	316, 316 + Ti	280-680	7-10	200-500	4	2/77
HFIR-CTR-13	Swelling and tensile properties	316, 316 + Ti	280-680	7-10	200-500	4	2/77
HFIR-CTR-14	Fatigue	316	430	9-15	400-1000	7	12/77
HFIR-CTR-15	Fatigue	316	550	6-9	200-400	4	10/78
HFIR-CTR-16	Weld characterization, swelling, and tensile properties	316, PE-16, Inconel 600	55	6-9	150-2700	4	8/77
HFIR-CTR-17	Weld characterization	316	280-620	7-13	180-460	5.5	10/77
HFIR-CTR-18	Swelling and tensile properties	316, PE-16	280-700	17-27	1600-5600	12	6/78
HFIR-CTR-19	Weld characterization	316	280-620	7-10	200-500	4	12/77
HFIR-CTR-20	Fatigue	316	430	6-9	200-400	4	1/78
HFIR-CTR-21	Fatigue	316	550	9-15	400-1000	7	7/78
HFIR-CTR-22	Fatigue	316	430	6-9	200-400	4	3/78
HFIR-CTR-23	Fatigue	PE-16	430	6-9	370-1000	3.5	2/79
HFIR-CTR-24	Temperature calibration and tensile properties	316	300-620	2.2	30	1	12/78
HFIR-CTR-26	Swelling and tensile properties	316	284-620	30	1900	10	4/80
HFIR-CTR-27	Swelling and tensile properties	316	284-620	56	3500	18	1/81
HFIR-CTR-28	Swelling and tensile properties	316	370-560	30	1900	10	12/80
HFIR-CTR-29	Swelling and tensile properties	316	370-560	56	3500	18	8/81
		Experiments in HFIR					
HFIR-CTR-30	Swelling, microstructure, and ductility	Paths A, B, C, D, and E	300-600	40	<15,000	14	11/81
HFIR-CTR-31	Swelling, microstructure, and ductility	Paths A, B, C, D, and E	300-600	20	<7,500	8	5/81
HFIR-CTR-32	Swelling, microstructure, and ductility	Paths A, B, C, D, and E	300-600	10	<3,000	4	12/81
HFIR-CTR-33	Swelling, tensile properties, and weld characterization	Paths A and E	55	10	<510	4	10/80
HFIR-CTR-34	Charpy	Path E	300, 400	10	0-75	4	5/82
HFIR-CTR-35	Charpy	Path E	300, 400	10	0-75	4	5/82
HFIR-CTR-36	Fatigue	316 PCA	430, 550	30	2,000	13	5/83
HFIR-CTR-39	Swelling and tensile properties	Path E	300-500	12	0-90	5	10/82
HFIR-CTR-40	Swelling and tensile properties	Path E	300-500	12	0-90	5	12/82
HFIR-CTR-41	Swelling and tensile properties	Path E	300-500	12	0-90	5	1/83
HFIR-CTR-42	Swelling, tensile microstructure	Paths A, B	300-600	20	1100	8	6/83

Table 10.1.1. (continued).

Experiment	Major objective	Alloy	Temperature (°C)	Displacement damage (dpa)	Helium (at. ppm)	Duration (months)	Date completed
HFIR-CTR-43		Similar to HFIR-CTR-42					
HFIR-CTR-44[a]	Swelling, tensile	Path A	250–400	10	500	4	5/83
HFIR-CTR-45		Similar to HFIR-CTR-44					
HFIR-CTR-46	Charpy	Path E	300–400	10	75	4	6/83
HFIR-MFE-RB1	Swelling, microstructure, crack growth, fracture toughness, Charpy, tensile, and fatigue	Path E	55	10	90	8	7/82
HFIR-MFE-RB2	Swelling, microstructure, crack growth, fracture toughness, Charpy, tensile, and fatigue	Path E	55	2	200	17	7/83
HFIR-MFE-T1	Swelling, tensile fatigue	Path E	55	30	<300	12	8/82
HFIR-MFE-T2	Swelling and tensile fatigue	Path E	55	9	<75	3	5/81
HFIR-MFE-T3	Impact properties	Path E	55	10	<85	4	12/81

[a]Joint U.S./EC/JP.

Table 10.1.2. Objectives and schedule for current and planned ADIP program reactor irradiation experiments

Experiment designation	Major objective
A. Oak Ridge Research Reactor	
ORR-MFE-4	Effect of irradiation on tensile, fatigue, and irradiation creep of path A PCA (Prime Candidate Alloy) and path B base research alloys. Spectral tailoring to maintain correct He/dpa ratio. Irradiation on continuing basis. 330–600°C (1)
ORR-MFE-6J	Swelling, tensile, irradiation creep fatigue, crack growth, and microstructure of Path A alloys. 60 and 200°C. Evaluated at 10 to 15 dpa intervals. Employs spectral tailoring to achieve fusion He:dpa value.
ORR-MFE-7J	Similar to ORR-MFE-6J but 300 and 400°C.
B. Experimental Breeder Reactor (EBR-II)	

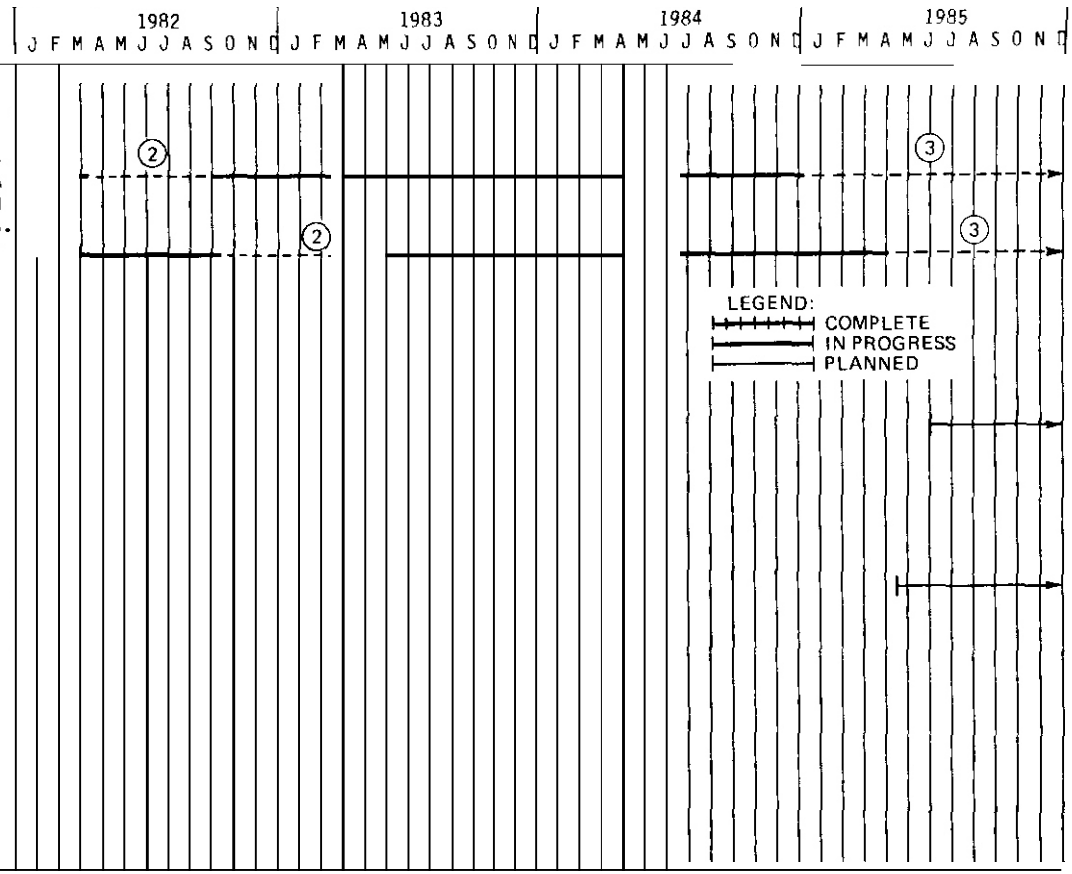

(1) MFE-4A operates at 330 and 400°C. MFE-4B operates at 500 and 600°C.

(2) Removed from reactor for reencapsulation at 5 dpa.

(3) Reconstituted at 14 dpa for insertion in HFIR spectral tailoring position.

(4) Interim examination. *Experiment out of reactor.* Reencapsulated in subassembly X 3 4

(5) Remove for specimen discharge.

(6) HFIR shut down for reflector replacement.

(7) The HFIR-JP experiment series is a joint program shared by the U.S. and Japan Fusion Reactor Materials activities.

Table 10.1.2. (continued)

Experiment designation	Major objective
AD-2 (6 pins in separate subassemblies of row 4)	To supplement present EBR-II data on ferritic alloys with data on crack growth, fatigue, and fatigue toughness. Temperature 390, 450, 500, and 550°C. 15 and 30 dpa.
C. Fast Flux Test Facility (FFTF)	
FFTF MOTA Fusion Experiment	Microstructural and mechanical properties of Path A, C, and E alloys.
D. High Flux Isotope Reactor (HFIR)	
HFIR-CTR-36	Fatigue properties of path A alloys. 30 dpa, 2000 ppm He.
HFIR-CTR-42	Swelling, tensile properties of path A alloys. 20 dpa, 1100 ppm He, 300 to 600°C.
HFIR-CTR-43	Swelling, tensile properties of path A alloys. 20 dpa, 1100 ppm He, 300 to 600°C.
HFIR-CTR-44	Swelling, tensile properties of path A alloys. 10 dpa, 500 ppm He, 250 to 400°C. Joint experiment of U.S., European Community, and Japan.
HFIR-CTR-45	Similar to HFIR-CTR-44.
HFIR-CTR-46	Impact properties of path E alloys. 10 dpa, 75 ppm He, 300 and 400°C.

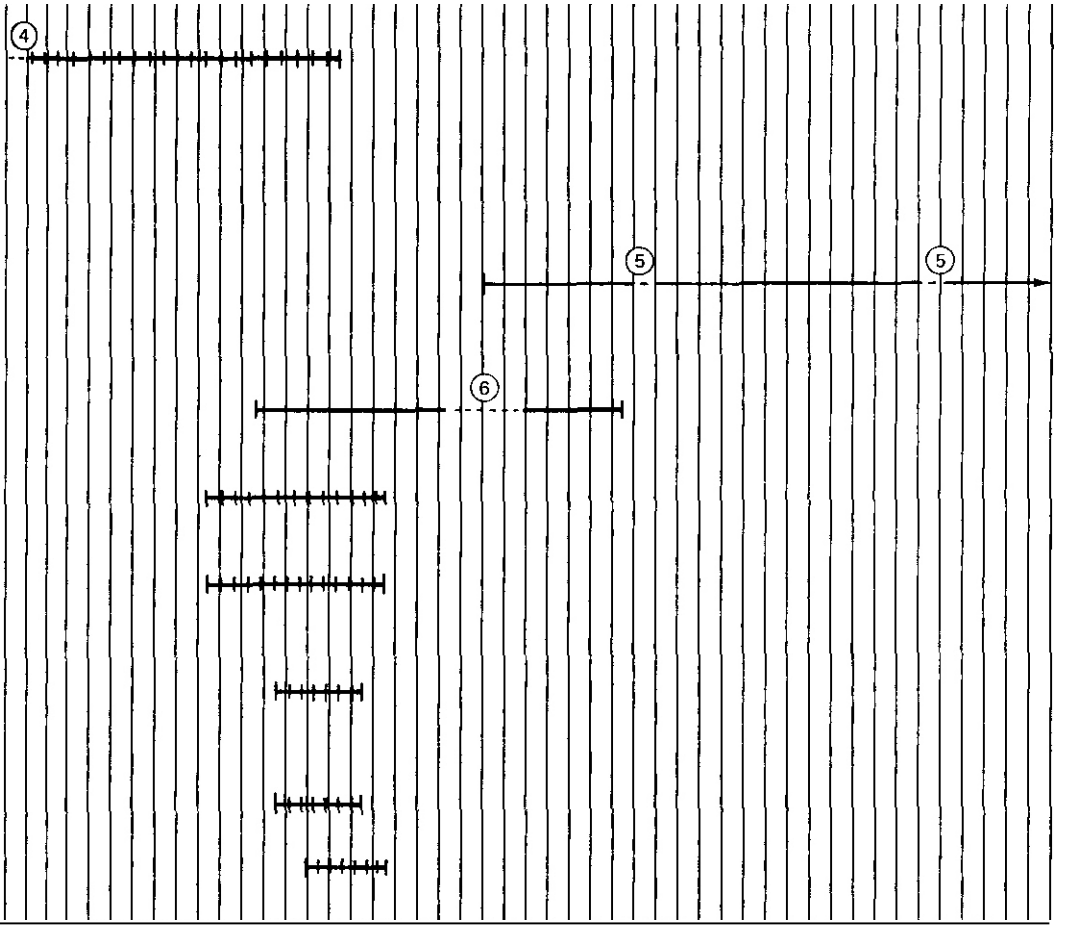

Table 10.1.2. (continued)

Experiment designation	Major objective
HFIR-CTR-47	Impact properties of path E alloys. 40 dpa, 400 ppm He, 300 and 400°C.
HFIR-CTR-48	Similar to HFIR-CTR-47.
HFIR-CTR-49	Tensile properties and microstructure of path E alloys. 50 dpa, 70 to 500 ppm He, 300 to 500°C.
HFIR-CTR-50	Tensile, swelling, microstructure of path E alloys, 100 dpa, 150 to 1000 ppm He, 400, 600°C.
HFIR-CTR-51	Swelling, tensile properties of low-activation alloys. 20 dpa, 300–600°C
HFIR-CTR-52	Fatigue properties of 316 SS. 10 dpa, 500 ppm He 430°C. Joint experiment with European community and Japan.
HFIR-CTR-53	Impact properties of path E alloys. 10 dpa 75 ppm He, 200, 300°C, one-third size Charpy.
HFIR-CTR-54	Similar to HFIR-CTR-53
HFIR-CTR-55	Tensile swelling, microstructure of path E and low activation alloys. 50 dpa, 400 ppm He, 400, 600°C.
HFIR-CTR-56	Tensile, swelling microstructure of path E and low activation alloys. 100 dpa, 150–1000 ppm He, 400, 600°C.

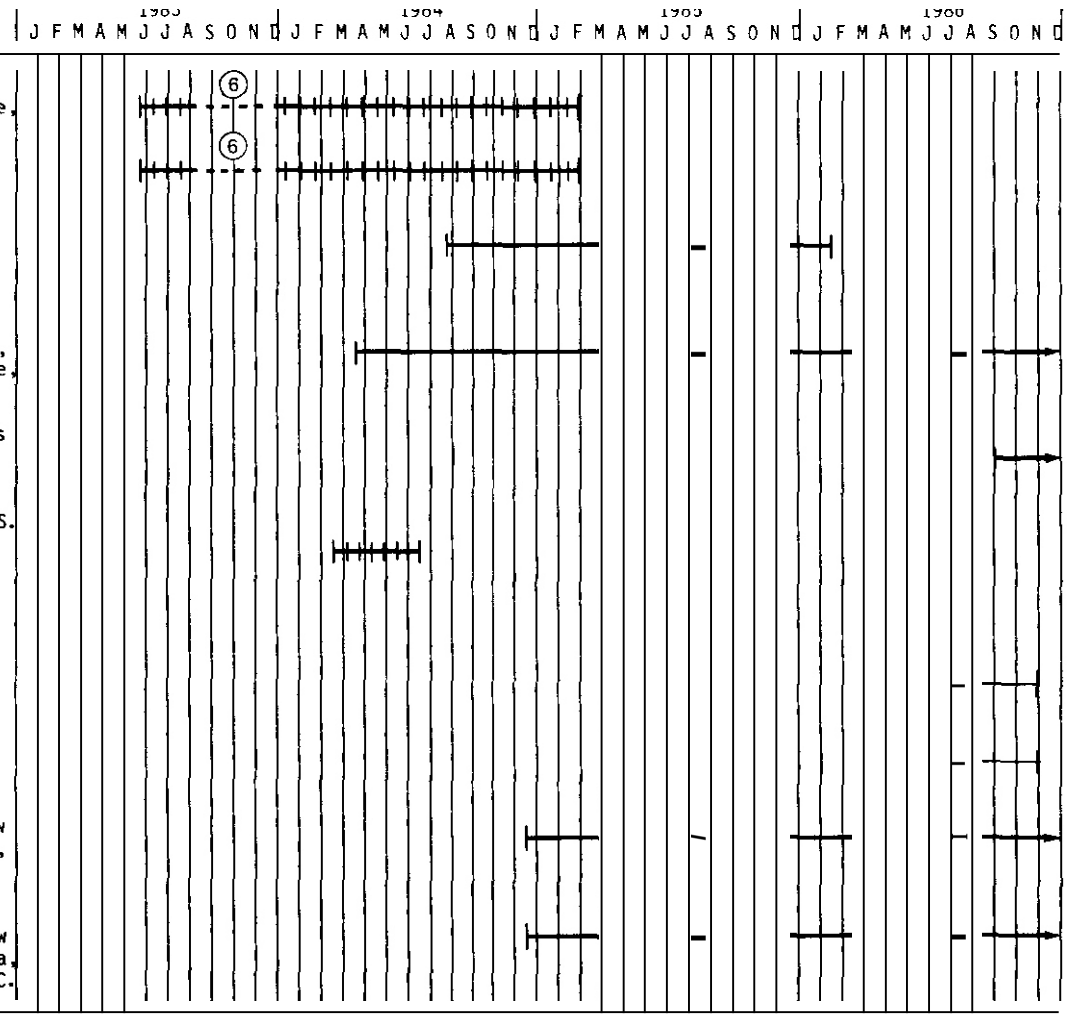

Table 10.1.2. (continued)

Experiment designation	Major objective
HFIR-JP-1(7)	Swelling, tensile and fatigue properties, and microstructure of path A alloys. 300–600°C, 30 dpa, 2000 ppm He.
HFIR-JP-2	Similar to HFIR-JP-1 but to 50 dpa, 3500 ppm He.
HFIR-JP-3	Similar to HFIR-JP-1.
HFIR-JP-4	Swelling, tensile properties and microstructure of path A alloys. 55°C, 50 dpa, 2000 ppm He.
HFIR-JP-5	Similar to HFIR-JP-2.
HFIR-JP-6	Similar to HFIR-JP-1.
HFIR-JP-7	Similar to HFIR-JP-1.
HFIR-JP-8	Similar to HFIR-JP-2.

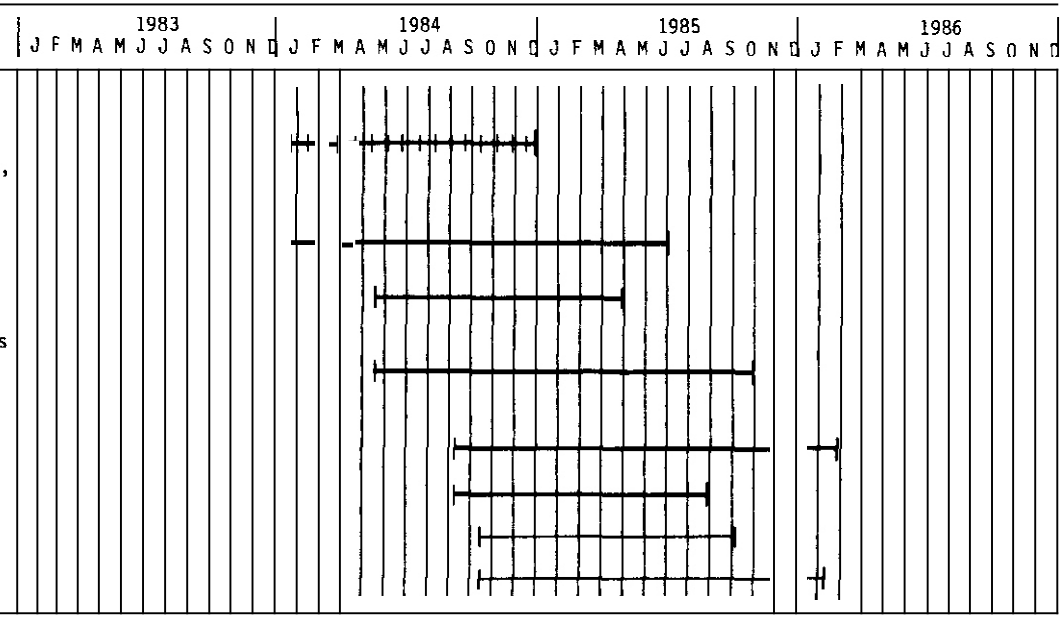

10.2 FUSION PROGRAM RESEARCH MATERIALS INVENTORY — T. K. Roche, F. W. Wiffen (Oak Ridge National Laboratory), J. W. Davis (McDonnell Douglas Astronautics Company — St. Louis Division), and T. A. Lechtenberg (GA Technologies)

10.2.1 ADIP Task

ADIP Task 1.D.1, Materials Stockpile for Magnetic Fusion Energy Programs.

10.2.2 Objective

Oak Ridge National Laboratory maintains a central inventory of research materials to provide a common supply of materials for the Fusion Reactor Materials program. This will minimize unintended material variations and provide for economy in procurement and for centralized record-keeping. Initially this inventory is to focus on materials related to first-wall and structural applications and related research, but various special purpose materials may be added in the future.

The use of materials from this inventory that is coordinated with or otherwise related technically to the Fusion Reactor Materials program of the Department of Energy is encouraged.

10.2.3 Materials Requests and Release

Materials requests shall be directed to the Fusion Program Research Materials Inventory at ORNL (Attention: F. W. Wiffen). Materials will be released directly if (a) the material is to be used for programs funded by the Office of Fusion Energy, with goals consistent with the approved Materials Program Plans of the Materials and Radiation Effects Branch and (b) the requested amount of material is available without compromising other intended uses.

Materials requests that do not satisfy both (a) and (b) will be discussed with the staff of the Reactor Technologies Branch, Office of Fusion Energy, for agreement on action.

10.2.4 Records

Chemistry and materials preparation records are maintained for all inventory mterials. All materials supplied to program users will be accompanied by summary characterization information.

10.2.5 Summary of Current Inventory and Material Movement During Period October 1, 1984, Through March 31, 1985

A condensed, qualitative description of the content of materials in the Fusion Program Research Materials Inventory is given in Table 10.2.1. This table indicates the nominal diameter of rod or thickness of sheet for product forms of each alloy and also indicates by weight the amount of each alloy in larger sizes available for fabrication to produce other product forms as needed by the program. There was no material added to the inventory during this reporting period. Table 10.2.2 gives the materials distributed from the Inventory.

Alloy compositions and more detail on the alloys and their procurement and/or fabrication are given in this and earlier ADIP progress reports.

Table 10.2.1. Summary status of materials available in the fusion program research materials inventory

Alloy	Product form			
	Ingot or Bar[a] Weight (kg)	Rod diameter (mm)	Sheet thickness (mm)	Thin-wall tubing wall thickness (mm)
		Path A Alloys		
Type 316 SS	900	16 and 7.2	13 and 7.9	0.25
Path A PCA[b]	490	12	13	0.25
USSR Cr-Mn Steel[c]		10.5	2.6	
NONMAGNE 30d		18.5	10	
		Path 8 Alloys		
PE-16	140	16 and 7.1	13 and 1.6	0.25
B-1	180			
B-2	180			
B-3	180			
B-4	180			
B-6	180			
		Path C Alloys		
Ti-64			2.5 and 0.76	
Ti-6242S		63	6.3, 3.2, and 0.76	
Ti-5621S			2.5 and 0.76	
Ti-38644			0.76 and 0.25	
Nb—1% Zr		6.3	2.5, 1.5, and 0.76	
Nb—5%Mo—1%Zr		6.3	2.5, 1.5, and 0.76	
V—20%Ti		6.3	2.5, 1.5, and 0.76	
V—15%Cr—5%Ti		6.3	2.5, 1.5, and 0.76	
VANSTAR-7		6.3	2.5, 1.5, and 0.76	
		Path D Alloy		
LRO-37[e]			3.3, 1.6, and 0.8	
		Path E Alloys		
HT9 (AOD fusion heat)[f]	3400		28.5. , 15.8. 9.5, and 3.1	
HT9 (AOD/ESR fusion heat)	7000	25, 50, and 75	28.5, 15.8, 9.5, and 3.1	
HT9			4.5 and 18	
HT9 + 1%Ni			4.5 and 18	
HT9 t 2% Ni			4.5 and 18	
HT9 + 2% Ni + Cr adjusted			4.5 and 18	
T-9 modified[g]			4.5 and 18	
T-9 modified + 2% Ni			4.5 and 18	
T-9 modified + 2% Ni + Cr adjusted			4.5 and 18	
2 1/4Cr-1Mo			h	

[a]Greater than 25 mm, minimum dimension.
[b]Prime candidate alloy.
[c]Rod and sheet of a USSR stainless steel supplied under the US-USSR Fusion Reactor Materials Exchange Program.
[d]NONMAGNE 30 is an austenitic steel with base composition Fe—14%Mn—2%Ni—2%Cr. It was supplied to the inventory by the Japanese Atomic Energy Research Institute.
[e]LRO-37 is the ordered alloy $(Fe,Ni)_3(V,Ti)$ with composition Fe—39.4%Ni—22.4%V—0.43%Ti.
[f]Alloy 12Cr-1MoVW, with composition equivalent to Sandvik alloy HT9.
[g]T-9 modified is the alloy 9Cr-1MoVNb.
[h]Material is thick-wall pipe, rerolled as necessary to produce sheet or rod.

Table 10.2.2. Fusion program research materials inventory disbursements October 1, 1984 through March 31, 1985

Alloy	Heat	Product form	Dimension[a] (mm)	Quantity (m)	Quantity (m^2)	Sent to
			Path A Alloys — Austenitic Stainless Steels			
Path A PCA	K-280	Tubing	4.57 OD × 0.254 wall	1.67		Radiation Effects Group, M&C Division, ORNL
			Path C Alloys — Reactive and Refractory Alloys			
V-15%Cr-5%Ti	CAM8356	Rod	6.35	2.89		Metals Processing Group, M&C Division, ORNL
	CAM8356	Rod	5.08	4.55		Radiation Effects Group, M&C Division, ORNL
	CAM834	Sheet	2.54		0.058	HEDL, Richland, WA
	CAM835A	Sheet	0.84		0.01	Materials Compatibility Group, M&C Division, ORNL
	CAM835A	Sheet	0.84		0.003	Kernforschungszentrum, Karlsruhe, Germany
	CAM834	Sheet	0.86		0.02	Radiation Effects Group, M&C Division, ORNL
VANSTAR-7	CAM837	Sheet	0.84		0.027	Radiation Effects Group, M&C Division, ORNL
			Path E Alloys — Ferritic Steels			
HT9	AOD/ESR-9607R2	Sheet	0.76		0.003	Kernforschungszentrum, Karlsruhe, Germany

[a]Characteristic dimension: Thickness for plate and sheet, diameter for rod and tubing.

DOE/ER-0045/14
Distribution
Categories
uc-20, 20c

DISTRIBUTION

1–6. Argonne National Laboratory, 9700 South Cass Avenue, Argonne, IL 60439

L. Greenwood
B. A Loomis
V. Maroni
R. F. Mattas
D. L. Smith
H. Wiedersich

7. Auburn university, Department of Mechanical Engineering, Auburn, AL 36849

B. A Chin

8. Battelle-Pacific Northwest Laboratory, P.O. Box 999, Richland, WA 99352

J. L. Brimhall

9. Brookhaven National Laboratory, Upton, NY 11973

C. L. Snead, Jr.

10. Carnegie-Mellon University, Pittsburgh, PA 15213

J. C. Williams

11. Colorado School of Mines, Golden, CO 80401

G. R. Edwards

12-195. Department of Energy, Technical Information Center, Office of Information Services, P.O. Box 62, Oak Ridge, TN 37831

For distribution as shown in DOE/TIC-4500 Distribution Categories, UC-20 (Magnetic Fusion Energy), and UC-20c (Reactor Materials)

196–202. Department of Energy, Office of Fusion Energy, Washington, DC 20545

M. M Cohen
G. M Haas
T. C. Reuther, Jr. (5 copies)

203. Department of Energy, Oak Ridge Operations Office, P.O. Box E, Oak Ridge, TN 37831

Office of Assistant Manager for Energy Research and Development

204. Energy Technology Engineering Center, P.O. Box 1449, Canoga Park, CA 91304

ETEC Library

205–206. GA Technologies, Inc., P.O. Box 81608, San Diego, CA 92138

T. A Lechtenberg
D. L. Roberts

207–209. Lawrence Livermore National Laboratory, P.O. Box 808, Livermore, CA 94550

E.N.C. Dalder
M. Guinan
C. M Logan

210. Los Alamos National Laboratory, P.O. Box 1663, Los Alamos, NM 87545

R. J. Livak

211. Massachusetts Institute of Technology, 138 Albany Street, Cambridge, MA 02139

O. K. Harling

212. Massachusetts Institute of Technology, 77 Massachusetts Ave., Cambridge, MA 02139
N. J. Grant

213. McDonnell Douglas Astronautics Company, East, P.O. Box 516, St. Louis, MO 63166
J. W. Davis

214. National Materials Advisory Board, 2101 Constitution Ave., Washington, DC 20418
K. M. Zwilsky

215–216. Naval Research Laboratory, Washington, DC 20375
Superintendent, Materials Science and Technology Division
J. A. Sprague

217–250. Oak Ridge National Laboratory, P.O. Box X, Oak Ridge, TN 37831
Central Research Library (2 copies)
Document Reference Section
Laboratory Records Department (2 copies)
Laboratory Records Deoartment, RC
ORNL Patent Section
L. A. Berry
E. E. Bloom
D. N. Braski
W. R. Corwin
J. H. DeVan
M. L. Grossbeck
R. L. Klueh
R. A. Lillie
C. T. Liu
K. C. Liu
L. K. Mansur
P. J. Maziasz
C. J. McHargue
T. K. Roche
A. F. Rowcliffe (2 copies)
M. J. Saltmarsh
J. L. Scott
I. Siman-Tov
K. R. Thoms
P. T. Thornton (3 copies)
P. F. Tortorelli
J. M. Vitek
C. O. West
F. W. Wiffen

251. Princeton University, Plasma Physics Laboratory, P.O. Box 451, Princeton, NJ 08544
P. Bonanos

252-253. Rensselaer Polytechnic Institute, Troy, NY 12181
D. Steiner
N. Stoloff

254–255. Sandia National Laboratories, Livermore Division 8316, Livermore, CA 94550
W. Bauer
J. C. Lippold

256–257. Sandia National Laboratories, P.O. Box 5800, Albuquerque, NM 87185
M. J. Davis
W. B. Gauster

258. Science Applications, Inc., 1200 Prospect, La Jolla, CA 92037
H. Gurol

259–261. University of California, Department of Chemical, Nuclear, and Thermal Engineering, Los Angeles, CA 90024

M. A. Abdou
R. W. Conn
N. M. Ghoniem

262. University of California, Santa Barbara, CA 93106

G. R. Odette

263. University of Missouri, Department of Mechanical and Aerospace Engineering, Columbia, MO 65211

M. Jolles

264. University of Virginia, Department of Materials Science, Charlottesville. VA 22901

W. A. Jesser

265. University of Wisconsin, 1500 Johnson Drive, Madison, WI 53706

G. L. Kulcinski

266. Westinghouse Electric Company, Advanced Energy Systems Division, P.O. Box 10864, Pittsburgh, PA 15236

W. A. Boltax

267'274. Westinghouse Hanford Company, P.O. Box 1970, Richland, WA 99352

H. R. Brager
D. G. Doran
A. M. Ermi
F. A. Garner
D. S. Gelles
E. C. Opperman
R. W. Powell
J. L. Straalsund

275. Westinghouse Research and Development Center, 1310 Beulah Road, Pittsburgh, PA 15235

J. A. Spitznagel

*U. S. GOVERNMENT PRINTING OFFICE: 1985-544-045/20097